



International Journal of  
*Molecular Sciences*

Special Issue Reprint

---

# Multifunctional Nanomaterials

Synthesis, Properties, and Applications 2.0

---

Edited by  
Raghvendra Singh Yadav

[www.mdpi.com/journal/ijms](http://www.mdpi.com/journal/ijms)



# **Multifunctional Nanomaterials: Synthesis, Properties, and Applications 2.0**



# **Multifunctional Nanomaterials: Synthesis, Properties, and Applications 2.0**

Editor

**Raghvendra Singh Yadav**

MDPI • Basel • Beijing • Wuhan • Barcelona • Belgrade • Manchester • Tokyo • Cluj • Tianjin



*Editor*

Raghvendra Singh Yadav  
Centre of Polymer Systems  
Tomas Bata University in Zlín  
Zlín  
Czech Republic

*Editorial Office*

MDPI  
St. Alban-Anlage 66  
4052 Basel, Switzerland

This is a reprint of articles from the Special Issue published online in the open access journal *International Journal of Molecular Sciences* (ISSN 1422-0067) (available at: [www.mdpi.com/journal/ijms/special\\_issues/Multifunctional\\_Nanomaterial](http://www.mdpi.com/journal/ijms/special_issues/Multifunctional_Nanomaterial)).

For citation purposes, cite each article independently as indicated on the article page online and as indicated below:

LastName, A.A.; LastName, B.B.; LastName, C.C. Article Title. <i>Journal Name</i> <b>Year</b> , <i>Volume Number</i> , Page Range.
--

**ISBN 978-3-0365-8325-9 (Hbk)**

**ISBN 978-3-0365-8324-2 (PDF)**

© 2023 by the authors. Articles in this book are Open Access and distributed under the Creative Commons Attribution (CC BY) license, which allows users to download, copy and build upon published articles, as long as the author and publisher are properly credited, which ensures maximum dissemination and a wider impact of our publications.

The book as a whole is distributed by MDPI under the terms and conditions of the Creative Commons license CC BY-NC-ND.

# Contents

<b>About the Editor</b> . . . . .	vii
<b>Preface to "Multifunctional Nanomaterials: Synthesis, Properties, and Applications 2.0"</b> . . . . .	ix
<b>Raghvendra Singh Yadav</b> Multifunctional Nanomaterials: Synthesis, Properties, and Applications 2.0 Reprinted from: <i>Int. J. Mol. Sci.</i> <b>2023</b> , <i>24</i> , 7619, doi:10.3390/ijms24087619 . . . . .	1
<b>Zijun Yan and Tao Wu</b> Highly Selective Electrochemical CO <sub>2</sub> Reduction to C <sub>2</sub> Products on a g-C <sub>3</sub> N <sub>4</sub> -Supported Copper-Based Catalyst Reprinted from: <i>Int. J. Mol. Sci.</i> <b>2022</b> , <i>23</i> , 14381, doi:10.3390/ijms232214381 . . . . .	3
<b>Sérgio R. S. Veloso, Raquel G. D. Andrade, Valéria Gomes, Carlos O. Amorim, Vítor S. Amaral and Verónica Salgueiriño et al.</b> Oxidative Precipitation Synthesis of Calcium-Doped Manganese Ferrite Nanoparticles for Magnetic Hyperthermia Reprinted from: <i>Int. J. Mol. Sci.</i> <b>2022</b> , <i>23</i> , 14145, doi:10.3390/ijms232214145 . . . . .	15
<b>Pornsuda Maraming, Nang Noon Shean Aye, Patcharee Boonsiri, Sakda Daduang, Onanong Buhome and Jureerut Daduang</b> Polydopamine Nanoparticles Functionalized Electrochemical DNA Aptasensor for Serum Glycated Albumin Detection Reprinted from: <i>Int. J. Mol. Sci.</i> <b>2022</b> , <i>23</i> , 13699, doi:10.3390/ijms232213699 . . . . .	31
<b>Daniel Rui Chen, Megha Chitranshi, Vesselin Shanov and Mark Schulz</b> Electrochemically Activated CNT Sheet as a Cathode for Zn-CO <sub>2</sub> Batteries Reprinted from: <i>Int. J. Mol. Sci.</i> <b>2022</b> , <i>23</i> , 12602, doi:10.3390/ijms232012602 . . . . .	45
<b>Yuan-Chang Liang, Shao-Yu You and Bo-Yue Chen</b> Crystal Design and Photoactivity of TiO <sub>2</sub> Nanorod Template Decorated with Nanostructured Bi <sub>2</sub> S <sub>3</sub> Visible Light Sensitizer Reprinted from: <i>Int. J. Mol. Sci.</i> <b>2022</b> , <i>23</i> , 12024, doi:10.3390/ijms231912024 . . . . .	59
<b>Giuseppa Biddeci, Gaetano Spinelli, Paolo Colomba and Francesco Di Blasi</b> Nanomaterials: A Review about Halloysite Nanotubes, Properties, and Application in the Biological Field Reprinted from: <i>Int. J. Mol. Sci.</i> <b>2022</b> , <i>23</i> , 11518, doi:10.3390/ijms231911518 . . . . .	73
<b>Peng Zhu, Luyao Feng, Zejun Ding and Xuechun Bai</b> Preparation of Spherical Cellulose Nanocrystals from Microcrystalline Cellulose by Mixed Acid Hydrolysis with Different Pretreatment Routes Reprinted from: <i>Int. J. Mol. Sci.</i> <b>2022</b> , <i>23</i> , 10764, doi:10.3390/ijms231810764 . . . . .	91
<b>Grégory Barbillon</b> Latest Advances in Metasurfaces for SERS and SEIRA Sensors as Well as Photocatalysis Reprinted from: <i>Int. J. Mol. Sci.</i> <b>2022</b> , <i>23</i> , 10592, doi:10.3390/ijms231810592 . . . . .	105
<b>Radu Nicolae Revnic, Gabriela Fabiola Ştiufiuc, Valentin Toma, Anca Onaciu, Alin Moldovan and Adrian Bogdan Ţigu et al.</b> Facile Microwave Assisted Synthesis of Silver Nanostars for Ultrasensitive Detection of Biological Analytes by SERS Reprinted from: <i>Int. J. Mol. Sci.</i> <b>2022</b> , <i>23</i> , 8830, doi:10.3390/ijms23158830 . . . . .	121

<b>Tianxin Gao, Pei Wang, Teng Gong, Ying Zhou, Ancong Wang and Xiaoying Tang et al.</b> Reporter Genes for Brain Imaging Using MRI, SPECT and PET Reprinted from: <i>Int. J. Mol. Sci.</i> <b>2022</b> , 23, 8443, doi:10.3390/ijms23158443 . . . . .	<b>137</b>
<b>Shuaijun Zou, Qianqian Wang, Peipei Zhang, Bo Wang, Guoyan Liu and Fuhai Zhang et al.</b> Biomimetic Nanosponges Enable the Detoxification of <i>Vibrio vulnificus</i> Hemolysin Reprinted from: <i>Int. J. Mol. Sci.</i> <b>2022</b> , 23, 6821, doi:10.3390/ijms23126821 . . . . .	<b>157</b>
<b>Arvind Mukundan, Shih-Wei Feng, Yu-Hsin Weng, Yu-Ming Tsao, Sofya B. Artemkina and Vladimir E. Fedorov et al.</b> Optical and Material Characteristics of MoS <sub>2</sub> /Cu <sub>2</sub> O Sensor for Detection of Lung Cancer Cell Types in Hydroplegia Reprinted from: <i>Int. J. Mol. Sci.</i> <b>2022</b> , 23, 4745, doi:10.3390/ijms23094745 . . . . .	<b>171</b>

# About the Editor

## **Raghvendra Singh Yadav**

Dr. Raghvendra Singh Yadav has been working as a senior scientist and a team leader of the scientifically independent research group “Two-dimensional Nanostructures (graphene, MXene, borophene, transition metal dichalcogenides, etc.) Based on Innovative Functional Nanocomposites and Their Advanced Applications” at the Center of Polymer Systems, Tomas Bata University in Zlin, Czech Republic. Dr. Yadav has authored more than 74 articles in reputable international journals, garnering 2805 citations with an h-index of 31. Additionally, Dr. Yadav has contributed to two book chapters and six books on materials science and nanotechnology. Additionally, Dr. Yadav has been a member of the editorial boards of several journals.



# **Preface to “Multifunctional Nanomaterials: Synthesis, Properties, and Applications 2.0”**

This reprint consists of scientific papers that had been published, covering the synthesis, characteristics, and applications of multifunctional nanomaterials. Smart nanoparticles with two or more engineered properties or characteristics make up multifunctional nanomaterials. These versatile nanomaterials have impressive structural and physical characteristics, which has expanded their industrial application. This reprint will be useful to academics, scientists, engineers, students, and industrial researchers.

**Raghvendra Singh Yadav**

*Editor*





Editorial

# Multifunctional Nanomaterials: Synthesis, Properties, and Applications 2.0

Raghvendra Singh Yadav 

Centre of Polymer Systems, Tomas Bata University in Zlin, Trida Tomase Bati 5678, 76001 Zlin, Czech Republic; yadav@utb.cz; Tel.: +420-576031725

This Special Issue, “Multifunctional Nanomaterials: Synthesis, Properties and Applications 2.0”, is composed of twelve published research articles, which include nine original research articles and three review articles.

An innovative method described by Zijun Yan et al. [1] was used to improve the efficiency of electrochemical CO<sub>2</sub> reduction (CO<sub>2</sub>R) as well as the ability to produce C<sub>2</sub> products. A simple hydrothermal process combined with calcination was used to create CuO/g-C<sub>3</sub>N<sub>4</sub> based on copper oxide catalysts, using g-C<sub>3</sub>N<sub>4</sub> as a carrier. The addition of g-C<sub>3</sub>N<sub>4</sub> boosted the specific surface area, which promoted the kinetics of mass transfer and created new opportunities for the exposure of active sites and CO<sub>2</sub> adsorption. Veloso, S.R.S. et al. [2] reported calcium-doped manganese ferrite nanoparticles via an oxidative precipitation approach for magnetic hyperthermia. The produced calcium-doped manganese ferrite nanoparticles had larger saturation magnetization and heating efficiency values, which made them suitable for therapeutic uses such as drug delivery and cancer treatment. Maraming, P. et al. [3] discussed the creation of an electrochemical aptasensor functionalized with polydopamine nanoparticles (PDA-NPs) for the rapid, accurate, and economical detection of glycated albumin (GA), a promising biomarker for glycemic control in diabetic patients. This suggested method demonstrated its potential use in GA measurement to improve diabetic patient screening and management in the future. Chen, D.R. et al. [4] reported a fabrication of a Zn-CO<sub>2</sub> battery using a carbon nanotube (CNT) sheet as a cathode and a Zn plate as an anode. This study emphasized the significance of the activation process, which made it possible to load more catalyst onto the cathode and create more active sites for the electroreduction process. In order to design TiO<sub>2</sub>-Bi<sub>2</sub>S<sub>3</sub> composites with high photoactive performance, a detailed vulcanization-process-dependent microstructure evolution and photoactive properties of TiO<sub>2</sub>-Bi<sub>2</sub>S<sub>3</sub> composites were proposed in the study of Liang, Y.-C. et al. [5]. Furthermore, Zhu, P. et al. [6] used commercial microcrystalline cellulose (MCC) as the raw material to develop spherical cellulose nanocrystal (CNC) via mixed acid hydrolysis. By choosing different pretreatment routes through mixed acid hydrolysis, the authors showed that it is possible to prepare spherical CNC with various properties economically from MCC. The fabrication of anisotropic silver nanostars (AgNS) that can be used as highly effective surface enhanced Raman spectroscopy (SERS) substrates for various bioanalytes, even in the case of a near-infrared (NIR) excitation laser, was described by Revnic, R.N. et al. [7]. In order to neutralize *V. vulnificus* hemolysin (VvhA), Zou, S. et al. [8] created a biocompatible nanoscale detoxification system. With regard to recombinant *V. vulnificus* hemolysin (rVvhA)-induced toxicity, nanosponges (NSs) demonstrated excellent protective effects, offering helpful insights into how to counter the growing dangers posed by severe *V. vulnificus* infections. For the purpose of detecting different lung cancer cell types in hydroplegia, Mukundan et al. [9] reported the optical and material properties of a MoS<sub>2</sub>/Cu<sub>2</sub>O sensor.

Halloysite nanotubes, their properties, and their use in the biological field were reviewed by Biddecì, G. et al. [10]. Recent developments in metasurfaces for photocatalysis, surface-enhanced infrared absorption (SEIRA), and surface-enhanced Raman scattering

**Citation:** Yadav, R.S. Multifunctional Nanomaterials: Synthesis, Properties, and Applications 2.0. *Int. J. Mol. Sci.* **2023**, *24*, 7619. <https://doi.org/10.3390/ijms24087619>

Received: 6 April 2023

Accepted: 11 April 2023

Published: 21 April 2023



**Copyright:** © 2023 by the author. Licensee MDPI, Basel, Switzerland. This article is an open access article distributed under the terms and conditions of the Creative Commons Attribution (CC BY) license (<https://creativecommons.org/licenses/by/4.0/>).

(SERS) sensors were reported by Barbillon, G. [11]. The applications of magnetic resonance imaging (MRI), single-photon emission computed tomography (SPECT), and positron emission tomography (PET) in reporter gene technologies for use in brain imaging were discussed in a review article by Gao, T. et al. [12].

**Funding:** I am thankful for the financial support of the Ministry of Education, Youth, and Sports of the Czech Republic-DKRVO (RP/CPS/2022/007).

**Conflicts of Interest:** The author declares no conflict of interest.

## References

1. Yan, Z.; Wu, T. Highly Selective Electrochemical CO<sub>2</sub> Reduction to C<sub>2</sub> Products on a g-C<sub>3</sub>N<sub>4</sub>-Supported Copper-Based Catalyst. *Int. J. Mol. Sci.* **2022**, *23*, 14381. [CrossRef] [PubMed]
2. Veloso, S.R.S.; Andrade, R.G.D.; Gomes, V.; Amorim, C.O.; Amaral, V.S.; Salgueiriño, V.; Coutinho, P.J.G.; Ferreira, P.M.T.; Correa-Duarte, M.A.; Castanheira, E.M.S. Oxidative Precipitation Synthesis of Calcium-Doped Manganese Ferrite Nanoparticles for Magnetic Hyperthermia. *Int. J. Mol. Sci.* **2022**, *23*, 14145. [CrossRef] [PubMed]
3. Maraming, P.; Aye, N.N.S.; Boonsiri, P.; Daduang, S.; Buhome, O.; Daduang, J. Polydopamine Nanoparticles Functionalized Electrochemical DNA Aptasensor for Serum Glycated Albumin Detection. *Int. J. Mol. Sci.* **2022**, *23*, 13699. [CrossRef] [PubMed]
4. Chen, D.R.; Chitranshi, M.; Shanov, V.; Schulz, M. Electrochemically Activated CNT Sheet as a Cathode for Zn-CO<sub>2</sub> Batteries. *Int. J. Mol. Sci.* **2022**, *23*, 12602. [CrossRef] [PubMed]
5. Liang, Y.-C.; You, S.-Y.; Chen, B.-Y. Crystal Design and Photoactivity of TiO<sub>2</sub> Nanorod Template Decorated with Nanostructured Bi<sub>2</sub>S<sub>3</sub> Visible Light Sensitizer. *Int. J. Mol. Sci.* **2022**, *23*, 12024. [CrossRef] [PubMed]
6. Zhu, P.; Feng, L.; Ding, Z.; Bai, X. Preparation of Spherical Cellulose Nanocrystals from Microcrystalline Cellulose by Mixed Acid Hydrolysis with Different Pretreatment Routes. *Int. J. Mol. Sci.* **2022**, *23*, 10764. [CrossRef] [PubMed]
7. Revnic, R.N.; Stiufiuc, G.F.; Toma, V.; Onaciu, A.; Moldovan, A.; Tigau, A.B.; Fischer-Fodor, E.; Tetean, R.; Burzo, E.; Stiufiuc, R.I. Facile Microwave Assisted Synthesis of Silver Nanostars for Ultrasensitive Detection of Biological Analytes by SERS. *Int. J. Mol. Sci.* **2022**, *23*, 8830. [CrossRef] [PubMed]
8. Zou, S.; Wang, Q.; Zhang, P.; Wang, B.; Liu, G.; Zhang, F.; Li, J.; Wang, F.; Wang, B.; Zhang, L. Biomimetic Nanosponges Enable the Detoxification of *Vibrio vulnificus* Hemolysin. *Int. J. Mol. Sci.* **2022**, *23*, 6821. [CrossRef] [PubMed]
9. Mukundan, A.; Feng, S.-W.; Weng, Y.-H.; Tsao, Y.-M.; Artemkina, S.B.; Fedorov, V.E.; Lin, Y.-S.; Huang, Y.-C.; Wang, H.-C. Optical and Material Characteristics of MoS<sub>2</sub>/Cu<sub>2</sub>O Sensor for Detection of Lung Cancer Cell Types in Hydroplegia. *Int. J. Mol. Sci.* **2022**, *23*, 4745. [CrossRef] [PubMed]
10. Biddeci, G.; Spinelli, G.; Colomba, P.; Di Blasi, F. Nanomaterials: A Review about Halloysite Nanotubes, Properties, and Application in the Biological Field. *Int. J. Mol. Sci.* **2022**, *23*, 11518. [CrossRef] [PubMed]
11. Barbillon, G. Latest Advances in Metasurfaces for SERS and SEIRA Sensors as Well as Photocatalysis. *Int. J. Mol. Sci.* **2022**, *23*, 10592. [CrossRef] [PubMed]
12. Gao, T.; Wang, P.; Gong, T.; Zhou, Y.; Wang, A.; Tang, X.; Song, X.; Fan, Y. Reporter Genes for Brain Imaging Using MRI, SPECT and PET. *Int. J. Mol. Sci.* **2022**, *23*, 8443. [CrossRef] [PubMed]

**Disclaimer/Publisher's Note:** The statements, opinions and data contained in all publications are solely those of the individual author(s) and contributor(s) and not of MDPI and/or the editor(s). MDPI and/or the editor(s) disclaim responsibility for any injury to people or property resulting from any ideas, methods, instructions or products referred to in the content.



Article

# Highly Selective Electrochemical CO<sub>2</sub> Reduction to C<sub>2</sub> Products on a g-C<sub>3</sub>N<sub>4</sub>-Supported Copper-Based Catalyst

Zijun Yan<sup>1</sup> and Tao Wu<sup>1,2,3,\*</sup>

<sup>1</sup> New Materials Institute, University of Nottingham Ningbo China, Ningbo 315100, China

<sup>2</sup> Key Laboratory of Carbonaceous Wastes Processing and Process Intensification of Zhejiang Province, University of Nottingham Ningbo China, Ningbo 315100, China

<sup>3</sup> Nottingham Ningbo Beacons of Excellence Research and Innovation Institute, Ningbo 315000, China

\* Correspondence: tao.wu@nottingham.edu.cn

**Abstract:** Herein, a novel approach used to enhance the conversion of electrochemical CO<sub>2</sub> reduction (CO<sub>2</sub>R), as well as the capacity to produce C<sub>2</sub> products, is reported. A copper oxide catalyst supported by graphite phase carbon nitride (CuO/g-C<sub>3</sub>N<sub>4</sub>) was prepared using a one-step hydrothermal method and exhibited a better performance than pure copper oxide nanosheets (CuO NSs) and spherical copper oxide particles (CuO SPs). The Faradaic efficiency reached 64.7% for all the C<sub>2</sub> products, specifically 37.0% for C<sub>2</sub>H<sub>4</sub>, with a good durability at −1.0 V vs. RHE. The results suggest that the interaction between CuO and the two-dimensional g-C<sub>3</sub>N<sub>4</sub> planes promoted CO<sub>2</sub> adsorption, its activation and C-C coupling. This work offers a practical method that can be used to enhance the activity of electrochemical CO<sub>2</sub>R and the selectivity of C<sub>2</sub> products through synergistic effects.

**Keywords:** electrochemical reduction of CO<sub>2</sub>; graphite phase carbon nitride; copper oxide; C<sub>2</sub> products; hydrothermal preparation for advantageous electrocatalyst

**Citation:** Yan, Z.; Wu, T. Highly Selective Electrochemical CO<sub>2</sub> Reduction to C<sub>2</sub> Products on a g-C<sub>3</sub>N<sub>4</sub>-Supported Copper-Based Catalyst. *Int. J. Mol. Sci.* **2022**, *23*, 14381. <https://doi.org/10.3390/ijms232214381>

Academic Editor: Raghvendra Singh Yadav

Received: 30 October 2022

Accepted: 17 November 2022

Published: 19 November 2022

**Publisher's Note:** MDPI stays neutral with regard to jurisdictional claims in published maps and institutional affiliations.



**Copyright:** © 2022 by the authors. Licensee MDPI, Basel, Switzerland. This article is an open access article distributed under the terms and conditions of the Creative Commons Attribution (CC BY) license (<https://creativecommons.org/licenses/by/4.0/>).

## 1. Introduction

According to statistics, the level of CO<sub>2</sub> in the air is rising, which has led to global warming [1]. Compared with other measures, the chemical transformation of CO<sub>2</sub> into carbon-containing chemicals is a promising option for CO<sub>2</sub> mitigation. Among these options, electrocatalysis is considered to have high potential because it uses clean energy generated by electrical power and reacts in an aqueous solution at room temperature and pressure under mild reducing conditions [2,3]. As a result, it is environmentally friendly and transforms CO<sub>2</sub> into fuels and chemical materials with significant added value [4].

Among the numerous metal catalysts, copper is the only one that has a moderate binding energy to intermediates, which can generate numerous C<sub>1</sub> and high-value C<sub>2</sub> and C<sub>2+</sub> products [5,6]. Compared to copper, as a simple substance, oxide-derived copper catalysts at lower potentials exhibit a considerably enhanced CO<sub>2</sub> electroreduction to C<sub>2</sub> [7]. However, in conventional thermal conversion, it is difficult to meet the need for the increased reaction rates and selectivity of the target products at present. Although several novel synthetic strategies for copper-based catalysts have been reported, such as electrodeposition and plasma treatments [7–10], these complex synthesis methods often require the adoption of harsh reaction conditions and the use of expensive equipment, which hinder the widespread application of the related technologies. Consequently, it is necessary to create new methods that are simple and environmentally friendly for the preparation of catalysts.

Thus far, a wide range of CO<sub>2</sub>R techniques for oxide-derived copper catalysts have been reported. Ager et al. [11] prepared oxide-derived Cu catalysts based on Cu<sub>2</sub>O through electroreduction and obtained a selectivity of the C<sub>2+</sub> products (FE = 60%) for at least 5 h at −1.0 V in 0.1 M potassium bicarbonate. Cui et al. [12] introduced N into Cu<sub>2</sub>O to produce nitrogen-doped Cu<sub>2</sub>O, which resulted in the enhanced CO<sub>2</sub> adsorption and

doubled Faradaic efficiency of ethylene (10%) compared to  $\text{Cu}_2\text{O}$ . However, despite the excellent electrocatalytic performance of copper metal in regard to  $\text{CO}_2$ , it is still affected by its complex reduction products and poor single-product selectivity and  $\text{CO}_2\text{R}$  activity. Moreover,  $\text{CO}_2$  is poorly soluble in water. Thus, the overpotentials related to  $\text{C}_2$  generation reactions are high, which makes it more difficult for  $\text{CO}_2$  to be adsorbed on the catalyst surface and renders the competing hydrogen precipitation side reactions significant [13,14]. In this regard, Luo et al. [15] proposed that high  $\text{CO}_2$  pressure at the same concentration of the electrolyte can lead to a lower local pH, which will increase the surface coverage of CO, thus promoting the formation of  $\text{C}_2$  products. Wang et al. [16] created a  $\text{Cu}/\text{N}_x\text{C}$  (nitrogen-doped carbon) interface and found that  $\text{CO}_2$  has a strong interaction with the  $\text{Cu}/\text{N}_x\text{C}$  interface and is enriched on  $\text{N}_x\text{C}$ , which increases the selectivity of  $\text{C}_2$  by 200–300%. Hence, there is a need to develop a novel catalyst that is more efficient and highly selective, following this line of reasoning.

Density functional theory (DFT) indicates that, for multi-carbon products, the ability of multiple  $^*\text{CO}$  intermediates to engage in a C-C coupling process and influence the strength of  $^*\text{CO}$  intermediate binding located in the catalytic active center are the determining factors [17]. In order to promote such an interaction, a number of enhancement studies have been undertaken, including the study of  $g\text{-C}_3\text{N}_4$ . It has a high thermal and chemical stability and special laminar structure, as well as a low cost, and its heterostructure provides a high  $\text{CO}_2$  adsorption and activation efficiency [18,19].  $g\text{-C}_3\text{N}_4$  contains a large amount of pyridine N. Theoretical calculations indicate that, as the main active site for electrocatalytic reactions, pyridine N, as a substrate, can complex with the metal nanoparticles to stabilize them and also provides an active center for  $\text{CO}_2\text{R}$ . The interaction of  $g\text{-C}_3\text{N}_4$  with metal also causes the metal surface to be highly electron-rich, thus enhancing the adsorption of reaction intermediates [20]. However, few experiments have been conducted to systematically verify this process. Jiao et al. [21] synthesized  $\text{Cu-C}_3\text{N}_4$  to provide experimental evidence for the calculation of the  $g\text{-C}_3\text{N}_4$  scaffold. In the synthesized samples, the analysis based on the N K-edge NEXAFS spectra and Cu 2p XPS confirmed the significant chemical interaction between N and Cu atoms. However, the main product of  $\text{CO}_2\text{R}$  of  $\text{Cu-C}_3\text{N}_4$  was still hydrogen (>50%). This suggests that the  $g\text{-C}_3\text{N}_4$ -loaded Cu-based catalysts still require further improvement. To date, there is no research that has been carried out to capitalize on the synergistic effects of  $g\text{-C}_3\text{N}_4$  and copper oxide to enhance electrochemical  $\text{CO}_2\text{R}$  and its selectivity.

In this work, starting with the material structure of electrocatalysts,  $\text{CuO}/g\text{-C}_3\text{N}_4$  was prepared based on copper oxide catalysts using  $g\text{-C}_3\text{N}_4$  as a carrier by a straightforward hydrothermal method combined with calcination. The morphology and components were analyzed, and the electrochemical performance and catalytic activity were investigated by drop coating the catalysts on carbon paper. During the discussion, the control experiments were performed using  $\text{CuO}$  NSs and  $\text{CuO}$  SPs, and the reasons for the efficient catalytic reduction to  $\text{C}_2$  products by the  $\text{CuO}/g\text{-C}_3\text{N}_4$  electrode were comprehensively analyzed.

## 2. Results and Discussion

### 2.1. Electrochemical Activity Tests

LSV curves of the  $\text{CuO}$  SP,  $\text{CuO}$  NS and  $\text{CuO}/g\text{-C}_3\text{N}_4$  catalysts in Ar- and  $\text{CO}_2$ -saturated 0.1 M  $\text{KHCO}_3$  solution are displayed in Figure 1a. In the  $\text{CO}_2$ -saturated electrolyte, clearly, all of the investigated catalysts showed higher current densities compared to those in the Ar-saturated electrolyte, demonstrating their great inherent activity for electrochemical  $\text{CO}_2\text{R}$ . Under the same solution conditions,  $\text{CuO}/g\text{-C}_3\text{N}_4$  also exhibited a smaller onset potential than the  $\text{CuO}$  NSs and  $\text{CuO}$  SPs. Additionally,  $\text{CuO}/g\text{-C}_3\text{N}_4$  exhibited a noticeably improved current density from onset potential to  $-1.3$  V vs. RHE relative to the other two  $\text{CuO}$  catalysts, thus implying its higher  $\text{CO}_2\text{R}$  performance. Tafel curves for the overpotential-log ( $\text{C}_2$  current density) are plotted in Figure 1b. Compared with the  $\text{CuO}$  NSs and  $\text{CuO}$  SPs ( $27.8$   $\text{mV}\cdot\text{dec}^{-1}$  and  $33.6$   $\text{mV}\cdot\text{dec}^{-1}$ ), the slope of  $\text{CuO}/g\text{-C}_3\text{N}_4$  exhibits a significant decrease ( $17.2$   $\text{mV}\cdot\text{dec}^{-1}$ ), which provides the further evidence

of the better intrinsic properties of the CuO/g-C<sub>3</sub>N<sub>4</sub> surface. The advantageous current density is also attributed to the lower charge transfer resistance of CuO/g-C<sub>3</sub>N<sub>4</sub>, reflecting the improved charge transfer process at the interface of the electrode and surrounding electrolyte, according to the EIS measurements and the fitting results in Figure S1 and Table S1.

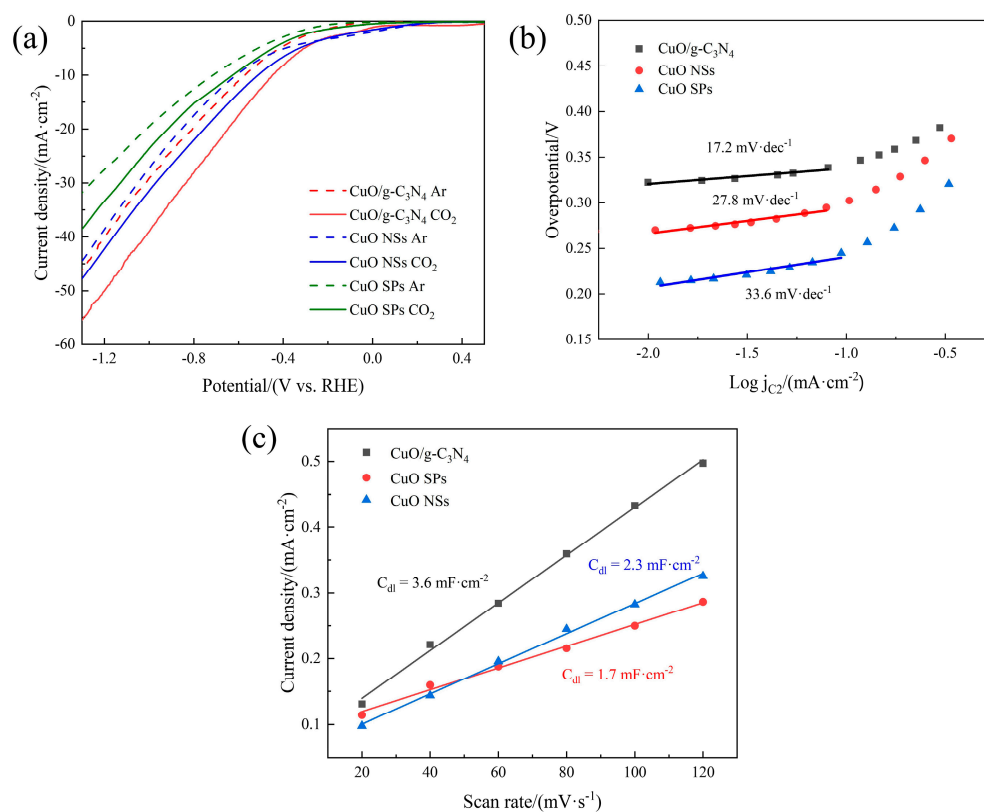


**Figure 1.** (a) LSV curves of CuO SPs, CuO NSs and CuO/g-C<sub>3</sub>N<sub>4</sub> in Ar- and CO<sub>2</sub>-saturated 0.1 M KHCO<sub>3</sub> solution, (b) Tafel slope calculation curves of CuO SPs, CuO NSs and CuO/g-C<sub>3</sub>N<sub>4</sub>, and (c) capacitive current at OCP as a function of the scan rate of CuO SPs, CuO NSs and CuO/g-C<sub>3</sub>N<sub>4</sub> in CO<sub>2</sub>-saturated KHCO<sub>3</sub> solution.

The ECSA of the CuO SP, CuO NS and CuO/g-C<sub>3</sub>N<sub>4</sub> electrodes were studied by contrast with the corresponding C<sub>dl</sub> (double-layer capacitance). The CVs of these three electrodes are presented in Figure S2. The slope of the non-faradaic capacitive current (current density at OCP) versus the scan rate was used to calculate the C<sub>dl</sub> value. In Figure 1c, it is clear that the C<sub>dl</sub> of CuO/g-C<sub>3</sub>N<sub>4</sub> (3.6 mF·cm<sup>-2</sup>) is much higher than that of the CuO NSs (2.3 mF·cm<sup>-2</sup>), indicating that CuO/g-C<sub>3</sub>N<sub>4</sub> has a larger electrochemical active surface area and more exposed active sites, which are advantageous for boosting the CO<sub>2</sub>R activity. This also proves that the larger active surface area is caused by the g-C<sub>3</sub>N<sub>4</sub> layer. Meanwhile, the C<sub>dl</sub> of the CuO NSs is larger than that of the CuO SPs (1.7 mF·cm<sup>-2</sup>), suggesting that the nanosheets of CuO have a larger active surface area than the spherical nanoparticles of CuO.

## 2.2. Electrochemical CO<sub>2</sub> Reduction Performance Tests

Furthermore, the CO<sub>2</sub>RR gaseous product distributions of the CuO SPs, CuO NSs and CuO/g-C<sub>3</sub>N<sub>4</sub> were comparatively studied using a potential region of -0.8~ -1.2 V vs. RHE. As given in Figure 2a, the CuO SPs consistently preferred CH<sub>4</sub> production in all the testing potential regions, while the C<sub>2</sub>H<sub>4</sub> selectivity was very low (<20%). This result indicates that regardless of the applied potentials, CuO SPs do not exhibit a particularly high C-C coupling activity. Comparatively to the CuO SPs, whose Faradaic efficiency was not higher than 5% at -0.8~ -1.2 V, that of CH<sub>4</sub> was suppressed for the CuO NSs. At the best applied

potential of  $-1.0$  V, the  $C_2H_4$  production increased from 16.5% to 31.7%, and some ethane was produced as well (Figure 2b). However, in terms of the CuO/g- $C_3N_4$  electrocatalyst, the  $CH_4$  and CO productions were considerably further suppressed, totaling less than 6% at the potential of  $-1.0$  V, as Figure 2c shows, while the CuO NS catalyst had an 8.1% Faradaic efficiency of  $C_1$  gaseous products at the same potential. Meanwhile, the  $C_2H_4$  selectivity in CuO/g- $C_3N_4$  was significantly improved, whereas the  $H_2$  production caused by the HER side reaction clearly decreased. In particular, at the potential of  $-1.0$  V, the  $C_2H_4$  Faradaic efficiency reached as high as 37.0%, which was accompanied with  $H_2$  formation at 25.8%. A very small amount of HCOOH (8.8%) was also detected at this potential in the liquid products. Ethanol was reliably detected as well. At  $-0.8\sim-1.0$  V, its Faradaic efficiency varied in the small range of 27.3~28.2%. The Faradaic efficiency for  $C_2$  was 64.7% for CuO/g- $C_3N_4$  at the respective optimal potential for  $C_2$  electroproduction. In brief, the CuO/g- $C_3N_4$  catalyst achieves a further improvement in the selectivity of  $C_2$  products.

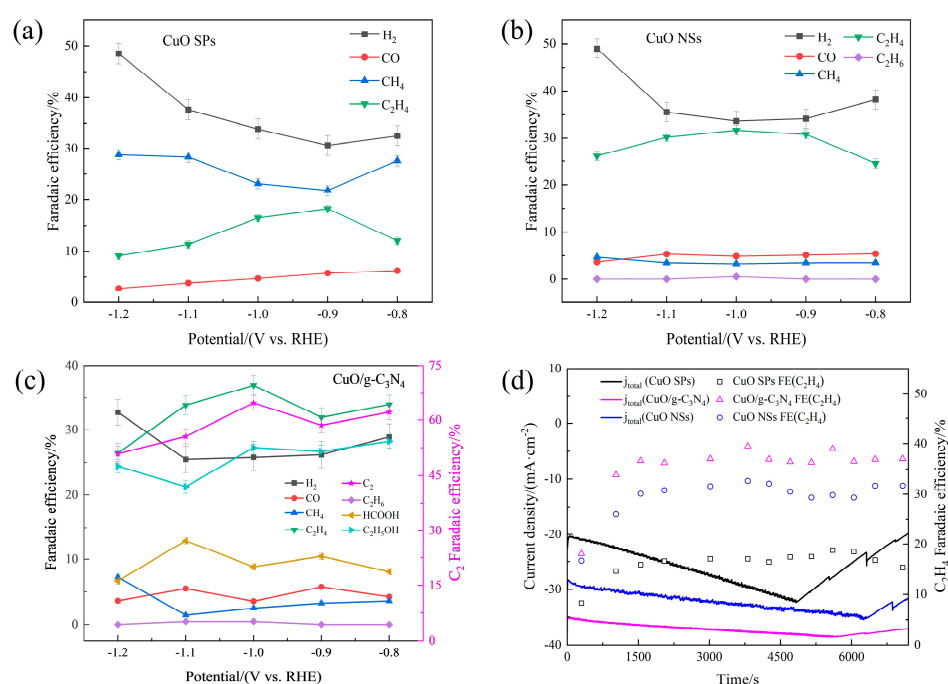


**Figure 2.** Faradaic efficiencies of CO<sub>2</sub> electroreduction products as a function of the potential: (a) CuO SPs, (b) CuO NSs and (c) CuO/g- $C_3N_4$ . (d) Stability tests for CuO SPs, CuO NSs and CuO/g- $C_3N_4$  at  $-1.0$  V vs. RHE.

Figure S3 compares the geometric partial current densities of several products for various electrodes. At each potential, the  $H_2$  formation rate for the electrodes follows the trend CuO/g- $C_3N_4$  < Cu NSs < CuO SPs, illustrating the  $H_2$  production caused by the competing HER was well controlled on CuO/g- $C_3N_4$ . Meanwhile, the maximum  $C_2H_4$  and  $C_2$  partial current densities occurred at  $-1.0$  V in CuO/g- $C_3N_4$ , reaching  $14.0$  mA·cm<sup>-2</sup> and  $24.5$  mA·cm<sup>-2</sup>, respectively. The above results show the exceptional performance of CO<sub>2</sub>R compared to that of the previously reported Cu-based electrocatalysts (Table S2).

CuO/g- $C_3N_4$  has an excellent activity and selectivity in addition to a good stability. Figure 2d shows its chronoamperometric responses after being biased for two hours at  $-1.0$  V (corresponding to the highest  $C_2H_4$  selectivity, especially for CuO/g- $C_3N_4$ ). The CuO/g- $C_3N_4$  and Cu NSs displayed an excellent stability in these two hours. In terms of CuO/g- $C_3N_4$ , the total cathodic current density tended to smooth out and was still maintained at  $37.0$  mA·cm<sup>-2</sup> at the end of the stability test. Its corresponding  $C_2H_4$  selectivity experienced an initial increase and was then retained at over 37.0% throughout the electroreduction. The CuO SPs catalyst, on the other hand, demonstrated a quick catalytic deactivation. The current density dropped rapidly by 40% after 5000s, and there

was also a downward trend in the Faradaic efficiency of  $C_2H_4$  at the end, despite the fact that it experienced a spike during the previous experiment.

### 2.3. Structure and Morphology Characterizations

The surface characteristics of nano-adsorbents can be identified using  $N_2$  adsorption/desorption measurements. In Figure 3, for the CuO/g- $C_3N_4$  material, there is a mesoporous structure, as evidenced by the large hysteresis loop from 0.47 to 1.00 of  $P/P_0$ , which can also be proved by its pore size distribution using the BJH method. Remarkably, the adsorbed quantity of CuO/g- $C_3N_4$  is more than that of the CuO NSs, demonstrating that CuO/g- $C_3N_4$  has a more consistent pore structure and a greater surface area [22,23]. The BET surface areas of the CuO NSs and CuO/g- $C_3N_4$ , as obtained, are  $7.62 \text{ m}^2/\text{g}$  and  $11.2 \text{ m}^2/\text{g}$ , respectively. Meanwhile, a higher average pore volume of  $0.048 \text{ cm}^3 \cdot \text{g}^{-1}$  is observed in CuO/g- $C_3N_4$  (versus  $0.029 \text{ cm}^3 \cdot \text{g}^{-1}$  of the CuO NSs sample). In a word, g- $C_3N_4$  contributes to the increase in the surface area as well as the pore volume. Thus,  $CO_2$  can be better adsorbed, combined with the synergistic effects between CuO and g- $C_3N_4$ .

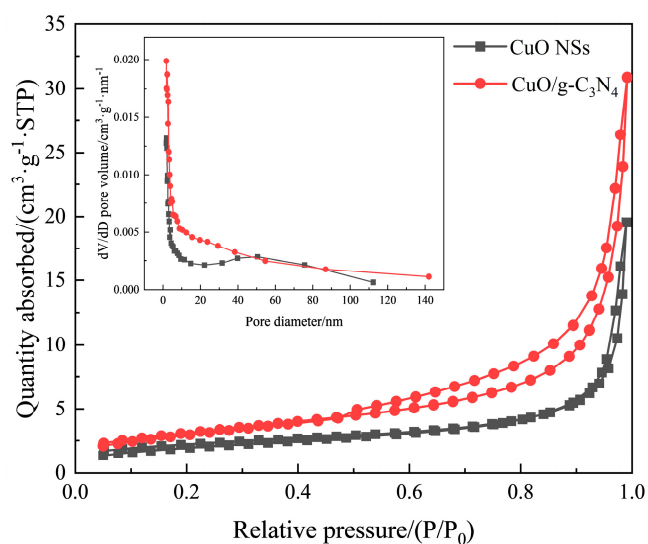


**Figure 3.**  $N_2$  adsorption–desorption isotherm and BJH pore size distribution plots (insets) of CuO NSs and CuO/g- $C_3N_4$ .

The crystal phase of the synthesized catalysts was revealed by the XRD patterns. According to Figure 4a, the graphitic materials with two specific diffraction planes, (100) and (002), correspond to the two typical diffraction peaks of pure g- $C_3N_4$  at  $13.08^\circ$  and  $27.17^\circ$ , which are caused by the interlayer stacking of conjugated aromatic rings and the in-plane structure of tri-s-triazine motifs [24,25]. In terms of the CuO NSs, the main peaks at  $32.50^\circ$ ,  $35.50^\circ$ ,  $38.73^\circ$ ,  $38.96^\circ$  and  $48.73^\circ$  can be attributed to the crystal facets ( $-110$ ), (002), (111), (200) and ( $-202$ ) of CuO (JCPDS#45-0937), some of which are also depicted in the HRTEM and SAED patterns (Figure S4). The CuO/g- $C_3N_4$  composite allows for the observation of both g- $C_3N_4$  and CuO XRD diffraction peaks, and the absence of any additional distinctive peaks indicates the high purity of the samples immediately after preparation. Meanwhile, the cluster bands between  $1248$  and  $1631 \text{ cm}^{-1}$  in the FTIR spectra of g- $C_3N_4$  (Figure 4b) can be classified as the classic stretching mode of C-N heterocycles, and the heptazine ring system is the source of the  $805 \text{ cm}^{-1}$  sharp peak. The peaks of Cu-O stretching vibrations are also very obvious. The distinctive bands seen in CuO NSs at  $425 \text{ cm}^{-1}$  correspond to the CuO Au mode, and those at the slightly higher wavenumber position of  $496 \text{ cm}^{-1}$  correspond to the CuO Bu mode [26–29]. All of them can be seen in CuO/g- $C_3N_4$ . This evidence prove that the two elements, g- $C_3N_4$  and CuO, coexist in the CuO/g- $C_3N_4$  material.

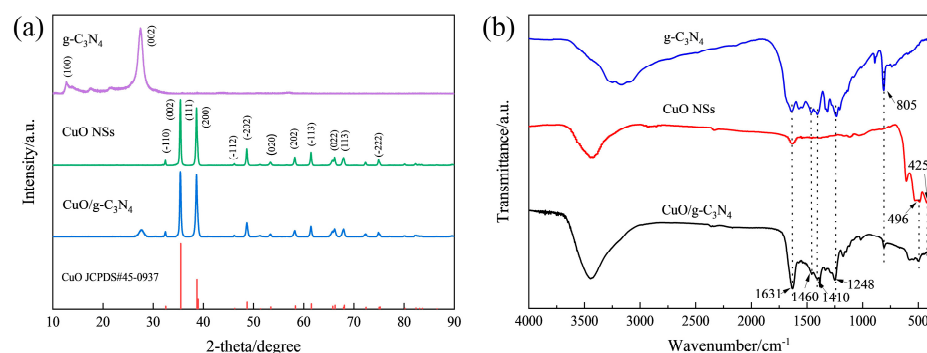


**Figure 4.** (a) XRD patterns of  $g\text{-C}_3\text{N}_4$ , CuO NSs and CuO/ $g\text{-C}_3\text{N}_4$ , (b) FTIR spectra of  $g\text{-C}_3\text{N}_4$ , CuO NSs and CuO/ $g\text{-C}_3\text{N}_4$ .

The elemental compositions of  $g\text{-C}_3\text{N}_4$  and CuO/ $g\text{-C}_3\text{N}_4$  were examined by XPS spectroscopy, and the binding energies obtained for each of them were compared. The investigated spectra in Figure 5a confirm that all the anticipated elements are present, namely N 1s and C 1s for  $g\text{-C}_3\text{N}_4$  and O 1s, Cu 2p, N 1s and C 1s for CuO/ $g\text{-C}_3\text{N}_4$ . In Figure 5b, the Cu 2p high-resolution peak of the composite CuO/ $g\text{-C}_3\text{N}_4$  is observed. The pattern of CuO/ $g\text{-C}_3\text{N}_4$  presents with a pair of peaks discovered at 932.7 and 952.5 eV that are associated with two typical energy levels of copper:  $2p_{3/2}$  and  $2p_{1/2}$ . CuO crystals are present, according to the nearly 20 eV spin-orbit energy difference. This also indicates that the Cu in the sample is in the +II oxidation state. The small peaks at 940–945 eV are satellite peaks, which are generally seen in Cu ions in the oxidation state of +II. Furthermore, in Figure 5c, a C 1s binding energy peak is shown at 284.8 eV, which refers to  $g\text{-C}_3\text{N}_4$  and CuO/ $g\text{-C}_3\text{N}_4$ , belonging to the C=N  $sp^2$  bond and the interaction of the metal oxide with  $g\text{-C}_3\text{N}_4$  in the mixture. Similarly, on the s-triazine ring of graphitic nitride of  $g\text{-C}_3\text{N}_4$  and CuO/ $g\text{-C}_3\text{N}_4$ , there are  $sp^2$  N-C=N bonds, which can be represented by the C 1s peaks at 288.1 and 287.9 eV. Assigned to pyridine nitrogen, pyrrolic nitrogen and graphitic nitrogen, respectively, the N 1s peak of  $g\text{-C}_3\text{N}_4$  can be deconvoluted into three chemical states, i.e., the peaks at 398.5, 399.0 and 400.6 eV. In terms of pyridine N, the binding energy of the CuO/ $g\text{-C}_3\text{N}_4$  sample (398.3 eV) is 0.2 eV lower than that of pure  $g\text{-C}_3\text{N}_4$  (398.5 eV), impacting the interaction between the two molecules at the interface (Figure 5d) [30–35].

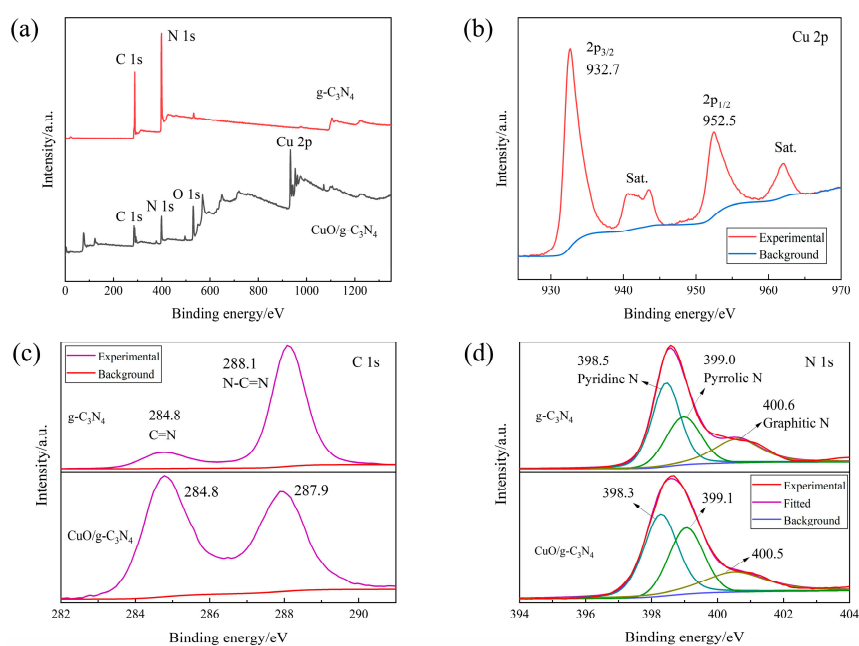


**Figure 5.** XPS spectra of  $g\text{-C}_3\text{N}_4$  and CuO/ $g\text{-C}_3\text{N}_4$ : (a) full scan, (b) Cu 2p, (c) C 1s, (d) N 1s.

The morphology of  $g\text{-C}_3\text{N}_4$ , CuO and CuO/ $g\text{-C}_3\text{N}_4$  were confirmed using FESEM (Figure 6) and TEM (Figure S5). In Figure 6a, the pure  $g\text{-C}_3\text{N}_4$  is composed of irregular and loose aggregates of sheet-like structures. The lamellae are formed as a result of the thermal breakdown of the urea fracture while producing a large number of pores, and this rough appearance confers a very high functionalization on the  $g\text{-C}_3\text{N}_4$  sheets. In Figure 6b, it can be seen that a large number of CuO nanosheets of varying lengths were synthesized, with an average width of about 300 nm. Figure 6c demonstrates that, in the case of the CuO/ $g\text{-C}_3\text{N}_4$  composites, it is evident that the particles with smooth surfaces in the connected sheets of agglomerates are considered as CuO NSs loaded onto the  $g\text{-C}_3\text{N}_4$  matrix. Meanwhile, the corresponding elemental mapping (Figure 6d–g) also shows that the C, N, O and Cu atoms are evenly distributed throughout the composite, indicating the emergence of the CuO/ $g\text{-C}_3\text{N}_4$  structure and the close contact between them.

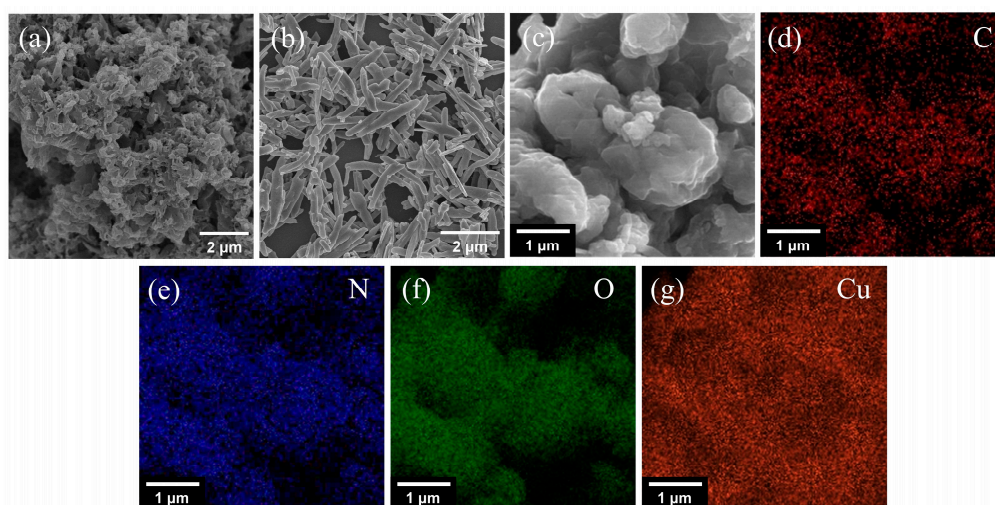


**Figure 6.** FESEM images of (a)  $g\text{-C}_3\text{N}_4$ , (b) CuO NSs, (c) CuO/ $g\text{-C}_3\text{N}_4$ , and (d–g) elemental mapping results of C (red), N (blue), O (green), and Cu (orange) of CuO/ $g\text{-C}_3\text{N}_4$ .

### 3. Materials and Methods

#### 3.1. Materials

Urea, polyvinyl pyrrolidone K30 (PVP-K30),  $\text{Cu}(\text{NO}_3)_2 \cdot 3\text{H}_2\text{O}$ , sodium acetate ( $\text{C}_2\text{H}_3\text{NaO}_2$ ), NaOH,  $\text{KHCO}_3$ , isopropanol ( $\text{C}_3\text{H}_8\text{O}$ ) and acetone ( $\text{C}_3\text{H}_6\text{O}$ ) were purchased from Sinopharm Chemical Reagent. Sodium dodecyl sulfate (SDS), ethanol (99.7%), Nafion-117 solution (~5%) and CuO SPs (40 nm, 99.5%) were purchased from Macklin. Carbon paper (GDS180S) was purchased from Ce Tech. Each chemical was used directly as received, and UP water ( $>18.2 \times 10^6 \Omega \cdot \text{cm}$ ) was employed to dispense the whole aqueous solution.

#### 3.2. Preparation of Catalysts

##### 3.2.1. Preparation of $g\text{-C}_3\text{N}_4$

A total of 20 g urea was placed into a 50 mL crucible, and after that, the prepared sample was placed in a muffle furnace, directly heated for 2 h in air conditions at  $540 \text{ }^\circ\text{C}$  and a rate of  $10 \text{ }^\circ\text{C min}^{-1}$ . After allowing it to naturally drop to an ambient temperature, the  $g\text{-C}_3\text{N}_4$  sample was obtained.

##### 3.2.2. Preparation of CuO NSs

A total of 0.238 g  $\text{Cu}(\text{NO}_3)_2 \cdot 3\text{H}_2\text{O}$ , 0.173 g  $\text{C}_2\text{H}_3\text{NaO}_2$ , 0.500 g PVP-K30 and 0.295 g SDS were dissolved in 100 mL  $\text{H}_2\text{O}$ . Then, under continuous rapid stirring, 0.1 M NaOH was added dropwise until a pH > 12 was obtained. The suspension was filled in a 200 mL stainless-steel autoclave with a Teflon lining and heated for 24 h at  $170 \text{ }^\circ\text{C}$ . The resultant sample was obtained by centrifuging the suspension, repeatedly washing it in  $\text{H}_2\text{O}$  and EtOH, and then heating it to  $550 \text{ }^\circ\text{C}$  ( $5 \text{ }^\circ\text{C min}^{-1}$ ) and holding it there for two hours in air.

### 3.2.3. Preparation of g-C<sub>3</sub>N<sub>4</sub>

The procedure was similar to that of CuO NSs, except for the fact that 0.100 g g-C<sub>3</sub>N<sub>4</sub> was introduced in the first instance.

### 3.3. Characterization

The morphology and structure of the studied samples were characterized by field emission scanning electron microscopy (FESEM, Regulus 8100, 5 kV) and transmission electron microscopy (TEM, Tecnai G2 F20, 200 kV). Energy-dispersive X-ray spectroscopy (EDS) mapping was conducted using FESEM Regulus 8100. The atomic valence states and some molecular structures were investigated by X-ray photoelectron spectroscopy (XPS, Thermo Escalab 250), and the source gun type was Al K $\alpha$ . X-ray diffraction (XRD) was carried out using D8 Advance, produced by German Bruker-AXS, operating at 40 kV and 40 mA with an accuracy of 0.01° (2 $\theta$ ) at room temperature. Fourier transform infrared spectrometer (FTIR) spectra were measured in the 400–4000 cm<sup>-1</sup> range using a Nicolet iS50 FT-IR spectrometer, with the samples prepared as KBr pellets. Brunauer–Emmett–Teller (BET) surface area measurements were performed at 77 K using a TriStar II 3020 adsorption analyzer in the N<sub>2</sub> adsorption mode.

### 3.4. Electrochemical Measurements

The carbon paper was pre-treated with acetone and washed at least 3 times with H<sub>2</sub>O and EtOH before being air-dried. A total of 4 mg of the sample (CuO/g-C<sub>3</sub>N<sub>4</sub>, CuO NSs or CuO SPs) was dispersed in 1 mL isopropanol and 30  $\mu$ L Nafion solution, followed by sonication for 30 min to create the sample ink. Then, the ink was homogeneously added drop by drop onto the carbon paper (2  $\times$  2 cm<sup>2</sup>) and dried on a hot plate, and then it was divided into working electrodes with a surface area of 1  $\times$  1 cm<sup>2</sup>.

The electrochemical measurements were performed using an electrochemistry workstation (Gamry Reference 300) in a three-electrode system. A Nafion-117 membrane divided the two compartments of the H-cell. As the counter electrode and reference electrode, respectively, platinum grid and Ag/AgCl electrode (saturated KCl) were employed. CO<sub>2</sub>-saturated (pH  $\approx$  6.8) or Ar-saturated 0.1 M KHCO<sub>3</sub> (pH  $\approx$  8.3) was used as the electrolyte. Additionally, each measurement potential was standardized to the reversible hydrogen electrode (RHE) reference scale, together with manual internal resistance compensation:

$$E_{RHE} = E_{Ag/AgCl} + 0.059 \times pH + 0.197 - iR_u \quad (1)$$

The  $iR_u$  was determined by potentiostatic electrochemical impedance spectroscopy measurements under an open circuit potential (OCP) at frequencies ranging from 10<sup>5</sup> Hz to 0.1 Hz. The linear sweep voltammetry (LSV) was tested in the same environment at a sweep rate of 10 mV·s<sup>-1</sup>. The current density equals the testing current divided by the geometric surface area of working electrode. The double-layer capacitance method was used to conduct the electrochemical active surface area (ECSA) tests. The potential range was OCP  $\pm$  50 mV, and cyclic voltammetry was performed at different sweep speeds. Gas chromatography (Agilent GC 8890) was used to identify the resulting gas phase products, and NMR (AVANCE III HD 400 MHz) was used to detect the products in the liquid phase.

### 3.5. Calculation of the Faradaic Efficiency

The following equation was used to calculate the Faradaic efficiency of the gas products:

$$FE_{gas} = \frac{nCGP \times 96485}{IRT} \quad (2)$$

Above,  $n$  is the amount of e<sup>-</sup> that is transferred to the product formation.  $C$  is the concentration (ppm) of the gases revealed by GC.  $G$  is rate of CO<sub>2</sub>.  $I$  is the cell current.  $P = 1.01 \times 10^5$  Pa.  $R$  is the universal gas constant.  $T = 273.15$  K.

The Faradaic efficiency of the liquid products was calculated by following equation:

$$FE_{liquid} = \frac{cV \cdot ne \times 6.022 \times 10^{23}}{\frac{Q}{e}} \quad (3)$$

Above,  $c$  is the concentration of the product.  $V$  is the total volume of the cathodic electrolyte and  $e$  is the electron.  $Q$  is the number of the transfer charge.

#### 4. Conclusions

In summary, a CuO/g-C<sub>3</sub>N<sub>4</sub> catalyst was fabricated by a simple hydrothermal method and achieved highly active and selective electrochemical CO<sub>2</sub>R to C<sub>2</sub> products. The catalyst demonstrates a significant advantage over pure CuO nanosheets and spherical CuO particles and shows a high Faradaic efficiency of 37.0% for C<sub>2</sub>H<sub>4</sub> at −1.0 V vs. RHE. It also has an ethylene catalytic stability that lasts for at least two hours. Meanwhile, the Faradaic efficiencies of all the C<sub>2</sub> products of the composite are 64.7%, performing better than many other Cu-based catalysts, which indicates a synergistic promotion of C-C coupling between CuO and g-C<sub>3</sub>N<sub>4</sub>. Moreover, the structure and morphology characterizations demonstrated that the composite is based on g-C<sub>3</sub>N<sub>4</sub>-supported uniform polycrystalline copper oxide. The introduction of g-C<sub>3</sub>N<sub>4</sub> increases the specific surface area, which promotes the mass transfer kinetics and provides new opportunities for the adsorption of CO<sub>2</sub> and the exposure of active sites. Additionally, the interaction of pyridine N with copper oxide was confirmed, which further increases the reaction activity of CO<sub>2</sub> reduction. This work provides an effective strategy that can be used to improve the selectivity and activity of C<sub>2</sub> formation during the electrochemical reduction of CO<sub>2</sub> and bridges the gap between the laboratory-based conversion of CO<sub>2</sub> to economically valuable chemicals and its industrial application.

**Supplementary Materials:** The following supporting information can be downloaded at: <https://www.mdpi.com/article/10.3390/ijms232214381/s1>. Refs. [36–47] are cited.

**Author Contributions:** Conceptualization, Z.Y.; formal analysis, Z.Y.; supervision, T.W.; validation, T.W.; writing—original draft, Z.Y. All authors have read and agreed to the published version of the manuscript.

**Funding:** This research was partially funded by the Ningbo Municipal Science and Technology Program (2018B10023).

**Institutional Review Board Statement:** Not applicable.

**Informed Consent Statement:** Not applicable.

**Data Availability Statement:** Not applicable.

**Conflicts of Interest:** The authors declare no conflict of interest.

#### References

- Pires, J.; Martins, F.; Alvim-Ferraz, M.; Simões, M. Recent developments on carbon capture and storage: An overview. *Chem. Eng. Res. Des.* **2011**, *89*, 1446–1460. [CrossRef]
- Nielsen, D.U.; Hu, X.-M.; Daasbjerg, K.; Skrydstrup, T. Chemically and electrochemically catalysed conversion of CO<sub>2</sub> to CO with follow-up utilization to value-added chemicals. *Nat. Catal.* **2018**, *1*, 244–254. [CrossRef]
- Kondratenko, E.V.; Mul, G.; Baltrusaitis, J.; Larrazábal, G.O.; Pérez-Ramírez, J. Status and perspectives of CO<sub>2</sub> conversion into fuels and chemicals by catalytic, photocatalytic and electrocatalytic processes. *Energy Environ. Sci.* **2013**, *6*, 3112–3135. [CrossRef]
- Fu, J.; Jiang, K.; Qiu, X.; Yu, J.; Liu, M. Product selectivity of photocatalytic CO<sub>2</sub> reduction reactions. *Mater. Today* **2020**, *32*, 222–243. [CrossRef]
- Nitopi, S.; Bertheussen, E.; Scott, S.B.; Liu, X.; Engstfeld, A.K.; Horch, S.; Seger, B.; Stephens, I.E.L.; Chan, K.; Hahn, C.; et al. Progress and Perspectives of Electrochemical CO<sub>2</sub> Reduction on Copper in Aqueous Electrolyte. *Chem. Rev.* **2019**, *119*, 7610–7672. [CrossRef]
- Bagger, A.; Ju, W.; Varela, A.S.; Strasser, P.; Rossmeisl, J. Electrochemical CO<sub>2</sub> reduction: A classification problem. *ChemPhysChem* **2017**, *18*, 3266–3273. [CrossRef] [PubMed]

7. Gao, D.; Zegkinoglou, I.; Divins, N.J.; Scholten, F.; Sinev, I.; Grosse, P.; Roldan Cuenya, B. Plasma-activated copper nanocube catalysts for efficient carbon dioxide electroreduction to hydrocarbons and alcohols. *ACS Nano* **2017**, *11*, 4825–4831. [CrossRef]
8. Scholten, F.; Sinev, I.; Bernal, M.; Roldan Cuenya, B. Plasma-modified dendritic Cu catalyst for CO<sub>2</sub> electroreduction. *ACS Catal.* **2019**, *9*, 5496–5502. [CrossRef]
9. Zhu, Q.; Sun, X.; Yang, D.; Ma, J.; Kang, X.; Zheng, L.; Zhang, J.; Wu, Z.; Han, B. Carbon dioxide electroreduction to C<sub>2</sub> products over copper-cuprous oxide derived from electrosynthesized copper complex. *Nat. Commun.* **2019**, *10*, 3851. [CrossRef]
10. Song, Y.; Peng, R.; Hensley, D.K.; Bonnesen, P.V.; Liang, L.; Wu, Z.; Meyer, H.M., III; Chi, M.; Ma, C.; Sumpter, B.G. High-selectivity electrochemical conversion of CO<sub>2</sub> to ethanol using a copper nanoparticle/N-doped graphene electrode. *ChemistrySelect* **2016**, *1*, 6055–6061. [CrossRef]
11. Lum, Y.; Ager, J.W. Stability of residual oxides in oxide-derived copper catalysts for electrochemical CO<sub>2</sub> reduction investigated with <sup>18</sup>O labeling. *Angew. Chem. Int. Ed.* **2018**, *57*, 551–554. [CrossRef] [PubMed]
12. Yan, C.; Luo, W.; Yuan, H.; Liu, G.; Hao, R.; Qin, N.; Wang, Z.; Liu, K.; Wang, Z.; Cui, D. Stabilizing intermediates and optimizing reaction processes with N doping in Cu<sub>2</sub>O for enhanced CO<sub>2</sub> electroreduction. *Appl. Catal. B* **2022**, *308*, 121191. [CrossRef]
13. Cheng, Y.; Yang, S.; Jiang, S.P.; Wang, S. Supported single atoms as new class of catalysts for electrochemical reduction of carbon dioxide. *Small Methods* **2019**, *3*, 1800440. [CrossRef]
14. Liu, H.; Zhu, Y.; Ma, J.; Zhang, Z.; Hu, W. Recent advances in atomic-level engineering of nanostructured catalysts for electrochemical CO<sub>2</sub> reduction. *Adv. Funct. Mater.* **2020**, *30*, 1910534. [CrossRef]
15. Mi, Y.; Peng, X.; Liu, X.; Luo, J. Selective formation of C<sub>2</sub> products from electrochemical CO<sub>2</sub> reduction over Cu<sub>1.8</sub>Se nanowires. *ACS Appl. Energy Mater.* **2018**, *1*, 5119–5123.
16. Li, Z.; Yang, Y.; Yin, Z.; Wei, X.; Peng, H.; Lyu, K.; Wei, F.; Xiao, L.; Wang, G.; Abruna, H.D. Interface-enhanced catalytic selectivity on the C<sub>2</sub> products of CO<sub>2</sub> electroreduction. *ACS Catal.* **2021**, *11*, 2473–2482. [CrossRef]
17. Chan, Y.-T.; Huang, I.-S.; Tsai, M.-K. Enhancing C–C bond formation by surface strain: A computational investigation for C<sub>2</sub> and C<sub>3</sub> intermediate formation on strained Cu surfaces. *Phys. Chem. Chem. Phys.* **2019**, *21*, 22704–22710. [CrossRef]
18. Ghosh, U.; Majumdar, A.; Pal, A. Photocatalytic CO<sub>2</sub> reduction over g-C<sub>3</sub>N<sub>4</sub> based heterostructures: Recent progress and prospects. *J. Environ. Chem. Eng.* **2021**, *9*, 104631. [CrossRef]
19. Shi, H.; Chen, G.; Zhang, C.; Zou, Z. Polymeric g-C<sub>3</sub>N<sub>4</sub> coupled with NaNbO<sub>3</sub> nanowires toward enhanced photocatalytic reduction of CO<sub>2</sub> into renewable fuel. *ACS Catal.* **2014**, *4*, 3637–3643. [CrossRef]
20. Zhao, S.; Tang, Z.; Guo, S.; Han, M.; Zhu, C.; Zhou, Y.; Bai, L.; Gao, J.; Huang, H.; Li, Y. Enhanced activity for CO<sub>2</sub> electroreduction on a highly active and stable ternary Au-CDots-C<sub>3</sub>N<sub>4</sub> electrocatalyst. *ACS Catal.* **2018**, *8*, 188–197. [CrossRef]
21. Jiao, Y.; Zheng, Y.; Chen, P.; Jaroniec, M.; Qiao, S.-Z. Molecular scaffolding strategy with synergistic active centers to facilitate electrocatalytic CO<sub>2</sub> reduction to hydrocarbon/alcohol. *J. Am. Chem. Soc.* **2017**, *139*, 18093–18100. [CrossRef] [PubMed]
22. Wang, H.; Wang, W.; Zhao, Y.; Xu, Z.; Chen, L.; Zhao, L.; Tian, X.; Sun, W. Superior adsorption of 3D nanoporous architectures for Ni (II) ions adsorption using polyvinyl alcohol as cross-linking agent and adsorption conveyor. *RSC Adv.* **2018**, *8*, 7899–7903. [CrossRef] [PubMed]
23. Yuan, T.; Zhang, W.; Li, W.-T.; Song, C.; He, Y.-S.; Razal, J.M.; Ma, Z.-F.; Chen, J. N-doped pierced graphene microparticles as a highly active electrocatalyst for Li-air batteries. *2D Mater.* **2015**, *2*, 024002. [CrossRef]
24. Mao, Z.; Chen, J.; Yang, Y.; Wang, D.; Bie, L.; Fahlman, B.D. Novel g-C<sub>3</sub>N<sub>4</sub>/CoO nanocomposites with significantly enhanced visible-light photocatalytic activity for H<sub>2</sub> evolution. *ACS Appl. Mater. Interfaces* **2017**, *9*, 12427–12435. [CrossRef] [PubMed]
25. Vattikuti, S.P.; Reddy, B.P.; Byon, C.; Shim, J. Carbon/CuO nanosphere-anchored g-C<sub>3</sub>N<sub>4</sub> nanosheets as ternary electrode material for supercapacitors. *J. Solid State Chem.* **2018**, *262*, 106–111. [CrossRef]
26. Bhattacharjee, A.; Ahmaruzzaman, M. Green synthesis of 2D CuO nanoleaves (NLs) and its application for the reduction of p-nitrophenol. *Mater. Lett.* **2015**, *161*, 79–82. [CrossRef]
27. Kliche, G.; Popovic, Z. Far-infrared spectroscopic investigations on CuO. *Phys. Rev. B* **1990**, *42*, 10060. [CrossRef]
28. Li, Y.; Zhang, J.; Wang, Q.; Jin, Y.; Huang, D.; Cui, Q.; Zou, G. Nitrogen-rich carbon nitride hollow vessels: Synthesis, characterization, and their properties. *J. Phys. Chem. B* **2010**, *114*, 9429–9434. [CrossRef]
29. Zheng, L.; Liu, X. Solution-phase synthesis of CuO hierarchical nanosheets at near-neutral pH and near-room temperature. *Mater. Lett.* **2007**, *61*, 2222–2226. [CrossRef]
30. Duan, Y. Facile preparation of CuO/g-C<sub>3</sub>N<sub>4</sub> with enhanced photocatalytic degradation of salicylic acid. *Mater. Res. Bull.* **2018**, *105*, 68–74. [CrossRef]
31. Zhao, L.; Kuang, X.; Liu, Z.; Hou, Y.; Wang, Z.; Wei, Q.; Lee, J.Y.; Kang, B. Anchoring CuO nanoparticles on C, N-codoped G-C<sub>3</sub>N<sub>4</sub> nanosheets from melamine-entrapped MOF gel for high-efficiency oxygen evolution. *ChemNanoMat* **2019**, *5*, 1170–1175. [CrossRef]
32. Li, X.; Wang, Y.; Tian, W.; Cao, J. Graphitic carbon nitride nanosheets decorated flower-like NiO composites for high-performance triethylamine detection. *ACS Omega* **2019**, *4*, 9645–9653. [CrossRef] [PubMed]
33. Fu, Y.; Zhu, C.; Wang, H.; Dou, Y.; Shi, W.; Shao, M.; Huang, H.; Liu, Y.; Kang, Z. High-performance NiO/g-C<sub>3</sub>N<sub>4</sub> composites for visible-light-driven photocatalytic overall water splitting. *Inorg. Chem. Front.* **2018**, *5*, 1646–1652. [CrossRef]
34. Cao, S.-W.; Yuan, Y.-P.; Barber, J.; Loo, S.C.J.; Xue, C. Noble-metal-free g-C<sub>3</sub>N<sub>4</sub>/Ni(dmgh)<sub>2</sub> composite for efficient photocatalytic hydrogen evolution under visible light irradiation. *Appl. Surf. Sci.* **2014**, *319*, 344–349. [CrossRef]

35. Sun, Q.; Lv, K.; Zhang, Z.; Li, M.; Li, B. Effect of contact interface between TiO<sub>2</sub> and g-C<sub>3</sub>N<sub>4</sub> on the photoreactivity of g-C<sub>3</sub>N<sub>4</sub>/TiO<sub>2</sub> photocatalyst: (0 0 1) vs (1 0 1) facets of TiO<sub>2</sub>. *Appl. Catal. B* **2015**, *164*, 420–427.
36. Wu, M.; Zhu, C.; Wang, K.; Li, G.; Dong, X.; Song, Y.; Xue, J.; Chen, W.; Wei, W.; Sun, Y. Promotion of CO<sub>2</sub> Electrochemical Reduction via Cu Nanodendrites. *ACS Appl. Mater. Interfaces* **2020**, *12*, 11562–11569. [CrossRef]
37. Altaf, N.; Liang, S.; Huang, L.; Wang, Q. Electro-derived Cu-Cu<sub>2</sub>O nanocluster from LDH for stable and selective C<sub>2</sub> hydrocarbons production from CO<sub>2</sub> electrochemical reduction. *J. Energy Chem.* **2019**, *48*, 169–180. [CrossRef]
38. Handoko, A.D.; Ong, C.W.; Huang, Y.; Lee, Z.G.; Lin, L.; Panetti, G.B.; Yeo, B.S. Mechanistic insights into the selective electroreduction of carbon dioxide to ethylene on Cu<sub>2</sub>O-derived copper catalysts. *J. Phys. Chem. C* **2016**, *120*, 20058–20067. [CrossRef]
39. Feng, Y.; Li, Z.; Liu, H.; Dong, C.; Wang, J.; Kulinich, S.A.; Du, X.-W. Laser-Prepared CuZn Alloy Catalyst for Selective Electrochemical Reduction of CO<sub>2</sub> to Ethylene. *Langmuir* **2018**, *34*, 13544–13549. [CrossRef]
40. Jeon, H.S.; Kunze, S.; Scholten, F.; Roldan Cuenya, B. Prism-shaped Cu nanocatalysts for electrochemical CO<sub>2</sub> reduction to ethylene. *ACS Catal.* **2018**, *8*, 531–535. [CrossRef]
41. Zhuang, T.-T.; Liang, Z.-Q.; Seifitokaldani, A.; Li, Y.; De Luna, P.; Burdyny, T.; Che, F.; Meng, F.; Min, Y.; Quintero-Bermudez, R.; et al. Steering post-C–C coupling selectivity enables high efficiency electroreduction of carbon dioxide to multi-carbon alcohols. *Nat. Catal.* **2018**, *1*, 421–428. [CrossRef]
42. De Luna, P.; Quintero-Bermudez, R.; Dinh, C.-T.; Ross, M.B.; Bushuyev, O.S.; Todorović, P.; Regier, T.; Kelley, S.O.; Yang, P.; Sargent, E.H. Catalyst electro-redeposition controls morphology and oxidation state for selective carbon dioxide reduction. *Nat. Catal.* **2018**, *1*, 103–110. [CrossRef]
43. Kim, D.; Kley, C.S.; Li, Y.; Yang, P. Copper nanoparticle ensembles for selective electroreduction of CO<sub>2</sub> to C<sub>2</sub>–C<sub>3</sub> products. *Proc. Natl. Acad. Sci. USA* **2017**, *114*, 10560–10565. [CrossRef] [PubMed]
44. Ting LR, L.; Pique, O.; Lim, S.Y.; Tanhaei, M.; Calle-Vallejo, F.; Yeo, B.S. Enhancing CO<sub>2</sub> electroreduction to ethanol on copper–silver composites by opening an alternative catalytic pathway. *ACS Catal.* **2020**, *10*, 4059–4069. [CrossRef]
45. Jiang, K.; Sandberg, R.B.; Akey, A.J.; Liu, X.; Bell, D.C.; Nørskov, J.K.; Chan, K.; Wang, H. Metal ion cycling of Cu foil for selective C–C coupling in electrochemical CO<sub>2</sub> reduction. *Nat. Catal.* **2018**, *1*, 111–119. [CrossRef]
46. Torelli, D.A.; Francis, S.A.; Crompton, J.C.; Javier, A.; Thompson, J.R.; Brunschwig, B.S.; Soriaga, M.P.; Lewis, N.S. Nickel–gallium-catalyzed electrochemical reduction of CO<sub>2</sub> to highly reduced products at low overpotentials. *ACS Catal.* **2016**, *6*, 2100–2104. [CrossRef]
47. Kim, T.; Palmore, G.T.R. A scalable method for preparing Cu electrocatalysts that convert CO<sub>2</sub> into C<sup>2+</sup> products. *Nat. Commun.* **2020**, *11*, 1–11. [CrossRef]





Article

# Oxidative Precipitation Synthesis of Calcium-Doped Manganese Ferrite Nanoparticles for Magnetic Hyperthermia

Sérgio R. S. Veloso <sup>1</sup>, Raquel G. D. Andrade <sup>1</sup>, Valéria Gomes <sup>1,2</sup>, Carlos O. Amorim <sup>3</sup>, Vítor S. Amaral <sup>3</sup>, Verónica Salgueiriño <sup>4,5</sup>, Paulo J. G. Coutinho <sup>1</sup>, Paula M. T. Ferreira <sup>2</sup>, Miguel A. Correa-Duarte <sup>4</sup>, and Elisabete M. S. Castanheira <sup>1,\*</sup>

- <sup>1</sup> Physics Centre of Minho and Porto Universities (CF-UM-UP) and LaPMET Associate Laboratory, University of Minho, Campus de Gualtar, 4710-057 Braga, Portugal  
<sup>2</sup> Centre of Chemistry (CQUM), University of Minho, Campus de Gualtar, 4710-057 Braga, Portugal  
<sup>3</sup> Physics Department and CICECO, University of Aveiro, Campus de Santiago, 3810-193 Aveiro, Portugal  
<sup>4</sup> CINBIO, Universidad de Vigo, 36310 Vigo, Spain  
<sup>5</sup> Departamento de Física Aplicada, Universidad de Vigo, 36310 Vigo, Spain  
\* Correspondence: [ecoutinho@fisica.uminho.pt](mailto:ecoutinho@fisica.uminho.pt); Tel.: +351-253-604-321

**Abstract:** Superparamagnetic nanoparticles are of high interest for therapeutic applications. In this work, nanoparticles of calcium-doped manganese ferrites ( $\text{Ca}_x\text{Mn}_{1-x}\text{Fe}_2\text{O}_4$ ) functionalized with citrate were synthesized through thermally assisted oxidative precipitation in aqueous media. The method provided well dispersed aqueous suspensions of nanoparticles through a one-pot synthesis, in which the temperature and Ca/Mn ratio were found to influence the particles microstructure and morphology. Consequently, changes were obtained in the optical and magnetic properties that were studied through UV-Vis absorption and SQUID, respectively. XRD and Raman spectroscopy studies were carried out to assess the microstructural changes associated with stoichiometry of the particles, and the stability in physiological pH was studied through DLS. The nanoparticles displayed high values of magnetization and heating efficiency for several alternating magnetic field conditions, compatible with biological applications. Hereby, the employed method provides a promising strategy for the development of particles with adequate properties for magnetic hyperthermia applications, such as drug delivery and cancer therapy.

**Keywords:** magnetic nanoparticles; superparamagnetism; citrate-stabilization; calcium ferrites; manganese ferrites; magnetic hyperthermia

**Citation:** Veloso, S.R.S.; Andrade, R.G.D.; Gomes, V.; Amorim, C.O.; Amaral, V.S.; Salgueiriño, V.; Coutinho, P.J.G.; Ferreira, P.M.T.; Correa-Duarte, M.A.; Castanheira, E.M.S. Oxidative Precipitation Synthesis of Calcium-Doped Manganese Ferrite Nanoparticles for Magnetic Hyperthermia. *Int. J. Mol. Sci.* **2022**, *23*, 14145. <https://doi.org/10.3390/ijms232214145>

Academic Editor: Raghvendra Singh Yadav

Received: 24 October 2022  
Accepted: 12 November 2022  
Published: 16 November 2022

**Publisher's Note:** MDPI stays neutral with regard to jurisdictional claims in published maps and institutional affiliations.

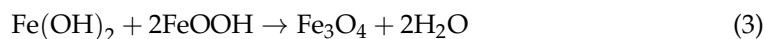


**Copyright:** © 2022 by the authors. Licensee MDPI, Basel, Switzerland. This article is an open access article distributed under the terms and conditions of the Creative Commons Attribution (CC BY) license (<https://creativecommons.org/licenses/by/4.0/>).

## 1. Introduction

Magnetic nanoparticles have been of high interest for several biomedical applications, such as drug and gene delivery [1], magnetic resonance imaging [2], and magnetic hyperthermia [3]. The iron oxides are the most widely used type of magnetic nanoparticles, owing to the high saturation magnetization, chemical stability, low cytotoxicity, and rather easy and scalable synthesis [4]. Particularly interesting is the case of nanoparticles of spinel ferrites, with a unit cell consisting of a cubic close-packed arrangement with 32 oxygen atoms, and 8 tetrahedral (A) and 16 octahedral (B) occupancies for cation doping and distribution, as by the general formula  $(\text{M}^{2+})^A[\text{Fe}_2^{3+}]^B\text{O}_4^{2-}$ , with the consequent tuning of their characteristic properties (e.g., optical, magnetic and dielectric) [4–6]. Particularly, the manganese ferrites' outstanding magnetic properties, high transition temperature, and chemical stability render these particles suitable for several applications, including hyperthermia [7] and MRI [8]. In addition, manganese can be consumed in the amount of 0.67–4.99 mg, with a mean value of 2.21 mg/day [9], and recently the  $\text{Mn}^{2+}$  released concentration from 3 to 18 nm nanoparticles was demonstrated to be in the range of safe doses [10]. Yet, as its cytotoxicity is still of concern [11], other chemical compositions, such as ferrites doped with calcium, have recently been proposed [12–14].

When it comes to the suitable applications of these nanoparticles, stabilization is a major factor to consider, so as to ensure the biocompatibility and prevent particle aggregation. Among the several functional groups that can be employed, the citrate has been commonly used for biomedical applications [15–18], including in commercial iron oxide nanoparticles such as the MRI contrast agent VSOP C184 [19]. Here, the citric acid coordinates the iron oxide surface, leaving at least one carboxylic acid group exposed, thus rendering the surface hydrophilic and avoiding particle aggregation. However, despite being commonly employed as a post-synthesis surface modification [20], if used during the synthetic process, the citric acid molecules can affect both the nucleation and growth, modifying the crystallite size and oxidation degree of the final nanoparticles [15,21–23]. Thus, there has been a growing search for one-pot strategies to obtain well-defined stabilized particles, either employing hydrothermal [18] or co-precipitation methods [15]. Recently, a thermally assisted oxidative precipitation was demonstrated to be a suitable and scalable method for the production of spherical and anisotropic magnetic particles [17,24,25]. In general, the synthesis reaction mechanism is described by an alkalization reaction of ferrous ion to ferrous hydroxide, and consequent dehydration reaction of iron hydroxide and ferric oxyhydroxide (resulting from  $\text{Fe}(\text{OH})_2$  oxidation) to magnetite [26], as follows:



The final size of these superparamagnetic magnetite nanoparticles, stabilized with citrate, was reported to be affected by precursor concentration, ionic strength and reaction time [26]. For instance, the partial oxidation of the initially formed  $\text{Fe}(\text{OH})_2$  into ferric oxyhydroxide is driven by the  $\text{O}_2$  dissolved in water, which, together with the lower ionic strength, leads to larger particles. However, a longer reaction time was reported to decrease the size of the particles. Hence, in this work, we describe the one-pot synthesis of ferrites doped with manganese and/or calcium stabilized with citrate through thermally assisted oxidative precipitation, requiring neither post-synthesis stabilization nor calcination treatment. The effect of the calcium/manganese cation ratio on the nanoparticle morphology and microstructure was studied, as well as the resulting magnetic properties. Further, the suitability of these magnetic nanoparticles for magnetic hyperthermia was assessed for several conditions adequate for biological applications.

## 2. Results and Discussion

### 2.1. Nanoparticles Morphology

A transmission electron microscopy (TEM) analysis (Figure 1) demonstrated that increasing the calcium/manganese ratio affected the final morphology of the nanoparticles, narrowing the size distribution and decreasing the average size (from ~20 nm to ~5 nm). For instance, the presence of only manganese led to larger polydisperse particles, comprising single and multicore particles (more images of obtained structures are in Figure S1 in Supplementary Material). Doaga et al. [7] also reported for manganese doped ferrites that a higher content of manganese favoured the formation of larger particles obtained through co-precipitation method. The addition of calcium strongly favoured the formation of smaller and more monodisperse particles (Figure S2), but also displayed nanorod/spindle like structures. The formation of rods can be associated with the lepidocrocite or goethite as by-products of ferrous ion oxidation [27].

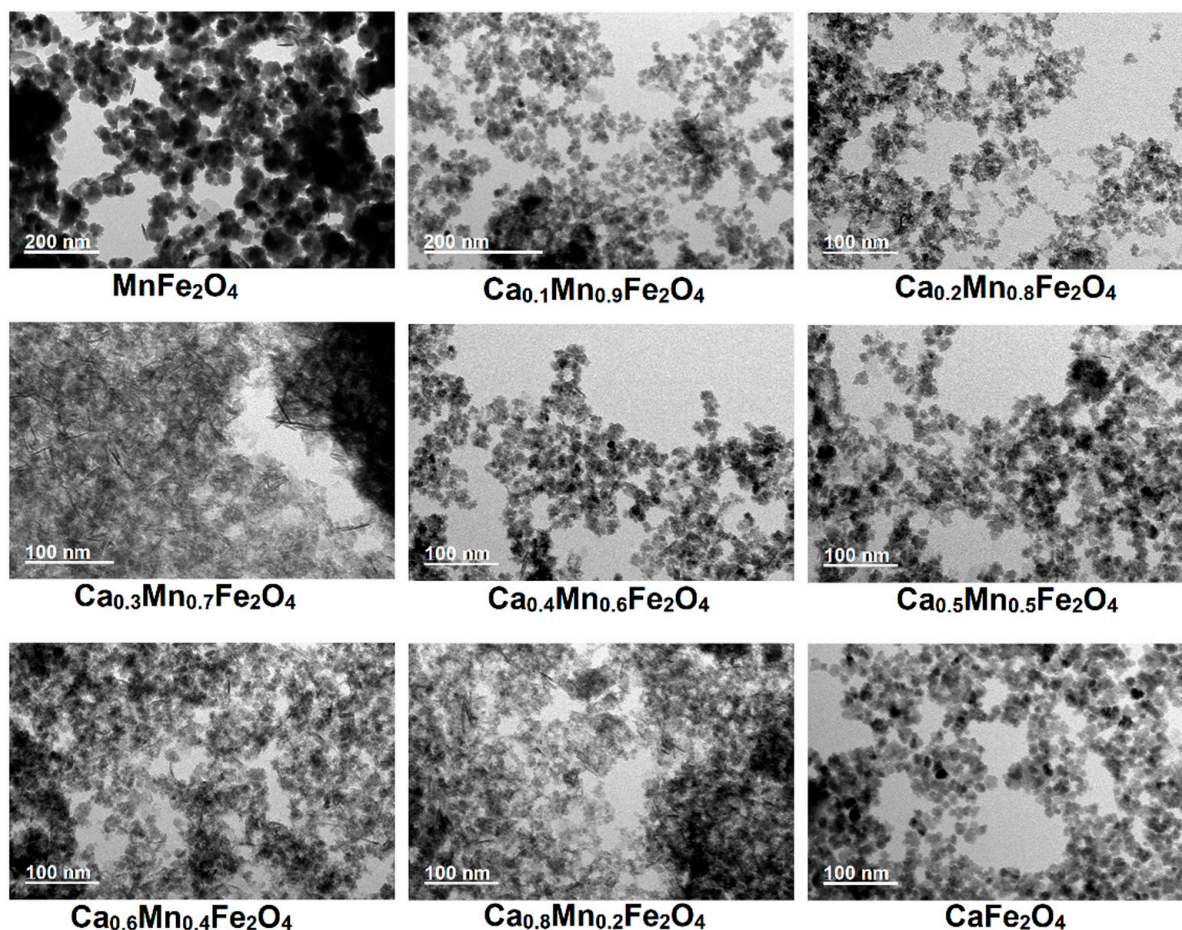


**Figure 1.** TEM images of the synthesized calcium and manganese-doped ferrites at 90 °C.

The multicore-like structures were mainly observed in the  $x = 0.4$ – $0.6$  calcium nominal fractions, and also in the  $x = 0.1$  and  $x = 0.2$  fractions, whereas a content of  $x = 0.3$  and  $x = 0.8$  presented a higher amount of small single core and rod-like structures. In the case of the samples synthesized with only calcium as dopant, (pseudo-)cubic and multicore-like particles were observed, and the sample was devoid of rod-like particles. The formation of multicore/flower-like particles was also reported by Gavilán et al. [28] from the oxidation of the  $\text{Fe}(\text{OH})_2$  intermediate in water in the presence of dextran.

The smaller size of the calcium (doped) ferrites can be associated with the prevention of crystal growth by  $\text{Ca}^{2+}$  as reported for other ferrites [29,30], in which the presence of citrate ions can provide additional electrostatic and steric repulsion, and thus hamper the fusing of the generated nuclei into larger particles. In addition, citrate is reported to not only prevent the oxidation of iron oxide to hematite [18], but also hamper the oxidation of  $\text{Fe}(\text{II})$ , as carboxylates are stronger complexing agents than the anions of simple ferrous salts [17], thus also delaying the nucleation. Nonetheless, the citrate role in ensuring a smaller size was clearly confirmed by the larger particle size obtained for manganese ferrites synthesized without citrate (Figure S3). In this sense, the presence of citrate is crucial to favor the repulsion between the initially formed nuclei, thus leading to the formation of smaller particles and also of multicore/flower-like particles, as the fusion between the formed cores is prevented.

Considering that the stabilization by citrate results from the chemical bonds between carboxyl groups of citrate and OH groups of the magnetic nanoparticles surface [15], a higher reaction temperature was tested to assess the impact of an increased chemical reaction rate. As displayed in Figure 2, a higher temperature (100 °C) led to samples devoid of rod-like structures and a predominance of the multicore particles, in both stoichiometric

manganese and calcium ferrites. The formation of smaller single cores of the magnetic nanoparticles was noticed in the case of the calcium ferrite, which decreased from  $\sim 7$  nm to  $\sim 4$  nm, but not in the case of the manganese ferrite, which kept the same average size ( $\sim 19$  nm). Both samples displayed a large content of multicore particles with average sizes of  $\sim 50$  nm and  $\sim 20$  nm for the manganese and calcium ferrite, respectively. Summarizing this part, the thermally assisted oxidative precipitation in the presence of citrate and at  $100^\circ\text{C}$  offers control over the production of multicore/flower-like nanoparticles, with the dopant ion playing a role in determining the final size of the small single cores. Nonetheless, the results are also promising for future research in the exploration of other reaction conditions, including the oxidant, as a means to assess other morphologies or tune the ones here described.

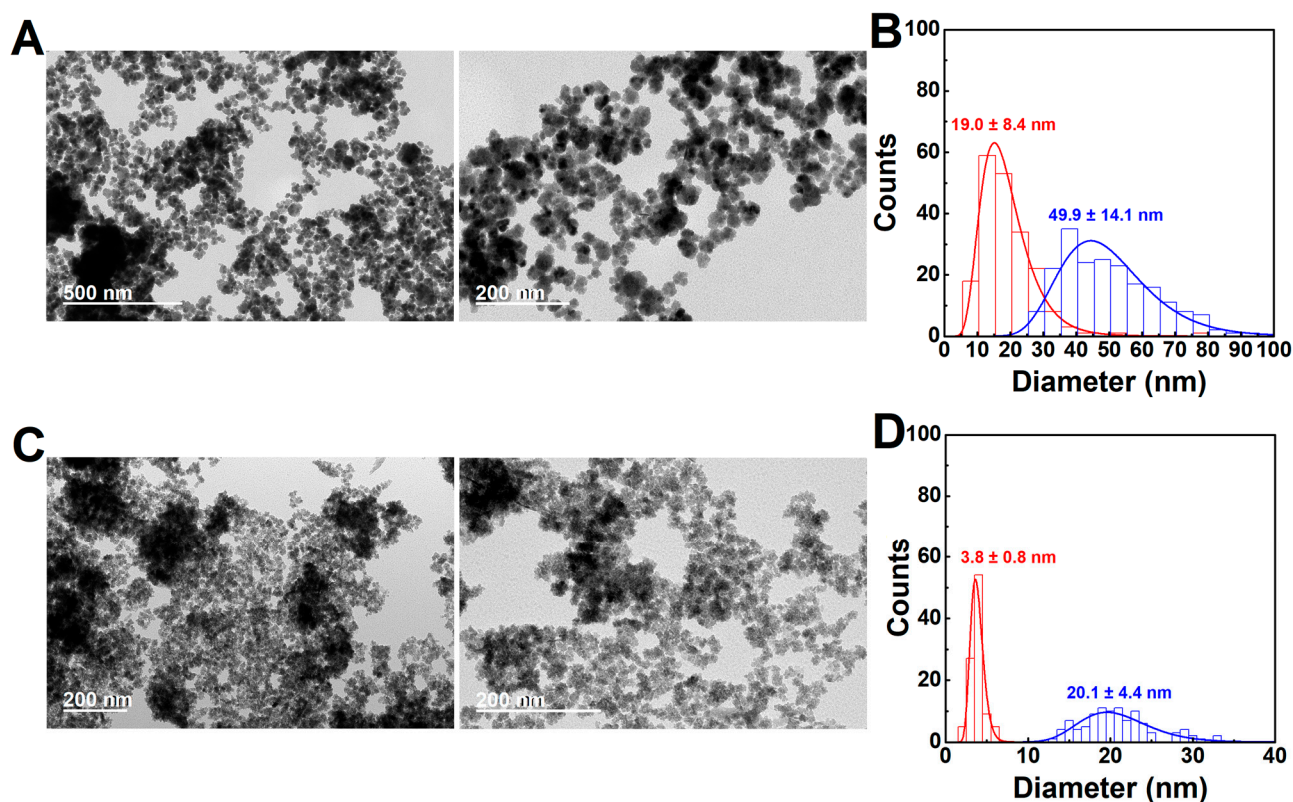


**Figure 2.** TEM images and histograms of the particles obtained from the synthesis of (A,B) manganese and (C,D) calcium ferrites at  $100^\circ\text{C}$ , in the presence of citric acid. The red histogram corresponds to the smaller single cores forming part of the multicore-like particles (blue histogram).

## 2.2. Microstructure Characterization

### 2.2.1. X-ray Diffraction Analysis

X-ray diffraction (XRD) studies were carried out to determine the phase composition and crystalline domain size of the nanoparticles, as well as to understand the changes observed in the particle size. The XRD patterns in Figure 3A–C revealed that all synthesized particles displayed crystalline nature, which endows the employed method suitable to achieve crystalline manganese and/or calcium ferrite nanoparticles, as other synthesis routes of calcium-doped ferrites require calcination after synthesis [14,29,30]. In all the cases, the patterns displayed Bragg's reflections characteristic of the  $Fd\bar{3}m$  space group, that can be indexed as (1 1 1), (2 2 0), (3 1 1), (4 2 0), (5 1 1), (4 4 0), and (6 2 0), reflecting the presence of manganese/calcium ferrites with a cubic structure [31–33]. Yet, another phase was formed in the samples with a larger calcium content ( $x > 0.2$ ), with peaks indexed as (1 0 4), (1 1 0), (1 1 3), (2 0 2), (0 2 4), (0 1 8) and (1 1 6), associated with the presence of calcite (calcium carbonate) rhombohedral structure belonging to the  $R\bar{3}c$  space group. Thus, the

results also suggest that the obtained rods are a shape by-product of the reaction, and not lepidocrocite or goethite.

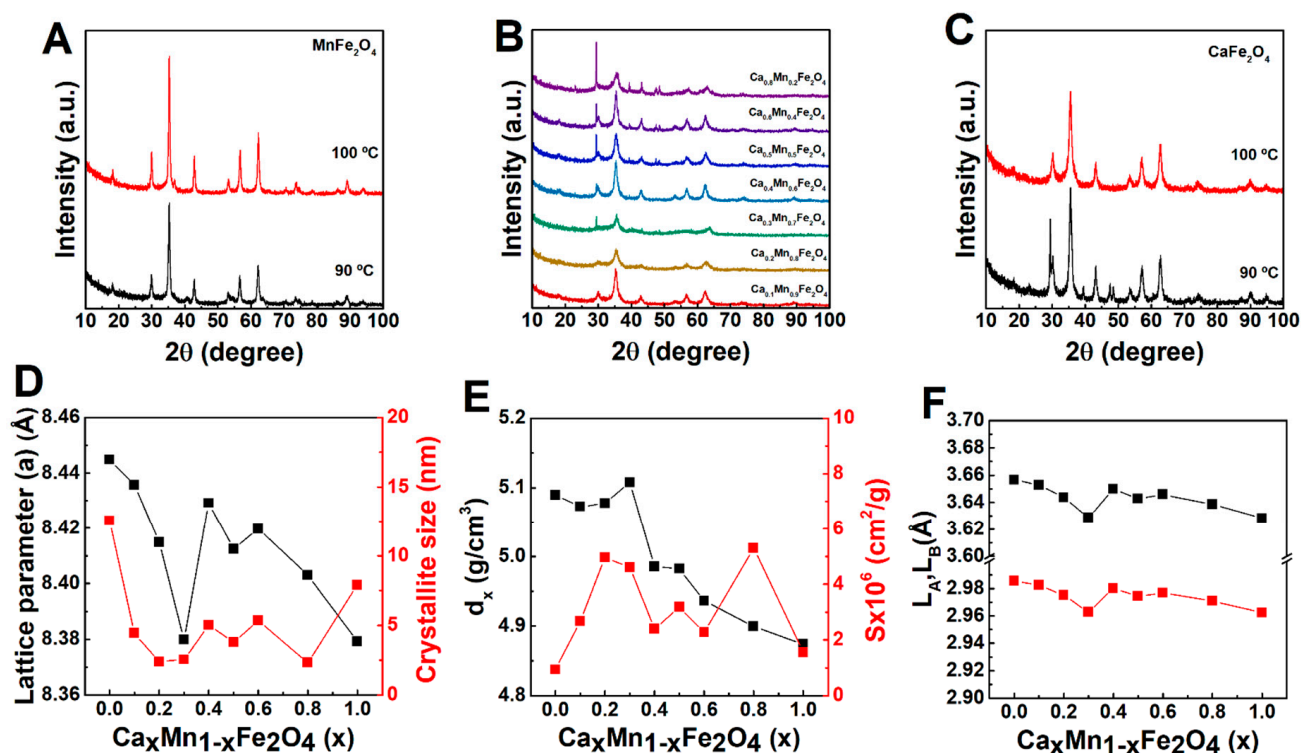


**Figure 3.** XRD patterns of (A) manganese ferrites, (B) calcium and manganese mixed ferrites, and (C) calcium ferrites. Dependence of (D) lattice parameter, crystallite size, (E) X-ray density ( $d_x$ ), specific surface area ( $S$ ), and (F) hopping length in tetrahedral ( $L_A$ ) and octahedral ( $L_B$ ) sites on the  $\text{Ca}^{2+}$  and  $\text{Mn}^{2+}$  content.

The synthesis of both stoichiometric manganese and calcium ferrites at 100 °C led to single-phase nanoparticles, suggesting that the calcium carbonate present in the mixed ferrites can be an intermediate of the reaction that is not completed at 90 °C. In this sense, the results suggest that  $\text{Ca}^{2+}$  might interfere with the nucleation and growth of the crystals, with a fraction of the iron ions remaining in an amorphous phase (mostly for  $x = 0.3$  in a  $\text{Ca}_x\text{Mn}_{1-x}\text{Fe}_2\text{O}_4$  ferrite). For instance, the formation of calcium carbonate has also been reported by Gomes et al. [34] in a sol-gel synthesis method, in which a single phase of  $\text{CaFe}_2\text{O}_4$  could be achieved through calcination at 1000 °C.

The Rietveld refinement method was employed to assess the crystallographic properties of the several synthesised particles (see the refinement of each profile in Figure S4). As displayed in Figure 3D, the replacement of  $\text{Mn}^{2+}$  (0.80 Å) with  $\text{Ca}^{2+}$  (0.99 Å) led to a decrease of the average crystallite size, which is in agreement with TEM results. Hashhash et al. [35] suggested that a decrease of the particle size with  $\text{Ca}^{2+}$  content could be associated with the reaching of the ion's solubility limit, which leads to its accumulation in the grain boundaries, thus suppressing the grain growth. In addition, the lattice parameter  $a$  also decreased, though an average increased value was obtained at  $x = 0.4$ . This behaviour can be associated with the occupation of the B-sites by  $\text{Ca}^{2+}$  ions, that have a larger ionic radius [35]. However, at  $x = 0.4$ , the migration of  $\text{Ca}^{2+}$  from B to A-sites might be favoured, promoting the migration of the smaller  $\text{Mn}^{2+}$  or  $\text{Fe}^{3+}$  ions to the B-sites. Chhaya et al. [36] reported that migration of  $\text{Ca}^{2+}$  to the A-sites replaces the smaller  $\text{Fe}^{3+}$  (0.64 Å), while a further increase might lead to a continuous reduction of  $\text{Ca}^{2+}$  ions in the A-sites and consequent reduction of lattice constant. Besides, Islam et al. [8] also reported that for a larger particle size the  $\text{Mn}^{2+}$  tended to occupy the A-sites. In this way, the hopping lengths in tetrahedral ( $L_A$ ) and octahedral ( $L_B$ ) sites displayed a decreasing trend with the  $\text{Ca}^{2+}$

content (except at  $x = 0.4$ ), which was also obtained for the particles synthesized at 100 °C (see Table S1 in Supplementary Material). Further, for a low  $\text{Ca}^{2+}$  content ( $x < 0.4$ ), the change in the molecular weight is not significant, so the decrease of the cell unit volume leads to an increase of the X-ray density and specific surface area, while both fell for larger  $\text{Ca}^{2+}$  content, except at  $x = 0.8$ , in which the concomitant reduction of crystallite size led to a larger specific surface area. Other parameters were calculated (Table S2), including the tetrahedral and octahedral radii, that further suggest the discussed transfer of  $\text{Ca}^{2+}$ ,  $\text{Mn}^{2+}$  and  $\text{Fe}^{3+}$  between A- and B-sites. The preferential occupation of the B-sites by  $\text{Ca}^{2+}$  and the formation of inverse spinels was also confirmed through estimation of the cation distribution using the Bertaut method (see discussion and Table S3 in Supplementary Material) [37].

### 2.2.2. Raman Spectroscopy Characterization

Raman spectroscopy studies were carried out to get further insight into microstructural changes of the nanoparticles. A comparison of the several samples of nanoparticles obtained through synthesis at 90 °C is displayed in Figure 4, and the deconvolution with Lorentzian curves is included in Figure S5 (Supplementary Material). The samples did not display the calcite bands, which are commonly observed at  $\sim 150\text{ cm}^{-1}$ ,  $280\text{ cm}^{-1}$  and  $712\text{ cm}^{-1}$  [38], possibly for being below the threshold of the device sensitivity. The group theory predicts five Raman active modes for spinels with  $\text{Fd}3\text{m}$  space group ( $\text{A}_{1\text{g}} + \text{E}_{\text{g}} + 3\text{T}_{2\text{g}}$  bands), associated with the motion of O ions in the A and B-sites [39–42]. In general, when considering nanoparticles, the  $\text{A}_{1\text{g}}$ ,  $\text{T}_{2\text{g}}(2)$ , and  $\text{E}_{\text{g}}$  Raman modes are the most intense, located in this case around  $\sim 670\text{ cm}^{-1}$ ,  $\sim 450\text{ cm}^{-1}$ , and  $\sim 320\text{ cm}^{-1}$ , respectively (values reported in Table S4), which closely match other reported values for manganese-doped ferrites [43,44]. Besides, the spectra displayed some resemblance to profiles commonly observed in inverted spinels [45]. Particularly, the  $\text{A}_{1\text{g}}$  is associated with the symmetric stretching of O ions with respect to the metal ion in A-sites, which occurs together with the deformation of three metal-oxygen bonds at the octahedral sites (as the tetrahedral sites are not isolated) [40], thus being sensitive to the mass of the tetrahedral cation and size of the nanoparticles [46]. Hence, the splitting of the  $\text{A}_{1\text{g}}$  mode in two modes, as displayed in Figure 4B,C, can be associated to the fact of having two different cations in A and/or B sites. In addition to the metal-doping associated changes, the increase of  $\text{Ca}^{2+}$  was accompanied by a decrease of particle size, which is also suggested by an overall downshift, broadening of the Raman bands and intensity decrease resulting from the increase of micro-deformation and/or the dominance of phonon confinement [39,46]. Further, the incremental  $\text{Ca}^{2+}$  content induced changes also displayed some relation with the variation of lattice parameter (see further discussion in Supplementary Material) that further confirmed the ions distribution in both A and B-sites.

### 2.3. Optical Properties

The nanoparticles optical properties also displayed changes associated with the synthesis temperature and Ca/Mn ratio. Regarding the latter, the UV-vis absorbance was observed to achieve an enhanced absorbance in the near-infrared region at larger  $\text{Mn}^{2+}$  content, which has been commonly reported for manganese-doped ferrites [47].

The Tauc plot was further employed (see plots in Figure S6 in Supplementary Material) to estimate the optical direct band gap, as also described for other ferrites [48,49]. Here, the increased content of  $\text{Mn}^{2+}$  ions was accompanied by a red-shift of the optical band gap, which was found to decrease by synthesizing the particles at 100 °C. The red-shift of calcium ferrites band gap has also been reported for doping with  $\text{Co}^{2+}$  [49], which was associated with the increased particle size leading to a larger distance between atoms, and thus a reduction of the potential energy of materials' electrons. In the work by Samira et al. [47], the substitution of Ni by Mn also produced a red-shift of the optical band gap, which was associated to Mn inducing inner bands that provided additional paths between the conduction and valence bands, producing a decrease of the band gap value.

In this sense, the results suggest that both the Ca/Mn ratio and synthesis temperature affect the optical band gap. Thus, both parameters can be employed to tune the specific capacitance that is commonly larger for smaller band gaps [47] and the energy harvesting ability of the nanoparticles, which can be of interest for photocatalysis applications in environmental cleaning.

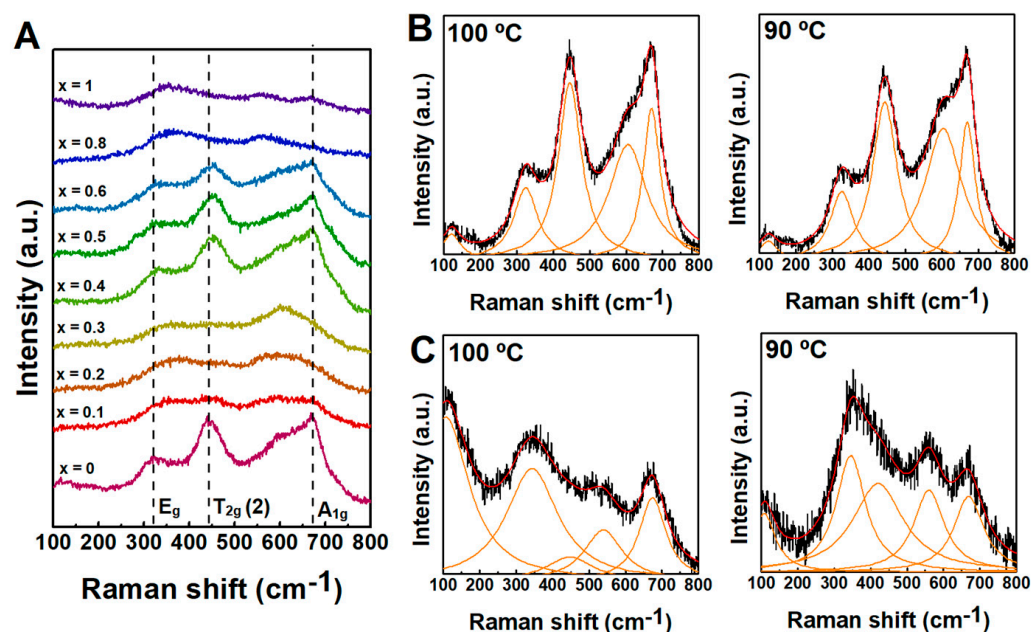


**Figure 4.** (A) A comparison of the Raman scattering spectra of the manganese- and/or calcium-doped ferrites obtained at 90 °C. The fitting of Lorentzian bands to Raman spectra of (B) manganese and (C) calcium ferrites synthesised at 90 °C and 100 °C.

#### 2.4. Hydrodynamic Diameter and Zeta Potential

The behaviour of nanoparticles in the solution was studied at a concentration of 0.01 mg/mL. In agreement with the TEM and XRD results, the increasing content of  $\text{Ca}^{2+}$  ions led to a decrease of the hydrodynamic diameter (Figure 5C), which was also decreased by carrying out the synthesis at 100 °C. The obtained hydrodynamic diameter was obviously larger than the physical particle size, which can be associated with the high stability of the nanoparticles, as resulting from the electrostatic double layer stabilizing the nanoparticles in the solution or the formation of aggregates [50]. Indeed, this increased stability is also suggested by the rather low polydispersity index (in the ~0.1–0.2 range, Figure 5D), which might result from the particles dispersing into quasi-monodisperse structures, as also pointed out by the correlograms single decay in the majority of the samples (see Figure S7 in Supplementary Material). Further proof of the stability is confirmed by the highly negative zeta potential (Figure 5E) associated with the citrate functionalization at the nanoparticles surface, and correlated with the lack of noise (absence of sedimentation) in the correlograms.

In line with these results, the stabilization with citrate has been demonstrated to endow nanoparticles with good colloidal stability and circulation time, very appropriate for the potential bio-related applications [51,52]. Though a protein corona is commonly formed upon contact of the nanoparticles with the biologic fluids, which can influence the particle size and, consequently, the biodistribution in vivo and blood-clearance [53,54], the magnetic hyperthermia (vide infra) ability should not become substantially affected. Besides, the citrate negative charge provides a means for the adsorption and delivery of chemotherapeutic drugs through electrostatic interactions, such as doxorubicin [55], rendering the particles a versatile platform for further developments in biomedical applications.

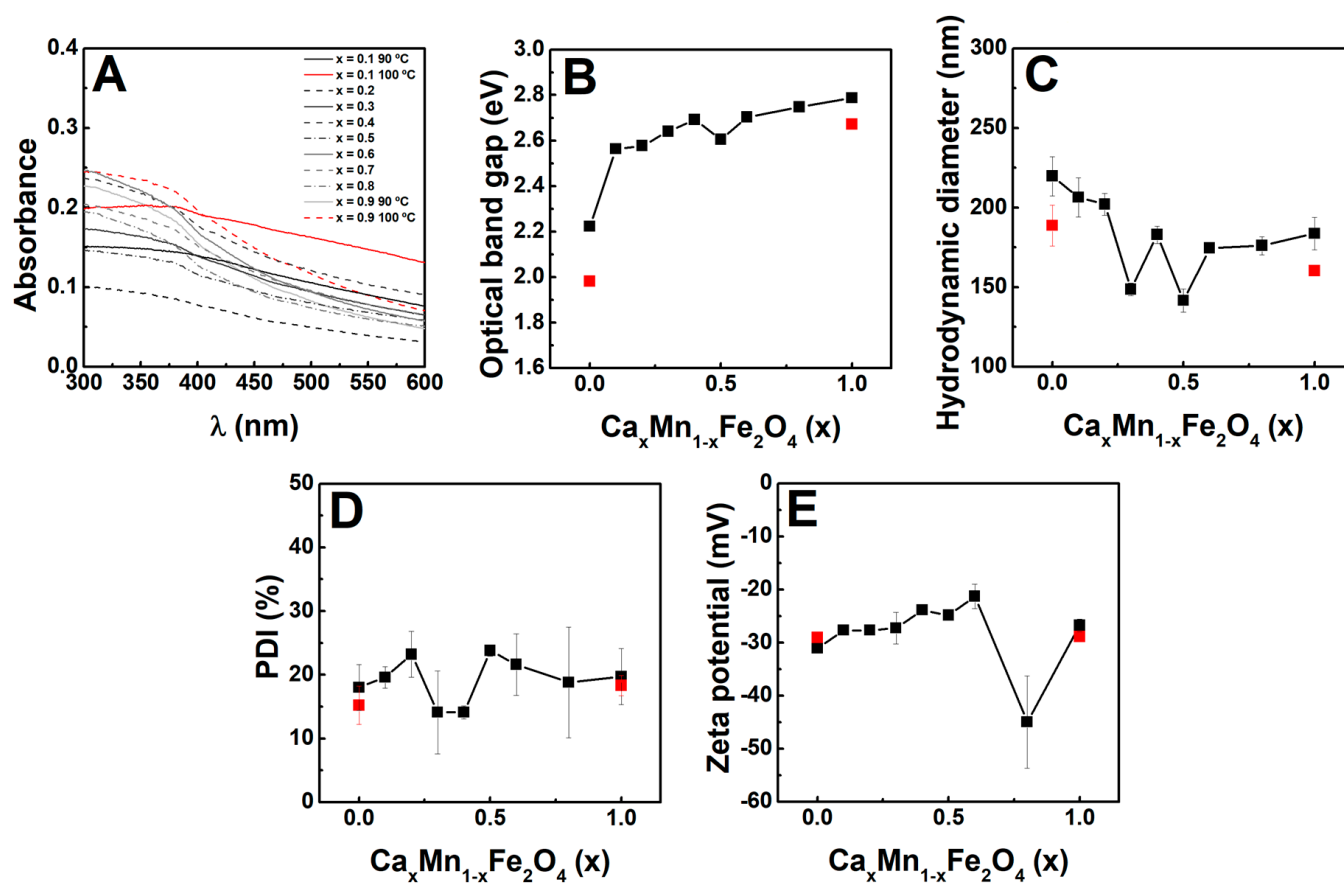


**Figure 5.** (A) UV-vis absorption spectra of the synthesized nanoparticles at 0.01 mg/mL and (B) dependence of the optical band gap on the Ca/Mn content for the particles synthesized at 90 °C (black squares) and 100 °C (red squares). The dependence of (C) hydrodynamic diameter, (D) polydispersity index (PDI), and (E) zeta potential on the particle type at 0.01 mg/mL is also included.

### 2.5. Magnetic Properties

Figure 6A includes the field-dependent magnetization of the different samples of Ca-doped manganese ferrite nanoparticles, offering relatively large values of saturation magnetization and negligible values of coercivity and remanence, at 300 K (see also Figure S8 and Table S5), reflecting superparamagnetic behaviour in all cases [56]. The largest values of saturation magnetization were registered for the stoichiometric manganese or calcium ferrite synthesised at 100 °C, stemming from the distribution of the magnetic cations ( $\text{Mn}^{2+}$  and  $\text{Fe}^{3+}$ ) in the crystalline structure (Figure 6B). The reproducibility of the method was also evidenced by the similarity of the stoichiometric manganese ferrite magnetic properties to other reported particles for the same synthesis method [57].

Regarding the particles with intermediary composition, the saturation magnetization displayed a Ca/Mn ratio dependence profile similar to the obtained in the crystallite and particle size, in which the obtained magnetization decreases for smaller sizes. This effect for individual particles is usually ascribed to the formation of a dead layer inversely proportional to the particle size, in which the spin canting and surface disorder (in-homogeneities, oxidation, and truncation of the crystalline lattice) are detrimental for the saturation magnetization [18,58,59]. However, this effect is very small and alone is not enough to explain the results, as the saturation magnetization remained reasonably high in some mixed ferrites, such as in the range  $x = 0.4$  to  $0.6$ , despite displaying smaller particle size than the  $\text{CaFe}_2\text{O}_4$  and  $\text{MnFe}_2\text{O}_4$  particles. Instead, as these samples were observed to display a cluster like morphology, in which close contacts are formed between the nanoparticles in each cluster, the minimization of the magnetic dead layer effect can be associated with the promotion of direct exchange and dipolar interactions that are described to minimize the decrease of

the saturation magnetization [59]. Nonetheless, the inversion degree and inter-sublattice A-B super-exchange interaction were found to well describe the saturation magnetization dependence on the Ca/Mn ratio (see discussion and Figure S9A,B in Supplementary Material) [4,32,33,60–65].

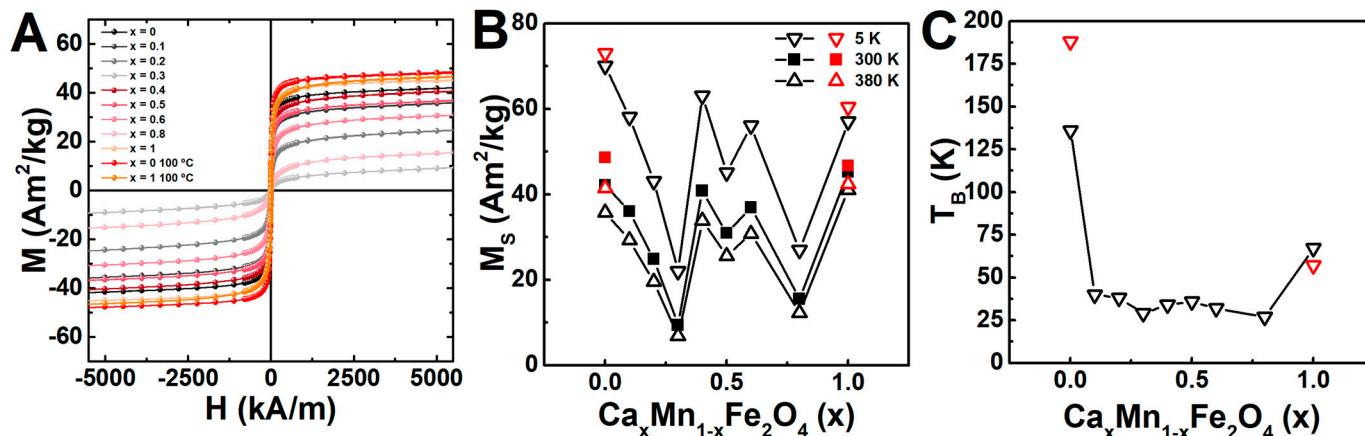


**Figure 6.** (A) Magnetization dependence on the applied magnetic field obtained for the manganese- and/or calcium-doped ferrites obtained at  $90^\circ\text{C}$  (from  $x = 0$  to  $x = 1$ ) and  $100^\circ\text{C}$  ( $x = 0$  and  $x = 1$ ) measured at  $300\text{ K}$ . Dependence of the (B) saturation magnetization and (C) blocking temperature on the Ca/Mn ratio obtained from ZFC and FC curves under a field of  $100\text{ Oe}$ .

In addition to the size and dipolar interactions between the clusters' nanoparticles, the ferrites magnetocrystalline anisotropy plays a huge role in the final magnetic behavior, as evidenced in the measurements at  $5\text{ K}$ , in which the coercivity displayed a  $\text{Ca}^{2+}$  content dependence profile (Figure S9C), in line with the pointed-out distribution of magnetic cations.

The magnetic properties were further characterized through zero field cooled (ZFC) and field cooled (FC) measurements under an applied field of  $100\text{ Oe}$ . The ZFC-FC magnetization curves are displayed in Figure S10 in Supplementary Materials. The broader ZFC curves suggested larger particle size dispersity [4], which is mainly noticeable in the samples with  $x = 0$  and in agreement with the TEM results. Nevertheless, the dipolar interactions between nanoparticles in the final flower-like structures should be taken into account as well [59], since this is suggested by the FC magnetization curve flatness observed in the low temperature range (mainly in the samples range from  $x = 0.4$  to  $x = 1$ ) [66,67]. Figure 6 includes the blocking temperature dependence on Ca/Mn ratio, obtained from the ZFC derivative ( $dM/dT$ , shown in Figure S10) [68], reflecting the highest values for the manganese ferrites. Furthermore, the obtained blocking temperatures for  $\text{CaFe}_2\text{O}_4$  and  $\text{MnFe}_2\text{O}_4$  particles were similar to other reported particles [69,70], proving therefore the reproducibility of the method. Overall, the magnetic characterization proves that the nanoparticles of  $\text{CaFe}_2\text{O}_4$ ,  $\text{MnFe}_2\text{O}_4$  and of intermediary formulations ( $x = 0.4$  to  $0.6$ ) are superparamagnetic at room temperature and therefore very promising for magnetic targeting applications, given the large values of saturation magnetization.

## 2.6. Magnetic Hyperthermia

The heating efficiency of the nanoparticles was evaluated considering alternating magnetic fields (AMF) of different amplitude and frequency, but fulfilling the medical threshold limit of  $H_0f \leq 5 \times 10^9\text{ A m}^{-1}\text{ s}^{-1}$  [71]. The heating profiles are displayed in Figure 7.

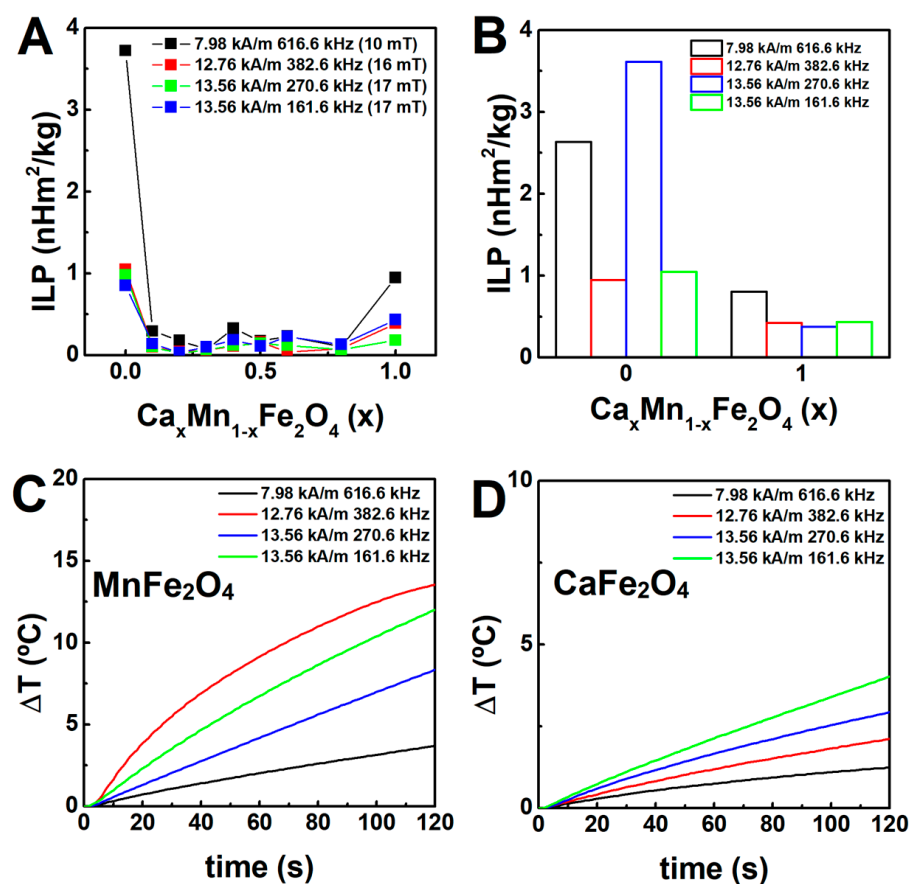


**Figure 7.** (A) Dependence of the intrinsic loss power (ILP) on the composition of the nanoparticles at 5 mg/mL. (B) ILP and (C,D) temperature variation over time of the manganese and calcium-doped ferrites obtained through synthesis at 100 °C. The equivalent magnetic flux density is also indicated in brackets.

In general, the incremental content of Ca<sup>2+</sup> ions (in substitution of Mn<sup>2+</sup> ions) led to a decrease of the heating efficiency (Figure 7A) that was quantitatively evaluated through the intrinsic loss power (ILP). However, a slight increase was obtained in the range  $x = 0.4$  to  $x = 0.6$ , given the particular distribution of magnetic cations in the spinel ferrite crystalline structure for these stoichiometries. Furthermore, the samples synthesized at 100 °C displayed similar or slightly improved heating efficiency (Figure 7B) than the batch obtained at 90 °C, owing to the absence of phase impurities. Both samples of nanoparticles considered in this analysis induced a rather large temperature variation in 2 min (~15 °C when applying a field of ~13 kA/m (17 mT) and 382.6 kHz, in the case of the manganese ferrite, and ~4 °C with a field of ~13 kA/m (17 mT) and 161.6 kHz, for the calcium ferrite, of which mild hyperthermia treatments can take advantage of, in a short period of time.

Compared to other reported magnetic nanoparticles, the developed CaFe<sub>2</sub>O<sub>4</sub> and MnFe<sub>2</sub>O<sub>4</sub> particles displayed similar or improved heating efficiency than other transition metal-doped [72], cobalt-doped [73,74], calcium-doped [75], manganese-doped [8], and multicore particles [76].

Hence, the high heating efficiency of the manganese- and calcium-doped ferrites, together with the superparamagnetic behaviour, endow the developed particles suitable for magnetic hyperthermia therapy. Nonetheless, the exploration of several synthesis parameters, including reaction time, salts/reagents/ligand concentration, and reducing agents, are envisioned as future works to fine-tune the shape and heating performance of the developed particles.

### 3. Materials and Methods

#### 3.1. Synthesis of Magnetic Nanoparticles

Citrate-stabilized iron oxide nanoparticles doped with calcium and/or manganese were synthesized through an oxidative precipitation method adapted from [26]. In general, trisodium citrate dehydrate (1 mmol) and NaOH (4 mmol) were added to 19 mL of ultrapure water at 90 °C or 100 °C. A 1 mL aqueous solution of FeSO<sub>4</sub>·7H<sub>2</sub>O (1.33 mmol) and the doping metal salt (MnSO<sub>4</sub>·H<sub>2</sub>O, Ca(CH<sub>3</sub>CO<sub>2</sub>)<sub>2</sub>) (0.66 mmol) was added, drop by drop, into the mixture under vigorous agitation and air open. After 2 h, the solution was cooled down to room temperature, washed through magnetic decantation with water/ethanol 1:1, and dried at 80 °C.

#### 3.2. General Spectroscopic Methods

Absorption spectra were recorded in a Shimadzu UV-3600 Plus UV-Vis-NIR spectrophotometer (Shimadzu Corporation, Kyoto, Japan). A conventional PAN'alytical X'Pert PRO diffractometer (Malvern Panalytical Ltd., Malvern, UK) was used for X-ray diffraction (XRD) analyses, operating with Cu K<sub>α</sub> radiation, in a Bragg-Brentano configuration, at the Electron Microscopy Unit, University of Trás-os-Montes and Alto Douro (UTAD), Vila Real, Portugal. Raman spectroscopy measurements were performed at room temperature with a Renishaw inVia Reflex Raman confocal microscope system (Wotton-under-Edge, Stroud, UK), equipped with a high-resolution grating of 1200 grooves mm<sup>-1</sup>. The excitation line, 785 nm, of a NIR diode laser was focused onto the sample by a ×20 objective with a numerical aperture (NA) value of 0.40 in a backscattering geometry. The spectra were acquired with a measured power of about 650 μW on the sample, with a spectral acquisition time of 120 s over one accumulation and the range 100–1000 cm<sup>-1</sup>. The average hydrodynamic diameter and zeta potential of the nanoparticles (n = 3 independent runs) were measured in phosphate buffer pH 7.4 at 0.01 mM in a Dynamic Light Scattering (DLS) equipment Litesizer™ 500 from Anton Paar (Anton Paar GmbH, Graz, Austria), using a semiconductor laser diode of 40 mW and λ = 658 nm, backscatter angle (175°), and a controlled temperature of 25 °C.

#### 3.3. Transmission Electron Microscopy (TEM)

TEM images of nanoparticles were recorded using a high contrast JEOL JEM-1010, operating at 100 kV (CACTI, Vigo, Spain). A small portion of the sample was placed onto a TEM 400 mesh copper grid with Formvar/Carbon (ref. S162-4 from Agar Scientific), held by tweezers and the excess solution was cleaned. The processing of STEM images was performed using ImageJ software (National Institutes of Health, NIH, Bethesda, MD, USA), which consisted in enhancing local contrast and adjusting brightness followed by manual selection of fibres.

#### 3.4. Magnetic Properties

Magnetic measurements were performed in an MPMS3 SQUID magnetometer (Quantum Design Inc., San Diego, CA, USA). The field-dependent magnetization (hysteresis cycles) of the samples were measured in the large field range (up to H = 5570.42 kA/m or B = 7 T) for each sample. In all the cases at 5 K, 300 K, and 380 K, given the room temperature applications they are designed for, a specific magnetic field correction for the trapped flux in the superconducting coil was conducted, achieving an accuracy of residual less than 0.16 kA/m [77].

#### 3.5. Hyperthermia Measurements

With the aim of evaluating the heating performance, magneto-caloric measurements were carried out using a hyperthermia system magneTherm (nanoTherics, Warrington, UK), working at f ≈ (162, 271, 383, 617) kHz and at the magnetic field H = (13.56, 12.76, 7.98) kA/m. For all experiments, the initial temperature was stabilized before starting the

measurement. Next, the AC magnetic field was applied for 10 min, and the temperature variation was recorded using a thermocouple.

#### 4. Conclusions

In this work, citrate-stabilized multicore nanoparticles of Ca-doped manganese ferrite ( $\text{Ca}_x\text{Mn}_{1-x}\text{Fe}_2\text{O}_4$ ) were synthesized through a thermally assisted oxidative precipitation in aqueous media. While the incremental content of calcium was found to decrease the average nanoparticle size, decreasing the synthesis temperature from 100 to 90 °C was accompanied by the formation of an impurity phase of calcite.

Regarding the resulting particle shape, the synthesis resulted in the formation of single, multicore and rod-like particles, but the synthesis carried out at 100 °C allowed to preferentially obtain the multicore nanoparticles. Furthermore, the variation in the Mn/Ca ratio led to changes in the microstructure, mainly in the lattice parameter and cation distribution, and consequently in the final magnetic properties.

The particles displayed great colloidal stability, with a low polydispersity, lack of sedimentation and highly negative zeta potential.

The obtained calcium-doped manganese ferrite nanoparticles displayed relatively large values of saturation magnetization and heating efficiency, higher than other reported superparamagnetic nanoparticles, which, together with the superparamagnetic behaviour, render them suitable for therapeutic applications, such as drug delivery and cancer therapy.

**Supplementary Materials:** The following supporting information can be downloaded at: <https://www.mdpi.com/article/10.3390/ijms232214145/s1>.

**Author Contributions:** Conceptualization, S.R.S.V. and E.M.S.C.; methodology, S.R.S.V., R.G.D.A., V.S., M.A.C.-D. and E.M.S.C.; validation, V.S.A., P.J.G.C., M.A.C.-D., and E.M.S.C.; formal analysis, S.R.S.V., V.G., C.O.A. and V.S.; investigation, S.R.S.V., R.G.D.A., V.G., V.S. and C.O.A.; writing—original draft preparation, S.R.S.V.; writing—review and editing, E.M.S.C.; visualization, V.S.A., P.M.T.F. and M.A.C.-D.; supervision, P.M.T.F., M.A.C.-D. and E.M.S.C.; project administration, P.J.G.C., P.M.T.F. and M.A.C.-D. All authors have read and agreed to the published version of the manuscript.

**Funding:** This work was funded by the Portuguese Foundation for Science and Technology (FCT) in the framework of the Strategic Funding of CF-UM-UP (UIDB/04650/2020, UIDP/04650/2020), CQUM (UIDB/00686/2020), CICECO Aveiro Institute of Materials (UIDB/50011/2020, UIDP/50011/2020 & LA/P/0006/2020) and by Ministerio de Economía y Competitividad de España (PID2020-113704RB-I00 and PID2020-119242RB-I00), Xunta de Galicia (Centro Singular de Investigación de Galicia—Accreditation 2019-2022 ED431G 2019/06 and IN607A 2018/5 and project ED431C 2020-06), and European Union (EU-ERDF Interreg V-A—Spain-Portugal 0245\_IBEROS\_1\_E, 0712\_ACUINANO\_1\_E, and 0624\_2IQBIONEURO\_6\_E, and Interreg Atlantic Area NANOCULTURE 1.102.531), and the European Union H2020-MSCA-RISE-2019 PEPSA-MATE project. S.R.S. Veloso acknowledges FCT for a PhD grant (SFRH/BD/144017/2019). Support from MAP-Fis Doctoral Programme is also acknowledged.

**Institutional Review Board Statement:** Not applicable.

**Informed Consent Statement:** Not applicable.

**Data Availability Statement:** Not applicable.

**Conflicts of Interest:** The authors declare no conflict of interest.

#### References

- Mitchell, M.J.; Billingsley, M.M.; Haley, R.M.; Wechsler, M.E.; Peppas, N.A.; Langer, R. Engineering Precision Nanoparticles for Drug Delivery. *Nat. Rev. Drug Discov.* **2021**, *20*, 101–124. [CrossRef] [PubMed]
- Caspani, S.; Magalhães, R.; Araújo, J.P.; Sousa, C.T. Magnetic Nanomaterials as Contrast Agents for MRI. *Materials* **2020**, *13*, 2586. [CrossRef] [PubMed]
- Liu, X.; Zhang, Y.; Wang, Y.; Zhu, W.; Li, G.; Ma, X.; Zhang, Y.; Chen, S.; Tiwari, S.; Shi, K.; et al. Comprehensive Understanding of Magnetic Hyperthermia for Improving Antitumor Therapeutic Efficacy. *Theranostics* **2020**, *10*, 3793–3815. [CrossRef] [PubMed]
- Kurian, J.; Lahiri, B.B.; Mathew, M.J.; Philip, J. High Magnetic Fluid Hyperthermia Efficiency in Copper Ferrite Nanoparticles Prepared by Solvothermal and Hydrothermal Methods. *J. Magn. Magn. Mater.* **2021**, *538*, 168233. [CrossRef]

5. Gahrouei, Z.E.; Labbaf, S.; Kermanpur, A. Cobalt Doped Magnetite Nanoparticles: Synthesis, Characterization, Optimization and Suitability Evaluations for Magnetic Hyperthermia Applications. *Phys. E Low-Dimens. Syst. Nanostruct.* **2020**, *116*, 113759. [CrossRef]
6. Chand, P.; Vaish, S.; Kumar, P. Structural, Optical and Dielectric Properties of Transition Metal (MFe<sub>2</sub>O<sub>4</sub>; M = Co, Ni and Zn) Nanoferrites. *Phys. B Condens. Matter* **2017**, *524*, 53–63. [CrossRef]
7. Doaga, A.; Cojocariu, A.M.; Amin, W.; Heib, F.; Bender, P.; Hempelmann, R.; Caltun, O.F. Synthesis and Characterizations of Manganese Ferrites for Hyperthermia Applications. *Mater. Chem. Phys.* **2013**, *143*, 305–310. [CrossRef]
8. Islam, K.; Haque, M.; Kumar, A.; Hoq, A.; Hyder, F.; Hoque, S.M. Manganese Ferrite Nanoparticles (MnFe<sub>2</sub>O<sub>4</sub>): Size Dependence for Hyperthermia and Negative/Positive Contrast Enhancement in MRI. *Nanomaterials* **2020**, *10*, 2297. [CrossRef]
9. Tripathi, R.M.; Mahapatra, S.; Raghunath, R.; Kumar, A.V.; Sadasivan, S. Daily Intake of Manganese by Adult Population of Mumbai, India. *Sci. Total Environ.* **2002**, *299*, 73–77. [CrossRef]
10. Ma, H.; Guo, L.; Zhang, H.; Wang, Y.; Miao, Y.; Liu, X.; Peng, M.; Deng, X.; Peng, Y.; Fan, H. The Metal Ion Release of Manganese Ferrite Nanoparticles: Kinetics, Effects on Magnetic Resonance Relaxivities, and Toxicity. *ACS Appl. Bio Mater.* **2022**, *5*, 3067–3074. [CrossRef]
11. Zhang, L.; Xiao, S.; Kang, X.; Sun, T.; Zhou, C.; Xu, Z.; Du, M.; Zhang, Y.; Wang, G.; Liu, Y.; et al. Metabolic Conversion and Removal of Manganese Ferrite Nanoparticles in Raw264.7 Cells and Induced Alteration of Metal Transporter Gene Expression. *Int. J. Nanomed.* **2021**, *16*, 1709–1724. [CrossRef] [PubMed]
12. Khanna, L.; Verma, N.K. Biocompatibility and Superparamagnetism in Novel Silica/CaFe<sub>2</sub>O<sub>4</sub> Nanocomposite. *Mater. Lett.* **2014**, *128*, 376–379. [CrossRef]
13. Noor, A.; Akhtar, M.N.; Khan, S.N.; Nazir, M.S.; Yousaf, M. Synthesis, Morphological and Electromagnetic Evaluations of Ca Doped Mn Spinel Nanoferrites for GHz Regime Applications. *Ceram. Int.* **2020**, *46*, 13961–13968. [CrossRef]
14. Khanna, L.; Verma, N.K. Size-Dependent Magnetic Properties of Calcium Ferrite Nanoparticles. *J. Magn. Magn. Mater.* **2013**, *336*, 1–7. [CrossRef]
15. Li, L.; Mak, K.Y.; Leung, C.W.; Chan, K.Y.; Chan, W.K.; Zhong, W.; Pong, P.W.T. Effect of Synthesis Conditions on the Properties of Citric-Acid Coated Iron Oxide Nanoparticles. *Microelectron. Eng.* **2013**, *110*, 329–334. [CrossRef]
16. Poller, W.C.; Löwa, N.; Schleicher, M.; Münster-Wandowski, A.; Taupitz, M.; Stangl, V.; Ludwig, A.; Wiekhorst, F. Initial Interaction of Citrate-Coated Iron Oxide Nanoparticles with the Glycocalyx of THP-1 Monocytes Assessed by Real-Time Magnetic Particle Spectroscopy and Electron Microscopy. *Sci. Rep.* **2020**, *10*, 3591. [CrossRef] [PubMed]
17. Granath, T.; Mandel, K.; Löbmann, P. Overcoming the Inhibition Effects of Citrate: Precipitation of Ferromagnetic Magnetite Nanoparticles with Tunable Morphology, Magnetic Properties, and Surface Charge via Ferrous Citrate Oxidation. *Part. Part. Syst. Charact.* **2021**, *38*, 2100098. [CrossRef]
18. Maurizi, L.; Bouyer, F.; Paris, J.; Demoisson, F.; Saviot, L.; Millot, N. One Step Continuous Hydrothermal Synthesis of Very Fine Stabilized Superparamagnetic Nanoparticles of Magnetite. *Chem. Commun.* **2011**, *47*, 11706–11708. [CrossRef]
19. Boyer, C.; Whittaker, M.R.; Bulmus, V.; Liu, J.; Davis, T.P. The Design and Utility of Polymer-Stabilized Iron-Oxide Nanoparticles for Nanomedicine Applications. *NPG Asia Mater.* **2010**, *2*, 23–30. [CrossRef]
20. Jawad, A.; Al-Abodi, E.E. Investigating (Fe<sub>3</sub>O<sub>4</sub>) Magnetic Nanoparticles Impregnated onto Tri-Sodium Citrate to Remove, of Methylene Blue Dye from Aqueous Solutions. *AIP Conf. Proc.* **2019**, *2123*, 020026. [CrossRef]
21. Ur Rahman, Z.; Dong, Y.L.; Ren, C.; Zhang, Z.Y.; Chen, X. Protein Adsorption on Citrate Modified Magnetic Nanoparticles. *J. Nanosci. Nanotechnol.* **2012**, *12*, 2598–2606. [CrossRef] [PubMed]
22. Saraswathy, A.; Nazeer, S.S.; Jeevan, M.; Nimi, N.; Arumugam, S.; Harikrishnan, V.S.; Varma, P.R.H.; Jayasree, R.S. Citrate Coated Iron Oxide Nanoparticles with Enhanced Relaxivity for in Vivo Magnetic Resonance Imaging of Liver Fibrosis. *Colloids Surf. B Biointerfaces* **2014**, *117*, 216–224. [CrossRef] [PubMed]
23. Cheraghipour, E.; Javadpour, S.; Mehdizadeh, A.R. Citrate Capped Superparamagnetic Iron Oxide Nanoparticles Used for Hyperthermia Therapy. *J. Biomed. Sci. Eng.* **2012**, *5*, 715–719. [CrossRef]
24. Asimakidou, T.; Makridis, A.; Veintemillas-Verdaguer, S.; Morales, M.P.; Kellartzis, I.; Mitrakas, M.; Vourlias, G.; Angelakeris, M.; Simeonidis, K. Continuous Production of Magnetic Iron Oxide Nanocrystals by Oxidative Precipitation. *Chem. Eng. J.* **2020**, *393*, 124593. [CrossRef]
25. Granath, T.; Löbmann, P.; Mandel, K. Oxidative Precipitation as a Versatile Method to Obtain Ferromagnetic Fe<sub>3</sub>O<sub>4</sub> Nano- and Mesocrystals Adjustable in Morphology and Magnetic Properties. *Part. Part. Syst. Charact.* **2021**, *38*, 2000307. [CrossRef]
26. Hui, C.; Shen, C.; Yang, T.; Bao, L.; Tian, J.; Ding, H.; Li, C.; Gao, H.-J. Large-Scale Fe<sub>3</sub>O<sub>4</sub> Nanoparticles Soluble in Water Synthesized by a Facile Method. *J. Phys. Chem. C* **2008**, *112*, 11336–11339. [CrossRef]
27. Sleiman, N.; Deluchat, V.; Wazne, M.; Courtin, A.; Saad, Z.; Kazpard, V.; Baudu, M. Role of Iron Oxidation Byproducts in the Removal of Phosphate from Aqueous Solution. *RSC Adv.* **2016**, *6*, 1627–1636. [CrossRef]
28. Gavilán, H.; Kowalski, A.; Heinke, D.; Sugunan, A.; Sommertune, J.; Varón, M.; Bogart, L.K.; Posth, O.; Zeng, L.; González-Alonso, D.; et al. Colloidal Flower-Shaped Iron Oxide Nanoparticles: Synthesis Strategies and Coatings. *Part. Part. Syst. Charact.* **2017**, *34*, 1700094. [CrossRef]
29. Hirazawa, H.; Kusamoto, S.; Aono, H.; Naohara, T.; Mori, K.; Hattori, Y.; Maehara, T.; Watanabe, Y. Preparation of Fine Mg<sub>1</sub>-XCaXFe<sub>2</sub>O<sub>4</sub> Powder Using Reverse Coprecipitation Method for Thermal Coagulation Therapy in an Ac Magnetic Field. *J. Alloys Compd.* **2008**, *461*, 467–473. [CrossRef]

30. Pereira, D.S.M.; Cardoso, B.D.; Rodrigues, A.R.O.; Amorim, C.O.; Amaral, V.S.A.; Almeida, B.G.; Queiroz, M.-J.R.P.; Martinho, O.; Baltazar, F.; Calhella, R.C.; et al. Magnetoliposomes Containing Calcium Ferrite Nanoparticles for Applications in Breast Cancer Therapy. *Pharmaceutics* **2019**, *11*, 477. [CrossRef]
31. Satalkar, M.; Kane, S.N. On the Study of Structural Properties and Cation Distribution of  $Zn_{0.75-x}Ni_xMg_{0.15}Cu_{0.1}Fe_2O_4$  Nano Ferrite: Effect of Ni Addition. *J. Phys. Conf. Ser.* **2016**, *755*, 012050. [CrossRef]
32. Nikam, D.S.; Jadhav, S.V.; Khot, V.M.; Bohara, R.A.; Hong, C.K.; Mali, S.S.; Pawar, S.H. Cation Distribution, Structural, Morphological and Magnetic Properties of  $Co_{1-x}Zn_xFe_2O_4$  ( $x = 0-1$ ) Nanoparticles. *RSC Adv.* **2015**, *5*, 2338–2345. [CrossRef]
33. Bamzai, K.K.; Kour, G.; Kaur, B.; Kulkarni, S.D. Preparation, and Structural and Magnetic Properties of Ca Substituted Magnesium Ferrite with Composition  $MgCa_xFe_{2-x}O_4$  ( $x = 0.00, 0.01, 0.03, 0.05, 0.07$ ). *J. Mater.* **2014**, *2014*, 184340. [CrossRef]
34. Gomes, H.C.; Teixeira, S.S.; Graça, M.P.F. Synthesis of Calcium Ferrite for Energy Storage Applications. *J. Alloys Compd.* **2022**, *921*, 166026. [CrossRef]
35. Hashhash, A.; Kaiser, M. Synthesis and Characterization of Calcium-Substituted Mg-Co-Cr Ferrite Nanoparticles with a Crystallite Size Less Than 10 Nm. *J. Supercond. Nov. Magn.* **2021**, *34*, 3403–3412. [CrossRef]
36. Chhaya, S.D.; Pandya, M.P.; Chhantbar, M.C.; Modi, K.B.; Baldha, G.J.; Joshi, H.H. Study of Substitution Limit, Structural, Bulk Magnetic and Electrical Properties of  $Ca^{2+}$  Substituted Magnesium Ferrite. *J. Alloys Compd.* **2004**, *377*, 155–161. [CrossRef]
37. Weil, L.; Bertaut, F.; Bochirol, L. Propriétés Magnétiques et Structure de La Phase Quadratique Du Ferrite de Cuivre. *J. Phys. Radium* **1950**, *11*, 208–212. [CrossRef]
38. Donnelly, F.C.; Purcell-Milton, F.; Framont, V.; Cleary, O.; Dunne, P.W.; Gun'ko, Y.K. Synthesis of  $CaCO_3$  Nano- and Micro-Particles by Dry Ice Carbonation. *Chem. Commun.* **2017**, *53*, 6657–6660. [CrossRef]
39. Massoudi, J.; Smari, M.; Nouri, K.; Dhahri, E.; Khirouni, K.; Bertaina, S.; Bessais, L.; Hlil, E.K. Magnetic and Spectroscopic Properties of Ni-Zn-Al Ferrite Spinel: From the Nanoscale to Microscale. *RSC Adv.* **2020**, *10*, 34556–34580. [CrossRef]
40. Testa-Anta, M.; Ramos-Docampo, M.A.; Comesaña-Hermo, M.; Rivas-Murias, B.; Salgueiriño, V. Raman Spectroscopy to Unravel the Magnetic Properties of Iron Oxide Nanocrystals for Bio-Related Applications. *Nanoscale Adv.* **2019**, *1*, 2086–2103. [CrossRef]
41. Wang, Z.; Schiferl, D.; Zhao, Y.; O'Neill, H.S.C. High Pressure Raman Spectroscopy of Spinel-Type Ferrite  $ZnFe_2O_4$ . *J. Phys. Chem. Solids* **2003**, *64*, 2517–2523. [CrossRef]
42. Freire, R.M.; Ribeiro, T.S.; Vasconcelos, I.F.; Denardin, J.C.; Barros, E.B.; Mele, G.; Carbone, L.; Mazzetto, S.E.; Fechine, P.B.A.  $MZnFe_2O_4$  ( $M = Ni, Mn$ ) Cubic Superparamagnetic Nanoparticles Obtained by Hydrothermal Synthesis. *J. Nanoparticle Res.* **2013**, *15*, 1616. [CrossRef]
43. Wang, W.; Ding, Z.; Zhao, X.; Wu, S.; Li, F.; Yue, M.; Liu, J.P. Microstructure and Magnetic Properties of  $MFe_2O_4$  ( $M = Co, Ni, and Mn$ ) Ferrite Nanocrystals Prepared Using Colloid Mill and Hydrothermal Method. *J. Appl. Phys.* **2015**, *117*, 17A328. [CrossRef]
44. Nekvapil, F.; Bunge, A.; Radu, T.; Cinta Pinzaru, S.; Turcu, R. Raman Spectra Tell Us so Much More: Raman Features and Saturation Magnetization for Efficient Analysis of Manganese Zinc Ferrite Nanoparticles. *J. Raman Spectrosc.* **2020**, *51*, 959–968. [CrossRef]
45. Babu, K.V.; Kumar, G.V.S.; Satyanarayana, G.; Sailaja, B.; Lakshmi, C.C.S. Microstructural and Magnetic Properties of  $Ni_{1-x}Cu_xFe_2O_4$  ( $x = 0.05, 0.1$  and  $0.15$ ) Nano-Crystalline Ferrites. *J. Sci. Adv. Mater. Devices* **2018**, *3*, 236–242. [CrossRef]
46. Galinetto, P.; Albini, B.; Bini, M.; Mozzati, M.C. Raman Spectroscopy in Zinc Ferrites Nanoparticles. In *Raman Spectroscopy*; Nascimento, G., Ed.; IntechOpen: London, UK, 2018.
47. Sharifi, S.; Yazdani, A.; Rahimi, K. Incremental Substitution of Ni with Mn in  $NiFe_2O_4$  to Largely Enhance Its Supercapacitance Properties. *Sci. Rep.* **2020**, *10*, 10916. [CrossRef]
48. Baig, M.M.; Zulfikar, S.; Yousuf, M.A.; Touqeer, M.; Ullah, S.; Agboola, P.O.; Warsi, M.F.; Shakir, I. Structural and Photocatalytic Properties of New Rare Earth  $La^{3+}$  Substituted  $MnFe_2O_4$  Ferrite Nanoparticles. *Ceram. Int.* **2020**, *46*, 23208–23217. [CrossRef]
49. Hashemi, A.; Naseri, M.; Ghiyasvand, S.; Naderi, E.; Vafai, S. Evaluation of Physical Properties, Cytotoxicity, and Antibacterial Activities of Calcium–Cadmium Ferrite Nanoparticles. *Appl. Phys. A Mater. Sci. Process.* **2022**, *128*, 236. [CrossRef]
50. Jitkang, L.; Pin, Y.S.; Xin, C.H.; Chun, L.S. Characterization of Magnetic Nanoparticle by Dynamic Light Scattering. *Nanoscale Res. Lett.* **2013**, *8*, 308–381.
51. Nowak-Jary, J.; Machnicka, B. Pharmacokinetics of Magnetic Iron Oxide Nanoparticles for Medical Applications. *J. Nanobiotechnology* **2022**, *20*, 305. [CrossRef] [PubMed]
52. Iacovita, C.; Fizeşan, I.; Pop, A.; Scorus, L.; Dudric, R.; Stiufiuc, G.; Vedeau, N.; Teteau, R.; Loghin, F.; Stiufiuc, R.; et al. In Vitro Intracellular Hyperthermia of Iron Oxide Magnetic Nanoparticles, Synthesized at High Temperature by a Polyol Process. *Pharmaceutics* **2020**, *12*, 424. [CrossRef] [PubMed]
53. Jedlovszky-Hajdú, A.; Bombelli, F.B.; Monopoli, M.P.; Tombácz, E.; Dawson, K.A. Surface Coatings Shape the Protein Corona of SPIONs with Relevance to Their Application in Vivo. *Langmuir* **2012**, *28*, 14983–14991. [CrossRef] [PubMed]
54. Yallapu, M.M.; Chauhan, N.; Othman, S.F.; Khalilzad-Sharghi, V.; Ebeling, M.C.; Khan, S.; Jaggi, M.; Chauhan, S.C. Implications of Protein Corona on Physico-Chemical and Biological Properties of Magnetic Nanoparticles. *Biomaterials* **2015**, *46*, 1–12. [CrossRef] [PubMed]
55. Nawara, K.; Romiszewski, J.; Kijewska, K.; Szczytko, J.; Twardowski, A.; Mazur, M.; Krysinski, P. Adsorption of Doxorubicin onto Citrate-Stabilized Magnetic Nanoparticles. *J. Phys. Chem. C* **2012**, *116*, 5598–5609. [CrossRef]
56. Caruntu, D.; Caruntu, G.; O'Connor, C.J. Magnetic Properties of Variable-Sized  $Fe_3O_4$  Nanoparticles Synthesized from Non-Aqueous Homogeneous Solutions of Polyols. *J. Phys. D Appl. Phys.* **2007**, *40*, 5801–5809. [CrossRef]

57. Veloso, S.R.S.; Silva, J.F.G.; Hilliou, L.; Moura, C.; Coutinho, P.J.G.; Martins, J.A.; Testa-Anta, M.; Salgueiriño, V.; Correa-Duarte, M.A.; Ferreira, P.M.T.; et al. Impact of Citrate and Lipid-Functionalized Magnetic Nanoparticles in Dehydropeptide Supramolecular Magnetogels: Properties, Design and Drug Release. *Nanomaterials* **2021**, *11*, 16. [CrossRef]
58. Karimi, Z.; Karimi, L.; Shokrollahi, H. Nano-Magnetic Particles Used in Biomedicine: Core and Coating Materials. *Mater. Sci. Eng. C* **2013**, *33*, 2465–2475. [CrossRef]
59. Otero-Lorenzo, R.; Fantechi, E.; Sangregorio, C.; Salgueiriño, V. Solvothermally Driven Mn Doping and Clustering of Iron Oxide Nanoparticles for Heat Delivery Applications. *Chem. A Eur. J.* **2016**, *22*, 6666–6675. [CrossRef]
60. Ouyahia, S.; Rais, A.; Bozzo, B.; Taibi, K.; Addou, A. Cations Distribution by Rietveld Refinement and Magnetic Properties of  $MgCr_xFe_{2-x}O_4$  Spinel Ferrites. *Appl. Phys. A Mater. Sci. Process.* **2020**, *126*, 666. [CrossRef]
61. Sharma, R.; Thakur, P.; Kumar, M.; Barman, P.B.; Sharma, P.; Sharma, V. Enhancement in A-B Super-Exchange Interaction with Mn Substitution in Mg-Zn Ferrites as a Heating Source in Hyperthermia Applications. *Ceram. Int.* **2017**, *43*, 13661–13669. [CrossRef]
62. Nitika; Rana, A.; Kumar, V. Evaluation of Structural, Magnetic, Optical, Electrical, and Humidity Sensing Properties of Manganese-Substituted Zinc Ferrite Nanoparticles. *Appl. Phys. A* **2021**, *127*, 860. [CrossRef]
63. Kumar, P.; Pathak, S.; Singh, A.; Jain, K.; Khanduri, H.; Wang, L.; Kim, S.-K.; Pant, R.P. Observation of Intrinsic Fluorescence in Cobalt Ferrite Magnetic Nanoparticles by  $Mn^{2+}$  Substitution and Tuning the Spin Dynamics by Cation Distribution. *J. Mater. Chem. C* **2022**, *10*, 12652–12679. [CrossRef]
64. Assar, S.T.; Abosheisha, H.F. Effect of Ca Substitution on Some Physical Properties of Nano-Structured and Bulk Ni-Ferrite Samples. *J. Magn. Magn. Mater.* **2015**, *374*, 264–272. [CrossRef]
65. Topkaya, R.; Baykal, A.; Demir, A. Yafet-Kittel-Type Magnetic Order in Zn-Substituted Cobalt Ferrite Nanoparticles with Uniaxial Anisotropy. *J. Nanopart. Res.* **2013**, *15*, 1359. [CrossRef]
66. Vargas, J.M.; Nunes, W.C.; Socolovsky, L.M.; Knobel, M.; Zanchet, D. Effect of Dipolar Interaction Observed in Iron-Based Nanoparticles. *Phys. Rev. B* **2005**, *72*, 184428. [CrossRef]
67. Félix, L.L.; Rodriguez Martínez, M.A.; Pacheco Salazar, D.G.; Huamani Coaquira, J.A. One-Step Synthesis of Polyethyleneimine-Coated Magnetite Nanoparticles and Their Structural, Magnetic and Power Absorption Study. *RSC Adv.* **2020**, *10*, 41807–41815. [CrossRef] [PubMed]
68. Bruvera, I.J.; Mendoza Zélis, P.; Pilar Calatayud, M.; Goya, G.F.; Sánchez, F.H. Determination of the Blocking Temperature of Magnetic Nanoparticles: The Good, the Bad, and the Ugly. *J. Appl. Phys.* **2015**, *118*, 184304. [CrossRef]
69. Yelenich, O.; Solopan, S.; Kolodiaznyi, T.; Tykhonenko, Y.; Tovstolytkin, A.; Belous, A. Magnetic Properties and AC Losses in  $AFe_2O_4$  ( $A = Mn, Co, Ni, Zn$ ) Nanoparticles Synthesized from Nonaqueous Solution. *J. Chem.* **2015**, *2015*, 1–9. [CrossRef]
70. Khanna, L.; Verma, N.K. PEG/ $CaFe_2O_4$  Nanocomposite: Structural, Morphological, Magnetic and Thermal Analyses. *Phys. B Condens. Matter* **2013**, *427*, 68–75. [CrossRef]
71. Mehdaoui, B.; Meffre, A.; Carrey, J.; Lachaize, S.; Lacroix, L.-M.; Gougeon, M.; Chaudret, B.; Respaud, M. Optimal Size of Nanoparticles for Magnetic Hyperthermia: A Combined Theoretical and Experimental Study. *Adv. Funct. Mater.* **2011**, *21*, 4573–4581. [CrossRef]
72. Gupta, R.; Tomar, R.; Chakraverty, S.; Sharma, D. Effect of Manganese Doping on the Hyperthermic Profile of Ferrite Nanoparticles Using Response Surface Methodology. *RSC Adv.* **2021**, *11*, 16942–16954. [CrossRef]
73. Aslibeiki, B.; Eskandarzadeh, N.; Jalili, H.; Ghotbi Varzaneh, A.; Kameli, P.; Orue, I.; Chernenko, V.; Hajalilou, A.; Ferreira, L.P.; Cruz, M.M. Magnetic Hyperthermia Properties of  $CoFe_2O_4$  Nanoparticles: Effect of Polymer Coating and Interparticle Interactions. *Ceram. Int.* **2022**, *48*, 27995–28005. [CrossRef]
74. Nasrin, S.; Chowdhury, F.U.Z.; Hoque, S.M. Study of Hyperthermia Temperature of Manganese-Substituted Cobalt Nano Ferrites Prepared by Chemical Co-Precipitation Method for Biomedical Application. *J. Magn. Magn. Mater.* **2019**, *479*, 126–134. [CrossRef]
75. Kheradmand, A.; Vahidi, O.; Masoudpanah, S.M. Magnetic, Hyperthermic and Structural Properties of Zn Substituted  $CaFe_2O_4$  Powders. *Appl. Phys. A Mater. Sci. Process.* **2018**, *124*, 255. [CrossRef]
76. Lopes, F.A.C.; Fernandes, A.V.F.; Rodrigues, J.M.; Queiroz, M.-J.R.P.; Almeida, B.G.; Pires, A.; Pereira, A.M.; Araújo, J.P.; Castanheira, E.M.S.; Rodrigues, A.R.O.; et al. Magnetoliposomes Containing Multicore Nanoparticles and a New Antitumor Thienopyridine Compound with Potential Application in Chemo/Thermotherapy. *Biomedicines* **2022**, *10*, 1547. [CrossRef]
77. Amorim, C.O.; Mohseni, F.; Dumas, R.K.; Amaral, V.S.; Amaral, J.S. A Geometry-Independent Moment Correction Method for the MPMS3 SQUID-Based Magnetometer. *Meas. Sci. Technol.* **2021**, *32*, 105602. [CrossRef]





Article

# Polydopamine Nanoparticles Functionalized Electrochemical DNA Aptasensor for Serum Glycated Albumin Detection

Pornsuda Maraming<sup>1</sup>, Nang Noon Shean Aye<sup>1</sup> , Patcharee Boonsiri<sup>2</sup>, Sakda Daduang<sup>3</sup>, Onanong Buhome<sup>4</sup> and Jureerut Daduang<sup>1,\*</sup>

<sup>1</sup> Centre for Research and Development of Medical Diagnostic Laboratories, Faculty of Associated Medical Sciences, Khon Kaen University, Khon Kaen 40002, Thailand

<sup>2</sup> Department of Biochemistry, Faculty of Medicine, Khon Kaen University, Khon Kaen 40002, Thailand

<sup>3</sup> Division of Pharmacognosy and Toxicology, Faculty of Pharmaceutical Sciences, Khon Kaen University, Khon Kaen 40002, Thailand

<sup>4</sup> Department of Medical Technology, Faculty of Allied Health Sciences, Nakhon Ratchasima College, Nakhon Ratchasima 30000, Thailand

\* Correspondence: jurpoo@kku.ac.th

**Abstract:** Polydopamine (PDA) has now been widely applied to electrochemical biosensing because of its excellent biocompatibility, abundant functional groups, and facile preparation. In this study, polydopamine nanoparticles (PDA-NPs)-functionalized electrochemical aptasensor was developed for the rapid, sensitive, and cost-effective detection of glycated albumin (GA), a promising biomarker for glycemic control in diabetic patients. PDA-NPs were synthesized at various pH conditions in Tris buffer. Cyclic voltammetry (CV) of PDA-NPs-coated screen-printed carbon electrodes (SPCEs) revealed that the materials were more conductive when PDA-NPs were synthesized at pH 9.5 and 10.5 than that at pH 8.5. At pH 10.5, the prepared PDA and PDA-aptamer NPs were monodispersed spherical morphology with an average size of  $118.0 \pm 1.9$  and  $127.8 \pm 2.0$  nm, respectively. When CV and electrochemical impedance spectrometry (EIS) were used for the characterization and detection of the electrochemical aptasensor under optimal conditions, the proposed aptasensor exhibited a broad linearity for detection of GA at a clinically relevant range of  $(1\text{--}10,000 \mu\text{g mL}^{-1})$ , provided a low detection limit of  $0.40 \mu\text{g mL}^{-1}$ , appreciable reproducibility (less than 10%), and practicality (recoveries 90–104%). In addition, our developed aptasensor presented a great selectivity towards GA, compared to interfering substances commonly present in human serum, such as human serum albumin, urea, glucose, and bilirubin. Furthermore, the evaluation of the aptasensor performance against GA-spiked serum samples showed its probable applicability for clinical use. The developed PDA aptasensor demonstrated excellent sensitivity and selectivity towards GA detection with a simple and facile fabrication process. This proposed technique shows its potential application in GA measurement for improving the screening and management of diabetic patients in the future.

**Keywords:** polydopamine nanoparticles; electrochemical sensor; aptamer; glycated albumin; diabetes mellitus

**Citation:** Maraming, P.; Aye, N.N.S.; Boonsiri, P.; Daduang, S.; Buhome, O.; Daduang, J. Polydopamine Nanoparticles Functionalized Electrochemical DNA Aptasensor for Serum Glycated Albumin Detection. *Int. J. Mol. Sci.* **2022**, *23*, 13699. <https://doi.org/10.3390/ijms232213699>

Academic Editor: Raghvendra Singh Yadav

Received: 5 October 2022

Accepted: 5 November 2022

Published: 8 November 2022

**Publisher's Note:** MDPI stays neutral with regard to jurisdictional claims in published maps and institutional affiliations.



**Copyright:** © 2022 by the authors. Licensee MDPI, Basel, Switzerland. This article is an open access article distributed under the terms and conditions of the Creative Commons Attribution (CC BY) license (<https://creativecommons.org/licenses/by/4.0/>).

## 1. Introduction

Diabetes mellitus (DM), affecting millions of people worldwide, is a chronic metabolic disorder with heterogenous etiologies resulting from insulin deficiency and/or insulin resistance [1]. Blood glucose level measurement is important in the diagnosis and glycemic monitoring of DM. However, human blood glucose levels are dependent upon food intake and can reflect the glycemic control within the past few hours. Hemoglobin A1c (HbA1c) is recognized as the gold standard for glycemic monitoring. It can provide the average blood glucose level over 2–3 months. Nevertheless, diseases that affect red blood cells (RBCs) including haemoglobinopathy, renal anaemia, haemolytic anaemia, and liver cirrhosis,

affect HbA1c measurements [2]. Moreover, due to the long lifespan of RBCs, HbA1c is not suitable for monitoring short-term blood glucose level fluctuations.

Glycated albumin (GA), formed by the non-enzymatic glycation of albumin, is a potential biomarker for monitoring the blood glucose level over the past few weeks. It is specific for the albumin glycation rates and can be used for shorter-term glycemic control than HbA1c and is more accurate than the blood glucose measurement. GA was unaffected by hemoglobin levels or hemoglobinopathies such as anemia, thalassemia, or variant hemoglobin [3]. There are various techniques for measuring GA such as immunoassays, capillary electrophoresis [4], high-performance liquid chromatography, refractive index measurement [5], ion-exchange chromatography, and Raman spectroscopy [6]. However, these techniques are frequently time-consuming, labor-intensive, and require expensive equipment. An electrochemical biosensor is an alternative method to the currently used conventional techniques gaining more attention in recent years [7–9]. Its advantages include easy and rapid detection, small volumes of samples, and low-cost instrument [10].

Aptamers are short-sequenced artificial single-strand DNA or RNA that can bind to specific biomolecules [11]. The aptamer can be identified and generated from the oligonucleotide library via a process of Sequential Evolution of Ligands by Exponential Enrichment (SELEX) [12]. Recently, novel techniques using capillary electrophoresis and microfluidic technology significantly enhanced the efficiency of aptamer discovery/selection [13]. Aptamers exhibit complicated three-dimensional structures that are highly selective and able to attach non-covalently to target molecules (small molecules, proteins, lipids, cells, etc.) [14]. Its advantages include low immunogenicity, the ability to be immobilized on various surfaces, high-temperature resistance, similar affinities and specificities compared to antibodies, and better consistency than antibodies [15,16]. Therefore, we developed an aptamer-based biosensor to measure serum GA levels.

Polydopamine (PDA) is a polymerized product from dopamine (3,4-dihydroxyphenethylamine) or other catecholamines under oxidative and basic conditions [17]. PDA was originally used to modify material surfaces that formed thin layers at the nanoscale ranging from a few to about 100 nm (e.g., metal films) [18]. It has good characteristics including biocompatibility, easy steps in preparation, simple functionalization, and thermal stability on practically any surface [19]. However, during PDA film is deposited on the surfaces, the oxidation reaction causes the formation of unwanted aggregation in the solution hindering success in surface modification. This major disadvantage led to PDA production in the form of nanoparticles with colloidal stabilization [18]. PDA nanostructures offer aqueous solubility, good optical and electrical properties, surface modification ability, and photothermal properties offering several applications in biomedical platform and analytical science [20,21]. As for the chemistry of the material surfaces, PDA layers can be modified via various mechanisms such as catechol–metal coordination, electrostatic interactions,  $\pi$ – $\pi$  interactions, hydrogen, and covalent bonds resulting in the success of surface functionalization [22].

PDA nanoparticles (PDA-NPs) have been applied for the development of the sensor, drug carrier, molecular imaging, gene targeting therapy, and tissue engineering [18]. Moreover, PDA-based films and nanoparticles have demonstrated a promise as sensing materials for a variety of analytes. The number of studies looking at possible uses of this material is still rising quickly. Previous electrochemical studies showed the most common binding molecules for biomarker detection in DM monitoring including antibodies [23], aptamers [24], and enzymes [25]. Until now, PDA-NPs-based electrochemical study has never been explored for serum GA measurement. In this study, a sensitive and selective electrochemical aptasensor was fabricated using the PDA-NPs nanocomposite for label-free GA detection in spiked clinical samples.

## 2. Results and Discussion

### 2.1. Characterization of PDA Nanoparticles

PDA is a biopolymer that is brown to black in color and contains significant amounts of phenol, catechol, and quinone functional groups, which provide a variety of molecular adsorption characteristics [26]. PDA-NPs exhibit the ability to chelate and bind many compounds. In addition to having biocompatibility, good adhesion, and anti-biofouling characteristics, PDA nanostructures are good candidates for biomedical applications [27,28]. There are various methods for synthesizing PDA-NPs. The most commonly used techniques are enzymatic/solution oxidation as well as electro-polymerization [22]. In this study, PDA-NPs were formed by the self-oxidative polymerization of  $0.5 \text{ mg mL}^{-1}$  dopamine under alkaline conditions. After 20 h of synthesis, PDA-NPs were characterized by scanning electron microscope (SEM), spectrophotometry, and attenuated total reflectance Fourier-transform infrared spectroscopy (FTIR). Morphologically, PDA-NPs observed under SEM were uniform, monodispersed, and spherical shape (see Figure 1A). The UV-Vis spectrum of the synthesized PDA-NPs is shown in Figure 1B. The absorbance pattern decreased with the increase of the wavelength from 250 to 830 nm.

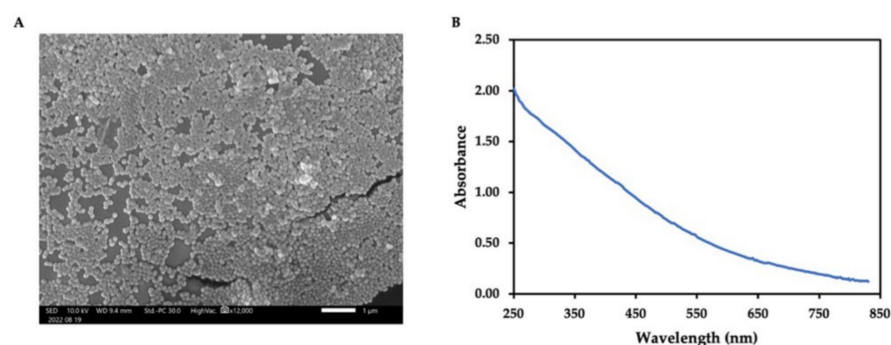


**Figure 1.** (A) SEM image and (B) UV-Vis spectrum of synthesized PDA-NPs.

The synthesized PDA-NPs were also subjected to FTIR examination in order to analyze further characteristic functional groups of the PDA NPs formation during dopamine oxidation and polymerization in the spectral range between  $500$  and  $4000 \text{ cm}^{-1}$  as shown in Figure 2. The peaks at  $3348 \text{ cm}^{-1}$  and  $2940 \text{ cm}^{-1}$  were observed in the PDA-NPs spectrum corresponding to O-H stretching vibrations and C-H stretching of the aromatic ring, respectively [28–30]. The characteristics of C=C and C–N–C stretching from the indole group of PDA-NPs were found by peaks at  $1580$  and  $1491 \text{ cm}^{-1}$ , respectively [20,31–33]. Moreover, a strong band of PDA-NPs at  $1044 \text{ cm}^{-1}$  was due to the stretching vibration of catechol hydroxyl C–O and/or C–N [32]. The presence of indole and indolequinone structures in the FTIR spectrum of the PDA sample demonstrated that dopamine was successfully polymerized to PDA-NPs [34].

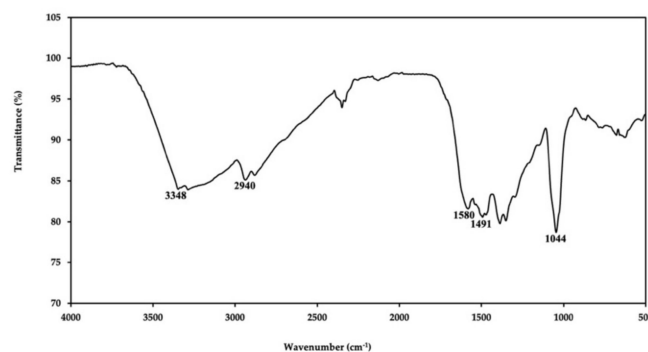


**Figure 2.** ATR-FTIR spectrum of synthesized PDA-NPs.

As shown in Figure 3A,B, under a transmission electron microscope (TEM), morphologically PDA-NPs and PDA-aptamer NPs had monodispersed spherical distribution. By dynamic light scattering (DLS) measurements, the prepared PDA-NPs were monodispersed with an average size of  $118.0 \pm 1.9$  nm. PDA surfaces are unable to link with nucleophiles (e.g., amine and thiol groups) by Schiff base or Michael addition reactions under alkaline conditions [19]. In this study, we conjugated DNA aptamer containing an amine group at 5' end on PDA surfaces through a covalent reaction. A reactant bearing an amine group can target the diketone or catechol groups expressed on the PDA layer via Michael addition and Schiff base reactions, which can modify the polymer surface properties [20]. To study the change of NP size after aptamer conjugation in a microcentrifuge tube, we used a similar protocol as that for the conjugation of it on SPCEs of the electrochemical sensor. After measurement by DLS, the hydrodynamic diameter of PDA aptamer NPs ( $127.8 \pm 2.0$ ) nm slightly increased than that of PDA-NPs, indicating successful surface modification (Figure 3C). The polydispersity index (PDI) of both PDA-NPs and PDA-aptamer NPs was within the range of 0.2 which is usually considered evidence of the homogeneity and monodispersity of NPs. After aptamer conjugation, PDA-NPs still maintained their stability. This may be due to performing conjugation under alkaline pH.

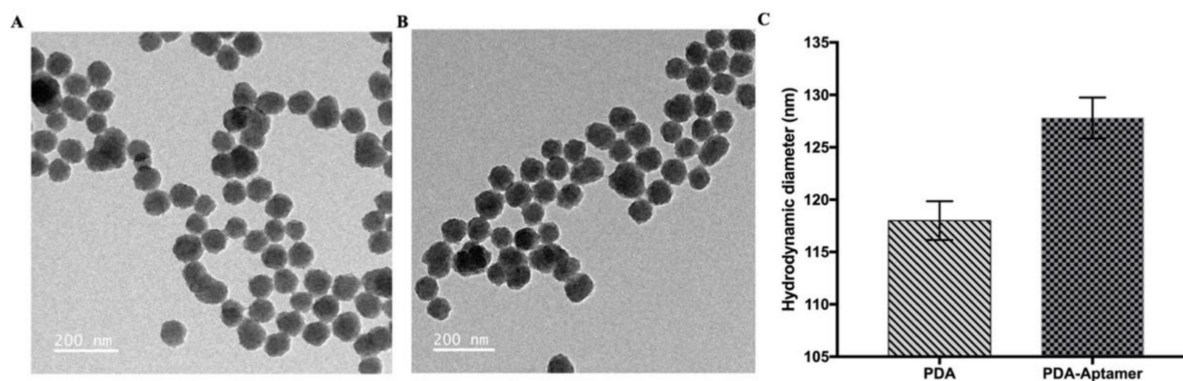


**Figure 3.** TEM images of (A) PDA-NPs and (B) PDA-aptamer NPs showing monodispersed spherical distribution. (C) DLS measurements of PDA-NPs and PDA-aptamer conjugates.

## 2.2. Characterization of Electrochemical Aptasensor

PDA has now been widely applied in electrochemical biosensing because of its excellent biocompatibility, abundant functional groups (catechol, amine), facile preparation, and anti-biofouling effect [35]. In this study, PDA-NPs were produced by polymerization of its monomer dopamine in Tris buffer under highly alkaline pH conditions. Various PDA-NP sizes were synthesized by varying the pH of the Tris buffer (pH 8.5, 9.5, and 10.5), with lower basic pH leading to the gradual color changes of the solution towards dark-brown (Figure 4A) and the increase of the sizes of NPs (Table S1, Supplementary Materials). The solution of PDA-NPs was dropped onto carbon electrode surfaces to modify their surfaces. The electrochemical characterization of the developed aptasensor was characterized by cyclic voltammetry (CV) from  $-0.5$  V to  $0.9$  V at a scan rate of  $100 \text{ mVs}^{-1}$  using  $5 \text{ mM } [\text{Fe}(\text{CN})_6]^{3-/4-}$ . The electrochemical characterization by CV of the PDA-NPs after immobilization is shown in Figure 4B. PDA-NPs coated SPCEs exhibited changes in the peak current properties due to the coating, confirming surface modification with a more conductive material at pH 9.5 and 10.5, whereas PDA-NPs synthesized at pH 8.5 decreased a current signal compared to PDA synthesized at pH 9.5 and 10.5. This was caused by the formation of larger size PDA-NPs.

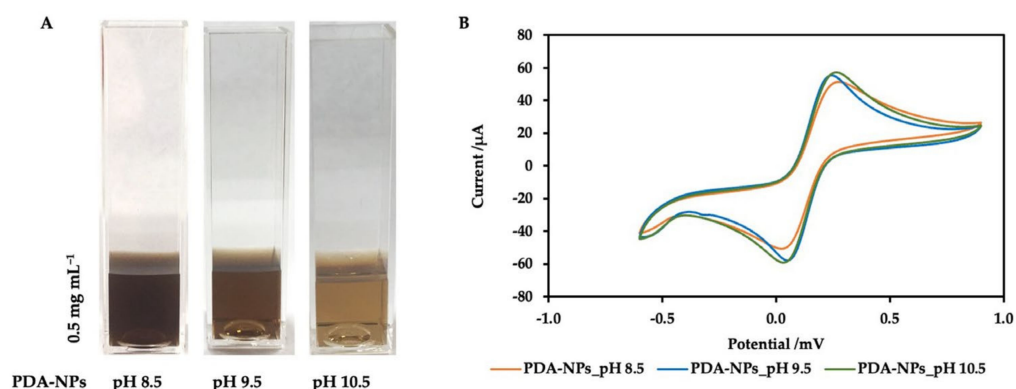


**Figure 4.** (A) PDA-NPs solution synthesized under different pH conditions. (B) Cyclic voltammograms of SPCEs modified with PDA-NPs synthesized at different pH.

Figure 5 shows the CV of the aptasensor after each immobilization. After coating SPCEs with PDA, both anodic ( $I_{pa}$ ) and cathodic ( $I_{pc}$ ) peak currents were slightly decreased with an increase in the peak-to-peak separation values. This indicated the successful coating of the surface with PDA-NPs. The decrease of the redox peak currents after aptamer immobilization was caused by the negative charge on the phosphate backbone of the aptamer and its large structure. This data showed that complete immobilization of the aptamer on the PDA modified SPCEs. The peak was further reduced after target incubation because of the conformational structure change of the aptamer after specific protein binding and blocking the electron transfer process. Then, the effect of the scan rate on the voltammetric behavior of PDA/SPCEs was investigated (Figure 6A). The scan rate parameters were in the range of 10–300  $\text{mVs}^{-1}$ . Figure 6B shows a linear relationship between the square root of the scan rate and peak currents ( $I_{pa}$  and  $I_{pc}$ ), with an  $R^2$  value of 0.9929 and 0.9918, suggesting the characteristics of the corresponding thin-layer type voltammetry [36]. The plot between the logarithms ( $\log$ ) of scan rates ( $\text{mVs}^{-1}$ ) and  $\log$  peak current ( $I_{pa}$  and  $I_{pc}$ ) indicated a linear relationship with the slope values of 0.49 and 0.51, respectively (data not indicated). The resulting values were in agreement with those for purely diffusion-controlled currents [37]. This implies that the PDA-modified SPCE surface was not fouled, and the electrochemical reaction was controlled by diffusion.

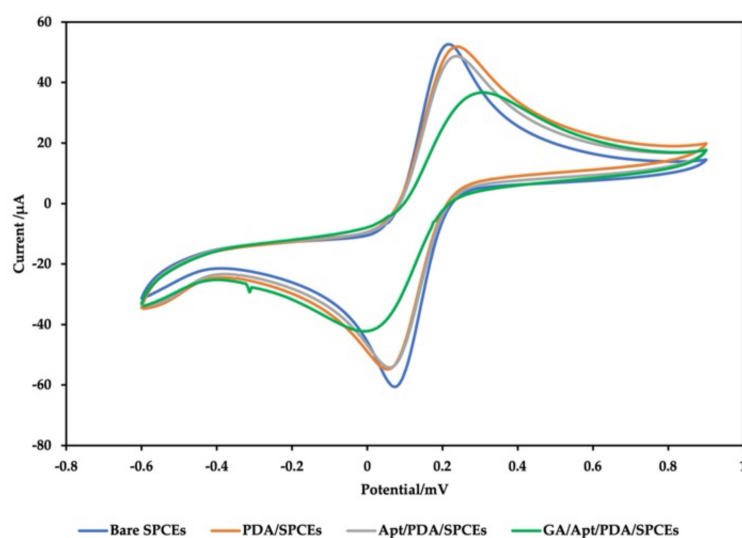


**Figure 5.** A Cyclic voltammograms of Bare SPCEs, PDA/SPCEs, Apt/PDA/SPCEs, GA/Apt/PDA/SPCEs showing successful immobilization/reaction of each layer.

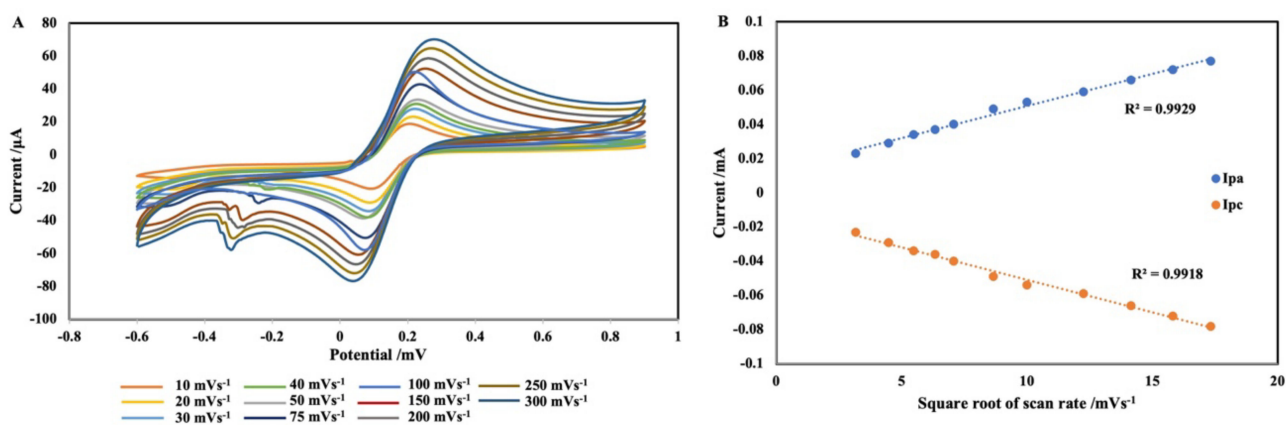


**Figure 6.** (A) Cyclic voltammograms of PDA/SPCEs at different scan rates from 10 to 300  $\text{mVs}^{-1}$  using 5 mM  $[\text{Fe}(\text{CN})_6]^{3-/4-}$  in phosphate-buffered saline (PBS) as redox probe. (B) plot between anodic ( $I_{pa}$ ) and cathodic ( $I_{pc}$ ) peak currents vs. square root of the scan rate ( $\text{mVs}^{-1}$ ).

### 2.3. Optimization of the Experimental Conditions

The optimization of experimental parameters is crucial for getting optimal experimental results. The optimal concentration of PDA was selected from 0.5, 0.75, and 1  $\text{mg mL}^{-1}$  PDA. However, the concentrations of PDA did not affect the electrochemical measurements (data not shown). Several conditions, including (a) measurement parameters, (b) aptamer concentration required for immobilization, (c) blocking, and (d) the reaction time with the target, were optimized. Electrochemical impedance spectrometry (EIS) is commonly used for surface characterization, batteries, corrosion studies, and semiconductors. It is also used for the biosensing of immunological reactions [38,39]. The observation of non-specific impedance changes may result in the inability to discriminate between specific and non-specific interactions [40]. Non-steady EIS signals also resulted from electrode contamination, additional voltammetric measurements, and repetitive measurements [41]. CV was used for the detection of GA concentration in this study.

#### 2.3.1. Optimization of GA Aptamer Immobilization

One of the most important steps in the development of electrochemical aptasensors is to optimize aptamer concentration. Various concentrations of aptamer (0.1–10  $\mu\text{M}$ ) were tested to optimize aptamer immobilization. The efficient electrochemical signal was not provided at a low concentration of the aptamer (0.1  $\mu\text{M}$ ). The sensitivity of the aptasensor was decreased at higher aptamer concentrations (5, 10  $\mu\text{M}$ ) due to dense immobilization on the electrode surface. In the context of CV current, an aptamer concentration of 1  $\mu\text{M}$  produced an appropriate signal and improved sensitivity (Figure 7A).

#### 2.3.2. Optimization of Blocking and Reaction Time

Various blocking agents such as bovine serum albumin (BSA), ethanolamine, and casein have been used. However, the similarity of the molecular structure of BSA with GA, BSA might interfere with detection. Therefore, ethanolamine was used as a blocking reagent in this study. Various concentrations of ethanolamine (0.1 M, 0.1 M, and 0.01 M) were used to determine optimal concentration. The maximum current change was observed at 0.01 M ethanolamine concentration (Figure 7B). The reaction time with the target solution was optimized ranging from 15 to 45 min. The optimal binding was achieved at 30 min with appropriate electrochemical signals (Figure 7C).

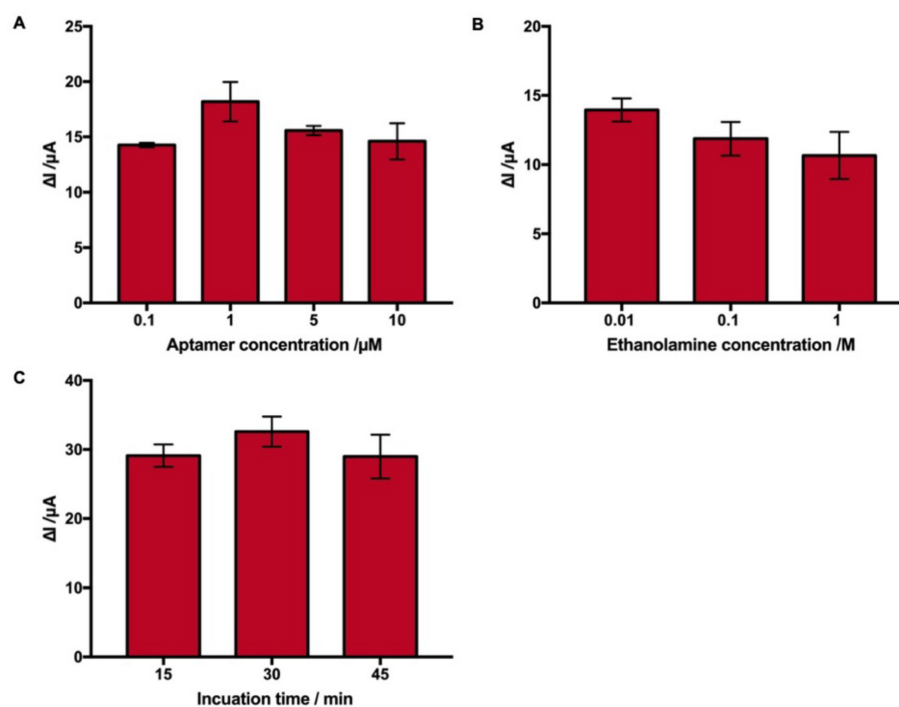


**Figure 7.** Optimization of (A) aptamer concentration, (B) concentration of blocking solution, and (C) reaction time with GA protein.

#### 2.4. Electrochemical Detection of GA

The sensitivity of the developed aptasensor was tested against various concentrations of GA (from 1 to 10,000  $\mu g mL^{-1}$ ) under optimal conditions. The aptamer immobilized on PDA-NPs/SPCEs provided a relatively significant current exhibiting a free and steady assembly on the electrode surface. When the aptamer changed conformational structure upon binding to the target, the captured GA-aptamer complex on the sensor surface acted as a kinetic barrier, inhibiting the electron transfer reaction, and thus lowering the peak current. The decrease of the CV oxidative peak current was observed corresponding to the increase in GA concentration (Figure 8A). Electrochemical measurements were carried out before and after target binding with the aptamer. The peak current changes were calculated as the following equation:  $\Delta I = I_0 - I_1$ , where  $\Delta I$  is the peak current change, and  $I_0$  and  $I_1$  are the peak current before and after incubation with the target protein, respectively. The efficient binding of GA by the aptasensor was indicated by a decrease in the maximum peak current. Figure 8B shows a standard curve plotted between the logarithm of the GA concentration and the peak current change ( $\mu A$ ). The peak current changes increased linearly with  $\log$  GA concentrations ( $I = 2.6166 \ln(c) + 3.326$ ), with a correlation coefficient ( $R^2$ ) of 0.9957 for GA detection over a range of 1–10,000  $\mu g mL^{-1}$ . The limit of detection (LOD) of GA was calculated from the equation;  $LOD = 3\sigma/S$ , where  $\sigma$  is the standard deviation of the average measurement of the lowest concentration of GA and  $S$  is the slope of the regression line. The calculated LOD value of the developed aptasensor was 0.40  $\mu g mL^{-1}$ , which is sensitive enough to detect GA concentrations due to the normal range of serum GA being 0.2–7  $mg mL^{-1}$  [42]. The aptasensor developed here is highly sensitive enough with a wide linearity range from 1 to  $1 \times 10^4 \mu g mL^{-1}$ . The calculated LOD in this study was compared to those of the previous studies (Table 1). Bunyarataphan et al. and Aye et al. reported the electrochemical aptasensors for GA detection with the low LOD of 3  $ng mL^{-1}$  and 31  $ng mL^{-1}$ , respectively [7,16]. However, the former sensor fabrication process involved prolonged incubation for streptavidin to be firmly immobilized on the electrode surface, which was resolved in this study with reduced fabrication time. The graphene oxide (GO)-modified aptasensor presented simple and sensitive biosensing functions [16]. However, the interference with high human serum

albumin (HSA) concentration limited the selectivity of the aptasensor which was surpassed in our study. A detailed comparison of the selectivity between these methods can be found in the following section. In the sensing systems, the binding affinity of aptamer and GA, the physical properties of the PDA-NPs, and the optimal conditions of aptamer concentration, blocking concentration, and reaction time, all have a significant impact on the detection sensitivity and specificity. In this study, PDA-NPs functionalized electrochemical aptasensor showed a linear response over a larger range ( $0.001\text{--}10\text{ mg mL}^{-1}$ ) of other approaches. Therefore, the aptasensor developed in this study can confidently be applied for sensitive detection of both low and high GA levels of clinical samples.

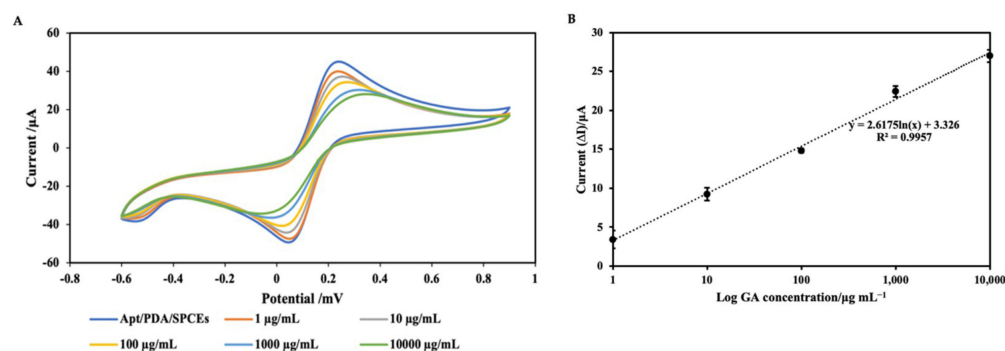


**Figure 8.** (A) CV response of Aptamer/PDA/SPCEs aptasensor after incubation with concentrations of  $1\ \mu\text{g mL}^{-1}$ ,  $10\ \mu\text{g mL}^{-1}$ ,  $100\ \mu\text{g mL}^{-1}$ ,  $1\ \text{mg mL}^{-1}$ , and  $10\ \text{mg mL}^{-1}$ . (B) The calibration curve for GA detection showing linear relationship between the logarithm of GA concentration  $1\text{--}10,000\ \mu\text{g mL}^{-1}$  and corresponding maximum current ( $\Delta I$ ) from CV. Mean current value of each concentration was plotted from three independent experiments.

**Table 1.** Comparison of limit of detection using various biosensors for the detection of serum glycosylated albumin.

No.	Techniques	Limit of Detection (LOD)	Linear Response Range	References
1.	Nanozyme-based electrochemical immunoassay	$3.8\ \mu\text{g mL}^{-1}$	$5\ \mu\text{g mL}^{-1}$ to $10\ \text{mg mL}^{-1}$	[43]
2.	rGO/AuNPs based electrochemical aptasensor	$0.07\ \mu\text{g mL}^{-1}$	$2\text{--}10\ \mu\text{g mL}^{-1}$	[8]
3.	Electrochemical-based aptasensor	$0.003\ \mu\text{g mL}^{-1}$	$0.002\text{--}16\ \text{mg mL}^{-1}$	[7]
4.	$\text{Cu}_2\text{O}$ -rGO nanozyme-based electrochemical sensor	$0.007\ \mu\text{g mL}^{-1}$	$0.02\text{--}1500\ \mu\text{g mL}^{-1}$	[44]
5.	Paper-based device with boronic acid-derived agarose beads	$7.1\ \mu\text{g mL}^{-1}$	$10\ \mu\text{g mL}^{-1}$ to $10\ \text{mg mL}^{-1}$	[45]
6.	Colorimetric immunoassay using Prussian blue nanoparticles	$7.32\ \mu\text{g mL}^{-1}$	$0.01\text{--}2.0\ \text{mg mL}^{-1}$	[46]
7.	Enzymatic assay-based sensor	$0.36\ \mu\text{g mL}^{-1}$	$0\text{--}0.6\ \text{mg mL}^{-1}$	[42]
8.	rGO-based aptasensor	$16.40\ \mu\text{g mL}^{-1}$	$0\text{--}125\ \mu\text{g mL}^{-1}$	[47]
9.	GO-fucntionalized electrochemical aptasensor	$0.031\ \mu\text{g mL}^{-1}$	$0.001\text{--}10\ \text{mg mL}^{-1}$	[16]
10.	PDA-NPs functionalized electrochemical aptasensor	$0.40\ \mu\text{g mL}^{-1}$	$0.001\text{--}10\ \text{mg mL}^{-1}$	This study

### 2.5. Selectivity and Reproducibility of the Electrochemical Aptasensor

To verify that the current changes were in fact caused by specific interaction between the aptamer and GA, the specificity of the aptasensor was evaluated using common interfering substances such as urea ( $2.5\ \text{mg mL}^{-1}$ ), glucose ( $125\ \text{mg dL}^{-1}$ ), bilirubin ( $2\ \text{mg dL}^{-1}$ ) and HSA ( $100\ \mu\text{g mL}^{-1}$ ). Apparently, as shown in Figure 9 the largest current change was observed with GA protein. In contrast, only small current changes ( $22 \pm 0.39\%$ ,  $19 \pm 0.53\%$ ,  $24 \pm 1.14\%$ ,  $19 \pm 0.09\%$ ) were observed with urea, glucose, bilirubin, and HSA, respectively. The concentrations of the interfering substances (except for HSA) used here were higher than their normal level in the normal human serum. Cross-reactivity with HSA is still a challenge for most GA biosensors as these two molecules possess a relatively similar molecular structure [7,9]. The present results indicate that the aptasensor developed here exhibited high specificity for the detection of GA without any labeling.

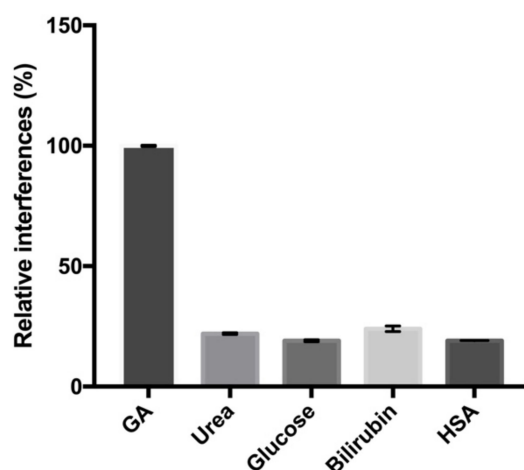


**Figure 9.** Specificity of electrochemical aptasensor to GA ( $1 \text{ mg mL}^{-1}$ ) compared with other biomaterials urea ( $2.5 \text{ mg mL}^{-1}$ ), glucose ( $125 \text{ mg dL}^{-1}$ ), bilirubin ( $2 \text{ mg dL}^{-1}$ ), and HSA ( $100 \text{ } \mu\text{g mL}^{-1}$ ).

Five independent experiments against three different concentrations of GA at 0, 0.1, and  $10 \text{ mg mL}^{-1}$  were carried out to test the reproducibility of the aptasensor detection. The relative standard deviations (RSDs) obtained were 8.28%, 1.77%, and 2.82%, respectively (Table 2). The RSD is lower than the acceptable value (less than 10%) [48] proving that the aptasensor can generate highly reproducible electrochemical signals and good precision. Moreover, the consistency of the electrode fabrication process was perceived. The stepwise electrode modification strengthened the reproducibility of the aptasensor. The relative interferences with HSA and reproducibility of the developed electrochemical aptasensor were compared to other methods in Table 3.

**Table 2.** Reproducibility of the aptasensor detection for various concentrations of GA (0, 1 and  $10 \text{ mg mL}^{-1}$ ).

GA Concentration ( $\text{mg mL}^{-1}$ )	Peak Current ( $\mu\text{A}$ )	Relative Standard Deviation (%) ( $n = 5$ )
0.00	$3.91 \pm 0.32$	8.28%
0.10	$14.83 \pm 0.26$	1.77%
10.00	$26.98 \pm 0.76$	2.82%

**Table 3.** Comparison of selectivity and reproducibility of the developed electrochemical sensor with other reported sensors.

No.	Biosensors	Relative Interferences with HSA (%)	Reproducibility (CV%)	References
1.	Electrochemical-based aptasensor	$29 \pm 3\%$	6.50%	[7]
2.	Immobilization free electrochemical sensor	$52.91 \pm 1.46\%$	9.88%	[9]
3.	GO-functionalized electrochemical aptasensor	$26.2 \pm 0.2\%$	2.50%	[16]
4.	PDA-NPs functionalized electrochemical aptasensor	$19 \pm 0.09\%$	2.82%	This study

### 2.6. Spike Recovery Assay

The accuracy of the GA detection of the electrochemical aptasensor developed in this study was evaluated using a GA-spiked human serum. Prior to spiking with GA, the serum was diluted from 1:1 to 1:1000 with PBS (1X, pH 7.4) to investigate the optimal serum dilution. The current changes were decreased in parallel with serum (Figure 10). Since relatively small interference with small current change was observed at 1:1000 dilution, this dilution was chosen to reduce the interference from other serum proteins.

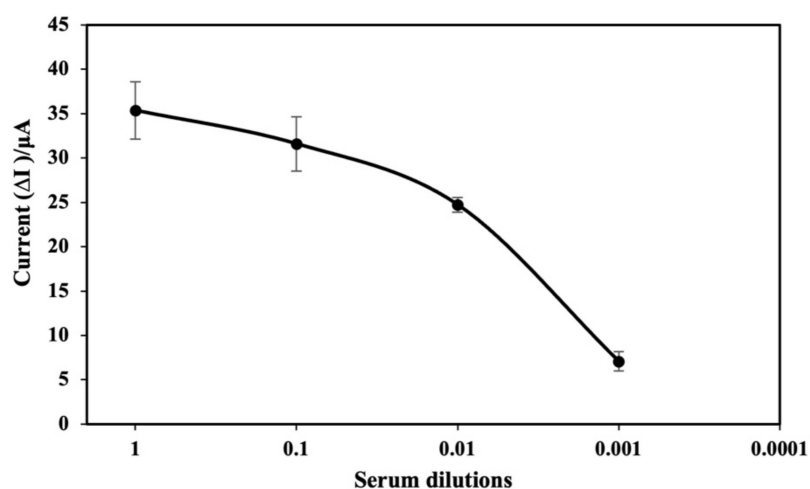


**Figure 10.** Evaluation of optimal serum dilution for spike recovery assay.

To demonstrate the applicability and feasibility of the fabricated aptasensor for clinical samples, two different concentrations ( $47.60$  and  $238.10 \mu\text{g mL}^{-1}$ ) of GA solutions were spiked into the diluted serum. The recovery rates of low and high GA concentrations were  $104\%$  and  $90\%$ , respectively, as shown in Table 4, which were within the acceptable range with RSD values of  $6.10\%$  and  $2.80\%$ , respectively. The data showed that the aptasensor developed here can detect GA levels accurately. Therefore, the developed aptasensor is observed to be reliable and can be used as a potential tool for the detection of GA in real clinical samples. However, further validation experiment including the comparison of the developed biosensor and a reference method for real sample analysis is required prior to implementation in the clinical laboratory.

**Table 4.** Recovery assay of GA in human serum using the developed aptasensor.

GA concentration Spiked in Serum ( $\mu\text{g mL}^{-1}$ )	Measured Concentration ( $\mu\text{g mL}^{-1}$ )	Recovery (%)	RSD <sup>a</sup> (%) ( $n = 3$ )
47.60	$53.1 \pm 0.79$	104	6.10
238.10	$217 \pm 0.56$	90	2.80

<sup>a</sup> The relative standard deviations.

### 3. Materials and Methods

#### 3.1. Reagents and Materials

The GA binding aptamer with a 33-nucleotide sequence of  $5'$ -GG TGG CTG GAG GGG GCG CGA ACG TTT TTT TTT T- $3'$  [49] was modified by an amino group ( $\text{NH}_2$ ) at  $5'$  end of the aptamer sequence (Integrated DNA Technologies Pte. Ltd., Singapore). The aptamer was reconstituted using Tris-EDTA (TE) buffer (1X, pH 8.2). Dopamine hydrochloride, GA, and ethanolamine were purchased from Sigma-Aldrich (Singapore). Disposable screen-printed carbon electrodes (SPCEs,  $30 \times 12.5$  mm) were purchased from Quasense, Thailand. As a redox indicator, potassium ferricyanide ( $\text{K}_3[\text{Fe}(\text{CN})_6]$ , 5 mM) together with 0.1 M potassium chloride (KCl) in phosphate-buffered saline (PBS) (1X, pH 7.4). All reagents were prepared in ultrapure deionized water (DI).

#### 3.2. Instruments

The electrochemical detection system was completed by the transducer (the electrode sensor) and the detector. The transducer was a disposable SPCE with a three-electrode system including a 3-mm working carbon electrode, a carbon counter electrode, and a silver/silver chloride reference electrode. The PalmSens4 potentiostat with PS Trace 5.8 software (PalmSens BV Co., Ltd., Houten, The Netherlands) was used for all

electrochemical experiments. The characterization of PDA-NPs was carried out by an Eppendorf BioSpectrometer® fluorescence (Hamburg, Germany), a Bruker TENSOR II ATR-FTIR spectrometer (Bruker, Germany), a transmission electron microscope (TEM, FEI, TECNAI G2 20, Nieuw-Vennep, The Netherlands), a scanning electron microscope (SEM, Jeol, JSM-IT200 InTouchScope™, Tokyo, Japan) and a dynamic light scattering (DLS, Malvern, UK).

### 3.3. Synthesis of PDA-NPs and In Vitro Conjugation of GA Aptamer on PDA-NPs

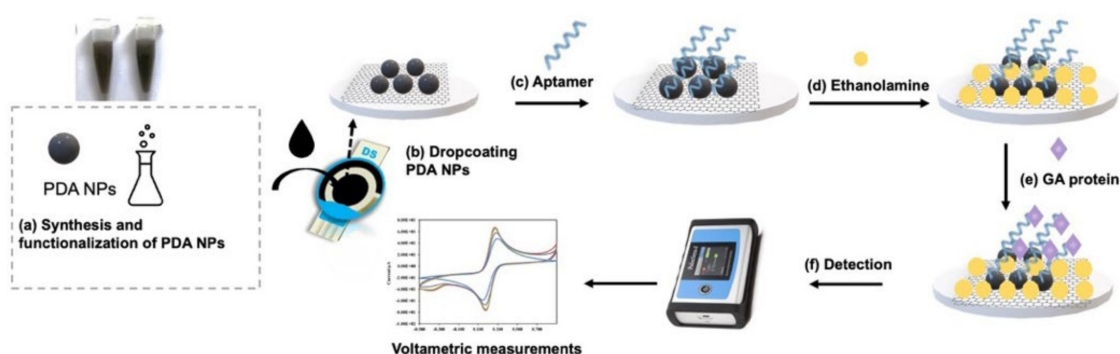
PDA-NPs were synthesized by simply dissolving 50 mg of dopamine hydrochloride into 100 mL of 10 mM Tris buffer (pH 8.5, 9.5, and 10.5). The suspension was stirred at 180 rpm for 20 h. The solution was then centrifuged at  $16,100\times g$  for 5 min at room temperature. PDA-NPs were washed twice with 1 mL of Tris buffer. The supernatant was discarded, and the remaining pellets were collected. The PDA-aptamer complex was prepared by mixing equal volumes of synthesized PDA-NPs and GA-specific aptamer. Aptamer conjugation was done 45 min after incubation.

### 3.4. Fabrication of the Electrochemical Aptasensor

The working carbon electrodes were coated with seven microliters of the PDA-NPs solution and dried in the oven at  $50\text{ }^{\circ}\text{C}$  for 30 min. To remove excess PDA-NPs, DI was used to thoroughly clean the electrodes. Then,  $7\text{ }\mu\text{L}$  of  $1\text{ }\mu\text{M}$  GA aptamer were immobilized and stabilized on the working electrode for 30 min to allow complete binding between the amino groups of the aptamers on the PDA surfaces. PBS (1X, pH 7.4) was used to completely wash the unbound aptamers. The surfaces were blocked with 0.1 M ethanolamine to reduce non-specific binding. After blocking for 15 min, the SPCEs were washed with PBS again. The layer-by-layer aptasensor was applied for the detection of GA in this study.

### 3.5. Electrochemical Analysis

The produced aptasensors were incubated with various GA concentrations for 30 min. Then, electrode surfaces were rinsed with PBS and  $130\text{ }\mu\text{L}$  of  $5\text{ mM}$   $[\text{Fe}(\text{CN})_6]^{3-/4-}$  was added until the surfaces were immersed. For the characterization of the fabrication process, CV and EIS analyses were carried out after each immobilization procedure. Both electrode characterization and GA detection were measured by CV with a potential of  $-0.5\text{ V}$  to  $0.9\text{ V}$  at a scan rate of  $100\text{ mVs}^{-1}$  using a redox indicator. The impedance spectra were measured using the open circuit potential at the frequency range of 100 mHz to 100 kHz. The flow diagram of the proposed electrochemical aptasensor is illustrated in Scheme 1.



**Scheme 1.** Schematic diagram of the proposed PDA-NPs functionalized electrochemical aptasensor for GA protein detection (a) Synthesis and functionalization of PDA-NPs (b) Drop-coating PDA-NPs onto SPCEs (c) Immobilization of aptamer (d) Blocking with ethanolamine (e) Incubation with GA and (f) Voltametric measurements using  $5\text{ mM}$   $[\text{Fe}(\text{CN})_6]^{3-/4-}$  as a redox indicator.

### 3.6. Real Sample Analysis

After optimal conditions were obtained, the capability of the proposed electrochemical biosensor was investigated in real samples. Serum samples were spiked with GA at final concentrations of 47.60 and 238.10  $\mu\text{g mL}^{-1}$  to test the clinical performance of the proposed biosensor. Known concentrations of GA spiked into diluted serum samples were determined by employing the electrochemical measurements that were described in the previous section.

## 4. Conclusions

PDA is quite a promising sensor material for a variety of analyses. In particular, it has been extensively applied for designing biochips for biomarker detection. In this study, we used functional PDA-NPs as a coating material on SPCE surfaces to create an electrochemical GA detector under a new concept, which has the potential to monitor glycemic control in DM patients. Here, we designed the sensing system to be convenient with a simple and facile fabrication process and label-free GA detection. The PDA aptasensor developed here showed excellent sensitivity, selectivity, and a low detection limit of 0.40  $\mu\text{g mL}^{-1}$  for GA detection. This proposed technique shows its potential application in serum/plasma GA measurement to improve the screening and management of diabetic patients in the future. It can be also applied to new PDA-based nanoconstructs to modify the electrode surfaces for a variety of biomedical applications.

**Supplementary Materials:** The following supporting information can be downloaded at: <https://www.mdpi.com/article/10.3390/ijms232213699/s1>, Table S1: Hydrodynamic diameter and polydispersity index (PDI) of PDA-NPs synthesized at different pH.

**Author Contributions:** Conceptual framework, P.M. and J.D.; Experimental design, N.N.S.A. and P.M.; Performing experiments, N.N.S.A. and P.M.; Data analysis and results interpretation, N.N.S.A. and P.M.; Drafting manuscript, P.M., O.B. and N.N.S.A.; Revision of the manuscript, P.M., S.D. and J.D.; Final approval version of the manuscript, P.B. and J.D. All authors have read and agreed to the published version of the manuscript.

**Funding:** This research is funded by the Young Researcher Development Project of Khon Kaen University Year 2022, Khon Kaen, Thailand.

**Institutional Review Board Statement:** The study was conducted in accordance with the Declaration of Helsinki, and the protocol was approved by the Centre for Ethics in Human Research, Khon Kaen University (HE651209).

**Informed Consent Statement:** Informed consent was obtained from all subjects involved in the study.

**Data Availability Statement:** Not applicable.

**Acknowledgments:** The author would like to acknowledge Yukifumi Nawa for editing the manuscript via the Publication Clinic, KKU, Thailand.

**Conflicts of Interest:** The authors declare no competing financial interest.

## References

1. Gu, Z.; Aimetti, A.A.; Wang, Q.; Dang, T.T.; Zhang, Y.; Veiseh, O.; Cheng, H.; Langer, R.S.; Anderson, D.G. Injectable Nano-Network for Glucose-Mediated Insulin Delivery. *ACS Nano* **2013**, *7*, 4194–4201. [CrossRef] [PubMed]
2. Koga, M.; Hashimoto, K.; Murai, J.; Saito, H.; Mukai, M.; Ikegame, K.; Ogawa, H.; Kasayama, S. Usefulness of Glycated Albumin as an Indicator of Glycemic Control Status in Patients with Hemolytic Anemia. *Clin. Chim. Acta* **2011**, *412*, 253–257. [CrossRef] [PubMed]
3. Danese, E.; Montagnana, M.; Nouvenne, A.; Lippi, G. Advantages and Pitfalls of Fructosamine and Glycated Albumin in the Diagnosis and Treatment of Diabetes. *J. Diabetes Sci. Technol.* **2015**, *9*, 169–176. [CrossRef]
4. Hinton, D.J.S.; Ames, J.M. Analysis of Glycated Protein by Capillary Electrophoresis. *Int. Congr. Ser.* **2002**, *1245*, 471–474. [CrossRef]
5. Zhernovaya, O.S.; Tuchin, V.V.; Meglinski, I.V. Monitoring of Blood Proteins Glycation by Refractive Index and Spectral Measurements. *Laser Phys. Lett.* **2008**, *5*, 460. [CrossRef]

6. Dingari, N.C.; Horowitz, G.L.; Kang, J.W.; Dasari, R.R.; Barman, I. Raman Spectroscopy Provides a Powerful Diagnostic Tool for Accurate Determination of Albumin Glycation. *PLoS ONE* **2012**, *7*, e32406. [CrossRef]
7. Bunyarataphan, S.; Dharakul, T.; Fucharoen, S.; Paiboonsukwong, K.; Japrun, D. Glycated Albumin Measurement Using an Electrochemical Aptasensor for Screening and Monitoring of Diabetes Mellitus. *Electroanalysis* **2019**, *31*, 2254–2261. [CrossRef]
8. Farzadfard, A.; Shayeh, J.S.; Habibi-Rezaei, M.; Omid, M. Modification of Reduced Graphene/Au-Aptamer to Develop an Electrochemical Based Aptasensor for Measurement of Glycated Albumin. *Talanta* **2020**, *211*, 120722. [CrossRef]
9. Waiwinya, W.; Putnin, T.; Pimalai, D.; Chawjiraphan, W.; Sathirapongsasuti, N.; Japrun, D. Immobilization-Free Electrochemical Sensor Coupled with a Graphene-Oxide-Based Aptasensor for Glycated Albumin Detection. *Biosensors* **2021**, *11*, 85. [CrossRef]
10. Mikula, E.; Wyslouch-Cieszynska, A.; Zhukova, L.; Verwilt, P.; Dehaen, W.; Radecki, J.; Radecka, H. Electrochemical Biosensor for the Detection of Glycated Albumin. *Curr. Alzheimer Res.* **2017**, *14*, 345–351. [CrossRef]
11. Sett, A. Aptamers: Magic Bullet for Theranostic Applications. In *Theranostics—An Old Concept in New Clothing*; IntechOpen: London, UK, 2020.
12. Liu, Q.; Zhang, W.; Chen, S.; Zhuang, Z.; Zhang, Y.; Jiang, L.; LIN, J.S. SELEX Tool: A Novel and Convenient Gel-Based Diffusion Method for Monitoring of Aptamer-Target Binding. *J. Biol. Eng.* **2020**, *14*, 1. [CrossRef] [PubMed]
13. Cho, M.; Soo Oh, S.; Nie, J.; Stewart, R.; Eisenstein, M.; Chambers, J.; Marth, J.D.; Walker, F.; Thomson, J.A.; Soh, H.T. Quantitative Selection and Parallel Characterization of Aptamers. *Proc. Natl. Acad. Sci. USA* **2013**, *110*, 18460–18465. [CrossRef] [PubMed]
14. Ruscito, A.; DeRosa, M.C. Small-Molecule Binding Aptamers: Selection Strategies, Characterization, and Applications. *Front. Chem.* **2016**, *4*, 14. [CrossRef]
15. Keefe, A.D.; Pai, S.; Ellington, A. Aptamers as Therapeutics. *Nat. Rev. Drug Discov.* **2010**, *9*, 537–550. [CrossRef] [PubMed]
16. Aye, N.N.S.; Maraming, P.; Tavichakorntrakool, R.; Chaibunruang, A.; Boonsiri, P.; Daduang, S.; Teawtrakul, N.; Prasongdee, P.; Amornkitbamrung, V.; Daduang, J. A Simple Graphene Functionalized Electrochemical Aptasensor for the Sensitive and Selective Detection of Glycated Albumin. *Appl. Sci.* **2021**, *11*, 10315. [CrossRef]
17. Davidsen, M.B.; Teixeira, J.F.L.; Dehli, J.; Karlsson, C.; Kraft, D.; Souza, P.P.C.; Foss, M. Post-Treatments of Polydopamine Coatings Influence Cellular Response. *Colloids Surf. B Biointerfaces* **2021**, *207*, 111972. [CrossRef]
18. Ball, V. Polydopamine Nanomaterials: Recent Advances in Synthesis Methods and Applications. *Front. Bioeng. Biotechnol.* **2018**, *6*, 109. [CrossRef]
19. Zmerli, I.; Michel, J.-P.; Makky, A. Multifunctional Polydopamine-Based Nanoparticles: Synthesis, Physico-Chemical Properties and Applications for Bimodal Photothermal/Photodynamic Therapy of Cancer. *Multifunct. Mater.* **2021**, *4*, 022001. [CrossRef]
20. Bolat, G.; Vural, O.A.; Yaman, Y.T.; Abaci, S. Polydopamine Nanoparticles-Assisted Impedimetric Sensor towards Label-Free Lung Cancer Cell Detection. *Mater. Sci. Eng. C* **2021**, *119*, 111549. [CrossRef]
21. Poinard, B.; Neo, S.Z.Y.; Yeo, E.L.L.; Heng, H.P.S.; Neoh, K.G.; Kah, J.C.Y. Polydopamine Nanoparticles Enhance Drug Release for Combined Photodynamic and Photothermal Therapy. *ACS Appl. Mater. Interfaces* **2018**, *10*, 21125–21136. [CrossRef]
22. Cortés, M.T.; Vargas, C.; Blanco, D.A.; Quinchanequa, I.D.; Cortés, C.; Jaramillo, A.M. Bioinspired Polydopamine Synthesis and Its Electrochemical Characterization. *J. Chem. Educ.* **2019**, *96*, 1250–1255. [CrossRef]
23. Molazemhosseini, A.; Magagnin, L.; Vena, P.; Liu, C.-C. Single-Use Disposable Electrochemical Label-Free Immunosensor for Detection of Glycated Hemoglobin (HbA1c) Using Differential Pulse Voltammetry (DPV). *Sensors* **2016**, *16*, 1024. [CrossRef] [PubMed]
24. Eissa, S.; Zourob, M. Aptamer-Based Label-Free Electrochemical Biosensor Array for the Detection of Total and Glycated Hemoglobin in Human Whole Blood. *Sci. Rep.* **2017**, *7*, 1016. [CrossRef] [PubMed]
25. Kausaite-Minkstimiene, A.; Mazeiko, V.; Ramanaviciene, A.; Ramanavicius, A. Evaluation of Amperometric Glucose Biosensors Based on Glucose Oxidase Encapsulated within Enzymatically Synthesized Polyaniline and Polypyrrole. *Sens. Actuators B Chem.* **2011**, *158*, 278–285. [CrossRef]
26. Sukeri, A.; Arjunan, A.; Bertotti, M. New Strategy to Fabricate a Polydopamine Functionalized Self-Supported Nanoporous Gold Film Electrode for Electrochemical Sensing Applications. *Electrochem. Commun.* **2020**, *110*, 106622. [CrossRef]
27. Khan, Z.; Shanker, R.; Um, D.; Jaiswal, A.; Ko, H. Bioinspired Polydopamine and Composites for Biomedical Applications. In *Electrically Conductive Polymer and Polymer Composites*; John Wiley & Sons, Ltd.: Hoboken, NJ, USA, 2018; pp. 1–29. ISBN 978-3-527-80791-8.
28. Yang, Y.; Song, C.; Wang, P.; Fan, X.; Xu, Y.; Dong, G.; Liu, Z.; Pan, Z.; Song, Y.; Song, C. Insights into the Impact of Polydopamine Modification on Permeability and Anti-Fouling Performance of Forward Osmosis Membrane. *Chemosphere* **2022**, *291*, 132744. [CrossRef]
29. Zangmeister, R.A.; Morris, T.A.; Tarlov, M.J. Characterization of Polydopamine Thin Films Deposited at Short Times by Autoxidation of Dopamine. *Langmuir* **2013**, *29*, 8619–8628. [CrossRef]
30. Li, S.; Hou, X.; Lu, S.; Xu, W.; Tao, J.; Zhao, Z.; Hu, G.; Gao, F. Fabrication and Simulation of a Layered Ultrahigh Thermal Conductive Material Made of Self-Assembled Graphene and Polydopamine on a Copper Substrate. *RSC Adv.* **2021**, *11*, 34676–34687. [CrossRef]
31. Nandiyanto, A.; Oktiani, R.; Ragadhita, R. How to Read and Interpret FTIR Spectroscopy of Organic Material. *Indones. J. Sci. Technol.* **2019**, *4*, 97–118. [CrossRef]
32. Batul, R.; Bhave, M.; Mahon, P.J.; Yu, A. Polydopamine Nanosphere with In-Situ Loaded Gentamicin and Its Antimicrobial Activity. *Molecules* **2020**, *25*, 2090. [CrossRef]

33. Samanta, A.; Ojha, K.; Mandal, A. Interactions between Acidic Crude Oil and Alkali and Their Effects on Enhanced Oil Recovery. *Energy Fuels* **2011**, *25*, 1642–1649. [CrossRef]
34. Ho, C.-C.; Ding, S.-J. The PH-Controlled Nanoparticles Size of Polydopamine for Anti-Cancer Drug Delivery. *J. Mater. Sci. Mater. Med.* **2013**, *24*, 2381–2390. [CrossRef] [PubMed]
35. Liu, Y.; Ai, K.; Lu, L. Polydopamine and Its Derivative Materials: Synthesis and Promising Applications in Energy, Environmental, and Biomedical Fields. *Chem. Rev.* **2014**, *114*, 5057–5115. [CrossRef] [PubMed]
36. Kanyong, P.; Krampa, F.D.; Aniweh, Y.; Awandare, G.A. Polydopamine-Functionalized Graphene Nanoplatelet Smart Conducting Electrode for Bio-Sensing Applications. *Arab. J. Chem.* **2020**, *13*, 1669–1677. [CrossRef]
37. Beck, F. Cyclic Voltammetry—Simulation and Analysis of Reaction Mechanisms. *Electroanalysis* **1995**, *7*, 298. [CrossRef]
38. Dijkema, M.; Kamp, B.; Hoogvliet, J.C.; Van Bennekom, W.P. Development of an Electrochemical Immunosensor for Direct Detection of Interferon- $\gamma$  at the Attomolar Level. *Anal. Chem.* **2001**, *73*, 901–907. [CrossRef]
39. Bardea, A.; Katz, E.; Willner, I. Biosensors with Amperometric Detection of Enzymatically Controlled PH-Changes. *Electroanalysis* **2000**, *12*, 731–735. [CrossRef]
40. Bogomolova, A.; Komarova, E.; Reber, K.; Gerasimov, T.; Yavuz, O.; Bhatt, S.; Aldissi, M. Challenges of Electrochemical Impedance Spectroscopy in Protein Biosensing. *Anal. Chem.* **2009**, *81*, 3944–3949. [CrossRef]
41. Li, L.; Zhao, H.; Chen, Z.; Mu, X.; Guo, L. Aptamer Biosensor for Label-Free Square-Wave Voltammetry Detection of Angiogenin. *Biosens. Bioelectron.* **2011**, *30*, 261–266. [CrossRef]
42. Kohzuma, T.; Yamamoto, T.; Uematsu, Y.; Shihabi, Z.K.; Freedman, B.I. Basic Performance of an Enzymatic Method for Glycated Albumin and Reference Range Determination. *J. Diabetes Sci. Technol.* **2011**, *5*, 1455–1462. [CrossRef]
43. Choi, H.; Son, S.E.; Hur, W.; Tran, V.-K.; Lee, H.B.; Park, Y.; Han, D.K.; Seong, G.H. Electrochemical Immunoassay for Determination of Glycated Albumin Using Nanozymes. *Sci. Rep.* **2020**, *10*, 9513. [CrossRef] [PubMed]
44. Li, Z.; Zhang, J.; Dai, G.; Luo, F.; Chu, Z.; Geng, X.; He, P.; Zhang, F.; Wang, Q. A Ratiometric Electrochemical Biosensor for Glycated Albumin Detection Based on Enhanced Nanozyme Catalysis of Cuprous Oxide-Modified Reduced Graphene Oxide Nanocomposites. *J. Mater. Chem. B* **2021**, *9*, 9324–9332. [CrossRef] [PubMed]
45. Ko, E.; Tran, V.-K.; Geng, Y.; Kim, M.K.; Jin, G.H.; Son, S.E.; Hur, W.; Seong, G.H. Determination of Glycated Albumin Using Boronic Acid-Derived Agarose Beads on Paper-Based Devices. *Biomicrofluidics* **2018**, *12*, 014111. [CrossRef] [PubMed]
46. Son, S.E.; Gupta, P.K.; Hur, W.; Choi, H.; Lee, H.B.; Park, Y.; Seong, G.H. Determination of Glycated Albumin Using a Prussian Blue Nanozyme-Based Boronate Affinity Sandwich Assay. *Anal. Chim. Acta* **2020**, *1134*, 41–49. [CrossRef]
47. Kim, A.-R.; Choi, Y.; Kim, S.-H.; Moon, H.-S.; Ko, J.-H.; Yoon, M.-Y. Development of a Novel SsDNA Sequence for a Glycated Human Serum Albumin and Construction of a Simple Aptasensor System Based on Reduced Graphene Oxide (RGO). *Biosensors* **2020**, *10*, 141. [CrossRef]
48. Karnes, H.T.; March, C. Precision, Accuracy, and Data Acceptance Criteria in Biopharmaceutical Analysis. *Pharm. Res.* **1993**, *10*, 1420–1426. [CrossRef]
49. Tsukakoshi, K.; Abe, K.; Sode, K.; Ikebukuro, K. Selection of DNA Aptamers That Recognize  $\alpha$ -Synuclein Oligomers Using a Competitive Screening Method. *Anal. Chem.* **2012**, *84*, 5542–5547. [CrossRef]



Article

# Electrochemically Activated CNT Sheet as a Cathode for Zn-CO<sub>2</sub> Batteries

Daniel Rui Chen <sup>1,†</sup>, Megha Chitranshi <sup>2,†</sup>, Vesselin Shanov <sup>1,3</sup> and Mark Schulz <sup>2,\*</sup>

<sup>1</sup> Department of Mechanical and Materials Engineering, University of Cincinnati, Cincinnati, OH 45221, USA

<sup>2</sup> Department of Electrical Engineering and Computer Science, University of Cincinnati, Cincinnati, OH 45221, USA

<sup>3</sup> Department of Chemical and Environmental Engineering, University of Cincinnati, Cincinnati, OH 45221, USA

\* Correspondence: schulzmk@ucmail.uc.edu

† These authors contributed equally to this work.

**Abstract:** High demand for electrochemical storage devices is increasing the need for high-performance batteries. A Zn-CO<sub>2</sub> battery offers a promising solution for CO<sub>2</sub> reduction as well as energy storage applications. For this study, a Zn-CO<sub>2</sub> battery was fabricated using a Carbon Nanotube (CNT) sheet as a cathode and a Zn plate as an anode. The electrochemical activation technique was used to increase the surface area of the CNT electrode by roughly 4.5 times. Copper (Cu) as a catalyst was then deposited onto the activated CNT electrode using electrodeposition method and different Cu loadings were investigated to optimize CO<sub>2</sub> reduction. The final assembled Zn-CO<sub>2</sub> battery has a 1.6 V output voltage at a current density of 0.063 mA/cm<sup>2</sup>, which is higher than most devices reported in the literature. This study demonstrates the importance of activation process which enabled more catalyst loading on the cathode resulted in additional active sites for electroreduction process. This paper presents the activated CNT sheet as a promising cathode material for Zn-CO<sub>2</sub> batteries.

**Keywords:** CNT/Cu composite; CO<sub>2</sub> reduction; Zn-CO<sub>2</sub> battery

**Citation:** Chen, D.R.; Chitranshi, M.; Shanov, V.; Schulz, M.

Electrochemically Activated CNT Sheet as a Cathode for Zn-CO<sub>2</sub> Batteries. *Int. J. Mol. Sci.* **2022**, *23*, 12602. <https://doi.org/10.3390/ijms232012602>

Academic Editor: Raghvendra Singh Yadav

Received: 8 August 2022

Accepted: 17 October 2022

Published: 20 October 2022

**Publisher's Note:** MDPI stays neutral with regard to jurisdictional claims in published maps and institutional affiliations.



**Copyright:** © 2022 by the authors. Licensee MDPI, Basel, Switzerland. This article is an open access article distributed under the terms and conditions of the Creative Commons Attribution (CC BY) license (<https://creativecommons.org/licenses/by/4.0/>).

## 1. Introduction

The Metal-CO<sub>2</sub> battery has attracted attention due to its unique approach to utilize CO<sub>2</sub> economically and efficiently. The discharging process of the battery is based on the mechanism that naturally occurred the oxidation process from the metal anode provide electron to reduce CO<sub>2</sub> to various hydrocarbon byproducts, electrons can pass through an external circuit to the cathode and generate electricity [1]. Although metal-CO<sub>2</sub> battery research is still at a very early stage, it is considered to be a promising solution to capture and recycle CO<sub>2</sub>. This technology is intended to address two major global issues that are currently faced by humanity: the energy crisis and climate change caused by the rapid rise of CO<sub>2</sub> levels.

Various successful metal-CO<sub>2</sub> batteries have been demonstrated in recent years including Li-CO<sub>2</sub> [2–5], Al-CO<sub>2</sub> [6], Na-CO<sub>2</sub> [7], and others. The most studied battery is Li-CO<sub>2</sub> battery due to its high theoretical energy density of 1876 Wh Kg<sup>-1</sup> [2], compared to other available batteries. However, these batteries have challenges including, use of high active metal anodes, solid discharge products, and cost limits the practical environmentally friendly applications [8–10]. Zn-CO<sub>2</sub> provides a promising alternative due to its low toxicity, safety, cost, low active metal anodes, and is environmentally friendly [4,8,9,11,12].

Reutilizing CO<sub>2</sub> to produce other high-value chemicals is deemed to be a more practical route. Electrochemical reduction of CO<sub>2</sub> (ERC) has many advantages, which include producing high economic value products such as methanol, ethylene, and formic acid, operating at room temperature and atmospheric pressure, and the process can be powered using renewable sources of energy [13].

However, ERC has also been associated with many constraints and disadvantages. These shortcomings are demonstrated in the following three points: (i). ERC has suffered from high electrode overpotential and low resultant current density [14,15]; (ii). The hydrogen evolution reaction competes with the ERC process at the high potential in the aqueous phase [16]; (iii). Product selectivity and low efficiency often plague the ERC process [15]. Using electrocatalysts has been suggested to lower the potential and increase the current density, and to improve the overall efficiency of the ERC process. Metal and semiconducting metals, such as Cu, Fe, Sn, Au, Pt, etc., are commonly used as cathode materials to reduce CO<sub>2</sub> electrocatalytically [17,18].

Among various metal catalysts, Cu has been considered the most appropriate candidate for the ERC process. In an aqueous phase, Cu can electrocatalytically reduce CO<sub>2</sub> to hydrocarbons with relatively low current density (around 5–10 mA cm<sup>-2</sup>) and high current efficiency (i.e., >69% at 0 °C) [19]. Furthermore, the selectivity of the products can be controlled by the atomic structure of Cu, for instance, a Cu (100) electrode with an optimal density of steps has shown higher selectivity for C-C coupling than other planar surfaces [20,21]; production of oxygenates is enhanced in the crystal with the plane of (100) and (110) [20,22]; recent DFT results also show that Cu (211) yields higher magnitude activity than other planes (100) and (111) for CO reduction to CH<sub>4</sub> [23].

CNT materials have been known for their great electrical and mechanical properties [24,25], chemical inertness, and electrocatalytic stability [26], as well as high surface area [27]. All these advantages make CNT a good substrate material for Cu deposition. By utilizing the porous surface morphology of the CNT sheet, Cu materials can penetrate and distribute more evenly inside the nanotubes. The inherent mechanical property of CNT also provides CNT-Cu composite materials with a great degree of flexibility. To ensure the formation of micro-sized Cu particles, a slow-paced organic deposition method was used to deposit Cu on the CNT sheet. Two Zn-CO<sub>2</sub> batteries were investigated using two tubular cathodes prepared from directly grown CNTs on copper and nickel mesh [28]. These batteries demonstrated excellent stability, high input voltage, and discharge performance. Another Zn-CO<sub>2</sub> was fabricated using hollow CNT fiber exhibited high selectivity and efficiency [10]. The battery showed energy density of 288.3 Wh Kg<sup>-1</sup> and was stable up to 8 days.

This paper discusses the use of CNT sheet as a cathode material for Zn-CO<sub>2</sub> battery. The CNT sheet was first acid-treated to make it hydrophilic and then electrochemical activation was performed on the acid-treated CNT sheet to increase the surface area for Cu deposition. The organic deposition method was used to deposit the Cu on the activated CNT sheet, different Cu depositions were achieved by varying the deposition time of the process. Optimum deposition time in terms of CO<sub>2</sub> reduction efficiency was studied. The aim of this research is to use activation process to increase the surface area of the electrode for more catalyst deposition. The additional area will provide more activation sites for electrochemical reduction activity and improve the performance of the device. The performance of Cu deposited CNT was then investigated and compared with non-activated CNT cathode electrode.

## 2. Results & Discussion

### 2.1. CNT Activation and Cu Deposition

During the final stage of the FCCVD process for CNT synthesis, the CNT sheet has lost a significant amount of surface area due to the densification process. Thus, electrochemical activation has been used as a practical approach to recover some of the losses. The activation is explained in detail in our previous paper [29]. Before the activation, CNTs sheets were acid-treated to increase their hydrophilicity. The hydrophobicity of as-synthesized CNT sheet has prevented electrolytes from wetting the electrode, which is mainly due to the nonpolar aromatic molecular structure. Acid treatment was used to functionalize the CNT sheet and promote the wetting [30]. Additionally, to not bring external chemical elements into the electrochemical cell, NaCl was used as the electrolyte to activate the CNT sheet. The duration of activation was limited to less than 10 min to prevent CNT structural damage

caused by excessive activation. During the activation process, electrolysis, and formation of  $H_2$  caused expansion and delamination of the CNT sheet. After 10 min activation, the activated CNT sheet exhibited sponge-like and multi-layer morphology, which was able to increase the inner surface area for the deposition of Cu. The illustration of activation and deposition process used for CNT sheet samples for  $CO_2$  reduction and battery part is shown in Figure 1.

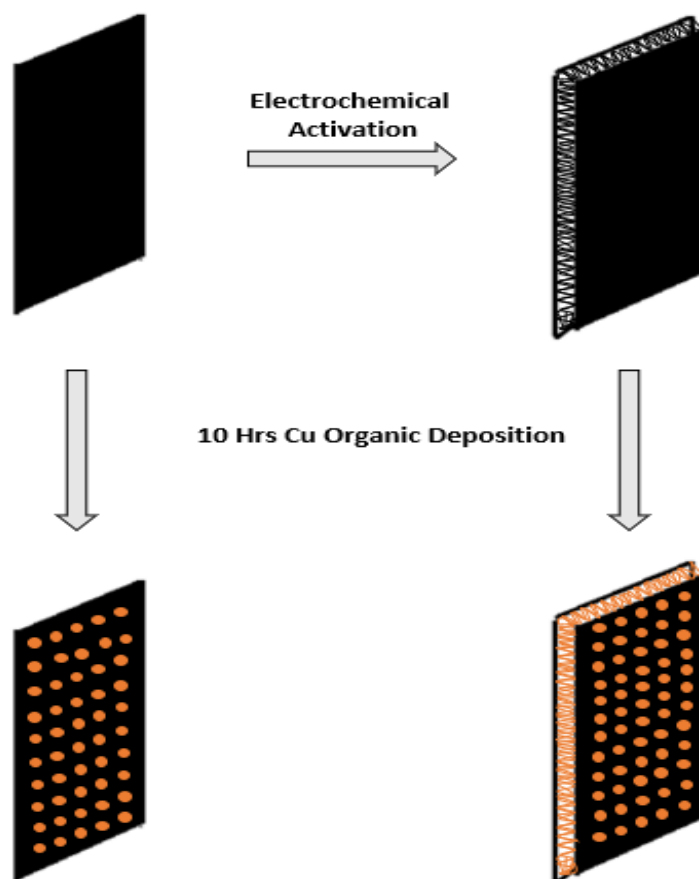


**Figure 1.** The illustration of process steps used for preparing CNT samples for analysis.

During the Cu deposition, organic electrolytes ( $Cu(CH_3COO)_2$  &  $CH_3CN$ ) were used for deposition. Organic deposition has been used as a Cu seeding method in some publications, it has helped to achieve a uniform and less congregated Cu distribution on CNT substrate due to its low Faradaic efficiencies and slow deposition rate [31]. In comparison to an aqueous electrolyte deposition method ( $CuSO_4$ ), organic deposition can infiltrate into the activated area and provide more balanced internal and surface deposition [31]. In this research, organic deposition was used to deposit Cu onto activated CNT sheet to maximize its surface area.

Cu deposition was achieved by electrochemical deposition of Cu onto a CNT electrode with a constant voltage by using the organic deposition method. The organic deposition method (OD) has been used to promote Cu deposition within CNT wires and control surface deposition to obtain a uniform and continuous Cu matrix. OD is the initial seeding process that deposit nano-sized Cu particle, under the following heat treatment, these nanosized Cu particles can agglomerate into micro-sized Cu particles, which catalyze  $CO_2$  reduction [31,32]. During the CV measurement, the three electrode method was used to measure the cyclic voltammetry at different scan rates (10, 25, 50, 100, and 150 mV/s), the CV curves were presented in Figures S1A–D and S2 (Sections S1 and S2) to study the electrochemical activity of various samples, according to which there is no redox peak for the acid-treated sample, whereas redox peaks are visible for the 2, 5, 10, 20 h for the Cu

deposited sample. The onset of the reduction peak is an indication of the occurrence of the  $\text{CO}_2$  reduction reaction. Due to the absence of Cu catalyst, a redox reaction is unlikely to have occurred on the acid-treated CNT sample.

Additionally, the relationship between current density and potential is shown in Figure S2, as it indicated that current density increases with the increase in potential. However, the acid-treated CNT sample shows the lowest negative current density increase compared with other samples. The 10 h Cu deposited sample showed the highest negative current density increase especially below  $-1$  V. Due to its great electrochemical activity at a negative potential, 10 h was considered the optimal OD time frame to provide most electrochemically active CNT sample for  $\text{CO}_2$  reduction.

## 2.2. The Surface Area Comparison

The electrochemical active surface area of acid-treated CNT as well as CNT after activation was estimated based on the double-layer capacitance ( $C_{dl}$ ) by using a cyclic voltammetry (CV) graph. According to the classic capacitance equation for double-layer capacitance:  $C_{dl} = \epsilon_0 * A / d$ , where  $A$  is the surface area and  $d$  is the distance between layers [33], the surface area of the electrode is proportional to the capacitance value.

During the measurement, CV was taken between  $-1.0$  and  $2.0$  V vs. RHE at scan rates of  $10$  mV/s and the electrolyte is  $1$  M NaCl saturated with  $\text{CO}_2$ . According to the CV graph in Figure 2, the capacitance of the sample was estimated using  $C_{dl} = \int Idv / v * m * \Delta V$ , where  $\int Idv$  is the integrated area under the CV curve,  $v$  is the scan rate,  $m$  is the weight of the electrode sample, and  $\Delta V$  is the voltage window. Because  $v$ ,  $m$ , and  $\Delta V$  are the same for the acid-treated and activated samples, the surface area ratio between activated CNT and acid-treated CNT is equivalent to the ratio of the integrated area of their respective CV curve. Based on the calculation,  $\int Idv$  of the activated CNT curve is around 4.5 times larger than the acid-treated CNT curve, which suggested a large increase in the electrochemical active area and higher surface roughness.

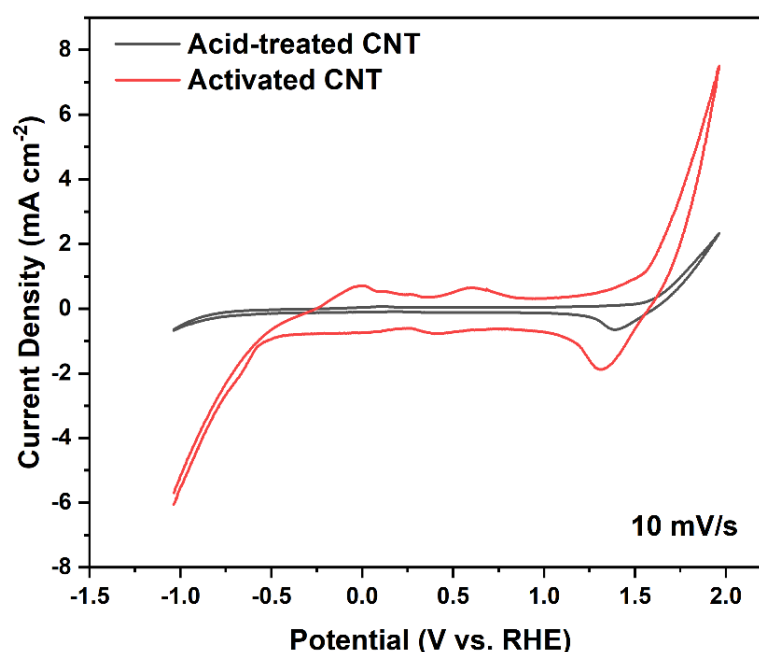
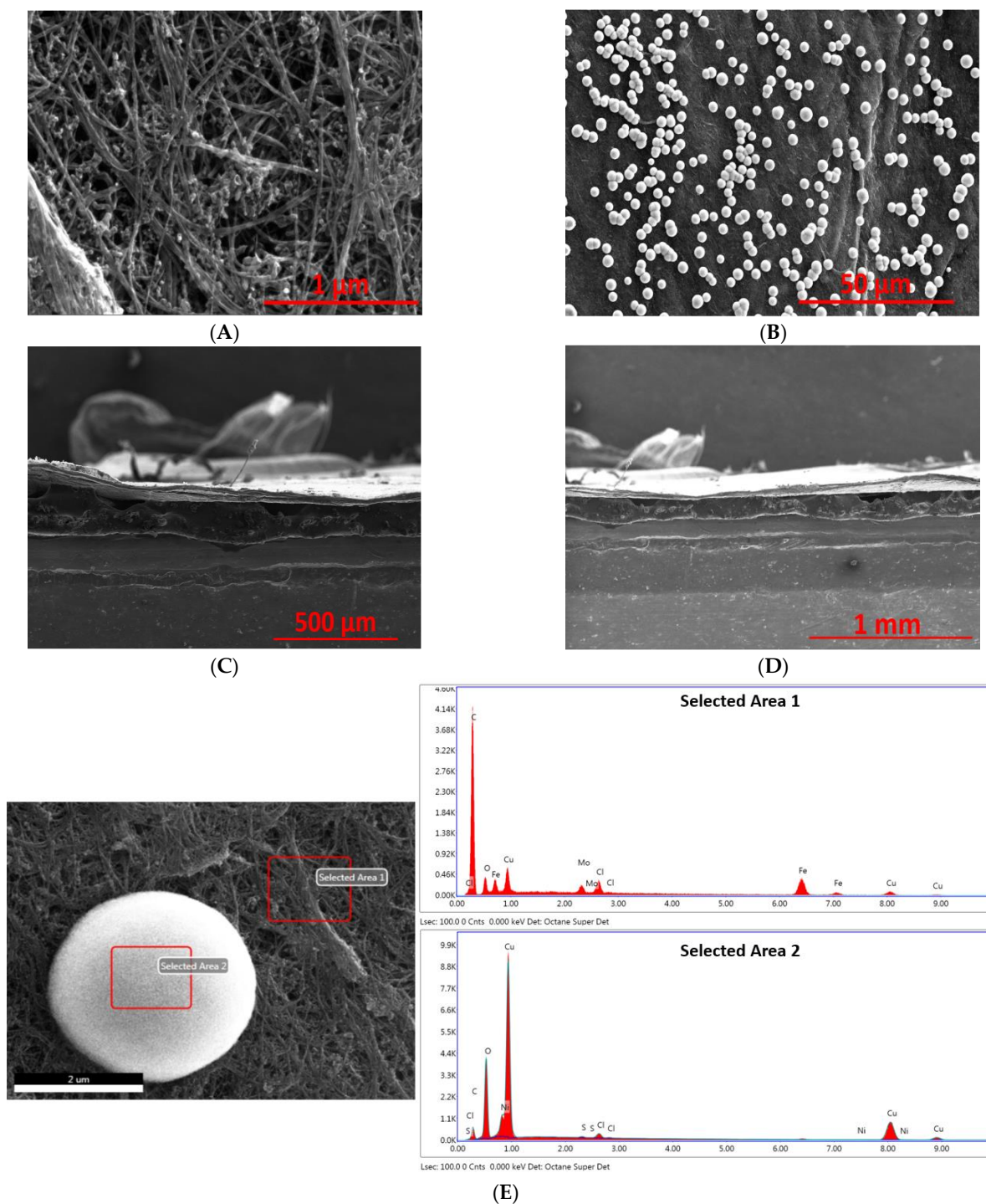


Figure 2. CV curve of acid-treated and activated CNT.

## 2.3. Structural Analysis

The SEM images of acid-treated and activated CNT with Cu deposition with different magnification as well as their EDX graph are shown in Figures 3 and 4, respectively. After organic deposition, Cu precipitant was first formed around CNT strands and deposited onto the surface of CNT sheet (Figure 3A). After the heat treatment, these precipitants

started to coalesce and formed large size spherical particles, which were uniformly distributed on the CNT surface as shown in Figure 3B, while the cross-section is non-activated (Figure 3C,D) and its compact structure prevents further infiltration of Cu. Additionally, EDX was used to verify the presence of Cu (Figure 3E). The presence of O indicates that Cu particles are partially oxidized, a small percentage of impurities such as Fe, S are from the catalyst source (Ferrocene) and growth promoter (Thiophene), respectively, used in the nanotube synthesis process. The elements of Mo and Cl are possibly from the ceramic tube used in the synthesis reactor.



**Figure 3.** SEM images of acid-treated CNT with Cu organic deposition: surface morphology (A,B), as well as cross-sectional images (C,D), and EDX spectrum of the selected area (E).

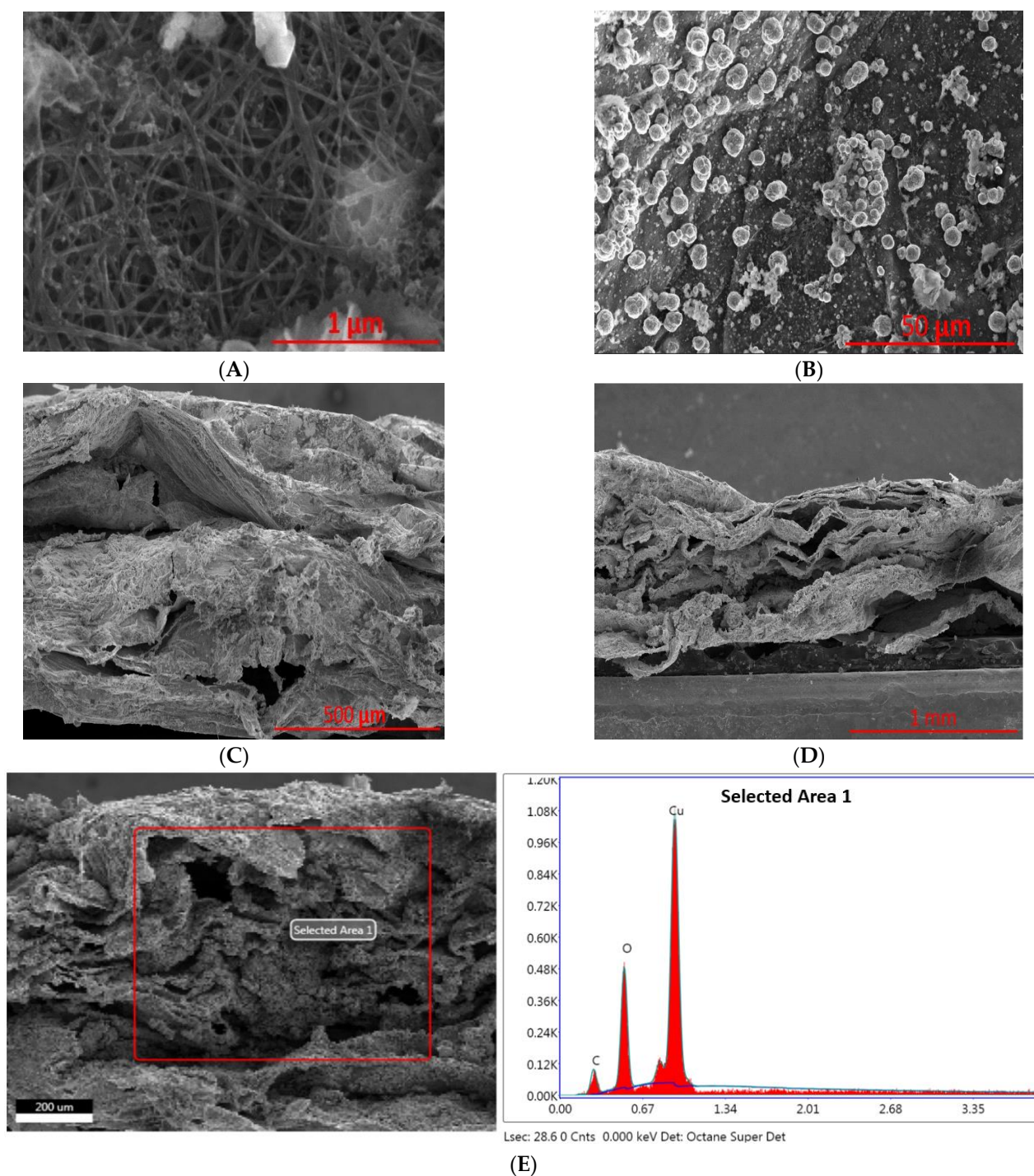


**Figure 4.** SEM images of activated CNT with Cu organic deposition: surface morphology (A,B), as well as cross-sectional images (C,D), and EDX spectrum from cross-sectional area of the activated sample (E).

In terms of the activated CNT sheet, due to the nature of the electrochemical activation process, which generates a copious amount of  $H_2$ ,  $H_2$  is not only able to delaminate the CNT sheet, but surface roughness has also been increased due to the bulge formation in the CNT sheet from  $H_2$  generation. The distance between CNT strands appears to be wider than that of non-activated ones (Figure 4A), the rough surface also gives rise to the rough Cu surface morphologies (Figure 4B). Past literature has shown that surface roughness has a direct relationship with activity and product selectivity of  $CO_2$  reduction [34,35]. There are more under-coordinated sites present in the roughened surface that showed more adsorption energies compared to highly coordinated sites. Cross-section SEM images showed the

multilayer and delaminated structure, which provide ample space for Cu deposition. An EDX spectrum of the cross-section indicates that Cu has a large presence, and the presence of O indicates Cu is partially oxidized.

#### 2.4. Linear Sweep Voltammetry Graph and Potentiostatic Curve

A linear sweep voltammetry (LSV) graph was used to estimate the electrochemical reduction potential of the electrodes. Enhanced current density at increased negative potential suggests high electrocatalytic activity of activated CNT/Cu for CO<sub>2</sub> reduction. The comparison was made between Cu deposited acid-treated CNT and Cu deposited activated CNT, before the LSV measurement, NaCl electrolyte was saturated with CO<sub>2</sub>, and CO<sub>2</sub> gas was continuously pumped into NaCl electrolyte during the experiment. The range of sweeping potential was kept between 0.4 and −0.6 vs. RHE, current density was normalized by the geometric area of the CNT sample. It can be seen from Figure 5A that, for the Cu deposited activated CNT sample, a rapid shift in current and increased current density indicate an intensified reduction reaction. The reduction current density initially decreased and increased with further increase of reduction potential. However, in terms of Cu deposited only in the acid-treated sample, the current density appeared to be stabilized at around 0.5 mA/cm<sup>2</sup> after the initial rapid decline, which indicates a minor occurrence of the electrochemical reduction reaction.

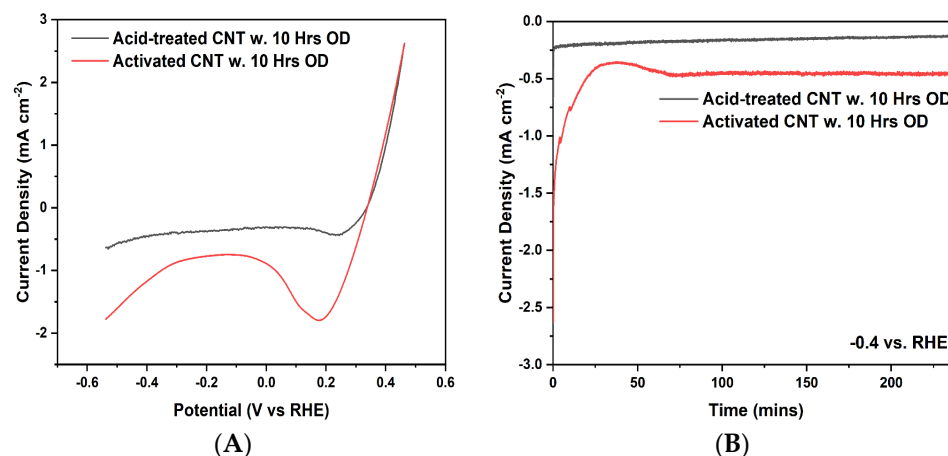


**Figure 5.** LSV curve (A) and potentiostatic curve (B) of acid-treated CNT with 10 Hrs Cu organic deposition and activated CNT with 10 Hrs organic deposition.

Potentiostatic testing was carried out and results are shown in Figure 5B. A constant voltage −0.4 vs. RHE was applied and the current density variation was measured during the 4 h running. Cu deposited activated CNT experienced initial decline and later became stabilized around 0.5 mA/cm<sup>2</sup>, while Cu deposited only acid-treated CNT was kept constant around 0.25 mA/cm<sup>2</sup>, which indicates that activated CNT provides extra space for Cu deposition to increase the activation sites, additionally rough surface morphology of Cu particles on the CNT sheet enhances the electrochemical activities.

#### 2.5. Zn-CO<sub>2</sub> Battery Performance

The Zn-CO<sub>2</sub> metal battery was constructed in the H-cell, which is schematically shown in Figure 6. Cu deposited activated CNT was used as the cathode material in the cathodic compartment, while the Zn plate was used as an anode in the anodic compartment. A Nafion membrane was used to stabilize the pH values of anolyte and catholyte. After NaCl was saturated with CO<sub>2</sub>, the gas was constantly bubbling into the electrolyte during the experiment. During the discharge process, the Zn plate can react with KOH to form Zn(OH)<sub>2</sub> and release electrons, at the same time, CO<sub>2</sub> reduction occurred on the Cu deposited CNT electrode, and Cu catalyzes to promote the CO<sub>2</sub> conversion.

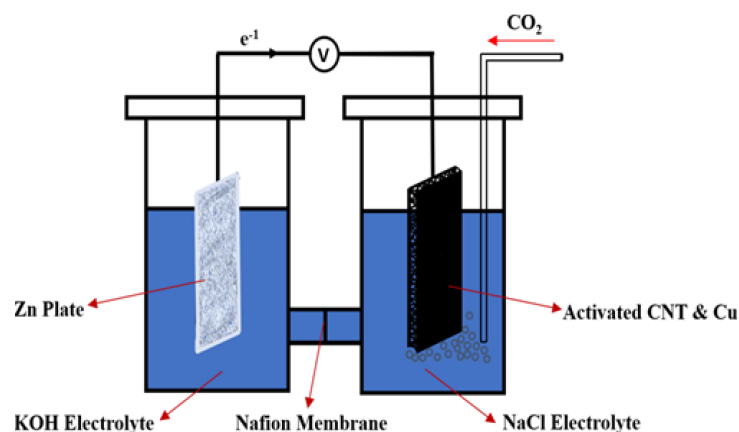


Figure 6. Schematic diagram of the Zn-CO<sub>2</sub> electrochemical cell.

The possible reaction occurred on both electrodes are shown below:



The potential stability of Zn-CO<sub>2</sub> in terms of discharging time before and after the saturation of CO<sub>2</sub> was measured. According to Figure 7A, the acid-treated CNT showed the lowest potential output and was followed by a sharp potential drop, while inactivated CNT. In Figure 7B, before the saturation of CO<sub>2</sub>, the output potential of a cell has been stabilized around 1.3 V, after the saturation of CO<sub>2</sub>, the potential has seen a steady drop, which is likely due to the increased internal resistance caused by CO<sub>2</sub> saturated electrolyte. Figure 7C,D, both demonstrate the potential to increase due to the introduction of CO<sub>2</sub>, furthermore, Cu deposited activated-CNT shows the highest potential increase of 0.4 V after CO<sub>2</sub> saturation, while Cu deposited acid treated-CNT has a 0.2 V increase after CO<sub>2</sub> saturation. During 20 min discharging process, the discharge current density was kept at 0.0625 mA/cm<sup>2</sup>. The potential change at different current densities was also measured and presented in Figure 7E, the potential was reduced from 1.2 V at a current density of 0.122 mA/cm<sup>2</sup> to 0.8 V at a current density of 0.37 mA/cm<sup>2</sup>. In comparison, when NaHCO<sub>3</sub> was used as electrolyte on both side of the cell, due to the low reactivity between Zn and NaHCO<sub>3</sub>, output potential show negligible improvement when Cu-CNT was cathode (Supplementary Materials Figure S3 in Sections S3).

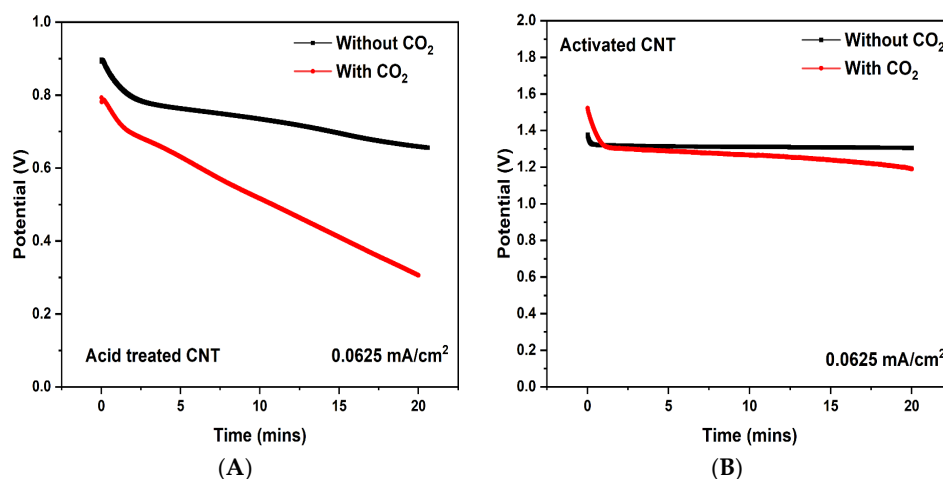
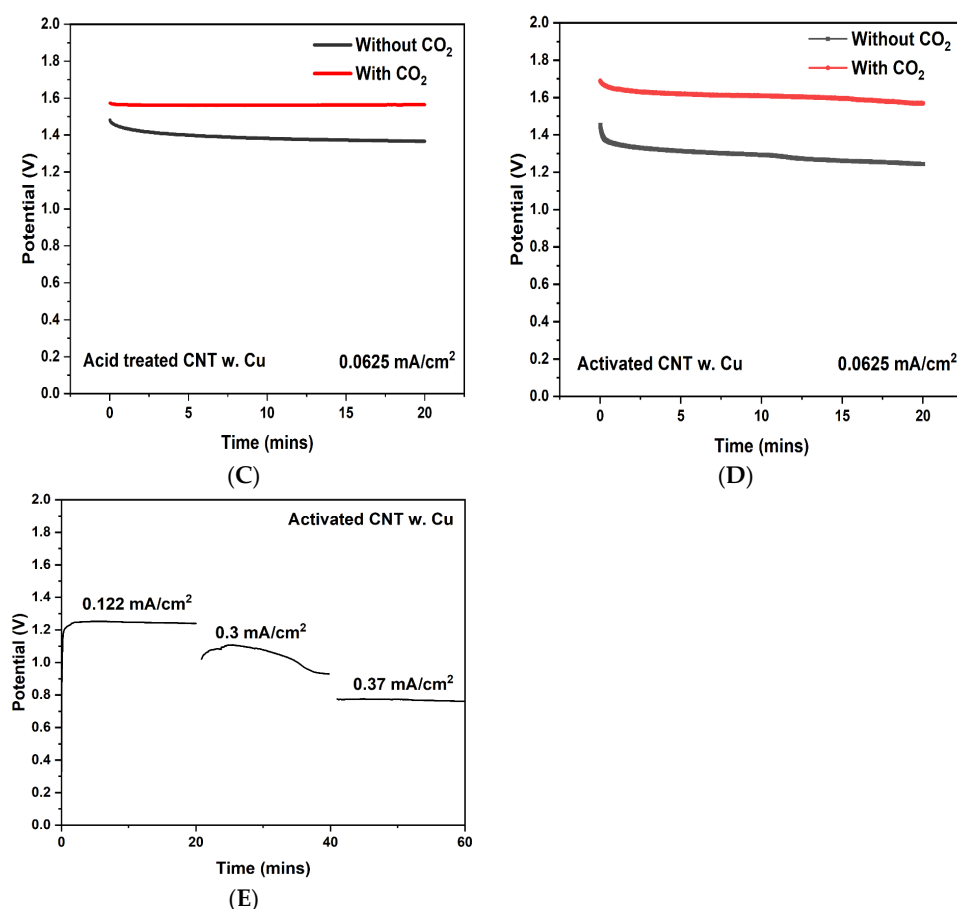


Figure 7. Cont.



**Figure 7.** Discharging curve of acid-treated CNT for 20 min (A), activated CNT (B), Cu-deposited acid-treated CNT (C), Cu deposited activated CNT (D), discharging curve of Cu deposited activated CNT at different current densities (E).

The formation of acetic acid ( $\text{CH}_3\text{COOH}$ ) in the electrolyte has been verified by Nuclear Magnetic Resonance (NMR) (Figure 8A). NMR is used to determine the molecular structure at the atomic level, in which all nuclei have multiple spins and are electrically charged. Inside of NMR magnetic field, radio wave excites the nuclei from lower to higher energy level in a single step and generates nuclear magnetic resonance, which can be detected by sensitive radio receiver. The resonance frequency gives access to the detailed information of the electronic structure and functional group of a molecule/chemical compounds [36,37].

According to various literature, pathways towards C2+ products are considered to be very complex and generates debate among researchers performing theoretical studies. Compared with C1 products, C2+ hydrocarbon by-products contain two or more carbon atoms and have higher energy densities, although most theoretically proposed mechanisms are based on density functional theory (DFT) simulations, however, the consensus is by transferring a concerted proton-electron ( $\text{H}^+/\text{e}^-$ ) from the electrolyte to adsorbed species, which in this case is Cu surface, a  $\text{CO}_2$  molecule can reduce to carboxyl intermediate  $^*\text{COOH}$  and then to  $^*\text{CO}$  and water molecule, further reaction include protonation of  $^*\text{CO}$  to  $^*\text{CH}_3\text{O}$  and following coupling with  $\text{CO}_2^-$  to form to acetate [38], which is illustrated in Figure 8B due to the complicated nature of the reaction as well as this could well be one of the possible routes to form acetic acid, further studies are needed to fully confirm. The Zn- $\text{CO}_2$  battery has a theoretical electromotive force of 4.557 V and a theoretical energy density of  $915.75 \text{ Wh Kg}^{-1}$  (Supplementary Materials Section S4). The comparison between this work and other works can be found in Table S1 in Section S5 which proves that this

Zn-CO<sub>2</sub> battery has a high open voltage of 1.6 V compared to other batteries reported in the literature.

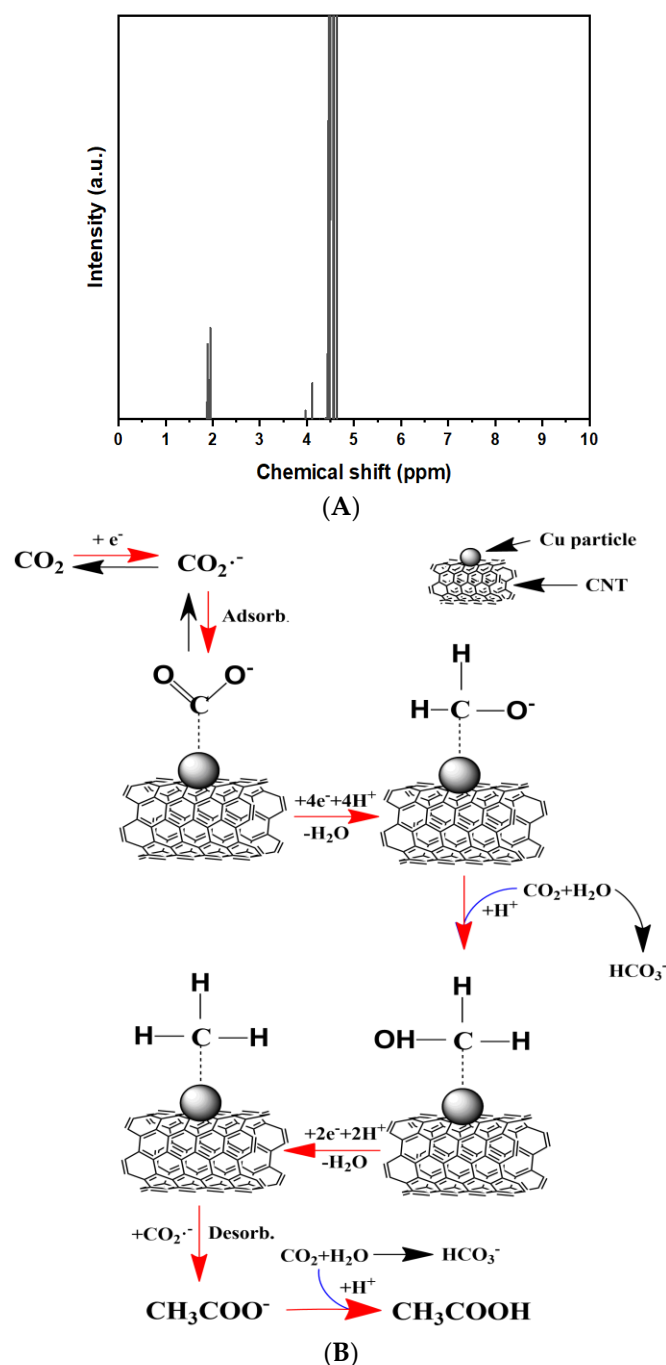


**Figure 8.** <sup>1</sup>H NMR graph of the by-product electrolyte (A) and acetic acid by possible product pathway from CO<sub>2</sub> reduction (B).

### 3. Materials and Methods

#### 3.1. The Synthesis and Activation of CNT Sheet

The CNT sheet used in this experiment was synthesized from Floating Catalyst Chemical Vapor Deposition (FCCVD) method. The FC-CVD process is a one-step continuous process and can produce industrial-scale nanotube sheet. The process is substrate-free and provides flexibility to tune the process and customize the material according to a specific application. In this process, we introduced a feedstock at the inlet of the reactor. The feedstock is composed of methanol, n-Hexane, ferrocene, and thiophene. The CNT sock

(web of nanotubes) forms in the high-temperature synthesis zone of the reactor and is collected at the outlet of the reactor onto a rotating drum. A detailed description of the synthesis process tuning, process analysis, and characterization techniques can be found in our previously published research articles [39–43,43–46]. The as-synthesized CNT sheet materials are cleaned and expanded through an acid treatment and activation process. The acid treatment follows the steps of immersing the sample inside a mixture of 3:1 ratio of H<sub>2</sub>SO<sub>4</sub> (Fisher Chemical) and HNO<sub>3</sub> (Fisher Chemical) followed by heat reflux (90 °C) for 2–3 h.

For activation of the CNT sheet [29], a three-electrode method was employed using an electrochemical workstation (Gamry, Interface 1000, Warminster, PA, USA). A rectangular CNT sheet (34 mm × 48 mm) served as the working electrode. Ag/AgCl and graphite rods were used as the reference and counter electrodes respectively. A 0.3 M NaCl solution was used as the electrolyte. A cyclic voltammetry (CV) sweep was conducted at a scan rate of 50 mV/s, with an applied voltage between −2 V and +2 V, to chemically activate which increases the surface area of the CNT sheet. Typically, 10–15 scan cycles were considered as the optimal number of cycles to fully activate the CNT without causing structural damage to the CNT sheet. The relationship between number of activation cycles and optimal electrochemical performance is given in [29].

### 3.2. Organic Deposition of Copper on Activated CNT

The Cu electrodeposition was carried out on a workstation equipped with a power supply (Circuit Specialists, CSI5003X5, AZ, USA), a voltage stabilizer (XY-SK35 CNC buck-boost, Econede, FL, USA), and a time relay device (XY-WJ01 Delay Relay Module, Hardware, TKXEC, China) were used to ensure constant voltage supply and accurate control of the electrodeposition time. The electrodeposition setup consisted of an activated CNT sheet sample as the cathode material that was mounted on a glass slide with a Cu strip attached to the upper edge of the sample. The CNT cathode material and Cu anode material were immersed and separated each other at a distance of ~20 mm in the electrolyte. Anhydrous 0.0075 g copper acetate (Cu (CH<sub>3</sub>COO)<sub>2</sub>, Sigma Aldrich, St. Louis, MO, USA) in 150 mL acetonitrile (CH<sub>3</sub>CN, Sigma Aldrich, St. Louis, MO, USA) was used as the electrolyte for organic deposition. Deposition times were 2 h, 5 h, 10 h, and 20 h, respectively, and the excess electrolyte after Cu organic deposition was removed from the sample by rinsing in deionized water. The sample was then dried in the air for 1 h.

### 3.3. Metal-CO<sub>2</sub> Battery Electrochemical Measurement

Electrochemical activity for CO<sub>2</sub> reduction experiments was conducted in a three-electrode method using an electrochemical workstation (Gamry, Interface 1000, Warminster, PA, USA) and a CV/linear sweep voltammetry (LSV) graph was recorded. All electrochemical data was collected vs. the Ag/AgCl reference electrode. The electrolyte used in both compartments was 1 M NaCl solution. The Ag/AgCl electrode and the Platinum electrode were used as the reference and counter electrode. The following equation was used to convert from the Ag/AgCl scale to the reversible hydrogen electrode (RHE) standard:

$$E(\text{vs. RHE}) = E(\text{vs. Ag/AgCl}) + 0.209V + 0.0591V \times pH \quad (4)$$

The pH value of the electrolyte in Equation (1) was measured using a digital pH meter (Digital pH tester pen, VIVUSUN, China).

A full Zn-CO<sub>2</sub> battery was assembled in an H-type cell separated by a Nafion membrane. A Zn plate (34 mm × 48 mm) and Cu deposited CNT were used as anode and cathode respectively. Before the experiment, ultra-pure CO<sub>2</sub> (99.99%, Wright Brother, Cincinnati, OH, USA) was pumped into the cathode compartment for 45 min at a rate of 0.25 sL/min to saturate the electrolyte. The whole system is air-tight to prevent leakage and increase CO<sub>2</sub> saturation concentration in the electrolyte (1 M NaCl).

### 3.4. Material Characterization

Scanning electron microscopy (SEM) (FEI SCIOS, 5 kV, Themofisher Scientific, Waltham, MA, USA) was used to characterize the surface morphology as well as the cross-section of the activated CNT/Cu sample. Nuclear magnetic resonance (NMR) (Bruker NEO 400 Billerica, MA, USA), with Bruker Ascend 9.4 T, 54 mm (narrow) bore, BOSS-336 shim system, equipped with Bruker 5 mm SMART  $^{15}\text{N}$ - $^{31}\text{P}$  and  $^{19}\text{F}$  observe with  $^1\text{H}$  decoupling and observe, Z-axis PFG, VT range from 150 to +150 °C, was used to analyze the by-product solution from the electrochemical reduction experiment.

### 4. Conclusions

A Zn-CO<sub>2</sub> battery with copper deposited CNT as a cathode and a zinc plate as an anode is proposed. The area of the CNT electrode was increased by 4.5 times using the electrochemical activation technique. Different copper loadings were studied for the CO<sub>2</sub> reduction process, and it was concluded that the ten hours of organic deposition is the optimum loading for our sample. A new approach for using activated CNT as the cathode is presented and the assembled battery showed an open circuit voltage of 1.6 V and a current density of 0.063 mA/cm<sup>2</sup>, which is higher than reported for most device in the literature. Moreover, the oxidized Zn plate is easily replaceable which extends the lifetime of the battery. However, the reduction reaction is still ambiguous and needs a better understanding of the reaction mechanism.

**Supplementary Materials:** The following supporting information can be downloaded at: <https://www.mdpi.com/article/10.3390/ijms232012602/s1>.

**Author Contributions:** Conceptualization, D.R.C. and M.C.; Formal analysis, D.R.C. and M.C.; Supervision, V.S. and M.S.; Validation, M.S.; Writing—original draft, D.R.C. and M.C. All authors have read and agreed to the published version of the manuscript.

**Funding:** This research study was supported by the National Institute for Occupational Safety and Health through the Pilot Research Project Training Program of the University of Cincinnati Education and Research Center Grant #T42OH008432.

**Informed Consent Statement:** Not applicable.

**Data Availability Statement:** The data that support the findings of this study are available from the corresponding author upon reasonable request.

**Conflicts of Interest:** The authors declare no conflict of interest.

### References

1. Qiao, Y.; Xu, S.; Liu, Y.; Dai, J.; Xie, H.; Yao, Y.; Mu, X.; Chen, C.; Kline, D.J.; Hitz, E.M.; et al. Transient, in situ synthesis of ultrafine ruthenium nanoparticles for a high-rate Li-CO<sub>2</sub> battery. *Energy Environ. Sci.* **2019**, *12*, 1100–1107. [CrossRef]
2. Li, C.; Guo, Z.; Yang, B.; Liu, Y.; Wang, Y.; Xia, Y. A Rechargeable Li-CO<sub>2</sub> Battery with a Gel Polymer Electrolyte. *Angew. Chem.* **2017**, *56*, 9126–9130. [CrossRef]
3. Zhang, Z.; Zhang, Q.; Chen, Y.; Bao, J.; Zhou, X.; Xie, Z.; Wei, J.; Zhou, Z. The first introduction of graphene to rechargeable Li-CO<sub>2</sub> batteries. *Angew. Chem.* **2015**, *127*, 6550–6553. [CrossRef]
4. Mu, X.; Pan, H.; He, P.; Zhou, H. Li-CO<sub>2</sub> and Na-CO<sub>2</sub> Batteries: Toward Greener and Sustainable Electrical Energy Storage. *Adv. Mater.* **2020**, *32*, 1903790. [CrossRef]
5. Xu, S.; Das, S.K.; Archer, L.A. The Li-CO<sub>2</sub> battery: A novel method for CO<sub>2</sub> capture and utilization. *RSC Adv.* **2013**, *3*, 6656–6660. [CrossRef]
6. Ma, W.; Liu, X.; Li, C.; Yin, H.; Xi, W.; Liu, R.; He, G.; Zhao, X.; Luo, J.; Ding, Y. Rechargeable Al-CO<sub>2</sub> Batteries for Reversible Utilization of CO<sub>2</sub>. *Adv. Mater.* **2018**, *30*, 1801152. [CrossRef] [PubMed]
7. Hu, X.; Sun, J.; Li, Z.; Zhao, Q.; Chen, C.; Chen, J. Rechargeable room-temperature Na-CO<sub>2</sub> batteries. *Angew. Chem.* **2016**, *55*, 6482–6486. [CrossRef] [PubMed]
8. Xie, J.; Wang, X.; Lv, J.; Huang, Y.; Wu, M.; Wang, Y.; Yao, J. Reversible Aqueous Zinc-CO<sub>2</sub> Batteries Based on CO<sub>2</sub>-HCOOH Interconversion. *Angew. Chem.* **2018**, *57*, 16996–17001. [CrossRef]
9. Gao, S.; Liu, Y.; Xie, Z.; Qiu, Y.; Zhuo, L.; Qin, Y.; Ren, J.; Zhang, S.; Hu, G.; Luo, J.; et al. Metal-Free Bifunctional Ordered Mesoporous Carbon for Reversible Zn-CO<sub>2</sub> Batteries. *Small Methods* **2021**, *5*, 2001039. [CrossRef] [PubMed]

10. Wang, K.; Wu, Y.; Cao, X.; Gu, L.; Hu, J. A Zn–CO<sub>2</sub> Flow Battery Generating Electricity and Methane. *Adv. Funct. Mater.* **2020**, *30*, 1908965. [CrossRef]
11. Fetrow, C.J.; Carugati, C.; Zhou, X.D.; Wei, S. Electrochemistry of metal-CO<sub>2</sub> batteries: Opportunities and challenges. *Energy Storage Mater.* **2022**, *45*, 911–933. [CrossRef]
12. Li, Y.; Dai, H. Recent advances in Zinc-air batteries. *Chem. Soc. Rev.* **2014**, *43*, 5257–5275. [CrossRef] [PubMed]
13. Safdar Hossain, S.; Rahman, S.U.; Ahmed, S. Electrochemical reduction of carbon dioxide over CNT-supported nanoscale copper electrocatalysts. *J. Nanomater.* **2014**, *2014*, 9. [CrossRef]
14. Centi, G.; Perathoner, S.; Winè, G.; Gangeri, M. Electrocatalytic conversion of CO<sub>2</sub> to long carbon-chain hydrocarbons. *Green Chem.* **2007**, *9*, 671–678. [CrossRef]
15. Gattrell, M.; Gupta, N.; Co, A. A review of the aqueous electrochemical reduction of CO<sub>2</sub> to hydrocarbons at copper. *J. Electroanal. Chem.* **2006**, *594*, 1–19. [CrossRef]
16. Whipple, D.T.; Kenis, P.J.A. Prospects of CO<sub>2</sub> Utilization via Direct Heterogeneous Electrochemical Reduction. *J. Phys. Chem. Lett.* **2010**, *1*, 3451–3458. [CrossRef]
17. Hori, Y.; Kikuchi, K.; Suzuki, S. Production of Co and CH<sub>4</sub> in Electrochemical Reduction of CO<sub>2</sub> at Metal Electrodes in Aqueous Hydrogencarbonate Solution. *Chem. Lett.* **1985**, *14*, 1695–1698. [CrossRef]
18. Goncalves, M.R.; Gomes, A.; Condeco, J.; Fernandes, R.; Pardal, T.; Sequeira, C.A.C.; Branco, J.B. Selective electrochemical conversion of CO<sub>2</sub> to C<sub>2</sub> hydrocarbons. *Energy Convers. Manag.* **2010**, *51*, 30–32. [CrossRef]
19. Schouten, K.J.P.; Gallent, E.P.; Koper, M.T.M. Structure Sensitivity of the Electrochemical Reduction of Carbon Monoxide on Copper Single Crystals. *ACS Catal.* **2013**, *3*, 1292–1295. [CrossRef]
20. Hori, Y.; Takahashi, I.; Koga, O.; Hoshi, N. Electrochemical reduction of carbon dioxide at various series of copper single crystal electrodes. *J. Mol. Catal. A Chem.* **2003**, *199*, 39–47. [CrossRef]
21. C, H.; T, H.; YG, K.; A, V.; JH, B.; DC, H.; SA, N.; MP, S.; TF, J. Engineering Cu surfaces for the electrocatalytic conversion of CO<sub>2</sub>: Controlling selectivity toward oxygenates and hydrocarbons. *Proc. Natl. Acad. Sci. USA* **2017**, *114*, 5918–5923. [CrossRef]
22. Takahashi, I.; Koga, O.; Hoshi, N.; Hori, Y. Electrochemical reduction of CO<sub>2</sub> at copper single crystal Cu(S)-[n(111) × (111)] and Cu(S)-[n(110) × (100)] electrodes. *J. Electroanal. Chem.* **2002**, *533*, 135–143. [CrossRef]
23. Liu, X.; Xiao, J.; Peng, H.; Hong, X.; Chan, K.; Nørskov, J.K. Understanding trends in electrochemical carbon dioxide reduction rates. *Nat. Commun.* **2017**, *8*, 15438. [CrossRef] [PubMed]
24. Ajayan, P.M.; Ebbesen, T.W.; Ichihashi, T.; Iijima, S.; Tanigaki, K.; Hiura, H. Opening carbon nanotubes with oxygen and implications for filling. *Nature* **1993**, *362*, 522–525. [CrossRef]
25. Zhu, Y.; Murali, S.; Cai, W.; Li, X.; Suk, J.W.; Potts, J.R.; Ruoff, R.S. Graphene and graphene oxide: Synthesis, properties, and applications. *Adv. Mater.* **2010**, *22*, 3906–3924. [CrossRef] [PubMed]
26. Koo, Y.; Malik, R.; Alvarez, N.; White, L.; Shanov, V.N.; Schulz, M.; Collins, B.; Sankar, J.; Yun, Y. Aligned carbon nanotube/copper sheets: A new electrocatalyst for CO<sub>2</sub> reduction to hydrocarbons. *RSC Adv.* **2014**, *4*, 16362–16367. [CrossRef]
27. Peigney, A.; Laurent, C.; Flahaut, E.; Bacsar, R.R.; Rousset, A. Specific surface area of carbon nanotubes and bundles of carbon nanotubes. *Carbon* **2001**, *39*, 507–514. [CrossRef]
28. Chen, Y.; Mei, Y.; Li, M.; Dang, C.; Huang, L.; Wu, W.; Wu, Y.; Yu, X.; Wang, K.; Gu, L.; et al. Highly selective CO<sub>2</sub> conversion to methane or syngas tuned by CNTs@non-noble-metal cathodes in Zn-CO<sub>2</sub> flow batteries. *Green Chem.* **2021**, *23*, 8138–8146. [CrossRef]
29. Chen, D.R.; Adusei, P.K.; Chitranshi, M.; Fang, Y.; Johnson, K.; Schulz, M.; Shanov, V. Electrochemical activation to enhance the volumetric performance of carbon nanotube electrodes. *Appl. Surf. Sci.* **2021**, *541*, 148448. [CrossRef]
30. Janas, D.; Stando, G. Unexpectedly strong hydrophilic character of free-standing thin films from carbon nanotubes. *Sci. Rep.* **2017**, *7*, 1–13. [CrossRef]
31. Sundaram, R.; Yamada, T.; Hata, K.; Sekiguchi, A. The influence of Cu electrodeposition parameters on fabricating structurally uniform CNT-Cu composite wires. *Mater. Today Commun.* **2017**, *13*, 119–125. [CrossRef]
32. Nitopi, S.; Bertheussen, E.; Scott, S.B.; Liu, X.; Engstfeld, A.K.; Horch, S.; Seger, B.; Stephens, I.E.L.; Chan, K.; Hahn, C.; et al. Progress and Perspectives of Electrochemical CO<sub>2</sub> Reduction on Copper in Aqueous Electrolyte. *Chem. Rev.* **2019**, *119*, 7610–7672. [CrossRef] [PubMed]
33. You, X.; Misra, M.; Gregori, S.; Mohanty, A.K. Preparation of an Electric Double Layer Capacitor (EDLC) Using Miscanthus-Derived Biocarbon. *ACS Sustain. Chem. Eng.* **2018**, *6*, 318–324. [CrossRef]
34. Jiang, K.; Huang, Y.; Zeng, G.; Toma, F.M.; Goddard, W.A.; Bell, A.T. Effects of Surface Roughness on the Electrochemical Reduction of CO<sub>2</sub> over Cu. *ACS Energy Lett.* **2020**, *5*, 1206–1214. [CrossRef]
35. Kim, T.; Palmore, G.T.R. A scalable method for preparing Cu electrocatalysts that convert CO<sub>2</sub> into C<sup>2+</sup> products. *Nat. Commun.* **2020**, *11*, 3622. [CrossRef] [PubMed]
36. Singh, M.K.; Singh, A. Nuclear Magnetic Resonance Spectroscopy. In *Characterization of Polymers and Fibres*; Elsevier: Amsterdam, The Netherlands, 2022; pp. 321–339. [CrossRef]
37. Snyder, J.; Noujaim, D.; Mikkelsen, T. Magnetic Resonance Spectroscopy. In *Handbook of Neuro-Oncology Neuroimaging*; Academic Press: Cambridge, MA, USA, 1995; pp. 419–467. [CrossRef]
38. Fan, Q.; Zhang, M.; Jia, M.; Liu, S.; Qiu, J.; Sun, Z. Electrochemical CO<sub>2</sub> reduction to C<sub>2</sub><sup>+</sup> species: Heterogeneous electrocatalysts, reaction pathways, and optimization strategies. *Mater. Today Energy* **2018**, *10*, 280–301. [CrossRef]

39. Chitranshi, M.; Pujari, A.; Ng, V.; Chen, D.; Chauhan, D.; Hudepohl, R.; Saleminik, M.; Kim, S.Y.; Kubley, A.; Shanov, V.; et al. Carbon nanotube sheet-synthesis and applications. *Nanomaterials* **2020**, *10*, 2023. [CrossRef]
40. Chen, D.R.; Chitranshi, M.; Adusei, P.K.; Schulz, M.; Shanov, V.; Cahay, M.M. Chlorosulfonic acid stretched carbon nanotube sheet for flexible and low-voltage heating applications. *Nanomaterials* **2021**, *11*, 2132. [CrossRef]
41. Schulz, M.J.; Chitranshi, M.; Chauhan, D.; Kubley, A.; Pujari, A.; Xu, C.; Chen, D.; Chaudhary, S.; Hou, G.; Bell, G.; et al. Pioneering carbon nanotube textile engineering & fashion technology. *J. Text. Eng. Fash. Technol.* **2019**, *5*, 89–92. [CrossRef]
42. Chitranshi, M. Carbon Nanotube Hybrid Material for Air Filtering Applications. *Video Proc. Adv. Mater.* **2021**, *2*, 2103160. [CrossRef]
43. Kim, S.Y.; Chitranshi, M.; Pujari, A.; Ng, V.; Kubley, A.; Hudepohl, R.; Shanov, V.; Anantharaman, D.; Chen, D.; Chauhan, D.; et al. Reactor Design for Manufacturing Carbon Hybrid Materials. *Adv. Mater. Lett.* **2022**, *13*, 1685–2201. [CrossRef]
44. Chitranshi, M.; Chen, D.; Schulz, M. Heat treatment of carbon nanotube hybrid material for textile applications. *J. Text. Eng. Fash. Technol.* **2021**, *7*, 121–125.
45. Chen, D.R.; Chitranshi, M.; Schulz, M.; Shanov, V. A Review of Three Major Factors Controlling Carbon Nanotubes Synthesis from the Floating Catalyst Chemical Vapor Deposition. *Nano Life* **2019**, *9*, 1930002. [CrossRef]
46. Kubley, A.; Chitranshi, M.; Hou, X.; Schulz, M. Manufacturing and Characterization of Customizable Flexible Carbon Nanotube Fabrics for Smart Wearable Applications. *Textiles* **2021**, *1*, 534–546. [CrossRef]



Article

# Crystal Design and Photoactivity of TiO<sub>2</sub> Nanorod Template Decorated with Nanostructured Bi<sub>2</sub>S<sub>3</sub> Visible Light Sensitizer

Yuan-Chang Liang \*, Shao-Yu You and Bo-Yue Chen

Department of Optoelectronics and Materials Technology, National Taiwan Ocean University, Keelung 20224, Taiwan

\* Correspondence: yuanvictory@gmail.com

**Abstract:** In this study, TiO<sub>2</sub>-Bi<sub>2</sub>S<sub>3</sub> composites with various morphologies were synthesized through hydrothermal vulcanization with sputtering deposited Bi<sub>2</sub>O<sub>3</sub> sacrificial layer method on the TiO<sub>2</sub> nanorod templates. The morphologies of decorated Bi<sub>2</sub>S<sub>3</sub> nanostructures on the TiO<sub>2</sub> nanorod templates are controlled by the duration of hydrothermal vulcanization treatment. The Bi<sub>2</sub>S<sub>3</sub> crystals in lumpy filament, nanowire, and nanorod feature were decorated on the TiO<sub>2</sub> nanorod template after 1, 3, and 5 h hydrothermal vulcanization, respectively. Comparatively, TiO<sub>2</sub>-Bi<sub>2</sub>S<sub>3</sub> composites with Bi<sub>2</sub>S<sub>3</sub> nanowires exhibit the best photocurrent density, the lowest interfacial resistance value and the highest photodegradation efficiency towards Rhodamine B solution. The possible Z-scheme photoinduced charge separation mechanism and suitable morphology of Bi<sub>2</sub>S<sub>3</sub> nanowires might account for the high photoactivity of TiO<sub>2</sub> nanorod-Bi<sub>2</sub>S<sub>3</sub> nanowire composites.

**Keywords:** composites; vulcanization; photoactivity

**Citation:** Liang, Y.-C.; You, S.-Y.; Chen, B.-Y. Crystal Design and Photoactivity of TiO<sub>2</sub> Nanorod Template Decorated with Nanostructured Bi<sub>2</sub>S<sub>3</sub> Visible Light Sensitizer. *Int. J. Mol. Sci.* **2022**, *23*, 12024. <https://doi.org/10.3390/ijms231912024>

Academic Editor: Raghvendra Singh Yadav

Received: 12 September 2022

Accepted: 6 October 2022

Published: 10 October 2022

**Publisher's Note:** MDPI stays neutral with regard to jurisdictional claims in published maps and institutional affiliations.



**Copyright:** © 2022 by the authors. Licensee MDPI, Basel, Switzerland. This article is an open access article distributed under the terms and conditions of the Creative Commons Attribution (CC BY) license (<https://creativecommons.org/licenses/by/4.0/>).

## 1. Introduction

Nanorod arrays of TiO<sub>2</sub> are beneficial to provide direct channels for electron transport, reducing the recombination probability of electrons in the transmission process. The rod morphology helps to improve the electron injection and collection efficiency of TiO<sub>2</sub> semiconductor [1–5]. However, the wide band gap nature of TiO<sub>2</sub> engenders poor response to visible light [6,7]. In order to improve the photoactivity of TiO<sub>2</sub>, the strategy of semiconductor coupling is often used to enhance the solar energy conversion and utilization of TiO<sub>2</sub> [8]. Several cases of TiO<sub>2</sub> coupled with a visible light sensitizer has been shown a promising approach to improve solar energy utilization efficiency. TiO<sub>2</sub> microspheres coupled with CdS nanoparticles enhance the light harvesting ability and suppress the electron-hole recombination of TiO<sub>2</sub> and CdS [9]. The electrospinning formed TiO<sub>2</sub>/CuO composite nanofibers enhance light absorbance and interparticle charge transfer and lower the band gap energy, thus promoting absorbance and utilization of photon energy from a broader light spectrum [10]. Precise control of Bi<sub>2</sub>O<sub>3</sub> coverage layer phase composition realizes the high photoactivity of the one-dimensional TiO<sub>2</sub>-Bi<sub>2</sub>O<sub>3</sub> composites [11]. The decoration of ZnFe<sub>2</sub>O<sub>4</sub> crystallites onto TiO<sub>2</sub> improves the photoactivity of TiO<sub>2</sub> and enhance the photodegradation performance towards Methylene orange [12]. The TiO<sub>2</sub>/Bi<sub>2</sub>S<sub>3</sub> core-shell nanowire arrays demonstrate improved photocurrent density than that of pristine TiO<sub>2</sub> because of the broadened light absorption ability and the increased charge carrier separation efficiency [13]. Similarly, Bi<sub>2</sub>S<sub>3</sub> nanowires/TiO<sub>2</sub> nanorod arrays exhibit an excellent photoelectrochemical activity [14]. Rosette-rod TiO<sub>2</sub>/Bi<sub>2</sub>S<sub>3</sub> shows substantial improvement in photoresponse in compared with pristine TiO<sub>2</sub> photoanode [15]. Furthermore, hydrothermal method deposition of TiO<sub>2</sub>/Bi<sub>2</sub>S<sub>3</sub> composite film is presented to be promising for applications of photoanode [16]. These examples clearly present the feasibility of construction of TiO<sub>2</sub>-Bi<sub>2</sub>S<sub>3</sub> heterogeneous system to be used in photoactive devices with an improved efficiency.

Among various visible-light sensitizers,  $\text{Bi}_2\text{S}_3$  has attracted much attention because it is environmentally friendly and non-toxic.  $\text{Bi}_2\text{S}_3$  has a high optical absorption coefficient and a suitable band gap, which can absorb most of the visible light spectrum [17].  $\text{Bi}_2\text{S}_3$  crystals with a large area growth and different morphologies have been realized through various chemical routes [18]. The photoactivity of  $\text{Bi}_2\text{S}_3$  crystals is highly dependent on shape, size, and crystalline quality. How to precisely control the microstructures of  $\text{Bi}_2\text{S}_3$  in order to fabricate  $\text{TiO}_2$ - $\text{Bi}_2\text{S}_3$  composites with satisfactory photoactivity is an important issue. In this study,  $\text{Bi}_2\text{S}_3$  crystals with various microstructures were decorated on  $\text{TiO}_2$  nanorod arrays via vulcanization of  $\text{Bi}_2\text{O}_3$  sacrificial layer. The vulcanization of metal oxide to obtain metal sulfide has been shown to be a promising and easy approach to synthesize the metal sulfides with controllable microstructures [17,19]. Using metal oxide sacrificial layer to form the metal sulfide through vulcanization is an easy approach to control the microstructure of the as-synthesized metal sulfide. This approach is suitable for microstructural control of the sulfide crystals and thus tuning the physical properties of the samples. However, studies on synthesis of  $\text{TiO}_2$ - $\text{Bi}_2\text{S}_3$  composites through vulcanization of  $\text{Bi}_2\text{O}_3$  layer and their photoactivities are lacking. A detailed vulcanization process-dependent microstructure evolution and photoactive properties of  $\text{TiO}_2$ - $\text{Bi}_2\text{S}_3$  composites are proposed in this study to realize the design of  $\text{TiO}_2$ - $\text{Bi}_2\text{S}_3$  composites with high photoactive performance.

## 2. Experiments

The synthesis of  $\text{TiO}_2$  nanorod template on the F-doped  $\text{SnO}_2$  (FTO) substrate was realized through a hydrothermal method at 170 °C. Other detailed parameters and preparation procedures have been described elsewhere [4]. The  $\text{Bi}_2\text{O}_3$  thin films were sputter deposited on the  $\text{TiO}_2$  nanorod template using a radio-frequency magnetron sputtering system. A metallic Bi disc was used as the target (99.9 wt%, 2 inches in diameter); the substrate temperature was fixed at 410 °C. The working atmosphere is mixed Ar/ $\text{O}_2$  with a ratio of 1/1, the working pressure is 20 mtorr and sputtering power is 30 W. The sputtering duration is 50 min. The  $\text{Bi}_2\text{O}_3$  thin-film coated  $\text{TiO}_2$  nanorod templates are further immersed in a 20 mL reaction solution containing 0.1M thiourea and sealed in a Teflon-lined autoclave for a hydrothermal reaction at 160 °C for 1, 3, and 5 h to obtain  $\text{TiO}_2$ - $\text{Bi}_2\text{S}_3$  composites (named as BT-1, BT-3, and BT-5, respectively.).

Crystallographic structures of as-synthesized samples were investigated by X-ray diffraction (XRD) analysis using  $\text{Cu K}\alpha$  radiation with a two-theta scan range of 20–60° and scan rate of four degrees per min. The morphologies of the as-synthesized samples were investigated using a field emission scanning electron microscopy (FE-SEM). The morphology, high resolution images, crystallographic structure, and composition of BT-1 and BT-3 composite samples were investigated by high-resolution transmission electron microscopy (HR-TEM). X-ray photoelectron spectroscopy (XPS) was used to analyze the elemental binding energies of the as-synthesized samples. The diffuse reflectance spectra of the as-synthesized samples were recorded by using UV-vis spectrophotometer (Jasco V750) at the wavelength range of 200–800 nm. Photoelectrochemical (PEC) and electrochemical impedance spectroscopy (EIS) properties of various photoanodes were investigated using the potentiostat (SP150, BioLogic, Orlando, FL, USA). During measurements, an Ag/AgCl electrode were used as the reference electrode herein. The 0.5 M  $\text{Na}_2\text{SO}_4$  solution was used as electrolyte and the light irradiation source for measurements is excited from 100 W Xe arc lamp. The 10 mL RhB solution ( $5 \times 10^{-5}$  M) was used as target dye solution for photodegradation experiments. The RhB solution containing various photocatalysts with different irradiation durations (0, 15, 30, 45, and 60 min) was carried out to understand the photocatalytic activity of various as-synthesized samples.

## 3. Results and Discussion

The morphology of initial pristine  $\text{TiO}_2$  rod array template was clearly observed from the SEM images in Figure 1a. As seen, the  $\text{TiO}_2$  rods are uniformly grown on the entire substrate; moreover,  $\text{TiO}_2$  rods have a regular cross-section and the side-wall surfaces are

smooth. Figure 1b displays the morphology of BT-1. A large number of lumpy filament-like crystals are covered on the top region of the TiO<sub>2</sub> rod template. Figure 1c shows that abundant nanowires with around 0.8 μm length were grafted on the TiO<sub>2</sub> rod template for the BT-3 sample. Such a morphology is similar to that of Bi<sub>2</sub>S<sub>3</sub> nanowire-decorated TiO<sub>2</sub> rod heterostructures synthesized via a facile two-step hydrothermal growth process reported by Liu et al. [14]. Compared to Figure 1c, after extending the hydrothermal duration to 5 h, the diameter of one dimensional Bi<sub>2</sub>S<sub>3</sub> thickened, and the length increases from 0.8 μm to 1.2 μm as exhibited in Figure 1d. Some aggregations of one-dimensional Bi<sub>2</sub>O<sub>3</sub> crystals appear on the TiO<sub>2</sub> rod template. It has been shown that Bi<sub>2</sub>O<sub>3</sub> oxide layer is easily etched and transfer to Bi<sub>2</sub>S<sub>3</sub> phase during a vulcanization process with sulfur ions in the reaction solution [20].

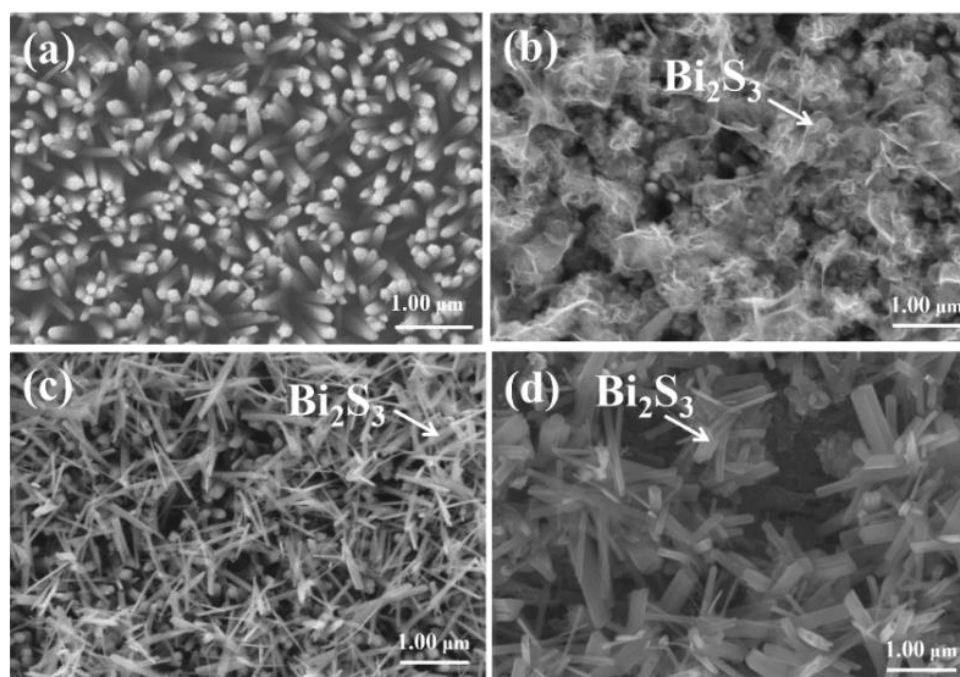


**Figure 1.** SEM images: (a) TiO<sub>2</sub> template, (b) BT-1, (c) BT-3, and (d) BT-5.

Figure 2 shows the possible formation processes of Bi<sub>2</sub>S<sub>3</sub> nanostructures on the TiO<sub>2</sub>-Bi<sub>2</sub>O<sub>3</sub> composite rod template via different vulcanization processes in this study. Notably, in aqueous solution the solubility of Bi<sub>2</sub>S<sub>3</sub> is much lower than that of Bi<sub>2</sub>O<sub>3</sub>. When the TiO<sub>2</sub>-Bi<sub>2</sub>O<sub>3</sub> composite rods are placed in a reaction solution containing a large amount of S<sup>2-</sup> ions, there is a high possibility of S<sup>2-</sup> ions transfer toward to the Bi<sub>2</sub>O<sub>3</sub> surface as exhibited in (a). Furthermore, due to solubility disparity, the formation of Bi<sub>2</sub>S<sub>3</sub> nuclei on Bi<sub>2</sub>O<sub>3</sub> will occur during the vulcanization process because of the ion exchange of S<sup>2-</sup> from the sulfur precursor solution and O<sup>2-</sup> from the Bi<sub>2</sub>O<sub>3</sub> surface. The generation of Bi<sub>2</sub>S<sub>3</sub> crystals will continually proceed with a result of Bi<sup>3+</sup> reacting with S<sup>2-</sup> as exhibited in schematic (b). Further extending reaction duration, the Bi<sub>2</sub>S<sub>3</sub> nuclei will slowly stack up to form loose filament structure at the given vulcanization condition of schematic (c). When an increase of the vulcanization reaction duration to 3 h, the loose and lumpy Bi<sub>2</sub>S<sub>3</sub> clusters will transfer into abundant, distinguishable, and separable nanowire crystals covered on the TiO<sub>2</sub> template as displayed in schematic (d). When the reaction duration reaches 5 h, the one-dimensional Bi<sub>2</sub>S<sub>3</sub> crystals continue to aggregate into a thicker rod structure, as shown in schematic (e).

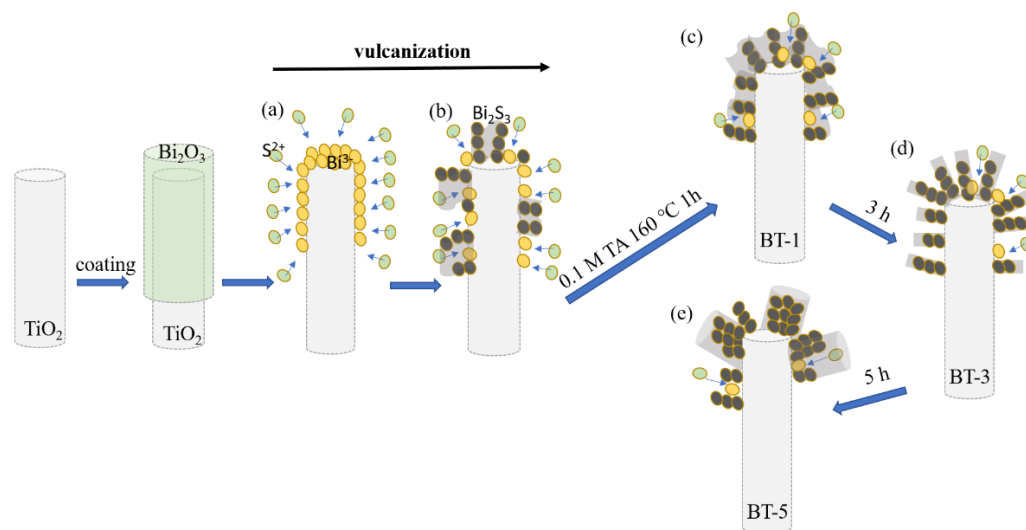


**Figure 2.** Schematic illustration of the formation processes of  $\text{Bi}_2\text{S}_3$  nanostructures.

Figure 3a–c demonstrate the XRD patterns of vulcanization-treated BT-1, BT-3, and BT-5 samples. In addition to the Bragg reflections originated from the FTO substrate, the characteristic diffraction peaks centered at approximately  $26.61^\circ$ ,  $36.18^\circ$ , and  $54.76^\circ$  can be indexed to (110), (101), and (211) planes of rutile  $\text{TiO}_2$  (JCPDS No. 00-021-1276), revealing high crystallinity of the  $\text{TiO}_2$  template. Notably, after hydrothermal vulcanization, several visible Bragg reflections originated from orthorhombic  $\text{Bi}_2\text{S}_3$  phase could be clearly observed (JCPDS No. 017-0320) in the BT-1, BT-3, and BT-5 samples. Figure 3a–c present that addition of thiourea in hydrothermal reaction solution can vulcanize the  $\text{Bi}_2\text{O}_3$  sacrificial oxide layer to transfer into the corresponding sulfide phase in BT-1, BT-3, and BT-5. The prolonged vulcanization process (from 1 to 5 h) improves Bragg reflection intensity of  $\text{Bi}_2\text{S}_3$  phase of the samples, revealing an improved crystallinity of the samples. This might be associated with crystal morphology transformation of the loose and lumpy filament-like  $\text{Bi}_2\text{S}_3$  crystals of BT-1 to one-dimensional  $\text{Bi}_2\text{S}_3$  rods of BT-5 with prolonged vulcanization process. No Bragg reflections associated with  $\text{Bi}_2\text{O}_3$  and other impurity phases were detected in the XRD patterns, revealing the vulcanization processes herein successfully synthesized the  $\text{TiO}_2$ - $\text{Bi}_2\text{S}_3$  composite structure, and the as-synthesized composite structures are crystalline.

Figure 4a shows the low-magnification TEM image of the BT-1. It can be observed that  $\text{Bi}_2\text{S}_3$  flakes decorated on the  $\text{TiO}_2$  rod. Figure 4b is the HRTEM image taken from the red square in Figure 3a. The distinct lattice fringes with a distance of approximately 0.28 nm are from the interplane spacing of orthorhombic  $\text{Bi}_2\text{S}_3$  (2 2 1) and the lattice fringes with a spacing of 0.33 nm are from the interplane spacing of tetragonal  $\text{TiO}_2$  (1 1 0). Figure 4c showed the selected area electron diffraction (SAED) pattern of several BT-1. Several clear diffraction spots arranged in centric rings are associated with the orthorhombic  $\text{Bi}_2\text{S}_3$  (2 1 1), (2 2 1), and (4 3 1) planes and the rutile  $\text{TiO}_2$  (1 1 0) plane, which agrees with the result observed by XRD analysis. This demonstrates the well-constructed  $\text{TiO}_2$ - $\text{Bi}_2\text{S}_3$  heterogeneous structure of BT-1, and a good crystallinity of the composites. The EDS spectrum in Figure 4d shows Ti, O, Bi, and S are the main elements in this composite structure. Furthermore, the particular element line scan intensity distributions displayed in Figure 4e reveals the construction of  $\text{Bi}_2\text{S}_3$  flakes on the  $\text{TiO}_2$  rod for the BT-1.

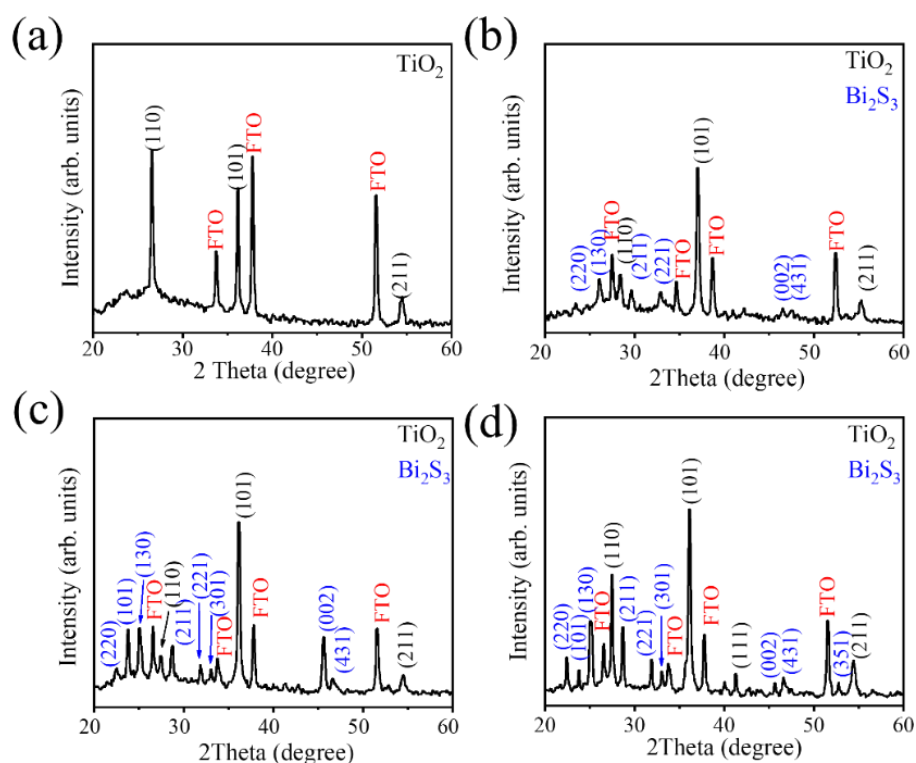


Figure 3. XRD patterns: (a) TiO<sub>2</sub> template, (b) BT-1, (c) BT-3, and (d) BT-5.

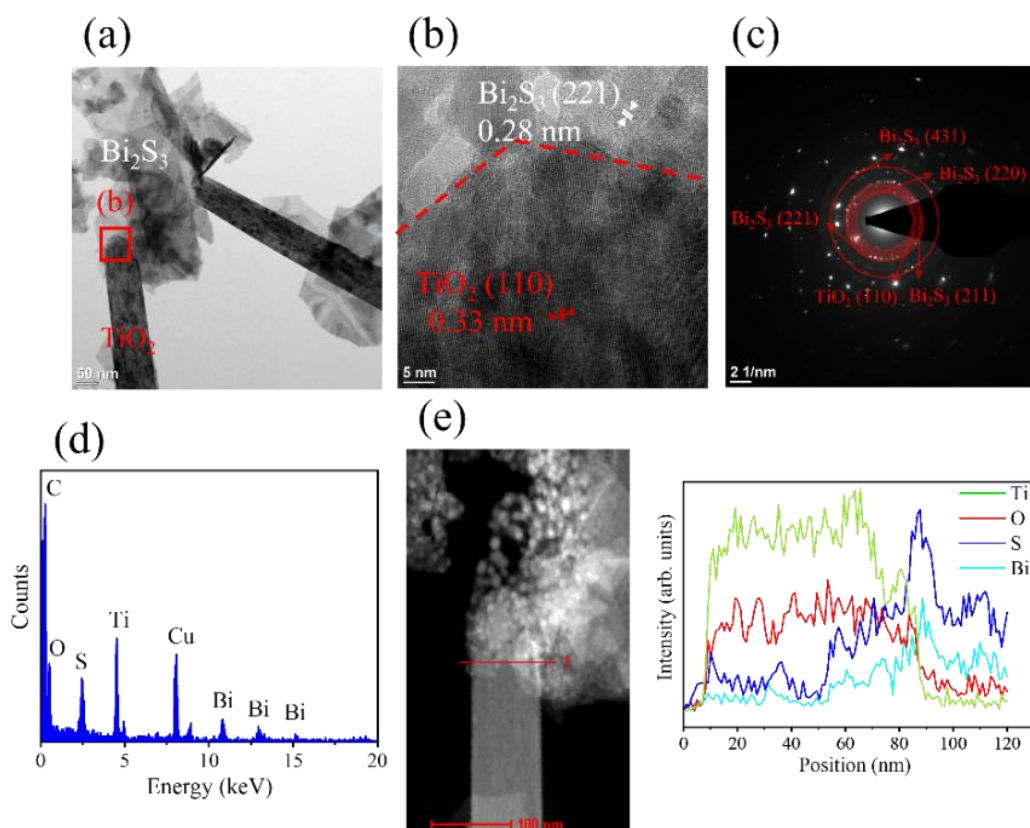
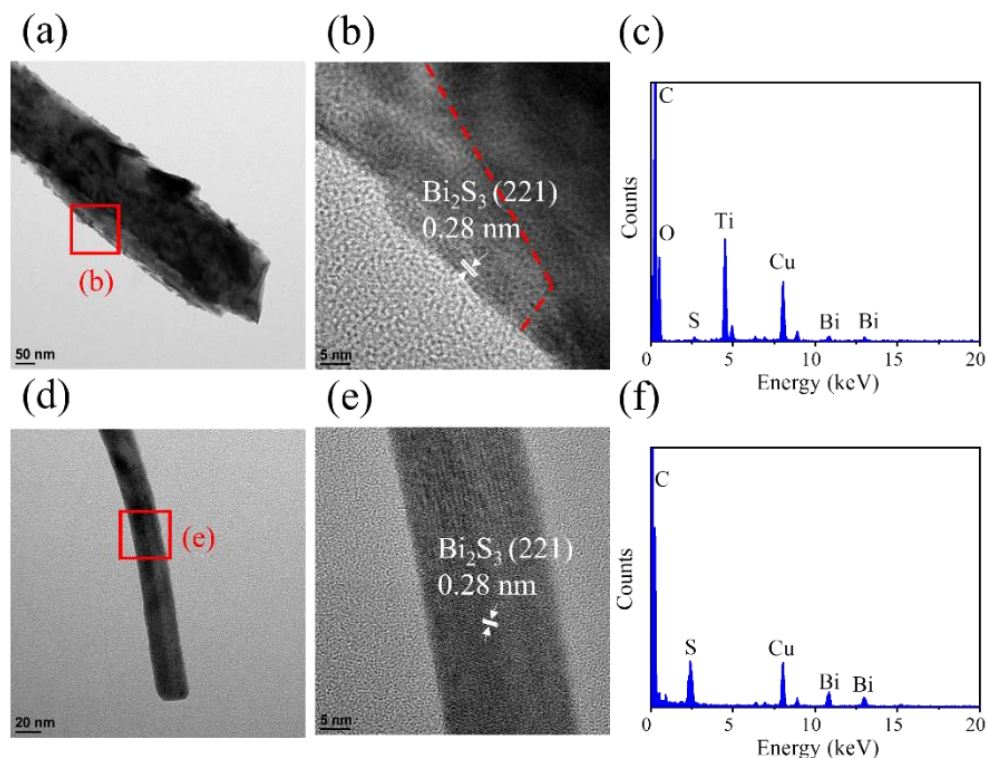


Figure 4. (a) Low magnification TEM image of BT-1. (b) HRTEM image taken from the local region of the sample in (a). (c) The SAED pattern of BT-1 in (a). (d) EDS spectrum taken from the sample in (a). (e) EDS line-scanning profiles across the composite.

Figure 5a shows the low-magnification TEM image of the BT-3 structure scratched from the sample. The sidewall of the composite showed an undulated feature because of the decoration of  $\text{Bi}_2\text{S}_3$  crystals. However, a broken top region of the structure was observed in Figure 5a. Because the preparation of TEM sample with a scratched off method will destroy the integrity of the BT-3 composite, the distinct two-layered structure of the BT-3 composite is not observed herein, as revealed in the aforementioned SEM observation. Figure 5b displays the HRTEM image taken from the red square region in Figure 5a. The distinct lattice fringes with a distance of approximately 0.28 nm are associated with the interplanar spacing of  $\text{Bi}_2\text{S}_3$  (2 2 1). Figure 5c demonstrates the EDS spectrum taken from the nanostructure in Figure 5a. In addition to Cu and C originated from the TEM grid, the Ti, O, Bi, and S are the main constituent elements in this composite structure, which proves that  $\text{TiO}_2$  and  $\text{Bi}_2\text{S}_3$  phases coexist in the composite structure. Figure 5d presents a low-magnification image of the scratched nanowire structure from BT-3 sample. The nanowire has the diameter of 23 nm, and the surface is smooth. The nanowire shows a little bent state. Figure 5e shows the HRTEM image taken from the red square in Figure 5d. The distinct and ordered lattice fringes shows the single crystalline quality of the  $\text{Bi}_2\text{S}_3$  nanowire. Similarity, a distinguishable  $\text{Bi}_2\text{S}_3$  (2 2 1) lattice image in the one-dimensional  $\text{Bi}_2\text{S}_3$  crystal in an orthorhombic structure has been shown in  $\text{WO}_3/\text{Bi}_2\text{S}_3$  composite synthesized via chemical bath deposition [21]. Figure 5f shows the EDS spectrum taken from the single  $\text{Bi}_2\text{S}_3$  nanowire, where the EDS spectrum indicates high purity of  $\text{Bi}_2\text{S}_3$  composition of the nanowire.



**Figure 5.** (a) Low-magnification TEM image of scratched BT-3. (b) HRTEM image taken from the local region of the sample in (a). (c) The EDS spectrum of BT-3 in (a). (d) Low magnification TEM image of  $\text{Bi}_2\text{S}_3$  nanowire scratched from BT-3. (e) HRTEM image taken from the local regions of the sample in (d). (f) The EDS spectrum of  $\text{Bi}_2\text{S}_3$  nanowire in (d).

Figure 6 shows the characteristic XPS spectral lines of various samples. The main constituent elements of Bi, S, Ti, and O are detected in BT-1, BT-3, and BT-5, supporting the existence of  $\text{Bi}_2\text{S}_3$  and  $\text{TiO}_2$  in the composite structure. Moreover, the relatively weak Ti signals from the spectra in comparison with that of the Bi signals, revealing the capping layer of  $\text{Bi}_2\text{S}_3$  phase on the  $\text{TiO}_2$  template for the test samples, and this spectral feature has

widely been observed in the composite structure, having obvious layering characteristics [9]. In addition to the C signal that originated from the sample contamination on exposure to ambient air, no impurity was detected in the as-synthesized samples. In order to further investigate the elemental binding states of the  $\text{Bi}_2\text{S}_3$  capping layer, the XPS narrow scan spectra of Bi 4f for BT-1, BT-3, and BT-5 are displayed in Figure 7a–c, respectively. Two sharp and distinct peaks centered at approximately 157.3 eV and 162.6 eV, which are assigned to  $\text{Bi } 4f_{7/2}$  and  $\text{Bi } 4f_{5/2}$  of  $\text{Bi}_2\text{S}_3$ , respectively [22]. The tiny peak located between the two distinct characteristic peaks of Bi 4f is originated from S 2p. The binding energies of Bi 4f core-level peaks corresponded to the characteristic binding state of  $\text{Bi}^{3+}$  in the  $\text{Bi}_2\text{S}_3$ , revealing the well formation of the  $\text{Bi}_2\text{S}_3$  phase through vulcanizing the  $\text{Bi}_2\text{O}_3$  layer. No metallic Bi or  $\text{Bi}_2\text{O}_3$  appeared after vulcanization.

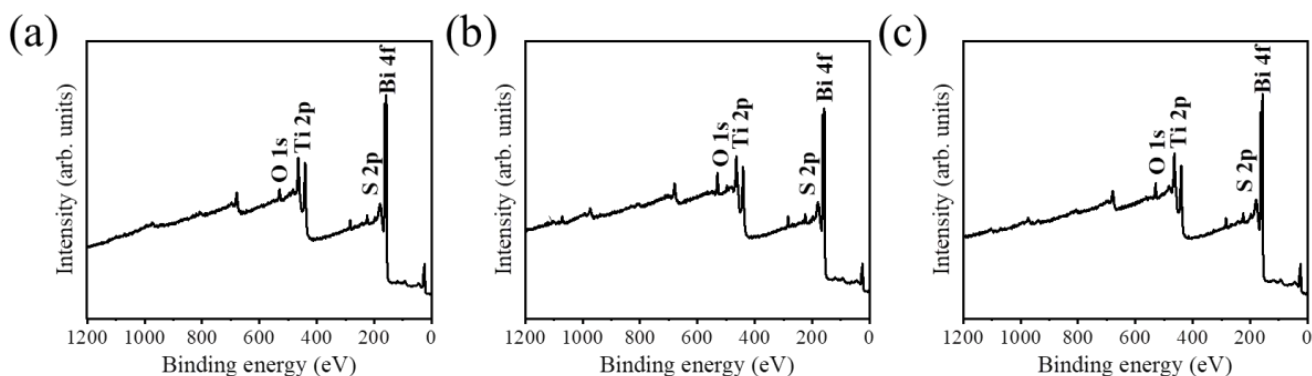


Figure 6. XPS survey scan spectra: (a) BT-1, (b) BT-3, and (c) BT-5.

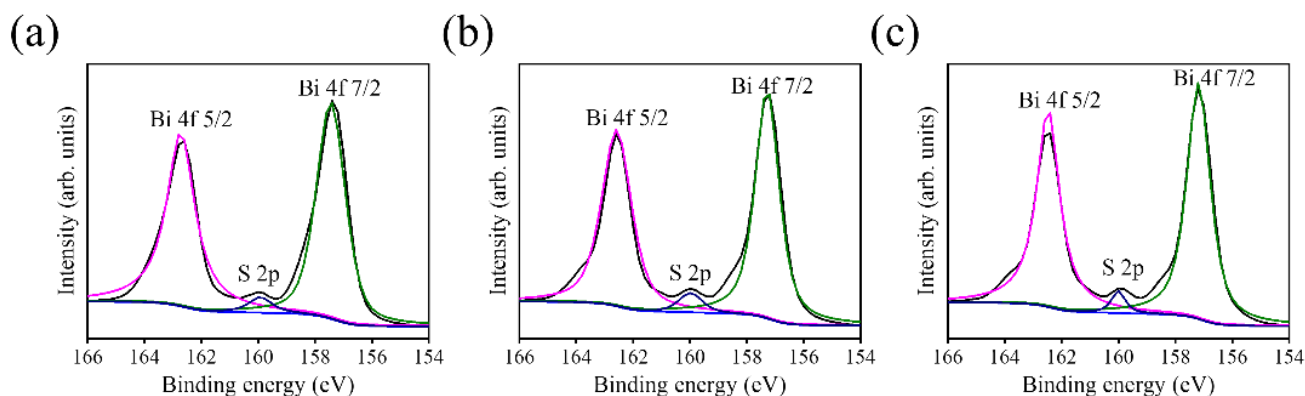


Figure 7. XPS analysis of narrow scan Bi 4f spectra: (a) BT-1, (b) BT-3, and (c) BT-5.

Notably, the narrow scan spectra of S 2p region of BT-1, BT-3, and BT-5 in Figure 8 reveal the characteristic peaks centered at approximately 162.6 eV and 160.1 eV, which are assigned to  $\text{S } 2p_{1/2}$  and  $\text{S } 2p_{3/2}$ , respectively. The S 2p binding energies herein associated with the aforementioned Bi 4f binding states evidenced the formation of Bi-S bonds in the capping layer synthesized via the given vulcanization processes in this study [23].

A comparison of the UV-vis absorption spectra of  $\text{TiO}_2$  template and various  $\text{TiO}_2$ - $\text{Bi}_2\text{S}_3$  samples are displayed in Figure 9a. The absorption of the  $\text{TiO}_2$  template is mainly in the UV light range. The decoration of  $\text{Bi}_2\text{S}_3$  extends the absorption range of the  $\text{TiO}_2$  template to the visible light range because of the narrow energy gap of  $\text{Bi}_2\text{S}_3$ . This is consistent with the feature of optical absorption spectra for  $\text{Bi}_2\text{S}_3$  nanorod/ $\text{TiO}_2$  nanoplate composites [24]. Moreover, in the previous  $\text{TiO}_2$ / $\text{Bi}_2\text{S}_3$  core-shell nanowire arrays synthesized via a successive ionic layer adsorption and reaction method, the absorption of the composite extends to cover the visible light range, and the decoration of  $\text{Bi}_2\text{S}_3$  phase increases the light absorption ability of the pristine  $\text{TiO}_2$  nanowires [8]. Notably, the band gap energies of the pristine  $\text{TiO}_2$  and  $\text{Bi}_2\text{S}_3$  are evaluated in Figure 9b,c, respectively, from Tauc plots based on

Kubelka–Munk function [25]. The  $\text{TiO}_2$  has a band gap energy of approximately 3.02 eV, and the band gap energy of the reference  $\text{Bi}_2\text{S}_3$  derived from the sputtering deposited  $\text{Bi}_2\text{O}_3$  layer and then vulcanized using 0.1 M thiourea is approximately 1.3 eV. Based on the evaluated band gap energy, the construction of the  $\text{TiO}_2/\text{Bi}_2\text{S}_3$  heterostructure herein improves the light harvesting ability.

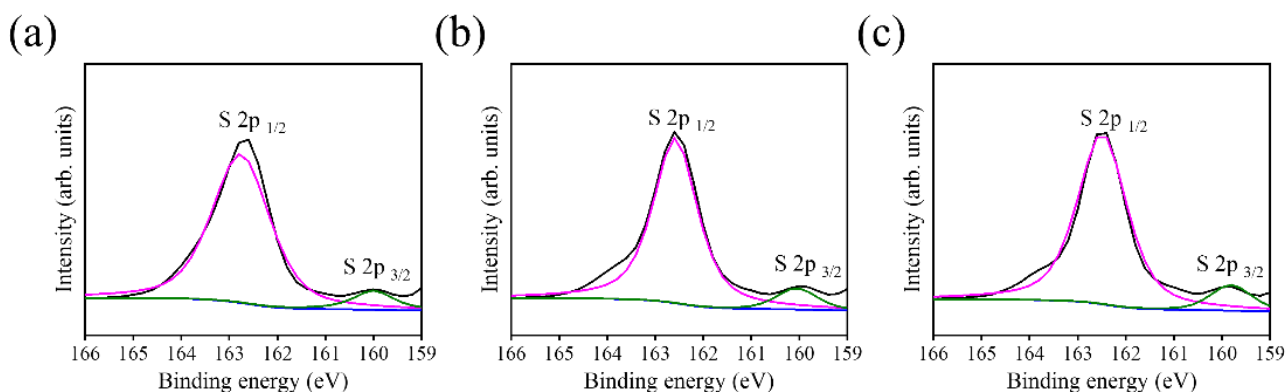


Figure 8. XPS analysis of narrow scan S 2p spectra: (a) BT-1, (b) BT-3, and (c) BT-5.

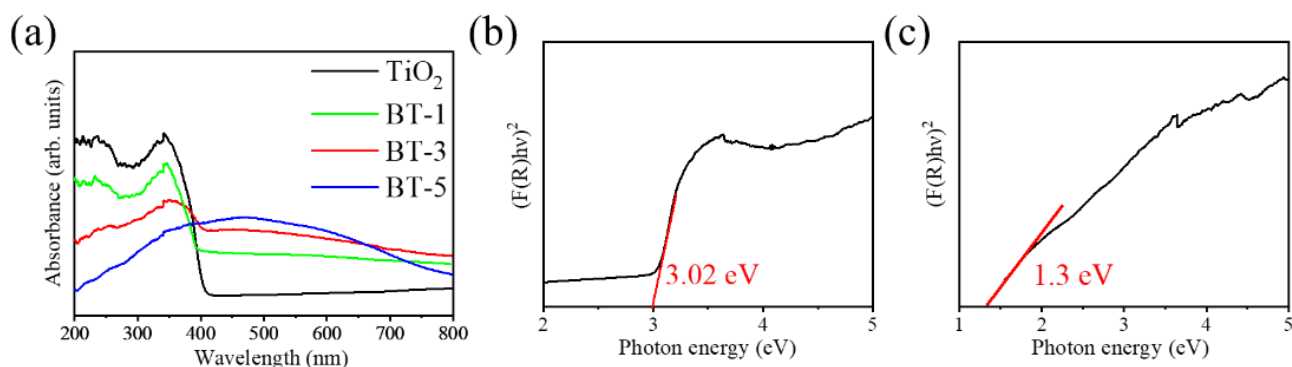
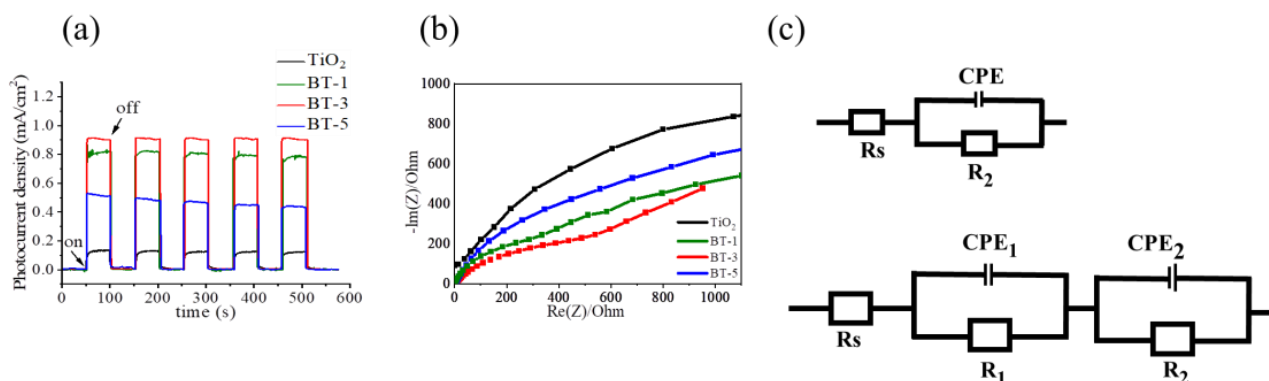


Figure 9. (a) UV-vis absorbance spectra of various samples. Band gap evaluation of (b) pristine  $\text{TiO}_2$  and (c) pristine  $\text{Bi}_2\text{S}_3$ .

Figure 10a shows the transient photocurrent performance of various photoelectrodes under repeated on/off irradiation cycles at 0.5 V (vs. Ag/AgCl). It is known that the transient photocurrent performance is highly associated with the photoresponse, charge carrier transport speed, charge carrier separation efficiency, and charge carrier recombination rate of samples. When the light is on, the photocurrent densities of all samples swiftly rise to a stable value of 0.12, 0.81, 0.93, and 0.47  $\text{mA}/\text{cm}^2$  for  $\text{TiO}_2$ , BT-1, BT-3, and BT-5, respectively. When the light is off, the photocurrent densities of the samples drop to their initial dark current density value instantaneously. Such a fast rise and fall process of the photocurrents indicates that carrier transport and separation in the prepared photoelectrodes proceed quickly [11]. Furthermore, the photoresponse of the BT-3 increased approximately three times higher than that of the  $\text{TiO}_2$  template. The BT-1 and BT-5 also exhibited enhanced photoresponses in comparison with the  $\text{TiO}_2$  template. Among various composite structure, the BT-3 has the highest photocurrent response, indicating it has the lowest photogenerated electron/hole recombination rate. By contrast, the BT-5 exhibits a lower photocurrent response among various composites. This might be attributed to the following reason. Substantially excessive  $\text{Bi}_2\text{S}_3$  deposition leads to an increase in the number of recombination centers, and as a result, a decrease in photocurrent density has been observed due to the loss of photogenerated electrons [15]. The results herein prove that decoration of  $\text{Bi}_2\text{S}_3$  crystals onto the  $\text{TiO}_2$  template can effectively improve the photoinduced charge separation efficiency of the  $\text{TiO}_2$  template, resulting in more efficient charge migration and

higher photocurrent density of the  $\text{TiO}_2\text{-Bi}_2\text{S}_3$  composite structure. A similar improved transient photocurrent performance because of decoration of visible light sensitizer onto the wide band gap semiconductor with a suitable band alignment has been demonstrated in  $\text{TiO}_2\text{-Bi}_2\text{O}_3$  and  $\text{ZnO-Sn}_2\text{S}_3$  heterostructures [11,25]. Figure 10b presents the Nyquist plots of various photoelectrodes. The semicircular radius of the Nyquist plots can reflect the charge transfer resistance of the photoelectrode materials. As shown in Figure 10b, the arc radius of the  $\text{TiO}_2\text{-Bi}_2\text{S}_3$  composites herein are smaller than that of the  $\text{TiO}_2$  template, revealing that formation of  $\text{TiO}_2/\text{Bi}_2\text{S}_3$  heterojunction is beneficial for interfacial charge transfer. Comparatively, BT-3 has the smallest radius of the Nyquist curve among various samples. The possible equivalent circuits shown in Figure 10c are used to fit the EIS Nyquist results, where  $R_s$ ,  $R_1$ ,  $R_2$ , and CPE represent the solution resistance, semiconductor depletion layer resistance, charge transfer resistance, and chemical capacitance, respectively [26]. Herein, the  $R_2$  is evaluated from the fitting results of the Nyquist plots at the low frequency region. The  $R_2$  values of the pristine  $\text{TiO}_2$ , BT-1, BT-3, and BT-5 are 3500, 583.3, 463.4, and 925  $\Omega$ , respectively. The BT-3 exhibited the smallest  $R_2$  value. As the vulcanization duration was further prolonged, a larger size of  $\text{Bi}_2\text{S}_3$  crystallites deposition occurred, which might prolong the electron diffusion path in the BT-5 composite, resulting a larger  $R_2$  value among various composites. Notably, charge transfer resistances of the BT-1, BT-3, and BT-5 are much lower than that of  $\text{TiO}_2$ . This indicates that decoration of  $\text{Bi}_2\text{S}_3$  onto the  $\text{TiO}_2$  could effectively reduce the photoinduced charge transfer resistance of the  $\text{TiO}_2$  template and enhance the separation efficiency of charge carriers. Both the transient photocurrent and Nyquist plot results herein support an effective separation of photogenerated electron–hole pairs and faster interfacial charge transfer occurred on the BT-3 interface, which might lead to the enhanced photocatalytic performance.



**Figure 10.** (a) Photocurrent density versus time curves of various samples at 0.5 V vs. Ag/AgCl under chopped illumination. (b) Nyquist plot of various samples at an open-circuit potential under illumination (c) Possible equivalent circuits used to fit  $R_2$  value of the pristine  $\text{TiO}_2$  and  $\text{TiO}_2\text{-Bi}_2\text{S}_3$  composite.

Figure 11 shows the Mott–Schottky (M–S) plots of  $\text{TiO}_2$ ,  $\text{Bi}_2\text{S}_3$ , and  $\text{TiO}_2\text{-Bi}_2\text{S}_3$  composites performed at 1 kHz. All the samples were measured with a positive slope in the M–S plots, revealing an n-type nature of the composed semiconductors. The flat band potential ( $E_{fb}$ ) of various samples can be calculated from the x intercept of the linear region in the M–S plots according to the M–S equation [27]. Furthermore, the normal hydrogen electrode (NHE) potential can be converted from the Ag/AgCl reference electrode as  $\text{NHE} = V(\text{Ag}/\text{AgCl}) - 0.197$  V. The  $E_{fb}$  of  $\text{TiO}_2$  and  $\text{Bi}_2\text{S}_3$  referenced samples are  $-0.21$  and  $-0.45$  V vs. NHE, respectively. Comparatively, the flat band potential of the  $\text{TiO}_2\text{-Bi}_2\text{S}_3$  composites has a negative shift compared to the  $\text{TiO}_2$  template as exhibited in Figure 11c–e. Moreover, the tangent slope in the linear region of the M–S plots for the  $\text{TiO}_2\text{-Bi}_2\text{S}_3$  composites is smaller than the  $\text{TiO}_2$  template, demonstrating the decoration of  $\text{Bi}_2\text{S}_3$  crystallites onto the  $\text{TiO}_2$  template increases carrier concentration and reduce the charge recombination rate of the composites. A more negative shift of the flat band potential with respect to  $\text{TiO}_2$  template is observed for the BT-3 among various  $\text{TiO}_2\text{-Bi}_2\text{S}_3$  composites; moreover,

the smaller tangent slope in the linear region of the M–S plot was observed for the BT-3. These reveal a superior electronic property of the BT-3 than that of other TiO<sub>2</sub>-Bi<sub>2</sub>S<sub>3</sub> composites. It has been shown that the crystallite size and number of visible-light sensitizers affect the photoinduced charge separation efficiency of the visible-light sensitizer-decorated TiO<sub>2</sub> [28]. Moreover, the crystal quality of the semiconductor has been proved to affect its photoactivity [29]. The BT-3 because of suitable Bi<sub>2</sub>S<sub>3</sub> crystallite quality and size shows the superior photogenerated carrier density and effective interface transfer ability among various composites in this study.

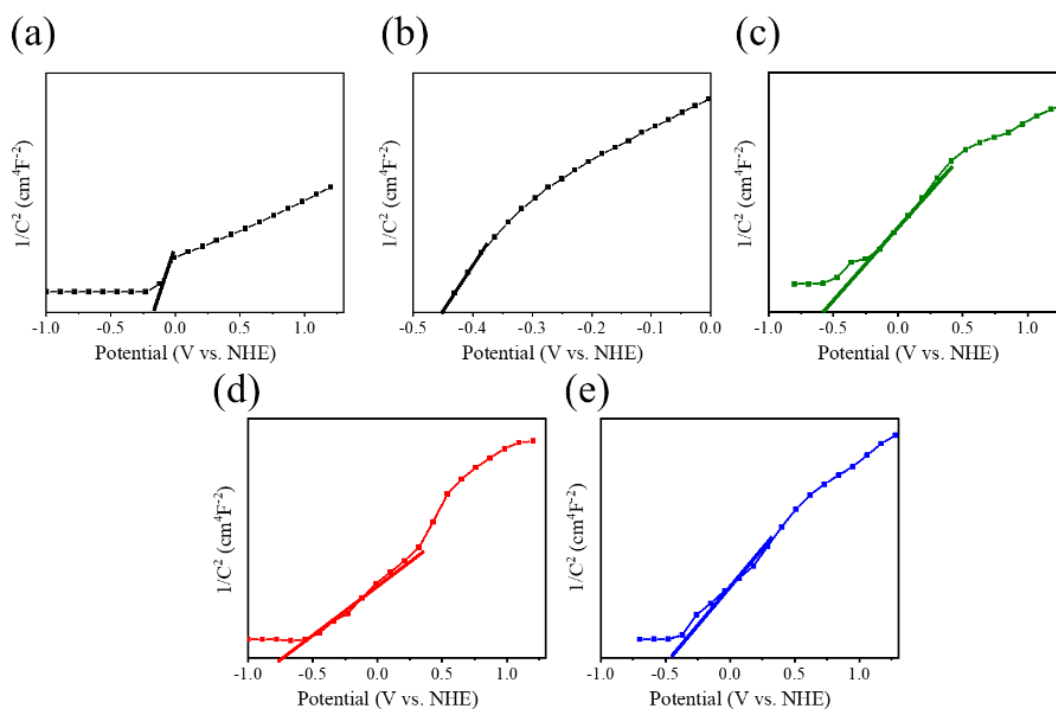


**Figure 11.** Mott–Schottky plots of various samples: (a) pristine TiO<sub>2</sub>, (b) pristine Bi<sub>2</sub>S<sub>3</sub>, (c) BT-1, (d) BT-3, and (e) BT-5.

Figure 12a shows the photodegradation level of various photocatalysts towards RhB solution. The percentage of photodegradation was calculated using the  $C/C_0 = I_t/I_0$ . The  $C_0$  and  $C$  are the initial and residual concentration of the RhB solution at  $t = 0$  and at irradiation duration  $t$ , respectively, and can be evaluated from the intensity variation of absorbance spectra of the RhB solution with and without photocatalytic reaction [30]. Figure 12a demonstrates that the BT-1, BT-3, BT-5, and TiO<sub>2</sub> degrades 60.3%, 65.6%, 50.8%, and 36.1% of RhB solution, respectively, after 30 min irradiation. Furthermore, the degradation level of RhB solution reached 77.8%, 87.2%, 71.2%, and 57.1% after 60 min irradiation for the BT-1, BT-3, BT-5, and TiO<sub>2</sub>, respectively. Notably, the dark balanced absorptions of various samples are also conducted to understand the initial catalysts' surface dye adsorption efficiency. The  $C/C_0$  of the BT-1, BT-3, BT-5, and TiO<sub>2</sub> after 30 min dark balanced adsorption is 7.1%, 7.6%, 5.8%, and 4.2%, respectively. Comparatively, the BT-1 and BT-3 exhibit a slightly larger surface dye adsorption ability than that of BT-5 and TiO<sub>2</sub>. Figure 12b demonstrates the discoloration of RhB solution with BT-3 under different irradiation durations. Apparent discoloration appeared in the RhB solution containing BT-3 with an increased irradiation duration. To quantitatively compare the photocatalytic activity of the as-prepared photocatalyst samples, the photodegradation data were fitted to the pseudo-first-order kinetics equation:  $\ln(C_0/C) = kt$ , where  $k$  is the apparent first-order rate constant [4]. Figure 12c presents the plot of  $\ln(C_0/C)$  versus  $t$  for various samples. The higher  $k$  value is observed for the TiO<sub>2</sub>-Bi<sub>2</sub>S<sub>3</sub> composites than that of pristine TiO<sub>2</sub>. Moreover, the BT-3 demonstrates the highest  $k$  value of  $0.03274 \text{ min}^{-1}$  among various samples, confirming the higher photocatalytic activity of BT-3 composite. The suitable

morphology and decoration content of  $\text{Bi}_2\text{S}_3$  crystallites on the  $\text{TiO}_2$  template might account for the observed result. This has also been supported by visible-light  $\text{CuO}$  sensitizer decorated  $\text{ZnO}$  composite photocatalysts that crystal morphology and content of the  $\text{CuO}$  substantially affect the photocatalytic activity of  $\text{CuO}$ - $\text{ZnO}$  nanocomposites [31]. Active groups of the photocatalytic degradation reaction were explored by the addition of free radical capture agents, as exhibited in Figure 12d. Herein, benzoquinone (BQ,  $\cdot\text{O}_2^-$  radical scavenger), tertiary butyl alcohol (t-BuOH,  $\cdot\text{OH}$  radical scavenger), and EDTA-2Na (EDTA-2Na,  $\text{h}^+$  radical scavenger) are used to explore the active groups of the photocatalytic degradation reaction. Notably, the photocatalytic efficiency of RhB solution with BT-3 was significantly inhibited after adding BQ, indicating that  $\cdot\text{O}_2^-$  is the main active substance for RhB degradation. Furthermore, the results herein reveal that a single scavenger could not completely prevent the dye degradation, and the  $\text{h}^+$  and  $\cdot\text{OH}$  also contribute some degrees of photodegradation towards RhB dyes.

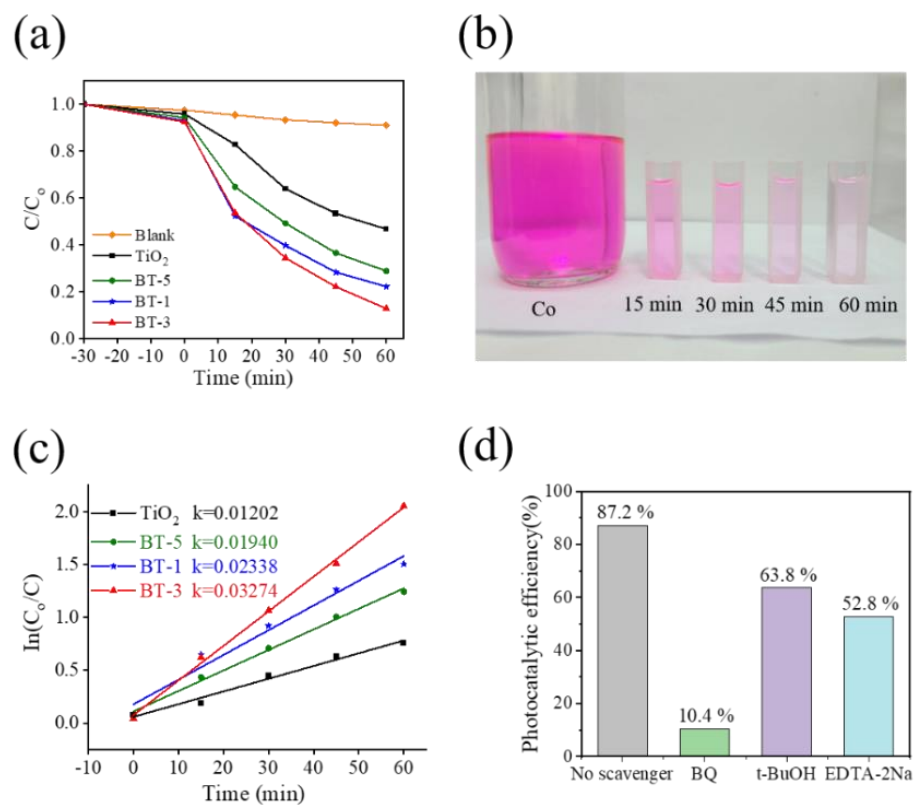


**Figure 12.** (a)  $C/C_0$  versus irradiation duration plot. (b) Discoloration of RhB solution with BT-3 under different irradiation durations. (c)  $\ln(C_0/C)$  versus irradiation duration plot. (d) The photocatalytic performance after adding various scavengers in BT-3/RhB solution.

In the M-S analysis, the flat band potentials of the  $\text{TiO}_2$  and  $\text{Bi}_2\text{S}_3$  are  $-0.21$  and  $-0.45$  eV, respectively. Furthermore, the  $E_{\text{CB}}$  bottoms of the  $\text{TiO}_2$  and  $\text{Bi}_2\text{S}_3$  can be evaluated to be  $-0.31$  and  $-0.55$  eV, respectively [32]. The valence band (VB) positions of the  $\text{TiO}_2$  and  $\text{Bi}_2\text{S}_3$  are evaluated to be  $2.71$  and  $0.75$  eV, respectively. According to the band structures of  $\text{TiO}_2$  and  $\text{Bi}_2\text{S}_3$ , there are two possible migration mechanisms of photoinduced charge carriers in the  $\text{TiO}_2/\text{Bi}_2\text{S}_3$  heterojunction as shown in Figure 13. However, the potential of  $\text{O}_2/\cdot\text{O}_2^-$  is  $-0.33$  eV, which is more negative than CB of  $\text{TiO}_2$ , and CB electrons are not easy to reduce  $\text{O}_2$ . At the same time, the photoinduced holes on  $\text{Bi}_2\text{S}_3$  VB cannot oxidize  $\text{H}_2\text{O}$  to produce  $\cdot\text{OH}$  radicals, because the VB edge potential of  $\text{Bi}_2\text{S}_3$  is more negative than the potential of  $\text{H}_2\text{O}/\text{OH}$  ( $2.27$  V), as shown in Figure 13a. Based on the aforementioned discussions, type II photodegradation mechanism is not suitable for the as-synthesized  $\text{TiO}_2$ - $\text{Bi}_2\text{S}_3$  composites in this study. By contrast, a direct Z-scheme mechanism

over the TiO<sub>2</sub>/Bi<sub>2</sub>S<sub>3</sub> heterostructure can be proposed in Figure 13b. Upon irradiation, TiO<sub>2</sub>/Bi<sub>2</sub>S<sub>3</sub> absorbs light greater than its band gap, electron-hole pairs are generated (Equations (1) and (2)), and RhB will also be excited to RhB\* by light irradiation at the same time (Equation (3)). The RhB\* injects electrons into the CB of Bi<sub>2</sub>S<sub>3</sub> (Equation (4)). A similar phenomenon of electron injection from RhB\* to the TiO<sub>2</sub> CB has been proposed in the literature [33]. The electrons in the TiO<sub>2</sub> CB position could migrate to the Bi<sub>2</sub>S<sub>3</sub> VB, resulting in the effective separation of photoinduced charge carriers (Equation (5)). The RhB<sup>+</sup> reacts with adsorbed dye to form intermediate products by the photosensitization process (Equation (6)). Parts of the holes in the TiO<sub>2</sub> VB will react with the intermediate product to degrade RhB dyes (Equation (7)). Moreover, the residual photoinduced holes in the TiO<sub>2</sub> VB will react with the H<sub>2</sub>O molecules to generate the ·OH radicals (Equation (8)), and the electrons are gathered on Bi<sub>2</sub>S<sub>3</sub> CB to produce ·O<sub>2</sub><sup>-</sup> radicals (Equation (9)) [34]. Therefore, the RhB dyes are effectively photodegraded with BT-3 under irradiation (Equation (10)). A similar Z-scheme mechanism is shown in other TiO<sub>2</sub>-based composite systems decorated with visible-light sensitizers [35–37].

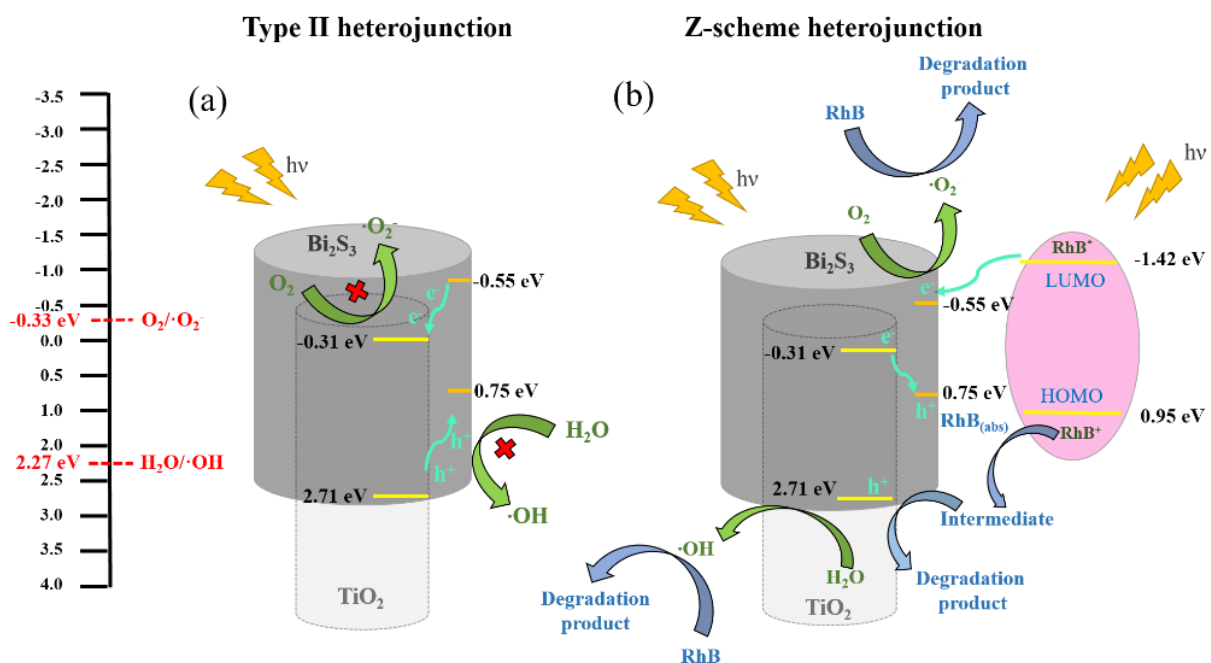
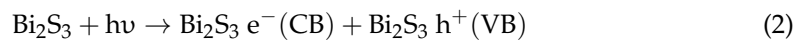
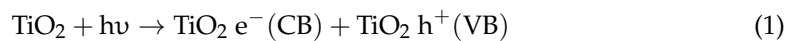


**Figure 13.** Schematic diagrams of the photogenerated electron–hole separation process for TiO<sub>2</sub>/Bi<sub>2</sub>S<sub>3</sub> composites: (a) Type II heterojunction and (b) Z-scheme heterojunction.

#### 4. Conclusions

TiO<sub>2</sub> nanorod array coated with Bi<sub>2</sub>O<sub>3</sub> layer was used to vulcanize to form TiO<sub>2</sub>-Bi<sub>2</sub>S<sub>3</sub> composites with various morphologies. The hydrothermal vulcanization duration profoundly affects the microstructure, optical properties, and photoactivity of TiO<sub>2</sub>-Bi<sub>2</sub>S<sub>3</sub> composites. The decorated Bi<sub>2</sub>S<sub>3</sub> crystals changed the morphology from filament, nanowire to nanorod with an increased vulcanization duration from 1, 3, and 5 h, respectively. The decoration of Bi<sub>2</sub>S<sub>3</sub> crystals enhanced the light absorption capacity of the TiO<sub>2</sub> nanorod template. The improved photodegradation performance of the composites can be reasonably attributed to the construction of the direct Z-scheme heterojunction between the TiO<sub>2</sub> and Bi<sub>2</sub>S<sub>3</sub>. This study demonstrates that design of TiO<sub>2</sub>-Bi<sub>2</sub>S<sub>3</sub> composites with suitable morphology of decorated Bi<sub>2</sub>S<sub>3</sub> crystals can tune the photoactivity of the composites, and the findings in this study may be of great value for the development of oxide-sulfide composites for ideal photosensitive device applications.

**Author Contributions:** Methodology, Y.-C.L. and S.-Y.Y.; formal analysis, S.-Y.Y. and B.-Y.C.; investigation, S.-Y.Y. and B.-Y.C.; writing—original draft preparation, Y.-C.L. and S.-Y.Y.; supervision, Y.-C.L. All authors have read and agreed to the published version of the manuscript.

**Funding:** This research was funded by the National Science and Technology Council of Taiwan, grant number MOST 111-2221-E-019 -062-MY3.

**Data Availability Statement:** Not applicable.

**Conflicts of Interest:** The authors declare no conflict of interest.

#### References

- Wei, L.; Li, F.; Hu, S.; Li, H.; Chi, B.; Pu, J.; Jian, L. CdS Quantum Dot-Sensitized Vertical TiO<sub>2</sub> Nanorod Arrays by a Simple Linker-Assisted SILAR Method. *J. Am. Ceram. Soc.* **2015**, *98*, 3173–3178. [CrossRef]
- Yang, H.; Chen, J.; Zuo, Y.; Zhang, M.; He, G.; Sun, Z. Enhancement of photocatalytic and photoelectrochemical properties of BiOI nanosheets and silver quantum dots co-modified TiO<sub>2</sub> nanorod arrays. *J. Am. Ceram. Soc.* **2019**, *102*, 5966–5975. [CrossRef]
- Wang, L.-L.; Wang, R.; Feng, L.; Liu, Y. Coupling TiO<sub>2</sub> nanorods with g-CN using modified physical vapor deposition for efficient photoelectrochemical water oxidation. *J. Am. Ceram. Soc.* **2020**, *103*, 6272–6279. [CrossRef]
- Liang, Y.-C.; Zhao, W.-C. Morphology-dependent photocatalytic and gas-sensing functions of three-dimensional TiO<sub>2</sub>-ZnO nanoarchitectures. *CrystEngComm* **2020**, *22*, 7575–7589. [CrossRef]
- Liang, Y.-C.; Zhao, W.-C. Crystal Growth and Design of Disk/Filament ZnO-Decorated 1D TiO<sub>2</sub> Composite Ceramics for Photoexcited Device Applications. *Nanomaterials* **2021**, *11*, 667–678.
- Lin, J.; Liu, X.; Zhu, S.; Chen, X. TiO<sub>2</sub> nanotube structures for the enhancement of photon utilization in sensitized solar cells. *Nanotechnol. Rev.* **2015**, *4*, 209–238. [CrossRef]
- Lozano, H.; Devis, S.; Aliaga, J.; Alegría, M.; Guzmán, H.; Villarroel, R.; Benavente, E.; González, G. Two-Dimensional Titanium Dioxide-Surfactant Photoactive Supramolecular Networks: Synthesis, Properties, and Applications for the Conversion of Light Energy. *Int. J. Mol. Sci.* **2022**, *23*, 4006. [CrossRef]
- Fawzi, T.; Rani, S.; Roy, S.C.; Lee, H. Photocatalytic Carbon Dioxide Conversion by Structurally and Materially Modified Titanium Dioxide Nanostructures. *Int. J. Mol. Sci.* **2022**, *23*, 8143. [CrossRef]
- Meng, A.; Zhu, B.; Zhong, B.; Zhang, L.; Cheng, B. Direct Z-scheme TiO<sub>2</sub>/CdS hierarchical photocatalyst for enhanced photocatalytic H<sub>2</sub>-production activity. *Appl. Surf. Sci.* **2017**, *422*, 518–527. [CrossRef]
- Lee, S.S.; Bai, H.; Liu, Z.; Sun, D.D. Novel-structured electrospun TiO<sub>2</sub>/CuO composite nanofibers for high efficient photocatalytic cogeneration of clean water and energy from dye wastewater. *Water Res.* **2013**, *47*, 4059–4073. [CrossRef] [PubMed]
- Liang, Y.-C.; Chiang, K.-J. Coverage Layer Phase Composition-Dependent Photoactivity of One-Dimensional TiO<sub>2</sub>-Bi<sub>2</sub>O<sub>3</sub> Composites. *Nanomaterials* **2020**, *10*, 1005. [CrossRef]
- Liang, Y.-C.; Liu, Y.-C. Microstructures and photodegradation performance toward methylene orange of sputtering-assisted decoration of ZnFe<sub>2</sub>O<sub>4</sub> crystallites onto TiO<sub>2</sub> nanorods. *Nanomaterials* **2019**, *9*, 205. [CrossRef]
- Ai, G.; Mo, R.; Chen, Q.; Xu, H.; Yang, S.; Li, H.; Zhong, J. TiO<sub>2</sub>/Bi<sub>2</sub>S<sub>3</sub> core-shell nanowire arrays for photoelectrochemical hydrogen generation. *RSC Adv.* **2015**, *5*, 13544–13549. [CrossRef]
- Liu, C.; Yang, Y.; Li, W.; Li, J.; Li, Y.; Chen, Q. A novel Bi<sub>2</sub>S<sub>3</sub> nanowire@TiO<sub>2</sub> nanorod heterogeneous nanostructure for photoelectrochemical hydrogen generation. *Chem. Eng. J.* **2016**, *302*, 717–724. [CrossRef]
- Ahmad, A.; Tezcan, F.; Yerlikaya, G.; Paksoy, H.; Kardaş, G. Three dimensional rosette-rod TiO<sub>2</sub>/Bi<sub>2</sub>S<sub>3</sub> heterojunction for enhanced photoelectrochemical water splitting. *J. Alloys Compd.* **2021**, *868*, 159133. [CrossRef]
- Li, X.; Han, X.; Zhu, D.; Chen, Y.; Li, L.; Ren, F.; Huang, J. Hydrothermal method deposition of TiO<sub>2</sub>/Bi<sub>2</sub>S<sub>3</sub> composite film for solar cell photoanode. *Mater. Res. Express* **2019**, *6*, 055910. [CrossRef]

17. Liang, Y.-C.; Li, T.-H. Controllable morphology of Bi<sub>2</sub>S<sub>3</sub> nanostructures formed via hydrothermal vulcanization of Bi<sub>2</sub>O<sub>3</sub> thin-film layer and their photoelectrocatalytic performances. *Nanotechnol. Rev.* **2022**, *11*, 284–297. [CrossRef]
18. Sun, B.; Feng, T.; Dong, J.; Li, X.; Liu, X.; Wu, J.; Ai, S. Green synthesis of bismuth sulfide nanostructures with tunable morphologies and robust photoelectrochemical performance. *Cryst. Eng. Comm.* **2019**, *21*, 1474–1481. [CrossRef]
19. Liang, Y.-C.; Xu, N.-C. Synthesis of TiO<sub>2</sub>–ZnS nanocomposites via sacrificial template sulfidation and their ethanol gas-sensing performance. *RSC Adv.* **2018**, *8*, 22437–22446. [CrossRef] [PubMed]
20. Chen, L.; He, J.; Yuan, Q.; Liu, Y.; Au, C.T.; Yin, S.F. Environmentally benign synthesis of branched Bi<sub>2</sub>O<sub>3</sub>–Bi<sub>2</sub>S<sub>3</sub> photocatalysts by an etching and re-growth method. *J. Mater. Chem. A* **2015**, *3*, 1096–1102. [CrossRef]
21. Wang, Y.; Tian, W.; Chen, L.; Cao, F.; Guo, J.; Li, L. Three-dimensional WO<sub>3</sub> nanoplate/Bi<sub>2</sub>S<sub>3</sub> nanorod heterojunction as a highly efficient photoanode for improved photoelectrochemical water splitting. *ACS Appl. Mater. Interfaces* **2017**, *9*, 40235–40243. [CrossRef] [PubMed]
22. Ma, G.Q.; Liu, F.S.; Wang, S.; Dang, Z.C.; Zhang, J.W.; Fu, X.J.; Hou, M.S. Preparation and characterization of Bi<sub>2</sub>S<sub>3</sub>/3DOM-TiO<sub>2</sub> for efficient photocatalytic degradation of rhodamine B. *Mater. Sci. Semicond. Process.* **2019**, *100*, 61–72. [CrossRef]
23. Xu, F.; Xu, C.; Chen, H.; Wu, D.; Gao, Z.; Ma, X.; Zhang, Q.; Jiang, K. The synthesis of Bi<sub>2</sub>S<sub>3</sub>/2D-Bi<sub>2</sub>WO<sub>6</sub> composite materials with enhanced photocatalytic activities. *J. Alloys Compd.* **2019**, *780*, 634–642. [CrossRef]
24. Huang, G.; Zhang, J.; Jiang, F.; Zhang, Z.; Zeng, J.; Qi, X.; Shen, Z.; Wang, H.; Kong, Z.; Ji, Z.; et al. Excellent photoelectrochemical activity of Bi<sub>2</sub>S<sub>3</sub> nanorod/TiO<sub>2</sub> nanoplate composites with dominant {001} facets. *J. Solid State Chem.* **2020**, *281*, 121041. [CrossRef]
25. Liang, Y.C.; Lung, T.W.; Xu, N.C. Photoexcited properties of tin sulfide nanosheet-decorated ZnO nanorod heterostructures. *Nanoscale Res. Lett.* **2017**, *12*, 1–8. [CrossRef]
26. Guan, Z.C.; Wang, X.; Jin, P.; Tang, Y.Y.; Wang, H.P.; Song, G.L.; Du, R.G. Enhanced photoelectrochemical performances of ZnS-Bi<sub>2</sub>S<sub>3</sub>/TiO<sub>2</sub>/WO<sub>3</sub> composite film for photocathodic protection. *Corros. Sci.* **2018**, *143*, 31–38. [CrossRef]
27. Hao, C.; Wang, W.; Zhang, R.; Zou, B.; Shi, H. Enhanced photoelectrochemical water splitting with TiO<sub>2</sub>@Ag<sub>2</sub>O nanowire arrays via p-n heterojunction formation. *Sol. Energy Mater. Sol. Cells* **2018**, *174*, 132–139. [CrossRef]
28. Wang, Q.; Liu, Z.; Jin, R.; Wang, Y.; Gao, S. SILAR preparation of Bi<sub>2</sub>S<sub>3</sub> nanoparticles sensitized TiO<sub>2</sub> nanotube arrays for efficient solar cells and photocatalysts. *Sep. Purif. Technol.* **2019**, *210*, 798–803. [CrossRef]
29. Liang, Y.-C.; Chang, C.-W. Preparation of orthorhombic WO<sub>3</sub> thin films and their crystal quality-dependent dye photodegradation ability. *Coatings* **2019**, *9*, 90. [CrossRef]
30. Liang, Y.-C.; Chiang, K.-J. Design and tuning functionality of rod-like titanium dioxide–nickel oxide composites via a combinational methodology. *Nanotechnology* **2020**, *31*, 195709. [CrossRef]
31. Das, S.; Srivastava, V.C. An overview of the synthesis of CuO–ZnO nanocomposite for environmental and other applications. *Nanotechnol. Rev.* **2018**, *7*, 267–282. [CrossRef]
32. Kavan, L.; Vlckova Zivcova, Z.; Zlamalova, M.; Zakeeruddin, S.M.; Grätzel, M. Electron-selective layers for dye-sensitized solar cells based on TiO<sub>2</sub> and SnO<sub>2</sub>. *J. Phys. Chem. C* **2020**, *124*, 6512–6521. [CrossRef]
33. Pan, L.; Zou, J.J.; Liu, X.Y.; Liu, X.J.; Wang, S.; Zhang, X.; Wang, L. Visible–light–induced photodegradation of rhodamine B over hierarchical TiO<sub>2</sub>: Effects of storage period and water-mediated adsorption switch. *Ind. Eng. Chem. Res.* **2012**, *51*, 12782–12786. [CrossRef]
34. Zhu, L.; Li, H.; Xia, P.; Liu, Z.; Xiong, D. Hierarchical ZnO decorated with CeO<sub>2</sub> nanoparticles as the direct Z-scheme heterojunction for enhanced photocatalytic activity. *ACS Appl. Mater. Interfaces* **2018**, *10*, 39679–39687. [CrossRef] [PubMed]
35. Xue, Y.; Wu, Z.; He, X.; Yang, X.; Chen, X.; Gao, Z. Constructing a Z-scheme Heterojunction of Egg-Like Core@shell CdS@TiO<sub>2</sub> Photocatalyst via a Facile Reflux Method for Enhanced Photocatalytic Performance. *Nanomaterials* **2019**, *9*, 222. [CrossRef]
36. Zhao, W.; Yang, X.; Liu, C.; Qian, X.; Wen, Y.; Yang, Q.; Sun, T.; Chang, W.; Liu, X.; Chen, Z. Facile Construction of All-Solid-State Z-Scheme g-C<sub>3</sub>N<sub>4</sub>/TiO<sub>2</sub> Thin Film for the Efficient Visible-Light Degradation of Organic Pollutant. *Nanomaterials* **2020**, *10*, 600. [CrossRef]
37. Sharma, S.; Ibhaddon, A.O.; Francesconi, M.G.; Mehta, S.K.; Elumalai, S.; Kansal, S.K.; Umar, A.; Baskoutas, S. Bi<sub>2</sub>WO<sub>6</sub>/C-Dots/TiO<sub>2</sub>: A Novel Z-Scheme Photocatalyst for the Degradation of Fluoroquinolone Levofloxacin from Aqueous Medium. *Nanomaterials* **2020**, *10*, 910. [CrossRef]



Review

# Nanomaterials: A Review about Halloysite Nanotubes, Properties, and Application in the Biological Field

Giuseppa Biddeci, Gaetano Spinelli, Paolo Colomba  and Francesco Di Blasi \*

Institute for Innovation and Biomedical Research (IRIB), 90146 Palermo, CNR, Italy

\* Correspondence: francesco.dibiasi@irib.cnr.it; Tel.: +39-0916809514

**Abstract:** The use of synthetic materials and the attention towards environmental hazards and toxicity impose the development of green composites with natural origins. Clay is one of the candidates for this approach. Halloysite is a natural clay mineral, a member of the Kaolin group, with characteristic tubular morphology, usually named halloysite nanotubes (HNTs). The different surface chemistry of halloysite allows the selective modification of both the external surface and the inner lumen by supramolecular or covalent interactions. An interesting aspect of HNTs is related to the possibility of introducing different species that can be released more slowly compared to the pristine compound. Due to their unique hollow morphology and large cavity, HNTs can be employed as an optimal natural nanocarrier. This review discusses the structure, properties, and application of HNTs in the biological field, highlighting their high biocompatibility, and analyse the opportunity to use new HNT hybrids as drug carriers and delivery systems.

**Keywords:** halloysite nanotubes; biocompatibility; drug delivery system; biomedical application

**Citation:** Biddeci, G.; Spinelli, G.; Colomba, P.; Di Blasi, F. Nanomaterials: A Review about Halloysite Nanotubes, Properties, and Application in the Biological Field. *Int. J. Mol. Sci.* **2022**, *23*, 11518. <https://doi.org/10.3390/ijms231911518>

Academic Editor: Christian M. Julien

Received: 2 August 2022

Accepted: 19 August 2022

Published: 29 September 2022

**Publisher's Note:** MDPI stays neutral with regard to jurisdictional claims in published maps and institutional affiliations.



**Copyright:** © 2022 by the authors. Licensee MDPI, Basel, Switzerland. This article is an open access article distributed under the terms and conditions of the Creative Commons Attribution (CC BY) license (<https://creativecommons.org/licenses/by/4.0/>).

## 1. Introduction

As emerging materials, nanomaterials have attracted much attention over the years due to their small size, but also due to the countless properties that distinguish them. In fact, the nanometric dimensions of material make it assume particular and different chemical-physical properties compared to conventional materials. These different properties, determined by the chemical composition, structure, surface, and increase in surface reactivity in relation to volume, solubility, and state of aggregation, have raised questions about potential human health and environmental risks [1]. In the past few years, there has been a growing interest in research aimed at the development of new organic or inorganic nanocomposites [2–5]. The attention of the scientific community has been drawn by nano clays, thanks to their natural origin, worldwide abundance, availability, biocompatibility, and sustainability [6–8]. Halloysite, largely known as halloysite nanotubes or HNTs, is a natural mineral clay composed of alternating layers of silica and alumina geologically laminated in mesoporous tubular particles with significant adsorption and loading capabilities [9]. Compared to other tubular nanomaterials, HNTs show some advantages in terms of processability and hydrodynamic properties [10]. In fact, for many years, much attention was focused on carbon nanotubes (CNTs) [11–14], showing that these nanotubes have a high cost, lower water dispersibility, and higher toxicity than HNTs [15]. The physicochemical properties of HNTs were fully described, disclosing their potential for various applications such as biomedicine and catalysis [16–19]. HNT-based composites are gaining interest in research aimed at the development of biomaterials for drug delivery vehicles in nanomedicine [20]. In this review, we aim to provide an overview of the properties and biomedical applications of halloysite nanotubes as drug delivery systems. We will discuss their possible application in biotechnology through a focus on HNT composites for biomedical applications. Herein, we aim to provide an overview of the structure, properties, and applicative aspects of halloysite nanotubes in the biomedical field. We start with a

brief background about HNTs then provide a brief discussion of their biocompatibility and application.

## 2. Halloysite Nanotubes

Halloysite is a two-layered aluminosilicate with a chemical composition similar to kaolinite (chemical formula:  $\text{Al}_2\text{Si}_2\text{O}_5(\text{OH})_4 \cdot n\text{H}_2\text{O}$ ) [21,22], and a hollow tubular structure in the sub-micrometre range [23–26]. Halloysite was first described in 1826 by the French chemist Pierre Berthier and was later given its name in honour of the Belgian geologist Omalius d’Halloy, who found it in the deposits of Angleur, Belgium [27]. Natural tubular halloysite clay has attracted great interest in materials development because it is one of the few inexpensive nanomaterials available in thousands of tons at a low price [28,29]. The nucleation of halloysite crystals occurs in different parts of the world, because of rock erosion due to weathering, pedogenesis, and hydrothermal alteration of ultramafic rocks [30,31]. New Zealand, Belgium, Brazil, France, China, Australia, and Turkey are rich in deposits of halloysite, and it has been shown that with the variation of the deposits it is possible to observe different characteristics that are maintained within the same deposit. Halloysite is defined as a 1:1 phyllosilicate in which a planar layer of tetrahedral silicates alternates with an octahedral geometry layer; these layers are bound together by oxygen bridges [32]. The fundamental unit for the octahedral sheet consists of three octahedrons. In particular, the siloxane groups are bonded via only one oxygen atom to octahedral rings at the outer part and the apical oxygen of tetrahedra becomes the vertices of octahedra [33]. However, under certain geological conditions, halloysite can also take on forms other than classical tubular. It is also possible to distinguish a spheroidal morphology, flat and almost rolled [34,35]. In the “Dragon Mine” deposits of Utah (USA), halloysite is characterized by a good degree of purity and looks like a white stone that can easily be transformed into soft, fine powder. In some deposits, the presence of metals as contaminants induces a colour change that becomes yellowish or brown [30]. Transmission electron microscopy (TEM) structural analysis has shown that halloysite with predominantly tubular morphology and heterogeneous dimensions is present in New Zealand, the United States, and Australian deposits [36]. A very interesting aspect is linked to the different chemical composition between the inner and outer surfaces, in which there are, respectively, aluminolic groups (Al-OH) that give a positive charge and siloxanes (Si-O-Si) that give a negative charge [37,38]. The charges that characterize the internal and external nanotube surfaces are due to the different dielectric and ionization properties of silicon oxides and aluminium. For pH values of 3–10, the positive charges are distributed in the inner lumen and the negative charges on the external surface; present on the edges is a negative/positive charge. In particular, the tubule lumen is positively charged with  $\text{pH} \leq 8.5$ , and the outer surface is negatively charged with  $\text{pH} \geq 1.5$  [39]. Generally, because of the O and OH atoms that carry negative charges, the halloysite nanotube is negatively charged. As a result of the tubular shape, on the outer surface only a few hydroxyl groups are present; these are more concentrated in the internal lumen and therefore are more reactive. In fact, for halloysite, it is possible to classify three types of Al-OH, according to their positioning on the surface, at the ends, and between the octahedral and tetrahedral sheets, as shown in Figure 1. All can be reactive and dissociate according to the pH of the solutions, except those placed between the octahedral and tetrahedral sheets, due to steric hindrance [40].

The halloysite nanotubes’ size may vary depending on the extraction site and the purification process they undergo, but they usually have an internal diameter of 10–30 nm, an external diameter of 40–70 nm [41], and a length between 200 and 2000 nm [42] (Figure 2a,b).

Nanotubes with a length between 3 and 5  $\mu\text{m}$  have been found in some deposits, although those with smaller sizes are more interesting from a biological point of view, as they are more suitable for use as drug carriers [44]. Halloysite is chemically like kaolinite, but the halloysite double layers are separated by a monolayer of water molecules. In the hydrated form of halloysite  $n = 2$  in the formula  $\text{Al}_2(\text{OH})_4\text{Si}_2\text{O}_5 \cdot n\text{H}_2\text{O}$ . One layer of water molecules is present between the multilayers and is named “halloysite-(10 Å)”, where

“10 Å” indicates the  $d_{001}$ -value of the layers. When the  $n$  value is 0 ( $n = 0$ ), the halloysite is named dehydrated or “halloysite-(7 Å)” and may be obtained through the loss of the interlayer water molecules [30,45]. The water present in halloysite-(10 Å) can be classified as “hole water” and “associated water”. In the first case, the water molecules are placed on the surface of the tetrahedral sheet with different orientations and make hydrogen bonds with the basal oxygens. The “associated” water has a greater degree of mobility at room temperature and is located at a different level in the interlayer space, with an ice-like configuration and forming hydrogen bonds with each other and/or with inner-surface hydroxyls [46–50]. Generally, HNT surfaces could be classified into three types. The inner lumen surface has a positive charge and is covered by Al-OH groups. It can undergo a variety of covalent modifications by which certain functional groups can be added. This method allows immobilizing several organic groups on the surface of the lumen stably. The external siloxane surface has a negative charge and can be used to establish covalent bonding with molecules such as organosilanes [51]. Moreover, it can be modified by coating with cationic substances, such as polymers, biopolymers, and surfactants. This type of modification can help to improve the dispersibility and biocompatibility of halloysite. Interstate surfaces, held together by hydrogen bridges, can be modified by direct or indirect intercalation of small organic molecules and some monovalent cationic salts. This, therefore, can lead to a weakening of the hydrogen bonds interstate and an increase in the surface between the various layers that can be understood as additional space for loading or adsorption [52].

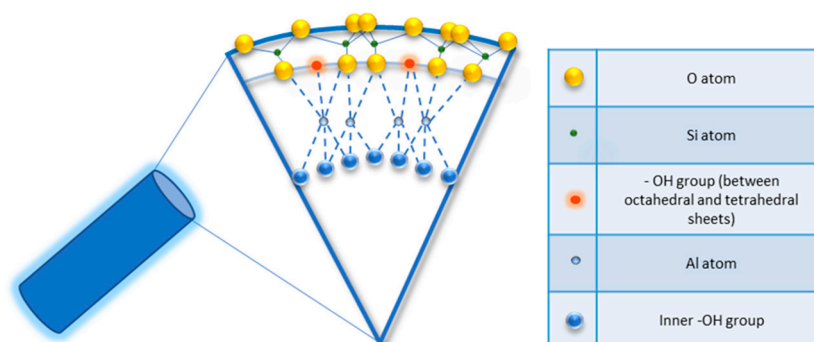


**Figure 1.** Detail of schematic illustration of the crystalline structure of halloysite nanotubes.

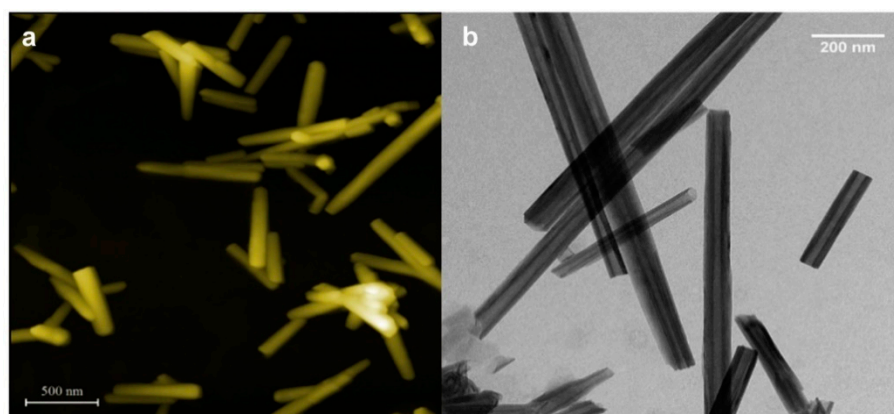


**Figure 2.** (a) Atomic force microscopy; (b) TEM images of halloysite nanotubes precipitated from aqueous dispersion. Adapted from [43].

### 3. Effects of Nanomaterial on Human Health

Despite nanomaterials having potential benefits, their interaction with biological systems may cause unpredicted risk to human life. One concern is the variation in dimensions of nanoparticles, which may affect chemical, thermodynamic, optical, biological,

spectroscopic, electronic, and electromagnetic processes, resulting in unexpected modifications [53–55]. An increasing exposure to different types of nanomaterials makes it essential to determine their possible negative impact on human health and potential toxic effects. For this reason, it is important to evaluate and characterize the chemical-physical properties, dimensions, solubility, chemical composition, surface area, surface energy, etc. [56]. Among these properties, size and surface are the most important for interaction with biological systems as they determine how the materials will respond [57]. It was observed that the mechanisms for cell internalization depend mainly on the material size [58] and that toxicity may also depend on this aspect. The size of nanomaterials depends on the ability to enter the biological systems, to interact with cellular functions by modifying the structure of macromolecules, and thus interfere with biological functions [59,60]. Nanomaterial internalisation can take place by many paths such as inhalation, oral intake, direct injection, or skin absorption (Figure 3), and is followed by their transportation into organs and their succeeding biological effects, including oxidative stress, inflammatory responses, cellular apoptosis, and DNA damage [61,62].

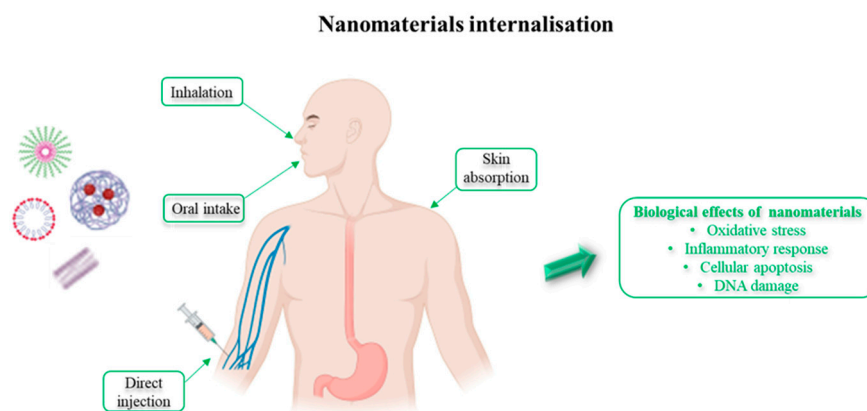


**Figure 3.** Nanomaterial internalisation and biological effects on the human body.

Nanostructures, once ingested, administered topically, or inhaled, can be transported by blood and accumulated in various organs [63]. Subsequent to entry into the systemic circulation, the absorption of nanoparticles by blood capillaries allows the distribution in various body districts. Depending on their surface characteristics, they can be recognized and degraded by macrophages [64]. Moreover, nanocarrier size also affects the *in vivo* fate. In fact, particles larger than 200 nanometres are shown to accumulate in the liver and spleen. Instead, nanoparticles smaller than five nanometres are filtered at the renal level [65]. It has been observed that the optimal size of a nano system for application in the biomedical field is around 100 nanometres [66]. *In vivo* studies have shown that once nanomaterials enter the bloodstream they can reach the central nervous system [67], induce pulmonary inflammatory reactions [68,69], and cause cardiovascular problems [70]. The toxic effects induced in the cells by contact with nanomaterials can be chemical or physical. Chemical mechanisms may include the production of reactive oxygen species (ROS) [71], disruption of electron and ion transport across the cell membrane [72], and lipid peroxidation with a consequent decrease in the fluidity of the membranes [73]. Concerning physical mechanisms, which depend on the size of the nanomaterial and the surface properties [74], these include rupture of the plasma membrane and interruption of related activities such as transport processes [75,76] and misfolding of proteins resulting in loss of their function [77]. The life cycle of nanomaterials in the human body, their metabolism, and their fate in human organs are dependent on the physical and chemical characteristics of the nanomaterials and on their exposure route [78]. The exposure of humans to nanomaterials requires an improved understanding of their potential toxicity to predict the consequences. Future research efforts should be towards developing easy, cost-effective, and highly biocompatible nanomaterials for their application in the biomedical field.

#### 4. Halloysite Biocompatibility

Thanks to their rheological properties, high interaction, and high binding capacity with biopolymers, the role of mineral clays as a drug carrier has become the subject of extensive research. The physical-chemical properties, including size, morphology, and surface charge density, which depend on the type of mineral clay and the crystalline structure, are the features that make them interesting [79]. The increased use of halloysite nanotubes, their purification, modification, and large-scale preparation lead to an increasing exposure to human society and environments. Therefore, it is important to do a systematic analysis before their use in biomedical applications and to consider the possible consequential effects of their use on human health. The different interactions of HNTs with living cells, encompassing electrostatic, van der Waals, and ion exchange, as well as cellular response, are decisive in determining the behaviour of halloysite nanotubes in biological systems [80]. Due to their abundance and perceived biocompatibility, in recent years halloysite nanotube toxicity has been evaluated in different *in vitro* and *in vivo* models. For example, Sawicka et al. investigated both short- (24 or 72 h) and long-term (seven days) cytotoxic effects of HNTs at doses ranging from 10 to 200  $\mu\text{g}/\text{mL}$  on human alveolar carcinoma epithelial cells (A549) and human bronchial epithelial cells (BEAS-2B). After 24 h of exposure, the  $\text{IC}_{50}$  of HNTs in A549 and BEAS-2B cells was  $152 \pm 6.4 \mu\text{g}/\text{mL}$  and  $> 400 \mu\text{g}/\text{mL}$ , respectively. After 72 h of exposure, the  $\text{IC}_{50}$  values decreased to  $49 \pm 3 \mu\text{g}/\text{mL}$  in A549 and  $45.1 \pm 8 \mu\text{g}/\text{mL}$ , in BEAS-2B cells. Thus, the results showed that cytotoxicity of HNTs depends on cell model, dose, and time of exposure [81]. Table 1 shows some of the toxicity threshold values reported for different concentrations of HNTs regarding cell types.

**Table 1.** Cytotoxicity of HNTs towards different cell lines.

Cell Type	Incubation Time	HNT Concentration	Reference
MCF7, HeLa	24–72 h	No toxic effect up to $75 \mu\text{g mL}^{-1}$	[25]
A549	24 h	No toxic effect up to $100 \mu\text{g mL}^{-1}$	[82]
Caco-2, HT29-MTX	6 h	No toxic effect up to $100 \mu\text{g mL}^{-1}$	[83]
A549	24–48–72 h	No toxic effect up to $100 \mu\text{g mL}^{-1}$	[84]
C6	24 h	No toxic effect up to $500 \mu\text{g mL}^{-1}$	[85]
Colo 320	24 h	No toxic effect up to $625 \mu\text{g mL}^{-1}$	[86]

Kamalieva et al., evaluated the internalization of pristine halloysite nanotubes using the A549 cell line. To assess the cytotoxicity, the cells were treated for 24 h with increasing concentrations of pristine HNT (ranging from 33 to  $900 \mu\text{g per } 10^5$  cells). Once the treatment was finished, the  $\text{IC}_{50}$  of halloysite nanotubes for A549 cells was determined to be  $300 \mu\text{g per } 10^5$  cells by MTT assay [87]. Regarding the nanomaterials for applications in the biomedical field, it is also important to verify their haemolytic potency when contacting the blood. To this end, the hemocompatibility of the hybrid system HNT/CURBO was investigated by exposing human red blood cells (HRBCs) both to pristine halloysite and HNT/CURBO for 24 h at  $37^\circ\text{C}$ . After exposure to different concentrations, a non-noticeable haemolytic effect was observed. The haemolysis percentage values induced by the exposition of HRBCs to different concentrations of HNT/CURBO (ranging from  $10 \mu\text{g}/\text{mL}$  to  $200 \mu\text{g}/\text{mL}$ ) were all less than 5% (Figure 4).

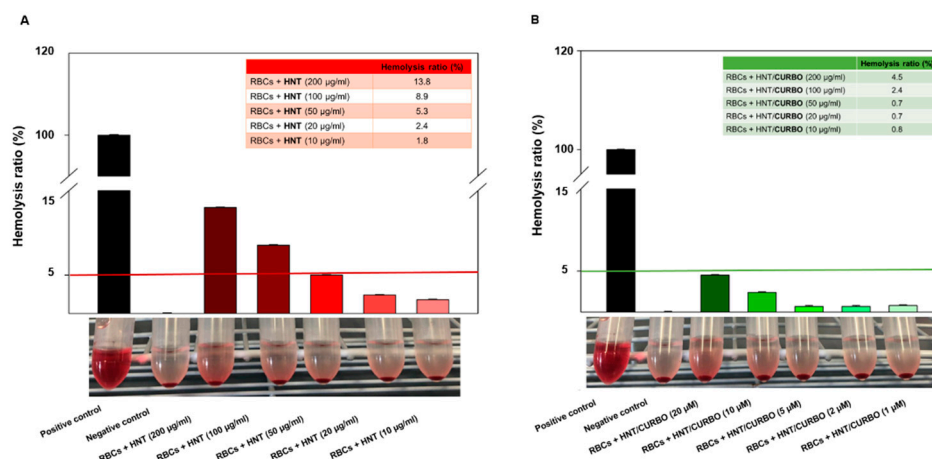


**Figure 4.** In vitro hemocompatibility assay of (A) raw HNT and (B) HNT/CURBO after incubation at 37 °C for 12 h. The positive control was in ultrapure water (100% lysis), and negative control was in PBS 1× (0% lysis). International Journal of NanoMedicine 2021:16 4755–4768 Originally published by and used with permission from Dove Medical Press Ltd. [88].

This result suggests that HNTs do not exhibit a significant haemolytic effect [88]. It has also been seen that HUVECs (human umbilical vein endothelial cells) and MCF-7 (human breast cancer) cells show high cell viability after being treated with different concentrations of HNTs for 24 h. For both cell lines, vitality remains above 85% even when the concentration of HNTs reaches up to 200 mg/mL. When incubation times increase (48 h and 72 h), a slight decrease is observed in cell viability. In particular, at 72 h in HUVEC cells viability is 62.1% at the maximum HNT concentration of 200 mg/mL. Furthermore, to investigate the cellular uptake of HNTs in HUVECs and MCF-7, the cells were incubated with FITC-HNTs and monitored using confocal laser scanning microscope (CLSM) as shown in Figure 5 [89].

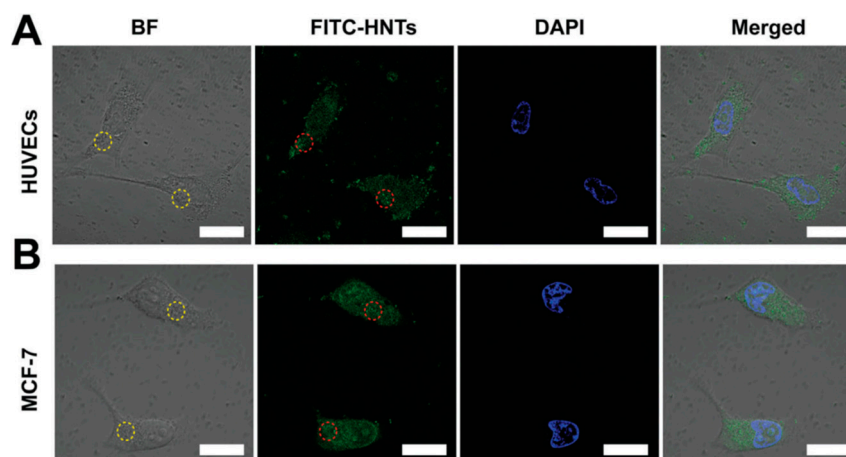


**Figure 5.** CLSM images of (A) HUVECs and (B) MCF-7 cells. Cells incubated with FITC-HNTs ( $50 \text{ mg mL}^{-1}$ ); FITC-HNTs and cell nucleus are indicated in green and blue, respectively. The circles in the images represent the FITC-HNT aggregates. Scale bar = 20 mm. Adapted from [89].

Halloysite nanotube toxicity was further evaluated against human peripheral lymphocytes by means of mitotic index assay. Different concentrations of HNTs (10, 100, 500, and 1000 µg/mL) were incubated with the peripheral lymphocyte culture. The mitotic index assay revealed inhibition of the proliferation of lymphocytes only at the highest concentration (1000 µg/mL) [90]. Despite many in vitro studies indicating that HNTs exhibit a high level of biocompatibility, the in vivo toxicity of HNTs remains unclear. HNT toxicity has been evaluated in in vivo models and in all cases, results show that this nanomaterial is

non-toxic or scarcely toxic depending on the tested condition. Several concentrations of HNTs (ranging from 0.25 to 50 mg/mL) were tested towards zebrafish embryos and larvae from 24 h post-fertilization (hpf) to 120 hpf and the results showed that the percent survival of zebrafish embryos and larvae have no significant changes at different developmental stages (24, 48, 72, 96, and 120 hpf) except at the highest concentrations (25 and 50 mg/mL) (Figure 6).

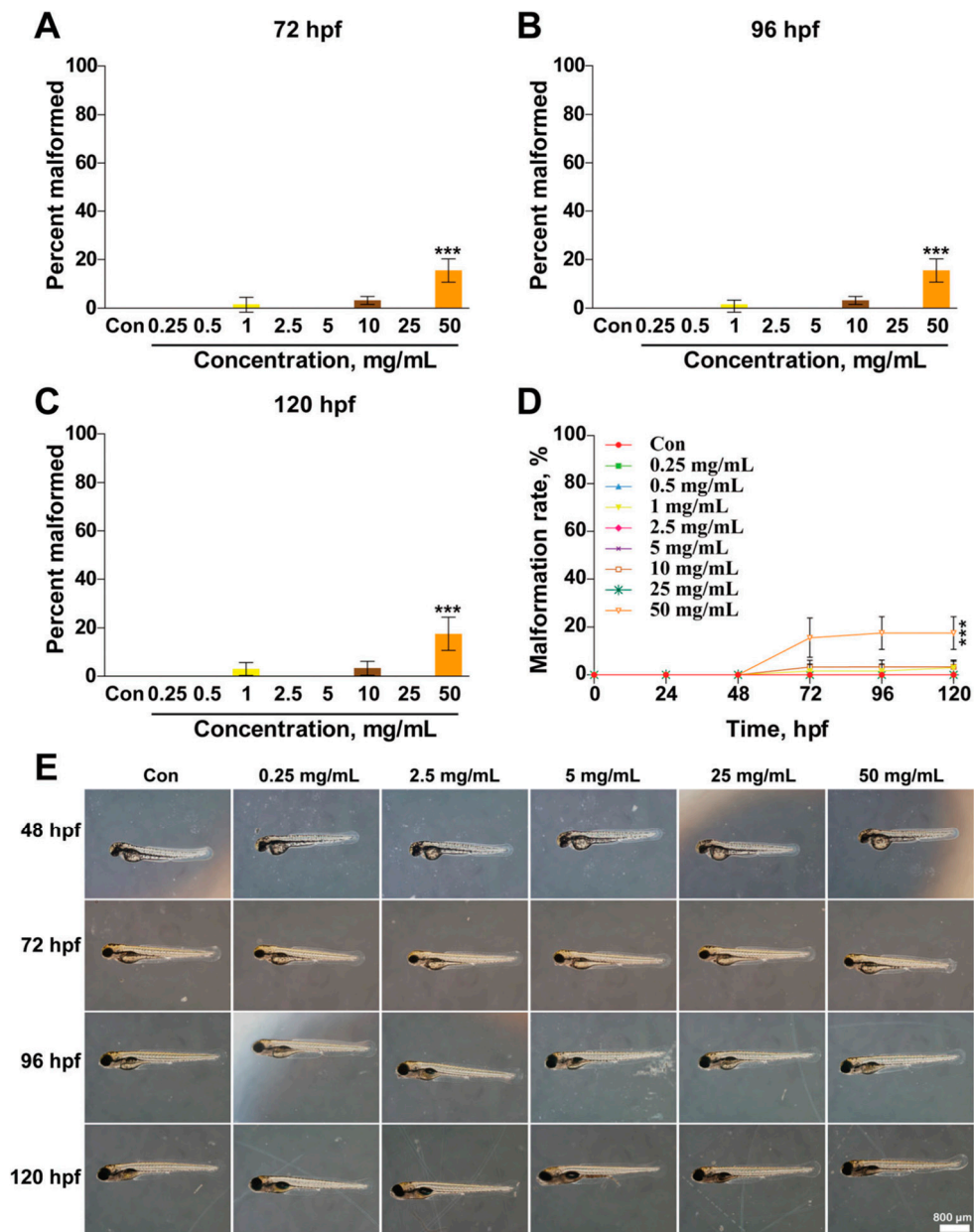


**Figure 6.** Effects of HNTs on the morphology of developing zebrafish. Embryos were treated with different concentrations of HNTs (0, 0.25, 2.5, 5, 25, and 50 mg mL<sup>-1</sup>) starting from 6 hpf. (A–D) Percent of malformed zebrafish was analysed at 72, 96, and 120 hpf. (E) Morphology of zebrafish larvae treated with HNTs was photographed using a microscope at 48, 72, 96, and 120 hpf. The values are represented as mean ± SD (*n* = 24). Each bar represents the collated data of three separate experiments. The data were analysed using Graph Prim 6 for one-way ANOVA and a Tukey’s post hoc test. \*\*\* *p* < 0.001 versus control group. Adapted from [89].

Following the treatment at relatively low HNT concentrations, the percent survival for all the hpf data sets increases slightly above 100%, then the HNTs increase the survival

of the zebrafish at low concentrations and have little effect on the survival, proving to be weakly toxic [89]. Fakhruddin et al. evaluated the *in vivo* toxicity of HNTs by using as a model organism the nematode *Caenorhabditis elegans*. The results showed that HNTs within the investigated concentrations, ranging from 0.05 mg/mL to 1 mg/mL, were not toxic to the nematode. They only induce mechanical stress in the digestive system, which is restored once the treatment is finished. In extended depth of field (EDF) microscopy images, halloysite nanotubes were found exclusively in the alimentary system of the worms (Figure 7) [91].

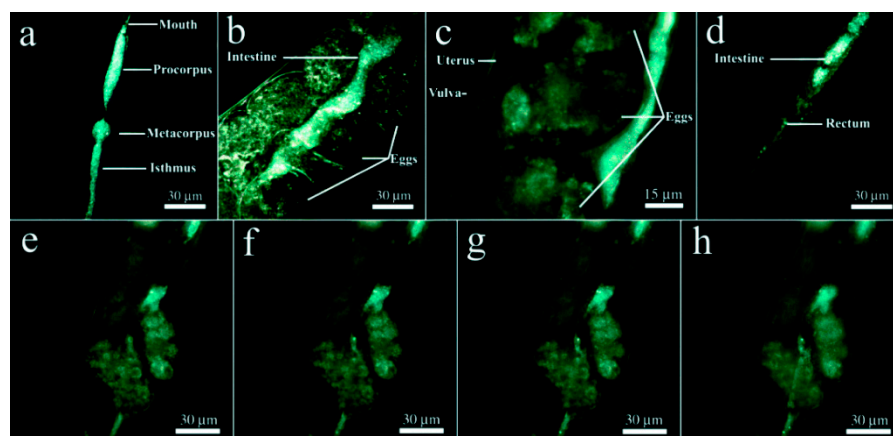


**Figure 7.** HNT localization in the nematode's intestines by EDF microscopy: (a) inside the foregut; (b,c) in the midgut; (d) inside the hindgut; (e–h) EDF images of the intestine near the uterus taken at different focal planes demonstrating the localisation of HNTs exclusively inside the intestine. Adapted from [91].

In addition, a phytotoxic study carried out on *Raphanus sativus* has shown that halloysite nanotubes do not affect the germination process, xylem differentiation, and development, thus demonstrating a high biocompatibility also with respect to plant species [92]. Another study evaluates the biodistribution and pulmonary toxicity of the purified HNTs in mice, following an intragastric administration for 30 days. The results showed that HNT oral administration caused considerable aluminium accumulation mainly in the lungs. Oral administration of HNTs stimulated the growth of the mice at low dose (5 mg/kg BW) with no pulmonary toxicity. When concentrations increased ten times (50 mg/kg BW), the mouse growth was inhibited and resulted in lung inflammation and oxidative stress [93]. An additional study instead showed normal mice weight gain at an oral dose of 5 mg kg<sup>-1</sup> and a reversible inflammation of the small intestine [94]. It is possible to state that HNTs have been shown to be almost non toxic under the tested conditions, and no cell toxicity makes HNTs suitable as safe materials for biomedical applications.

## 5. Halloysite Nanotube Application in Drug Delivery

Clay minerals are commonly used in the pharmaceutical industry either as excipients or activated ingredients. Indeed, it is known that when drugs and clay mineral are administered simultaneously the absorption capacity reduces by interacting with the drug. These kinds of interactions can represent advantages, for example in drug release [95]. Research has recently focused on the development of new drug delivery systems based on the use of nanomaterials, with the aim of improving the efficacy from the therapeutic point of view and reducing the side effects, especially, in cancer treatment. In several studies HNTs have been used as nanocontainers or nanocarriers for drug delivery. Since unmodified halloysite nanotubes have been shown to establish weak interaction with the drugs, several methods of modification have been developed, for example, tubular entrapment, adsorption, or intercalation [96–98]. Commonly, the methods used for the HNT loading consists of three steps. The first step is mixing the clay dry powder with

the saturated solution of the guest molecule; the second step is the sonication and stirring of the HNT/guest molecule dispersion; and the last step is the vacuum pumping in/out operation, in which the dispersion is transferred from atmospheric pressure to a vacuum jar. The third step was introduced to optimize the quantity of active molecules loaded inside the nanotubes by keeping the system under vacuum and then cycling it back to atmospheric pressure [99]. Thanks to hydroxyl groups present both on the outer and inner surface, HNTs can be functionalized and used as delivery vehicles of drugs [18,100]. In fact, thanks to the structural properties, high surface area (up to 184.9 m<sup>2</sup>/g), and the large pore volume (up to 0.353 cm<sup>3</sup>/g), over the last few years, halloysite has attracted increasing attention in several areas such as carriers for drug delivery, adsorbents, photocatalysts, etc. [101]. The functional groups of external (Si-OH) and internal (Al-OH) surfaces affect the loading of molecules of interest into HNTs. The negative charge of HNTs at pH above three, is due to silanol group deprotonation. The anionic nature of the external HNT surface enables it to interact with cationic compounds, while aluminol groups located on the internal lumen surface carry a positive charge and support the loading of anionic molecules. Moreover, interactions between HNTs and molecules can take place by van der Waals, hydrogen binding, or other specific interactions [102]. Due to the unique properties mentioned in the previous sections, HNTs have attracted research interest for application in drug delivery. In fact, drug molecules could be encapsulated inside the tube lumen or might be adsorbed on the outer surface [103–105]. Furthermore, the tubular morphology allows an increase in tensile and bending strength [106]. Taking advantage of the hollow tubular shape and the large cavity volume, HNTs can be used as desirable natural nanocarriers for biologically active agents. Drug therapy is the main approach in cancer treatment. Due to the poor loading capacity of hydrophobic molecules commonly used in cancer therapy, as for example curcumin, doxorubicin, and paclitaxel, halloysite nanotubes are not considered as an efficient carrier system for cancer drug therapy [107–109]. Since the surface of halloysite nanotubes is negatively charged, polycations such as chitosan can be coated onto HNTs. Thanks to this type of approach, drugs released from the HNT lumen may be sustained over a long period of time. Following this reasoning, curcumin was entrapped into the lumen of halloysite with the aid of vacuum suction and release obtaining drug-loaded halloysite nanotubes (DLHNTs). Then, the DLHNTs were coated with chitosan (DLHNTs-CH). The viability assay performed on MCF7 cells showed that polycationic coated HNTs have the potential to serve as a drug carrier [110]. Following surface modification of distearoyl phosphoethanolamine (DSPE), paclitaxel (PTX) is successfully loaded onto HNT surfaces with different inner lumen diameters giving rise to the system DSPE-HNTs-PTX, designed to deliver this drug to cancer cells. The antitumoral effects of the DSPE-HNTs-PTX system were evaluated on MDA-MB-231-bearing mice. The results showed that the system can inhibit tumour growth, suggesting a good anticancer effect [111]. Another study was conducted to evaluate the anticancer effect of chitosan-modified HNT loaded with curcumin-gold hybrid nanoparticles (HNT@CUR-Au/CS). This HNT hybrid system consisted of AuNP which have near-infrared (NIR) responsive property and pH-responsive curcumin release. The anticancer efficacy of HNT@CUR-Au/CS was tested on MCF-7 breast cancer cells showing more effective anticancer activity at pH 5.5 (intracellular tumour environment) than at a pH value of 7.4 (extracellular conditions) [112]. Taheri-Ledari et al. exploiting the properties of HNTs and gold nanoparticles (AuNPs), proposed a new system for controlled release of docetaxel (DTX), a cytotoxic anticancer agent. The DTX@HNT/Au-SORT system is composed of HNTs conjugated with monoclonal antibody as a biologically active agent for targeted drug delivery and small plasmonically active AuNPs included in the HNT pores. In vitro cytotoxicity assay performed on 3T3 (human normal fibroblast) and caov-4 (human ovarian cancer) cell lines showed high selectivity of DTX@HNT/Au-SORT in cell adhesion and internalization. At a concentration of DTX@HNT/Au-SORT equal to 50 µg mL<sup>-1</sup> the cytotoxicity was approximately 90% for caov-4 cells and 16% for the 3T3 cell line demonstrating that it could be a promising system to use in the treatment of ovarian cancer [113]. In recent years, various methods have been developed to functionalize

HNTs and allow them to be used as delivery systems for anticancer drugs. In Table 2 we summarize literature reports with respect to some anticancer drugs entrapped in HNTs.

**Table 2.** HNT nanocomposites for controlled and sustained anticancer drug delivery.

Anticancer Drug	Cell Type	HNT Modifications	Reference
Anthocyanins	MCF-7, HT-29	HNT-Anth	[114]
Atorvastatin	Caco-2, HT-29	HNT-ATV@HF-CEL	[115]
Camptothecin	HeLa	f-HNT/CPT and Fmoc-F/f-HNT/CPT	[116]
Camptothecin	Caco-2	CPT@COS/MHNTs and CPT@FA-COS/MHNTs	[117]
Curcumin	Caco-2	HNT-APT-PMVEMA@MF	[118]
Curcumin	HepG2, MCF-7, SV-HUC-1, EJ, CaSki, HeLa	HNT-COOH/Chitosan	[119]
Curcumin	SUM 149, MDA-MB-231, HL60, HL60R	f-Hal-1, 2, 4, 5, 6, and 7	[120]
Curcumin	MCF-7	PCL/PEO-Cur/HNT, PCL/PEO-Cur/HNT-GPTMS, and PCL/PEO-Cur/HNT-APTES	[121]
Doxorubicin	MCF-7	DOX@HNTs-g-COS	[122]
Doxorubicin	A549	DNA-wrapped HNTs	[123]
Doxorubicin	SKOV3, 293T	DOX@HNTs-S-S- $\beta$ -CD-Ad-PEG-FA	[124]
Doxorubicin	MCF-7	DOX@HNTs-PEG-FA	[125]
Doxorubicin	HeLa	DOX loaded Fe <sub>3</sub> O <sub>4</sub> @HNT	[126]
Doxorubicin	MCF-7	Au-HNT-DOX@BSA-FA	[127]
Doxorubicin	MCF-7, COLO 205	HNT-liposome-coated surfaces	[128]
Doxorubicin	HeLa, MCF-7	HNTs-DOX conjugated with anti-EpCAM antibody	[129]

Changes in the HNTs surface are important to improve their hydrophilicity and compatibility. One of the advantages of the use of clay nanomaterials is the ability to protect drugs against degradation by chemicals and enzymes while extending the drug release rate [130]. In the inner cavity of HNTs is possible to load not only small drug molecules but also proteins, DNA, or antibacterial agents [131–134]. Various modifications of the HNTs' lumen can increase the affinity of the drug towards the HNTs, thereby controlling the release rate [135]. Molecules and drugs released from HNTs' lumen can take place by diffusion from the lumen or by desorption from the external surface. Release from the lumen can be controlled by the tube diameter or by addition of tube-end stoppers [136,137]. The functionalization of HNTs with stimuli-responsive materials, for example with thermosensitive polymers, allows the release profile to be adjusted [138]. Kartogenin is a small molecule that promotes the selective differentiation of multipotent mesenchymal stem cells into chondrocytes, stimulating the repair of damaged cartilage. Unfortunately, like most organic molecules with biological properties, it possesses short-term stability in an aqueous medium. As an efficient treatment for osteoarthritis, halloysite nanotubes have been proposed as a carrier system for potential intra-articular delivery of KGN by means of laponite hydrogel (HNT/KGN/Lap). The cytotoxicity of the hybrid hydrogels was evaluated in human liver HepG2 cells. The efficacy of HNT/Lap hydrogel as a carrier for KGN was proved by in vitro release experiments performed at pH 7.4 and in ex vivo synovial fluid at 37 °C and it was observed that KGN has a slower release in synovial fluid than that of phosphate buffer at pH 7.4 [139]. Alternative approaches can be

employed for HNT surface modifications before the loading of drugs. One of these is the modification through (3-Aminopropyl) triethoxysilane (APTES), known for the functionalization of surfaces due to their ease of use and low toxicity. Its role is to introduce a silanol group on the surfaces of halloysite nanotubes to establish a bond with hydroxyl groups [95]. Pristine HNTs and APTES-modified HNTs were tested as drug carriers for loading and release of ibuprofen (IBU) that was encapsulated into the lumen and partially loaded onto the external surface. When unmodified halloysite nanotubes are used as a carrier for ibuprofen, a low loading rate and rapid release is achieved because the only established interactions between HNTs and ibuprofen are weak bonds (Van der Waals). HNT surface modification with APTES increases the loading of IBU by creating an electrostatic attraction between the introduced aminopropyl groups of the grafted APTES and the carboxyl group of ibuprofen and induces a delay in the release from the lumen of nanotubes [140]. In addition to exploiting the HNT lumen for drug encapsulation, it is possible to adsorb or add by covalent bonding molecules on the outer surface of nanotubes. By combining both, it is possible to obtain a system that can release the drug from the external surface initially and subsequently, in a slow and controlled way, that of the lumen. This type of system can be obtained through the functionalization of the external surface, for example, with some linkers. It has been observed that the functionalisation of the outer surface of nanotubes by the addition of triazolium salts is useful for the transport of curcumin. This system, in addition to demonstrating high efficiency for curcumin encapsulation and for controlled and prolonged release capacity, shows cytotoxic effects against different tumour cell lines [141]. The bioavailability of ciprofloxacin (CIP), due to its complexation with iron present in the body, decreases subsequent to administration. Entrapping the drug in a carrier could be a solution. To this end, CIP was loaded onto APTES modified halloysite nanotubes. The result was a high adsorption capacity in modified HNTs for CIP ( $70\% \pm 1.7\%$ ), compared to that of pristine halloysite nanotubes [142]. A multi-layered polylactic acid (PLA)/HNT porous membrane encapsulated with gentamicin was prepared for use in bone regeneration as antibacterial membrane. The membrane was shown to have good antibacterial efficacy against both Gram-negative and Gram-positive bacteria, suggesting that it could be used in the prevention of infection in bone regeneration applications [143]. Over the years, systems for pulmonary drug delivery systems have been developed to treat lung disease. Jeremi et al. designed a clay-based system with release capability of dexamethasone (Dex), to be used in coronavirus disease (COVID-19) treatment. They designed the system  $ZnFe_2O_4$ /Hal/DEX/PEG (Dex 5% wt/wt) sensitive to pH 5.6, able to release Dex at pulmonary infectious pH conditions [144]. Bordini et al. have developed an injectable GelMA-based nanotube modified hydrogel for controlled release of dexamethasone, illustrating the potential of this system for mineralized tissue regeneration. The DEX-loaded nanotube modified GelMA hydrogel (GelMA + 5.0% HNT-DEX10%) showed relevant properties from a mechanical point of view, but also biodegradability and cytocompatibility with mesenchymal stem cells from human exfoliated deciduous teeth (SHEDs). Moreover, the system had *in vivo* biocompatibility, and it also supported bone regeneration *in vivo* [145]. Phototherapy is described as a safe and secure way to destroy cancer cells when light waves of a particular wavelength are used with appropriate activating agents. Li et al. developed halloysite nanotubes decorated with poly(sodium-p-styrenesulfonate) (PSS) to enhance the biocompatibility, and further functionalized by lumen loading the type-II photosensitizer indocyanine green (ICG) to obtain a biomimetic nanocarrier platform for target-specific delivery of phototherapeutic agents. The obtained system, HNT-PSS-ICG, showed an excellent *in vivo* phototherapeutic effect against breast cancer in model mice [146]. Tan et al. developed a system of HNT-based multifunctional nanoparticles designed for tumour targeting and phototherapy in breast cancer treatment. Fluorescein isothiocyanate (FITC) was adsorbed on the HNT surfaces, and indocyanine green (ICG) was loaded as the photothermal agent into the lumen. To enhance the biocompatibility, the system was wrapped with red blood cell membrane (RBCM). Finally, anti-EpCAM was conjugated with HNTs-FITC-ICG-RBCM with the assistance of strepta-

vidin to improve the specific uptake of breast cancer cells. The cell viability assay results for MCF-7 cells indicated that the HNTs-FITC-ICG-RBCM cytotoxicity was irradiation time and concentration dependent and that this could be potentially used in breast cancer treatment [147]. As evidenced by Lisuzzo et al., HNTs are excellent candidates as interfacially active inorganic particles for the formation of Pickering emulsions thanks to their advantages, as for example low cost, biocompatibility, mechanical strength, tubular morphology, etc. [148]. The functionalization of HNT surfaces allows the synthesis of infinite nano-architectures which have different properties and can be modulated according to the desired performance and the field of application. It is, therefore, clear why it has led to a deepening of the research for their possible applications.

## 6. Conclusions

Halloysite nanotubes are naturally occurring and cost-effective nanomaterials that are finding applications in several areas, some discussed here. Several types of functionalisation of HNT have been discussed, including the advantageous tubular structure that has given it numerous roles as drug delivery and gene delivery agents or nanocarriers. Recent studies demonstrate the potential of halloysite clay nanotubes for life science applications since results suggest that HNTs are a safe nanomaterial which can be used in biomaterials without serious side effects. However, more studies are needed to clarify the in vivo outcomes of long and chronic oral exposure to HNTs, which seems to depend on the administered concentration. Overall, the results obtained to date open wide prospects of investigation to better understand the use of these systems for a potential application as drug carrier and delivery systems. The combination of the innumerable properties of halloysite nanotubes, together with their biocompatibility and the possibility of functionalising the surfaces, makes them ideal candidates for the development of an innovative therapeutic approach.

**Funding:** This research received no external funding.

**Institutional Review Board Statement:** Not applicable.

**Informed Consent Statement:** Not applicable.

**Data Availability Statement:** Not applicable.

**Acknowledgments:** We thank Daniele Francofonte for his excellent assistance and technical support for images and table realization.

**Conflicts of Interest:** The authors declare no conflict of interest.

## References

1. Boverhof, D.R.; Bramante, C.M.; Butala, J.H.; Clancy, S.F.; Lafranconi, M.; West, J.; Gordon, S.C. Comparative assessment of nanomaterial definitions and safety evaluation considerations. *Regul. Toxicol. Pharmacol.* **2015**, *73*, 137–150. [CrossRef]
2. Ahmad, H.; Fan, M.; Hui, D. Graphene oxide incorporated functional materials: A review. *Compos. Part B Eng.* **2018**, *145*, 270–280. [CrossRef]
3. Guo, S.; Fu, D.; Utupova, A.; Sun, D.; Zhou, M.; Jin, Z.; Zhao, K. Applications of polymer-based nanoparticles in vaccine field. *Nanotechnol. Rev.* **2019**, *8*, 143–155. [CrossRef]
4. Yang, Z.; Yang, J.; Liu, A.; Fu, J. Nonlinear in-plane instability of functionally graded multilayer graphene reinforced composite shallow arches. *Compos. Struct.* **2018**, *204*, 301–312. [CrossRef]
5. Tam, M.; Yang, Z.; Zhao, S.; Yang, J. Vibration and Buckling Characteristics of Functionally Graded Graphene Nanoplatelets Reinforced Composite Beams with Open Edge Cracks. *Materials* **2019**, *12*, 1412. [CrossRef]
6. Zhou, C.H.; Keeling, J. Fundamental and applied research on clay minerals: From climate and environment to nanotechnology. *Appl. Clay Sci.* **2013**, *74*, 3–9. [CrossRef]
7. Moraes, J.D.D.; Bertolino, S.R.A.; Cuffini, S.L.; Ducart, D.F.; Bretzke, P.E.; Leonardi, G.R. Clay minerals: Properties and applications to dermocosmetic products and perspectives of natural raw materials for therapeutic purposes—A review. *Int. J. Pharm.* **2017**, *534*, 213–219. [CrossRef]
8. Aguzzi, C.; Cerezo, P.; Viseras, C.; Caramella, C. Use of clays as drug delivery systems: Possibilities and limitations. *Appl. Clay Sci.* **2007**, *36*, 22–36. [CrossRef]
9. Joussein, E.; Petit, S.; Fialips, C.I.; Vieillard, P.; Righi, D. Differences in the Dehydration-Rehydration Behavior of Halloysites: New Evidence and Interpretations. *Clays Clay Miner.* **2006**, *54*, 473–484. [CrossRef]

10. Ventrapragada, L.K.; Creager, S.E.; Rao, A.M.; Podila, R. Carbon nanotubes coated paper as current collectors for secondary Li-ion batteries. *Nanotechnol. Rev.* **2019**, *8*, 18–23. [CrossRef]
11. Moniruzzaman, M.; Winey, K.I. Polymer nanocomposites containing carbon nanotubes. *Macromolecules* **2006**, *39*, 5194–5205. [CrossRef]
12. Zakaria, M.R.; Akil, H.M.; Kudus, M.H.A.; Ullah, F.; Javed, F.; Nosbi, N. Hybrid carbon fiber-carbon nanotubes reinforced polymer composites: A review. *Compos. Part B Eng.* **2019**, *176*, 107313. [CrossRef]
13. Munir, K.S.; Wen, C.; Li, Y. Carbon nanotubes and graphene as nanoreinforcements in metallic biomaterials: A review. *Adv. Biosyst.* **2019**, *3*, 1800212. [CrossRef]
14. Gohari, G.; Safai, F.; Panahirad, S.; Akbari, A.; Rasouli, F.; Dadpour, M.R.; Fotopoulos, V. Modified multiwall carbon nanotubes display either phytotoxic or growth promoting and stress protecting activity in *Ocimum basilicum* L. in a concentration-dependent manner. *Chemosphere* **2020**, *249*, 126171. [CrossRef]
15. Lampropoulou, P.; Papoulis, D. Halloysite in Different Ceramic Products: A Review. *Materials* **2021**, *14*, 5501. [CrossRef]
16. Rahmani, S.; Maroufkhani, M.; Mohammadzadeh-Komuleh, S.; Khoubi-Arani, Z. Polymer nanocomposites for biomedical applications. In *Micro and Nano Technologies, Fundamentals of Bionanomaterials*; Barhoum, A., Jeevanandam, J., Danquah, M.K., Eds.; Elsevier: Amsterdam, The Netherlands, 2022; pp. 175–215.
17. Liu, M.; Fakhruddin, R.; Novikov, A.; Panchal, A.; Lvov, Y. Tubule Nanoclay-Organic Heterostructures for Biomedical Applications. *Macromol. Biosci.* **2019**, *19*, e1800419. [CrossRef]
18. Satish, S.; Tharmavaram, M.; Rawtani, D. Halloysite nanotubes as a nature's boon for biomedical applications. *Nanobiomedicine* **2019**, *6*, 1849543519863625. [CrossRef]
19. Zhao, X.; Zhou, C.; Liu, M. Self-assembled structures of halloysite nanotubes: Towards the development of high-performance biomedical materials. *J. Mater. Chem. B* **2020**, *8*, 838–851. [CrossRef]
20. Ghalei, S.; Hopkins, S.; Douglass, M.; Garren, M.; Mondal, A.; Handa, H. Nitric oxide releasing halloysite nanotubes for biomedical applications. *J. Colloid Interface Sci.* **2021**, *590*, 277–289. [CrossRef]
21. Prishchenko, D.A.; Zenkov, E.V.; Mazurenko, V.V.; Fakhruddin, R.W.; Lvov, Y.M.; Mazurenko, V.G. Molecular dynamics of the halloysite nanotubes. *Phys. Chem. Chem. Phys.* **2018**, *20*, 5841–5849. [CrossRef]
22. Santos, A.C.; Ferreira, C.; Veiga, F.; Ribeiro, A.J.; Panchal, A.; Lvov, Y.; Agarwal, A. Halloysite clay nanotubes for life sciences applications: From drug encapsulation to bioscaffold. *Adv. Colloid Interface Sci.* **2018**, *257*, 58–70. [CrossRef]
23. Hasani, M.; Abdouss, M.; Shojaei, S. Nanocontainers for drug delivery systems: A review of Halloysite nanotubes and their properties. *Int. J. Artif. Organs* **2020**, *44*, 426–433. [CrossRef]
24. Kotova, O.; Sun, S.; Kotova, E.; Ponariyadov, A.; Brodskaya, R. Aluminosilicates: Interphase boundary interactions and nature engineering of nanostructures. *J. Phys. Conf. Ser.* **2022**, *2315*, 012003. [CrossRef]
25. Vergaro, V.; Abdullayev, E.; Lvov, Y.M.; Zeitoun, A.; Cingolani, R.; Rinaldi, R.; Leporatti, S. Cytocompatibility and Uptake of Halloysite Clay Nanotubes. *Biomacromolecules* **2010**, *11*, 820–826. [CrossRef]
26. Massaro, M.; Cavallaro, G.; Colletti, C.G.; Lazzara, G.; Milioto, S.; Noto, R.; Riela, S. Chemical modification of halloysite nanotubes for controlled loading and release. *J. Mater. Chem. B* **2018**, *6*, 3415–3433. [CrossRef]
27. Churchman, G.; Carr, R.M. The Definition and Nomenclature of Halloysites. *Clays Clay Miner.* **1975**, *23*, 382–388. [CrossRef]
28. Massaro, M.; Lazzara, G.; Milioto, S.; Noto, R.; Riela, S. Covalently modified halloysite clay nanotubes: Synthesis, properties, biological and medical applications. *J. Mater. Chem. B* **2017**, *5*, 4246. [CrossRef]
29. Lvov, Y.; Panchal, A.; Fu, Y.; Fakhruddin, R.; Kryuchkova, M.; Batasheva, S.; Stavitskaya, A.; Glotov, A.; Vinokurov, V. Interfacial Self-Assembly in Halloysite Nanotube Composites. *Langmuir* **2019**, *35*, 8646–8657. [CrossRef]
30. Chow, W.S.; Tham, W.L.; Seow, P.C. Effects of maleated-PLA compatibilizer on the properties of poly(lactic acid)/halloysite clay composites. *J. Thermoplast. Compos. Mater.* **2013**, *26*, 1349–1363. [CrossRef]
31. Wilson, I.; Keeling, J. Global occurrence, geology and characteristics of tubular halloysite deposits. *Clay Miner.* **2016**, *51*, 309–324. [CrossRef]
32. Teo, Z.X.; Chow, W.S. Impact, thermal, and morphological properties of poly(lactic acid)/poly(methyl methacrylate)/halloysite nanotube nanocomposites. *Polym.-Plast. Technol. Eng.* **2016**, *55*, 1474–1480. [CrossRef]
33. Duarte, H.A.; Lourenço, M.P.; Heine, T.; Guimarães, L. Clay Mineral Nanotubes: Stability, Structure and Properties. In *Stoichiometry and Materials Science—When Numbers Matter*, 1st ed.; Innocenti, A., Kamarulzaman, N., Eds.; Intech Open: London, UK, 2012. [CrossRef]
34. Du, M.; Guo, B.; Jia, D. Newly emerging applications of halloysite nanotubes: A review. *Polym. Int.* **2010**, *59*, 574–582. [CrossRef]
35. Pasbakhsh, P.; Churchman, G.J.; Keeling, J.L. Characterisation of properties of various halloysites relevant to their use as nanotubes and microfibre fillers. *Appl. Clay Sci.* **2013**, *74*, 47–57. [CrossRef]
36. Daraie, M.; Bagheri, D.; Malmir, M.; Heravi, M.M. Investigation of halloysite nanotubes and Schiff base combination with deposited copper iodide nanoparticles as a novel heterogeneous catalytic system. *Sci. Rep.* **2021**, *11*, 23658. [CrossRef]
37. Guimaraes, L.; Enyashin, A.N.; Seifert, G.; Duarte, H.A. Structural, electronic, and mechanical properties of single-walled halloysite nanotube models. *J. Chem. Phys.* **2010**, *114*, 11358–11363. [CrossRef]
38. Joo, Y.; Sim, J.H.; Jeon, Y.; Lee, S.U.; Sohn, D. Opening and blocking the inner-pores of Halloysite. *Chem. Commun.* **2013**, *49*, 4519–4521. [CrossRef]

39. Bugatti, V.; Sorrentino, A.; Gorrasi, G. Encapsulation of Lysozyme into halloysite nanotubes and dispersion in PLA: Structural and physical properties and controlled release analysis. *Eur. Polym. J.* **2017**, *93*, 495–506. [CrossRef]
40. Albdiry, M.T.; Yousif, B.F. Role of silanized halloysite nanotubes on structural, mechanical properties and fracture toughness of thermoset nanocomposites. *Mater. Des.* **2014**, *57*, 279–288. [CrossRef]
41. Abdullayev, E.; Lvov, Y. Halloysite clay nanotubes as a ceramic “skeleton” for functional biopolymer composites with sustained drug release. *J. Mater. Chem. B* **2013**, *1*, 2894–2903. [CrossRef]
42. Pereira, I.; Saleh, M.; Nunes, C.; Reis, S.; Veiga, F.; Paiva-Santos, A.C. Preclinical developments of natural-occurring halloysite clay nanotubes in cancer therapeutics. *Adv. Colloid Interface Sci.* **2021**, *291*, 102406. [CrossRef]
43. Yendluri, R.; Lvov, Y.; De Villiers, M.M.; Vinokurov, V.; Naumenko, E.; Tarasova, E.; Fakhrullin, R. Paclitaxel Encapsulated in Halloysite Clay Nanotubes for Intestinal and Intracellular Delivery. *J. Pharm. Sci.* **2017**, *10*, 3131–3139. [CrossRef] [PubMed]
44. Massaro, M.; Lazzara, G.; Noto, R.; Riela, S. Halloysite nanotubes: A green resource for materials and life sciences. *Rend. Lincei Sci. Fis. Nat.* **2020**, *31*, 213–221. [CrossRef]
45. Joussein, E.; Petit, S.; Delvaux, B. Behavior of halloysite clay under formamide treatment. *Appl. Clay Sci.* **2007**, *35*, 17–24. [CrossRef]
46. Hillier, S.; Ryan, P.C. Identification of halloysite (7 Å) by ethylene glycol solvation: The ‘MacEwan effect’. *Clay Miner.* **2002**, *37*, 487–496. [CrossRef]
47. Fisher, G.B.; Ryan, P.C. The smectite-to-disordered kaolinite transition in a tropical soil chrono sequence, Pacific coast, Costa Rica. *Clays Clay Miner.* **2006**, *54*, 571–586. [CrossRef]
48. Hendricks, S.B.; Jefferson, M.E. Structures of kaolin and talc-pyrophyllite hydrates and their bearing on water sorption of the clays. *Am. Mineral.* **1938**, *23*, 863–875.
49. Lipsicas, M.; Straley, C.; Costanzo, P.M.; Giese, R.F., Jr. Static and dynamic structure of water in hydrated kaolinites. II. The dynamic structure. *J. Colloid Interface Sci.* **1985**, *107*, 221–230. [CrossRef]
50. Smirnov, K.S.; Bougeard, D. A molecular dynamics study of structure and short-time dynamics of water in kaolinite. *J. Phys. Chem. B* **1999**, *103*, 5266–5273. [CrossRef]
51. Yuan, P.; Southon, P.D.; Liu, Z.; Green, M.E.R.; Hook, J.M.; Antill, S.J.; Kepert, C.J. Functionalization of Halloysite Clay Nanotubes by grafting with  $\gamma$ -Aminopropyltriethoxysilane. *J. Phys. Chem. C* **2008**, *112*, 15742–15751. [CrossRef]
52. Tan, D.; Yuan, P.; Liu, D.; Du, P. Surface Modifications of Halloysite in Nanosized Tubular Clay Minerals. In *Developments in Clay Science*; Chapter 8; Elsevier: Amsterdam, The Netherlands, 2016; Volume 7, pp. 167–201.
53. Peer, D.; Karp, J.; Hong, S.; Farokhzad, O.C.; Margalit, R.; Langer, R. Nanocarriers as an emerging platform for cancer therapy. *Nat. Nanotechnol.* **2007**, *2*, 751–760. [CrossRef]
54. Xia, Y.; Xiong, Y.; Lim, B.; Skrabalak, S.E. Shape-Controlled Synthesis of Metal Nanocrystals: Simple Chemistry Meets Complex Physics? *Angew. Chem. Int.* **2009**, *48*, 60–103. [CrossRef] [PubMed]
55. Zielińska, A.; Costa, B.; Ferreira, M.V.; Miguéis, D.; Louros, J.M.S.; Durazzo, A.; Lucarini, M.; Eder, P.; Chaud, M.V.; Morsink, M.; et al. Nanotoxicology and Nanosafety: Safety-By-Design and Testing at a Glance. *Int. J. Environ. Res. Public Health* **2020**, *13*, 4657. [CrossRef] [PubMed]
56. Gato, M.A.; Naseem, S.; Arfat, M.Y.; Dar, A.M.; Qasim, K.; Zubair, S. Physicochemical Properties of Nanomaterials: Implication in Associated Toxic Manifestations. *BioMed Res. Int.* **2014**, *2014*, 498420. [CrossRef] [PubMed]
57. Powers, K.W.; Palazuelos, M.; Moudgil, B.M.; Roberts, S.M. Characterization of the size, shape, and state of dispersion of nanoparticles for toxicological studies. *Nanotoxicology* **2007**, *1*, 42–51. [CrossRef]
58. Foroozandeh, P.; Aziz, A.A. Insight into Cellular Uptake and Intracellular Trafficking of Nanoparticles. *Nanoscale Res. Lett.* **2018**, *13*, 339. [CrossRef]
59. Zhang, X.Q.; Xu, X.; Bertrand, N.; Pridgen, E.; Swami, A.; Farokhzad, O.C. Interactions of nanomaterials and biological systems: Implications to personalized nanomedicine. *Adv. Drug Deliv. Rev.* **2012**, *64*, 1363–1384. [CrossRef]
60. Gehr, P. Interaction of nanoparticles with biological systems. *Colloids Surf. B Biointerfaces* **2018**, *172*, 395–399. [CrossRef]
61. Yah, C.S.; Iyuke, S.E.; Simate, G.S. A review of nanoparticles toxicity and their routes of exposures. *Iran. J. Pharm. Sci.* **2012**, *8*, 299–314.
62. Teleanu, D.M.; Negut, I.; Grumezescu, V.; Grumezescu, A.M.; Teleanu, R.I. Nanomaterials for Drug Delivery to the Central Nervous System. *Nanomaterials* **2019**, *9*, 371. [CrossRef]
63. De Jong, W.H.; Hagens, W.I.; Krystek, P.; Burger, M.C.; Sips, A.J.; Geertsma, R.E. Particle size-dependent organ distribution of gold nanoparticles after intravenous administration. *Biomaterials* **2008**, *29*, 1912–1919. [CrossRef]
64. Rizvi, S.A.A.; Saleh, A.M. Applications of nanoparticle systems in drug delivery technology. *Saudi Pharm. J.* **2018**, *26*, 64–70. [CrossRef] [PubMed]
65. Choi, H.S.; Liu, W.; Misra, P.; Tanaka, E.; Zimmer, J.P.; Iyke, B.; Bawendi, M.G.; Frangioni, J.V. Renal clearance of quantum dots. *Nat. Biotechnol.* **2007**, *25*, 1165–1170. [CrossRef] [PubMed]
66. Blanco, E.; Shen, H.; Ferrari, M. Principles of nanoparticle design for overcoming biological barriers to drug delivery. *Nat. Biotechnol.* **2015**, *33*, 941–951. [CrossRef] [PubMed]
67. Wang, S.; Li, Y.; Fan, J.; Wang, Z.; Zeng, X.; Sun, Y.; Song, P.; Ju, D. The role of autophagy in the neurotoxicity of cationic PAMAM dendrimers. *Biomaterials* **2014**, *35*, 7588–7597. [CrossRef]

68. Cullen, R.T.; Searl, A.; Miller, B.G.; Davis, J.M.; Jones, A.D. Pulmonary and intraperitoneal inflammation induced by cellulose fibres. *J. Appl. Toxicol.* **2000**, *20*, 49–60. [CrossRef]
69. Huang, Y.C.; Vieira, A.; Huang, K.L.; Yeh, M.K.; Chiang, C.H. Pulmonary inflammation caused by chitosan microparticles. *J. Biomed. Mater. Res.* **2005**, *75*, 283–287. [CrossRef]
70. Kim, J.Y.; Kim, H.H.; Cho, K.H. Acute cardiovascular toxicity of sterilizers, PHMG, and PGH: Severe inflammation in human cells and heart failure in zebrafish. *Cardiovasc. Toxicol.* **2013**, *13*, 148–160. [CrossRef]
71. Yu, Z.; Li, Q.; Wang, J.; Yu, Y.; Wang, Y.; Zhou, Q.; Li, P. Reactive Oxygen Species-Related Nanoparticle Toxicity in the Biomedical Field. *Nanoscale Res. Lett.* **2020**, *15*, 115. [CrossRef]
72. Auffan, M.; Achouak, W.; Rose, J.; Roncato, M.A.; Chanéac, C.; Waite, D.T.; Masion, A.; Woicik, J.C.; Wiesner, M.R.; Bottero, J.Y. Relation between the redox state of iron-based nanoparticles and their cytotoxicity toward *Escherichia coli*. *Environ. Sci. Technol.* **2008**, *42*, 6730–6735. [CrossRef]
73. Kamat, J.P.; Devasagayam, T.P.; Priyadarsini, K.I.; Mohan, H. Reactive oxygen species mediated membrane damage induced by fullerene derivatives and its possible biological implications. *Toxicology* **2000**, *155*, 55–61. [CrossRef]
74. Walczyk, D.; Bombelli, F.B.; Monopoli, M.P.; Lynch, I.; Dawson, K.A. What the Cell ‘Sees’ in Bionanoscience. *J. Am. Chem. Soc.* **2010**, *132*, 5761–5768. [CrossRef] [PubMed]
75. Hussain, S.M.; Hess, K.L.; Gearhart, J.M.; Geiss, K.T.; Schlager, J.J. In vitro toxicity of nanoparticles in BRL 3A rat liver cells. *Toxicol. In Vitro* **2005**, *19*, 975–983. [CrossRef] [PubMed]
76. Leroueil, P.R.; Berry, S.A.; Duthie, K.; Han, G.; Rotello, V.M.; McNerny, D.Q.; Baker, J.R., Jr.; Orr, B.G.; Holl, M.M. Wide varieties of cationic nanoparticles induce defects in supported lipid bilayers. *Nano Lett.* **2008**, *8*, 420–424. [CrossRef]
77. Hauck, T.S.; Ghazani, A.A.; Chan, W.C.W. Assessing the effect of surface chemistry on gold nanorod uptake, toxicity, and gene expression in mammalian cells. *Small* **2008**, *4*, 153–159. [CrossRef]
78. Gupta, R.; Xie, H. Nanoparticles in daily life: Applications, toxicity and regulations. *J. Environ. Pathol. Toxicol. Oncol.* **2018**, *37*, 209–230. [CrossRef] [PubMed]
79. Mousa, M.; Evans, N.D.; Oreffo, R.O.C.; Dawson, J.I. Clay nanoparticles for regenerative medicine and biomaterial design: A review of clay bioactivity. *Biomaterials* **2018**, *159*, 204–214. [CrossRef]
80. Setter, O.F.; Segal, E. Halloysite nanotubes—The nano-bio interface. *Nanoscale* **2020**, *12*, 23444–23460. [CrossRef]
81. Sawicka, D.; Zapor, L.; Chojnacka-Puchta, L.; Miranowicz-Dzierzawska, K. The in vitro toxicity evaluation of halloysite nanotubes (HNTs) in human lung cells. *Toxicol. Res.* **2020**, *37*, 301–310. [CrossRef]
82. Verma, N.K.; Moore, E.; Blau, W.; Volkov, Y.; Babu, R.P. Cytotoxicity evaluation of nanoclays in human epithelial cell line A549 using high content screening and real-time impedance analysis. *J. Nanopart. Res.* **2012**, *14*, 1137. [CrossRef]
83. Lai, X.; Agarwal, M.; Lvov, Y.M.; Pachpande, C.; Varahramyan, K.; Witzmann, F.A. Proteomic profiling of halloysite clay nanotube exposure in intestinal cell co-culture. *J. Appl. Toxicol.* **2013**, *11*, 1316–1329. [CrossRef]
84. Liu, H.Y.; Du, L.; Zhao, Y.T.; Tian, W.Q. In Vitro Hemocompatibility and Cytotoxicity Evaluation of Halloysite Nanotubes for Biomedical Application. *J. Nanomater.* **2015**, *16*, 685323. [CrossRef]
85. Sánchez-Fernández, A.; Peña-Parás, L.; Vidaltamayo, R.; Cué-Sampedro, R.; Mendoza-Martínez, A.; Zomosa-Signoret, V.C.; Rivas-Estilla, A.M.; Riojas, P. Synthesis, Characterization, and In Vitro Evaluation of Cytotoxicity of Biomaterials Based on Halloysite Nanotubes. *Materials* **2014**, *7*, 7770–7780. [CrossRef] [PubMed]
86. Khodzhaeva, V.; Makeeva, A.; Ulyanova, V.; Zelenikhin, P.; Evtugyn, V.; Hardt, M.; Rozhina, E.; Lvov, Y.; Fakhrullin, R.; Ilinskaya, O. Binase Immobilized on Halloysite Nanotubes Exerts Enhanced Cytotoxicity toward Human Colon Adenocarcinoma Cells. *Front. Pharmacol.* **2017**, *8*, 631. [CrossRef]
87. Kamaliev, R.F.; Ishmukhametov, I.R.; Batasheva, S.N.; Rozhina, E.V.; Fakhrullin, R.F. Uptake of halloysite clay nanotubes by human cells: Colourimetric viability tests and microscopy study. *Nano-Struct. Nano-Objects* **2018**, *15*, 54–60. [CrossRef]
88. Biddeci, G.; Spinelli, G.; Massaro, M.; Riela, S.; Bonaccorsi, P.; Barattucci, A.; Di Blasi, F. Study of Uptake Mechanisms of Halloysite Nanotubes in Different Cell Lines. *Int. J. Nanomed.* **2021**, *16*, 4755–4768. [CrossRef] [PubMed]
89. Long, Z.; Wu, Y.P.; Gao, H.Y.; Zhang, J.; Ou, X.; He, R.R.; Liu, M. In vitro and in vivo toxicity evaluation of halloysite nanotubes. *J. Mater. Chem. B* **2018**, *6*, 7204–7216. [CrossRef] [PubMed]
90. Ahmed, F.R.; Shoaib, M.H.; Azhar, M.; Um, S.H.; Yousuf, R.I.; Hashmi, S.; Dar, A. In-vitro assessment of cytotoxicity of halloysite nanotubes against HepG2, HCT116 and human peripheral blood lymphocytes. *Colloids Surf. B Biointerfaces* **2015**, *135*, 50–55. [CrossRef]
91. Fakhrullin, G.I.; Akhatova, F.S.; Lvov, Y.M.; Fakhrullin, R.F. Toxicity of halloysite clay nanotubes in vivo: A *Caenorhabditis elegans* study. *Environ. Sci. Nano* **2015**, *2*, 54–59. [CrossRef]
92. Bellani, L.; Giorgetti, L.; Riela, S.; Lazzara, G.; Scialabba, A.; Massaro, M. Ecotoxicity of halloysite nanotube-supported palladium nanoparticles in *Raphanus sativus* L. *Environ. Toxicol.* **2016**, *35*, 2503–2510. [CrossRef]
93. Wang, X.; Gong, J.; Rong, R.; Gui, Z.; Hu, T.; Xu, X. Halloysite Nanotubes-Induced AI Accumulation and Fibrotic Response in Lung of Mice after 30-Day Repeated Oral Administration. *J. Agric. Food Chem.* **2018**, *66*, 2925–2933. [CrossRef]
94. Hu, T.; Wang, X.; Tan, W.; Nie, K.; Xu, X. Nitric oxide synthase-mediated sub-chronic injury and recovery in the small intestine of mice after oral administration with halloysite nanotubes. *Environ. Sci. Pollut. Res. Int.* **2020**, *15*, 17730–17737. [CrossRef] [PubMed]

95. Khatoon, N.; Chub, M.Q.; Zhou, C.H. Nanoclay-based drug delivery systems and their therapeutic potentials. *J. Mater. Chem. B* **2020**, *8*, 7335–7351. [CrossRef]
96. Veerabadran, N.G.; Price, R.R.; Lvov, Y.M. Clay nanotubes for encapsulation and sustained release of drugs. *Nano* **2007**, *2*, 115–120. [CrossRef]
97. Hanif, M.; Jabbar, F.; Sharif, S.; Abbas, G.; Farooq, A.; Aziz, M. Halloysite nanotubes as a new drug-delivery system: A review. *Clay Miner.* **2016**, *51*, 469–477. [CrossRef]
98. Price, R.R.; Gaber, B.P.; Lvov, Y. In-vitro release characteristics of tetracycline HCl, khellin and nicotinamide adenine dinucleotide from halloysite; a cylindrical mineral. *J. Microencapsul.* **2001**, *18*, 713–722. [CrossRef] [PubMed]
99. Lisuzzo, L.; Cavallaro, G.; Pasbakhsh, P.; Milioto, S.; Lazzara, G. Why does vacuum drive to the loading of halloysite nanotubes? The key role of water confinement. *J. Colloid Interface Sci.* **2019**, *547*, 361–369. [CrossRef] [PubMed]
100. Yang, Y.; Chen, Y.; Leng, F.; Huang, L.; Wang, Z.; Tian, W. Recent Advances on Surface Modification of Halloysite Nanotubes for Multifunctional Applications. *Appl. Sci.* **2017**, *7*, 1215. [CrossRef]
101. Danyliuk, N.; Tomaszewska, J.; Tatarchuk, T. Halloysite nanotubes and halloysite-based composites for environmental and biomedical applications. *J. Mol. Liq.* **2020**, *309*, 113077. [CrossRef]
102. Lvov, Y.M.; DeVilliers, M.M.; Fakhrullin, R.F. The application of halloysite tubule nanoclay in drug delivery. *Expert Opin. Drug Deliv.* **2016**, *13*, 977–986. [CrossRef]
103. Lvov, Y.; Abdullayev, E. Functional polymer–clay nanotube composites with sustained release of chemical agents. *Prog. Polym. Sci.* **2013**, *38*, 1690–1719. [CrossRef]
104. Massaro, M.; Amorati, R.; Cavallaro, G.; Guernelli, S.; Lazzara, G.; Milioto, S.; Noto, R.; Poma, P.; Riela, S. Direct chemical grafted curcumin on halloysite nanotubes as dual-responsive prodrug for pharmacological applications. *Colloids Surf. B Biointerfaces* **2016**, *140*, 505–513. [CrossRef] [PubMed]
105. Massaro, M.; Noto, R.; Riela, S. Past, Present and Future Perspectives on Halloysite Clay Minerals. *Molecules* **2020**, *25*, 4863. [CrossRef] [PubMed]
106. Lu, D.; Chen, H.; Wu, J.; Chan, C.M. Direct measurements of the Young’s modulus of a single halloysite nanotube using a transmission electron microscope with a bending stage. *J. Nanosci. Nanotechnol.* **2011**, *11*, 7789–7793. [CrossRef] [PubMed]
107. Fakhrullina, G.; Khakimova, E.; Akhatova, F.; Lazzara, G.; Parisi, F.; Fakhrullin, R. Selective Antimicrobial Effects of Curcumin@Halloysite Nanoformulation: A *Caenorhabditis elegans* Study. *ACS Appl. Mater. Interfaces* **2019**, *26*, 23050–23064. [CrossRef]
108. Luo, X.; Zhang, J.; Wu, Y.P.; Yang, X.; Kuang, X.P.; Li, W.X.; Li, Y.F.; He, R.R.; Liu, M. Multifunctional HNT@Fe<sub>3</sub>O<sub>4</sub>@PPy@DOX Nanoplatfrom for Effective Chemo-Photothermal Combination Therapy of Breast Cancer with MR Imaging. *ACS Biomater. Sci. Eng.* **2020**, *6*, 3361–3374. [CrossRef]
109. Massaro, M.; Poma, P.; Cavallaro, G.; García-Villén, F.; Lazzara, G.; Notarbartolo, M.; Muratore, N.; Sánchez-Espejo, R.; Viseras Iborra, C.; Riela, S. Prodrug based on halloysite delivery systems to improve the antitumor ability of methotrexate in leukemia cell lines. *Colloids Surf. B Biointerfaces* **2022**, *213*, 112385. [CrossRef]
110. Nyankson, E.; Aboagye, S.O.; Efavi, J.K.; Agyei-Tuffour, B.; Paemka, L.; Asimeng, B.O.; Balapangu, S.; Arthur, P.K.; Tiburu, E.K. Chitosan-Coated Halloysite Nanotubes As Vehicle for Controlled Drug Delivery to MCF-7 Cancer Cells In Vitro. *Materials* **2021**, *14*, 2837. [CrossRef]
111. Liao, J.; Wang, D.; Tang, A.; Fu, L.; Ouyang, J.; Yang, H. Surface modified halloysite nanotubes with different lumen diameters as drug carriers for cancer therapy. *Chem. Commun.* **2021**, *57*, 9470–9473. [CrossRef]
112. Rao, K.M.; Kumar, A.; Suneetha, M.; Han, S.S. pH and near-infrared active; chitosan-coated halloysite nanotubes loaded with curcumin-Au hybrid nanoparticles for cancer drug delivery. *Int. J. Biol. Macromol.* **2018**, *112*, 119–125. [CrossRef]
113. Taheri-Ledari, R.; Zhang, W.; Radmanesh, M.; Cathcart, N.; Maleki, A.; Kitaev, V. Plasmonic photothermal release of docetaxel by gold nanoparticles incorporated onto halloysite nanotubes with conjugated 2D8-E3 antibodies for selective cancer therapy. *J. Nanobiotechnol.* **2021**, *19*, 239. [CrossRef]
114. Hamedi, S.; Koosha, M. Designing a pH-responsive drug delivery system for the release of black-carrot anthocyanins loaded in halloysite nanotubes for cancer treatment. *Appl. Clay Sci.* **2020**, *197*, 105770. [CrossRef]
115. Li, W.; Liu, D.; Zhang, H.; Correia, A.; Mäkilä, E.; Salonen, J.; Hirvonen, J.; Santos, H.A. Microfluidic assembly of a nano-in-micro dual drug delivery platform composed of halloysite nanotubes and a pH-responsive polymer for colon cancer therapy. *Acta Biomater.* **2017**, *48*, 238–246. [CrossRef] [PubMed]
116. Rizzo, C.; Arrigo, R.; D’Anna, F.; Di Blasi, F.; Dintcheva, N.T.; Lazzara, G.; Parisi, F.; Riela, S.; Spinelli, G.; Massaro, M.J. Hybrid supramolecular gels of Fmoc-F/halloysite nanotubes: Systems for sustained release of camptothecin. *J. Mater. Chem. B* **2017**, *5*, 3217–3229. [CrossRef] [PubMed]
117. Dramou, P.; Fizir, M.; Taleb, A.; Itatahine, A.; Dahiru, N.S.; Mehdi, Y.A.; Wei, L.; Zhang, J.; He, H. Folic acid-conjugated chitosan oligosaccharide-magnetic halloysite nanotubes as a delivery system for camptothecin. *Carbohydr. Polym.* **2018**, *197*, 117–127. [CrossRef] [PubMed]
118. Kerdakundee, N.; Li, W.; Martins, J.P.; Liu, Z.; Zhang, F.; Kemell, M.; Correia, A.; Ding, Y.; Airavaara, M.; Hirvonen, J.; et al. Multifunctional Nanotube-Mucoadhesive Poly (methyl vinyl ether-co-maleic acid) @ Hydroxypropyl Methylcellulose Acetate Succinate Composite for Site-Specific Oral Drug Delivery. *Adv. Healthc. Mater.* **2017**, *20*, 1700629. [CrossRef]

119. Liu, M.; Chang, Y.; Yang, J.; You, Y.; He, R.; Chen, T.; Zhou, C. Functionalized halloysite nanotube by chitosan grafting for drug delivery of curcumin to achieve enhanced anticancer efficacy. *J. Mater. Chem. B* **2016**, *4*, 2253–2263. [CrossRef]
120. Massaro, M.; Poma, P.; Colletti, C.G.; Barattucci, A.; Bonaccorsi, P.M.; Lazzara, G.; Nicotra, G.; Parisi, F.; Salerno, T.M.G.; Spinella, C.; et al. Chemical and biological evaluation of cross-linked halloysite-curcumin derivatives. *Appl. Clay Sci.* **2020**, *184*, 105400. [CrossRef]
121. Bulbul, Y.E.; Okur, M.; Demirtas-korkmaz, F.; Dilsiz, N. Development of PCL/PEO electro spun fibrous membranes blended with silane-modified halloysite nanotube as a curcumin release system. *Appl. Clay Sci.* **2020**, *186*, 105430. [CrossRef]
122. Yang, J.; Wu, Y.; Shen, Y.; Zhou, C.; Li, Y.-F.; He, R.-R.; Liu, M. Enhanced therapeutic efficacy of doxorubicin for breast cancer using chitosan oligosaccharide-modified halloysite nanotubes. *ACS Appl. Mater. Interfaces* **2016**, *8*, 26578–26590. [CrossRef]
123. Lee, Y.; Jung, G.E.; Cho, S.J.; Geckeler, K.E.; Fuchs, H. Cellular interactions of doxorubicin-loaded DNA-modified halloysite nanotubes. *Nanoscale* **2013**, *5*, 8577–8585. [CrossRef]
124. Hu, Y.; Chen, J.; Li, X.; Sun, Y.; Huang, S.; Li, Y.; Zhong, S. Multifunctional halloysite nanotubes for targeted delivery and controlled release of doxorubicin in-vitro and in-vivo studies. *Nanotechnology* **2017**, *28*, 375101. [CrossRef] [PubMed]
125. Wu, Y.P.; Yang, J.; Gao, H.Y.; Shen, Y.; Jiang, L.; Zhou, C.; Li, Y.F.; He, R.R.; Liu, M. Folate-Conjugated Halloysite Nanotubes, an Efficient Drug Carrier, Deliver Doxorubicin for Targeted Therapy of Breast Cancer. *ACS Appl. Nano Mater.* **2018**, *1*, 595–608. [CrossRef]
126. Guo, M.; Wang, A.; Muhammad, F.; Qi, W.; Ren, H.; Guo, Y.; Zhu, G. Halloysite nanotubes, a multifunctional nanovehicle for anticancer drug delivery. *Chin. J. Chem.* **2012**, *30*, 2115–2120. [CrossRef]
127. Zhang, J.; Luo, X.; Wu, Y.P.; Wu, F.; Li, Y.F.; He, R.R.; Liu, M. Rod in Tube: A Novel NanoplatforM for Highly Effective Chemo-Photothermal Combination Therapy toward Breast Cancer. *ACS Appl. Mater. Interfaces* **2019**, *11*, 3690–3703. [CrossRef]
128. Mitchell, M.J.; Castellanos, C.A.; King, M.R. Nanostructured surfaces to target and kill circulating tumor cells while repelling leukocytes. *J. Nanomater.* **2012**, *2012*, 831263. [CrossRef]
129. He, R.; Liu, M.; Shen, Y.; Liang, R.; Liu, W.; Zhou, C. Simple fabrication of rough halloysite nanotubes coatings by thermal spraying for high performance tumor cells capture. *Mater. Sci. Eng. C* **2018**, *85*, 170–181. [CrossRef]
130. Lazzara, G.; Riela, S.; Fakhrullin, R.F. Clay-based drug delivery systems: What does the future hold? *Ther. Deliv.* **2017**, *8*, 633–646. [CrossRef]
131. Saleh, M.Y.; Prajapati, N.; DeCoster, M.A.; Lvov, Y. Tagged Halloysite Nanotubes as a Carrier for Intercellular Delivery in Brain Microvascular Endothelium. *Front. Bioeng. Biotechnol.* **2020**, *8*, 451. [CrossRef]
132. Fizir, M.; Dramou, P.; Dahiru, N.S.; Ruya, W.; Huang, T.; He, H. Halloysite nanotubes in analytical sciences and in drug delivery: A review. *Microchim. Acta* **2018**, *185*, 389. [CrossRef]
133. Lvov, Y.; Wang, W.; Zhang, L.; Fakhrullin, R. Halloysite clay nanotubes for loading and sustained release of functional compounds. *Adv. Mater.* **2016**, *28*, 1227–1250. [CrossRef]
134. Patel, S.; Jammalamadaka, U.; Sun, L.; Tappa, K.; Mills, D.K. Sustained release of antibacterial agents from doped Halloysite nanotubes. *Bioengineering* **2015**, *3*, 1. [CrossRef] [PubMed]
135. Zhang, H. Selective modification of inner surface of halloysite nanotubes: A review. *Nanotechnol. Rev.* **2017**, *6*, 573–581. [CrossRef]
136. Joshi, A.; Abdullayev, E.; Vasiliev, A.; Volkova, O.; Lvov, Y. Interfacial modification of clay nanotubes for the sustained release of corrosion inhibitors. *Langmuir* **2013**, *29*, 7439–7448. [CrossRef] [PubMed]
137. Dzamukova, M.R.; Naumenko, E.A.; Lvov, Y.M.; Fakhrullin, R.F. Enzyme-activated intracellular drug delivery with tubule clay nanoformulation. *Sci. Rep.* **2015**, *5*, 10560. [CrossRef] [PubMed]
138. Cavallaro, G.; Lazzara, G.; Massaro, M.; Milioto, S.; Noto, R.; Parisi, F.; Riela, S. Biocompatible Poly(N-isopropylacrylamide)-halloysite Nanotubes for Thermo-responsive Curcumin Release. *J. Phys. Chem. C* **2015**, *119*, 8944–8951. [CrossRef]
139. Massaro, M.; Buscemi, G.; Arista, L.; Biddeci, G.; Cavallaro, G.; D’Anna, F.; Di Blasi, F.; Ferrante, A.; Lazzara, G.; Rizzo, C.; et al. Multifunctional Carrier Based on Halloysite/Laponite Hybrid Hydrogel for Kartogenin Delivery. *ACS Med. Chem. Lett.* **2018**, *10*, 419–424. [CrossRef]
140. Tan, D.; Yuan, P.; Annabi-Bergaya, F.; Liu, D.; Wang, L.; Liu, H.; He, H. Loading and in vitro release of ibuprofen in tubular halloysite. *Appl. Clay Sci.* **2014**, *96*, 50–55. [CrossRef]
141. Riela, S.; Massaro, M.; Colletti, C.G.; Bommarito, A.; Giordano, C.; Milioto, S.; Noto, R.; Poma, P.; Lazzara, G. Development and characterization of co-loaded curcumin/triazole-halloysite systems and evaluation of their potential anticancer activity. *Int. J. Pharm.* **2014**, *475*, 613–623. [CrossRef]
142. Rawtani, D.; Pandey, G.; Tharmavaram, M.; Pathak, P.; Akkireddy, S.; Agrawal, Y.K. Development of a novel ‘nanocarrier’ system based on Halloysite Nanotubes to overcome the complexation of ciprofloxacin with iron: An in vitro approach. *Appl. Clay Sci.* **2017**, *150*, 293–302. [CrossRef]
143. Pierchala, M.K.; Makaremi, M.; Tan, H.L.; Pushpamalar, J.; Muniyandy, S.; Solouk, A.; Lee, S.M.; Pasbakhsh, P. Nanotubes in nanofibers: Antibacterial multilayered polylactic acid/halloysite/gentamicin membranes for bone regeneration application. *Appl. Clay Sci.* **2018**, *160*, 95–105. [CrossRef]
144. Jermy, B.R.; Ravinayagam, V.; Almohazey, D.; Alamoudi, W.A.; Dafalla, H.; Akhtar, S.; Tanimu, G. PEGylated green halloysite/spinel ferrite nanocomposites for pH sensitive delivery of dexamethasone: A potential pulmonary drug delivery treatment option for COVID-19. *Appl. Clay Sci.* **2022**, *216*, 106333. [CrossRef] [PubMed]

145. Bordini, E.A.F.; Ferreira, J.A.; Dubey, N.; Ribeiro, J.S.; De Souza Costa, C.A.; Soares, D.G.; Bottino, M.C. Injectable Multifunctional Drug Delivery System for Hard Tissue Regeneration under Inflammatory Microenvironments. *ACS Appl. BioMater.* **2021**, *4*, 6993–7006. [CrossRef] [PubMed]
146. Li, L.Y.; Zhou, Y.M.; Gao, R.Y.; Liu, X.C.; Du, H.H.; Zhang, J.L.; Ai, X.C.; Zhang, J.P.; Fu, L.M.; Skibsted, L.H. Naturally occurring nanotube with surface modification as biocompatible, target-specific nanocarrier for cancer phototherapy. *Biomaterials* **2019**, *190–191*, 86–96. [CrossRef] [PubMed]
147. Tan, C.; Zheng, J.; Feng, Y.; Liu, M. Cell Membrane-Coated Halloysite Nanotubes for Target-Specific Nanocarrier for Cancer Phototherapy. *Molecules* **2021**, *26*, 4483. [CrossRef] [PubMed]
148. Lisuzzo, L.; Cavallaro, G.; Milioto, S.; Lazzara, G. Pickering Emulsions Stabilized by Halloysite Nanotubes: From General Aspects to Technological Applications. *Adv. Mater. Interfaces* **2022**, *9*, 2102346. [CrossRef]



Article

# Preparation of Spherical Cellulose Nanocrystals from Microcrystalline Cellulose by Mixed Acid Hydrolysis with Different Pretreatment Routes

Peng Zhu \* , Luyao Feng, Zejun Ding and Xuechun Bai

College of Textile Science and Engineering (International Institute of Silk), Zhejiang Sci-Tech University, Hangzhou 310018, China

\* Correspondence: zhupeng@zstu.edu.cn

**Abstract:** Spherical cellulose nanocrystal (CNC), as a high value cellulose derivative, shows an excellent application potential in biomedicine, food packaging, energy storage, and many other fields due to its special structure. CNC is usually prepared by the mixed acid hydrolysis method from numerous cellulose raw materials. However, the pretreatment route in preparing spherical CNC from cellulose fiber is still used when choosing microcrystalline cellulose (MCC) as the raw material, which is not rigorous and economical. In this work, pretreatment effects on the properties of spherical CNC produced from MCC by mixed acid hydrolysis were systematically studied. Firstly, the necessity of the swelling process in pretreatment was examined. Secondly, the form effects of pretreated MCC (slurry or powder form) before acid hydrolysis in the preparation of spherical CNC were carefully investigated. The results show that the swelling process is not indispensable. Furthermore, the form of pretreated MCC also has a certain influence on the morphology, crystallinity, and thermal stability of spherical CNC. Thus, spherical CNC with different properties can be economically prepared from MCC by selecting different pretreatment routes through mixed acid hydrolysis.

**Keywords:** spherical cellulose nanocrystals; pretreatment; microcrystalline cellulose; mixed acid hydrolysis; crystallinity; thermal stability

**Citation:** Zhu, P.; Feng, L.; Ding, Z.; Bai, X. Preparation of Spherical Cellulose Nanocrystals from Microcrystalline Cellulose by Mixed Acid Hydrolysis with Different Pretreatment Routes. *Int. J. Mol. Sci.* **2022**, *23*, 10764. <https://doi.org/10.3390/ijms231810764>

Academic Editor: Raghvendra Singh Yadav

Received: 5 August 2022

Accepted: 12 September 2022

Published: 15 September 2022

**Publisher's Note:** MDPI stays neutral with regard to jurisdictional claims in published maps and institutional affiliations.



**Copyright:** © 2022 by the authors. Licensee MDPI, Basel, Switzerland. This article is an open access article distributed under the terms and conditions of the Creative Commons Attribution (CC BY) license (<https://creativecommons.org/licenses/by/4.0/>).

## 1. Introduction

In pursuit of environmentally friendly and sustainable development, the preparation and application of biomass materials have attracted great attention [1]. Cellulose is considered to be the most abundant, biodegradable, renewable, and sustainable biopolymer on Earth and its biosynthesis, chemistry, and ultrastructure remains an active field of research [2–4]. As one of the most important derivatives of cellulose, nanocellulose has great potential in biomedicine, food packaging, energy storage, environmental remediation, and many other fields [5]. Cellulose nanofibril (CNF) and CNC are the two main forms of nanocellulose [6–8]. CNF ( $\geq 1 \mu\text{m}$  of length) has a larger aspect ratio than CNC, which can form a unique entangled network structure. CNC (about 100–200 nm of length) is much shorter than CNF, while it has a higher crystallinity and a nanometer size. Moreover, CNC has the advantages of great mechanical properties, good biocompatibility, a high specific surface area, biodegradability, and a low thermal expansion coefficient [9,10].

In the past decades, various approaches have been proposed for CNC preparation. The size, shape, morphology, and structural properties of the cellulose nanomaterials were determined by these methods [11]. The morphology of a cellulose nanomaterial is closely related to its application characteristics, which will have a great impact on its application prospects. According to the existing literature, Ding et al. first prepared spherical CNC by a mixed acid hydrolysis method (sulfuric acid/hydrochloric acid) from short-staple cotton in 2000 [12]. As one of the nanocelluloses, spherical CNC has a large specific surface area, uniform particle size, higher bulk density, and higher thermal stability [1]. It has

more prominent advantages in many aspects, which has attracted the attention of many researchers. Yu et al. changed the type of mixed acid and also prepared spherical CNC from Lyocell fiber using formic acid/hydrochloric acid, as well as acetic acid/hydrochloric acid [13–15]. Furthermore, enzymatic hydrolysis is also a common method to prepare spherical CNC from cotton fiber [16], pulp fiber [1,5,17,18], or bacterial cellulose [19]. Moreover, Cheng et al. prepared spherical CNC through the chemical hydrolysis of Lyocell fiber in an ammonium persulfate solution [20]. In addition, a single acid combined with mechanical action was used to prepare spherical CNC from oil palm empty fruit bunch pulp [21] or sesame husk [22]. Meanwhile, other approaches were also proposed to prepare spherical CNC [2,23,24].

Among the above methods, the mixed acid hydrolysis method (sulfuric acid and hydrochloric acid) is a widely used method to prepare spherical CNC. In these studies, the pretreatment and hydrolysis processes are basically the same as shown in Figure 1a [3,12,25]. Even when the raw material was replaced by commercial MCC, the pretreatment process used was still the same as that of cellulose fibers (Figure 1b) [4]. The sizes of MCC and cellulose fibers are not in the same order of magnitude, and their chemical composition and physical structure are distinctly different [26–28]. Moreover, some series of MCC are obtained by acid hydrolysis from cellulose fibers through many high energy consuming steps [29–31]. Therefore, using the same pretreatment process from different raw materials is not rigorous and economical, although spherical CNC can be prepared.

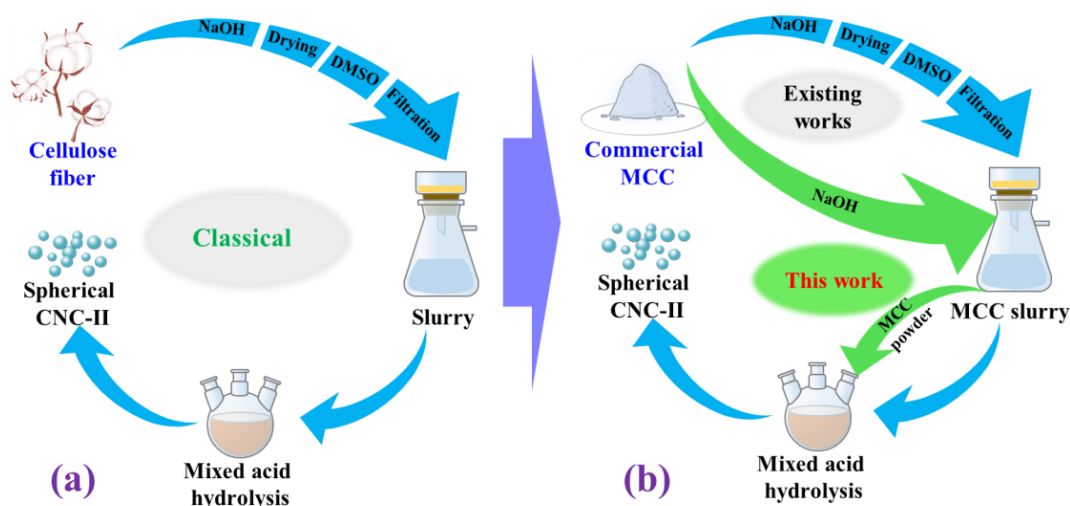


**Figure 1.** Schematic process flow of (a) spherical cellulose nanocrystal (CNC) preparation from cellulose fiber, and (b) spherical CNC preparation from commercial microcrystalline cellulose (MCC).

In the pretreatment process for cellulose fibers, sodium hydroxide is chosen to hydrolyze the amorphous region and swell fibers at the same time [3,16,22]. Meanwhile, the crystal type can be changed during the sodium hydroxide treatment from a cellulose I to a cellulose II structure, from which it is easier to fabricate spherical CNC [15,24]. DMSO is mainly used to swell cellulose fibers [3,12]. At present, the necessity of the DMSO swelling process in the preparation of spherical CNC by the mixed acid hydrolysis method from MCC requires investigation.

Furthermore, the obtained substance in slurry form after the DMSO swelling process will be hydrolyzed with mixed acid [3,4]. On the one hand, the form of slurry is conducive to maintaining the swelling effect, making it easier for mixed acid to enter the amorphous region or even the crystalline region of cellulose fibers [21]. On the other hand, the water content in the slurry cannot be easily controlled, resulting in poor repeatability, poor long-term storage stability, and excessive acid needed to ensure the product quality.

In the present work, commercial MCC was used as the raw material to prepare spherical CNC by mixed acid hydrolysis. The necessity of the swelling process in pretreatment

during the preparation of spherical CNC from commercial MCC was examined. In addition, the form effects of pretreated MCC (slurry or powder form) before mixed acid hydrolysis on the preparation of spherical CNC were carefully investigated. This work will provide support for selecting the pretreatment routes of MCC to prepare desired spherical CNC for further studies.

## 2. Results and Discussion

### 2.1. Chemical Structure

FTIR spectroscopy was used to evaluate the chemical structure of MCC before and after the pretreatment processes. Figure 2a illustrates FTIR spectra of MCC, MCC after alkaline treatment (MCC+NaOH), and MCC after alkaline treatment and swelling treatment by DMSO (MCC+NaOH+DMSO). It can be observed that all samples have the common peaks representative of cellulose: O–H stretching vibrations and flexural vibrations of intra- and intermolecular hydrogen bonds near 3000–3700  $\text{cm}^{-1}$  [16,19], C–H stretching vibrations at 2900  $\text{cm}^{-1}$  [21], O–H bending of absorbed water at 1647  $\text{cm}^{-1}$  [16], H–C–H and O–C–H in-plane bending vibrations at 1430  $\text{cm}^{-1}$  [4], C–H deformation vibrations at 1372  $\text{cm}^{-1}$  [32], C–O stretching vibrations at 1160  $\text{cm}^{-1}$  [22], O–H bending in  $\beta$ -glycosidic linkages between the anhydroglucose units at 897  $\text{cm}^{-1}$  [21,33], and C–OH out-of-plane bending at 667  $\text{cm}^{-1}$  are characteristic peaks of cellulose [4,32].

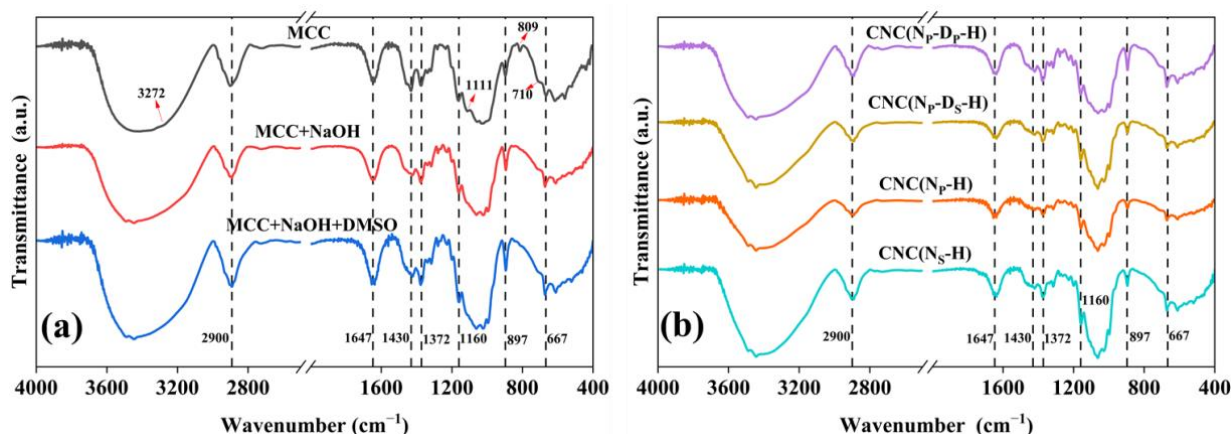


**Figure 2.** (a) FTIR spectra of MCC, MCC after alkaline treatment, and MCC after alkaline treatment and swelling treatment; (b) FTIR spectra of CNC samples prepared through different pretreatment routes.

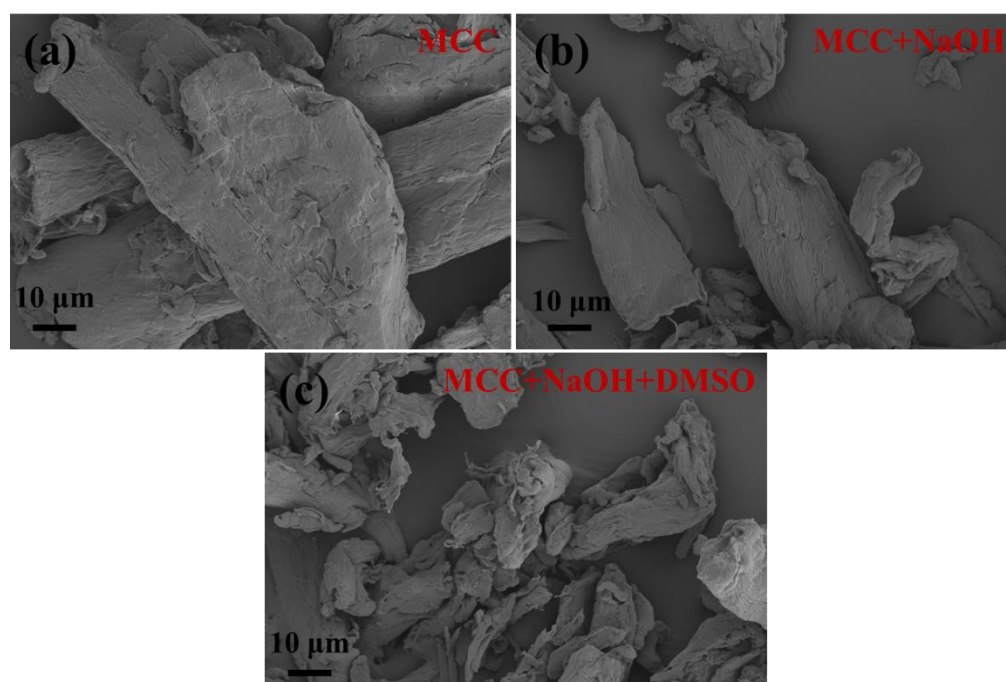
The main differences between the FTIR spectra in Figure 2a are the crystalline I characteristic peaks presented in the commercial MCC, O–H stretching vibrations at 3272  $\text{cm}^{-1}$ , and O–H out-of-plane bending at 710  $\text{cm}^{-1}$  [34]. Furthermore, the 1430 and 1111  $\text{cm}^{-1}$  absorption peaks can also be used to study the type of crystalline cell and the crystallinity changes because the crystalline cellulose I spectra differs clearly in these peaks from cellulose II [35]. Ring asymmetric stretching at 1111  $\text{cm}^{-1}$  is a characteristic peak of cellulose I. Meanwhile, the peak near 1430  $\text{cm}^{-1}$  is attributed to H–C–H symmetric bending or a scissoring motion which is known to be the sum of the cellulose I peak at 1430  $\text{cm}^{-1}$  and the cellulose II peak at 1420  $\text{cm}^{-1}$  [36]. Comparing the FTIR spectra of MCC before and after alkaline treatment, it can be seen that the intensity of peak at 1430  $\text{cm}^{-1}$  is significantly reduced and characteristic peaks at 3272  $\text{cm}^{-1}$ , 1111  $\text{cm}^{-1}$ , and 710  $\text{cm}^{-1}$  are absent, indicating the complete conversion of cellulose I to cellulose II after alkaline treatment. In addition, the peak at 809  $\text{cm}^{-1}$  in the commercial MCC spectra is due to glucomannan from hemicellulose [37], which disappeared in the sample spectra after alkaline treatment, meaning that the residual hemicellulose is completely removed during alkaline treatment.

Based on the FTIR analysis from Figure 2a, the molecular structures of pretreated MCC were changed from cellulose I to cellulose II through the alkaline treatment. As shown in

Figure 2b, all CNC samples prepared with different pretreatments maintain the cellulose II structure, due to the absence of characteristic peaks of cellulose I at  $3272\text{ cm}^{-1}$ ,  $1111\text{ cm}^{-1}$ , and  $710\text{ cm}^{-1}$ .

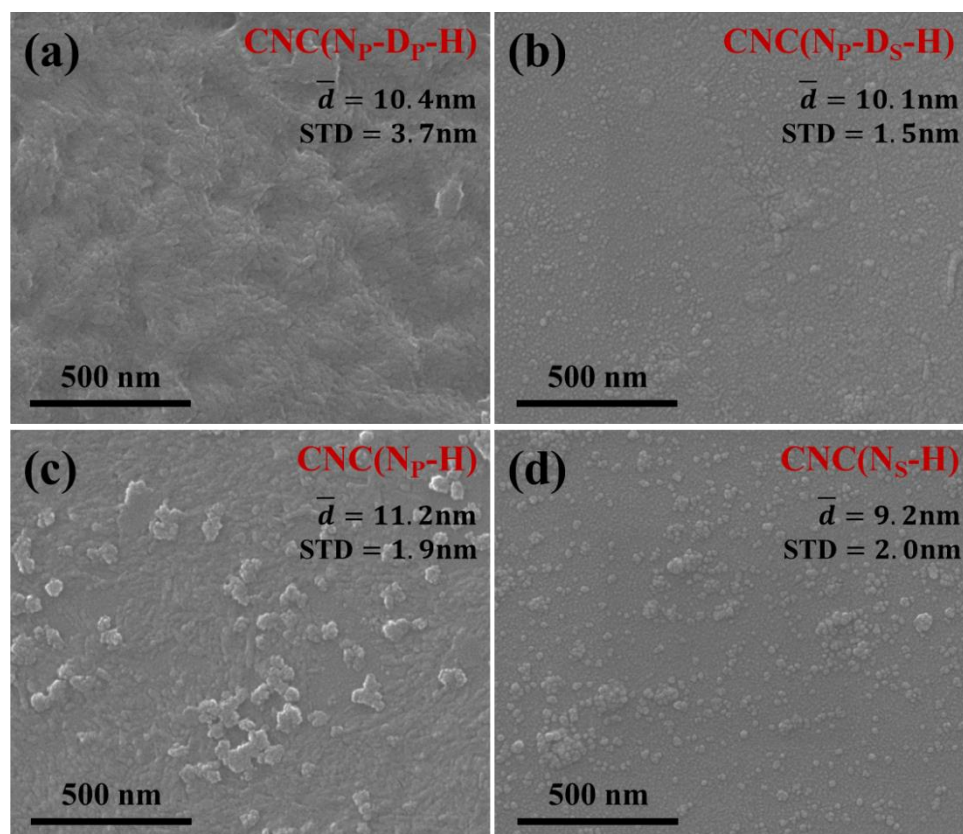
## 2.2. Micromorphology

Figure 3 demonstrates the FE-SEM images of MCC before and after different pretreatment routes. Compared with original MCC (Figure 3a), MCC+NaOH is smoother and more fragmented, as shown in Figure 3b. Due to the alkaline hydrolysis of cellulose, the surface and some amorphous regions of MCC are hydrolyzed first, leading to the above morphological structure. With further swelling by DMSO (Figure 3c), MCC+NaOH+DMSO becomes much more fragmented as some small organic molecules are dissolved in DMSO. In addition, their morphology becomes more irregular because of the deformation during the drying process from the swelling state.



**Figure 3.** FE-SEM images of (a) MCC, (b) MCC after alkaline treatment, and (c) MCC after alkaline treatment and swelling treatment ( $1000\times$  magnification).

FE-SEM images of CNC samples prepared with different pretreatments are presented in Figure 4. It can be seen that all CNC samples show an approximately spherical appearance and exhibit a very small size with a narrow size distribution, which has been annotated in Figure 4. In particular, the roundness of CNC( $N_P$ - $D_S$ -H) and CNC( $N_S$ -H) is improved, which is attributed to the easier entry of mixed acid into MCC when MCC is in slurry form. In Figure 4c,d, some nanoparticles with larger sizes are actually aggregates of small spherical CNC, which are easily formed during the natural evaporation of water in the sample preparation process for FE-SEM observation. Through the analysis and calculation of ImageJ software, the average diameters of CNC( $N_P$ - $D_P$ -H) and CNC( $N_P$ - $D_S$ -H) are  $10.4 \pm 3.7\text{ nm}$  and  $10.1 \pm 1.5\text{ nm}$ , respectively. Meanwhile, without any additional swelling treatment, CNC( $N_P$ -H) and CNC( $N_S$ -H) display an average diameter of  $11.2 \pm 1.9\text{ nm}$  and  $9.2 \pm 2.0\text{ nm}$ , respectively. It can be seen that the average particle size of CNC( $N_P$ - $D_S$ -H) and CNC( $N_S$ -H) is a bit smaller because the MCC has swollen, which makes it easier for the mixed acid solution to enter the MCC, resulting in a higher hydrolysis efficiency. It should be noted that in the preparation of CNC samples without any additional swelling treatment, MCC in slurry form has been initially swelled in the alkaline treatment [3,16,22].



**Figure 4.** FE-SEM images of CNC samples prepared through different pretreatment routes (200,000 $\times$  magnification).

These FE-SEM images strongly demonstrate that spherical CNC can be appropriately prepared from commercial MCC by mixed acid hydrolysis combined with ultrasonication, whether there is an additional swelling treatment or not and whether the form of MCC before mixed acid hydrolysis is powder or slurry. In addition, all the obtained suspensions of spherical CNC exhibited an excellent dispersion stability, as shown in Figure S1; thus, they are convenient for long-term storage without any special protection measures.

### 2.3. Crystallinity

XRD was performed to examine the changes in the crystalline structure and the crystallinity of MCC during the pretreatment. Figure 5a shows the XRD patterns of MCC, MCC+NaOH, and MCC+NaOH+DMSO. In the XRD pattern of MCC, there are diffraction peaks at  $2\theta$  around  $14.9^\circ$ ,  $16.3^\circ$ ,  $22.5^\circ$ , and  $34.6^\circ$  that correspond to the  $(1\bar{1}0)$ ,  $(110)$ ,  $(200)$ , and  $(004)$  crystallographic planes, in accordance with the characteristic diffraction peaks of cellulose  $I_\beta$  [16,38,39]. The diffractograms of other samples show peaks located at  $2\theta$  around  $12.0^\circ$ ,  $20.0^\circ$ , and  $22.0^\circ$ , which are characteristic of the  $(1\bar{1}0)$ ,  $(110)$ , and  $(200)$  crystallographic planes of cellulose II. The results indicate that the crystal type of pretreated MCC has been transformed from cellulose I to cellulose II through alkaline treatment, whereas the swelling treatment by DMSO has no effect on the crystal type. These XRD findings are supportive of and consistent with the FTIR results.

The crystallinity of different samples was calculated according to the XRD results as listed in Table 1. Compared with the 78.85% crystallinity of commercial MCC, the crystallinity of MCC+NaOH is lower—only 58.56%—which is attributed to the transformation of crystal type. In Liu's study, the crystallinity of cellulose also decreased significantly after alkaline treatment [24]. Meanwhile, the crystallinity of MCC+NaOH+DMSO increased to 64.81% because of the removal of residual small molecules by DMSO.

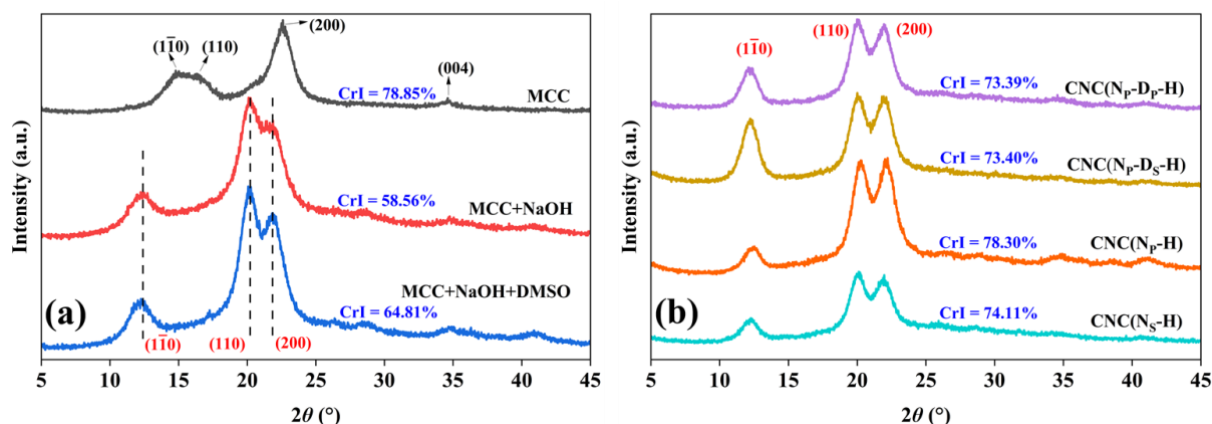


**Figure 5.** (a) XRD patterns of MCC, MCC after alkaline treatment and MCC after alkaline treatment and swelling treatment; (b) XRD patterns of CNC samples prepared through different pretreatment routes.

**Table 1.** The crystallinity and crystallite size for different samples.

Sample	CrI (%)	Crystallite Size (D, nm)		
		$(1\bar{1}0)$	(110)	(200)
MCC	78.85	4.06	3.81	5.06
MCC+NaOH	58.56	3.81	4.52	4.08
MCC+NaOH+DMSO	64.81	4.36	5.18	4.65
CNC( $N_P$ -D $_P$ -H)	73.39	7.15	5.98	5.87
CNC( $N_P$ -D $_S$ -H)	73.40	7.42	6.13	5.65
CNC( $N_P$ -H)	78.30	7.51	6.10	5.47
CNC( $N_S$ -H)	74.11	7.24	5.99	5.69

The average cross-sectional dimensions of the elementary crystallites perpendicular to the  $(1\bar{1}0)$ ,  $(110)$ , and  $(200)$  crystallographic planes of different samples were quantified using the XRD results and the Scherrer equation as listed in Table 1 [39]. Due to the transformation of crystal type, there was no correlation between the crystallite size data of commercial MCC and pretreated MCC. After further swelling treatment by DMSO, the regularity of the crystallite size data is consistent with that of alkaline treatment only, in which the crystallite size of  $(110)$  is the largest,  $(200)$  is the second, and  $(1\bar{1}0)$  is the smallest, but all values are increased. This indicates that the swelling treatment by DMSO contributes to the growth of cellulose unit cells through swelling and drying processes.

The diffractograms in Figure 5b show the characteristic peaks of cellulose II, indicating that the crystal type of pretreated MCC is maintained in all the obtained CNC samples. As there is a crystal transformation during the pretreatment, it is meaningless to compare the crystallinity of commercial MCC and CNC samples. Therefore, compared with the pretreated MCC, the crystallinity of all the obtained CNC samples is obviously increased, as listed in Table 1. This indicates that mixed acid hydrolysis causes a preferential degradation of amorphous regions in the material structure, whereas crystalline regions are domains with a higher resistant ability to the mixed acid [19,21]. Acid hydrolysis treatment increasing the crystallinity of CNC by the removal of disordered structure in MCC or cellulose fibers can be found in previous reports [2,15,21], but some studies still support the opposite conclusion [40,41].

The crystallinity of CNC( $N_P$ -H) is 78.30%, which is higher than that of CNC( $N_S$ -H) at 74.11%, meaning that the form of slurry or powder before the mixed acid hydrolysis exerts

a certain impact on the crystallinity of these CNC samples. It can be inferred that in slurry form, the mixed acid can enter the pretreated MCC, which provides easier contact with the crystalline region. While the amorphous region is hydrolyzed, a small part of the crystalline region will be destroyed as well. While in powder form, MCC can only be hydrolyzed gradually from the outside, giving priority to the amorphous region; thus, its crystallinity is higher. However, the crystallinity of CNC( $N_5$ -D $_P$ -H) and CNC( $N_5$ -D $_S$ -H) is nearly the same, meaning that the form before the mixed acid hydrolysis has no impact on the crystallinity of the CNC samples obtained with the pretreatments of alkaline treatment and swelling treatment. This may be due to the good swelling effect of DMSO. In powder form, there are many cracks caused by the incomplete recovery of deformation after swelling by DMSO, providing the mixed acid easy contact with the crystalline region [42]. Therefore, there is basically no difference in their crystallinity.

The crystallite size of CNC samples was also calculated (Table 1). The regularity of the crystallite size data is different from that of the pretreated MCC, in which the crystallite size of (110) is the largest, (110) is the second, and (200) is the smallest, and all values are clearly increased. This phenomenon also exists in other works [2,15,43]. Ahmed-Haras explained that the growth of cellulose crystals may be due to the partial removal of the MCC amorphous region by acid hydrolysis [2]. Although mixed acid may destroy the crystalline region, it is more inclined to hydrolyze the amorphous region, resulting in an increase in crystallinity at the macro level and the rearrangement of cellulose chains or cellulose cell units at the micro level.

#### 2.4. Thermal Stability

To evaluate the thermal stability of commercial MCC and pretreated MCC, thermogravimetric analysis was performed as shown in Figure 6a,b. Their thermal degradation processes can be divided into four steps: the loss of absorbed water before 100 °C, the appearance of a plateau until 220 °C, the degradation of cellulose at temperatures ranging from 220 to 400 °C, and the carbonation of the residual products over 400 °C [20].

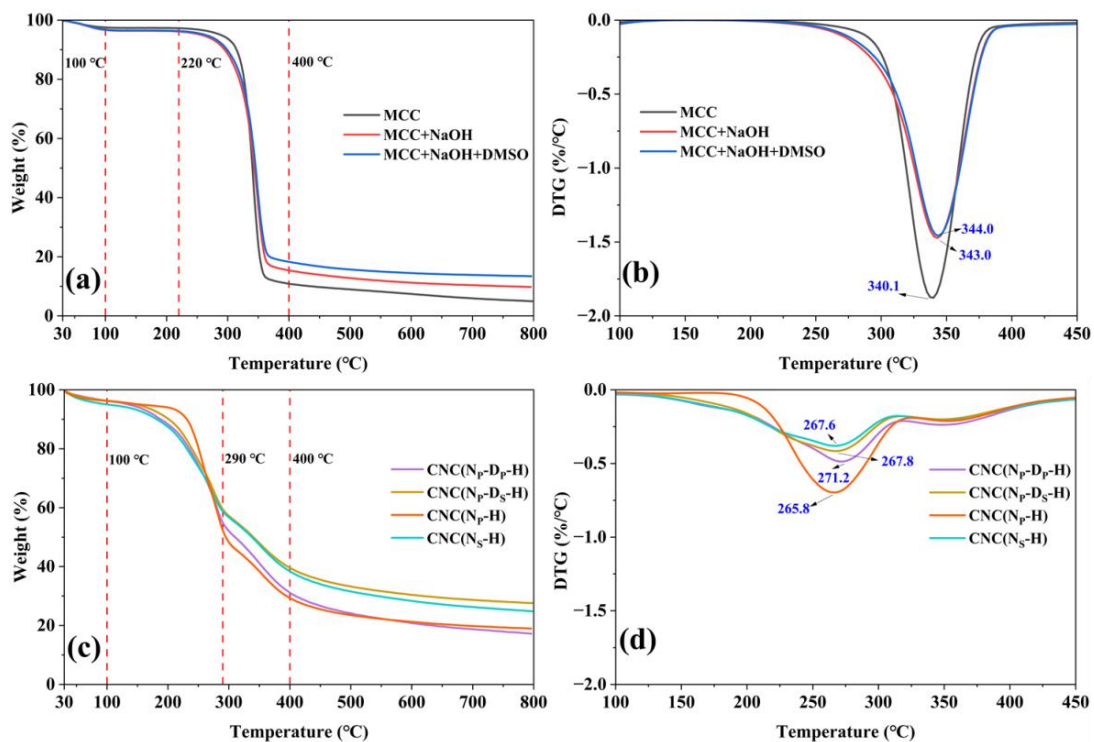


**Figure 6.** (a) TG and (b) DTG curves of MCC, MCC after alkaline treatment and MCC after alkaline treatment and swelling treatment; (c) TG and (d) DTG curves of CNC samples prepared through different pretreatment routes.

The thermal degradation parameters such as the onset degradation temperature ( $T_0$ ), the maximum degradation temperature ( $T_{Max}$ ), and the corresponding weight loss (WL) are calculated from the TG and DTG curves as listed in Table 2. Compared with commercial MCC, the water absorption capacity of pretreated MCC increases significantly, which is attributed to the full exposure of cellulose [43]. In particular, the hydrogen bond in MCC can be destroyed by hot water, and new hydroxyl groups will be introduced obtaining more adsorbed water. Due to its higher crystallinity, the  $T_0$  of MCC is higher than that of pretreated MCC, while their  $T_{Max}$  is basically the same. The above results show that the thermal stability of MCC decreased slightly after pretreatment, but the hydrophilicity increased.

**Table 2.** Thermal degradation parameters of different samples.

Sample	Initial Weight Loss (%)	$T_0$ (°C)	Main Stage I		Main Stage II		Final Residue (%)
			$T_{Max}$ (°C)	WL (%)	$T_{Max}$ (°C)	WL (%)	
MCC	2.45	315.1	340.1	84.62	–	–	4.97
MCC+NaOH	3.34	295.5	343.0	78.22	–	–	9.79
MCC+NaOH+DMSO	3.28	299.0	344.0	75.60	–	–	13.41
CNC( $N_P$ - $D_P$ -H)	3.70	220.5	271.2	42.56	348.7	22.94	16.72
CNC( $N_P$ - $D_S$ -H)	3.67	206.3	267.8	36.96	347.8	19.82	27.60
CNC( $N_P$ -H)	3.77	236.3	265.8	48.18	353.3	18.81	18.97
CNC( $N_S$ -H)	4.95	198.1	267.6	36.37	350.1	20.29	24.86

Figure 6c,d shows the thermogravimetric analysis diagram of CNC samples prepared with different pretreatments. Their thermal degradation processes can be divided into another four steps: the loss of absorbed water before 100 °C, the loss of bonded water and degradation of cellulose at temperatures ranging from 100 to 290 °C (main stage I as listed in Table 2), the slow charring process of the solid residue at temperatures ranging from 290 to 400 °C (main stage II as listed in Table 2), and the carbonation of the residual products over 400 °C. Previous literature also mentions these two main stages in the thermal decomposition process of CNC [16,33,34,40].

The thermal degradation parameters of CNC samples were calculated from the TG and DTG curves which are also listed in Table 2. Compared with the  $T_0$  (at around 300 °C) of pretreated MCC, the  $T_0$  of CNC samples is sharply decreased to about 200 °C. The  $T_{Max}$  of CNC samples in main stage I is much lower than the  $T_{Max}$  of pretreated MCC, while the  $T_{Max}$  of CNC samples in main stage II is slightly higher than that of pretreated MCC. The obvious decrease in the thermal stability of CNC samples is because the sulfate groups introduced on cellulose chains can catalyze the thermal degradation of cellulose [20,34,41]. Furthermore, the high surface area of CNC samples may also play an important role in diminishing their thermal stability due to the increased exposure of the surface area to heat [1,16]. Moreover, the decomposition of CNC samples occurring at lower temperatures may also indicate a faster heat transfer in CNC samples [34,38]. It also can be seen that the amount of char residue in CNC samples is noticeably larger than that of pretreated MCC [34]. Wang et al. explained that CNC particles had a great number of free end chains due to their small particle size, which started decomposition at a lower temperature facilitating the increase in the char yield of CNC [40].

In comparison with the thermal degradation parameters of CNC samples, CNC samples with different thermal stability can be obtained from different pretreatments. The initial weight loss of CNC( $N_S$ -H) is higher than other CNC samples because of more absorbed water and bonded water. At the same time, more bonded water will lead to a significant decrease in its  $T_0$ , which is 198.1 °C. Due to its higher crystallinity, the  $T_0$  of CNC( $N_P$ -H) is 236.3 °C. Meanwhile, the  $T_0$  of CNC( $N_P$ - $D_S$ -H) is lower than that of

CNC(N<sub>p</sub>-D<sub>p</sub>-H): 206.3 and 220.5 °C, respectively. A reasonable explanation is that the amorphous regions are more concentrated in CNC(N<sub>p</sub>-D<sub>p</sub>-H) than in CNC(N<sub>p</sub>-D<sub>s</sub>-H), which is more readily thermally decomposed. In addition, the T<sub>Max</sub> values of CNC samples in main stage I show no significant differences, ranging from 265.8 to 271.2 °C. Interestingly, the T<sub>Max</sub> and WL of all CNC samples in main stage II are basically the same, meaning that the slow charring process of the solid residue at temperatures ranging from 290 to 400 °C has nothing to do with the pretreatment of MCC.

From the above results, it can be concluded that the pretreatment of MCC has a certain influence on the properties of the spherical CNC subsequently obtained by mixed acid hydrolysis. Table 3 shows the pretreatment and hydrolysis processes of preparing spherical CNC by mixed acid hydrolysis in existing works. Among them, cellulose fiber and MCC were usually pretreated in the same way, and the rationality of this was not systematically investigated. Meanwhile, spherical CNC can also be obtained from MCC by acid hydrolysis without any pretreatment, from which can be drawn the same argument as this work—that DMSO swelling is not indispensable for the preparation of spherical CNC by acid hydrolysis. In addition, the mixed acid hydrolysis time of 2 h is sufficient, which can reduce carbonization and energy consumption.

**Table 3.** Spherical CNC (cellulose II) prepared by mixed acid hydrolysis with different pretreatments.

Raw Material	Pretreatment	Form before Hydrolysis	Mixed Acid Hydrolysis	CrI (%)	T <sub>0</sub> (°C)	Particle Size (nm)	Ref.
Cotton fiber	NaOH, 75 °C, 4 h; DMSO, 75 °C, 4 h	Slurry	H <sub>2</sub> SO <sub>4</sub> :HCl = 3:1; 75 °C, Ultrasonic, 8 h	-	-	50	[12]
Cellulose fiber	NaOH, 80 °C, 3 h; DMSO, 80 °C, 3 h	Slurry	H <sub>2</sub> SO <sub>4</sub> :HCl = 3:1; 80 °C, Ultrasonic, 8 h	82.0	-	80	[3]
Cellulose fiber	NaOH, 80 °C, 3 h; DMSO, 80 °C, 3 h	Slurry	H <sub>2</sub> SO <sub>4</sub> :HCl = 3:1; 80 °C, Ultrasonic, 8 h	-	-	5.9–10.9	[25]
MCC	NaOH, 80 °C, 3 h; DMSO, 80 °C, 3 h	Slurry	H <sub>2</sub> SO <sub>4</sub> :HCl = 3:1; 80 °C, Ultrasonic, 8 h	81.3	-	60	[4]
MCC	NaOH, 80 °C, 3 h; DMSO, 80 °C, 3 h	Powder	H <sub>2</sub> SO <sub>4</sub> :HCl = 3:1; 80 °C, Ultrasonic, 2 h	73.4	220.5	10.4	This work
MCC	NaOH, 80 °C, 3 h; DMSO, 80 °C, 3 h	Slurry	H <sub>2</sub> SO <sub>4</sub> :HCl = 3:1; 80 °C, Ultrasonic, 2 h	73.4	206.3	10.1	This work
MCC	NaOH, 80 °C, 3 h	Powder	H <sub>2</sub> SO <sub>4</sub> :HCl = 3:1; 80 °C, Ultrasonic, 2 h	78.3	236.3	11.2	This work
MCC	NaOH, 80 °C, 3 h	Slurry	H <sub>2</sub> SO <sub>4</sub> :HCl = 3:1; 80 °C, Ultrasonic, 2 h	74.1	198.1	9.2	This work

### 3. Materials and Methods

#### 3.1. Materials

MCC with a particle size of 25 µm and sodium hydroxide (NaOH, 96%) were purchased from Macklin Biochemical Co, Ltd. (Shanghai, China). Dimethyl sulfoxide (DMSO, ≥98%) was supplied by Aladdin Biochemical Technology Co., Ltd. (Shanghai, China). Sulfuric acid (H<sub>2</sub>SO<sub>4</sub>, 95–98%) and hydrochloric acid (HCl, 36–38%) were bought from Shuanglin Chemical Reagent Co., Ltd. (Hangzhou, China). All chemicals were used as received.

#### 3.2. Pretreatment of MCC

##### 3.2.1. Alkaline Treatment of MCC

MCC (30 g) was treated with a 5 M NaOH (250 mL) aqueous solution under mechanical stirring at 80 °C for 3 h, then filtered and washed with distilled water until pH < 8. The

slurry form was obtained at a vacuum of 0.06 MPa. Meanwhile, the powder form was obtained after drying at 40 °C for 24 h.

### 3.2.2. Swelling Treatment of Alkaline Treated MCC

The obtained powder of alkaline-treated MCC was immersed into DMSO (250 mL) under mechanical stirring at 80 °C for 3 h, then filtered and washed with distilled water. The slurry form after swelling treatment by DMSO was obtained at a vacuum of 0.06 MPa. Meanwhile, the powder form was obtained after drying at 40 °C for 24 h. The pretreatment routes of MCC are shown by a flow diagram in Figure 7.

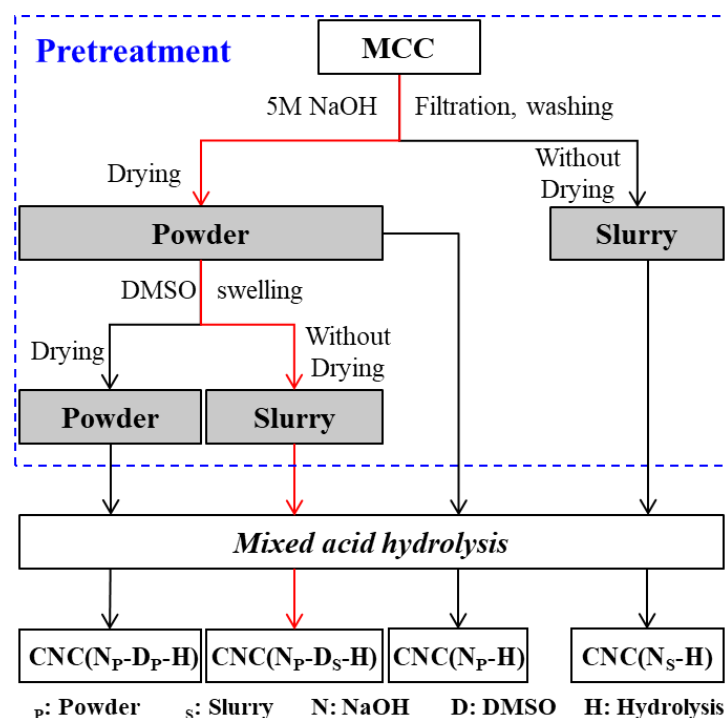


**Figure 7.** Pretreatment routes of MCC and its products after mixed acid hydrolysis (the common method in existing works is marked with red lines).

### 3.3. Mixed Acid Hydrolysis

One quarter of pretreated MCC (slurry form or powder form) was hydrolyzed with mixed acid (250 mL) at 80 °C under mechanical stirring and ultrasonication (40 KHz, 100 W, KQ2200DV, Shumei, China). The mixed acid was prepared by mixing sulfuric acid, hydrochloric acid, and distilled water at a ratio of 3:1:6 (*v/v*). Due to the ultrasonication during spherical CNC preparation, the acid molecules quickly penetrated into the inner amorphous region of the cellulose fibrils. Therefore, the hydrolysis reaction simultaneously occurred at the surface and in the inner amorphous regions of MCC. This caused MCC to first hydrolyze to the sub-micrometer fragments, instead of directly obtaining the CNC. Moreover, because the mixed acid concentration was mild, the dissolving capability of the cellulose fragments was very limited. Thus, the sub-micrometer fragments were further hydrolyzed by the mixed acid to form spherical CNC particles gradually [11,12,39,42].

The hydrolysis time in this work was fixed at 2 h to avoid the carbonization caused by further hydrolysis as shown in Figure S2. After hydrolysis, the suspensions were immediately diluted using an 8 times volume of distilled water to terminate the hydrolysis reaction. Then, the suspensions were centrifuged at 10,000 rpm for 10 min to remove the excessive acid solution and washed with distilled water several times. Finally, the washed CNC was dialyzed using dialysis membranes (MWCO 8000–14,000, 44 mm) against distilled water for three days until the pH was constant. Samples prepared through different routes are recorded as CNC(N<sub>p</sub>-D<sub>p</sub>-H), CNC(N<sub>p</sub>-D<sub>s</sub>-H), (CNC(N<sub>p</sub>-H) and CNC(N<sub>s</sub>-H),

respectively. Among them, the route of preparing CNC(N<sub>p</sub>-D<sub>S</sub>-H) is the common method in existing works as marked with red lines.

### 3.4. Characterization

#### 3.4.1. Fourier Transform Infrared (FTIR) Spectroscopy

MCC or CNC samples were mixed with KBr to produce tablets. FTIR spectra were conducted on a Nicolet 5700 spectrophotometer (MI, USA) in the range of 4000 to 400 cm<sup>-1</sup> at a resolution of 2 cm<sup>-1</sup> over 30 scans.

#### 3.4.2. Morphological Investigation

The morphology of MCC and CNC samples was observed using a field-emission scanning electron microscope (FE-SEM, FEI Quanta FEG 650, Hillsboro, OR, USA). MCC samples were directly laid on the conductive adhesive. The CNC suspensions were diluted to 0.01 wt.% with distilled water, and then dropped on the conductive adhesive and dried at room temperature. Then, these samples were coated with platinum to make them conductive prior to the analysis. The ImageJ software was used to calculate the particle size of CNC samples from the FE-SEM images.

#### 3.4.3. X-ray Diffraction (XRD) Analysis

The XRD spectra of MCC and CNC samples were measured with the X-ray diffractometer (D8 Advance, Bruker, Germany) using Cu-K $\alpha$  radiation ( $\lambda = 0.15418$  nm) at an accelerating voltage of 40 kV and a current of 40 mA.

The data were collected in the range of  $2\theta = 5^\circ$  to  $45^\circ$ . The degree of crystallinity could be relatively expressed by the percentage crystallinity index (CrI, %). The equation used to calculate the CrI was described by Segal et al. [44] in the following form,

$$\text{CrI (\%)} = [(I_{200} - I_{\text{am}})/I_{200}] \times 100 \quad (1)$$

where,  $I_{200}$  is the counter reading at peak intensity at a  $2\theta$  angle close to  $22^\circ$  representing the crystalline part and  $I_{\text{am}}$  is the counter reading at peak intensity at  $2\theta = 18^\circ$  representing the amorphous part in cellulose.

The crystallite size was calculated using the Scherrer equation,

$$D = K\lambda/\beta \cos\theta \quad (2)$$

where,  $D$  is the "apparent crystallite size",  $\beta$  is the full width of the diffraction peak measured at half maximum height (FWHM) by Lorentz function, and the constant  $K$  is equal to 0.94 [45].

#### 3.4.4. Thermal Analysis

Thermogravimetry (TG) and derivative thermogravimetry (DTG) curves of MCC and CNC samples were obtained using a Netzsch TG209 F3 instrument (Bavaria, Germany) over a temperature range of 30 °C to 800 °C at a heating rate of 10 °C/min under nitrogen supply.

## 4. Conclusions

In this study, spherical CNC samples with an average size of around 10 nm were successfully prepared by mixed acid hydrolysis from commercial MCC with different pretreatment routes. The physicochemical properties of spherical CNC were evaluated by FT-IR, FE-SEM, XRD, and TG. The characterization results revealed that an additional swelling process is not indispensable for the preparation of spherical CNC from MCC by mixed acid hydrolysis. Spherical CNC can also be readily obtained from alkaline-treated MCC without any other pretreatment. Furthermore, the form of pretreated MCC before acid hydrolysis (slurry or powder form) also has a certain influence on the morphology, crystallinity, and thermal stability of spherical CNC. This comparative study provides

support for further studies in selecting pretreatment processes of MCC to economically prepare desired spherical CNC with a high repeatability.

**Supplementary Materials:** The supporting information can be downloaded at: <https://www.mdpi.com/article/10.3390/ijms231810764/s1>.

**Author Contributions:** P.Z.: conceptualization, investigation, formal analysis, writing—original draft; L.F., Z.D. and X.B.: writing—original draft, data curation. All authors have read and agreed to the published version of the manuscript.

**Funding:** This work was financially supported by the Key Research and Development Program of Zhejiang Province: 2020C01234.

**Data Availability Statement:** Not applicable.

**Acknowledgments:** We would like to thank Danling Wang and Daye Huang from Zhongce Rubber Group Co., Ltd. for their guidance on this work.

**Conflicts of Interest:** The authors declare no conflict of interest.

## References

1. Xu, J.T.; Chen, X.Q. Preparation and characterization of spherical cellulose nanocrystals with high purity by the composite enzymolysis of pulp fibers. *Bioresource Technol.* **2019**, *291*, 121842. [CrossRef] [PubMed]
2. Ahmed-Haras, M.R.; Kao, N.; Ward, L. Single-step heterogeneous catalysis production of highly monodisperse spherical nanocrystalline cellulose. *Int. J. Biol. Macromol.* **2020**, *154*, 246–255. [CrossRef] [PubMed]
3. Zhang, J.; Elder, T.J.; Pu, Y.; Ragauskas, A.J. Facile synthesis of spherical cellulose nanoparticles. *Carbohydr. Polym.* **2007**, *69*, 607–611. [CrossRef]
4. Dong, H.; Ding, Q.; Jiang, Y.; Li, X.; Han, W. Pickering emulsions stabilized by spherical cellulose nanocrystals. *Carbohydr. Polym.* **2021**, *265*, 118101. [CrossRef]
5. Xu, J.T.; Chen, X.Q.; Shen, W.H.; Li, Z. Spherical vs. rod-like cellulose nanocrystals from enzymolysis: A comparative study as reinforcing agents on polyvinyl alcohol. *Carbohydr. Polym.* **2021**, *256*, 117493. [CrossRef]
6. Liu, S.; Qamar, S.A.; Qamar, M.; Basharat, K.; Bilal, M. Engineered nanocellulose-based hydrogels for smart drug delivery applications. *Int. J. Biol. Macromol.* **2021**, *181*, 275–290. [CrossRef] [PubMed]
7. Zhang, W.; Zhang, Y.; Cao, J.; Jiang, W. Improving the performance of edible food packaging films by using nanocellulose as an additive. *Int. J. Biol. Macromol.* **2020**, *166*, 288–296. [CrossRef]
8. Yadav, C.; Saini, A.; Zhang, W.B.; You, X.Y.; Chauhan, I.; Mohanty, P.; Li, X.P. Plant-based nanocellulose: A review of routine and recent preparation methods with current progress in its application as rheology modifier and 3D bioprinting. *Int. J. Biol. Macromol.* **2021**, *166*, 1586–1616. [CrossRef]
9. Chen, R.; Ma, Z.H.; Sun, D.Y.; Wang, X.; Han, Y. Cellulose I nanocrystals (CNCs I) prepared in mildly acidic lithium bromide trihydrate (MALBTH) and their application for stabilizing Pickering emulsions. *Int. J. Biol. Macromol.* **2022**, *201*, 59–66. [CrossRef]
10. Zhang, W.; Yang, G.; Deng, F.J.; Liang, J.; Huang, Q.; Dou, J.B.; Liu, M.Y.; Cao, Q.Y.; Zhang, X.Y.; Wei, Y. Direct grafting of cellulose nanocrystals with poly(ionic liquids) via Gamma-ray irradiation and their utilization for adsorptive removal of CR. *Int. J. Biol. Macromol.* **2022**, *194*, 1029–1037. [CrossRef]
11. Pandi, N.; Sonawane, S.H.; Anand Kishore, K. Synthesis of cellulose nanocrystals (CNCs) from cotton using ultrasound-assisted acid hydrolysis. *Ultrason. Sonochem.* **2021**, *70*, 105353. [CrossRef]
12. Li, X.F.; Ding, E.Y.; Li, G.K. A method of preparing spherical nano-crystal cellulose with mixed crystalline forms of cellulose I and II. *Chin. J. Polym. Sci.* **2001**, *19*, 291–296.
13. Lu, F.F.; Yu, H.Y.; Yan, C.F.; Yao, J.M. Polylactic acid nanocomposite films with spherical nanocelluloses as efficient nucleation agents: Effects on crystallization, mechanical and thermal properties. *RSC Adv.* **2016**, *6*, 46008–46018. [CrossRef]
14. Yu, H.Y.; Zhang, H.; Abdalkarim, S.Y.H.; Yang, L.; Zhu, J.; Gu, J.; Yao, J. Interfacial compatible poly (ethylene glycol) chains modified cellulose nanosphere as bifunctional reinforcements in green polylactic acid for food packagings. *J. Taiwan Inst. Chem.* **2019**, *95*, 583–593. [CrossRef]
15. Yan, C.F.; Yu, H.Y.; Yao, J.M. One-step extraction and functionalization of cellulose nanospheres from Lyocell fibers with cellulose II crystal structure. *Cellulose* **2015**, *22*, 3773–3788. [CrossRef]
16. Meyabadi, T.F.; Dadashian, F.; Sadeghi, G.M.M.; Asl, H.E.Z. Spherical cellulose nanoparticles preparation from waste cotton using a green method. *Powder Technol.* **2014**, *261*, 232–240. [CrossRef]
17. Beaumont, M.; Nypelö, T.; König, J.; Zirbs, R.; Opietnik, M.; Potthast, A.; Rosenau, T. Synthesis of redispersible spherical cellulose II nanoparticles decorated with carboxylate groups. *Green Chem.* **2016**, *18*, 1465–1468. [CrossRef]
18. Chen, X.Q.; Deng, X.Y.; Shen, W.H.; Jia, M.Y. Preparation and characterization of the spherical nanosized cellulose by the enzymatic hydrolysis of pulp fibers. *Carbohydr. Polym.* **2018**, *181*, 879–884. [CrossRef]

19. Lam, N.T.; Saewong, W.; Sukyai, P. Effect of varying hydrolysis time on extraction of spherical bacterial cellulose nanocrystals as a reinforcing agent for poly(vinyl alcohol) composites. *J. Polym. Res.* **2017**, *24*, 71. [CrossRef]
20. Cheng, M.; Qin, Z.Y.; Liu, Y.N.; Qin, Y.F.; Li, T.; Chen, L.; Zhu, M.F. Efficient extraction of carboxylated spherical cellulose nanocrystals with narrow distribution through hydrolysis of Lyocell fibers by using ammonium persulfate as an oxidant. *J. Mater. Chem. A* **2014**, *2*, 251–258. [CrossRef]
21. Azrina, Z.A.Z.; Beg, M.D.H.; Rosli, M.Y.; Ramlib, R.; Junadi, N.; Alam, A.K.M.M. Spherical nanocrystalline cellulose (NCC) from oil palm empty fruitbunch pulp via ultrasound assisted hydrolysis. *Carbohydr. Polym.* **2017**, *162*, 115–120. [CrossRef] [PubMed]
22. Purkait, B.S.; Ray, D.; Sengupta, S.; Kar, T.; Mohanty, A.; Misra, M. Isolation of cellulose nanoparticles from sesame husk. *Ind. Eng. Chem. Res.* **2011**, *50*, 871–876. [CrossRef]
23. Evdokimova, O.L.; Svensson, F.G.; Agafonov, A.V.; Håkansson, S.; Seisenbaeva, G.A.; Kessler, V.G. Hybrid drug delivery patches based on spherical cellulose nanocrystals and colloid titania-synthesis and antibacterial properties. *Nanomaterials* **2018**, *8*, 228. [CrossRef] [PubMed]
24. Liu, B.; Li, T.; Wang, W.Y.; Sagis, L.M.C.; Yuan, Q.P.; Lei, X.G.; Stuart, M.A.C.; Li, D.; Bao, C.; Bai, J.; et al. Corn cob cellulose nanosphere as an eco-friendly detergent. *Nat. Sustain.* **2020**, *3*, 448–458. [CrossRef]
25. Ibrahim, M.M.; El-Zawawy, W.K.; Nassar, M.A. Synthesis and characterization of polyvinyl alcohol/nanospherical cellulose particle films. *Carbohydr. Polym.* **2010**, *79*, 694–699. [CrossRef]
26. Bai, H.J.; Chen, J.H.; Zhou, X.Y.; Hu, C.Z. Single and binary adsorption of dyes from aqueous solutions using functionalized microcrystalline cellulose from cotton fiber. *Korean J. Chem. Eng.* **2020**, *37*, 1926–1932. [CrossRef]
27. Anju, T.R.; Ramamurthy, K.; Dhamodharan, R. Surface modified microcrystalline cellulose from cotton as a potential mineral admixture in cement mortar composite. *Cement Concrete Comp.* **2016**, *74*, 147–153. [CrossRef]
28. Shi, S.; Zhang, M.L.; Ling, C.; Hou, W.S.; Yan, Z.F. Extraction and characterization of microcrystalline cellulose from waste cotton fabrics via hydrothermal method. *Waste Manag.* **2018**, *82*, 139–146. [CrossRef]
29. Hou, W.S.; Ling, C.; Shi, S.; Yan, Z.F. Preparation and characterization of microcrystalline cellulose from waste cotton fabrics by using phosphotungstic acid. *Int. J. Biol. Macromol.* **2019**, *123*, 363–368. [CrossRef]
30. Sun, X.W.; Lu, C.H.; Liu, Y.; Zhang, W.; Zhang, X.X. Melt-processed poly(vinyl alcohol) composites filled with microcrystalline cellulose from waste cotton fabrics. *Carbohydr. Polym.* **2014**, *101*, 642–649. [CrossRef]
31. Rashid, M.; Gafur, M.A.; Sharafat, M.K.; Minami, H.; Miah, M.A.J.; Ahmad, H. Biocompatible microcrystalline cellulose particles from cotton wool and magnetization via a simple in situ co-precipitation method. *Carbohydr. Polym.* **2017**, *170*, 72–79. [CrossRef]
32. Oh, S.Y.; Dong, I.Y.; Shin, Y.; Hwan, C.K.; Hak, Y.K.; Yong, S.C.; Won, H.P.; Ji, H.Y. Crystalline structure analysis of cellulose treated with sodium hydroxide and carbon dioxide by means of X-ray diffraction and FTIR spectroscopy. *Carbohydr. Res.* **2005**, *340*, 2376–2391. [CrossRef]
33. Ayouch, I.; Barrak, I.; Kassem, I.; Kassab, Z.; Draoui, K.; Achaby, M.E. Ultrasonic-mediated production of carboxylated cellulose nanospheres. *J. Environ. Chem. Eng.* **2021**, *9*, 106302. [CrossRef]
34. Lu, P.; Hsieh, Y.L. Preparation and properties of cellulose nanocrystals: Rods, spheres, and network. *Carbohydr. Polym.* **2010**, *82*, 329–336. [CrossRef]
35. Carrillo, F.; Colom, X.; Suñol, J.J.; Saurina, J. Structural FTIR analysis and thermal characterisation of Lyocell and viscose-type fibres. *Eur. Polym. J.* **2004**, *40*, 2229–2234. [CrossRef]
36. Wang, W.; Liang, T.; Bai, H.Y.; Dong, W.F.; Liu, X.Y. All cellulose composites based on cellulose diacetate and nanofibrillated cellulose prepared by alkali treatment. *Carbohydr. Polym.* **2018**, *179*, 297–304. [CrossRef]
37. Schwanninger, M.; Rodrigues, J.C.; Pereira, H.; Hinterstoisser, B. Effects of short-time vibratory ball milling on the shape of FT-IR spectra of wood and cellulose. *Vib. Spectrosc.* **2004**, *36*, 23–40. [CrossRef]
38. Ren, R.W.; Chen, X.Q.; Shen, W.H. Preparation and separation of pure spherical cellulose nanocrystals from microcrystalline cellulose by complex enzymatic hydrolysis. *Int. J. Biol. Macromol.* **2022**, *202*, 1–10. [CrossRef]
39. Guo, J.; Guo, X.X.; Wang, S.Q.; Yin, Y.F. Effects of ultrasonic treatment during acid hydrolysis on the yield, particle size and structure of cellulose nanocrystals. *Carbohydr. Polym.* **2016**, *135*, 248–255. [CrossRef]
40. Wang, N.; Ding, E.Y.; Cheng, R.S. Thermal degradation behaviors of spherical cellulose nanocrystals with sulfate groups. *Polymer* **2007**, *48*, 3486–3493. [CrossRef]
41. Xiong, R.; Zhang, X.X.; Tian, D.; Zhou, Z.H.; Lu, C.H. Comparing microcrystalline with spherical nanocrystalline cellulose from waste cotton fabrics. *Cellulose* **2012**, *19*, 1189–1198. [CrossRef]
42. Wang, N.; Ding, E.Y.; Cheng, R.S. Preparation and liquid crystalline properties of spherical cellulose nanocrystals. *Langmuir* **2008**, *24*, 5–8. [CrossRef] [PubMed]
43. Lourdin, D.; Peixinho, J.; Bréard, J.; Cathala, B.; Leroy, E.; Duchemin, B. Concentration driven cocrystallisation and percolation in all-cellulose nanocomposites. *Cellulose* **2016**, *23*, 529–543. [CrossRef]
44. Segal, L.; Creely, J.J.; Martin, A.E.; Comrad, C.M., Jr. An empirical method for estimating the degree of crystallinity of native cellulose using the X-ray diffractometer. *Text. Res. J.* **1959**, *29*, 786–794. [CrossRef]
45. Revol, J.F.; Dietrich, A.; Goring, D.A.I. Effect of mercerization on the crystallite size and crystallinity index in cellulose from different sources. *Can. J. Chem.* **1987**, *65*, 1724–1725. [CrossRef]





Review

# Latest Advances in Metasurfaces for SERS and SEIRA Sensors as Well as Photocatalysis

Grégory Barbillon

EPF-Ecole d'Ingénieurs, 55 Avenue du Président Wilson, 94230 Cachan, France; gregory.barbillon@epf.fr

**Abstract:** Metasurfaces can enable the confinement of electromagnetic fields on huge surfaces and zones, and they can thus be applied to biochemical sensing by using surface-enhanced Raman scattering (SERS) and surface-enhanced infrared absorption (SEIRA). Indeed, these metasurfaces have been examined for SERS and SEIRA sensing thanks to the presence of a wide density of hotspots and confined optical modes within their structures. Moreover, some metasurfaces allow an accurate enhancement of the excitation and emission processes for the SERS effect by supporting resonances at frequencies of these processes. Finally, the metasurfaces allow the enhancement of the absorption capacity of the solar light and the generation of a great number of catalytic active sites in order to more quickly produce the surface reactions. Here, we outline the latest advances in metasurfaces for SERS and SEIRA sensors as well as photocatalysis.

**Keywords:** metasurfaces; SERS; SEIRA; photocatalysis; plasmonics; sensors

**Citation:** Barbillon, G. Latest Advances in Metasurfaces for SERS and SEIRA Sensors as Well as Photocatalysis. *Int. J. Mol. Sci.* **2022**, *23*, 10592. <https://doi.org/10.3390/ijms231810592>

Academic Editor: Raghvendra Singh Yadav

Received: 28 August 2022

Accepted: 12 September 2022

Published: 13 September 2022

**Publisher's Note:** MDPI stays neutral with regard to jurisdictional claims in published maps and institutional affiliations.



**Copyright:** © 2022 by the author. Licensee MDPI, Basel, Switzerland. This article is an open access article distributed under the terms and conditions of the Creative Commons Attribution (CC BY) license (<https://creativecommons.org/licenses/by/4.0/>).

## 1. Introduction

During the last two decades, the using of metasurfaces has increased significantly with applications in various domains such as light nanosources [1,2], quantum devices [3,4], photovoltaics [5–7], photodetectors [8–10], planar optics [11–13], holography [14–16], lenses [17–19], an optical cloak [20–23], far-field thermal emission [24–27], near-field radiative energy transfer [28–31], second and third harmonic generation [32–35], refractive index sensing [36], surface-enhanced infrared absorption (SEIRA) [37–41], surface-enhanced Raman scattering (SERS) [42–46] and photocatalysis [47–50]. The metasurfaces are generally constituted of nanoresonators (building blocks) named meta-atoms whose dimensions are smaller than the incident light wavelength. Indeed, these blocks of meta-atoms can be periodically organized to realize an one-dimensional chain, a two-dimensional metasurface and a three-dimensional metamaterial. Their properties derive not from those of the materials of natural origin but come from their artificial nanostructuration, which can be controlled by adjusting their geometric parameters (organization, shape and size) [51,52]. Thus, myriad applications are workable compared to naturally arising materials. Metasurfaces have several key advantages such as the confinement of electromagnetic fields on huge surfaces, greater absorption compared to conventional materials under their bulk form, a spatially localized absorption, a tunable light absorption on a whole solar spectrum and a focusing of densities of charge-carriers in the vicinity of active reaction locations. Moreover, metasurfaces can operate like open cavity structures where light is confined by structuring the building blocks of meta-atoms [53,54]. In addition, the metasurfaces mainly used in the literature can be classified into two groups—the first one being dielectric metasurfaces and the second one being plasmonic metasurfaces. The dielectric metasurfaces are based on the Mie resonances of dielectric nanostructures which have a high refractive index [55–57] and for the plasmonic metasurfaces on surface plasmon resonances of metallic nanostructures [53,58,59].

In this review paper, the aim was to introduce the latest advances (2019–2022) in metasurfaces for sensing by surface-enhanced spectroscopies and for photocatalysis. In

addition, several review papers on metasurfaces already exist in the scientific literature but with different focus points [11–13,51,53,54]. Here, we will concentrate on the metasurfaces for SERS sensors, then for SEIRA sensors, and lastly for photocatalysis.

## 2. Metasurfaces for Surface-Enhanced Raman Scattering Sensors

In this first part, the latest advances in metasurfaces for surface-enhanced Raman scattering (SERS) are introduced (see Table 1). For SERS sensors, the plasmonic or dielectric metasurfaces enable one to confine local electromagnetic fields in the vicinity of optical antennas resonating in a large spectral range matching with the excitation or Raman emission wavelengths or both, on huge domains. The SERS signal can be improved with an enhancement factor (EF) of  $|E|^4/|E_0|^4$ .

**Table 1.** Unit cell of metasurfaces, detected molecules and the enhancement factor (EF) for surface-enhanced Raman scattering sensors (4-mPBA = 4-mercaptoPhenylBoronic Acid; AuNPHs = gold NanoPolyHedrons; 4-ATP = 4-AminoThiophenol; 4-MBA = 4-MercaptoBenzoic Acid; HAV = Hepatitis A Virus; ZnO = Zinc Oxide; MIM NS = Metal-Insulator-Metal NanoStructures; Al<sub>2</sub>O<sub>3</sub> = Alumina; MG = Malachite Green; PS = PolyStyrene; CV = Crystal Violet).

Unit Cell of Metasurfaces	Detected Molecules	EF	References
One Ag nanohole	4-mPBA	–	[60]
Six AuNPHs	4-ATP	$1.7 \times 10^6$	[61]
Three Au pyramidal nanoholes	4-MBA, HAV	$5 \times 10^6$ – $6 \times 10^6$	[62]
Three Au triangular nanocavities	4-MBA, Shiga Toxins	$9 \times 10^7$	[63]
One Ag cellulose disk-hole matrix	1,4-benzenedithiol	–	[64]
Seven vertical Au/ZnO nanorods	Rhodamine 6G	$2 \times 10^4$	[65]
Quasi-(dis)ordered MIM NS	Human tear uric acid	$10^6$ – $5 \times 10^6$	[66]
Seven Au nanoholes	Benzenethiol	$10^6$	[67]
Truncated Au/Al <sub>2</sub> O <sub>3</sub> cones	4-ATP	$10^6$	[68]
Au nanoparticle assembly	4-MBA	$10^5$	[69]
Au/Ag microcracks	MG	–	[70]
Ag-coated PS microspheres	Rhodamine 6G	$10^8$	[71]
Ag aggregates on one Ag NP	Rhodamine 6G	$4 \times 10^7$ – $9 \times 10^7$	[72]
Ag nanocube superlattice	CV, drugs	$10^7$	[73]
Seven ring-shaped nanogaps	Rhodamine 6G	$3 \times 10^8$	[74]
Seven Au nanospheres	Benzenethiol	$10^4$ – $10^5$	[75]
Seven Au chiral nanogaps	L/D-cysteine	–	[76]
Au nanogrooves	Graphene	–	[77]
Au-coated silica nanoflowers	Benzoic acid	$10^6$	[78]

Sarychev et al. related the use of a metal-dielectric metasurface for the SERS detection of molecules of 4-mercaptophenylboronic acid (4-mPBA). This metasurface was constituted of a modulated dielectric coated by a silver layer, permitting the matching of plasmonic resonances to the excitation wavelength (785 nm) [60]. Chen et al. demonstrated a SERS detection of 4-aminothiophenol (4-ATP) molecules via a plasmonic metasurface consisting of a superlattice sheet of gold nanopolyhedrons (AuNPHs). An EF of  $1.7 \times 10^6$  was achieved thanks to the matching of the plasmonic resonance of this superlattice sheet of AuNPHs with the excitation wavelength of 633 nm, whose associated electric fields were strongly confined and induced by powerful interparticle coupling [61]. The group of Petti demonstrated the SERS detection of the hepatitis A virus (HAV) and 4-mercaptobenzoic acid (4-MBA) molecules by employing a metasurface constituted of gold inverted nanopyramids. An EF comprised between  $5 \times 10^6$  and  $6 \times 10^6$  was reached. This enhancement owed to a significant peak in absorbance (plasmonic resonance) near the excitation wavelength (532 nm) [62]. In addition, this same group reported the SERS detection of Shiga toxins by using a metasurface composed of gold octupolar nanostructures. The authors obtained an EF of  $9 \times 10^7$  due to the presence of a plasmonic double resonance in the visible and near-infrared regions, one of which had a plasmonic resonance close to the excitation

wavelength (785 nm) used for SERS measurements [63]. Caligiuri et al. introduced the SERS detection of 1,4-benzenedithiol molecules via a plasmonic metasurface consisting of a square array of cellulose nanoholes covered by a thin layer of silver. The authors attained an enhancement factor of 6 for the SERS signal from the metasurface compared to a flat silver film. This increase in the SERS signal was due to the overlapping of the plasmonic mode corresponding to the low-energy bonding optical mode with the excitation wavelength of 785 nm [64].

Additionally, Gabinet and Osuji showed a SERS detection of rhodamine 6G (R6G) molecules through a plasmonic metasurface (see Figure 1a,b) consisting of an array of zinc oxide (ZnO) vertical nanorods (NRs) coated with a gold layer. An EF of  $2 \times 10^4$  was reached by a dint of the overlapping of a plasmonic resonance of this Au/ZnO NR array with the excitation wavelength (532 nm employed for SERS measurements, see Figure 1c), and the spatial localization (vicinity of Au/ZnO NR tops, see inset of Figure 1c) of the electric field [65]. In another way, Narasimhan et al. realized a flexible metasurface composed of a quasi-(dis)ordered group of Au nanodisks on nanoholes isolated by a silicon dioxide nanogap (in a metal–insulator–metal arrangement) for the SERS detection of human tear uric acid (UA). Enhancement factors comprised between  $10^6$  and  $5 \times 10^6$  were achieved due to the broadband plasmonic resonance overlapping with the excitation wavelength as well as the emission wavelengths of some Raman peaks [66]. Yang et al. have fabricated a metasurface constituted of Au nanoholes hexagonally arranged on a SiO<sub>2</sub> film itself deposited on a gold mirror for the SERS detection of benzenethiol molecules. The authors demonstrated by adjusting the structure parameters that a very strong absorption and a significant enhancement of electric near-fields at the wavelength used for SERS measurements were reached, thus allowing to obtain an EF of  $10^6$  [67]. Zhao et al. employed a metasurface consisting of hyperbolic metaparticles composed of five gold layers isolated by alumina (Al<sub>2</sub>O<sub>3</sub>) layers for the SERS sensing of 4-ATP molecules. The dimensions of these hyperbolic metaparticles were tuned to obtain a scattering resonance at 785 nm, thus overlapping with the excitation wavelength employed for Raman measurements, resulting in an EF of  $10^6$  [68]. Furthermore, Ma et al. created an electro-tunable plasmonic metasurface for the SERS detection of 4-mercaptobenzoic acid (4-MBA) molecules. This metasurface consisted of Au nanoparticle arrays deposited on titanium nitride (TiN)/Ag substrate (electrode).

The authors observed an EF of  $10^5$  for a potential of 0.7 V versus potential of zero charge (PZC) where the gold nanoparticles were densely assembled (see Figure 2a,b). This EF was due to a stronger plasmonic coupling between gold nanoparticles (NPs) and the redshift of plasmonic resonance towards the excitation wavelength (633 nm; see the red curve in Figure 2c) upon the densification of these gold NPs when a potential of 0.7 V vs. PZC was applied [69]. In another way, Kovalets et al. have created a metasurface by metallic deposition (thermal sputtering of gold or silver) on track-etched membranes, then stretched leading the generation of microcracks in the metal layer for SERS sensing of malachite green (MG) molecules. The authors have noted that the number of microcracks increased when the deformation (stretching) of samples increased, thus inducing an increase in the SERS signal of MG molecules. This increase in the SERS signal is owed to the increase in the number of hotspots (zones of strong electric fields) at the level of microcracks [70]. Nguyen et al. studied the SERS sensing of R6G molecules via a metasurface consisting of a monolayer of polystyrene (NS) nanospheres coated by a thin layer of silver deposited on silver mirror. An EF of  $10^8$  was achieved thanks to the matching of the broadband plasmonic resonance of the metasurface with the excitation wavelength as well as the emission wavelengths of Raman bands of R6G molecules [71]. Zhang's group realized a broadband SERS substrate for the detection of R6G molecules consisting of a plasmonic metasurface composed of large silver (Ag) nanoparticles on which small aggregates of silver were obliquely deposited. Enhancement factors from  $4 \times 10^7$  to  $9 \times 10^7$  were achieved due to the matching of the broadband plasmonic resonance of the metasurface with the three excitation wavelengths using Raman measurements [72]. Wang et al. investigated

a plasmonic metasurface composed of Ag nanocube (NC) arrays with an average gap between NCs of 1 nm for the detection of crystal violet (CV) molecules and several drugs such as lidocaine and methotrexate. An EF of  $10^7$  was obtained, and this was due to the strong electric fields located in the nanogaps between Ag NCs at the excitation wavelength used for Raman experiments [73]. To finish this section dedicated to the metasurfaces for SERS sensors, the last three works concern studies based on metasurfaces using metallic nanogaps. For the first example, Luo et al. fabricated a plasmonic metasurface composed of ring-shaped nanogap arrays realized in gold film for the SERS sensing of R6G molecules. The authors obtained an EF of  $3 \times 10^8$  owing to the matching of the broad plasmonic resonance with the excitation wavelength for SERS measurements, and regions of strong electric fields located in the gap zone [74].

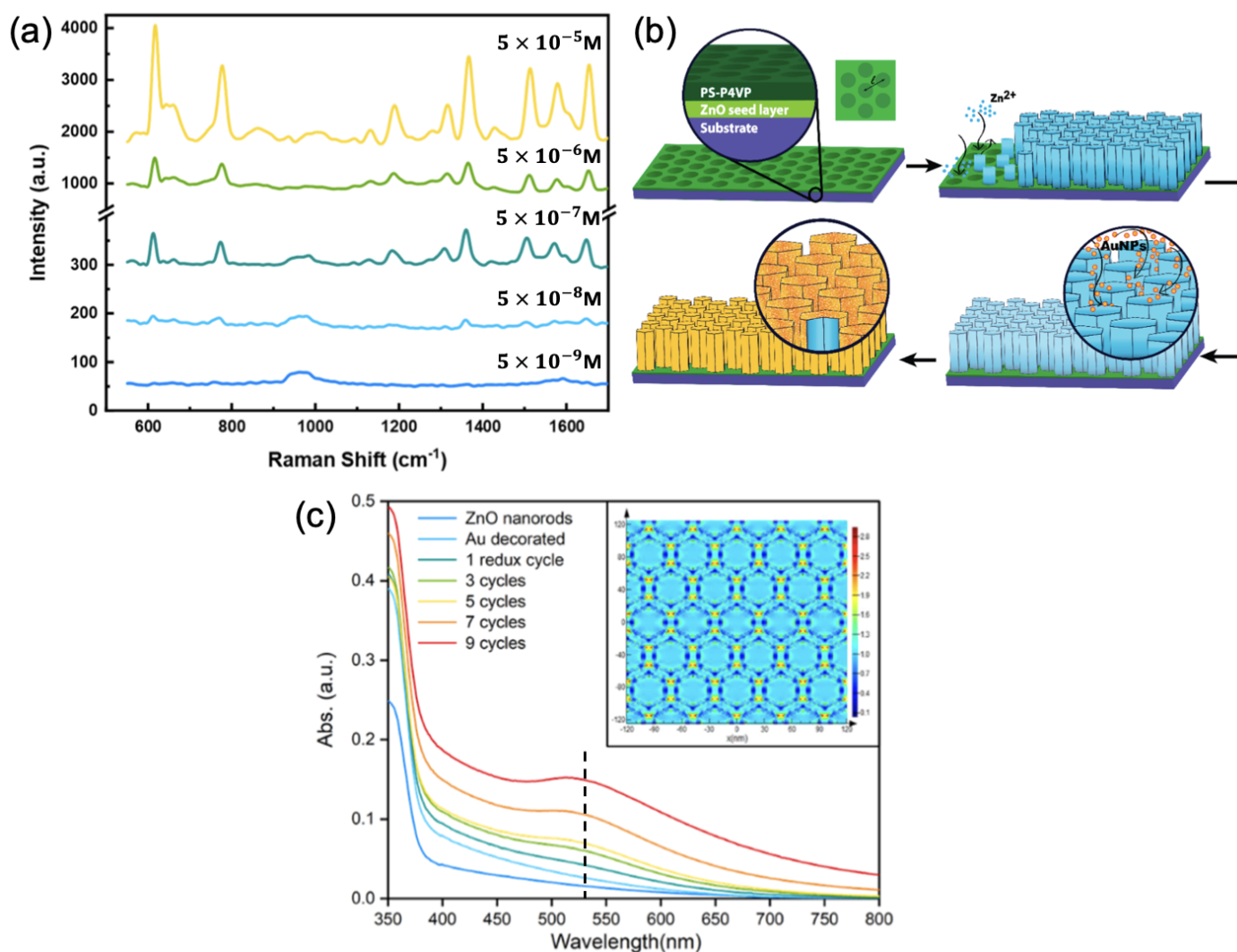


**Figure 1.** (a) SERS spectra of R6G molecules on the plasmonic metasurface for different R6G concentrations; (b) illustration of the fabrication process of the plasmonic metasurface composed of gold-coated ZnO nanorods; and (c) absorbance spectra of the plasmonic metasurface at different reduction cycles. The black dashed line corresponds to the excitation wavelength for SERS measurements. Inset displays the electric field mapping in the Au/ZnO nanorod array. All the figures are reprinted (adapted) with permission from [65], Copyright 2021 American Chemical Society.

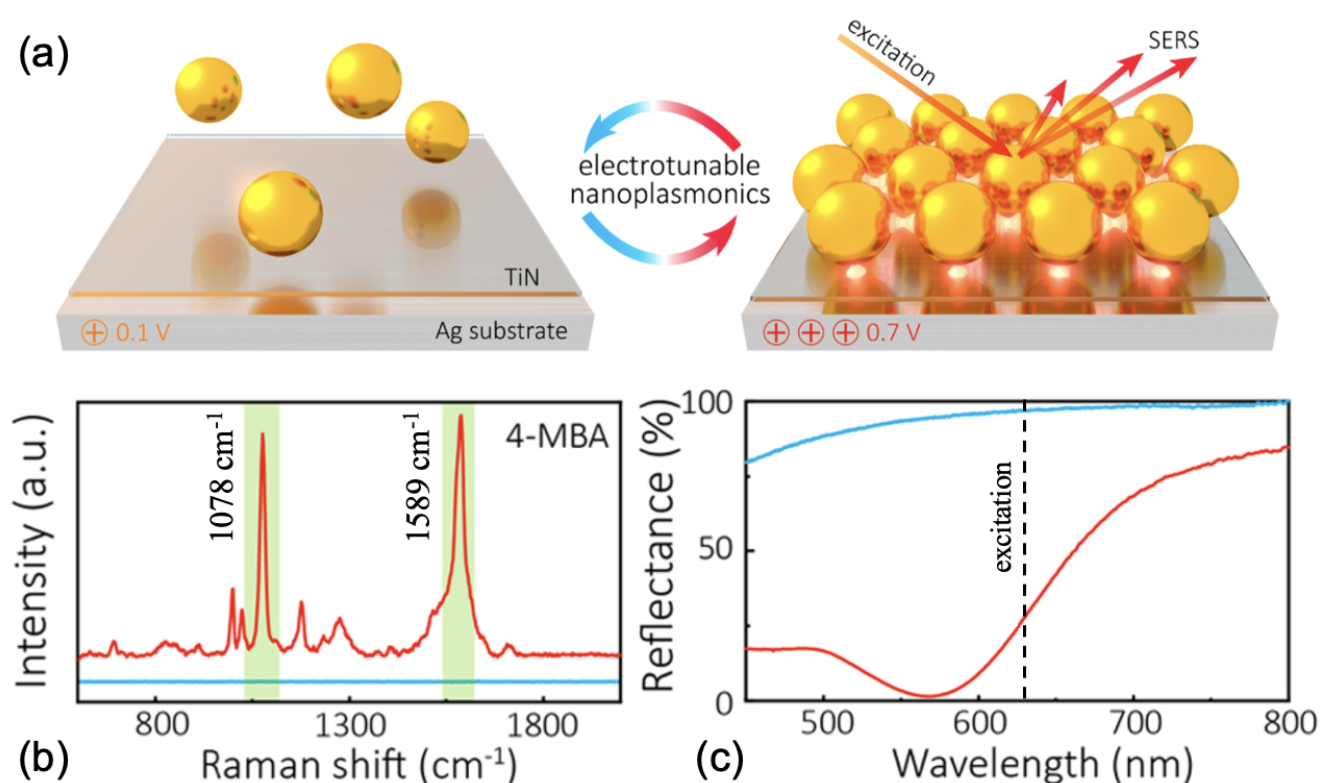


**Figure 2.** (a) Illustration of the electro-tunable plasmonic metasurface composed of gold nanoparticles assembled on TiN/Ag substrate at 0.1 V vs. PZC (at left) and 0.7 V vs. PZC (at right). (b) SERS spectra of 4-MBA adsorbed on the metasurface at 0.1 V vs. PZC (blue color) and 0.7 V vs. PZC (red color). (c) Reflectance spectra of the plasmonic metasurface at 0.1 V vs. PZC (blue color) and 0.7 V vs. PZC (red color). The dashed black line corresponds to the excitation wavelength used for SERS measurements. All the figures are reprinted (adapted) with permission from [69], Copyright 2020 American Chemical Society.

Then, Bauman et al. reported the SERS detection of benzenethiol molecules through a plasmonic metasurface composed of gold nanospheres (AuNS) with a tunable gap between AuNS (see Figure 3a,b). EFs from  $10^4$  to  $10^5$  were obtained thanks to the overlapping of the excitation wavelength and the wavelength of the absorbance peak of the metasurface as well as to strong electric fields obtained in the nanogaps at the excitation wavelength (see Figure 3c), for an optimal gap width of 0.55 nm [75]. Zhang et al. related the fabrication of a plasmonic metasurface consisting of an array of chiral nanogaps for the selective SERS detection of the L-cysteine and D-cysteine molecules. The authors showed that chiral nanogaps with a gap size of 5 nm were optimal for this SERS detection because their circular dichroism activity and g-factor were more important. These L-chiral nanogaps allowed obtaining the SERS spectrum of L-cysteine with more intense peaks than for the D-cysteine, and the R-chiral nanogaps allowed obtaining the SERS spectrum of D-cysteine with more intense peaks than for the L-cysteine [76]. In addition, Thareja et al. reported the use of anisotropic plasmonic metasurface composed of an array of the parallel nanogrooves fabricated into a gold film for the SERS detection of characteristic Raman peaks (G and 2D) of graphene. The SERS intensities of G and 2D Raman peaks for graphene were improved of a factor of 25–50. This enhancement of the SERS signal was owing to the excitation of propagating gap plasmons in the nanogrooves generating stronger electric fields in controlled directions [77]. To finish this first part, Jiang et al. fabricated a plasmonic metasurface composed of an array of Au-coated silica nanoflowers for the SERS sensing of benzoic acid molecules. An EF of  $10^6$  was reached and this was due to the significant electric fields located in the gaps between nanopetals generated by the near-field coupling between these same nanopetals [78].

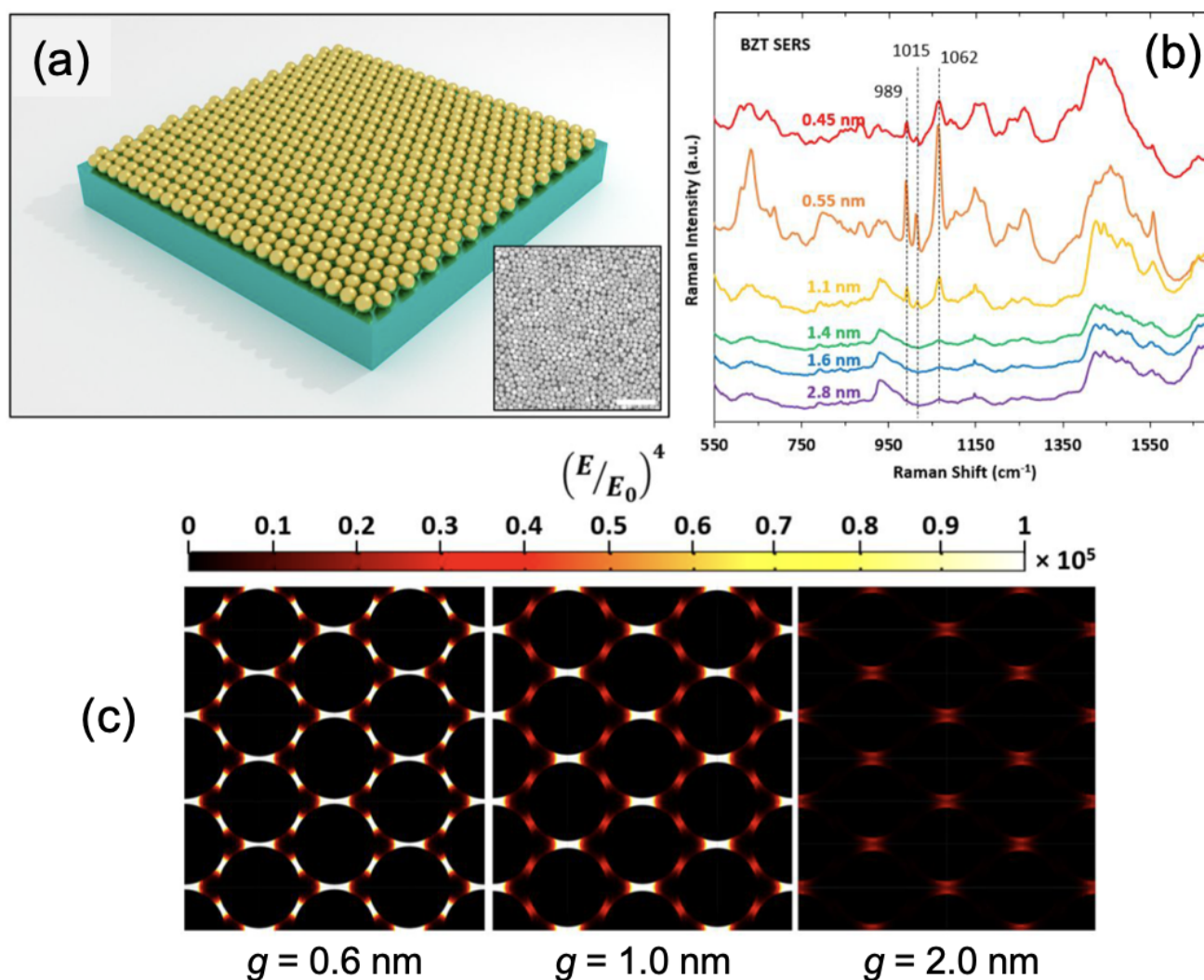


**Figure 3.** (a) Illustration of the plasmonic metasurface composed of gold nanospheres self-assembled on silicon substrate. Inset corresponds to a TEM picture of the plasmonic metasurface with gaps of 0.55 nm (white bar = 100 nm) (b) SERS spectra of benzenethiol adsorbed on the metasurface with different values of nanogap. (c) Mappings of the electric field enhancement for three values of nanogap ( $g = 0.6$  nm, 1.0 nm and 2.0 nm). All the figures are reprinted (adapted) with permission from [75], Copyright 2022 American Chemical Society.

### 3. Metasurfaces for Surface-Enhanced Infrared Absorption Sensors

In this part, we present the latest advances in metasurfaces for surface-enhanced infrared absorption (SEIRA) (see Table 2). For this application, the plasmonic or dielectric metasurfaces allow the improvement of the infrared absorption of molecules by the confinement of local electromagnetic fields in the vicinity of optical antennas resonating in the mid-infrared (mid-IR) domain on vast areas. The SEIRA signal will increase with an enhancement factor (EF) of  $|E|^2/|E_0|^2$ , when the frequency matching between plasmonic or dielectric nanostructures and molecular vibration modes occurs.

**Table 2.** Unit cell of metasurfaces, detected molecules and the enhancement factor (EF) for surface-enhanced infrared absorption sensors (ssDNA = single-stranded DNA; ODAM = human odontogenic ameloblast-associated protein; a-Si:H = anisotropic hydrogenated amorphous silicon; 4H-SiC = 4H-silicium carbide; h-BN = hexagonal boron nitride; CBP = 4,4'-bis(N-carbazolyl)-1,1'-biphenyl).

Unit Cell of Metasurfaces	Detected Molecules	EF	References
Two germanium ellipses	Polylysine, ssDNA, ODAM	6000	[79,80]
Two a-Si:H ellipses	Proteins A/G	1500	[80]
Two 4H-SiC teeth	Cyclohexane	–	[81]
Five aluminum ellipses	Liposomes	30–160	[82]
Two monoisotopic h-BN ribbons	CBP	10	[83]

As first example, Altug's group showed the detection of human odontogenic ameloblast-associated protein (ODAM), polylysine and single-stranded DNA (ssDNA) by using dielectric metasurfaces with high-quality factors. The resonance for this dielectric metasurface was controlled with the incidence angle of light and the polarization in order to obtain molecular fingerprint details. In addition, the building block (meta-atom) of this dielectric metasurface was composed of two elliptical shapes in germanium realized on a calcium fluoride ( $\text{CaF}_2$ ) substrate (see Figure 4a), and the principal axes of two ellipses were rotated asymmetrically between them. This metasurface thus permitted enhancing the electromagnetic near-fields ( $\text{EF} = 6000$ ) located at the tips of elliptical shapes, where the interactions between biomolecules and light occur. Finally, by employing this approach, the detection of mid-IR absorption fingerprints of biomolecules (here: polylysine, ssDNA, and ODAM, see Figure 4b,c) was realized without any tunable laser and/or expensive spectrometers that take up space [79,80]. Another example of this same research group is presented. In this example, the authors used pixelated dielectric metasurfaces for the detection of proteins A/G by SEIRA. Each metapixel of this metasurface was constituted of an array of anisotropic hydrogenated amorphous silicon ellipses (with an  $\text{EF} = 1500$  and the same geometry as the previous example, as can be seen in Figure 4a), whose resonance can be set over a given range of fingerprints of target molecules by adjusting the lateral dimensions of the unit cell by a factor named  $S$ . Thus, thanks to this pixelated dielectric metasurface, they accessed the signals of biomolecules over an expanded spectrum of wavelength with a great sensitivity [80].

Folland et al. demonstrated the sensing of cyclohexane using a metasurface composed of 4H-silicium carbide (4H-SiC) high-aspect-ratio gratings (HAGs, see Figure 5a,b). Thanks to this metasurface, a vibrational coherent coupling between the epsilon-near-zero (ENZ) waveguide mode and a vibrational mode of cyclohexane was evidenced by the mode splitting coming from the interaction between these two modes and following a dependence in  $\sqrt{C}$  with the cyclohexane concentration (see Figure 5c,d) [81]. The work of Leitis et al. has related the use of plasmonic metasurfaces in order to observe the liposome catching. These plasmonic metasurfaces were fabricated on alumina ( $\text{Al}_2\text{O}_3$ ) membranes and they were composed of aluminum (Al) nanoantennas (or meta-atoms), thus enabling a conception with various resonances in the mid-IR. Thereby, these resonances enhanced and overlapped the absorption bands of the liposomes in this case. To resume, the authors succeeded in demonstrating the catching of liposomes by SEIRA thanks to the high electric field enhancements ( $\text{EF} = 30\text{--}160$ ) located at the hotspots of Al nanoantennas whose resonances overlapped with the absorption bands of the liposomes [82]. To finish this section, Autore et al. reported the sensing of 4,4'-bis(N-carbazolyl)-1,1'-biphenyl (CBP) molecules using a metasurface composed of monoisotopic hexagonal boron nitride (h-BN) ribbon arrays realized on a  $\text{CaF}_2$  substrate. They observed a SEIRA signal increase of a factor of 10 for CBP molecules with this monoisotopic h-BN metasurface compared to the reference sample without the metasurface. This increase in the SEIRA signal was due to coupling between hyperbolic phonon-polariton modes and vibration modes of CBP molecules [83].

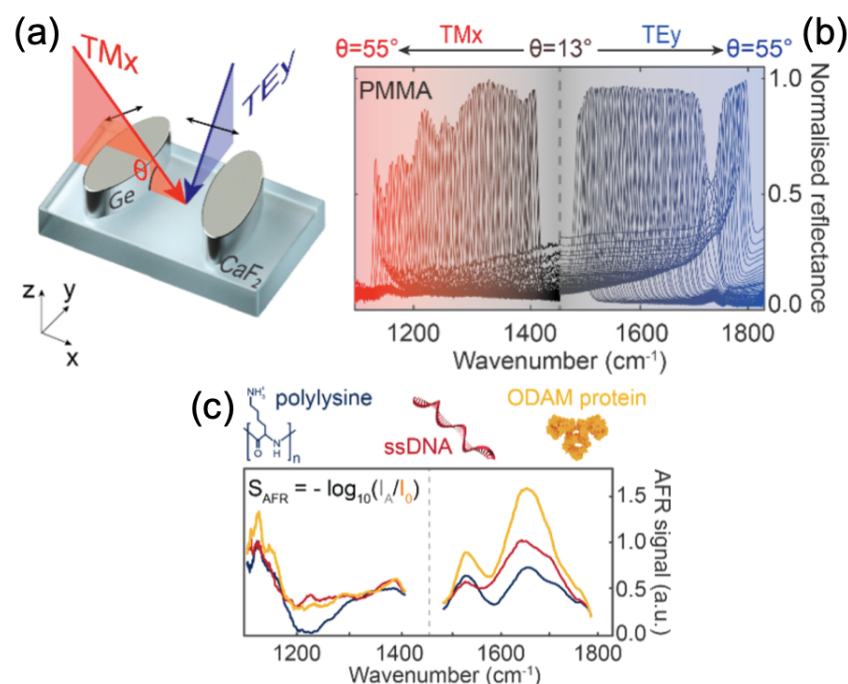


**Figure 4.** (a) Principle scheme of the unit cell for the dielectric metasurface. (b) Normalized reflectance spectra for the different incidence angles of light. (c) Absorbance spectra of polylysine, ssDNA and ODAM. All the figures are reprinted (adapted) with permission from [80], Copyright 2021 American Chemical Society.

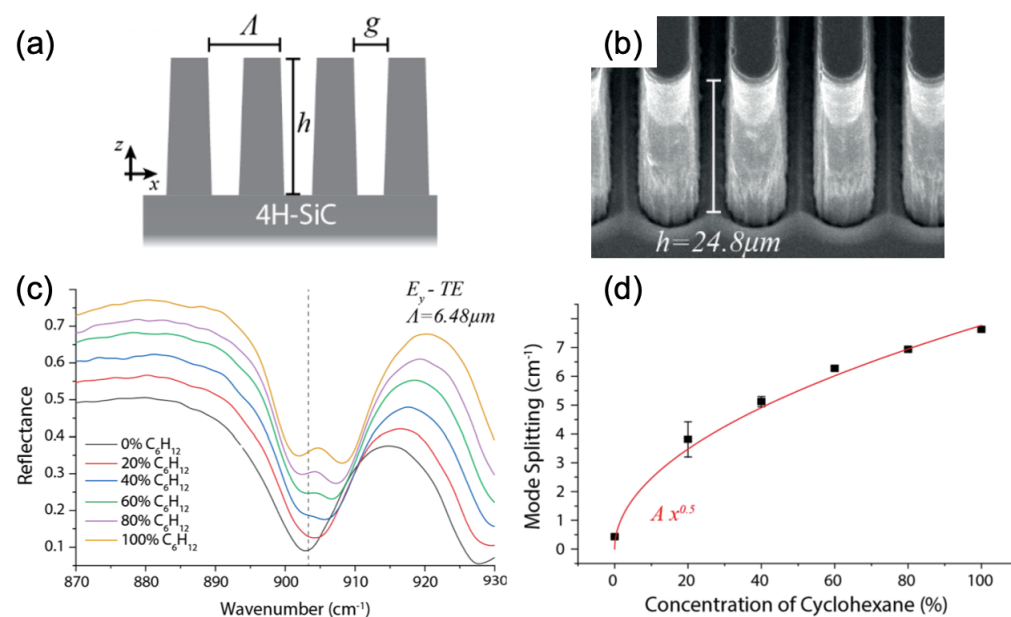


**Figure 5.** (a) Principle scheme of 4H-SiC high-aspect-ratio gratings (HAGs) with the tooth height  $h$  of grating, the grating period  $\Lambda$  and the tooth spacing of grating  $g$ . (b) SEM image of the 4H-SiC HAG. (c) Reflectance spectra with different concentrations of cyclohexane. The dashed line corresponds to the vibration mode of cyclohexane located at  $903 \text{ cm}^{-1}$ . (d) Mode splitting versus cyclohexane concentration. The red line corresponds to the fit with a square root function. All the figures are reprinted (adapted) with permission from [81], Copyright 2020 American Chemical Society.

#### 4. Metasurfaces for Photocatalysis

In this last part, we introduce the latest advances in metasurfaces for photocatalysis (see Table 3). For photocatalysis, a broadband absorption of light and an enhancement of

photocurrents are required. Thus, by adjusting the size, shape and organization of building blocks, the plasmonic or dielectric metasurfaces will improve the photon–electron energy conversion, thus enabling the enhancement of this absorption capacity of the solar light and the generation of a great number of catalytic active sites in order to more quickly produce the surface reactions. In addition, the enhancement factor is defined for the following examples as the ratio of photocurrents or reaction rates obtained for the metasurface and the reference sample (metasurface/reference).

**Table 3.** Unit cell of metasurfaces, reactions of photocatalysis and their EF ( $\text{CrO}_x$  = *p*-type Chromium Oxide;  $\text{NiO}_x$  = *p*-type Nickel Oxide; NRs = Nanorods; PEC = Photoelectrochemical; a-GaP = amorphous Gallium Phosphide; AuPd = Gold/Palladium; NPs = Nanoparticles; Cu@Pt = Copper–Platinum Core–Shell; Zn/Cu = Zinc/Copper;  $\text{TiO}_2$  = Titanium Dioxide; NO = Nitrogen Monoxide;  $\text{TiO}_{2-x}$  = Loss-engineered Substoichiometric Titanium Oxide; TiN = Titanium Nitride; HM = Hematite).

Unit Cell of Metasurfaces	Photocatalysis	EF	References
Random $\text{CrO}_x$ – $\text{NiO}_x$ NRs	PEC hydrogen generation	30	[84]
One a-GaP nanodisk	PEC hydrogen generation	5.7	[85]
Random AuPd NPs	PEC reduction of water	5–20	[86]
One Cu@Pt NP	PEC hydrogen generation	5–20	[87]
One Zn/Cu nanocube	Methanol production	93–181	[88]
One $\text{TiO}_2$ nanohole	NO oxidation reaction rate	5.7	[89]
Two $\text{TiO}_{2-x}$ ellipses	Ag reduction reaction	7	[90]
One TiN nanodisk	Hydrogen evolution rate	3.2	[91]
Au nanodisk on HM/Au bilayer	Water splitting	2–6	[92]

At first, Ozbay’s group demonstrated a catalyzed reaction of the hydrogen evolution (HER) using a metasurface constituted of random  $\text{CrO}_x$ – $\text{NiO}_x$  nanorods.  $\text{CrO}_x$  nanorods were chosen for their quality of light absorption in zones close to the surface thanks to hotspots generated by this geometry of random nanorods, and for easing the separation of charges.  $\text{NiO}_x$  was chosen as an HER catalyst. For the  $\text{CrO}_x$ – $\text{NiO}_x$  metasurface ( $\text{CrO}_x$  metasurface covered by a  $\text{NiO}_x$  layer, and then annealed at 600 °C over 30 min), the authors have shown an increase in the photocurrent values of a factor of 30 and 3 compared to those of a planar conception and those of a bare  $\text{CrO}_x$ -30 metasurface (30 = annealing at 600 °C over 30 min), respectively. This increase was due to the separation of charges which triggered the HER. This separation of charges was possible thanks to a good band alignment between the conduction bands of  $\text{CrO}_x$ ,  $\text{NiO}_x$  and the HER potential. In addition to the increase in photocurrent values, the ICPE measurements exhibited an enhancement of the efficiency in the conversion process [84]. Furthermore, based on similar principles, the group of Cortes also reported an increase in the photocurrent values of a factor of 5.7 compared to those of a planar conception upon HER conditions by using a different metasurface composed of amorphous gallium phosphide (a-GaP) nanodisks deposited on an indium tin oxide film itself deposited on a  $\text{SiO}_2$  substrate [85].

Building upon the above, Xiao et al. reported an increase in the photocurrent values of a factor 5–20 upon the reduction of water by using a plasmonic metasurface composed of AuPd nanoparticles deposited on a bilayer film of titanium dioxide and gold itself deposited on a glass substrate (see Figure 6a,b and blue curve in Figure 6b). This increase in photocurrent was due to the mixed photon-to-energy conversion of gold and palladium through plasmonic resonances for gold and interband transitions of Pd. Moreover, the incident photon conversion efficiency (IPCE) exposed an efficiency improvement in the conversion process (see blue curve in Figure 6c) [86].

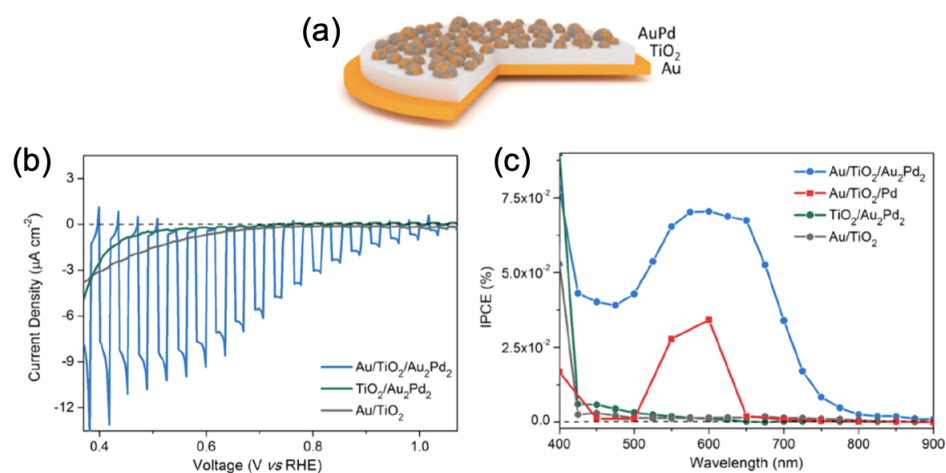


**Figure 6.** (a) Principle scheme of the plasmonic metasurface. (b) Linear sweep voltammogram scans with chopped visible light. (c) Incident photon conversion efficiency (IPCE) versus wavelength. All the figures are reprinted (adapted) with permission from [86], Copyright 2021 American Chemical Society.

Finally, Deng et al. have shown an improvement in photocurrent of a factor of 5–20 during the HER by employing a metasurface constituted of lattices of copper–platinum core–shell nanoparticles deposited on an ITO/quartz substrate (see Figure 7a–c). This best improvement in photocurrent is owed to the surface lattice resonances of lattices of Cu@Pt nanoparticles inducing robust absorption of light (see the IR part of Figure 7d, where the dip indicates the presence of a surface lattice resonance) and electromagnetic fields [87]. A work of Kherani’s group has reported on the enhancement of the rate of methanol production of a factor 93–181 via the use of a metasurface constituted of ZnO/Cu nanocubes on an Au/Cu bilayer film. This enhancement was obtained by combining the broadband absorption and the plasmonics, thus inducing strong electric fields over the (nonplasmonic) absorption range [88]. Capitolis et al. demonstrated an enhancement of a factor 5.7 on the reaction rate of the NO oxidation through the use of a metasurface formed of nanohole arrays realized in a silicon nitride ( $\text{SiN}_x$ ) film, then covered by a  $\text{TiO}_2$  layer. This enhancement was due to the significant absorption of the incident light (UV-light in this case) via slow light modes produced by the periodic lattice of metasurface [89]. Additionally, Hu et al. created a metasurface composed of loss-engineered substoichiometric titanium oxide ( $\text{TiO}_{2-x}$ ) ellipses and based on the bound states in the continuum (BIC) for increasing the reaction rate of silver (Ag) reduction. The authors have reported an EF of 7 for the reaction rate of Ag reduction with the low-defect  $\text{TiO}_{2-x}$  (named  $\text{TiO}_{2-L}$ ), which was due to the matching of the excitation wavelength with the quasi-BIC resonance of the metasurface by adjusting all the geometric parameters of the unit cell of metasurface. This matching enabled an optimal absorption of the visible light and an optimal enhancement of near-fields, thus inducing a better reaction rate [90].

Yu et al. reported an improvement of a factor 3.2 for the hydrogen evolution rate by employing a metasurface composed of titanium nitride (TiN) nanodisks fabricated on a thin TiN film and arranged in square array, then covered by a photocatalyst polymer (see Figure 8a–c; TiN film without any nanodisk serves as reference). This improvement of the HER was obtained thanks to the broadband plasmon resonance of the metasurface (see Figure 8d) producing strong electric fields and thus increasing different rates, such as those of absorption light, carrier separation and the transfer of hot carriers in photocatalyst polymers [91]. To terminate this part on metasurfaces for photocatalysis, Dutta et al. reported the use of a plasmonic metasurface for the water splitting. This metasurface consisted of arrays of gold nanodisks deposited on a hematite film—itsself deposited on gold film. Enhancement factors of 2 and 6 in the photocurrent of the water oxidation were obtained above and below the bandgap of hematite, respectively. The EF of 2 in the

photocurrent obtained above the bandgap was owed to an improved scattering by the Au nanodisks and a back-reflection from the Au mirror. The EF of 6 in the photocurrent obtained below the bandgap was due to the hot electrons produced by plasmon decay [92].

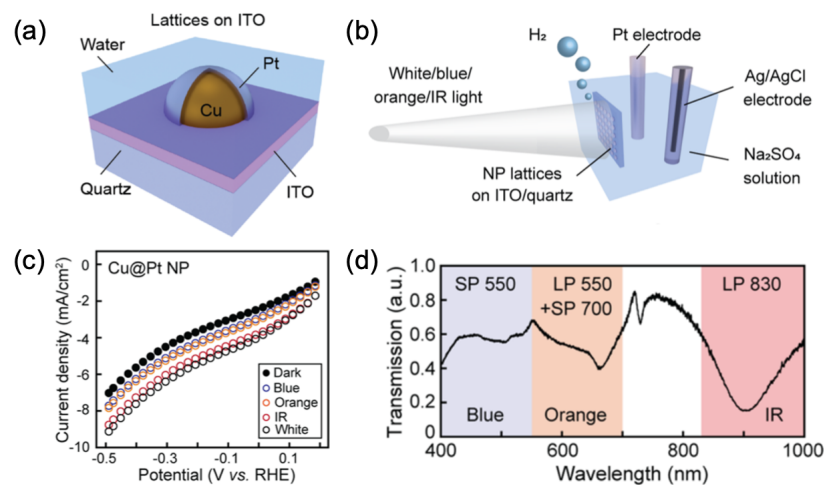


**Figure 7.** (a) Principle scheme of the unit cell of the metasurface. (b) Illustration of HER measurements. (c) Linear sweep voltammogram scans of HER at different wavelengths (see the caption in the curves). (d) Transmission spectrum of the Cu@Pt nanoparticle array, where three ranges of light are indicated by the shading of each. All the figures are reprinted (adapted) with permission from [87], Copyright 2021 American Chemical Society.

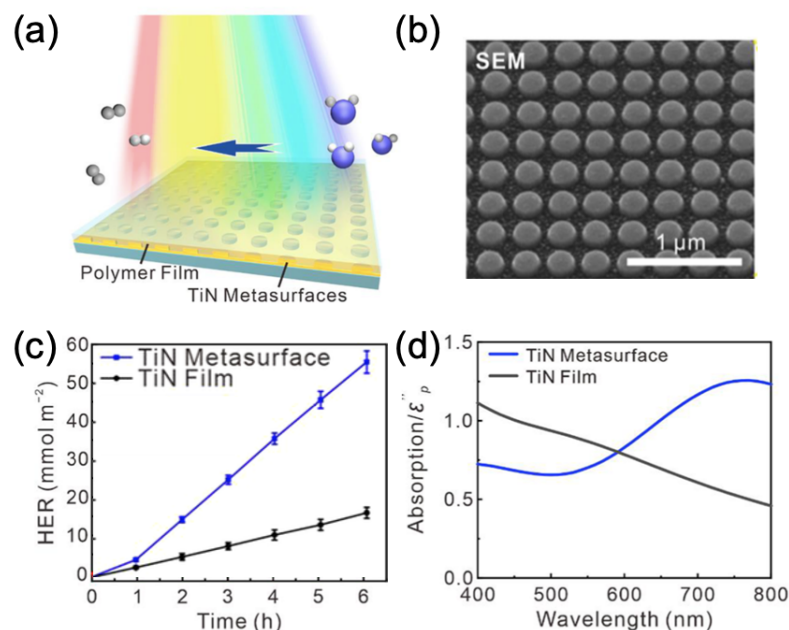


**Figure 8.** (a) Principle scheme of the hydrogen evolution induced by visible light by employing the TiN metasurface covered by the photocatalyst polymer. (b) SEM picture of the metasurface composed of TiN nanodisks. (c) HER rate of the photocatalyst polymer deposited on a TiN metasurface and TiN film (reference) versus time. (d) Calculated absorption spectra of the photocatalyst polymer deposited on the TiN metasurface and TiN film (reference). All the figures are reprinted (adapted) with permission from [91], Copyright 2021 American Chemical Society.

## 5. Conclusions and Outlook

In summary, we depicted the latest advances in the performance of plasmonic or dielectric metasurfaces for SERS and SEIRA sensors as well as photocatalysis. Thanks to the performances of these metasurfaces, enhancement factors were obtained ranging from 2

to 81 for photocatalysis, from 10 to 6000 for SEIRA sensors and from  $10^4$  to  $3 \times 10^8$  for SERS sensors. These enhancement factors were due to the confinement of local electromagnetic fields in the vicinity of optical antennas that had resonances in a large spectral range being thus able to increase the SERS and SEIRA signals. Furthermore, some metasurfaces enabled an accurate enhancement of the excitation and emission processes for the SERS effect by supporting resonances at frequencies of these processes. Another advantage of using metasurfaces is to achieve the good reproducibility and uniformity of the SERS signal on the whole substrate thanks to the present fabrication techniques, which permit the identical realization of plasmonic or dielectric nanostructures. Finally, these metasurfaces permitted the enhancement of the absorption capacity of the solar light and the generation of a great number of catalytic active sites in order to more quickly produce the surface reactions. A couple of interesting perspectives concerning the metasurfaces to be used would be chemo-tunable metasurfaces that can allow a chemical modulation to control their optical properties alternately to electrotunable metasurfaces (presented here in one or two examples), or surface-functionalized metasurfaces for handling their properties. For instance, proteins can be functionalized on metasurfaces in order to obtain very selective biochemical interactions for improving the sensing of antibodies or antigens. Finally, we think that, in the near future, chemo-tunable or surface-functionalized metasurfaces will offer perspectives for photocatalysis and sensing based on surface-enhanced spectroscopies.

**Funding:** This research received no external funding.

**Institutional Review Board Statement:** Not applicable.

**Informed Consent Statement:** Not applicable.

**Data Availability Statement:** Not applicable.

**Conflicts of Interest:** The author declares no conflict of interest.

## References

1. Wang, D.; Wang, W.; Knudson, M.P.; Schatz, G.C.; Odom, T.W. Structural Engineering in Plasmon Nanolasers. *Chem. Rev.* **2018**, *118*, 2865–2881. [CrossRef] [PubMed]
2. Staude, I.; Pertsch, T.; Kivshar, Y.S. All-Dielectric Resonant Meta-Optics Lightens up. *ACS Photonics* **2019**, *6*, 802–814. [CrossRef]
3. Wang, K.; Titchener, J.G.; Kruk, S.S.; Xu, L.; Chung, H.-P.; Parry, M.; Kravchenko, I.I.; Chen, Y.-H.; Solntsev, A.S.; Kivshar, Y.S.; et al. Quantum metasurface for multiphoton interference and state reconstruction. *Science* **2018**, *361*, 1104–1108. [CrossRef] [PubMed]
4. Li, L.; Liu, Z.; Ren, X.; Wang, S.; Su, V.-C.; Chen, M.-K.; Chu, C.H.; Kuo, H.Y.; Liu, B.; Zang, W.; et al. Metalens-array-based high-dimensional and multiphoton quantum source. *Science* **2020**, *368*, 1487–1490. [CrossRef]
5. Ou, Q.-D.; Xie, H.-J.; Chen, J.-D.; Zhou, L.; Tang, J.-X. Enhanced light harvesting in flexible polymer solar cells: Synergistic simulation of a plasmonic meta-mirror and a transparent silver mesowire electrode. *J. Mater. Chem. A* **2016**, *4*, 18952–18962. [CrossRef]
6. Voroshilov, P.M.; Ovchinnikov, V.; Papadimitratos, A.; Zakhidov, A.A.; Simovski, C.R. Light Trapping Enhancement by Silver Nanoantennas in Organic Solar Cells. *ACS Photonics* **2018**, *5*, 1767–1772. [CrossRef]
7. Chang, C.-C.; Kort-Kamp, W.J.M.; Nogan, J.; Luk, T.S.; Azad, A.K.; Taylor, A.J.; Dalvit, D.A.R.; Sykora, M.; Chen, H.-T. High-Temperature Refractory Metasurfaces for Solar Thermophotovoltaic Energy Harvesting. *Nano Lett.* **2018**, *18*, 7665–7673. [CrossRef]
8. Fang, J.; Wang, D.; DeVault, C.T.; Chung, T.-F.; Chen, Y.P.; Boltasseva, A.; Shalaev, V.M.; Kildishev, A.V. Enhanced Graphene Photodetector with Fractal Metasurface. *Nano Lett.* **2017**, *17*, 57–62. [CrossRef]
9. Li, L.; Wang, J.; Kang, L.; Liu, W.; Yu, L.; Zheng, B.; Brongersma, M.L.; Werner, D.H.; Lan, S.; Shi, Y.; et al. Monolithic Full-Stokes Near-Infrared Polarimetry with Chiral Plasmonic Metasurface Integrated Graphene–Silicon Photodetector. *ACS Nano* **2020**, *14*, 16634–16642. [CrossRef]
10. Sharma, N.; Bar-David, J.; Mazurki, N.; Levy, U. Metasurfaces for Enhancing Light Absorption in Thermoelectric Photodetectors. *ACS Photonics* **2020**, *7*, 2468–2473. [CrossRef]
11. Yu, N.; Capasso, F. Flat optics with designer metasurfaces. *Nat. Mater.* **2014**, *13*, 139–150. [CrossRef]
12. Genevet, P.; Capasso, F.; Aieta, F.; Khorasaninejad, M.; Devlin, R. Recent Advances in Planar Optics: From Plasmonic to Dielectric Metasurfaces. *Optica* **2017**, *4*, 139–152. [CrossRef]
13. Ding, F.; Pors, A.; Bozhevolnyi, S.I. Gradient Metasurfaces: A Review of Fundamentals and Applications. *Rep. Prog. Phys.* **2018**, *81*, 026401. [CrossRef]
14. Dolev, I.; Epstein, I.; Arie, A. Surface-Plasmon Holographic Beam Shaping. *Phys. Rev. Lett.* **2012**, *109*, 203903. [CrossRef]

15. Zheng, G.X.; Mühlenbernd, H.; Kenney, M.; Li, G.X.; Zentgraf, T.; Zhang, S. Metasurface holograms reaching 80% efficiency. *Nat. Nanotechnol.* **2015**, *10*, 308–312. [CrossRef]
16. Deng, Z.L.; Jin, M.K.; Ye, X.; Wang, S.; Shi, T.; Deng, J.H.; Mao, N.B.; Cao, Y.Y.; Guan, B.O.; Alu, A.; et al. Full-Color Complex-Amplitude Vectorial Holograms Based on Multi-Freedom Metasurfaces. *Adv. Funct. Mater.* **2020**, *30*, 1910610. [CrossRef]
17. Aieta, F.; Genevet, P.; Kats, M.A.; Yu, N.; Blanchard, R.; Gaburro, Z.; Capasso, F. Aberration-Free Ultrathin Flat Lenses and Axicons at Telecom Wavelengths Based on Plasmonic Metasurfaces. *Nano Lett.* **2012**, *12*, 4932–4936. [CrossRef]
18. Pors, A.; Nielsen, M.G.; Eriksen, R.L.; Bozhevolnyi, S.I. Broadband Focusing Flat Mirrors Based on Plasmonic Gradient Metasurfaces. *Nano Lett.* **2013**, *13*, 829–834. [CrossRef]
19. Ni, X.J.; Ishii, S.; Kildishev, A.V.; Shalaev, V.M. Ultra-thin, planar, Babinet-inverted plasmonic metalenses. *Light Sci. Appl.* **2013**, *2*, e72. [CrossRef]
20. Valentine, J.; Li, J.S.; Zentgraf, T.; Bartal, G.; Zhang, X. An optical cloak made of dielectrics. *Nat. Mater.* **2009**, *8*, 568–571. [CrossRef]
21. Gharghi, M.; Gladden, C.; Zentgraf, T.; Liu, Y.M.; Yin, X.B.; Valentine, J.; Zhang, X. A Carpet Cloak for Visible Light. *Nano Lett.* **2011**, *11*, 2825–2828. [CrossRef]
22. Chen, H.S.; Zheng, B.; Shen, L.; Wang, H.P.; Zhang, X.M.; Zheludev, N.I.; Zhang, B.L. Ray-optics cloaking devices for large objects in incoherent natural light. *Nat. Commun.* **2013**, *4*, 2652. [CrossRef]
23. Hu, J.; Bandyopadhyay, S.; Liu, Y.-H.; Shao, L.-Y. A Review on Metasurface: From Principle to Smart Metadevices. *Front. Phys.* **2021**, *8*, 586087. [CrossRef]
24. De Zoysa, M.; Asano, T.; Mochizuki, K.; Oskooi, A.; Inoue, T. Conversion of Broadband to Narrowband Thermal Emission Through Energy Recycling. *Nat. Photonics* **2012**, *6*, 535–539. [CrossRef]
25. Barbillon, G.; Sakat, E.; Hugonin, J.-P.; Biehs, S.-A.; Ben-Abdallah, P. True thermal antenna with hyperbolic metamaterials. *Opt. Express* **2017**, *25*, 23356–23363. [CrossRef]
26. Xie, X.; Li, X.; Pu, M.; Ma, X.; Liu, K.; Guo, Y.; Luo, X. Plasmonic Metasurfaces for Simultaneous Thermal Infrared Invisibility and Holographic Illusion. *Adv. Funct. Mater.* **2018**, *28*, 1706673. [CrossRef]
27. Zhang, X.; Zhang, Z.; Wang, Q.; Zhu, S.; Liu, H. Controlling Thermal Emission by Parity-Symmetric Fano Resonance of Optical Absorbers in Metasurfaces. *ACS Photonics* **2019**, *6*, 2671–2676. [CrossRef]
28. Joulain, K.; Drevillon, J.; Ben-Abdallah, P. Noncontact heat transfer between two metamaterials. *Phys. Rev. B* **2010**, *81*, 165119. [CrossRef]
29. Liu, B.; Shen, S. Broadband near-field radiative thermal emitter/absorber based on hyperbolic metamaterials: Direct numerical simulation by the Wiener chaos expansion method. *Phys. Rev. B* **2013**, *87*, 115403. [CrossRef]
30. Liu, X.; Zhang, Z. Near-Field Thermal Radiation between Metasurfaces. *ACS Photonics* **2015**, *2*, 1320–1326. [CrossRef]
31. Fernandez-Hurtado, V.; Garcia-Vidal, F.J.; Fan, S.; Cuevas, E.C. Enhancing Near-Field Radiative Heat Transfer with Si-based Metasurfaces. *Phys. Rev. Lett.* **2017**, *118*, 203901. [CrossRef] [PubMed]
32. Lee, J.; Nookala, N.; Gomez-Diaz, J.S.; Tymchenko, M.; Demmerle, F.; Boehm, G.; Amann, M.-C.; Alu, A.; Belkin, M.A. Ultrathin Second-Harmonic Metasurfaces with Record-High Nonlinear Optical Responses. *Adv. Opt. Mater.* **2016**, *4*, 664–670. [CrossRef]
33. Fedotova, A.; Younesi, M.; Sautter, J.; Vaskin, A.; Löchner, F.J.F.; Steinert, M.; Geiss, R.; Pertsch, T.; Staude, I.; Setzpfandt, F. Second-Harmonic Generation in Resonant Nonlinear Metasurfaces Based on Lithium Niobate. *Nano Lett.* **2020**, *20*, 8608–8614. [CrossRef] [PubMed]
34. Yang, Y.; Wang, W.; Boulesbaa, A.; Kravchenko, I.I.; Briggs, D.P.; Poretzky, A.; Geohegan, D.; Valentine, J. Nonlinear Fano-Resonant Dielectric Metasurfaces. *Nano Lett.* **2015**, *15*, 7388–7393. [CrossRef]
35. Shorokhov, A.S.; Melik-Gaykazyan, E.V.; Smirnova, D.A.; Hopkins, B.; Chong, K.E.; Choi, D.-Y.; Shcherbakov, M.R.; Miroshnichenko, A.E.; Neshev, D.N.; Fedyanin, A.A.; et al. Multifold Enhancement of Third-Harmonic Generation in Dielectric Nanoparticles Driven by Magnetic Fano Resonances. *Nano Lett.* **2016**, *16*, 4857–4861. [CrossRef]
36. Qin, J.; Jiang, S.; Wang, Z.; Cheng, X.; Li, B.; Shi, Y.; Tsai, D.P.; Liu, A.Q.; Huang, W.; Zhu, W. Metasurface Micro/Nano-Optical Sensors: Principles and Applications. *ACS Nano* **2022**, *16*, 11598–11618. [CrossRef]
37. Wu, C.; Khanikaev, A.B.; Adato, R.; Arju, N.; Yanik, A.A.; Altug, H.; Shvets, G. Fano-resonant asymmetric metamaterials for ultrasensitive spectroscopy and identification of molecular monolayers. *Nat. Mater.* **2012**, *11*, 69–75. [CrossRef]
38. Brown, L.V.; Yang, X.; Zhao, K.; Zheng, B.Y.; Nordlander, P.; Halas, N.J. Fan-Shaped Gold Nanoantennas above Reflective Substrates for Surface-Enhanced Infrared Absorption (SEIRA). *Nano Lett.* **2015**, *15*, 1272–1280. [CrossRef]
39. Chen, X.; Ciraci, C.; Smith, D.R.; Oh, S.-H. Nanogap-Enhanced Infrared Spectroscopy with Template-Stripped Wafer-Scale Arrays of Buried Plasmonic Cavities. *Nano Lett.* **2015**, *15*, 107–113. [CrossRef]
40. Chae, J.; Lahiri, B.; Centrone, A. Engineering Near-Field SEIRA Enhancements in Plasmonic Resonators. *ACS Photonics* **2016**, *3*, 87–95. [CrossRef]
41. Neubrech, F.; Huck, C.; Weber, K.; Pucci, A.; Giessen, H. Surface-Enhanced Infrared Spectroscopy Using Resonant Nanoantennas. *Chem. Rev.* **2017**, *117*, 5110–5145. [CrossRef]
42. Zhang, N.; Liu, K.; Liu, Z.; Song, H.; Zeng, X.; Ji, D.; Cheney, A.; Jiang, S.; Gan, Q. Ultrabroadband Metasurface for Efficient Light Trapping and Localization: A Universal Surface-Enhanced Raman Spectroscopy Substrate for “All” Excitation Wavelengths. *Adv. Mater. Interfaces* **2015**, *2*, 1500142. [CrossRef]
43. Zhang, X.; Zheng, Y.; Liu, X.; Lu, W.; Dai, J.; Lei, D.Y.; MacFarlane, D.R. Hierarchical Porous Plasmonic Metamaterials for Reproducible Ultrasensitive Surface-Enhanced Raman Spectroscopy. *Adv. Mater.* **2015**, *27*, 1090–1096. [CrossRef]

44. Yang, Y.; Lee, Y.H.; Phang, I.Y.; Jiang, R.; Sim, H.Y.F.; Wang, J.; Ling, X.Y. A Chemical Approach To Break the Planar Configuration of Ag Nanocubes into Tunable Two-Dimensional Metasurfaces. *Nano Lett.* **2016**, *16*, 3872–3878. [CrossRef]
45. Gwo, S.; Wang, C.-Y.; Chen, H.-Y.; Lin, M.-H.; Sun, L.; Li, X.; Chen, W.-L.; Chang, Y.-M.; Ahn, H. Plasmonic Metasurfaces for Nonlinear Optics and Quantitative SERS. *ACS Photonics* **2016**, *3*, 1371–1384. [CrossRef]
46. Abdulhalim, I. Coupling configurations between extended surface electromagnetic waves and localized surface plasmons for ultrahigh field enhancement. *Nanophotonics* **2018**, *7*, 1891–1916. [CrossRef]
47. Gao, H.; Liu, C.; Jeong, H.E.; Yang, P. Plasmon-Enhanced Photocatalytic Activity of Iron Oxide on Gold Nanopillars. *ACS Nano* **2012**, *6*, 234–240. [CrossRef]
48. Li, J.; Cushing, S.K.; Zheng, P.; Meng, F.; Chu, D.; Wu, N. Plasmon-induced photonic and energy-transfer enhancement of solar water splitting by a hematite nanorod array. *Nat. Commun.* **2013**, *4*, 2651. [CrossRef]
49. Clavero, C. Plasmon-induced hot-electron generation at nanoparticle/metal-oxide interfaces for photovoltaic and photocatalytic devices. *Nat. Photonics* **2014**, *8*, 95–103. [CrossRef]
50. Aslam, U.; Chavez, S.; Linic, S. Controlling energy flow in multimetallic nanostructures for plasmonic catalysis. *Nat. Nanotechnol.* **2017**, *12*, 1000–1005. [CrossRef]
51. Kildishev, A.V.; Boltasseva, A.; Shalae, V.M. Planar Photonics with Metasurfaces. *Science* **2013**, *339*, 1289. [CrossRef]
52. Monticone, F.; Alu, A. Metamaterial, plasmonic and nanophotonic devices. *Rep. Prog. Phys.* **2017**, *80*, 036401. [CrossRef]
53. Meinzer, N.; Barnes, W.L.; Hooper, I.R. Plasmonic meta-atoms and metasurfaces. *Nat. Photonics* **2014**, *8*, 889–898. [CrossRef]
54. Vaskin, A.; Kolkowski, R.; Femius Koenderink, A.; Staude, I. Light-emitting metasurfaces. *Nanophotonics* **2019**, *8*, 1151–1198. [CrossRef]
55. Tittl, A.; Leitis, A.; Liu, M.; Yesilkoy, F.; Choi, D.-Y.; Neshev, D.N.; Kivshar, Y.S.; Altug, H. Imaging-based molecular barcoding with pixelated dielectric metasurfaces. *Science* **2018**, *360*, 1105–1109. [CrossRef]
56. Romano, S.; Zito, G.; Manago, S.; Calafiore, G.; Penzo, E.; Cabrini, S.; De Luca, A.C.; Mocella, V. Surface-Enhanced Raman and Fluorescence Spectroscopy with an All-Dielectric Metasurface. *J. Phys. Chem. C* **2018**, *122*, 19738–19745. [CrossRef]
57. Koshelev, K.; Kivshar, Y. Dielectric Resonant Metaphotonics. *ACS Photonics* **2021**, *8*, 102–112. [CrossRef]
58. Shi, X.; Ueno, K.; Oshikiri, T.; Sun, Q.; Sasaki, K.; Misawa, H. Enhanced water splitting under modal strong coupling conditions. *Nat. Nanotechnol.* **2018**, *13*, 953–958. [CrossRef]
59. Gao, J.; Zhang, N.; Ji, D.; Song, H.; Liu, Y.; Zhou, L.; Sun, Z.; Jornet, J.M.; Thompson, A.C.; Collins, R.L.; et al. Superabsorbing Metasurfaces with Hybrid Ag—Au Nanostructures for Surface-Enhanced Raman Spectroscopy Sensing of Drugs and Chemicals. *Small Methods* **2018**, *2*, 1800045. [CrossRef]
60. Sarychev, A.K.; Ivanov, A.; Lagarkov, A.N.; Ryzhikov, I.; Afanasev, K.; Bykov, I.; Barbillon, G.; Bakholdin, N.; Mikhailov, M.; Smyk, A.; et al. Plasmon Localization and Giant Fields in an Open-Resonator Metasurface for Surface-Enhanced-Raman-Scattering Sensors. *Phys. Rev. Appl.* **2022**, *17*, 044029. [CrossRef]
61. Chen, Y.; Yin, H.; Sikdar, D.; Yan, L.; Zhou, Z.; Sun, J.; Wang, C. Gold Nanopolyhedron-Based Superlattice Sheets as Flexible Surface-Enhanced Raman Scattering Sensors for Detection of 4-Aminothiophenol. *ACS Appl. Nano Mater.* **2021**, *4*, 12498–12505. [CrossRef]
62. Palermo, G.; Rippa, M.; Conti, Y.; Vestri, A.; Castagna, R.; Fusco, G.; Suffredini, E.; Zhou, J.; Zyss, J.; De Luca, A.; et al. Plasmonic Metasurfaces Based on Pyramidal Nanoholes for High-Efficiency SERS Biosensing. *ACS Appl. Mater. Interfaces* **2021**, *13*, 43715–43725. [CrossRef] [PubMed]
63. Rippa, M.; Sagnelli, D.; Vestri, A.; Marchesano, V.; Munari, B.; Carnicelli, D.; Varrone, E.; Brigotti, M.; Tozzoli, R.; Montalbano, M.; et al. Plasmonic Metasurfaces for Specific SERS Detection of Shiga Toxins. *ACS Appl. Mater. Interfaces* **2022**, *14*, 4969–4979. [CrossRef] [PubMed]
64. Caligiuri, V.; Tedeschi, G.; Palei, M.; Miscuglio, M.; Martin-Garcia, B.; Guzman-Puyol, S.; Hedayati, M.K.; Kristensen, A.; Athanassiou, A.; Cingolani, R.; et al. Biodegradable and Insoluble Cellulose Photonic Crystals and Metasurfaces. *ACS Nano* **2020**, *14*, 9502–9511. [CrossRef]
65. Gabinet, U.R.; Osuji, C.O. Plasmonic Sensing from Vertical Au-Coated ZnO Nanorod Arrays Templated by Block Copolymers. *ACS Appl. Nano Mater.* **2021**, *4*, 8556–8563. [CrossRef]
66. Narasimhan, V.; Siddique, R.H.; Park, H.; Choo, H. Bioinspired Disordered Flexible Metasurfaces for Human Tear Analysis Using Broadband Surface-Enhanced Raman Scattering. *ACS Omega* **2020**, *5*, 12915–12922. [CrossRef]
67. Yang, K.; Wang, J.; Yao, X.; Lyu, D.; Zhu, J.; Yang, Z.; Liu, B.; Ren, B. Large-Area Plasmonic Metamaterial with Thickness-Dependent Absorption. *Adv. Optical Mater.* **2021**, *9*, 2001375. [CrossRef]
68. Zhao, Y.; Hubarevich, A.; Iarossi, M.; Borzda, T.; Tantussi, F.; Huang, J.-A.; De Angelis, F. Hyperbolic Nanoparticles on Substrate with Separate Optical Scattering and Absorption Resonances: A Dual Function Platform for SERS and Thermoplasmonics. *Adv. Optical Mater.* **2021**, *9*, 2100888. [CrossRef]
69. Ma, Y.; Sikdar, D.; Fedosyuk, A.; Velleman, L.; Klemme, D.J.; Oh, S.-H.; Kucernak, A.R.J.; Kornyshev, A.A.; Edel, J.B. Electrotunable Nanoplasmonics for Amplified Surface Enhanced Raman Spectroscopy. *ACS Nano* **2020**, *14*, 328–336. [CrossRef]
70. Kovalets, N.P.; Kozhina, E.P.; Razumovskaya, I.V.; Bedin, S.A.; Piryazev, A.A.; Grigoriev, Y.V.; Naumov, A.V. Toward single-molecule surface-enhanced Raman scattering with novel type of metasurfaces synthesized by crack-stretching of metallized track-etched membranes. *J. Chem. Phys.* **2022**, *156*, 034902. [CrossRef]

71. Nguyen, T.V.; Pham, L.T.; Khuyen, B.X.; Duong, D.C.; Nghiem, L.H.T.; Nguyen, N.T.; Vu, D.; Hoa, D.Q.; Lam, V.D.; Nguyen, H.M. Effects of metallic underlayer on SERS performance of a metal film over nanosphere metasurface. *J. Phys. D Appl. Phys.* **2022**, *55*, 025101. [CrossRef]
72. Mao, P.; Liu, C.; Chen, Q.; Han, M.; Maier, S.A.; Zhang, S. Broadband SERS detection with disordered plasmonic hybrid aggregates. *Nanoscale* **2020**, *12*, 93–102. [CrossRef]
73. Wang, Y.; Zhao, C.; Wang, J.; Luo, X.; Xie, L.; Zhan, S.; Kim, J.; Wang, X.; Liu, X.; Ying, Y. Wearable plasmonic-metasurface sensor for noninvasive and universal molecular fingerprint detection on biointerfaces. *Sci. Adv.* **2021**, *7*, eabe4553. [CrossRef]
74. Luo, S.; Mancini, A.; Berté, R.; Hoff, B.H.; Maier, S.A.; de Mello, J.C. Massively Parallel Arrays of Size-Controlled Metallic Nanogaps with Gap-Widths Down to the Sub-3-nm Level. *Adv. Mater.* **2021**, *33*, 2100491. [CrossRef]
75. Bauman, S.J.; Darweesh, A.A.; Furr, M.; Magee, M.; Argyropoulos, C.; Herzog, J.B. Tunable SERS Enhancement via Sub-nanometer Gap Metasurfaces. *ACS Appl. Mater. Interfaces* **2022**, *14*, 15541–15548. [CrossRef]
76. Zhang, W.; Ai, B.; Gu, P.; Guan, Y.; Wang, Z.; Xiao, Z.; Zhang, G. Plasmonic Chiral Metamaterials with Sub-10 nm Nanogaps. *ACS Nano* **2021**, *15*, 17657–17667. [CrossRef]
77. Thareja, V.; Esfandyarpour, M.; Kik, P.G.; Brongersma, M.L. Anisotropic Metasurfaces as Tunable SERS Substrates for 2D Materials. *ACS Photonics* **2019**, *6*, 1996–2004. [CrossRef]
78. Jiang, T.; Goel, P.; Zhao, H.; Ma, R.; Zhu, L.; Liu, X.; Tang, L. Internal Structure Tailoring in 3D Nanoplasmonic Metasurface for Surface-Enhanced Raman Spectroscopy. *Part. Part. Syst. Character.* **2020**, *37*, 1900345. [CrossRef]
79. Leitis, A.; Tittl, A.; Liu, M.; Lee, B.H.; Gu, M.B.; Kivshar, Y.S.; Altug, H. Angle-multiplexed all-dielectric metasurfaces for broadband molecular fingerprint retrieval. *Sci. Adv.* **2019**, *5*, eaaw2871. [CrossRef]
80. Tseng, M.L.; Jahani, Y.; Leitis, A.; Altug, H. Dielectric Metasurfaces Enabling Advanced Optical Biosensors. *ACS Photonics* **2021**, *8*, 47–60. [CrossRef]
81. Folland, T.G.; Lu, G.; Bruncz, A.; Nolen, J.R.; Tadjer, M.; Caldwell, J.D. Vibrational Coupling to Epsilon-Near-Zero Waveguide Modes. *ACS Photonics* **2020**, *7*, 614–621. [CrossRef]
82. Leitis, A.; Tseng, M.L.; John-Herpin, A.; Kivshar, Y.S.; Altug, H. Wafer-Scale Functional Metasurfaces for Mid-Infrared Photonics and Biosensing. *Adv. Mater.* **2021**, *33*, 2102232. [CrossRef]
83. Autore, M.; Dolado, I.; Li, P.; Esteban, R.; Alfaro-Mozaz, F.J.; Atxabal, A.; Liu, S.; Edgar, J.H.; Velez, S.; Casanova, F.; et al. Enhanced Light–Matter Interaction in <sup>10</sup>B Monoisotopic Boron Nitride Infrared Nanoresonators. *Adv. Optical Mater.* **2021**, *9*, 2001958. [CrossRef]
84. Ulusoy Ghobadi, T.G.; Ghobadi, A.; Odabasi, O.; Karadas, F.; Ozbay, E. Subwavelength Densely Packed Disordered Semiconductor Metasurface Units for Photoelectrochemical Hydrogen Generation. *ACS Appl. Energy Mater.* **2022**, *5*, 2826–2837. [CrossRef]
85. Hüttenhofer, L.; Golibrzuch, M.; Bienek, O.; Wendisch, F.J.; Lin, R.; Becherer, M.; Sharp, I.D.; Maier, S.A.; Cortes, E. Metasurface Photoelectrodes for Enhanced Solar Fuel Generation. *Adv. Energy Mater.* **2021**, *11*, 2102877. [CrossRef]
86. Xiao, Q.; Kinnear, C.; Connell, T.U.; Kashif, M.K.; Easton, C.D.; Seeber, A.; Bourgeois, L.; Bonin, G.O.; Duffy, N.W.; Chesman, A.S.R.; et al. Dual Photolytic Pathways in an Alloyed Plasmonic Near-Perfect Absorber: Implications for Photoelectrocatalysis. *ACS Appl. Nano Mater.* **2021**, *4*, 2702–2712. [CrossRef]
87. Deng, S.; Zhang, B.; Choo, P.; Smeets, P.J.M.; Odom, T.W. Plasmonic Photoelectrocatalysis in Copper–Platinum Core–Shell Nanoparticle Lattices. *Nano Lett.* **2021**, *21*, 1523–1529. [CrossRef]
88. Loh, J.Y.Y.; Safari, M.; Mao, C.; Viasus, C.J.; Eleftheriades, G.V.; Ozin, G.A.; Kherani, N.P. Near-Perfect Absorbing Copper Metamaterial for Solar Fuel Generation. *Nano Lett.* **2021**, *21*, 9124–9130. [CrossRef]
89. Capitolis, J.; Hamandi, M.; Hochedel, M.; El-Jallal, S.; Drouard, E.; Chevalier, C.; Leclercq, J.-L.; Penuelas, J.; Dursap, T.; Brottet, S.; et al. Two-dimensional photonic metasurfaces for slow light-controlled photocatalysis. *Nano Select* **2022**, *3*, 108–117. [CrossRef]
90. Hu, H.; Weber, T.; Bienek, O.; Wester, A.; Hüttenhofer, L.; Sharp, I.D.; Maier, S.A.; Tittl, A.; Cortes, E. Catalytic Metasurfaces Empowered by Bound States in the Continuum. *ACS Nano* **2022**, *16*, 13057–13068. [CrossRef]
91. Yu, M.-J.; Chang, C.-L.; Lan, H.-Y.; Chiao, Z.-Y.; Chen, Y.-C.; Lee, H.W.H.; Chang, Y.-C.; Chang, S.-W.; Tanaka, T.; Tung, V.; et al. Plasmon-Enhanced Solar-Driven Hydrogen Evolution Using Titanium Nitride Metasurface Broadband Absorbers. *ACS Photonics* **2021**, *8*, 3125–3132. [CrossRef]
92. Dutta, A.; Naldoni, A.; Malara, F.; Govorov, A.O.; Shalaev, V.M.; Boltasseva, A. Gap-plasmon enhanced water splitting with ultrathin hematite films: The role of plasmonic-based light trapping and hot electrons. *Faraday Discuss.* **2019**, *214*, 283–295. [CrossRef] [PubMed]





Article

# Facile Microwave Assisted Synthesis of Silver Nanostars for Ultrasensitive Detection of Biological Analytes by SERS

Radu Nicolae Revnic<sup>1</sup>, Gabriela Fabiola Știufiuc<sup>2,3,\*</sup>, Valentin Toma<sup>3</sup>, Anca Onaciu<sup>3,4</sup>, Alin Moldovan<sup>3</sup>, Adrian Bogdan Țigu<sup>5</sup>, Eva Fischer-Fodor<sup>6</sup>, Romulus Tetean<sup>2</sup>, Emil Burzo<sup>2</sup> and Rareș Ionuț Știufiuc<sup>3,4,\*</sup>

- <sup>1</sup> Department of Family Medicine, "Iuliu Hatieganu" University of Medicine and Pharmacy, 2-4 Clinicilor Street, 400006 Cluj-Napoca, Romania
- <sup>2</sup> Faculty of Physics, "Babes-Bolyai" University, 1 Kogalniceanu Street, 400084 Cluj-Napoca, Romania
- <sup>3</sup> Department of BioNanoPhysics, MedFuture Research Center for Advanced Medicine, "Iuliu Hatieganu" University of Medicine and Pharmacy, 4-6 Pasteur Street, 400337 Cluj-Napoca, Romania
- <sup>4</sup> Department of Pharmaceutical Physics & Biophysics, Faculty of Pharmacy, "Iuliu Hatieganu" University of Medicine and Pharmacy, 6 Pasteur Street, 400349 Cluj-Napoca, Romania
- <sup>5</sup> Department of Translational Medicine, MedFuture Research Center for Advanced Medicine, "Iuliu Hatieganu" University of Medicine and Pharmacy, 4-6 Pasteur Street, 400337 Cluj-Napoca, Romania
- <sup>6</sup> Oncology Institute "Prof. Dr. Ion Chiricuta", 400015 Cluj-Napoca, Romania
- \* Correspondence: gabriela.stiufiuc@ubbcluj.ro (G.F.Ș.); rares.stiufiuc@umfcluj.ro (R.I.Ș.); Tel.: +40-726-340-278 (R.I.Ș.)

**Abstract:** We report a very simple, rapid and reproducible method for the fabrication of anisotropic silver nanostars (AgNS) that can be successfully used as highly efficient SERS substrates for different bioanalytes, even in the case of a near-infra-red (NIR) excitation laser. The nanostars have been synthesized using the chemical reduction of Ag<sup>+</sup> ions by trisodium citrate. This is the first research reporting the synthesis of AgNS using only trisodium citrate as a reducing and stabilizing agent. The key elements of this original synthesis procedure are rapid hydrothermal synthesis of silver nanostars followed by a cooling down procedure by immersion in a water bath. The synthesis was performed in a sealed bottom flask homogeneously heated and brought to a boil in a microwave oven. After 60 s, the colloidal solution was cooled down to room temperature by immersion in a water bath at 35 °C. The as-synthesized AgNS were washed by centrifugation and used for SERS analysis of test molecules (methylene blue) as well as biological analytes: pharmaceutical compounds with various Raman cross sections (doxorubicin, atenolol & metoprolol), cell lysates and amino acids (methionine & cysteine). UV-Vis absorption spectroscopy, (Scanning) Transmission Electron Microscopy ((S)TEM) and Atomic Force Microscopy (AFM) have been employed for investigating nanostars' physical properties.

**Keywords:** anisotropic silver nanostars; SERS; bioanalytes; cell lysates; pharmaceutical compounds

**Citation:** Revnic, R.N.; Știufiuc, G.F.; Toma, V.; Onaciu, A.; Moldovan, A.; Țigu, A.B.; Fischer-Fodor, E.; Tetean, R.; Burzo, E.; Știufiuc, R.I. Facile Microwave Assisted Synthesis of Silver Nanostars for Ultrasensitive Detection of Biological Analytes by SERS. *Int. J. Mol. Sci.* **2022**, *23*, 8830. <https://doi.org/10.3390/ijms23158830>

Academic Editor: Antonino Mazzaglia

Received: 28 June 2022

Accepted: 6 August 2022

Published: 8 August 2022

**Publisher's Note:** MDPI stays neutral with regard to jurisdictional claims in published maps and institutional affiliations.



**Copyright:** © 2022 by the authors. Licensee MDPI, Basel, Switzerland. This article is an open access article distributed under the terms and conditions of the Creative Commons Attribution (CC BY) license (<https://creativecommons.org/licenses/by/4.0/>).

## 1. Introduction

Plasmonic nanoparticles are in the limelight of modern nanotechnology applications, basically owing to their unique optical properties that are strongly dependent on their shape and size. The possible use of plasmonic nanoparticles as highly effective Surface Enhanced Raman Spectroscopy (SERS) substrates when using a NIR excitation laser led to the development of a plethora of synthesis methods for different types of noble metal nanoparticles, both isotropic or anisotropic [1,2]. Over time, it turned out that spherical isotropic plasmonic nanoparticles have a limited applicability as SERS substrates given their relatively low electromagnetic field enhancement. As a result, different aggregation techniques, leading to the creation of randomly oriented hot-spots capable of locally amplifying the Raman spectra of the analytes have been reported in the literature [3].

From the point of view of analytical quantitative analysis, the aggregation technique holds a major drawback since the process cannot be controlled and the amplified Raman spectra of analytes lack reproducibility [4,5]. The random orientation of the hot-spots

and the very poor reproducibility of the amplified Raman spectra represent the two most important obstacles that must be overcome for the introduction of SERS spectroscopy in clinical ultrasensitive biodetection applications.

On the other hand, it has been demonstrated that the strong Surface Plasmon Resonance (SPR) effect observed in the case of anisotropic nanoparticles significantly influences the SERS effect [6,7]. SERS enhancement depends on the size but mostly on the shape of the plasmonic substrates. For instance, in the case of anisotropic silver nanoparticles, it has been shown that the amplification can be 20 times higher than that of silver nanospheres [8].

In this paper, we present a very simple and rapid method for the creation of a new class of SERS substrates able to generate highly reproducible SERS spectra for molecules of biomedical interest, possessing a very low Raman cross section (e.g., pharmaceutical compounds, cell lysates). The here-proposed plasmonic substrates have the capacity to operate even in the case of using a NIR excitation laser, which represents a *sine qua non* condition for SERS measurements performed on bio analytes. The plasmonic substrates consist of silver nanostars, synthesized using an original method developed in MedFuture's Research Center laboratory. The only chemical precursors employed in this wet-chemical procedure are silver nitrate and trisodium citrate, with no addition of any other reagents. The microwave-assisted synthesis of the nanostars has been performed in a sealed bottom flask, which turned out to be a critical parameter in the synthesis process. The chemical reaction took place inside of a microwave oven capable of generating an almost uniform temperature in the whole volume of the liquid in a very short period. By the end of the synthesis process, the colloidal solution was immersed in a water bath at 35 °C. The SERS activity of the here-proposed AgNS has been evaluated on test molecules (Methylene Blue) as well as on pharmaceutical compounds with low Raman cross section (doxorubicin, atenolol & metoprolol), cell lysates and amino acids (cysteine & methionine), by pouring a very small volume of colloidal solution (~1.5 µL) onto a MgF<sub>2</sub> glass plate heated at 50 °C, prior to the deposition of the analytes. The quality of the vibrational spectra collected using the here-proposed plasmonic substrates represents strong experimental evidence of their versatility, especially in the case of bioanalytes.

## 2. Results and Discussion

In this study we proposed an original procedure for the microwave-assisted synthesis of silver nanostars by involving trisodium citrate as a reducing and stabilizing agent of Ag<sup>+</sup> ions. The role of microwave heating is to create a more homogenous thermal environment for the synthesis procedure and to speed up the process as shown in literature [9]. Once the synthesis procedure was completed, the nanostars' morphology was analyzed by microscopic complementary techniques (TEM/STEM, AFM). Their plasmonic properties have been tested on several biological analytes by means of SERS using a NIR excitation wavelength (785 nm). The SERS experiments were carried out on interconnected AgNS that can be regarded as solid plasmonic substrates, as well as on individual nanostars that can be easily localized on the MgF<sub>2</sub> port-probe using an optical microscope.

### 2.1. Characterization of AgNS Colloids by UV-Vis Spectroscopy

UV-Vis absorption spectroscopy is the first experiment that can be employed for the characterization of colloidal solutions containing nanoparticles of different types and shapes. The UV-Vis absorption spectrum of the colloidal solution containing silver nanostars is presented in Figure 1 together with the optical images of the colloids, right after synthesis (inset a) and after purification (inset b) through centrifugation, respectively.

The spectrum is characterized by the occurrence of a strong absorption peak located around 420 nm, specific for silver nanoparticles. The broadness of this peak is quite high with respect to isotropic silver nanoparticles [10–12], and this is a direct consequence of the presence of anisotropic silver nanostars in the solution. The full-width half-maximum (FWHM) value is ~200 nm in this case, which is more than double as compared to silver spherical nanoparticles. However, this property allows the use of NIR excitation lasers

(785/830 nm) for SERS analysis of biological samples, strongly decreasing their intrinsic fluorescence and facilitating the recording of highly qualitative SERS spectra of pharmaceutical compounds, amino acids or even cell lysates.

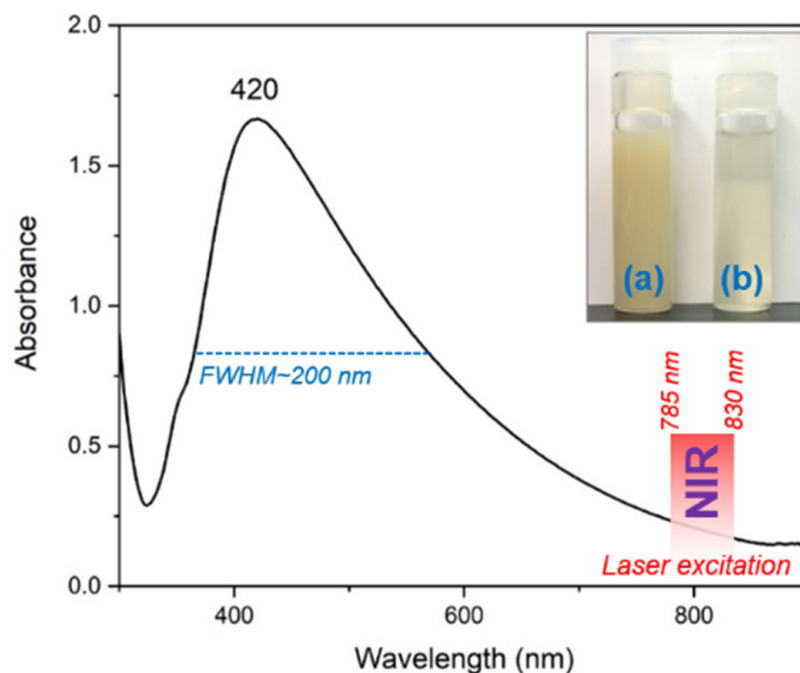


**Figure 1.** UV-Vis absorption spectra of the colloidal solution containing AgNS. The inset shows an optical image of the colloidal solutions before (a) and after purification through centrifugation (b) respectively.

## 2.2. Transmission Electron Microscopy (TEM) and Scanning Transmission Electron Microscopy (STEM) Characterization

TEM together with STEM has been employed for a proper characterization of AgNS. A typical TEM image of an individual nanostar is presented in Figure 2a, together with a zoom image of its central part (Figure 2b).

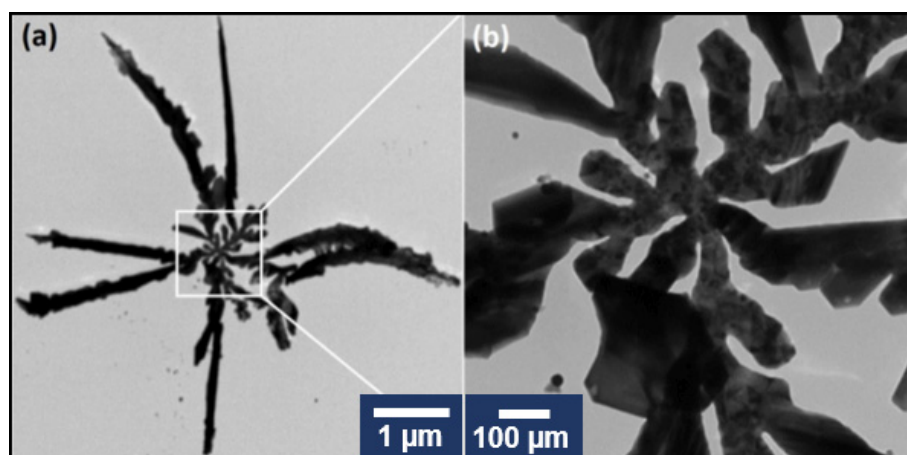


**Figure 2.** TEM image of a typical individual silver nanostar (a). TEM image of the central zone of the nanostar (b).

One can clearly distinguish that our AgNS consist of a central nanoparticle interconnected with several highly one-dimensional individual arms. The Energy Dispersive Analysis (EDS) confirmed that AgNS are composed of silver atoms (Figure S1). The STEM images of similar AgNS are presented in Figure 3.

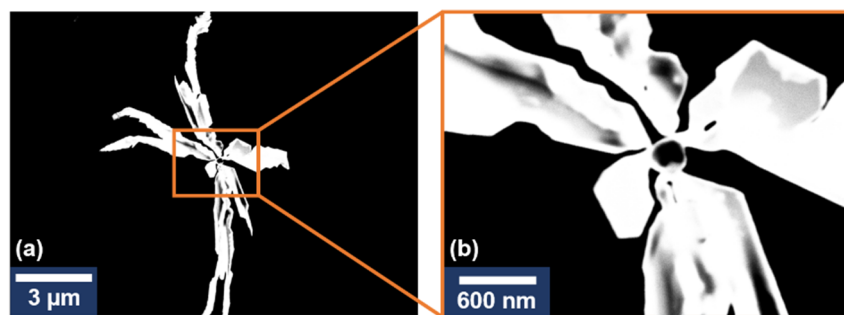


**Figure 3.** STEM image of an individual silver nanostar (a). STEM image of the central zone of the nanostar (b).

The STEM images revealed the same structure as the one obtained from TEM images. The AgNS appear as branched 3D structures with high electron-scattering capacities. The structure points towards a {1 1 1} oriented crystalline structure [13] with a single center seed particle being the origin of the branching arms. Differences in the contrast of the outer section of the nanostars (Figure 3b) are also indicative of a {1 0 0} preferential growth of the crystals as presented in [14] and, thus, could be interpreted as having a 2D structure. These results are complementary to the TEM morphological analysis of the nanostars presented in Figure 2.

### 2.3. Atomic Force Microscopy (AFM) Characterization

The evolution of the AgNS deposited onto the heated MgF<sub>2</sub> glass slides was evaluated by means of AFM measurements (Figure 4). All the measurements were performed on semi-contact operating mode. The 2D and 3D topographic images (height images) were recorded together with phase contrast ones (data not shown). The phase contrast images gave us a clear indication regarding the substrate's composition which is a very homogenous one (very small phase variations have been detected on the samples). On the other hand, the topographic images confirmed the presence on the substrate of interconnected AgNS that coexist with individual ones (Figure 4a). Their sizes vary between a few hundred nanometers and a few microns. The cross-sectional analysis of the individual nanoflowers revealed they have a maximum height of 600 nm, which is much smaller (~one order of magnitude) than their lateral dimensions.

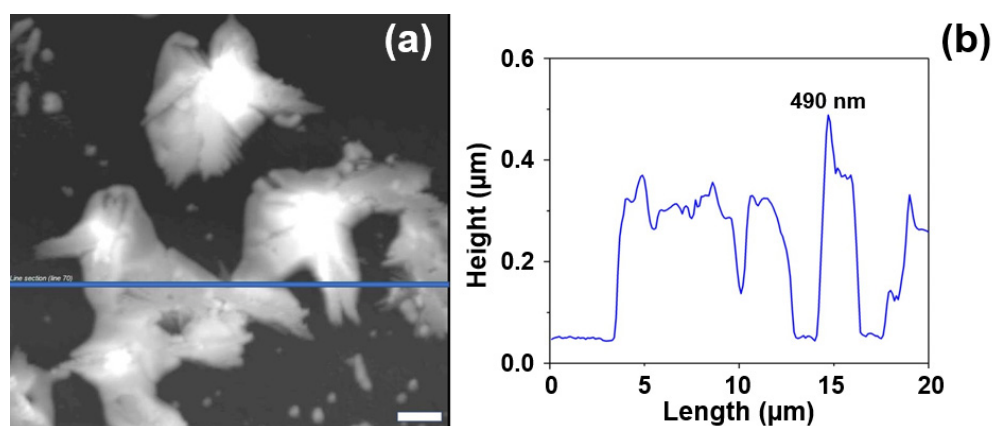


**Figure 4.** AFM topological image of several interconnected nanostars self-organized on the MgF<sub>2</sub> surface (a). Corresponding cross-sectional analysis of AgNS (b). The scale bar represents 2 μm.

As a result of the slow heating process, the space between the individual one-directional arms (identified in the TEM images) has been completely filled, as can be noticed in the high-resolution topographic image presented in Figure 5. The formation of the 2D network has been also observed.

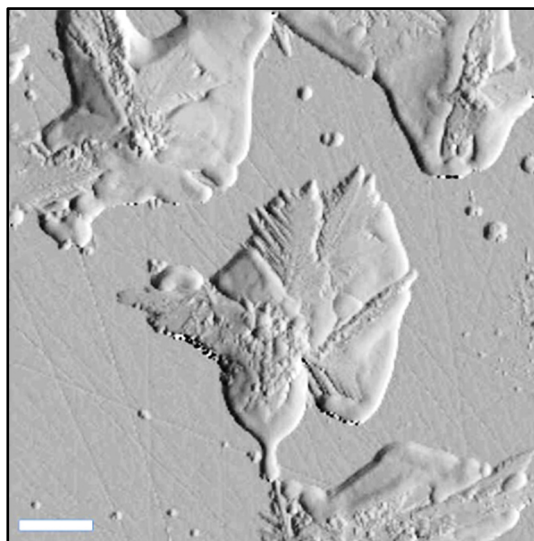


**Figure 5.** High resolution AFM topographical image of silver nanostars. The scale bar represents 2  $\mu\text{m}$ .

#### 2.4. SERS and Raman Analysis

All SERS measurements included in this study were performed on plasmonic substrates obtained by pouring colloidal solutions containing silver nanostars on Raman transparent  $\text{MgF}_2$  glass slides heated at 50  $^\circ\text{C}$ . The as-obtained plasmonic substrates allowed the recording of very reproducible SERS spectra on different regions of the substrate for all the bioanalytes here presented.

All Raman measurements were performed on  $\text{MgF}_2$  transparent glass using a 785 nm laser excitation.

The SERS spectrum of the pristine silver substrate were recorded under the same experimental conditions and can be observed in Figure 6. The intensity of the vibrational bands is very low as can be seen in the figure, emphasizing, the capacity of the here-proposed plasmonic substrates to be employed for SERS analysis of various bioanalytes.

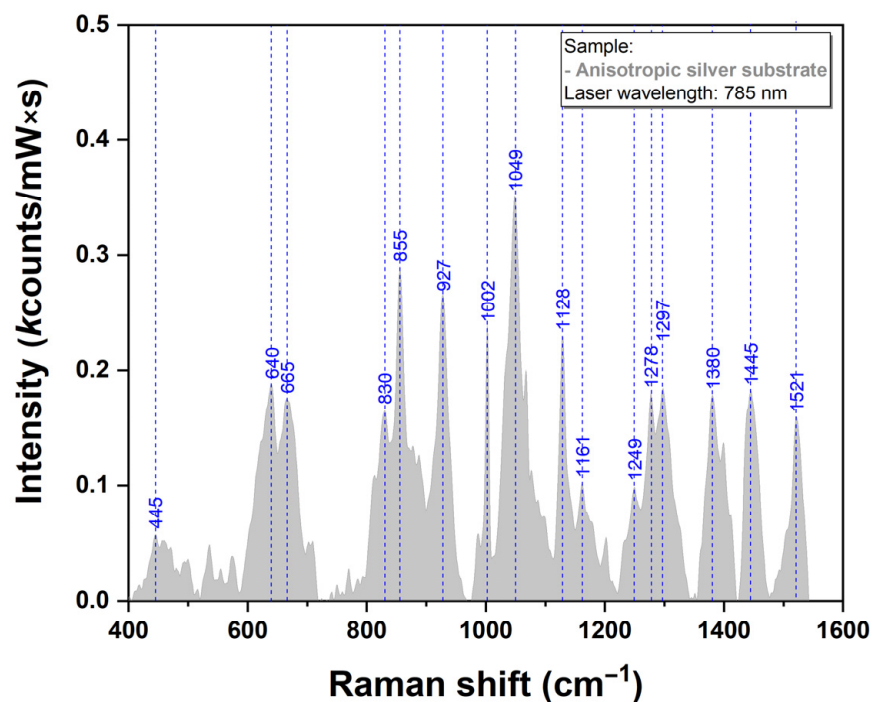


**Figure 6.** Raman spectra of AgNS recorded using a 785 nm laser excitation.

The enhancement capabilities of the plasmonic substrate were first tested on rhodamine 6G (R6G). This analyte was used in a first instance for testing the reproducibility of the recorded spectra. Finally, the Raman and SERS spectra of R6G were employed for the calculation of the substrate's enhancement factor (EF). In the case of SERS, 1  $\mu\text{L}$  solution of 1 mM R6G was deposited on the plasmonic substrate and left to dry. In the case of Raman, 1  $\mu\text{L}$  solution of 1 mM R6G was poured on a  $\text{MgF}_2$  glass slide and left to dry. The SERS spectrum of R6G is presented in Figure S2b. A value of  $\sim 8 \times 10^3$  was calculated for the substrate's enhancement factor (EF). This value was obtained by comparing Raman (Figure S2a) and SER spectra of R6G (Figure S2b).

For a proper assessment of the substrates' plasmonic properties, we performed SERS measurements using as analytes a standard test molecule (methylene blue-MB) and three pharmaceutical compounds having different Raman cross sections: doxorubicin (DOX), atenolol (ATE), and metoprolol (MET). The capacity of our AgNS to perform as very efficient plasmonic substrates was further tested on cell lysates (DLD1 cells) and two amino acids (methionine and cysteine) The spectra were recorded using NIR excitation laser (785 nm).

In the case of MB and DOX, previous studies reported comprehensive analysis of their SERS spectra collected on different plasmonic substrates together with a complete vibrational band assignment. Given their great Raman cross section, they can be considered "standard" analytes for the evaluation of the plasmonic properties for new substrates [10,12,15]. The MB Raman and SERS spectra, collected on our substrates, are presented in Figure 7.

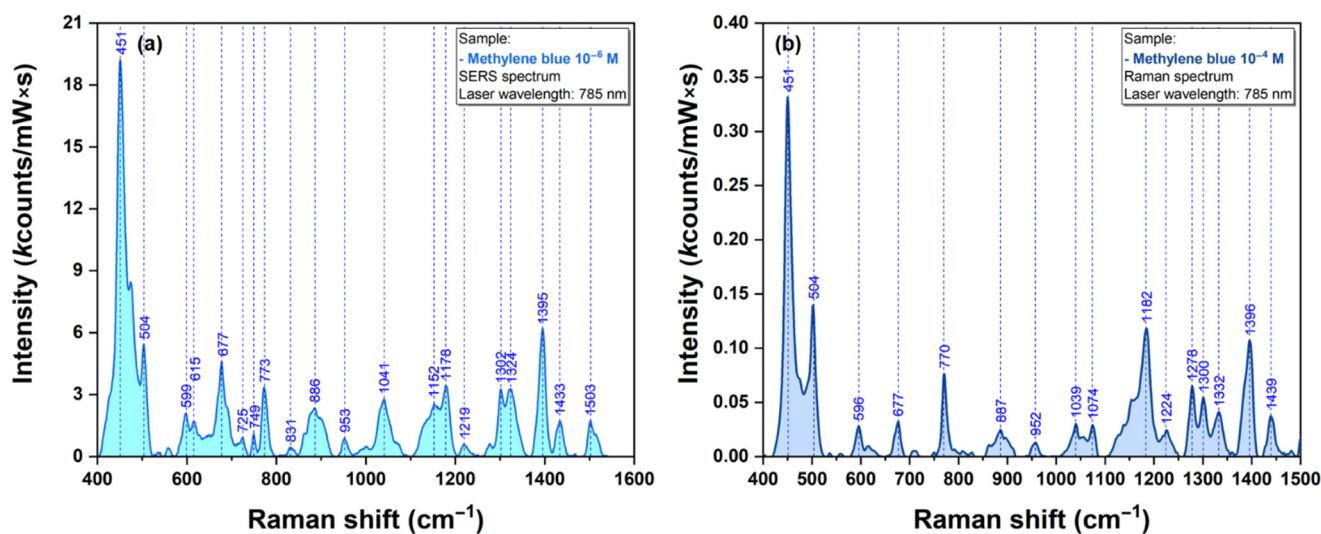


**Figure 7.** SERS spectrum of dried MB solution (1  $\mu\text{M}$ ) using a 785 nm excitation laser (a). Raman spectrum of dried MB solution (1  $\mu\text{M}$ ) using a 785 nm excitation laser (b).

The major vibrational peaks of MB, as described in the literature, are clearly visible even for an analyte concentration of  $\mu\text{M}$ . The main vibrational bands of MB are located at 451, 504, 677, 773, 1178 and 1395  $\text{cm}^{-1}$ . The most visible ones can be assigned to C-N-C skeletal deformations (447 and 500  $\text{cm}^{-1}$ ) and asymmetric C-N stretching (1395  $\text{cm}^{-1}$ ). The assignment of the most important bands is presented in Table S1. The spectrum is similar with the one recorded using other types of plasmonic substrates, suggesting a similar geometry of interaction between the substrate and the analyte.

The first pharmaceutical compound that was employed for testing the plasmonic substrate was doxorubicin. The typical vibrational frequencies of DOX are presented in Figure 8. The SERS spectrum of DOX included in this figure were collected using the individual nanostar highlighted in the inset of Figure 8. This spectrum is very similar to those reported in the scientific literature [16] recorded using other plasmonic substrates. The majority of DOX vibrational bands originate from the conjugated aromatic chromophore of

the drug molecule. A tentative assignment of the most important bands is summarized in Table S1.

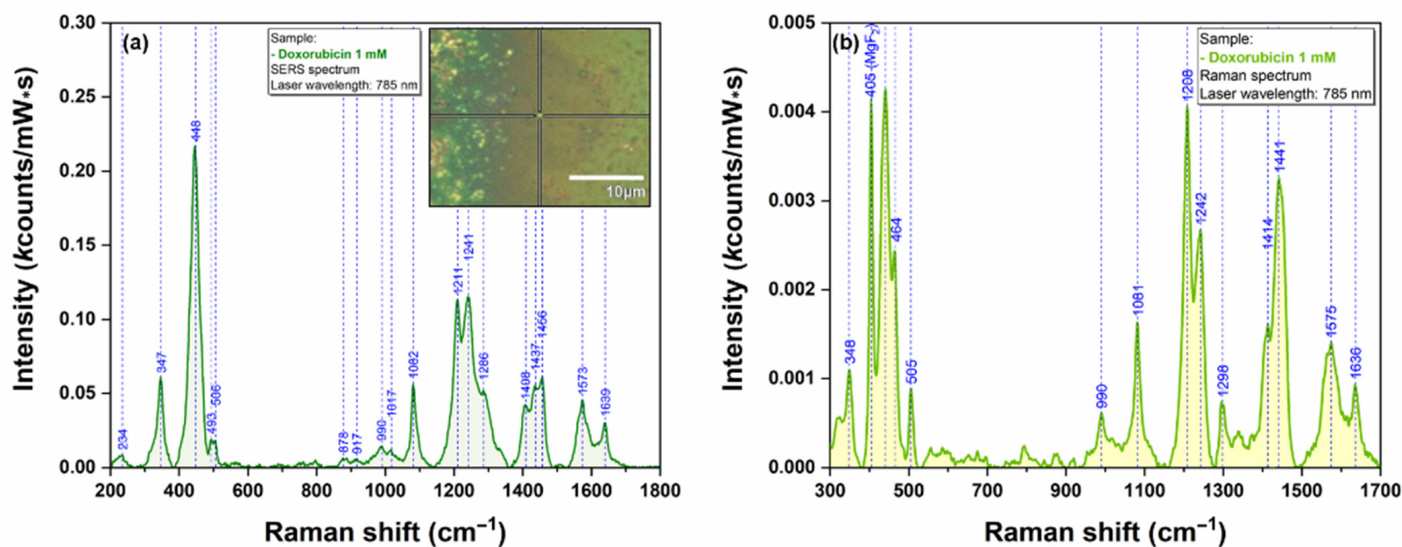


**Figure 8.** SERS spectrum of dried DOX solution (1 mM) collected on an isolated nanostar using a 785 nm excitation laser (a). The inset shows an optical image of the individual nanostar that has been used as plasmonic substrate. Raman spectrum of dried DOX solution (1 mM) collected using a 785 nm excitation laser (b).

In order to prove the capacity of the here-reported AgNS to be used as plasmonic substrates for biomolecules with low Raman cross section, we have performed SERS measurements on Metoprolol (Figure 9) and Atenolol (Figure 10). The spectra were recorded on an individual AgNS (MET) and on a solid substrate containing interconnected AgNS (ATE), respectively. The Raman spectra of MET and ATE are also presented (Figures 9b and 10b, respectively).

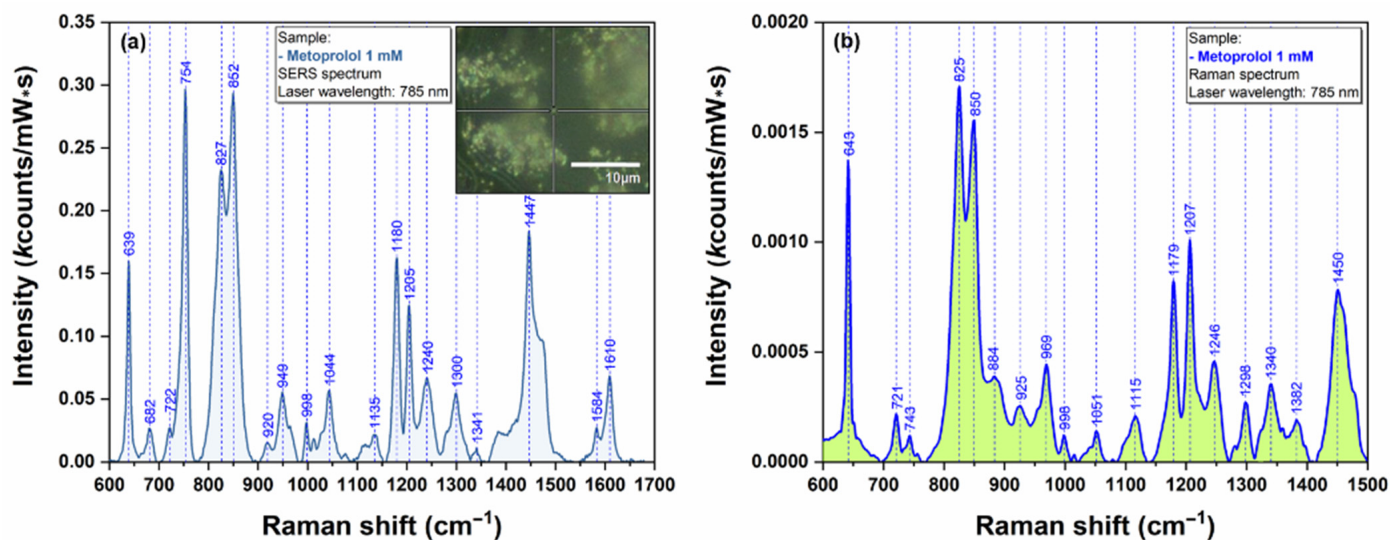


**Figure 9.** SERS spectrum of MET 1mM (a) collected on individual AgNS using a 785 nm laser. The inset in figure (a) shows an optical image of the individual nanostar that has been used for recording the spectra. Raman spectrum of MET 1 mM (b) collected using a 785 nm laser.

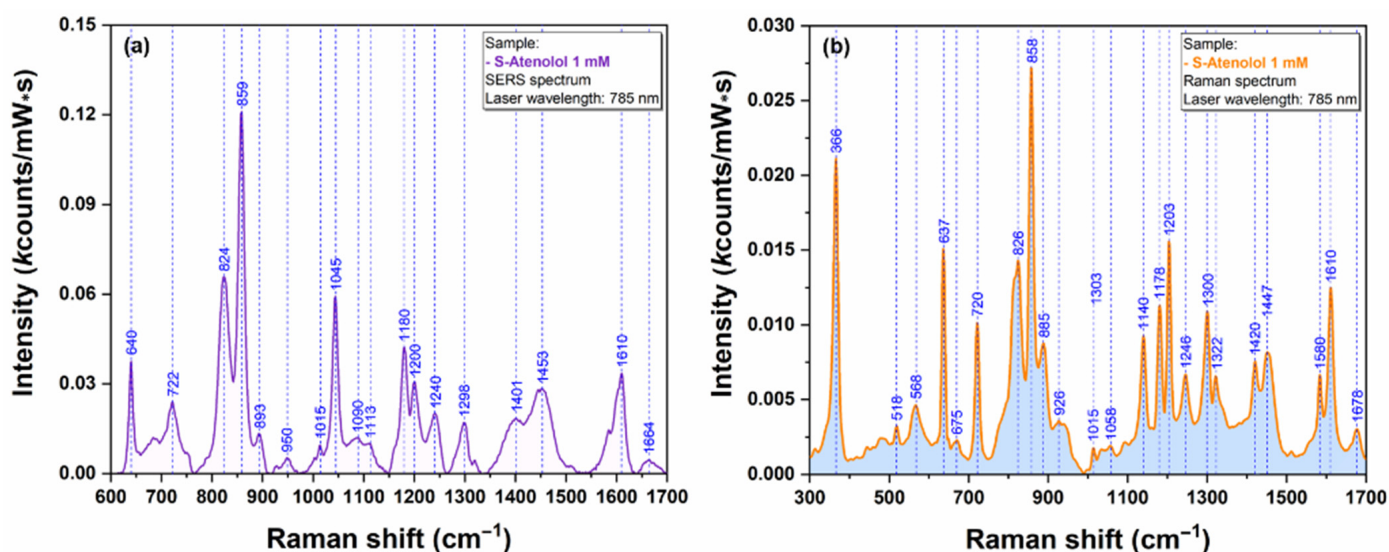


**Figure 10.** SERS spectrum of ATE 1 mM (a) collected on individual AgNS using a 785 nm laser. Raman spectrum of ATE 1 mM (b) collected using a 785 nm laser.

In the scientific literature, there are very few studies reporting a SERS analysis of these two pharmaceutical compounds belonging to the class of beta-blockers [11]. These two drug molecules have a very similar chemical structure. The central part of both molecules consists of a phenyl ring linked to an amine alkanol side chain containing the asymmetric carbon atom.

As expected, both spectra included in Figures 9 and 10 are very similar, being dominated by the bands assigned to the vibrational breathing mode of the central phenyl ring located at  $852\text{ cm}^{-1}$  (MET) and  $859\text{ cm}^{-1}$  (ATE), respectively. Other significant vibrational bands with their corresponding attributions are listed in Table S1. According to Moskovits' surface selection rules, this is a direct proof of a similar geometry of interaction between these two molecules and the plasmonic substrates [17]. On the other hand, the quality, reproducibility, and ease of recording of the SERS spectra can be attributed to the unique plasmonic properties of AgNS.

Very recently it has been shown that Raman/SERS spectroscopy has the potential to provide very useful information related to the nanoscale molecular interactions between analytes and plasmonic substrate [5,18].

As such, cell lysates were used for testing the plasmonic properties of our AgNS. A typical SERS spectrum of DLD1 cell lysate is presented in Figure 11a, while the Raman spectrum is presented in Figure 11b.

The spectrum from Figure 11 is dominated by a very intense vibrational peak at  $725\text{ cm}^{-1}$ . This peak can be assigned to the presence of adenine and adenosine as it has been recently shown by Genova et al. [19]. The presence of adenosine triphosphate in relatively high concentration could be an explanation for the strong intensity of this vibrational band. In the spectral fingerprint region ( $600\text{--}900\text{ cm}^{-1}$ ) one can detect the presence of another two distinct peaks at  $627\text{ cm}^{-1}$  and  $656\text{ cm}^{-1}$ . The latest peak can be assigned to guanine ring breathing vibrational mode. This behavior represents a strong proof of the fact that, in the case of untreated cells, one can detect the presence of the same biomolecular species responsible for the occurrence of specific vibrational bands. According to Barhoumi et al. [20], the rest of the prominent vibrational bands observed in the lysate spectrum can be assigned to vibration modes of  $\text{PO}_2$  ( $1094\text{ cm}^{-1}$ ) and adenine ( $1328$  &  $1586\text{ cm}^{-1}$ ), respectively.

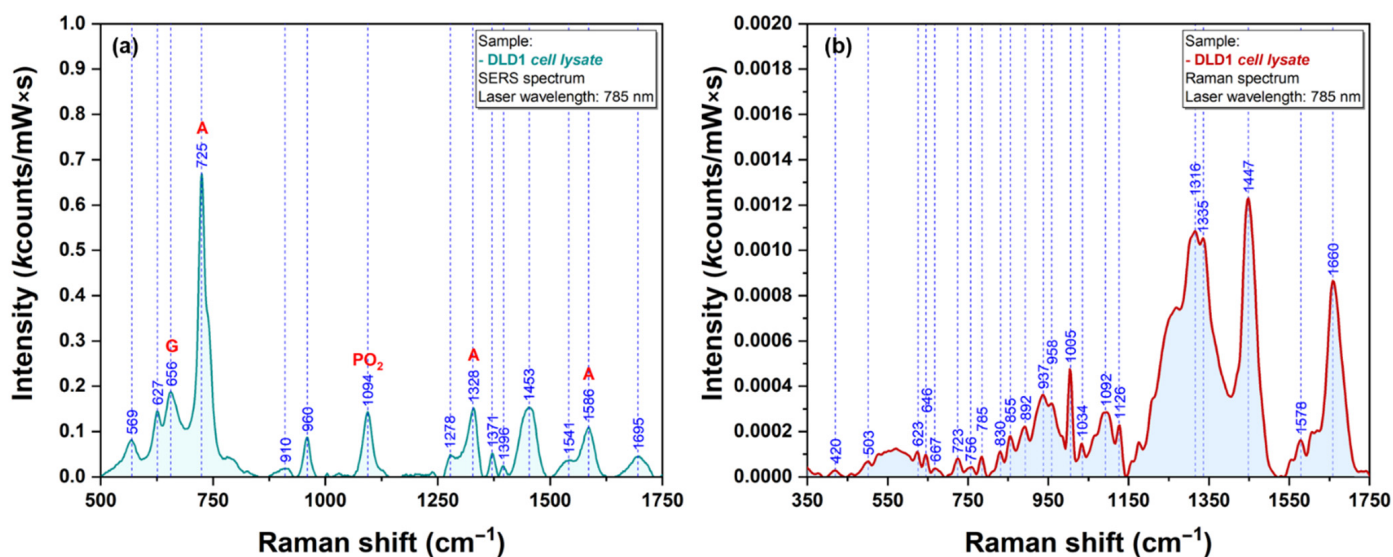


Figure 11. SERS spectra of DLD1 cell lysate obtained using a 785 nm excitation laser (a). Raman spectra of DLD1 cell lysate obtained using a 785 nm excitation laser (b).

The last class of bio analytes that were used for testing the Raman signal enhancing capacities of our plasmonic AgNS were the amino acids. We have chosen Cysteine (Cys) and Methionine (Met) because their sidechain contains one sulfur atom that has the capacity to interact directly with the silver surface [21]. SERS and Raman spectra of Cys and Met are presented in Figures 12 and 13, respectively.

The strong affinity of Sulphur atoms for silver surface is confirmed by the presence of two very intense vibrational bands ( $665\text{ cm}^{-1}$  for Cys &  $682\text{ cm}^{-1}$  for Met) that have been assigned to C-S stretching vibrations of the two amino acid, in SERS spectra of Cys (Figure 12a) and Met (Figure 13a). Nevertheless, the presence of a strong vibrational peak around  $1050\text{ cm}^{-1}$  ( $1054\text{ cm}^{-1}$  for Cys/ $1049\text{ cm}^{-1}$  in the case of Met) indicates a possible interaction of amino acids with the silver substrate through the amino group.

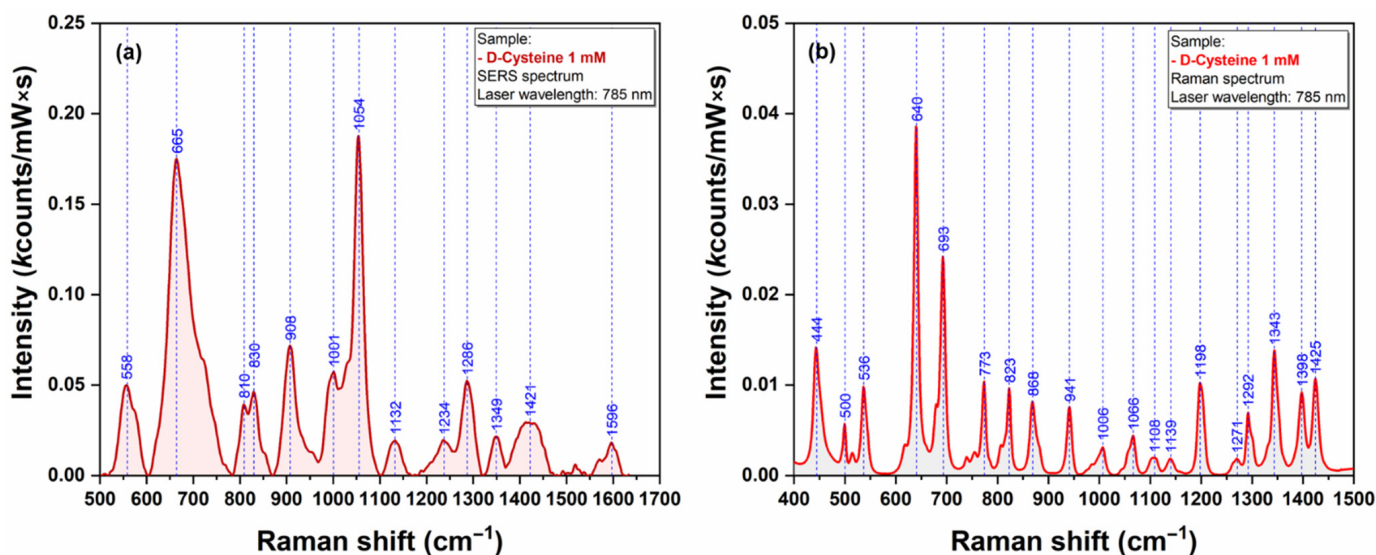
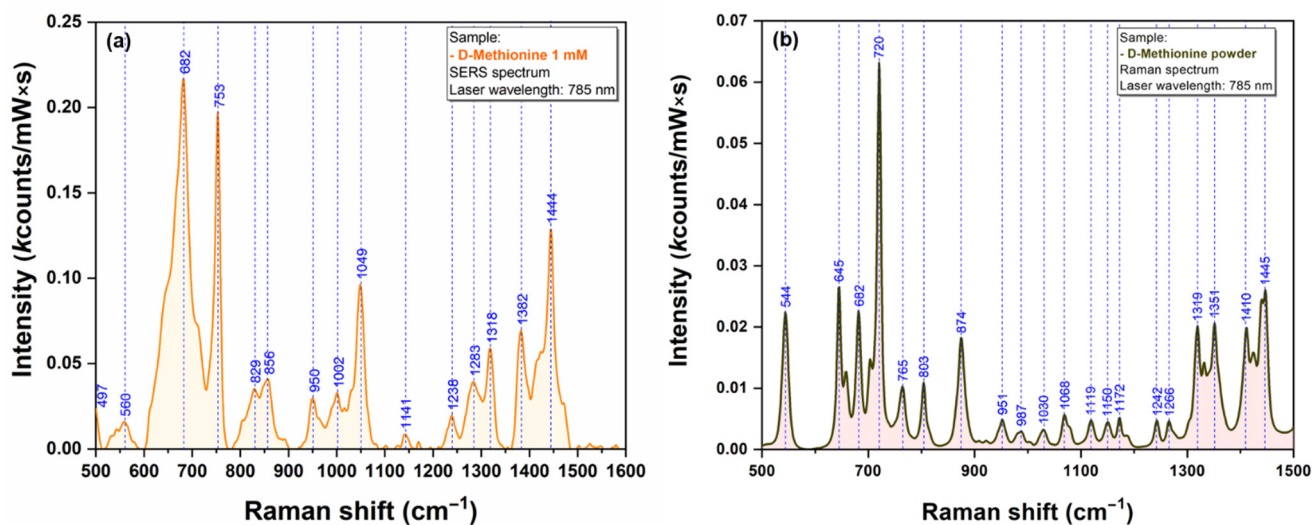


Figure 12. SERS (a) and Raman (b) spectra of Cysteine (1 mM) recorded using a 785 nm excitation laser.



**Figure 13.** SERS (a) and Raman (b) spectra of Methionine (1 mM) (a) recorded using a 785 nm excitation laser.

Table S1 represents a tentative assignment of the main vibrational bands for all the samples that were analyzed in this study.

### 3. Materials and Methods

#### 3.1. Materials

All chemical compounds employed in this paper were of analytical grade. Silver nitrate ( $\text{AgNO}_3$ ) and trisodium citrate were purchased from Roth (Karlsruhe, Germany) and Merck (Darmstadt, Germany), respectively. The aqueous solutions were prepared in Milli-Q water (Milli-Q®Direct Water Purification System, Darmstadt, Germany).  $\text{MgF}_2$  polished glasses (Crystran Ltd., Poole, UK), having a diameter of 20 mm, were used as port probes for the creation of the solid SERS substrates. The analytes and the pharmaceutical compounds used for SERS measurements (methylene blue MB, doxorubicin DOX, atenolol ATE, metoprolol MET, cysteine Cys and methionine Met) were purchased from Sigma-Aldrich (St. Louis, MO, USA). Cell culture products: Roswell Park Memorial Institute (RPMI 1640) cell culture medium, Fetal Bovine Serum (FBS), Glutamine, Penicillin/Streptomycin and Phosphate Buffered Saline solution (PBS 1X) were purchased from Gibco (Grand Island, NY, USA).

#### 3.2. Cell Culture and Lysates

DLD1 (ATCC® CCL-221™) colorectal carcinoma cells were acquired from American Type Culture Collection (ATCC, Manassas, VA, USA) and were maintained in RPMI 1640 cell culture medium, supplemented with 10% FBS, 1% Glutamine and 1% Penicillin/Streptomycin. During the experiment, the cells were stored in a humidified incubator at 37 °C and 5%  $\text{CO}_2$ .

For obtaining the cell lysates, the cells were detached from the culture flasks and washed three times with fresh complete medium, followed by three washing steps with PBS 1X. Then the cell pellet was washed three times with UltraPure DNase/RNase free water. The washing steps were performed by centrifugation of the cells at  $600\times g$ , for 5 min at room temperature. After the washing procedures, the cell pellet was resuspended in 333  $\mu\text{L}$  of UltraPure DNase/RNase free water and stored at  $-80\text{ }^\circ\text{C}$  until further use.

The lysate processing involved mechanical lysis steps. The samples were removed from  $-80\text{ }^\circ\text{C}$  and placed in the heating block at 37 °C for 15 min. The samples were sonicated with the following settings for the EpiShear 5/64' (2 mm) Probe Sonicator (Active Motif, Carlsbad, CA, USA): 18 s with pulse of 3 s and 80% amplitude (from a maximum intensity level of 200  $\mu\text{m}$ ). After the sonication process, the samples were stored at  $-80\text{ }^\circ\text{C}$  for 15 min, and the samples were sonicated and frozen two more times.

The cell lysate, processed as mentioned above, was stored at  $-80\text{ }^{\circ}\text{C}$  and thawed only when the sample was analyzed.

### 3.3. Fabrication of Silver NanoStars (AgNS)

Colloidal suspensions of silver nanostars (AgNS) were prepared using an original method developed in MedFuture's laboratories. The chemical reduction of  $\text{Ag}^+$  ions by trisodium citrate molecules were performed in a sealed-bottom flask introduced in the center of a microwave oven having a nominal power of 2100 W, operating at 2450 MHz capable of inducing water boiling ( $100\text{ }^{\circ}\text{C}$ ) after 30 s of irradiation. After 60 s of heating, the vials were removed from the oven, immersed in a water bath at  $35\text{ }^{\circ}\text{C}$  and let to accommodate at this temperature for 5 min, with no stirring. In a typical synthesis procedure, 10 mg of  $\text{AgNO}_3$  were dissolved in 50 mL of Milli-Q water and introduced in an empty 100 mL bottom flask. Trisodium citrate solution (1%, 1 mL) was added to the flask. The two solutions were gently stirred for 20 s, and then the bottom flask was sealed and introduced in the microwave oven. No sign of chemical reaction between the silver ions and the citrate molecules was observed at this stage. Afterwards, the solution was exposed to microwaves for 1 min. It was noted that, after 30 s of microwave exposure, the aqueous solution started to boil in the whole volume. After 15 more seconds, the solution suddenly changed its color from colorless to milky grey, indicating the successful formation of silver nanostars. By the end of the process, the colloidal solution was cooled down at room temperature using a two-step process. First the vials were immersed in a water bath at  $35\text{ }^{\circ}\text{C}$  for 5 min, and then they were brought to room temperature and left for another 5 min in air. The whole synthesis procedure took no more than 15 min.

### 3.4. Preparation of SERS Substrates

The SERS substrates were prepared by pouring  $1.5\text{ }\mu\text{L}$  of as-synthesized AgNS solution onto a  $\text{MgF}_2$  glass slide heated at  $50\text{ }^{\circ}\text{C}$ . After 2 min from the deposition, the glass slides were removed from the heated plate and the substrates were let to accommodate at room temperature for 15 min. Once this final procedure was completed, the SERS substrates containing self-aggregated as well as individual nanostars were ready for use.

### 3.5. Preparation of Samples for SERS and Raman Investigation

Stock aqueous solutions of standard Raman-test molecules (methylene blue MB) as well as of therapeutic agents (doxorubicin DOX, atenolol ATE, metoprolol MET) and amino acids (cysteine Cys and methionine Met) were prepared. The concentration of all stock solution was 1 mM. Further dilutions were prepared using Milli-Q water. Once the drying process of the solid SERS substrates was completed, a very small volume of analytes aqueous solution ( $1\text{ }\mu\text{L}$ ) was poured in the center of the solid substrate. The solution was left to dry for 30 min at room temperature. By the end of this process the samples were ready for SERS measurements, using a NIR excitation laser (785 nm).

The Raman spectra were recorded on dry solutions poured over Raman transparent  $\text{MgF}_2$  glass, using the same 785 nm laser excitation.

### 3.6. Characterization of Silver Nanostars and Solid Plasmonic Substrates

The colloidal solutions containing silver nanostars and the solid plasmonic substrates they formed were characterized by UV-VIS, STEM, TEM, AFM and SERS.

UV-Vis absorption measurements of the silver colloid were performed using a T92+ Spectrophotometer (PG Instruments, Lutterworth, UK) in the 190–900 nm wavelength range with a 2 nm resolution.

Electron microscopy measurements were performed on a Hitachi HT7700 Transmission Electron Microscope (Hitachi, Tokyo, Japan) operating at 120 kV, in the high-resolution mode.

The topography of the substrates was investigated by an Atomic Force Microscope (NT-MDT NTEGRA, NT-MDT Spectrum Instruments, Zelenograd, Russia) coupled with a

micro-Raman system. The topographic images presented in this paper were acquired in the semi-contact operating mode.

The SERS spectra were recorded using a multilaser confocal Renishaw InVia Reflex Raman spectrometer. The wavelength calibration was performed on an internal reference sample (silicon). The 785 and 830 nm laser lines were employed as the excitation sources, but preliminary tests have been performed also on 532 and 633 nm laser lines. The emitting laser power was measured for each laser and for each objective on top of the sample. The SERS spectra presented in this paper were recorded using a 50× objective and different acquisition times ranging from few seconds to 50 s. The spectral resolution of the spectrometer was  $0.5 \text{ cm}^{-1}$ . Baseline correction was applied to all SERS spectra, in order to eliminate the background. Each spectrum represents the average of a minimum of 30 spectral acquisitions. The baseline correction was performed by using the Wire 4.2 software provided by Renishaw (Gloucestershire, UK), with the inVia spectrometer. For all the spectra included in this study, the intensity of the vibrational bands is represented in  $\text{kcounts}/(\text{mW} \times \text{s})$  units.

The calculations of EF have been performed according to the procedure developed by Gupta and Weimar [22], using the following equation:

$$EF = \frac{M_{\text{Raman}} \times S_{\text{Surf}} \times I_{\text{Surf}}}{M_{\text{Surf}} \times S_{\text{Raman}} \times I_{\text{Raman}}}$$

where  $M_{\text{Surf}}$  and  $M_{\text{Raman}}$  are the numbers of molecules,  $S_{\text{Surf}}$  and  $S_{\text{Raman}}$  are the geometrical areas of the molecular films and  $I_{\text{Surf}}$  and  $I_{\text{Raman}}$  are the SERS/Raman intensities of the most intense vibrational band that was used for the calculation of EF ( $1510 \text{ cm}^{-1}$ ). Both measurements were performed using a 50× objective and an excitation laser of 785 nm. In the case of Raman measurements, a 100% laser power was used, the acquisition time was 10 s and the number of spectral acquisitions was 4. In the case of SERS measurement, the only modification that was made was the laser power which was set to 0.1%. The laser intensity, measured on sample surface, was 113 mW (100 % laser power) and 0.22 mW (0.1% laser power), respectively. The intensities of all vibrational bands included in this study were plotted in  $\text{kcounts}/(\text{mW} \times \text{s})$  units. In the case of Raman/SERS measurements employed for EF calculation, 1 mM aqueous solutions of R6G were used. The diameter of the circular spot was ~2 mm in both cases. The Raman/SERS values of  $1510 \text{ cm}^{-1}$  band intensities were 43.3 and 0.0054  $\text{kcounts}/(\text{mW} \times \text{s})$ , respectively.

#### 4. Conclusions

In this research, we report a very simple, rapid and reproducible microwave-assisted method for the fabrication of anisotropic silver nanostars (AgNS) that can be successfully used as highly efficient SERS substrates for a broad range of bioanalytes: pharmaceutical compounds, cell lysates and/or amino acids. The AgNS consist of a central nanoparticle interconnected with several highly one-dimensional individual arms having a star shape. The microwave-assisted synthesis of the nanostars was performed in a sealed-bottom flask in a very short time interval (less than 3 min). The only chemical precursors employed in this wet-chemical procedure were silver nitrate and trisodium citrate, with no addition of any other reagents. Based on their unique properties, our plasmonic substrates have the capacity to generate very intense SERS spectra even in the case of using a NIR excitation laser, which represents a sine qua non condition for SERS measurements on biological samples.

The high quality and reproducibility of the vibrational spectra collected using the here-proposed plasmonic substrates represents strong experimental evidence of their versatility and application potential, especially in the case of bioanalytes.

**Supplementary Materials:** The supporting information can be downloaded at: <https://www.mdpi.com/article/10.3390/ijms23158830/s1>. References [11,16,22–44] are cited in the supplementary materials.

**Author Contributions:** Conceptualization, R.N.R., R.I.Ș. and G.F.Ș.; methodology, V.T., A.B.T., A.M., E.F.-F. and R.I.Ș.; software, V.T., E.F.-F. and R.T.; validation, E.B., G.F.Ș. and R.I.Ș.; formal analysis, V.T.; investigation, A.B.T. and E.F.-F.; resources, R.I.Ș.; data curation, V.T., G.F.Ș. and A.O.; writing—original draft preparation, G.F.Ș., A.B.T., A.M., A.O., V.T. and R.I.Ș.; writing—review and editing, G.F.Ș. and R.I.Ș.; visualization, A.M. and V.T.; supervision, R.N.R., E.B., R.T. and R.I.Ș.; project administration, R.N.R.; funding acquisition, R.I.Ș. All authors have read and agreed to the published version of the manuscript.

**Funding:** This research was part of grant no. PN-III-P4-ID-PCCF-2016-0112 funded by Executive Agency for Higher Education, Research, Development and Innovation Funding (UEFISCDI), Romanian Ministry of Education and Research.

**Institutional Review Board Statement:** Not applicable.

**Informed Consent Statement:** Not applicable.

**Data Availability Statement:** Not applicable.

**Acknowledgments:** This work was granted by project PDI-PFE-CDI 2021, entitled Increasing the Performance of Scientific Research, Supporting Excellence in Medical Research and Innovation, PROGRES, no. 40PFE/30.12.2021.

**Conflicts of Interest:** The authors declare no conflict of interest.

## References

1. Parak, W.J.; Gerion, D.; Pellegrino, T.; Zanchet, D.; Micheel, C.; Williams, S.C.; Boudreau, R.; Le Gros, M.A.; Larabell, C.A.; Alivisatos, A.P. Biological applications of colloidal nanocrystals. *Nanotechnology* **2003**, *14*, R15–R27. [CrossRef]
2. Reguera, J.; Langer, J.; Jiménez de Aberasturi, D.; Liz-Marzán, L.M. Anisotropic metal nanoparticles for surface enhanced Raman scattering. *Chem. Soc. Rev.* **2017**, *46*, 3866–3885. [CrossRef] [PubMed]
3. Yamamoto, S.; Fujiwara, K.; Watarai, H. Surface-Enhanced Raman Scattering from Oleate-Stabilized Silver Colloids at a Liquid/Liquid Interface. *Anal. Sci.* **2004**, *20*, 1347–1352. [CrossRef] [PubMed]
4. Garcia-Leis, A.; Garcia-Ramos, J.V.; Sanchez-Cortes, S. Silver Nanostars with High SERS Performance. *J. Phys. Chem. C* **2013**, *117*, 7791–7795. [CrossRef]
5. Stiuftuc, R.; Iacovita, C.; Stiuftuc, G.; Bodoki, E.; Chis, V.; Lucaciu, C.M. Surface mediated chiral interactions between cyclodextrins and propranolol enantiomers: A SERS and DFT study. *Phys. Chem. Chem. Phys.* **2015**, *17*, 1281–1289. [CrossRef] [PubMed]
6. Wrzosek, B.; Kitahama, Y.; Ozaki, Y. SERS Blinking on Anisotropic Nanoparticles. *J. Phys. Chem. C* **2020**, *124*, 20328–20339. [CrossRef]
7. Caro, C.; Quaresma, P.; Pereira, E.; Franco, J.; Pernia Leal, M.; García-Martín, M.; Royo, J.; Oliva-Montero, J.; Merklings, P.; Zaderenko, A.; et al. Synthesis and Characterization of Elongated-Shaped Silver Nanoparticles as a Biocompatible Anisotropic SERS Probe for Intracellular Imaging: Theoretical Modeling and Experimental Verification. *Nanomaterials* **2019**, *9*, 256. [CrossRef] [PubMed]
8. Mai Ngoc, T.A.; Nguyen, D.T.D.; Ngo, V.K.T.; Nguyen Thi, P.P.; Nguyen, D.H.; Nguyen-Le, M.-T. A Systematic Study of the One-Pot Fabrication of Anisotropic Silver Nanoplates with Controllable Size and Shape for SERS Amplification. *Plasmonics* **2020**, *15*, 2185–2194. [CrossRef]
9. Barani, H.; Mahltig, B. Microwave-Assisted Synthesis of Silver Nanoparticles: Effect of Reaction Temperature and Precursor Concentration on Fluorescent Property. *J. Clust. Sci.* **2022**, *33*, 101–111. [CrossRef]
10. Stiuftuc, G.F.; Toma, V.; Buse, M.; Mărginean, R.; Morar-Bolba, G.; Culic, B.; Tetean, R.; Leopold, N.; Pavel, I.; Lucaciu, C.M.C.M.; et al. Solid Plasmonic Substrates for Breast Cancer Detection by Means of SERS Analysis of Blood Plasma. *Nanomaterials* **2020**, *10*, 1212. [CrossRef]
11. Farcas, A.; Iacovita, C.; Vinteler, E.; Chis, V.; Stiuftuc, R.; Lucaciu, M. The Influence of Molecular Structure Modifications on Vibrational Properties of Some Beta Blockers: A Combined Raman and DFT Study. *J. Spectrosc.* **2016**, *2016*, 1–9. [CrossRef]
12. Stiuftuc, R.; Iacovita, C.; Lucaciu, C.M.; Stiuftuc, G.; Dutu, A.G.; Braescu, C.; Leopold, N. SERS-active silver colloids prepared by reduction of silver nitrate with short-chain polyethylene glycol. *Nanoscale Res. Lett.* **2013**, *8*, 47. [CrossRef]
13. Zaheer, Z. Rafiuddin Multi-branched flower-like silver nanoparticles: Preparation and characterization. *Colloids Surf. A Physicochem. Eng. Asp.* **2011**, *384*, 427–431. [CrossRef]
14. Bakshi, M.S. Room Temperature Surfactant Assisted Crystal Growth of Silver Nanoparticles to Nanoribbons. *J. Nanosci. Nanotechnol.* **2010**, *10*, 1757–1765. [CrossRef]

15. Colceriu-Şimon, I.M.; Hedeşiu, M.; Toma, V.; Armencea, G.; Moldovan, A.; Ştiufiuc, G.; Culic, B.; Țărmure, V.; Dinu, C.; Berindan-Neagoe, I.; et al. The Effects of Low-Dose Irradiation on Human Saliva: A Surface-Enhanced Raman Spectroscopy Study. *Diagnostics* **2019**, *9*, 101. [CrossRef]
16. Gautier, J.; Munnier, E.; Douziech-Eyrolles, L.; Paillard, A.; Dubois, P.; Chourpa, I. SERS spectroscopic approach to study doxorubicin complexes with Fe<sup>2+</sup> ions and drug release from SPION-based nanocarriers. *Analyst* **2013**, *138*, 7354. [CrossRef]
17. Moskovits, M. Surface selection rules. *J. Chem. Phys.* **1982**, *77*, 4408–4416. [CrossRef]
18. Ştiufiuc, G.F.; Toma, V.; Onaciu, A.; Chiş, V.; Lucaciu, C.M.; Ştiufiuc, R.I. Proving Nanoscale Chiral Interactions of Cyclodextrins and Propranolol Enantiomers by Means of SERS Measurements Performed on a Solid Plasmonic Substrate. *Pharmaceutics* **2021**, *13*, 1594. [CrossRef]
19. Genova, E.; Pelin, M.; Decorti, G.; Stocco, G.; Sergio, V.; Ventura, A.; Bonifacio, A. SERS of cells: What can we learn from cell lysates? *Anal. Chim. Acta* **2018**, *1005*, 93–100. [CrossRef]
20. Barhoumi, A.; Zhang, D.; Tam, F.; Halas, N.J. Surface-Enhanced Raman Spectroscopy of DNA. *J. Am. Chem. Soc.* **2008**, *130*, 5523–5529. [CrossRef]
21. Stewart, S.; Fredericks, P. Surface-enhanced Raman spectroscopy of amino acids adsorbed on an electrochemically prepared silver surface. *Spectrochim. Acta Part A Mol. Biomol. Spectrosc.* **1999**, *55*, 1641–1660. [CrossRef]
22. Gupta, R.; Weimer, W.A. High enhancement factor gold films for surface enhanced Raman spectroscopy. *Chem. Phys. Lett.* **2003**, *374*, 302–306. [CrossRef]
23. Dutta Roy, S.; Ghosh, M.; Chowdhury, J. Adsorptive parameters and influence of hot geometries on the SER(R) S spectra of methylene blue molecules adsorbed on gold nanocolloidal particles. *J. Raman Spectrosc.* **2015**, *46*, 451–461. [CrossRef]
24. Ikramova, S.B.; Utegulov, Z.N.; Dikhanbayev, K.K.; Gaipov, A.E.; Nemkayeva, R.R.; Yakunin, V.G.; Savinov, V.P.; Timoshenko, V.Y. Surface-Enhanced Raman Scattering from Dye Molecules in Silicon Nanowire Structures Decorated by Gold Nanoparticles. *Int. J. Mol. Sci.* **2022**, *23*, 2590. [CrossRef]
25. Ruan, C.; Wang, W.; Gu, B. Single-molecule detection of thionine on aggregated gold nanoparticles by surface enhanced Raman scattering. *J. Raman Spectrosc.* **2007**, *38*, 568–573. [CrossRef]
26. Harpster, M.H.; Zhang, H.; Sankara-Warrier, A.K.; Ray, B.H.; Ward, T.R.; Kollmar, J.P.; Carron, K.T.; Mecham, J.O.; Corcoran, R.C.; Wilson, W.C.; et al. SERS detection of indirect viral DNA capture using colloidal gold and methylene blue as a Raman label. *Biosens. Bioelectron.* **2009**, *25*, 674–681. [CrossRef]
27. Eliasson, C.; Lorén, A.; Murty, K.V.G.K.; Josefson, M.; Käll, M.; Abrahamsson, J.; Abrahamsson, K. Multivariate evaluation of doxorubicin surface-enhanced Raman spectra. *Spectrochim. Acta Part A Mol. Biomol. Spectrosc.* **2001**, *57*, 1907–1915. [CrossRef]
28. Chul, J.L.; Jae, S.K.; Mak, S.K.; Kwang, P.L.; Mu, S.L. The study of doxorubicin and its complex with DNA by SERS and UV-resonance Raman spectroscopy. *Bull. Korean Chem. Soc.* **2004**, *25*, 1211–1216. [CrossRef]
29. Beljebbar, A.; Sockalingum, G.D.; Angiboust, J.F.; Manfait, M. Comparative FT SERS, resonance Raman and SERRS studies of doxorubicin and its complex with DNA. *Spectrochim. Acta Part A Mol. Spectrosc.* **1995**, *51*, 2083–2090. [CrossRef]
30. Minati, L.; Maniglio, D.; Benetti, F.; Chiappini, A.; Speranza, G. Multimodal Gold Nanostars as SERS Tags for Optically-Driven Doxorubicin Release Study in Cancer Cells. *Materials* **2021**, *14*, 7272. [CrossRef] [PubMed]
31. Cozar, I.B.; Szabó, L.; Leopold, N.; Chiş, V.; David, L. Raman, sers and dft study of atenolol and metoprolol cardiovascular drugs. *Rom. Rep. Phys.* **2010**, *55*, 772–781.
32. Guerrini, L.; Garcia-Rico, E.; O’Loghlen, A.; Giannini, V.; Alvarez-Puebla, R.A. Surface-Enhanced Raman Scattering (SERS) Spectroscopy for Sensing and Characterization of Exosomes in Cancer Diagnosis. *Cancers* **2021**, *13*, 2179. [CrossRef]
33. Bruzas, I.; Lum, W.; Gorunmez, Z.; Sagle, L. Advances in surface-enhanced Raman spectroscopy (SERS) substrates for lipid and protein characterization: Sensing and beyond. *Analyst* **2018**, *143*, 3990–4008. [CrossRef]
34. Liu, M.; Liu, X.; Huang, Z.; Tang, X.; Lin, X.; Xu, Y.; Chen, G.; Kwok, H.F.; Lin, Y.; Feng, S. Rapid discrimination of colon cancer cells with single base mutation in KRAS gene segment using laser tweezers Raman spectroscopy. *J. Biophotonics* **2019**, *12*. [CrossRef]
35. Cao, Z.; Pan, X.; Yu, H.; Hua, S.; Wang, D.; Chen, D.Z.; Zhou, M.; Wu, J. A Deep Learning Approach for Detecting Colorectal Cancer via Raman Spectra. *BME Front.* **2022**, *2022*, 1–10. [CrossRef]
36. Liu, W.; Sun, Z.; Chen, J.; Jing, C. Raman Spectroscopy in Colorectal Cancer Diagnostics: Comparison of PCA-LDA and PLS-DA Models. *J. Spectrosc.* **2016**, *2016*, 1–6. [CrossRef]
37. Kneipp, J.; Kneipp, H.; Wittig, B.; Kneipp, K. Novel optical nanosensors for probing and imaging live cells. *Nanomed. Nanotechnol. Biol. Med.* **2010**, *6*, 214–226. [CrossRef]
38. Brozek-Pluska, B.; Musial, J.; Kordek, R.; Abramczyk, H. Analysis of Human Colon by Raman Spectroscopy and Imaging—Elucidation of Biochemical Changes in Carcinogenesis. *Int. J. Mol. Sci.* **2019**, *20*, 3398. [CrossRef]
39. Beton, K.; Wysocki, P.; Brozek-Pluska, B. Mevastatin in colon cancer by spectroscopic and microscopic methods—Raman imaging and AFM studies. *Spectrochim. Acta Part A Mol. Biomol. Spectrosc.* **2022**, *270*, 120726. [CrossRef]
40. Yao, G.; Huang, Q. DFT and SERS Study of L-Cysteine Adsorption on the Surface of Gold Nanoparticles. *J. Phys. Chem. C* **2018**, *122*, 15241–15251. [CrossRef]
41. Chang, C.; Chen, Y.; Huang, Y.; Lai, C.-H.; Jeng, U.-S.; Lai, Y.-H. Nanostructured silver dendrites for photon-induced Cysteine dimerization. *Sci. Rep.* **2019**, *9*, 20174. [CrossRef]

42. Melo, W.D.C.; Freire, P.T.C.; Filho, J.M.; Melo, F.E.A.; Lima, J.A.; Paraguassu, W. Raman spectroscopy of d-methionine under high pressure. *Vib. Spectrosc.* **2014**, *72*, 57–61. [CrossRef]
43. Graff, M.; Bukowska, J. Surface-enhanced Raman scattering (SERS) spectroscopy of enantiomeric and racemic methionine on a silver electrode-evidence for chiral discrimination in interactions between adsorbed molecules. *Chem. Phys. Lett.* **2011**, *509*, 58–61. [CrossRef]
44. Podstawka, E.; Ozaki, Y.; Proniewicz, L.M. Part II: Surface-Enhanced Raman Spectroscopy Investigation of Methionine Containing Heterodipeptides Adsorbed on Colloidal Silver. *Appl. Spectrosc.* **2004**, *58*, 581–590. [CrossRef]





Review

# Reporter Genes for Brain Imaging Using MRI, SPECT and PET

Tianxin Gao<sup>1</sup>, Pei Wang<sup>1</sup>, Teng Gong<sup>2</sup>, Ying Zhou<sup>1</sup>, Ancong Wang<sup>1</sup> , Xiaoying Tang<sup>1,3</sup>, Xiaolei Song<sup>2,\*</sup> and Yingwei Fan<sup>3,\*</sup>

<sup>1</sup> School of Life Science, Beijing Institute of Technology, Beijing 100081, China; gtx@bit.edu.cn (T.G.); wpei02288@sina.com (P.W.); zhouying2587@gmail.com (Y.Z.); awang@bit.edu.cn (A.W.); xiaoying@bit.edu.cn (X.T.)

<sup>2</sup> Center for Biomedical Imaging Research, School of Medicine, Tsinghua University, Beijing 100084, China; gongt923@163.com

<sup>3</sup> School of Medical Technology, Beijing Institute of Technology, Beijing 100081, China

\* Correspondence: songxl@tsinghua.edu.cn (X.S.); fanyingwei@bit.edu.cn (Y.F.)

**Abstract:** The use of molecular imaging technologies for brain imaging can not only play an important supporting role in disease diagnosis and treatment but can also be used to deeply study brain functions. Recently, with the support of reporter gene technology, optical imaging has achieved a breakthrough in brain function studies at the molecular level. Reporter gene technology based on traditional clinical imaging modalities is also expanding. By benefiting from the deeper imaging depths and wider imaging ranges now possible, these methods have led to breakthroughs in preclinical and clinical research. This article focuses on the applications of magnetic resonance imaging (MRI), single-photon emission computed tomography (SPECT), and positron emission tomography (PET) reporter gene technologies for use in brain imaging. The tracking of cell therapies and gene therapies is the most successful and widely used application of these techniques. Meanwhile, breakthroughs have been achieved in the research and development of reporter genes and their imaging probe pairs with respect to brain function research. This paper introduces the imaging principles and classifications of the reporter gene technologies of these imaging modalities, lists the relevant brain imaging applications, reviews their characteristics, and discusses the opportunities and challenges faced by clinical imaging modalities based on reporter gene technology. The conclusion is provided in the last section.

**Keywords:** reporter gene; MRI; radionuclide imaging; brain imaging

**Citation:** Gao, T.; Wang, P.; Gong, T.; Zhou, Y.; Wang, A.; Tang, X.; Song, X.; Fan, Y. Reporter Genes for Brain Imaging Using MRI, SPECT and PET. *Int. J. Mol. Sci.* **2022**, *23*, 8443. <https://doi.org/10.3390/ijms23158443>

Academic Editor: Raghendra Singh Yadav

Received: 30 June 2022

Accepted: 25 July 2022

Published: 30 July 2022

**Publisher's Note:** MDPI stays neutral with regard to jurisdictional claims in published maps and institutional affiliations.



**Copyright:** © 2022 by the authors. Licensee MDPI, Basel, Switzerland. This article is an open access article distributed under the terms and conditions of the Creative Commons Attribution (CC BY) license (<https://creativecommons.org/licenses/by/4.0/>).

## 1. Introduction

Molecular imaging is an imaging technique that visualizes, characterizes, and measures biological processes *in vivo* at the molecular and cellular levels [1]. Reporter gene imaging is a critical technical route for molecular imaging, which introduces or expresses imaging agents into cells through so-called reporter genes. Reporter genes are those genes that, when introduced into target cells (e.g., brain tissues, cancer, and circulating white cells), produce a protein receptor or enzyme that binds, transports, or traps a subsequently injected imaging probe, which becomes the contrast agent for reporter gene imaging [2]. Reporter gene imaging is developing very rapidly for monitoring cell therapy and gene therapy by providing critical information on the biodistributions, magnitudes, and durations of viral gene expressions. Imaging the brains of large animals or humans on a large scale has become the next challenge of reporter gene imaging.

Among multiple imaging modalities, fluorescence reporter genes have drawn great attention; however, penetration depths limit their *in vivo* application [3]. Recently, other imaging modalities, including magnetic resonance imaging (MRI), single-photon emission computed tomography (SPECT), positron emission tomography (PET), and ultrasound (US) imaging, have been explored in the field of reporter genes [2]. The advantages of genetically

encoded fluorescent imaging are high spatiotemporal resolution, high sensitivity, and high molecular specificity, while some conventional imaging modalities that use modern reporter gene indicators are effective in clearly examining the brains of larger subjects in deep organs and on large scales. Compared with optical reporter gene imaging, other types of reporter gene imaging have a variety of properties, as shown in Table 1. For the imaging depths and scales, clinical imaging techniques provide better performance, while fluorescence reporters are excellent in terms of their temporal–spatial resolution, noninvasiveness, molecular and cell specificity, and sensitivity.

**Table 1.** Pros and cons of reporter gene brain imaging techniques.

	MRI	PET	SPECT	US	Optical Imaging
Penetration depth	Limitless	Limitless	Limitless	>10 cm, limited in hard and air-containing tissue	250–500 $\mu\text{m}$
Field of view	Whole body	Whole body	Whole body	Whole organ	1–2 $\text{mm}^2$
Spatial resolution	100–1000 $\mu\text{m}$	4–7 mm	1 cm	50–500 $\mu\text{m}$	Poor at greater depths
Temporal resolution	100–1000 ms	s	min	1–100 ms	Good
Detection capability	$\mu\text{M}$	pM–fM	pM	pM	nM
Imaging time	min–h	min–h	min–h	s–min	ms–min
Ionization radiation	No	Yes	Yes	No	No
Clinical utility	Yes	Yes	Yes	Yes	Limited
Sensitivity	poor	Excellent	Excellent	excellent	Excellent
Information	Anatomical, physiological, molecular	Physiological, molecular	Physiological, molecular	Anatomical physiological	Physiological, molecular

Brain imaging includes imaging of diseases, such as neurodegenerative disease and glioma, and foundational brain research, which can be divided into two categories: macroscopic, noninvasive human cognitive neuroscience and invasive reductionist neurobiology [4]. Reporter gene base brain imaging includes both of these categories. Nonoptical imaging modalities are commonly used in clinics, which means that such studies involve direct human applications.

Observing brain activity is a dream of researchers. Gene-encoded fluorescent indicators that are used to dynamically monitor neurotransmitters and neuromodulators with fluorescence imaging have recently achieved great breakthroughs and have been reviewed in excellent studies [3]. We note that, for clinical imaging modalities, such as MRI, radionuclide imaging, and US, some breakthroughs have been achieved in reporter gene-based brain studies. A number of positive reviews have summarized reporter gene materials [5], the history of MRI in brain activity detection [4], transgene-based strategies in nuclear-based imaging [6], nanoparticle-mediated brain imaging [7], and reporter gene imaging in oncolytic virotherapy and gene therapy [2]. Here, we focus on the recently developed nonoptical techniques of reporter gene imaging used in brain imaging.

## 2. Principle of Reporter Gene Imaging

The two basic elements of reporter gene imaging consist of reporter genes and their respective imaging probes (which are also referred to as imaging agents, substrates, or imaging reporters in other references). The accumulation of imaging probes directly depends on the protein products of reporter gene expression, thereby imaging the reporter

gene. Because it only monitors living cells, it can accurately provide important information such as that of survival, proliferation, migration, differentiation, and functional integration of transplanted cells in vivo [1,8,9].

### 2.1. Reporter Gene Imaging with MRI

MRI employs the resonance properties of atomic nuclei subjected to strong magnetic fields and radiofrequency pulses to generate signals and reconstruct images. MRI reporter genes can directly or indirectly produce magnetic resonance contrast signals that are based on the expressions of coding enzymes, receptors, metalloproteins, etc., which can specifically combine with MRI contrast agent [10–13]. MRI reporter genes can be used to longitudinally monitor the cell migration process and gene expressions by using noninvasive imaging [14]. The main types of existing MRI reporter genes include reporter genes that encode enzymes (e.g., tyrosinase), reporter genes that encode receptors on cells (e.g., transferrin receptor (TfR)), endogenous reporter genes (e.g., ferritin and aquaporin 1 (AQP1)), and reporter genes that express CEST-detectable proteins (e.g., lysine rich-protein (LRP)) [15].

As shown in Figure 1A,B, the most classic contrast agent for MRI reporter genes is iron. As a ubiquitous protein in the cells of various organisms, ferritin is assembled by two subunits, a heavy chain and a light chain. The proportions of light and heavy chains vary in different tissues. The ferritin heavy chain (FTH1) contains ferrous oxidase and can combine with iron oxide to transform unstable  $Fe^{2+}$  into stable, insoluble, and nontoxic  $Fe^{3+}$  forms. The light chain mainly increases the activity of FTH1 and stabilizes ferritin. Ferritin can specifically bind to iron, which results in accumulations of intracellular iron particles and decreases in T2 signals [16], and it is one of the most commonly used reporter genes in MRI (Figure 1A). The transferrin receptor (TfR) is another commonly used MRI reporter gene. TfR can bind to transferrin and transfer iron into cells via endocytosis, thus reducing the T2 relaxation time (Figure 1B) [14,17]. Lysine-rich protein (LRP) is an artificially designed gene. Due to the uniquely high chemical exchange rate of poly-L-lysine, LRP can be used as a reporter gene in chemical exchange saturation transfer (CEST) MRI (Figure 1C) [18,19]. The CEST mechanism occurs because exchangeable protons have chemical shifts that are different from water. These protons are selectively saturated and exchanged with water molecules, thus reducing the water signal. Magnetic resonance diffusion-weighted imaging (DWI) is an imaging method that uses MRI to observe the microdiffusion movements of water molecules in living tissues. It can noninvasively image the structures and physiological functions of living brain tissues. The apparent diffusion coefficient (ADC) is used to describe the diffusion rate of water molecules in DWI. A positive correlation exists between them. When water molecules with freer diffusion are dephasing, the level of signal loss is greater, the signal is weaker, and it appears darker in DWI, and vice versa [20,21]. Aquaporins mediate the selective exchange of water-conducting molecules across plasma membranes in many cell types, and their expressions are related to water diffusivity and DWI signals in several disease states [22,23]. Previous studies have shown that overexpression of aquaporin can increase tissue water diffusivity without affecting viability, and contrasts are observed in diffusion-weighted MRI (Figure 1D) [24].

### 2.2. Reporter Gene Imaging with Radionuclides

Radionuclide imaging refers to SPECT and PET. SPECT detects gamma rays that are produced by the decay of the radioactive isotopes used in imaging, and it has been developed to elucidate the basic molecular neurodegeneration mechanism in PD, AD, and drug addiction, as well as to improve therapeutic strategies with minimum adverse effects. PET uses the annihilation of positrons (emitted by decaying radioisotopes in the imaging agent) and electrons to generate 510 keV collinear photons, which are detected simultaneously to generate a three-dimensional map of radioactivity distributions in the body [6]. Radionuclide imaging has very high sensitivity and good penetration ability in

tissues, and it can be used in clinical practice. It has been widely used for noninvasive tracing and monitoring of living cells.

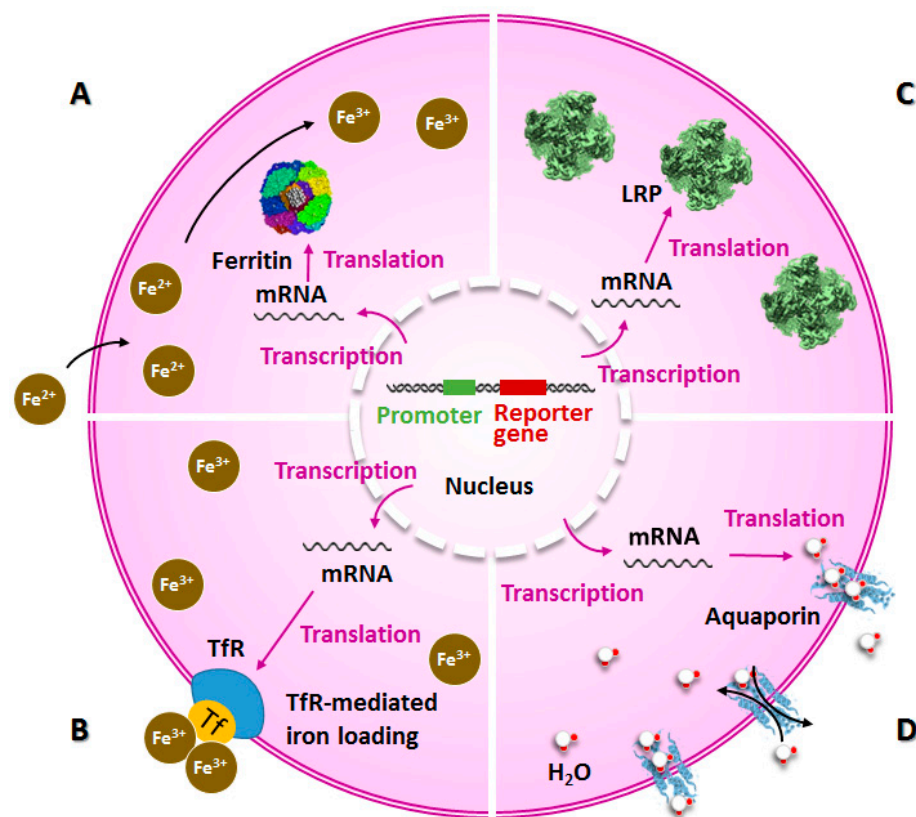


**Figure 1.** The principle of MRI reporter genes commonly used in brain imaging. (A) The expression of ferritin will cause intracellular iron particles to aggregate, resulting in a decrease in the T2 signal in MRI images. (B) The expression of TfR increases the iron uptake of cells and shows low signal intensity on T2 images of MRI. (C) LRP has a high chemical exchange rate and can be used in CEST MRI. (D) Aquaporin can increase water diffusivity and produce contrast in diffusion-weighted MRI.

PET imaging of reporter gene expression utilizes reporter gene imaging agents that are labeled by positron radionuclides. Currently, there are three types of commonly used radionuclide reporter gene imaging systems based on enzymes, receptors, and transporters, as shown in Figure 2 [6,25]. The most common reporter genes of enzymes are herpes simplex virus 1 thymine kinase (HSV1-tk) [9] and human  $\Delta$ -mitochondrial thymine kinase type 2 (h $\Delta$ tk2) [26]. The most common reporter genes are human somatostatin receptor type 2 (hSSTR2) [27] and dopamine D2 receptor (D2R) [28]. The most common reporter genes of transporters are human sodium–iodide symporter (hNIS) [29] and human norepinephrine transporter (hNET) [2,30].

One of the first and hence most intensively studied reporter genes, HSV1-tk, is also a suicide gene that adds an extra layer of control to ensure safety. NIS imaging is the most mature reporter gene imaging method used in human clinical trials and is more sensitive and longer lasting than HSV1-tk.

The SPECT imaging system was developed to elucidate the basic molecular neurodegeneration mechanism in PD, AD, and drug addiction, as well as to improve therapeutic strategies with minimum amounts of adverse effects. PET imaging can provide diagnosis and treatment guidance for tumors and cardiovascular and brain diseases. PET imaging of reporter gene expressions is capable of monitoring gene and cell therapy [6]. In brain studies, brain cancer and neurodegenerative disorders are the major diseases diagnosed and monitored by reporter gene expression PET imaging, as discussed thoroughly in Section 3.2.

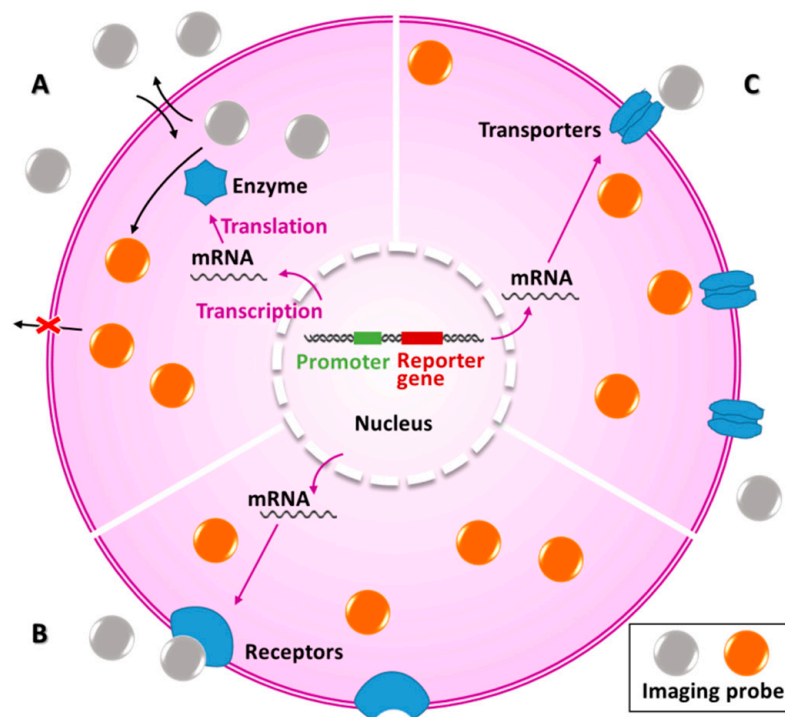


**Figure 2.** The major types of reporter gene expression in radionuclide imaging, based on (A) enzymes, (B) receptors, and (C) transporters.

### 3. Reporter Gene Imaging in Brain Studies

#### 3.1. Brain Imaging of Reporter Genes with MRI

In view of the diversity, high resolution, and noninvasive nature of MRI, MRI imaging of the brain can be used in a variety of applications, such as observing the process of virus infection through in vivo imaging, longitudinally monitoring cell migration and proliferation during cell therapy, noninvasive detection of neural connections, and monitoring neurogenesis. The majority of studies of MRI reporter genes in brain imaging are listed in Table 2.

**Table 2.** Reporter genes in brain imaging of MRI.

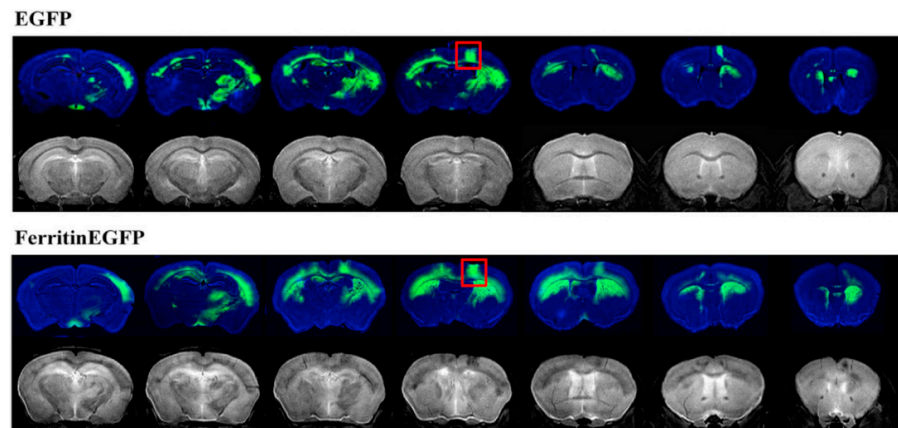
Class	Reporter Gene	Imaging Mode	Properties	Ref.
Receptor	TfR-FTH	T2WI	Shows increased contrast on T2-weighted brain images.	[31]
	Ferritin-EGFP	T2WI, FI	Synaptically connected neural network can be detected by ex vivo MRI and fluorescence imaging.	[32]
Endogenous reporter genes	Ferritin	T2WI	Realizes the accumulation of iron ions, resulting in a change in MR signal in the infected regions. Allows in vivo MRI to observe the process of virus infection and detect the neural circuits of living animals.	[33]
	FTH-EGFP	T2WI, FI	Tracks the tropism and fate of MSCs after systematic transplantation into orthotopic gliomas	[34]
	FTH1	DWI, SWI, T2WI	Allows in vivo detection of BMSCs transplanted due to cerebral ischemia/reperfusion injury and to treat intervention. FTH1-BMSC transplantation in the treatment of focal cerebral infarction is safe, reliable, and traceable by MRI; SWI is more sensitive than T2WI.	[35]

Table 2. Cont.

Class	Reporter Gene	Imaging Mode	Properties	Ref.
	FerrH	T2WI	Allows noninvasive visualization of neurogenesis in normal and ischemic rat brains using T2-weighted MRI	[36]
	IFN $\beta$ -FTH	T2WI	Traces MSCs and detects the therapeutic effect of IFN $\beta$ on glioma.	[37]
	FTH1-iRFP-EGFP	T2WI, NIF, FI	Tracks cells transplanted into the brain of mice during cell therapy by multimodal imaging.	[38]
	AQP1	DWI	The expression of AQP1 can provide DWI image contrast, which makes it possible to image the gene expression of intracranial tumor xenografts.	[24]
	EGFP-AQP1	DWI	Detection of astrocytes by fluorescence imaging and diffusion-weighted MRI.	[39]
	AQP1	DWI	Detection of brain-wide neural networks in vivo by metal-free MRI.	[40]
CEST	LRP	CEST MRI	Increases the contrast of CEST images of cell lysates and rat gliomas.	[18]
	rd LRP	CEST MRI	The CEST MRI contrast of mouse brain tumor is higher than that of LRP.	[41]
	dNKs	CEST MRI	Accurate localization in mouse intracranial tumor model. Realizes noninvasive two-color imaging of polygenes in deep tissue of living animals.	[42]

Visualization of neural networks helps provide a better understanding of the mechanisms of some brain functions and brain diseases. In the study of Wang et al. [32], vesicular stomatitis virus (VSV), a neurovirus that can spread sequentially in synaptic networks, was used to carry chimeric genes that encode ferritin and enhanced green fluorescent protein (EGFP). After recombinant VSV (rVSV) was injected into the somatosensory cortex (SC) of mice, the structural nerve connections were detected by MRI and fluorescence imaging. However, due to the high toxicity of VSV, mice infected with rVSV cannot survive for long periods, and in vivo MRI research is not allowed. The MRI and fluorescence images obtained after the death of mice are shown in Figure 3. In another study conducted by the team [33], hypotoxicity virus adeno-associated virus (AAV) was used as a vector to integrate the ferritin coding gene to obtain a ferritin coding viral vector (e.g., rAAV2-retro-CAG-Ferritin), which was injected into the caudate putamen (CPu) of mice to achieve noninvasive detection of neural networks in vivo. The CPu connection area was displayed by MRI at different time points after rAAV2-retro-CAG-ferritin injection (Figure 4). The team then focused on describing the activity of astrocytes, which are a major component of the central nervous system. They used the EGFP-AQP1 fusion gene of EGFP and aquaporin 1 (AQP1) as the reporter gene, detected astrocytes by fluorescence imaging and diffusion-weighted MRI, and established a new technique for the noninvasive detection of astrocytes in vivo for the first time [39]. In the newly published work [40] of the team, a tool virus rAAV-retro-AQP1-EGFP expressing nonmetallic magnetic resonance reporter gene AQP1 was prepared and used for in vivo brain-wide neural network detection. Three weeks after microinjection of virus rAAV-retro-AQP1-EGFP into the CPU brain area of mice, the changes in magnetic resonance signals in multiple brain regions (CPU, Ctx, BLA, Ins, Tha, HIP, etc) were observed by diffusion-weighted MRI, and the rapid imaging of specific brain region-related brain networks was successfully realized (increase from 60 days [33] to 21 days). The project also combined with the Cre-loxP system to prepare a brain network expressing Cre-dependent AQP1-related tool virus rAAV-retro-DIO-AQP1-EGFP for in vivo detection of specific neuronal types in specific

brain regions. This strategy provides a solid foundation for the visualization of neural networks in rodents and nonhuman primates.



**Figure 3.** Brain MRI (lower in both groups) and fluorescence images (upper). Four days after rVSV-EGFP or rVSV-Ferritin-EGFP was injected into the SC (red box) of mice, the mice were killed, and the images were obtained. Reproduced with permission from Ref. [32], 2019, Elsevier.

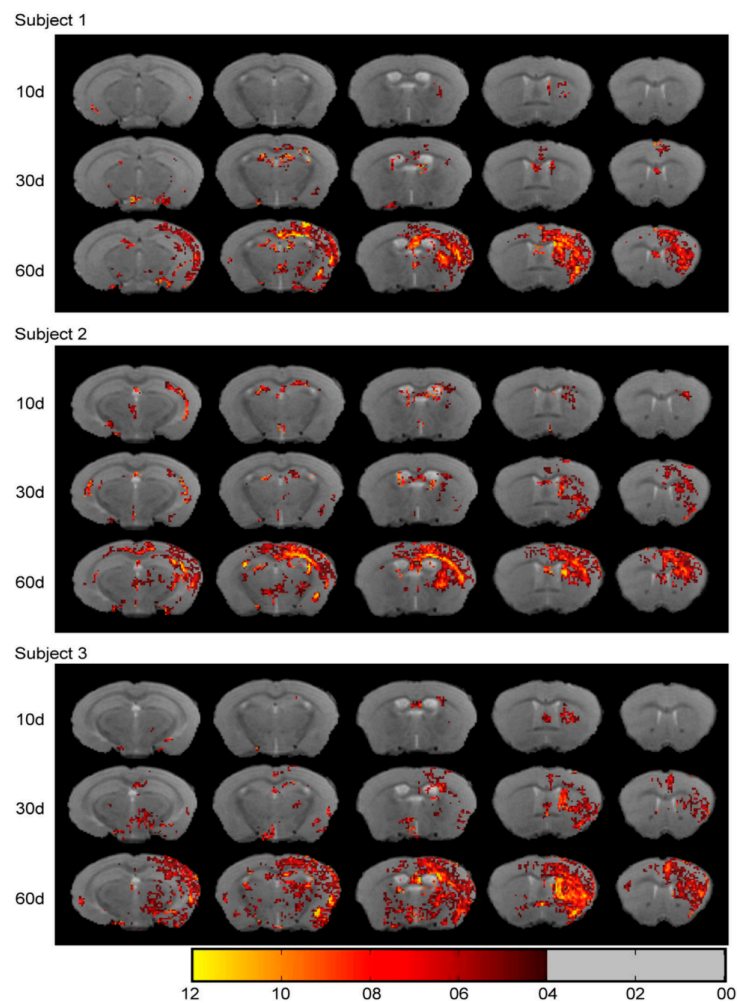


**Figure 4.** After different times (10 days, 30 days, or 60 days) of the rAAV2-retro-CAG-Ferritin injection, the CPU connection area is displayed by MRI in vivo (expressed by the change in T2 relaxation times). A color change (red–yellow) is used to indicate a change in T2 relaxation time (4–12 ms). Reproduced with permission from Ref. [33], 2021, Wiley.

Mesenchymal stem cells (MSCs) can cross the blood–brain barrier and tend to accumulate in tumors [43]; hence, they can be developed as cell carriers to treat gliomas [44–46]. Longitudinal *in vivo* monitoring of the migration and fate of MSCs is very important for the development of MSCs as cell carriers. Cao et al. [34] used a lentivirus as a vector to carry the ferritin heavy chain (FTH) and EGFP genes and transferred it to MSCs. MSCs expressing reporter genes were injected into a rat glioma model using different injection methods (e.g., arterial injection, intravenous injection, and stereotactic injection), and the homing and migration behaviors of MSCs were detected by MRI. The results showed that arterial injections of MSCs had a clear ability to treat glioma. MRI based on the ferritin reporter gene can be used to trace the tendency of MSCs to accumulate in glioma *in vivo*. Mao et al. [37] constructed MSCs with high expressions of interferon- $\beta$  (IFN $\beta$ ) and FTH in a similar manner. MRI was used to evaluate whether MSCs can be used as cell carriers to carry IFN $\beta$  to treat brain tumors, which provides a new option for treating brain tumors. Studies have shown that FTH-based MRI can monitor this treatment process.

MRI reporter genes are also used to study brain viral infections and for brain tumor imaging. Oncolytic viruses can be used to treat malignant tumors, such as glioblastoma [47,48]. The infection process is expected to be observed by MRI. In clinical trials, Christian et al. [18] integrated the lysine-rich protein (LRP) gene into a herpes simplex virus-derived oncolytic virus G47 $\Delta$  virus. CEST MRI was used to detect gliomas in rats before and 8 h after injection of G47 $\Delta$ -LRP or a control G47 $\Delta$ -empty virus. The contrast increased in tumors of CEST images after infection with G47 $\Delta$ -LRP virus. This study shows that LRP can be used as a reporter gene for real-time monitoring of virus transmission, but the highly repeated gene sequence of LRP may lead to DNA recombination events and expression of a series of truncated LRP protein fragments, which limits the sensitivity of CEST imaging. To address this problem, Perlman et al. [41] redesigned an LRP reporter (rd LRP) without DNA repeat sequences and improved its CEST MRI contrast. The *in vivo* CEST MRI of brain tumors in mice is shown in Figure 5.

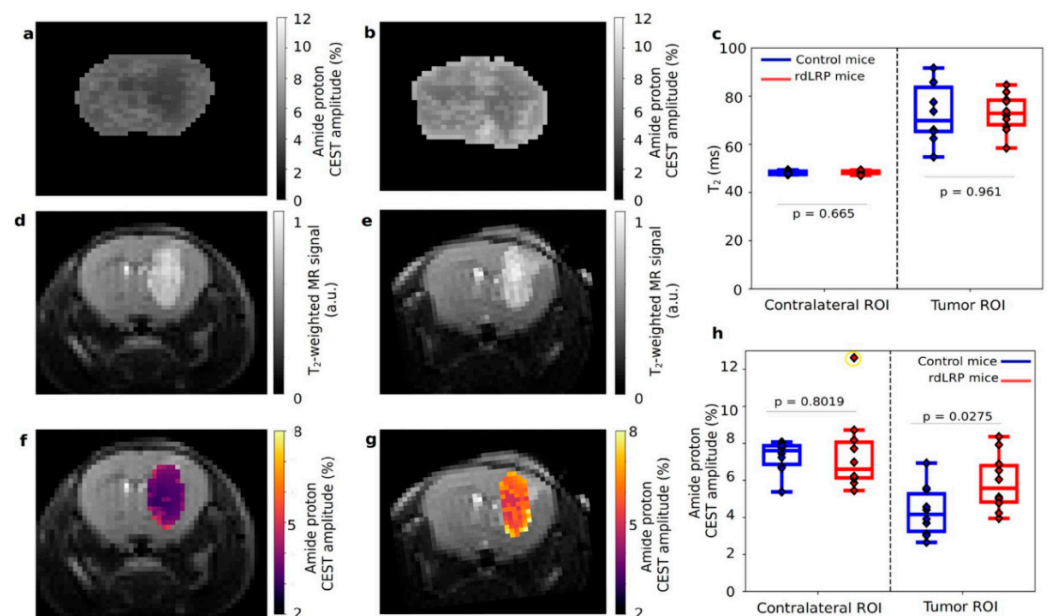


**Figure 5.** *In vivo* imaging of the rd LRP. (a,b) The amide proton CEST amplitudes of glioma cells that did not express rd LRP (a) and expressed rd LRP (b) in mouse brain. (c) Comparison of the T<sub>2</sub> relaxation time of the two groups. The results showed no significant difference, and there was edema in the tumor area. (d,e) T<sub>2</sub>-weighted imaging corresponding to (a,b) respectively. (f,g) Overlay of the amide proton CEST contrast (obtained using a frequency selective saturation pulse (a,b)) on the (d,e) image. (h) Comparison of CEST amplitudes of amide proton. CEST signal increased significantly in rd LRP group. Reproduced with permission from Ref. [41], 2020.

Additional innovative studies have been reported. Hyla et al. [42] developed a system called GeneREFORM, calculated and designed a group of two-color reporter genes and probes, and established a two-color gene imaging system. With the aid of existing MRI technology, GeneREFORM can accurately locate and achieve noninvasive two-color imaging of multiple genes in the deep tissues of living animals. The GeneREFORM system is also applicable to nontumor models.

There are also potential MRI reporter genes that can be used for brain imaging, notably gas vesicles (GVs). GV [49] are gas-filled protein nanostructures that are originally located in the cells of some bacteria and archaea that regulate cell buoyancy in aqueous environments [50,51]. GV is gene-encoded nanoscale probes composed of the primary structural protein, GvpA, the optional external scaffolding protein, GvpC, for structure reinforcement, and several secondary proteins that function as essential minor constituents or chaperones [52]. GV consists of external hydrophilic and internal hydrophobic protein structures, which cause their interiors to form gas cavities filled with gas that is separated from the surrounding medium and realizes the simultaneous free exchange of internal and external gas [53]. In the biological world, photosynthetic bacteria use the contents of gas contained in vesicles to regulate buoyancy and accomplish their own floating behavior. The magnetic susceptibility of GV is quite different from that of water, which can produce large contrasts in magnetic resonance imaging, even at sub-nanomolar concentrations. The gas cavities of the vesicles can scatter sound waves and produce ultrasonic contrasts. When the pressure on the air wall is greater than the threshold, the vesicles collapse; thus, background-free imaging can be achieved by acoustically modulated magnetic resonance imaging. The mechanical and surface characteristics of GvpC can be genetically modified by replacing the natural external GvpC with its recombinant variant, thus changing its magnetic susceptibility and collapse pressure, with the potential to obtain multichannel imaging. George et al. [54] showed that background-free imaging can be achieved by acoustic modulation MRI after injection of GV into the striatum of mice. When using the same method, MRI contrast could not be obtained after injections of phosphate buffer without GV. These results indicate that GV is expected to become an MRI reporter gene for brain imaging.

Vasoactive peptides are another potential MRI reporter gene for use in brain imaging. Their expression can cause vasodilation and facilitate hemodynamic imaging. Designed probes based on vasodilating peptides can image brain regions [55] and can be used to detect important molecules in the brain, such as neurochemicals [56]. Its use provides the potential to examine a wide variety of molecular phenomena in the brain and other organs.

### 3.2. Brain Imaging of Reporter Genes with Radionuclide

The majority of radionuclide imaging studies in the brain are related to cell/gene therapy monitoring, as shown in Table 3 [57–74]. They must be able to address challenges such as penetrating the blood–brain barrier (BBB), imaging in regions of high endogenous gene expressions in the central nervous system (CNS), low specificity, and endogenous expressions of reporter genes in microglia [73]. Shimojo [57] used bacterial dihydrofolate reductase (ecDHFR) as a reporter gene and [<sup>18</sup>F]FE-TMP as an imaging probe, which functioned as a dual probe in both fluorescence and PET imaging to image the CNS system. As a result, PET could analyze mammalian brain circuits at the molecular level.

**Table 3.** Reporter genes and corresponding radiotracer in radionuclide brain imaging.

Class	Reporter Gene	Imaging Probe	Properties	Refs.
Enzyme	ecDHFR	[ <sup>18</sup> F]FE-TMP	Allows PET analyses of mammalian brain circuits at the molecular level. TMP can be conjugated with fluorophores, while the radioactive analogs, [ <sup>11</sup> C]TMP and [ <sup>18</sup> F]TMP are compatible with PET.	[57]

Table 3. Cont.

Class	Reporter Gene	Imaging Probe	Properties	Refs.
	HSV1-TK	[ <sup>18</sup> F]FHBG	Safely enables the longitudinal imaging of T cells stably transfected with a PET reporter gene in patients. Allows noninvasive monitoring of cell fate in cell therapy. Does not cross BBB.	[58–60]
	HSV1-TK	[ <sup>18</sup> F]FHBT	Shows no statistically significant improvement of BBB permeability compared with [ <sup>18</sup> F]FHBG.	[61]
	HSV1-TK	[ <sup>18</sup> F]FIAU, [ <sup>18</sup> F]FEAU	Potential PET imaging agents for suicide gene expression.	[62]
	HSV1-TK	[ <sup>124</sup> I]FIAU	FIAU does not penetrate the intact BBB significantly.	[63]
	HSV1716	[ <sup>131</sup> I]FIAU	SPECT in patients, intratumoral injection.	[64]
	HSV1-TK	[ <sup>131</sup> I]FIAU	SPECT in rat. Local injection of stem cells is needed.	[65]
	HSV1-TK	[ <sup>76</sup> Br]FBAU	Shows intracranial tumors.	[66]
Receptor	D2R	[ <sup>11</sup> C]NMSP	Can assess the neural stem-cell-induced D2R expression in rat model.	[68]
	D2R80A	[ <sup>18</sup> F]fallypride	A potent reporter to detect hMSCs (human mesenchymal stem cells) by PET in vivo.	[69,70]
	hCB(2)	[ <sup>11</sup> C]GW405833	Dual-modality imaging viral vectors encoding hCB(2)(D80N) reporter system has potential clinical use as a PET reporter in the intact brain.	[71]
Transporter	hNIS	99mTc	SPECT in rat, for neural stem-cell tracing.	[72]
	Pyruvate kinase M2	[ <sup>18</sup> F]DASA-23	Applicable in all areas of the CNS of mice without breaking the blood–brain barrier.	[73]
	DMT1	[ <sup>52</sup> Mn <sup>2+</sup> ]	Dual-modality PET/MR tracking of transplanted stem cells in the central nervous system.	[74]

ecDHFR, bacterial dihydrofolate reductase; D2R, the dopamine type 2 receptor; [<sup>11</sup>C]NMSP, [<sup>11</sup>C]N-methylspiperone; D2R80A, a mutant of the dopamine type 2 receptor; hCB(2), human type 2 cannabinoid receptor; [<sup>11</sup>C]-GW405833, [<sup>11</sup>C]-labeled CB(2) ligand; DMT1, divalent metal transporter 1; FIAU, fluoro-5-iodo-1-beta-D-arabinofuranosyluracil; FEAU, fluoro-5-ethyl-1-beta-D-arabinofuranosyluracil; FLT, fluoro-3'-deoxy-3'-L-fluorothymidine; [<sup>52</sup>Mn<sup>2+</sup>], Mn based PET contrast agents.

SPECT and PET are useful in neuroscience research, especially in studies of neurodegeneration and neuro-oncology [64,75]. Stem = cell therapy offers new strategies for treating neurological diseases, such as Alzheimer's disease, Parkinson's disease, Huntington's disease, and multiple sclerosis caused by the loss of different types of neurons and glial cells in the brain. SPECT [65,72] and PET [68,69,73] can trace and evaluate the function of stem cells in the nervous system [76]. Multimodality imaging using several reporter genes used dual [77,78] or triple [79] fusion reporter vectors to enable high-sensitivity detection of cells in living animals. A dual-membrane protein positron and gamma-imaging reporter system using sodium iodide symporter and mutant dopamine D-2 receptor transgenes was developed for brain tumor detection.

HSV1-TK using the imaging probe, FHBG, has been used in glioma treatments to monitor chimeric antigen receptor (CAR) T-cell biodistributions and proliferation [58,59]. A study of the imaging probe, FIAU, in patients showed that FIAU cannot penetrate an intact BBB [63,64]. After gene therapy, substantial levels of FIAU may be detected within areas of BBB disruption; hence, clinically relevant levels of HSV-1-tk gene expression in brain tumors can be detected [63]. FBAU [66] is another promising imaging probe that has been studied in glioma imaging based on a mouse model.

In addition to glioma, bone marrow stem cells (BMSCs) used in experimental middle cerebral artery occlusion (MCAO) rat models have been imaged with a reporter gene–probe

system [65], consisting of the HSV1-tk and [ $^{131}$ I]FIAU pair. BMSCs were introduced into MCAO rat models via local injections into the brain or via injections into the lateral ventricle, carotid artery, or tail vein. The quantity of injected dose per gram in infarcted brain tissue in rats receiving injections into the brain was significantly higher than that in rats receiving injections elsewhere. No differences were seen in the other cell transplantation groups. SPECT imaging with [ $^{131}$ I]FIAU 24 h after injection provides peak target-to-nontarget count ratios. Neural stem cells have also been traced by SPECT [72]. The human sodium iodide symporter (hNIS) has been used as a reporter gene to track neural stem cells after transplantation in the brains of rats by using SPECT/CT imaging with technetium-99m to indicate the effectiveness and lack of interference with neural stem cell functioning. Dopamine type 2 receptor (D2R) and its mutant (D2R80A) have been used for neural stem cell tracing in the central nervous system. [ $^{11}$ C]N-methylspiperone microPET has been proven useful in imaging neural stem-cell-induced D2R expressions in a rat model of traumatic brain injury [68]. It has also been proven in athymic rats that D2R80A is an effective reporter gene for human mesenchymal stem-cell detection in vivo [69]. In another study with mice and cats, a separate adeno-associated virus type 1 vector with identical gene expression control elements was co-injected with the D2R80A vector. This dual-vector approach allows the D2R80A gene to be used with any therapeutic gene and to be injected into a single site for monitoring [70].

The BBB penetration ability of imaging probes hampers the usage of reporter gene imaging. FHBT was studied to improve BBB permeability [61], but there were no significant improvements compared with the traditional probe, FHBG. It was demonstrated that the novel scaffold proposed in this study supports the development of a new imaging probe with better BBB permeability for HSV1-tk and its mutant in the future. This imaging probe combined with reporter genes other than HSV1-TK provides a better solution for crossing the intact BBB. The human-type 2 cannabinoid receptor (hCB(2)) related ligand, [ $^{11}$ C]GW405833, for example, is readily distributed across the BBB. hCB(2)(D80N) was locoregionally overexpressed in the rat striatum by stereotactic injections of lentiviral and adeno-associated viral vectors. Kinetic PET revealed specific and reversible CB(2) binding of [ $^{11}$ C]GW405833 in the transduced rat striatum. The hCB(2) expressions were followed for 9 months, which demonstrates the potential future clinical use of CB(2) as a PET reporter in the intact brain [71]. In another study [73], the PKM2 reporter gene was delivered to the brains of mice by adeno-associated virus (AAV9) via stereotactic injection. PET imaging at 8 weeks post AAV delivery showed that the AAV-injected mice had increases in [ $^{18}$ F]DASA-23 brain uptake in the transduced sites. PKM2 can be used in the central nervous system to monitor gene and cell therapy without breaking the BBB.

Shimojo et al. [57] used bacterial dihydrofolate reductase, ecDHFR, and its unique antagonist, TMP, to visualize the neuronal circuit activities elicited by chemogenetic manipulation in the mouse hippocampus. In addition to mice, a 3.4 year old common marmoset underwent PET scans 45 days after AAV injection, when ecDHFR-EGFP was expressed in the brain. The PET results and postmortem fluorescence images are shown in Figure 6.

Biological variables are the byproducts of reporter gene expression PET imaging. Xu et al. [80] described a method that minimizes both the design and variability of vector delivery vehicles for alternative PET reporter genes (PRG) and the biological variability of the in vivo target when comparing the efficacy, sensitivity, and specificity of alternative PET reporter gene/PET reporter probe (PRP) combinations for in vivo PRG imaging. The Xu group described the process of comparing the standard HSVsr39TK/[ $^{18}$ F]FHBG PRG/PRP reporter system to four other PRGs, which were all coupled with the same PRP,  $^{18}$ F-L-FMAU.

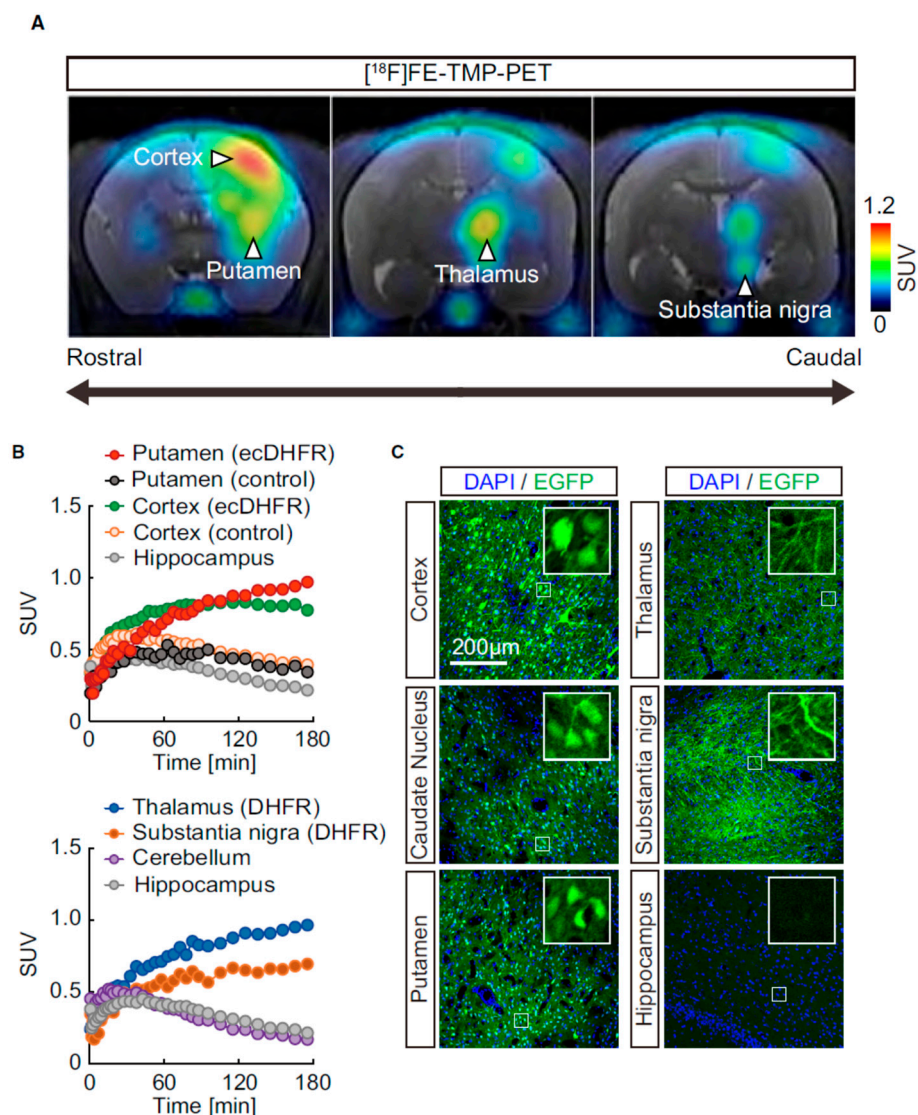


**Figure 6.** PET imaging of ecDHFR/TMP reporters in primate brain. (A) Representative coronal PET images generated by averaging dynamic scan data at 60–180 min after i.v. injection of [<sup>18</sup>F]FE-TMP. Note that reporter molecules were densely distributed in thalamus and substantia nigra pars compacta, which are connected to the neocortex and putamen via direct neuronal tract, respectively. PET images are overlaid with an individual MRI. Scale bar represents the SUV. (B) Time–radioactivity curves for [<sup>18</sup>F]FE-TMP in the putamen and neocortex carrying ecDHFR-EGFP or control AAV, and in the hippocampus are displayed in the upper panel. Curves in the thalamus, substantia nigra, and cerebellum along with hippocampus data are also shown in the lower panel. (C) Postmortem analysis of ecDHFR-EGFP expression in brain slices of different part with high-magnification image frames in inserts. Reproduced with permission from the authors (2021) [57].

#### 4. Opportunities and Challenges

##### 4.1. About the Modalities

Four clinical imaging modalities have the potential for conducting reporter gene imaging. MRI is the most common modality in brain detection and study. The limitations of MRI are the sensitivity of available imaging agents, the cost, and the imaging time. PET and SPECT have been used in gene and cell therapy because of their high sensitivity. SPECT needs strict collimation to maintain resolution, which may cause an increase in radioisotope dose. PET is more sensitive and has higher resolution than SPECT. SPECT and PET are often combined with CT for co-registered anatomical and functional imaging. The reporter genes for ultrasound, namely, the acoustic reporter gene (ARG), are exclusively

GVs. Studies in prokaryotic cells and mammalian cells have been carried out. Traditionally, imaging with probes that directly interact with target cells or molecules is called direct imaging. Imaging with probes that react to surrogate components that are related to the target cells or molecules is called indirect imaging. Imaging based on reporter genes is indirect. In existing brain studies, GVs can be used in brain imaging as probes but are not produced by target cells through transgenic technology. Further studies are needed to indirectly correlate GVs with target cells or molecules. The future of GVs as reporter genes or imaging contrast or therapy methods is very promising.

#### 4.2. MRI

The high spatial resolution of MRI leads to its wide use in brain imaging research. The use of targeted contrast agents [81] has further improved its signal-to-noise ratio, and reporter gene technology has further improved the sensitivity and specificity of imaging. Some MR reporter genes (e.g.,  $\beta$ -galactosidase) need to be used together with contrast agents to be detected, while some MR reporter genes (e.g., ferritin) do not need to add exogenous contrast agents, which has unique advantages compared with targeted contrast agents. On the one hand, the use of only reporter genes avoids the biological barriers that need to be overcome by injecting contrast media and the clearance barriers that contrast agents retain in the blood and tissue. Moreover, these reporter genes are generally not diluted with cell division-like targeted contrast agents (e.g., SPIO [82,83]), which can achieve more long-term and effective MRI monitoring [84,85]. On the other hand, reporter genes are generally expressed only in living cells, and they generally do not report both living and dead cells like imaging probes (e.g., the perfluorocarbon tracer), resulting in false-positive results [86–88].

Reporter gene-based MRI has great potential for use in brain imaging applications, but there are still many limitations to be overcome. Low sensitivity is a major limitation of MRI, while reporter genes based on CEST need high expression levels to achieve observable contrasts, which greatly limits the sensitivity of CEST. Reporter genes based on metal proteins or metal ion transporters may be hindered by the bioavailability or toxicity of metal ions. Therefore, there is a great demand for new MRI reporter genes that do not require metals and can be detected at low expression levels. The emergence of the aquaporin reporter gene improves these problems to some extent, but a potential limitation of aquaporin is its negative contrast enhancement.

In recent years, with the rapid development of MRI reporter genes, many innovative studies have been conducted. An interesting research direction is to integrate several types of reporter genes and combine the advantages of multiple imaging methods to achieve multimodal imaging. The search for new MRI reporter molecules is also an important research direction. In recent years, some studies have suggested that additional new molecules can be used as MRI reporter genes. For example, gas vesicles may become unique and powerful reporter genes in background-free MRI [54]. The ability to map several transgenes expressed at the same time by MRI will further enrich the gene transform palette and add additional “colors”, thus expanding the “multicolor” imaging toolbox to image previously inaccessible deep tissues [42]. However, most current research is currently in the animal experiment stage, and there is still a long way to go before they can be applied in clinics.

#### 4.3. Radionuclide Imaging

Radionuclide brain imaging has been used in molecular imaging for tumor detection and therapy and has even exhibited the possibility of brain function studies. The SPECT-based reporter gene technique has been studied in patients [64]. The progress of gene expression, posttranscriptional events, and brain circuit function can be noninvasively visualized by repetitively using reporter genes. Most of the paired imaging probes of the studied reporter genes are already clinically approved, which causes reporter gene radionuclide imaging to be close to clinical usage. Cell tracking studies have experienced

great improvements. [<sup>18</sup>F]FHBG imaging was safe in tracking HSV1-tk reporter gene expressions present in chimeric antigen receptor-engineered cytotoxic T lymphocytes and enabled the longitudinal imaging of T cells that were stably transfected with a PET reporter gene in patients [58].

The difficulty when choosing a reporter is that host-compatible reporters have no immune rejection risks, while their endogenous expressions may interfere with the real signal. Radionuclide imaging cannot be used in long-term studies due to decay of the imaging probe. The reporter gene will be expressed by the undiluted target cells for the lifetime of the cells and even for expanding cells. Until the design of viral tools for noninvasive gene delivery can apply these reporters to biomedical radionuclide imaging of human brains [89], researchers must face safety, cost-effectiveness, and ethics challenges.

HSV1-tk and its mutant are the most popular reporter genes for PET imaging. The inability to pass through the blood–brain barrier makes it difficult for them to be used in brain studies [68]. Imaging probes (e.g., PET tracers and reporter probes) that can cross the BBB have been developed [61,71,73]. A central nervous system multiparameter PET optimization (CNS PET MPO) algorithm was developed by a group from Pfizer that provides predictions of the required physicochemical properties of clinically useful CNS PET agents [61,90]. Reporter gene PET imaging is combined with other modalities, such as MRI [74] and optical imaging [71].

#### 4.4. Pharmacodynamic and Pharmacokinetic Assessment

A wide spectrum of therapeutic viruses, genes, and cells have been developed in recent years for personalized treatment of cancers. Despite of many undergoing clinical trials and some now licensed for clinical use, the safety, accuracy, and efficiency of these therapies remain big concerns [91,92]. In vivo imaging tools are in urgent need for the longitudinal monitoring of the biological distribution and fate of these exogenous cells, genes, and viruses, as well as an evaluation of the therapeutic response and promotion of their clinical translation [91,93]. As one of the most promising approaches, reporter genes feature a high level of cellular specificity, without signal dilution, such as cellular proliferation or tumor metastasis. Among all the modalities, reporter genes expressing PET tracers have progressed quickly and are considered most valuable for clinical translation. Notably, the combination of PET and MRI reporter genes exhibits translational potential with superiority in both specificity and localization [94].

However, in practice, multiple factors need to be taken into accounts, including the background signal contaminations, the favorable dosage over radiation exposure, and the limited or no biological effect deriving from expression of the transgene. Additionally, the potential for nonhuman reporter genes to be immunogenic must also be taken into consideration when addressing ideal system design, since this may affect functionality and survival of transduced cells once injected into humans [2,14].

In addition to the performance improvement of reporter gene and imaging probe, the clinical usage of reporter gene imaging faces some major problems such as the stable transfer of reporter gene safely and efficient delivery of reporter gene into primary cells that cannot be cultured *ex vivo* for long period. Early collaborations between molecular imagers and cell gene therapists may solve these problems, which would afford a parallel approach starting with pre-clinical studies so that reporter gene imaging can be incorporated into the cell or gene therapy. Members of the molecular–genetic imaging industry such as CellSight Technologies have bridged the gap between reporter gene technologies and clinical trials [2,91].

#### 4.5. Neuron Imaging with Reporter Gene

Reporter gene imaging for neuron imaging is a new rising direction with only a few studies reported. Wang's group imaged astrocytes in the whole brain with engineered AAVs and DWI *in vivo* [39]. They also use ferritin-encoding trans-synaptic [32] and adeno-associated virus [33] to detect neural connections *ex vivo* and longitudinal neural

connections in vivo, respectively. Shimojo et al. [57] used ecDHFR and TMP to visualize the neuronal circuit activities elicited by chemo-genetic manipulation in the mouse hippocampus. These studies provide substitutes for genetically encoded fluorescent probes, enabling in vivo gene targeted neuronal activity observation to be carried out in real time in larger animals. Hence, more mechanisms of neuron activity will be discovered in nonhuman primates or even humans in the future.

## 5. Conclusions

Reporter genes for use with clinical imaging modalities have greatly improved in recent years. For brain imaging studies, in addition to tumor detection and therapy, brain function-related studies cut a striking figure. Advances in gene techniques will bring great progress in brain imaging. The development of molecular functional MRI tools for animal research is accelerating, but the maximum benefits of this technology will eventually be achieved in human subjects. The abovementioned reporter gene technologies should be used and should not be limited to proof-of-concept experiments. Only in this way will it be possible to recognize the practical limitations of the emerging reporting mechanisms and identify important ways to improve them.

**Funding:** This research was funded by the National Natural Science Foundation of China grant number 81901907 and 82172112, the Beijing Institute of Technology Research Fund Program for Young Scholars, and the Fundamental Research Funds for the Central Universities grant number LY2022-22 and 2021CX11018.

**Conflicts of Interest:** The authors declare no conflict of interest.

## Abbreviations

Abbreviations	Full name
MRI	Magnetic resonance imaging
TfR	Transferrin receptor
AQP1	Aquaporin 1
CEST	Chemical exchange saturation transfer
LRP	Lysine-rich protein
FTH	Ferritin heavy chain
FerrH	Ferritin heavy chain
DWI	Diffusion-weighted imaging
ADC	Apparent diffusion coefficient
EGFP	Enhanced green fluorescent protein
T2WI	T2-weighted image
FI	Fluorescence imaging
MSCs	Mesenchymal stem cells
SWI	Susceptibility-weighted imaging
BMSCs	Bone marrow mesenchymal stromal cells
IFN $\beta$	Interferon- $\beta$
iRFP	Near-infrared fluorescent protein
rd LRP	Redesigned LRP reporter
dNKs	Deoxyribonucleoside kinases
VSV	Vesicular stomatitis virus
rVSV	Recombinant VSV
SC	Somatosensory cortex
AAV	Adeno-associated virus
CPU	Caudate putamen
Ctx	Cerebral cortex
BLA	Basolateral amygdala
Ins	Insular cortex
Tha	Thalamus

HIP	Hippocampus
GVs	Gas vesicles
PET	Positron emission tomography
SPECT	Single-photon emission computed tomography
US	Ultrasound
HSV1-tk	Herpes simplex virus-1 thymine kinase
hΔtk2	Human Δ-mitochondrial thymine kinase type 2
hSSTR2	Human somatostatin receptor type 2
D2R	Dopamine type 2 receptor
hNIS	Human sodium-iodide symporter
hNET	Human norepinephrine transporter
ecDHFR	Bacterial dihydrofolate reductase
[ <sup>11</sup> C]NMSP	[ <sup>11</sup> C]N-methylspiperone
D2R80A	Mutant of the dopamine type 2 receptor
hCB(2)	Human type 2 cannabinoid receptor
[ <sup>11</sup> C]-GW405833	[ <sup>11</sup> C]-labeled CB(2) ligand
DMT1	Divalent metal transporter 1
FIAU	Fluoro-5-iodo-1-beta-D-arabinofuranosyluracil
FEAU	Fluoro-5-ethyl-1-beta-D-arabinofuranosyluracil
FLT	Fluoro-3'-deoxy-3'-L-fluorothymidine
[ <sup>52</sup> Mn <sup>2+</sup> ]	Mn-based PET contrast agents
CAR	Chimeric antigen receptor
BMSCs	Bone marrow stem cells
MCAO	Middle cerebral artery occlusion
PRG	PET reporter gene
PRP	PET reporter probe
ARG	Acoustic reporter gene
CNS PET MPO	Central nervous system multiparameter PET optimization

## References

- Li, M.; Wang, Y.; Liu, M.; Lan, X. Multimodality reporter gene imaging: Construction strategies and application. *Theranostics* **2018**, *8*, 2954–2973. [CrossRef]
- Concilio, S.C.; Russell, S.J.; Peng, K.-W. A brief review of reporter gene imaging in oncolytic virotherapy and gene therapy. *Mol. Ther.-Oncolytics* **2021**, *21*, 98–109. [CrossRef] [PubMed]
- Wu, Z.; Lin, D.; Li, Y. Pushing the frontiers: Tools for monitoring neurotransmitters and neuromodulators. *Nat. Rev. Neurosci.* **2022**, *23*, 257–274. [CrossRef] [PubMed]
- Ghosh, S.; Harvey, P.; Simon, J.C.; Jasanoff, A. Probing the brain with molecular fMRI. *Curr. Opin. Neurobiol.* **2018**, *50*, 201–210. [CrossRef]
- Farhadi, A.; Sigmund, F.; Westmeyer, G.G.; Shapiro, M.G. Genetically encodable materials for non-invasive biological imaging. *Nat. Mater.* **2021**, *20*, 585–592. [CrossRef]
- Volpe, A.; Pillarsetty, N.V.K.; Lewis, J.S.; Ponomarev, V. Applications of nuclear-based imaging in gene and cell therapy: Probe considerations. *Mol. Ther.-Oncolytics* **2021**, *20*, 447–458. [CrossRef] [PubMed]
- Pan, C.-T.; Chang, W.-H.; Kumar, A.; Singh, S.P.; Kaushik, A.C.; Sharma, J.; Long, Z.-J.; Wen, Z.-H.; Mishra, S.K.; Yen, C.-K.; et al. Nanoparticles-mediated Brain Imaging and Disease Prognosis by Conventional as well as Modern Modal Imaging Techniques: A Comparison. *Curr. Pharm. Des.* **2019**, *25*, 2637–2649. [CrossRef]
- Brader, P.; Serganova, I.; Blasberg, R.G. Noninvasive Molecular Imaging Using Reporter Genes. *J. Nucl. Med.* **2013**, *54*, 167–172. [CrossRef] [PubMed]
- Higuchi, T.; Anton, M.; Dumler, K.; Seidl, S.; Pelisek, J.; Saraste, A.; Welling, A.; Hofmann, F.; Oostendorp, R.A.; Gansbacher, B.; et al. Combined Reporter Gene PET and Iron Oxide MRI for Monitoring Survival and Localization of Transplanted Cells in the Rat Heart. *J. Nucl. Med.* **2009**, *50*, 1088–1094. [CrossRef]
- Qin, C.; Cheng, K.; Hu, X.; Liu, Y.; Lan, X.; Zhang, Y.; Liu, H.; Xu, Y.; Bu, L.; Su, X.; et al. Tyrosinase as a multifunctional reporter gene for Photoacoustic/MRI/PET triple modality molecular imaging. *Sci. Rep.* **2013**, *3*, 1490. [CrossRef]
- Louie, A.Y.; Hüber, M.M.; Ahrens, E.T.; Rothbächer, U.; Moats, R.; Jacobs, R.E.; Fraser, S.E.; Meade, T.J. In vivo visualization of gene expression using magnetic resonance imaging. *Nat. Biotechnol.* **2000**, *18*, 321–325. [CrossRef] [PubMed]
- Paproski, R.J.; Forbrich, A.E.; Wachowicz, K.; Hitt, M.M.; Zemp, R.J. Tyrosinase as a dual reporter gene for both photoacoustic and magnetic resonance imaging. *Biomed. Opt. Express* **2011**, *2*, 771–780. [CrossRef] [PubMed]
- Weissleder, R.; Moore, A.; Mahmood, U.; Bhorade, R.; Benveniste, H.; Chiocca, E.A.; Bacion, J.P. In vivo magnetic resonance imaging of transgene expression. *Nat. Med.* **2000**, *6*, 351–355. [CrossRef] [PubMed]

14. Vandsburger, M.H.; Radoul, M.; Cohen, B.; Neeman, M. MRI reporter genes: Applications for imaging of cell survival, proliferation, migration and differentiation. *NMR Biomed.* **2013**, *26*, 872–884. [CrossRef]
15. Yang, C.; Tian, R.; Liu, T.; Liu, G. MRI Reporter Genes for Noninvasive Molecular Imaging. *Molecules* **2016**, *21*, 580. [CrossRef] [PubMed]
16. Ono, K.; Fuma, K.; Tabata, K.; Sawada, M. Ferritin reporter used for gene expression imaging by magnetic resonance. *Biochem. Biophys. Res. Commun.* **2009**, *388*, 589–594. [CrossRef] [PubMed]
17. Zhang, R.; Feng, G.; Zhang, C.J.; Cai, X.; Cheng, X.; Liu, B. Real-Time Specific Light-Up Sensing of Transferrin Receptor: Image-Guided Photodynamic Ablation of Cancer Cells through Controlled Cytomembrane Disintegration. *Anal. Chem.* **2016**, *88*, 4841–4848. [CrossRef] [PubMed]
18. Farrar, C.T.; Buhrman, J.S.; Liu, G.; Kleijn, A.; Lamfers, M.L.L.; McMahon, M.T.; Gilad, A.A.; Fulci, G. Establishing the Lysine-rich Protein CEST Reporter Gene as a CEST MR Imaging Detector for Oncolytic Virotherapy. *Radiology* **2015**, *275*, 746–754. [CrossRef] [PubMed]
19. Ward, K.M.; Aletras, A.H.; Balaban, R.S. A new class of contrast agents for MRI based on proton chemical exchange dependent saturation transfer (CEST). *J. Magn. Reson.* **2000**, *143*, 79–87. [CrossRef]
20. Le Bihan, D. Diffusion MRI: What water tells us about the brain. *EMBO Mol. Med.* **2014**, *6*, 569–573. [CrossRef]
21. Le Bihan, D. Looking into the functional architecture of the brain with diffusion MRI. *Nat. Rev. Neurosci.* **2003**, *4*, 469–480. [CrossRef] [PubMed]
22. Fukuda, A.M.; Adami, A.; Pop, V.; Bellone, J.A.; Coats, J.S.; Hartman, R.E.; Ashwal, S.; Obenaus, A.; Badaut, J. Posttraumatic reduction of edema with aquaporin-4 RNA interference improves acute and chronic functional recovery. *J. Cereb. Blood Flow Metab.* **2013**, *33*, 1621–1632. [CrossRef]
23. Badaut, J.; Ashwal, S.; Adami, A.; Tone, B.; Recker, R.; Spagnoli, D.; Terson, B.; Obenaus, A. Brain water mobility decreases after astrocytic aquaporin-4 inhibition using RNA interference. *J. Cereb. Blood Flow Metab.* **2011**, *31*, 819–831. [CrossRef] [PubMed]
24. Mukherjee, A.; Wu, D.; Davis, H.C.; Shapiro, M.G. Non-invasive imaging using reporter genes altering cellular water permeability. *Nat. Commun.* **2016**, *7*, 13891. [CrossRef] [PubMed]
25. Chao, F.; Shen, Y.; Zhang, H.; Tian, M. Multimodality Molecular Imaging of Stem Cells Therapy for Stroke. *BioMed Res. Int.* **2013**, *2013*, 849819. [CrossRef] [PubMed]
26. Chung, J.K. Sodium iodide symporter: Its role in nuclear medicine. *J. Nucl. Med.* **2002**, *43*, 1188–1200.
27. Filetti, S.; Bidart, J.M.; Arturi, F.; Caillou, B.; Russo, D.; Schlumberger, M. Sodium/iodide symporter: A key transport system in thyroid cancer cell metabolism. *Eur. J. Endocrinol.* **1999**, *141*, 443–457. [CrossRef]
28. Smanik, P.A.; Liu, Q.; Furminger, T.L.; Ryu, K.; Xing, S.; Mazzaferri, E.L.; Jhiang, S.M. Cloning of the human sodium iodide symporter. *Biochem. Biophys. Res. Commun.* **1996**, *226*, 339–345. [CrossRef] [PubMed]
29. Ahn, B.-C. Sodium Iodide Symporter for Nuclear Molecular Imaging and Gene Therapy: From Bedside to Bench and Back. *Theranostics* **2012**, *2*, 392–402. [CrossRef]
30. Seo, J.H.; Jeon, Y.H.; Lee, Y.J.; Yoon, G.S.; Won, D.-I.; Ha, J.-H.; Jeong, S.Y.; Lee, S.W.; Ahn, B.C.; Lee, J. Trafficking Macrophage Migration Using Reporter Gene Imaging with Human Sodium Iodide Symporter in Animal Models of Inflammation. *J. Nucl. Med.* **2010**, *51*, 1637–1643. [CrossRef]
31. Deans, A.E.; Wadghiri, Y.Z.; Bernas, L.M.; Yu, X.; Rutt, B.K.; Turnbull, D.H. Cellular MRI contrast via coexpression of transferrin receptor and ferritin. *Magn. Reson. Med.* **2006**, *56*, 51–59. [CrossRef] [PubMed]
32. Zheng, N.; Su, P.; Liu, Y.; Wang, H.; Nie, B.; Fang, X.; Xu, Y.; Lin, K.; Lv, P.; He, X.; et al. Detection of neural connections with ex vivo MRI using a ferritin-encoding trans-synaptic virus. *Neuroimage* **2019**, *197*, 133–142. [CrossRef] [PubMed]
33. Cai, A.; Zheng, N.; Thompson, G.J.; Wu, Y.; Nie, B.; Lin, K.; Su, P.; Wu, J.; Manyande, A.; Zhu, L.; et al. Longitudinal neural connection detection using a ferritin-encoding adeno-associated virus vector and in vivo MRI method. *Hum. Brain Mapp.* **2021**, *42*, 5010–5022. [CrossRef] [PubMed]
34. Cao, M.; Mao, J.; Duan, X.; Lu, L.; Zhang, F.; Lin, B.; Chen, M.; Zheng, C.; Zhang, X.; Shen, J. In vivo tracking of the tropism of mesenchymal stem cells to malignant gliomas using reporter gene-based MR imaging. *Int. J. Cancer* **2018**, *142*, 1033–1046. [CrossRef]
35. Huang, X.; Xue, Y.; Wu, J.; Zhan, Q.; Zhao, J. MRI Tracking of SPIO- and Fth1-Labeled Bone Marrow Mesenchymal Stromal Cell Transplantation for Treatment of Stroke. *Contrast Media Mol. Imaging* **2019**, *2019*, 5184105. [CrossRef]
36. Khodanovich, M.Y.; Akulov, A.E.; Anan'ina, T.V.; Kudabaeva, M.S.; Pishchelko, A.O.; Krutenkova, E.P.; Nemirovich-Danchenko, N.M.; Svetlik, M.V.; Tumentceva, Y.A.; Van den Haute, C.; et al. Tissue-Specific Ferritin- and GFP-Based Genetic Vectors Visualize Neurons by MRI in the Intact and Post-Ischemic Rat Brain. *Int. J. Mol. Sci.* **2020**, *21*, 8951. [CrossRef]
37. Mao, J.; Cao, M.; Zhang, F.; Zhang, J.; Duan, X.; Lu, L.; Yang, Z.; Zhang, X.; Zhu, W.; Zhang, Q.; et al. Peritumoral administration of IFN $\beta$  upregulated mesenchymal stem cells inhibits tumor growth in an orthotopic, immunocompetent rat glioma model. *J. Immunother. Cancer* **2020**, *8*, e000164. [CrossRef] [PubMed]
38. Zhang, Y.C.; Wang, J.W.; Wu, Y.; Tao, Q.; Wang, F.F.; Wang, N.; Ji, X.R.; Li, Y.G.; Yu, S.; Zhang, J.Z. Multimodal Magnetic Resonance and Fluorescence Imaging of the Induced Pluripotent Stem Cell Transplantation in the Brain. *Mol. Biol.* **2022**, *56*, 453–462. [CrossRef]
39. Li, M.; Liu, Z.; Wu, Y.; Zheng, N.; Liu, X.; Cai, A.; Zheng, D.; Zhu, J.; Wu, J.; Xu, L.; et al. In vivo imaging of astrocytes in the whole brain with engineered AAVs and diffusion-weighted magnetic resonance imaging. *Mol. Psychiatry* **2022**. [CrossRef] [PubMed]

40. Zheng, N.; Li, M.; Wu, Y.; Kaewborisuth, C.; Li, Z.; Gui, Z.; Wu, J.; Cai, A.; Lin, K.; Su, K.P.; et al. A novel technology for in vivo detection of cell type-specific neural connection with AQP1-encoding rAAV2-retro vector and metal-free MRI. *Neuroimage* **2022**, *258*, 119402. [CrossRef]
41. Perlman, O.; Ito, H.; Gilad, A.A.; McMahon, M.T.; Chiocca, E.A.; Nakashima, H.; Farrar, C.T. Redesigned reporter gene for improved proton exchange-based molecular MRI contrast. *Sci. Rep.* **2020**, *10*, 20664. [CrossRef]
42. Allouche-Arnon, H.; Khersonsky, O.; Tirukoti, N.D.; Peleg, Y.; Dym, O.; Albeck, S.; Brandis, A.; Mehlman, T.; Avram, L.; Harris, T.; et al. Computationally designed dual-color MRI reporters for noninvasive imaging of transgene expression. *Nat. Biotechnol.* **2022**, *40*, 1143–1149. [CrossRef] [PubMed]
43. Binello, E.; Germano, I.M. Stem cells as therapeutic vehicles for the treatment of high-grade gliomas. *Neuro-Oncology* **2012**, *14*, 256–265. [CrossRef] [PubMed]
44. Nakamura, K.; Ito, Y.; Kawano, Y.; Kurozumi, K.; Kobune, M.; Tsuda, H.; Bizen, A.; Honmou, O.; Niitsu, Y.; Hamada, H. Antitumor effect of genetically engineered mesenchymal stem cells in a rat glioma model. *Gene Ther.* **2004**, *11*, 1155–1164. [CrossRef] [PubMed]
45. Xu, G.; Jiang, X.D.; Xu, Y.; Zhang, J.; Huang, F.H.; Chen, Z.Z.; Zhou, D.X.; Shang, J.H.; Zou, Y.X.; Cai, Y.Q.; et al. Adenoviral-mediated interleukin-18 expression in mesenchymal stem cells effectively suppresses the growth of glioma in rats. *Cell Biol. Int.* **2009**, *33*, 466–474. [CrossRef]
46. Nakamizo, A.; Marini, F.; Amano, T.; Khan, A.; Studeny, M.; Gumin, J.; Chen, J.; Hentschel, S.; Vecil, G.; Dembinski, J.; et al. Human Bone Marrow-Derived Mesenchymal Stem Cells in the Treatment of Gliomas. *Cancer Res.* **2005**, *65*, 3307–3318. [CrossRef]
47. Fulci, G.; Chiocca, E.A. The status of gene therapy for brain tumors. *Expert Opin. Biol. Ther.* **2007**, *7*, 197–208. [CrossRef]
48. Russell, S.J.; Peng, K.-W.; Bell, J.C. Oncolytic virotherapy. *Nat. Biotechnol.* **2012**, *30*, 658–670. [CrossRef]
49. Wang, R.; Wang, L.; Chen, Y.; Xie, Y.; He, M.; Zhu, Y.; Xu, L.; Han, Z.; Chen, D.; Jin, Q.; et al. Biogenic Gas Vesicles for Ultrasound Imaging and Targeted Therapeutics. *Curr. Med. Chem.* **2022**, *29*, 1316–1330. [CrossRef]
50. Blaurock, A.E.; Wober, W. Structure of the wall of Halobacterium halobium gas vesicles. *J. Mol. Biol.* **1976**, *106*, 871–878. [CrossRef]
51. Walsby, A.E. Gas vesicles. *Microbiol. Rev.* **1994**, *58*, 94–144. [CrossRef] [PubMed]
52. Bourdeau, R.W.; Lee-Gosselin, A.; Lakshmanan, A.; Farhadi, A.; Kumar, S.R.; Nety, S.P.; Shapiro, M.G. Acoustic reporter genes for noninvasive imaging of microorganisms in mammalian hosts. *Nature* **2018**, *553*, 86–90. [CrossRef] [PubMed]
53. Pfeifer, F. Distribution, formation and regulation of gas vesicles. *Nat. Rev. Microbiol.* **2012**, *10*, 705–715. [CrossRef] [PubMed]
54. Lu, G.J.; Farhadi, A.; Szablowski, J.O.; Lee-Gosselin, A.; Barnes, S.R.; Lakshmanan, A.; Bourdeau, R.W.; Shapiro, M.G. Acoustically modulated magnetic resonance imaging of gas-filled protein nanostructures. *Nat. Mater.* **2018**, *17*, 456–463. [CrossRef]
55. Desai, M.; Slusarczyk, A.L.; Chapin, A.; Barch, M.; Jasanoff, A. Molecular imaging with engineered physiology. *Nat. Commun.* **2016**, *7*, 13607. [CrossRef] [PubMed]
56. Ohlendorf, R.; Wiśniewska, A.; Desai, M.; Barandov, A.; Slusarczyk, A.L.; Li, N.; Jasanoff, A. Target-responsive vasoactive probes for ultrasensitive molecular imaging. *Nat. Commun.* **2020**, *11*, 2399. [CrossRef] [PubMed]
57. Shimojo, M.; Ono, M.; Takuwa, H.; Mimura, K.; Nagai, Y.; Fujinaga, M.; Kikuchi, T.; Okada, M.; Seki, C.; Tokunaga, M.; et al. A genetically targeted reporter for PET imaging of deep neuronal circuits in mammalian brains. *EMBO J.* **2021**, *40*, e107757. [CrossRef]
58. Keu, K.V.; Witney, T.H.; Yaghoubi, S.; Rosenberg, J.; Kurien, A.; Magnusson, R.; Williams, J.; Habte, F.; Wagner, J.R.; Forman, S.; et al. Reporter gene imaging of targeted T cell immunotherapy in recurrent glioma. *Sci. Transl. Med.* **2017**, *9*, eaag2196. [CrossRef]
59. Hasenbach, K.; Wiehr, S.; Herrmann, C.; Mannheim, J.; Cay, F.; von Kürthy, G.; Bolmont, T.; Grathwohl, S.A.; Weller, M.; Lengerke, C.; et al. Monitoring the glioma tropism of bone marrow-derived progenitor cells by 2-photon laser scanning microscopy and positron emission tomography. *Neuro-Oncology* **2012**, *14*, 471–481. [CrossRef] [PubMed]
60. Yaghoubi, S.; Barrio, J.R.; Dahlbom, M.; Iyer, M.; Namavari, M.; Goldman, R.; Herschman, H.R.; Phelps, M.E.; Gambhir, S.S. Human pharmacokinetic and dosimetry studies of F-18 FHBG: A reporter probe for imaging herpes simplex virus type-1 thymidine kinase reporter gene expression. *J. Nucl. Med.* **2001**, *42*, 1225–1234.
61. Fuchigami, T.; Haywood, T.; Gowrishankar, G.; Anders, D.; Namavari, M.; Wardak, M.; Gambhir, S.S. Synthesis and Characterization of 9-(4-[<sup>18</sup>F]Fluoro-3-(hydroxymethyl)butyl)-2-(phenylthio)-6-oxopurine as a Novel PET Agent for Mutant Herpes Simplex Virus Type 1 Thymidine Kinase Reporter Gene Imaging. *Mol. Imaging Biol.* **2020**, *22*, 1151–1160. [CrossRef] [PubMed]
62. Alauddin, M.M.; Shahinian, A.; Park, R.; Tohme, M.; Fissekis, J.D.; Conti, P.S. In vivo evaluation of 2'-deoxy-2'-[<sup>18</sup>F]fluoro-5-iodo-1-β-D-arabinofuranosyluracil ([<sup>18</sup>F]FIAU) and 2'-deoxy-2'-[<sup>18</sup>F]fluoro-5-ethyl-1-β-D-arabinofuranosyluracil ([<sup>18</sup>F]FEAU) as markers for suicide gene expression. *Eur. J. Nucl. Med. Mol. Imaging* **2007**, *34*, 822–829. [CrossRef] [PubMed]
63. Jacobs, A.; Bräunlich, I.; Graf, R.; Lercher, M.; Sakaki, T.; Voges, J.; Hesselmann, V.; Brandau, W.; Wienhard, K.; Heiss, W.D. Quantitative kinetics of I-124 FIAU in cat and man. *J. Nucl. Med.* **2001**, *42*, 467–475. [PubMed]
64. Dempsey, M.F.; Wyper, D.; Owens, J.; Pimlott, S.; Papanastassiou, V.; Patterson, J.; Hadley, D.M.; Nicol, A.; Rampling, R.; Brown, S.M. Assessment of I-123-FIAU imaging of herpes simplex viral gene expression in the treatment of glioma. *Nucl. Med. Commun.* **2006**, *27*, 611–617. [CrossRef]
65. Wu, T.; Lang, J.; Sun, X.; Zhang, B.; Liu, Y.; An, R. Monitoring Bone Marrow Stem Cells with a Reporter Gene System in Experimental Middle Cerebral Artery Occlusion Rat Models. *J. Nucl. Med.* **2013**, *54*, 984–989. [CrossRef]
66. Cho, S.Y.; Ravasi, L.; Szajek, L.P.; Seidel, J.; Green, M.V.; Fine, H.A.; Eckelman, W.C. Evaluation of Br-76-FBAU as a PET reporter probe for HSV1-tk gene expression imaging using mouse models of human glioma. *J. Nucl. Med.* **2005**, *46*, 1923–1930.

67. Joya, A.; Martin, A. Evaluation of glial cell proliferation with non-invasive molecular imaging methods after stroke. *Neural Regen. Res.* **2021**, *16*, 2209–2210.
68. Zhang, H.; Zheng, X.; Yang, X.; Fang, S.; Shen, G.; Zhao, C.; Tian, M. C-11-NMSP/F-18-FDG microPET to monitor neural stem cell transplantation in a rat model of traumatic brain injury. *Eur. J. Nucl. Med. Mol. Imaging* **2008**, *35*, 1699–1708. [CrossRef]
69. Schoenitzer, V.; Haasters, F.; Kaesbauer, S.; Ulrich, V.; Mille, E.; Gildehaus, F.J.; Carlsen, J.; Pape, M.; Beck, R.; Delker, A.; et al. In Vivo Mesenchymal Stem Cell Tracking with PET Using the Dopamine Type 2 Receptor and F-18-Fallypride. *J. Nucl. Med.* **2014**, *55*, 1342–1347. [CrossRef]
70. Yoon, S.Y.; Gay-Antaki, C.; Ponde, D.E.; Poptani, H.; Vite, C.H.; Wolfe, J.H. Quantitative, noninvasive, in vivo longitudinal monitoring of gene expression in the brain by co-AAV transduction with a PET reporter gene. *Mol. Ther. Methods Clin. Dev.* **2014**, *1*, 14016. [CrossRef]
71. Vandeputte, C.; Evens, N.; Toelen, J.; Deroose, C.M.; Bosier, B.; Ibrahimi, A.; Van der Perren, A.; Gijssbers, R.; Janssen, P.; Lambert, D.M.; et al. A PET Brain Reporter Gene System Based on Type 2 Cannabinoid Receptors. *J. Nucl. Med.* **2011**, *52*, 1102–1109. [CrossRef] [PubMed]
72. Micci, M.-A.; Boone, D.R.; Parsley, M.A.; Wei, J.; Patrikeev, I.; Motamedi, M.; Hellmich, H.L. Development of a novel imaging system for cell therapy in the brain. *Stem Cell Res. Ther.* **2015**, *6*, 131. [CrossRef] [PubMed]
73. Haywood, T.; Beinart, C.; Gowrishankar, G.; Patel, C.B.; Alam, I.S.; Murty, S.; Gambhir, S.S. Positron emission tomography reporter gene strategy for use in the central nervous system. *Proc. Natl. Acad. Sci. USA* **2019**, *116*, 11402–11407. [CrossRef]
74. Lewis, C.M.; Graves, S.A.; Hernandez, R.; Valdovinos, H.F.; Barnhart, T.E.; Cai, W.; Meyerand, M.E.; Nickles, R.J.; Suzuki, M. <sup>52</sup>Mn Production for PET/MRI Tracking of Human Stem Cells Expressing Divalent Metal Transporter 1 (DMT1). *Theranostics* **2015**, *5*, 227–239. [CrossRef] [PubMed]
75. Jacobs, A.H.; Li, H.; Winkeler, A.; Hilker, R.; Knoess, C.; Ruger, A.; Galldiks, N.; Schaller, B.; Sobesky, J.; Kracht, L.; et al. PET-based molecular imaging in neuroscience. *Eur. J. Nucl. Med. Mol. Imaging* **2003**, *30*, 1051–1065. [CrossRef] [PubMed]
76. Wang, J.; Tian, M.; Zhang, H. PET molecular imaging in stem cell therapy for neurological diseases. *Eur. J. Nucl. Med. Mol. Imaging* **2011**, *38*, 1926–1938. [CrossRef]
77. Hwang, D.W.; Kang, J.H.; Chang, Y.S.; Jeong, J.M.; Chung, J.-K.; Lee, M.C.; Kim, S.; Lee, D.S. Development of a dual membrane protein reporter system using sodium iodide symporter and mutant dopamine D-2 receptor transgenes. *J. Nucl. Med.* **2007**, *48*, 588–595. [CrossRef]
78. Miletic, H.; Fischer, Y.; Litwak, S.; Giroglou, T.; Waerzeggers, Y.; Winkeler, A.; Li, H.; Himmelreich, U.; Lange, C.; Stenzel, W.; et al. Bystander killing of malignant glioma by bone marrow-derived tumor-infiltrating progenitor cells expressing a suicide gene. *Mol. Ther.* **2007**, *15*, 1373–1381. [CrossRef]
79. Ray, P.; Tsien, R.; Gambhir, S.S. Construction and validation of improved triple fusion reporter gene vectors for molecular imaging of living subjects. *Cancer Res.* **2007**, *67*, 3085–3093. [CrossRef]
80. Xu, S.; Herschman, H.R. Comparison of the Efficacy and Sensitivity of Alternative PET Reporter Gene/PET Reporter Probe Systems That Minimize Biological Variables. *Methods Mol. Biol.* **2020**, *2126*, 177–190.
81. Artemov, D. Molecular magnetic resonance imaging with targeted contrast agents. *J. Cell. Biochem.* **2003**, *90*, 518–524. [CrossRef] [PubMed]
82. Pohland, M.; Pohland, C.; Kiwit, J.; Glumm, J. Magnetic labeling of primary murine monocytes using very small superparamagnetic iron oxide nanoparticles. *Neural Regen. Res.* **2022**, *17*, 2311–2315. [PubMed]
83. Sun, R.; Wang, X.; Nie, Y.; Hu, A.; Liu, H.; Zhang, K.; Zhang, L.; Wu, Q.; Li, K.; Liu, C.; et al. Targeted trapping of endogenous endothelial progenitor cells for myocardial ischemic injury repair through neutrophil-mediated SPIO nanoparticle-conjugated CD34 antibody delivery and imaging. *Acta Biomater.* **2022**, *146*, 421–433. [CrossRef]
84. Yuan, Y.; Wang, C.; Kuddannaya, S.; Zhang, J.; Arifin, D.R.; Han, Z.; Walczak, P.; Liu, G.; Bulte, J.W.M. In vivo tracking of unlabelled mesenchymal stromal cells by mannose-weighted chemical exchange saturation transfer MRI. *Nat. Biomed. Eng.* **2022**, *6*, 658–666. [CrossRef] [PubMed]
85. Walczak, P.; Kedziorek, D.A.; Gilad, A.A.; Barnett, B.P.; Bulte, J. Applicability and limitations of MR tracking of neural stem cells with asymmetric cell division and rapid turnover: The case of the Shiverer dysmyelinated mouse brain. *Magn. Reson. Med.* **2010**, *58*, 261–269. [CrossRef]
86. Fink, C.; Smith, M.; Gaudet, J.M.; Makela, A.; Foster, P.J.; Dekaban, G.A. Fluorine-19 Cellular MRI Detection of In Vivo Dendritic Cell Migration and Subsequent Induction of Tumor Antigen-Specific Immunotherapeutic Response. *Mol. Imaging Biol.* **2019**, *22*, 549–561. [CrossRef] [PubMed]
87. Bar-Shir, A.; Alon, L.; Korner, M.J.; Lim, H.S.; Yadav, N.N.; Kato, Y.; Pathak, A.P.; Bulte, J.W.M.; Gilad, A.A. Quantification and tracking of genetically engineered dendritic cells for studying immunotherapy. *Magn. Reson. Med.* **2018**, *79*, 1010–1019. [CrossRef]
88. Gaudet, J.M.; Ribot, E.J.; Chen, Y.; Gilbert, K.M.; Foster, P.J. Tracking the Fate of Stem Cell Implants with Fluorine-19 MRI. *PLoS ONE* **2015**, *10*, e0118544. [CrossRef]
89. Chan, K.Y.; Jang, M.J.; Yoo, B.B.; Greenbaum, A.; Ravi, N.; Wu, W.-L.; Sanchez-Guardado, L.; Lois, C.; Mazmanian, S.K.; Deverman, B.E.; et al. Engineered AAVs for efficient noninvasive gene delivery to the central and peripheral nervous systems. *Nat. Neurosci.* **2017**, *20*, 1172–1179. [CrossRef]

90. Zhang, L.; Villalobos, A.; Beck, E.M.; Bocan, T.; Chappie, T.A.; Chen, L.; Grimwood, S.; Heck, S.D.; Helal, C.J.; Hou, X.; et al. Design and Selection Parameters to Accelerate the Discovery of Novel Central Nervous System Positron Emission Tomography (PET) Ligands and Their Application in the Development of a Novel Phosphodiesterase 2A PET Ligand. *J. Med. Chem.* **2013**, *56*, 4568–4579. [CrossRef]
91. Yaghoubi, S.S.; Campbell, D.O.; Radu, C.G.; Czernin, J. Positron Emission Tomography Reporter Genes and Reporter Probes: Gene and Cell Therapy Applications. *Theranostics* **2012**, *2*, 374–391. [CrossRef] [PubMed]
92. Lechermann, L.M.; Lau, D.; Attili, B.; Aloj, L.; Gallagher, F.A. In Vivo Cell Tracking Using PET: Opportunities and Challenges for Clinical Translation in Oncology. *Cancers* **2021**, *13*, 4042. [CrossRef] [PubMed]
93. Rakhshandehroo, T.; Smith, B.R.; Glockner, H.J.; Rashidian, M.; Pandit-Taskar, N. Molecular Immune Targeted Imaging of Tumor Microenvironment. *Nanotheranostics* **2022**, *6*, 286–305. [CrossRef] [PubMed]
94. Shalaby, N.; Kelly, J.; Martinez, F.; Fox, M.; Qi, Q.; Thiessen, J.; Hicks, J.; Scholl, T.J.; Ronald, J.A. A Human-derived Dual MRI/PET Reporter Gene System with High Translational Potential for Cell Tracking. *Mol. Imaging Biol.* **2022**, *24*, 341–351. [CrossRef] [PubMed]



Article

# Biomimetic Nanosponges Enable the Detoxification of *Vibrio vulnificus* Hemolysin

Shuaijun Zou <sup>1,†</sup>, Qianqian Wang <sup>1,†</sup>, Peipei Zhang <sup>2</sup>, Bo Wang <sup>1</sup>, Guoyan Liu <sup>1</sup>, Fuhai Zhang <sup>1</sup>, Jie Li <sup>1</sup>, Fan Wang <sup>1</sup>, Beilei Wang <sup>1,\*</sup> and Liming Zhang <sup>1,\*</sup> 

<sup>1</sup> Department of Marine Biomedicine and Polar Medicine, Naval Special Medical Center, Naval Medical University, Shanghai 200433, China; smmuzsj@163.com (S.Z.); abc\_w@163.com (Q.W.); m18817365409@163.com (B.W.); lgy\_laurie@aliyun.com (G.L.); zhangfh1105@163.com (F.Z.); 18260199036m@sina.com (J.L.); fanwang1130@126.com (F.W.)

<sup>2</sup> Department of Marine Biological Injury and Dermatology, Naval Special Medical Center, Naval Medical University, Shanghai 200052, China; zpp19841113@sina.com

\* Correspondence: beileiwang@smmu.edu.cn (B.W.); lmzhang@smmu.edu.cn (L.Z.); Tel.: +86-021-81871128 (B.W.); +86-021-81871129 (L.Z.)

† These authors contributed equally to this work.

**Abstract:** *Vibrio vulnificus* (*V. vulnificus*) infection-associated multiple antibiotic resistance has raised serious public health concerns. Recently, nanosponges (NSs) have been expected to provide innovative platforms for addressing antibacterial and drug-resistant challenges by targeting various pore-forming toxins (PFTs). In the present study, we constructed NSs to explore the effects and possible mechanism of recombinant *V. vulnificus* hemolysin (rVvhA)-induced injuries. In vitro, NSs significantly reversed rVvhA-induced apoptosis and necrosis, and improved toxin-induced intracellular reactive oxygen species (ROS) production, adenosine triphosphate (ATP) depletion, and apoptosis signaling pathway disruption. To explore the clinical translation potential of NSs, we established VvhA-induced septicemia and wound infection mouse models, respectively, and further found NSs could notably attenuate rVvhA-induced acute toxicity and septicemia-associated inflammation, as well as local tissue damage. In a conclusion, NSs showed excellent protective effects against rVvhA-induced toxicity, thus providing useful insights into addressing the rising threats of severe *V. vulnificus* infections.

**Keywords:** *Vibrio vulnificus*; nanosponge; VvhA; pore-forming toxins; biotransformation

**Citation:** Zou, S.; Wang, Q.; Zhang, P.; Wang, B.; Liu, G.; Zhang, F.; Li, J.; Wang, F.; Wang, B.; Zhang, L. Biomimetic Nanosponges Enable the Detoxification of *Vibrio vulnificus* Hemolysin. *Int. J. Mol. Sci.* **2022**, *23*, 6821. <https://doi.org/10.3390/ijms23126821>

Academic Editor: Francesco Trotta

Received: 14 May 2022

Accepted: 17 June 2022

Published: 19 June 2022

**Publisher's Note:** MDPI stays neutral with regard to jurisdictional claims in published maps and institutional affiliations.



**Copyright:** © 2022 by the authors. Licensee MDPI, Basel, Switzerland. This article is an open access article distributed under the terms and conditions of the Creative Commons Attribution (CC BY) license (<https://creativecommons.org/licenses/by/4.0/>).

## 1. Introduction

*Vibrio vulnificus* (*V. vulnificus*) is an alkalophilic, halophilic, rod-shaped, gram-negative bacterium of the *Vibrio* genus [1,2]. Exposure to *V. vulnificus*-contaminated seawater usually results in hemorrhagic necrotic skin lesions and secondary sepsis, while ingestion of contaminated raw or undercooked seafood mainly leads to primary septicemia [3–5]. Septicemia caused by *V. vulnificus* exerts high mortality (>50%), especially in patients with chronic liver diseases or immunocompromising conditions [6–9]. Currently, combination antibiotic therapy is the first choice for *V. vulnificus* infections and includes doxycycline, third-generation cephalosporin, fluoroquinolone, and trimethoprim-sulfamethoxazole, as well as aminoglycosides [10]; however, due to the excessive use of antibiotics in humans, agricultural and aquaculture systems, multiple antibiotic resistance has emerged in up to 50% of *V. vulnificus* strains in various countries, which raises serious public health and economic concerns [10,11]. Thus, the development of alternative agents is urgently needed.

*V. vulnificus* hemolysin (VvhA) is a pore-forming toxin (PFT) encoded by *vvhA*, which is a key virulence factor in the pathogenesis of *V. vulnificus* infections. Earlier studies [12,13] have shown that local and systemic administration of VvhA in animal models reproduces the same clinical and pathological manifestations as live *V. vulnificus*, and purified VvhA

can induce lethal effects in vivo, including hypotension, tachycardia, and pulmonary damage; moreover, VvhA may also contribute to pathogen invasion, vasodilatation and septic shock [14–17]. These results indicate that VvhA should be a logical target for the development of alternative therapeutics to combat *V. vulnificus* infection. More importantly, targeting the VvhA strategy could effectively prevent drug resistance since it exerts less selective pressure on pathogens themselves; however, the cellular targeting sites of VvhA remain controversial and unclear [16]. For example, the cholesterol on cell membranes was believed to be the receptor for VvhA, while some other reports suggested that VvhA localized on both cholesterol and glycan moieties rich membrane domain and other membrane domains [18,19]; conversely, the molecular mechanism of cell damage after the interaction between VvhA and the host cell during *V. vulnificus* infection has also not been clarified yet. For example, some studies demonstrate that VvhA induced NF- $\kappa$ B-dependent mitochondrial cell death via lipid raft-mediated reactive oxygen species (ROS) production [20]; some other studies proposed that VvhA induced autophagy upregulation through the lipid raft-mediated c-Src/NOX signaling pathway and ERK/eIF2 $\alpha$  activation [18]. Collectively, structure-specific PFT-targeting strategies or some signal pathway inhibitors would be insufficient to thoroughly combat VvhA-induced injuries.

Recently, Hu et al. [21,22] proposed a broad-spectrum detoxification strategy, known as “nanosponges (NSs)”, which focused on the whole membranes of affected host cells instead of targeting specific structures. Wrapped with red blood cell (RBC) membranes, NSs provide sufficient, intact, and natural targets for PFTs to bind with, and divert them away from the host cells; moreover, the natural membrane shells endow NSs with lower immunogenicity and prolonged circulation time in vivo [23]. Currently, the NS platform has been proven to be effective against injuries from gram-positive pathogen-derived toxins [24,25]; however, fewer studies have been conducted to investigate the protective effects and possible molecular mechanisms of NSs against gram-negative pathogen-derived PFTs.

In this study, we tried to construct NSs by fusing RBC vesicles onto poly (DL-lactide-co-glycolide) (PLGA) nanoparticles (NPs), which are the biocompatible polymers approved by the US Food and Drug Administration [26–28]. In vitro, we chose human pulmonary artery endothelial cells (HPAECs) as effector cells, which are the most common target cells in *V. vulnificus*-related sepsis. Then, we examined the effects and possible mechanisms of NSs on toxin-induced intracellular oxidative stress, adenosine triphosphate (ATP) depletion, and the activation of apoptosis signaling pathways. In vivo, we respectively constructed VvhA-induced septicemia and wound infection mouse models to simulate clinical cases, then tested the protective effects of NSs against VvhA by recording the animal survival rates, inflammatory cascades as well as lung and tissue damage.

## 2. Results

### 2.1. Characterization of NSs

To characterize the hydrodynamic size and zeta potential, PLGA NPs and RBC-derived NSs were measured by dynamic light scattering (DLS). The results revealed that the diameters of NPs increased from  $61.3 \pm 1.1$  to  $77.2 \pm 1.4$  nm with a narrow size distribution, corresponding to the bilayered membrane coating on a polymeric core; moreover, the zeta-potential of the PLGA NPs decreased from  $-35.8 \pm 0.3$  to  $-26.5 \pm 0.6$  mV, and the latter one corresponds to the potential of RBC vesicles (Figure 1A). These results demonstrated fusion between the NP cores and the RBC membranes. To characterize the nanostructures, the resulting NS sample was dried and examined by transmission electron microscopy (TEM). Compared to bare NPs, the resulting NSs exhibited a typical core-shell structure with PLGA cores enwrapped with thin membrane shells, verifying the formation of NSs (Figure 1B). To further characterize the protein contents retained on NSs, the resulting NS sample was examined by SDS-PAGE. The results showed that most membrane proteins were retained on NS shells, which were consistent with those of RBC ghosts and extruded RBC vesicles with a negligible loss during preparation (Figure 1C). Finally, NSs were suspended in

1 × phosphate-buffered saline (PBS) and 100% fetal bovine serum (FBS) and showed only negligible increases in particle size over 7 d at 4 °C, confirming the excellent stability of the prepared NSs (Figure 1D).

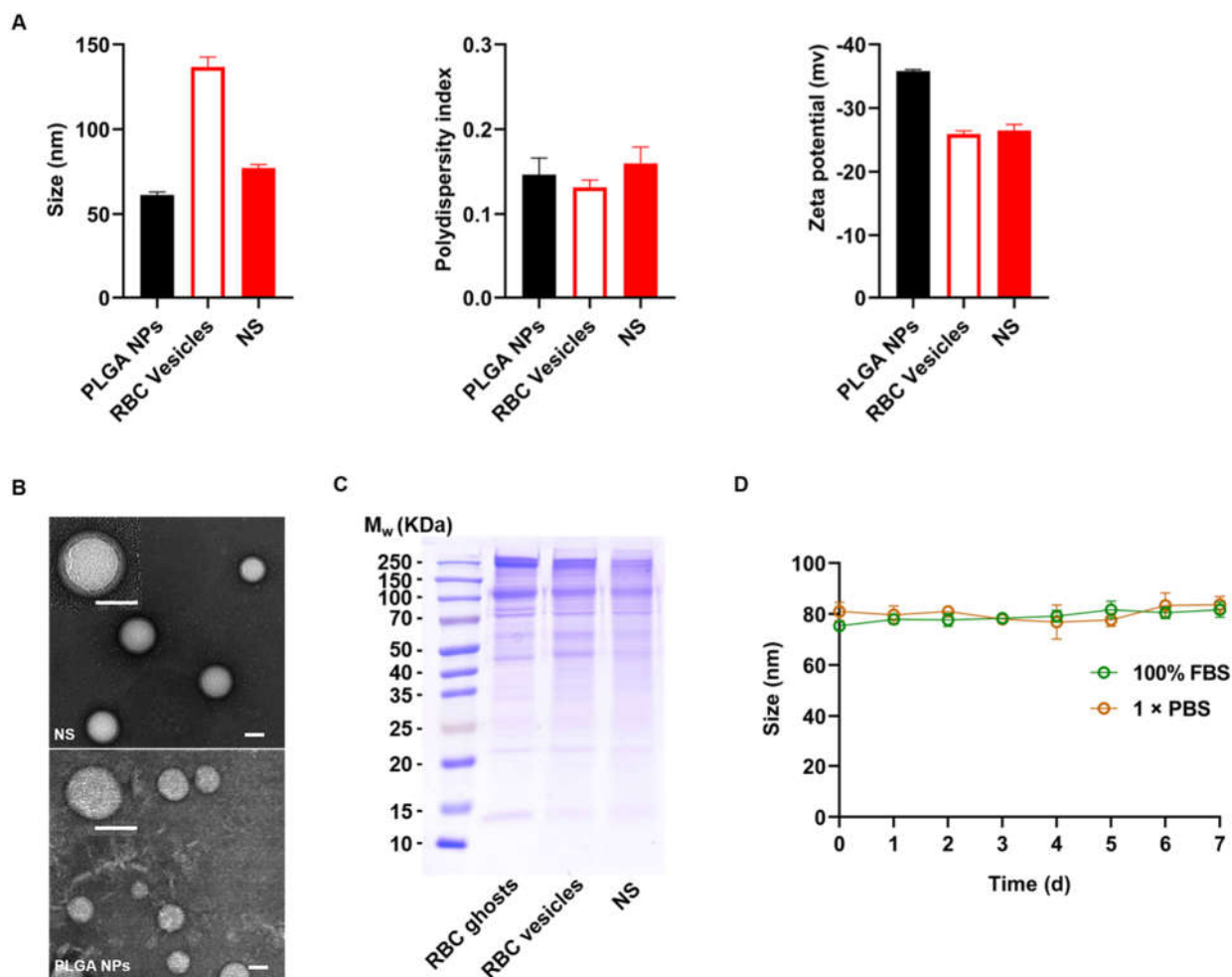


**Figure 1.** Characterization of NSs. (A) Hydrodynamic size, polydispersity index and zeta potential of PLGA NPs, RBC vesicles, and NSs. (B) TEM image showing the structure of PLGA NPs (lower) and NSs (upper). (Scale bar: 50 nm.) (C) Proteins in RBC ghosts, RBC vesicles, and NSs were examined by SDS-PAGE. (D) NSs were suspended in 1 × PBS or 100% FBS, and the hydrodynamic size was monitored for 7 d.

## 2.2. Inhibitory Effect of NSs on Cell Viability and Apoptosis Induced by Recombinant VvhA (rVvhA)

After expression and purification of rVvhA (Figures S1 and S2) [29], we then used HPAECs as target cells to investigate the protective effect of NSs against VvhA-induced cytotoxicity. According to the dose-effect and time-effect relationship of the toxin (Figure 2A,B), we chose the optimal dose of rVvhA (500 ng/mL, the dose producing 50% inhibition) and exposure time (4 h) for subsequent detoxification study. rVvhA-induced cytotoxicity was significantly inhibited by NSs (10–40 µg/mL), and 40 µg/mL NSs almost completely reversed the cytotoxicity of rVvhA, while NSs exerted no effect on cell viability (Figure 2C,D). Similar detoxification effects of NSs (40 µg/mL) were also observed in the context of rVvhA (500 ng/mL)-induced cell apoptosis (Figure 2E,F).

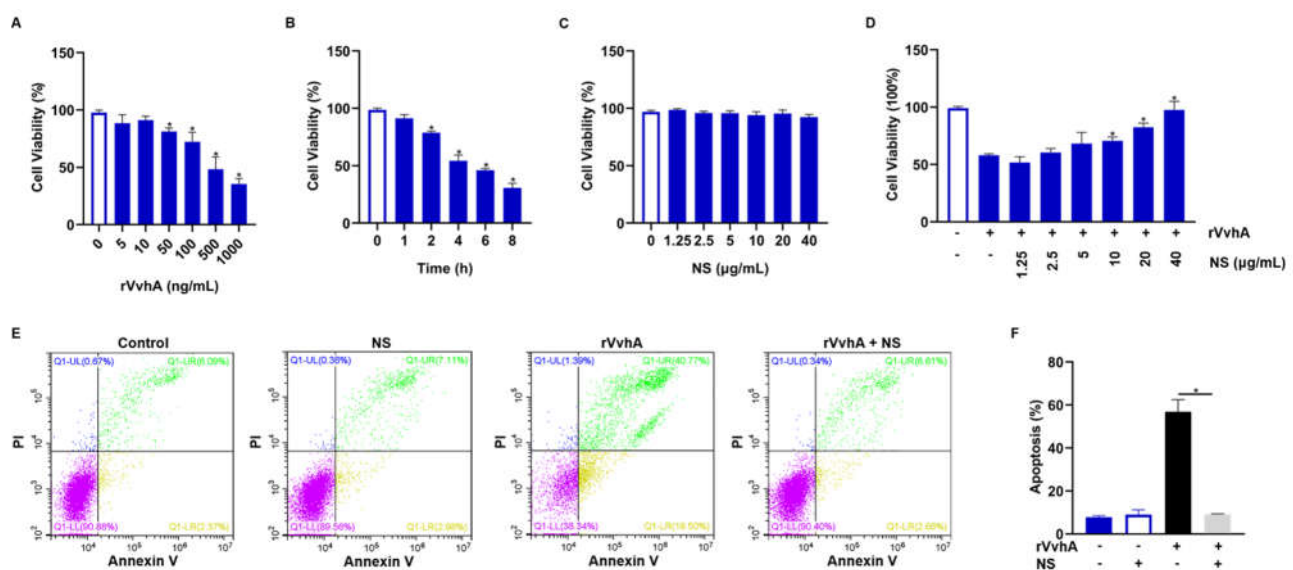


**Figure 2.** Inhibitory effects of NSs on rVvhA-induced cell death and apoptosis in HPAECs. (A) Dose-response of cell viability in HPAECs treated with rVvhA for 4 h. (B) Time response of HPAECs treated with rVvhA (500 ng/mL) over a period of 8 h (0, 1, 2, 4, 6, 8 h). (C) HPAECs were treated with increasing concentrations of NSs (0, 1.25, 2.5, 5, 10, 20 and 40 µg/mL) for 4 h. (D) HPAECs were treated with increasing concentrations of NSs (0, 1.25, 2.5, 5, 10, 20 and 40 µg/mL) in the presence of rVvhA (500 ng/mL) for 4 h. (E,F) HPAECs were treated with PBS, NSs (40 µg/mL), rVvhA (500 ng/mL), rVvhA (500 ng/mL) plus NSs (40 µg/mL) for 4 h, respectively. The percentages of total apoptotic cells were measured and quantified by using Annexin V/PI staining and flow cytometry. (The data represent the means  $\pm$  SE.  $n = 3$ . \*  $p < 0.05$ ).

### 2.3. NSs Inhibited ROS Production and ATP Depletion Induced by rVvhA

It was reported that oxidative stress and intracellular ATP depletion were associated with cell necrosis and apoptosis [30,31]; thus, we measured intracellular ROS and ATP levels in this study. As shown in Figure 3A, rVvhA (500 ng/mL) induced a significant increase in intracellular ROS levels, which reached a peak at 1 h; however, NS treatment (40 µg/mL) completely attenuated rVvhA-induced ROS production. Concretely, fluorescence detection via flow cytometry revealed decreased fluorescence in NS-treated cells, and ROS-related fluorescence was quantitatively weak under a fluorescence microscope after treatment (Figure 3B–D), indicating that NSs could prevent toxin-induced oxidative stress. Since ATP depletion is a terminal outcome of oxidative stress injuries in mitochondria, we further explored the effects of NSs on intracellular ATP depletion. Our results showed that rVvhA (500 ng/mL) caused a reduction in intracellular ATP in a time-dependent manner, and ATP was reduced by over 90% over a period of 12 h (Figure 3E,F); however, NSs also substantially prevented toxin-induced ATP depletion after 12 h (Figure 3G,H). Accordingly, we demonstrated that NSs may exert protective effects against rVvhA by improving oxidative stress and mitochondrial injury.

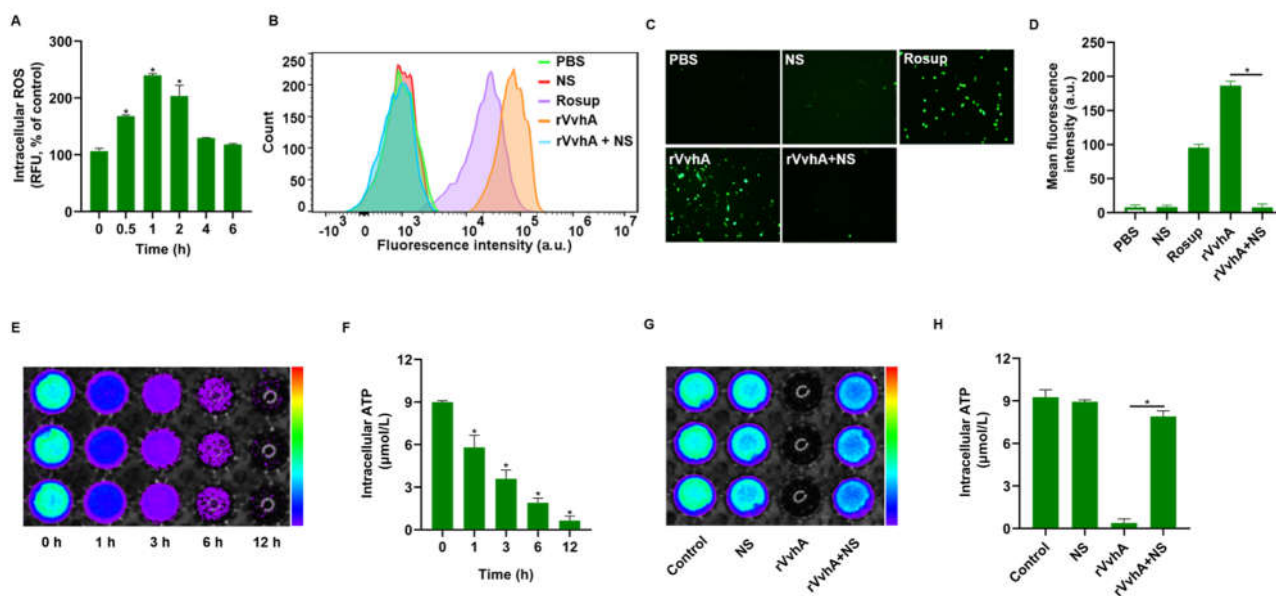


**Figure 3.** Inhibitory effects of NSs on rVvhA-induced ROS production and ATP reduction in HPAECs. (A) Time response of ROS production in HPAECs treated with rVvhA (500 ng/mL). (B) Flow cytometry results showing ROS production in HPAECs with various treatments. (C) ROS production (green) was visualized by fluorescence microscopy in HPAECs treated with PBS, NSs (40 μg/mL), rVvhA (500 ng/mL), rVvhA (500 ng/mL) plus NSs (40 μg/mL), respectively. (Original magnification × 200). (D) The quantification of ROS production in (C). (E,F) Time response of ATP levels in rVvhA-stimulated cells over a period of 12 h (0, 1, 3, 6, 12 h) were examined by a luminometer and bioluminescence imaging. (G,H) Analysis of ATP levels for 12 h in HPAECs treated with PBS, NSs (40 μg/mL), rVvhA (500 ng/mL), rVvhA (500 ng/mL) plus NSs (40 μg/mL), respectively, as detected by a luminometer and bioluminescence imaging. (The data represent the means ± SE.  $n = 3$ . \*  $p < 0.05$ ).

#### 2.4. NSs Inhibit PKC/ERK/JNK and NF-κB Pathway Activation Induced by rVvhA

According to previous studies, VvhA exposure can activate PKC/JNK/ERK phosphorylation, stimulate lipid raft-mediated ROS production, and ultimately cause NF-κB-dependent cell apoptosis in intestinal epithelial cells [20,32]. We, thus, measured the protein expression of these signaling pathways in HPAECs to explore the intracellular changes and protective effects of NSs against VvhA. In our study, we confirmed that rVvhA could stimulate PKC phosphorylation and induce the phosphorylation of both JNK and ERK from 30 to 90 min (Figure 4A), and these events were responsible for the activation of the transcription factor NF-κB; however, NSs significantly blocked rVvhA-induced PKC/JNK/ERK phosphorylation (Figure 4B). Next, we examined the effect of rVvhA on the activation of the NF-κB pathway, which is a direct transcriptional target of the apoptotic signaling pathway. Our results showed that rVvhA (500 ng/mL) increased the phosphorylation level of NF-κB from 15 min to 60 min (Figure 4C); however, NSs notably attenuated toxin-induced NF-κB signaling pathway activation (Figure 4D). A similar inhibitory effect of NSs on NF-κB accumulation in the nucleus was also confirmed by immunofluorescence staining (Figure 4E). Finally, the expression of the main apoptosis factors, including Bcl-2, Bax, Caspase-9, and Caspase-3, was measured, and these factors play key roles in mitochondrial pathways. Our results revealed that rVvhA altered the Bcl-2/Bax ratio from 60 to 180 min, and these proteins are two NF-κB-dependent apoptosis-determining factors (Figure 4F). Consistently, rVvhA also stimulated caspase-9/-3 activation while promoting apoptotic cell death; however, NSs notably reversed VvhA-mediated changes in mitochondrial apoptotic indicators (Figure 4G).

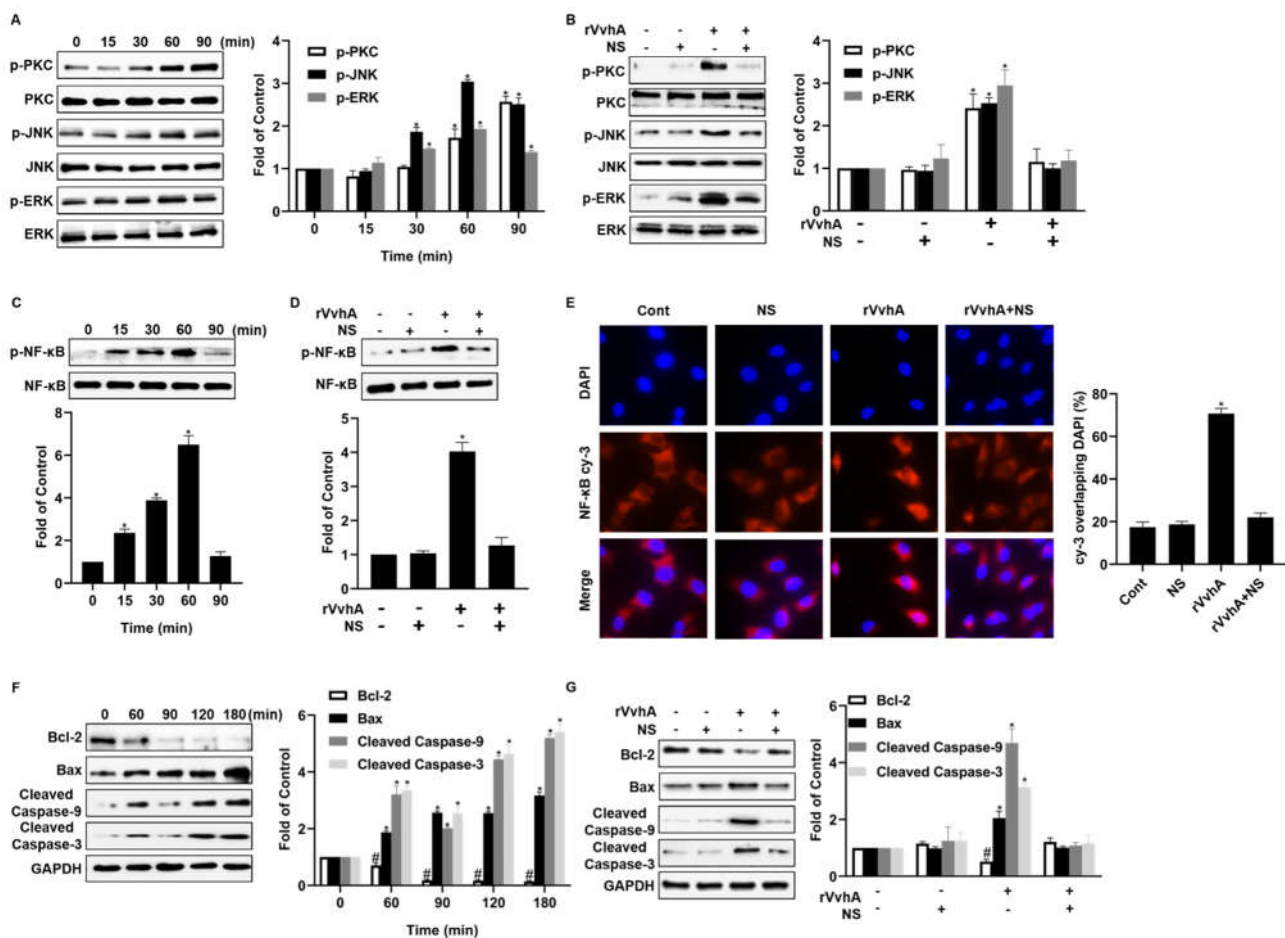


**Figure 4.** NSs inhibited rVvhA-induced activation of the PKC/JNK/ERK and NF-κB pathways. (A) The phosphorylation of PKC/JNK/ERK in HPAECs treated with rVvhA (500 ng/mL) was examined by Western blotting. The data represent the means ± SE.  $n = 3$ . \*  $p < 0.05$  versus 0 min. (B) The phosphorylation of PKC/JNK/ERK in HPAECs treated with NSs (40 μg/mL) and rVvhA (500 ng/mL) for 60 min. The data represent the means ± SE.  $n = 3$ . \*  $p < 0.05$  versus Cont. (C) The phosphorylation of NF-κB in HPAECs treated with rVvhA (500 ng/mL) was examined by Western blotting. The data represent the means ± SE.  $n = 3$ . \*  $p < 0.05$  versus 0 min. (D) The phosphorylation of NF-κB in HPAECs treated with NSs (40 μg/mL) and rVvhA (500 ng/mL) for 60 min. The data represent the mean ± SE.  $n = 3$ . \*  $p < 0.05$  versus Cont. (E) Nuclear accumulation of NF-κB was examined after 60 min by immunostaining with a Cy3-labeled NF-κB p65 antibody (Original magnification × 400). (F) HPAECs were incubated with rVvhA (500 ng/mL) for 180 min, and then Bcl-2 and Bax were analyzed by Western blotting. The data represent the means ± SE.  $n = 3$ . \*  $p < 0.05$  versus 0 min, #  $p < 0.05$  versus 0 min. (G) The expression of Bcl-2 and Bax was measured in the presence of NSs. The data represent the means ± SE.  $n = 3$ . \*  $p < 0.05$  versus Cont, #  $p < 0.05$  versus Cont.

### 2.5. In Vivo Neutralization of rVvhA by NSs

To examine the systemic detoxification effects of NSs against rVvhA in vivo, we first analyzed rVvhA-induced acute toxicity by injecting various amounts of rVvhA via the tail vein. Our results showed that the mortality of mice increased with increasing doses of rVvhA (Figure 5A). The survival curve shown in Figure 5B revealed that NS treatment dose-dependently improved the survival of mice that received lethal doses of rVvhA. When the dose of NSs exceeded 200 mg/kg, the survival rate was greater than 80%. Then, NSs (200 mg/kg) were used to examine the reduction in inflammatory cascade reactions caused by rVvhA (3.7 mg/kg,  $0.75 \times LD_{50}$ , a rational dose to trigger inflammatory and lung damage without lethality). NSs dramatically reversed rVvhA-induced interleukin-6

(IL-6) and tumor necrosis factor- $\alpha$  (TNF- $\alpha$ ) accumulation after 3 h (Figure 5C–F). NSs also apparently improved rVvhA-induced lung damage, such as typical hemorrhagic injuries, neutrophil aggregation, and alveolar structural changes (Figure 5G).

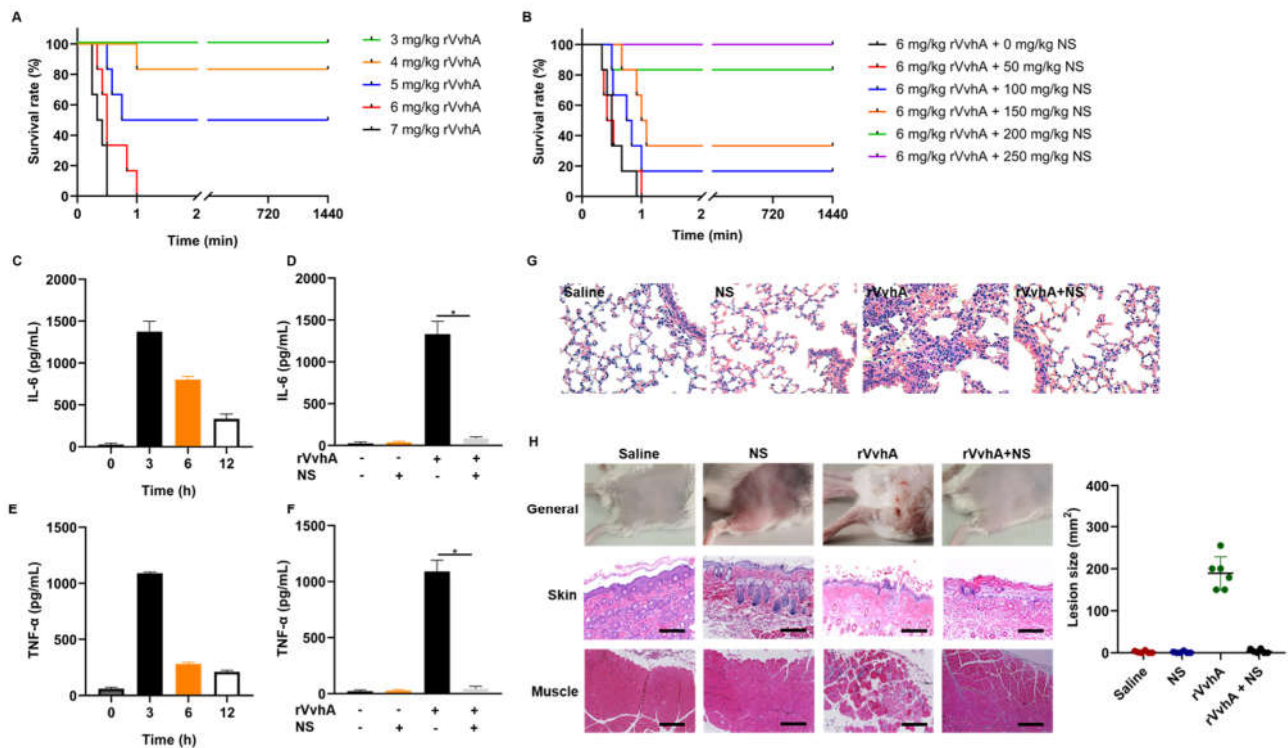


**Figure 5.** Protective effects of NSs in vivo. (A) Different doses of rVvhA (3, 4, 5, 6, 7 mg/kg) were injected intravenously, and mouse mortality was recorded. (B) A lethal dose of rVvhA (6 mg/kg) was injected via the tail vein, and different doses of NSs (0, 50, 100, 150, 200, 250 mg/kg) were immediately administered for treatment. (C,E) Mice were exposed to sublethal doses of rVvhA (3.7 mg/kg), and inflammatory factors, including IL-6 and TNF- $\alpha$ , were examined at predetermined times (0, 3, 6, 12 h). (D,F) NSs (200 mg/kg) were used to neutralize rVvhA (3.7 mg/kg) for 3 h in vivo, and then IL-6 and TNF- $\alpha$  in the blood were measured. (G) rVvhA (3.7 mg/kg) was used to stimulate mice for 3 h with or without NSs (200 mg/kg), and the lungs were harvested for hematoxylin and eosin (H&E) staining and pathological observations. Untreated mice and mice injected with NSs were used as controls. (Original magnification  $\times 400$ ) (H) rVvhA (30  $\mu$ g) was injected subcutaneously to imitate local infections, and NSs (50 mg/kg) were used for treatment. After 3 d, the injection sites were measured and photographed, and then the topical skin and muscle tissues were harvested for H&E staining and pathological observations. (Scale bar: 50  $\mu$ m. The data represent the means  $\pm$  SE.  $n = 6$ . \*  $p < 0.05$ ).

To examine the local detoxification effects of NSs against rVvhA in vivo, we further examined the effects of NSs (50 mg/kg) on a rVvhA-induced wound infection mouse model. Histological analyses showed that rVvhA induced obvious reddish ecchymosis and ulcerations on topical skin at 3 d, with typical edema, cell death and inflammation in the skin and muscles, while NS treatment significantly alleviated this tissue damage, confirming the local detoxification effects of NSs (Figure 5H).

### 3. Discussion

*V. vulnificus* is a highly fatal human pathogen that is increasingly being considered an emerging pathogen associated with public health concerns [33]; however, current antibiotic resistance combined with a lack of broad-spectrum virulence factor-targeting strategies highlights the need for innovative research into alternative strategies to combat

diseases [10]. In this study, a stable and biocompatible biomimetic nanodetoxification system was developed to neutralize VvhA for the first time. Specifically, NSs showed significant inhibitory effects on not only VvhA-induced apoptosis/necrosis but also toxin-induced septicemia and wound infections. In contrast to traditional strategies, NSs prevent the recognition and interaction between toxins and cells by absorbing and neutralizing VvhA toxins regardless of their specific structures, and further avoiding customization of inhibitors against VvhA-activating cell signaling molecules in treatment. Our work may offer significant potential for the treatment of severe *V. vulnificus* infections.

Multiple-organ failure caused by *V. vulnificus*-associated sepsis always begins with pulmonary dysfunction, which is characterized by increased vascular permeability due to pulmonary endothelial cell damage [34–37]. We, thus, used HPAECs as target cells to investigate the protective effect of NSs against VvhA-induced cytotoxicity. We first found that NSs could dramatically improve VvhA-induced apoptosis and necrosis in HPAECs. Since oxidative stress and intracellular ATP depletion are associated with necrosis and apoptosis [38–40], we further explored the effects of NSs on intracellular ROS production and ATP levels. Our results confirmed that NSs could prevent toxin-induced oxidative stress; moreover, we also found that NSs could apparently improve toxin-induced ATP depletion, which is a terminal outcome of oxidative stress injuries in mitochondria [38,40]. Accordingly, the above results revealed that NSs may exert protective effects against VvhA-induced apoptosis and necrosis by improving oxidative stress and mitochondrial injury. Then, we further explored the effects of NSs on various cell signaling pathways related to oxidative stress and mitochondrial injury. We confirmed that VvhA could induce NF- $\kappa$ B-dependent cell apoptosis via ROS production through the distinct activation of PKC/JNK/ERK in HPAECs. Additionally, NS treatment significantly blocked the activation of the above signaling pathways, as well as apoptosis-related proteins, confirming the protective mechanism of NSs on molecular levels. In previous studies [21,24,41–43], NSs were indicated to bind and neutralize toxins via lipid membrane interactions with a high natural affinity and prevent host-toxin interactions. Thus, we hypothesize that the protective mechanism of NSs against VvhA-induced cell apoptosis and necrosis may be associated with toxin sequestration and blocking toxin-host cell interactions, thus radically avoiding the downstream activation of toxin-induced cell signaling disruptions, as well as further cellular injuries. Therefore, for VvhA-induced sepsis, especially pulmonary dysfunction, the sequestration of VvhA by NSs can exert broadly protective effects without consideration of customization of inhibitors against disease-related cell signaling molecules in clinical trials.

To explore the clinical translation potential of NSs, we further established VvhA-induced septicemia mouse models and tested the systemic detoxification effects of NSs against VvhA in vivo. Our work showed that isolated VvhA toxins were fatal but NS injection significantly reversed VvhA-induced mortality, inflammation, and target organ damage, demonstrating that VvhA was indeed a vital virulence factor and NSs exerted significant anti-inflammatory and detoxification effects in vivo. In addition, given that *V. vulnificus* infection often occurs in exposed skin wounds [44], and VvhA can reproduce the same clinical and pathological manifestations as live *V. vulnificus*, we also subcutaneously injected VvhA into mice to simulate local wound infections. Similarly, we found that NSs could alleviate VvhA-induced skin and muscle lesions. These results indicated that NSs have great potential for treating local or systematic *V. vulnificus* infections clinically; however, many challenges should be tackled in preclinical trials [45,46]. First, immune responses are still very critical, and blood-type dependent biological applications may be a good strategy since NSs exert effects via natural RBC membranes. Second, the long-term compatibility of NSs should be further confirmed in large animal models (e.g., primates) before human trials [47]. Finally, the challenge of batch-to-batch quality control should also be addressed before scale-production. Overall, there is still a long way to go before practical application.

## 4. Materials and Methods

### 4.1. Cells, Animals and Reagents

HPAECs were obtained from Xinyu Biotechnology (Shanghai, China) and cultured at 37 °C in a humidified atmosphere of 5% CO<sub>2</sub> in Roswell Park Memorial Institute 1640 (RPMI 1640) medium containing 10% FBS and antibiotics. All the animal experiments were performed according to the Guide for the Care and Use of Laboratory Animals and were approved by the Medical Ethics Committee of Naval Medical University. FBS, PBS, tris buffered saline tween (TBST) and 0.25% (*w/v*) trypsin–0.03% (*w/v*) ethylenediaminetetraacetic acid (EDTA) solution were purchased from Grand Island Biological Co. (New York, NY, USA). RPMI 1640 medium was purchased from Solarbio Co. (Beijing, China). Cell-counting (CCK-8) kit was purchased from Dojindo Molecular Technologies, Inc. (Rockville, MD, USA). ROS and ATP detection kits were purchased from Beyotime Biotechnology (Shanghai, China). Carboxy-terminated 50:50 PLGA (Mw 48 000, 0.67 dL/g) was purchased from Lactel Co. (Birmingham, UK). Monoclonal antibodies against PKC (#2056), phosphorylated PKC (p-PKC, #9379), NF-κB (#8242), p-NF-κB(#3033), Bcl-2 (#), caspase-3 (#9664) and caspase-9 (#9509) were purchased from Cell Signaling Technology (Shanghai, China). Monoclonal antibodies against JNK (#AF1048), phosphorylated JNK (p-JNK, #AF1762), ERK (#AF1051), phosphorylated ERK (p-ERK, #AF1891) and Bax (#AF1270) were purchased from Beyotime Biotechnology (Shanghai, China). Tryptone and yeast extract were purchased from Thermo Fisher Scientific (Oxoid, Waltham, MA, USA). All other reagents were of analytical grade, commercially available, and used as received.

### 4.2. Preparation and Characterization of NSs

#### 4.2.1. Preparation of RBC Ghosts and Vesicles

RBC ghosts were prepared as described previously with slight modifications [48]. First, whole blood was collected from male ICR mice (25–30 g) via a cardiac puncture protocol [49]. Then, the cells were washed three times with cold 1 × PBS (pH 7.4) to remove plasma and the buffy coat. Sequentially, to obtain RBC ghosts, the sediments were repeatedly resuspended in 0.25 × PBS for 30 min followed by centrifugation at 14,000 rpm for 20 min at 4 °C until a white pellet was obtained. Finally, to obtain RBC-derived vesicles, the collected RBC ghosts were sonicated for 3 min at a frequency of 45 kHz and power of 200 W (SB-5200DT bath sonicator, Scientz, Ningbo, China) and then serially extruded through 400 nm and 200 nm polycarbonate porous membranes (Avanti mini extruder, Avanti Polar Lipids, Birmingham, UK).

#### 4.2.2. Preparation of PLGA Cores and NSs

PLGA NPs were prepared via the nanoprecipitation method [50]. Briefly, the PLGA polymer was first dissolved in 1 mL of acetone solution (5 mg/mL) and then injected into 3 mL of distilled water. The mixture was subsequently stirred for 1 h and then placed into a vacuum for complete evaporation of the acetone. The resulting NPs were examined by DLS. RBC vesicles and PLGA NPs were mixed at a 1:1 ratio (*w/w*) and then sonicated in a bath sonicator for 2 min. As a result, NSs were formed by sequentially extruding the mixture through 400 nm, 200 nm, and 100 nm polycarbonate porous membranes 12 times.

#### 4.2.3. Characterization of NSs

First, the hydrodynamic size and zeta potential of RBC-derived NSs were measured by DLS. Then, the NS structure was examined by TEM with 1% uranyl acetate for negative staining. Additionally, the membrane protein characteristics of RBC ghosts, RBC vesicles, and NSs (with an equivalent protein concentration of 1 mg/mL) were examined by SDS-PAGE on a 6–12% Bis-Tris gel that was run at 150 V for 1 h. The resulting gels were stained with Coomassie Blue (Sangon, Shanghai, China) for visualization. Finally, the stability of NSs was measured by DLS in both PBS and 100% FBS at 4 °C for 7 d.

#### 4.3. Cell Viability and Apoptosis/Necrosis Detection in HPAECs

HPAECs were grown on 96-well plates and synchronized in the G<sub>0</sub>/G<sub>1</sub> phase by culture in a serum-free medium for 24 h. Then, various doses of rVvhA (0, 5, 10, 50, 100, 500, 1000 ng/mL) were added and incubated for an additional 4 h, after which cell viability was analyzed using a CCK-8 kit. Subsequently, the time-dose effect of the toxin was also examined using rVvhA (500 ng/mL, the dose producing 50% inhibition) to treat HPAECs. For toxin neutralization, various doses of NSs (0, 1.25, 2.5, 5, 10, 20, 40 µg/mL) were added and incubated with rVvhA (500 ng/mL) for 30 min and then centrifuged at 10,000 rpm for 10 min. The resulting supernatant was harvested and used to treat cells for 4 h, after which cell viability was examined. A similar detoxification effect of NSs was also examined by measuring cell apoptosis with flow cytometry (FACSCalibur, BD, New York, NY, USA). First, NSs (40 µg/mL) were incubated with rVvhA (500 ng/mL) for 30 min and then centrifuged at 10,000 rpm for 10 min. Subsequently, cells were treated with the supernatants for 4 h and processed with an Annexin V and PI staining kit (Beyotime, Shanghai, China). PBS and NSs were used as controls.

#### 4.4. Intracellular ROS and ATP Detection

To quantify intracellular ROS levels, HPAECs were grown on 6-well plates and treated with 10 mM 2'-7'-dichlorofluorescein diacetate (DCFH-DA) probes for 20 min before being exposed to rVvhA (500 ng/mL). As a well-established ROS-inducing agent, Rosup (50 µg/mL) was used as a positive control. At predetermined times (0, 0.5, 1, 2, 4, 6 h), the cells were harvested for fluorescence detection at excitation and emission wavelengths of 488 and 525 nm, respectively. To examine the protective effect of NSs, a toxin-containing culture medium was immediately incubated with NSs (40 µg/mL) for 30 min and then centrifuged at 10,000 rpm for 10 min. The supernatants were obtained and used to treat cells for 1 h, and then intracellular ROS levels were measured using flow cytometry or fluorescence microscopy.

For ATP detection, HPAECs were incubated with rVvhA (500 ng/mL) for various times (0, 1, 3, 6, 12 h), lysed and centrifuged at 14,000 rpm for 5 min at 4 °C. The supernatants were harvested, and the intracellular ATP concentration was measured using a luminometer and bioluminescence imaging. Next, toxins were pre-incubated with NSs in medium for 30 min, followed by centrifugation for harvesting supernatants. After that, HPAECs were treated with harvested supernatants for 12 h. Then, all the cells were harvested for fluorescence intensity detection via a luminometer or bioluminescence imaging. Cells treated with PBS or NSs served as controls.

#### 4.5. Analysis of PKC/ERK/JNK and NF-κB Pathway in HPAECs

First, we explored the effects of rVvhA (500 ng/mL) on apoptosis-related signaling pathways. At predetermined time points (0, 15, 30, 60, and 90 min), rVvhA-treated HPAECs were harvested, washed, and then lysed to obtain cellular proteins to detect PKC-JNK-ERK and NF-κB pathways. Similarly, at different time points (0, 60, 90, 120, and 180 min), rVvhA-treated cells were harvested to detect apoptosis-related proteins. After determining the optimal exposure time, the effects of NSs (40 µg/mL) on apoptosis-related factors were then investigated. NSs were first pre-incubated with rVvhA (500 ng/mL) in RPMI 1640 medium for 30 min, followed by centrifugation to obtain supernatants. The cells were then treated with the supernatants and harvested at the optimal time point for apoptotic factor analysis.

Specifically, for Western blotting experiments, 20 micrograms of protein were resolved by 10% SDS-PAGE and transferred to a polyvinylidene difluoride membrane. The membrane was blocked with 5% skim milk for 2 h and incubated with the appropriate primary antibody (1:500) at 4 °C overnight. Next, the membrane was washed with TBST and incubated with a horseradish peroxidase-conjugated secondary antibody (1:2000) for 1 h. Subsequently, the protein bands were visualized by a ChemiDoc XRS+ System (Bio-Rad, Richmond, VA, USA) and quantified using ImageJ software (Version 1.8.0, NIH, Bethesda,

MD, USA). For immunofluorescence staining, the cells were fixed for 10 min at room temperature, rinsed with PBS, blocked, and then incubated with NF- $\kappa$ B p65 antibodies overnight at 4 °C. After being washed with PBS three times, the cells were incubated with conjugated antibodies for 1 h at room temperature. After that, 4',6-diamidino-2-phenylindole (DAPI) dye was added and incubated for 5 min before an anti-fluorescence quenching liquid was used and the cells were observed under a fluorescence microscope.

#### 4.6. *In Vivo* rVvhA Detoxification by NSs

To analyze rVvhA-induced acute toxicity, male ICR mice (18–20 g) were randomly divided into five groups ( $n = 6$ ), and different doses of rVvhA (3, 4, 5, 6, 7 mg/kg) were injected intravenously via the tail vein. The survival rate of each group was then recorded and analyzed. For systemic detoxification experiments, various amounts of NSs (0, 50, 100, 150, 200, 250 mg/kg) were injected via the tail immediately after exposure to a lethal intravenous dose of rVvhA (6 mg/kg), and the survival rate was recorded. For anti-inflammatory experiments, the mice were first injected with a sub-lethal dose of rVvhA (3.7 mg/kg,  $0.75 \times LD_{50}$ ). Then, at predetermined times (0, 3, 6, 12 h), the inflammatory factors, including IL-6 and TNF- $\alpha$ , were measured using ELISA kits. After that, the optimal time point (3 h), when rVvhA exerted the most obvious inflammatory injuries, was chosen to examine the inhibitory effects of NSs on toxin-induced inflammatory cascades. Finally, the mice were sacrificed, the lungs were harvested, and the tissues were fixed for H&E staining and pathological observations.

The local detoxification abilities of NSs against rVvhA were also tested. First, rVvhA (30  $\mu$ g) was injected subcutaneously into the right flanks of mice to imitate local infections. Then, NSs (50 mg/kg) were injected immediately into the same regions to test their protective effects against rVvhA-induced wound injuries. An equal amount of PBS was used in the negative control group. After 3 d, the injection sites were measured and photographed, and then the topical skin and muscle tissues were harvested for H&E staining and pathological observations.

#### 4.7. Statistical Analysis

The data are presented as the mean  $\pm$  standard error (SE). Statistical significance was evaluated using one-way ANOVA ( $p < 0.05$ ).

## 5. Conclusions

In conclusion, we synthesized a biocompatible nanoscale detoxification system (NSs) and used it for VvhA neutralization for the first time. NSs exerted significant protective effects on VvhA-induced damage both *in vitro* and *in vivo*, which may be associated with toxin sequestration and blockage of toxin-host cell interactions. These results provide new insights into how NS is a novel treatment strategy for the detoxification of PFTs from antibiotic-resisted *V. vulnificus*.

**Supplementary Materials:** The following supporting information can be downloaded at: <https://www.mdpi.com/article/10.3390/ijms23126821/s1>.

**Author Contributions:** Conceptualization, S.Z. and L.Z.; methodology, S.Z. and Q.W.; software, S.Z. and F.W.; validation, B.W. (Beilei Wang), P.Z. and B.W. (Bo Wang); formal analysis, S.Z. and G.L.; investigation, S.Z., P. Z. and F.Z.; resources, P. Z. and L. Z.; data curation, J.L. and B.W. (Bo Wang); writing—original draft preparation, S.Z., Q.W. and P.Z.; writing—review and editing, B.W. (Beilei Wang) and L.Z.; supervision, L.Z.; and project administration, L.Z. All authors have read and agreed to the published version of the manuscript.

**Funding:** The authors thank the National Natural Science Foundation of China (81974496) and the National Key R&D Program of China (2019YFC0312605) for financial support.

**Institutional Review Board Statement:** Not applicable.

**Informed Consent Statement:** Not applicable.

**Data Availability Statement:** Not applicable.

**Conflicts of Interest:** The authors declare no conflict of interest.

## References

- Zhao, H.; Xu, L.; Dong, H.; Hu, J.; Gao, H.; Yang, M.; Zhang, X.; Chen, X.; Fan, J.; Ma, W. Correlations between clinical features and mortality in patients with *Vibrio vulnificus* infection. *PLoS ONE* **2015**, *10*, e0136019. [CrossRef] [PubMed]
- Yun, N.R.; Kim, D.M. *Vibrio vulnificus* infection: A persistent threat to public health. *Korean J. Intern. Med.* **2018**, *33*, 1070–1078. [CrossRef] [PubMed]
- Park, J.; Lee, C.S. *Vibrio vulnificus* infection. *N. Engl. J. Med.* **2018**, *379*, 375. [CrossRef] [PubMed]
- Horseman, M.A.; Surani, S. A comprehensive review of *Vibrio vulnificus*: An important cause of severe sepsis and skin and soft-tissue infection. *Int. J. Infect. Dis.* **2011**, *15*, e157–e166. [CrossRef]
- Bhat, P.; Bhaskar, M.; Sistla, S.; Kadhiraivan, T. Fatal case of necrotising fasciitis due to *Vibrio vulnificus* in a patient with alcoholic liver disease and diabetes mellitus. *BMJ Case Rep.* **2019**, *12*, bcr-2018-227851. [CrossRef] [PubMed]
- Baker-Austin, C.; Oliver, J.D.; Alam, M.; Ali, A.; Waldor, M.K.; Qadri, F.; Martinez-Urtaza, J. *Vibrio* spp. infections. *Nat. Rev. Dis. Primers* **2018**, *4*, 8. [CrossRef]
- Lee, Y.C.; Hor, L.I.; Chiu, H.Y.; Lee, J.W.; Shieh, S.J. Prognostic factor of mortality and its clinical implications in patients with necrotizing fasciitis caused by *Vibrio vulnificus*. *Eur. J. Clin. Microbiol. Infect. Dis.* **2014**, *33*, 1011–1018. [CrossRef]
- King, M.; Rose, L.; Fraimow, H.; Nagori, M.; Danish, M.; Doktor, K. *Vibrio vulnificus* infections from a previously nonendemic area. *Ann. Intern. Med.* **2019**, *171*, 520–521. [CrossRef]
- Blake, P.A.; Merson, M.H.; Weaver, R.E.; Hollis, D.G.; Heublein, P.C. Disease caused by a marine *Vibrio*—clinical characteristics and epidemiology. *N. Engl. J. Med.* **1979**, *300*, 1–5. [CrossRef]
- Elmahdi, S.; DaSilva, L.V.; Parveen, S. Antibiotic resistance of *Vibrio parahaemolyticus* and *Vibrio vulnificus* in various countries: A review. *Food Microbiol.* **2016**, *57*, 128–134. [CrossRef]
- Mok, J.S.; Ryu, A.; Kwon, J.Y.; Park, K.; Shim, K.B. Abundance, antimicrobial resistance, and virulence of pathogenic *Vibrio* strains from molluscan shellfish farms along the Korean coast. *Mar. Pollut. Bull.* **2019**, *149*, 110559. [CrossRef] [PubMed]
- Larry, D.; Gray, A.S.K. Mouse skin damage caused by cytotoxin from *Vibrio vulnificus* and by *V. vulnificus* infection. *J. Infect. Dis.* **1987**, *155*, 236–241.
- Park, J.W.; Ma, S.N.; Song, E.S.; Park, B.H.; Rho, H.W.; Song, C.H.; Park, S.D.; Kim, H.R. Pulmonary damage by *Vibrio vulnificus* cytotoxin. *Infect. Immun.* **1996**, *64*, 2873–2876. [CrossRef] [PubMed]
- Jeong, H.G.; Satchell, K.J. Additive function of *Vibrio vulnificus* MARTX<sub>VV</sub> and VvhA cytotoxins promotes rapid growth and epithelial tissue necrosis during intestinal infection. *PLoS Pathog.* **2012**, *8*, e1002581. [CrossRef]
- Lee, S.E.; Ryu, P.Y.; Kim, S.Y.; Kim, Y.R.; Koh, J.T.; Kim, O.J.; Chung, S.S.; Choy, H.E.; Rhee, J.H. Production of *Vibrio vulnificus* hemolysin in vivo and its pathogenic significance. *Biochem. Biophys. Res. Commun.* **2004**, *324*, 86–91. [CrossRef]
- Yuan, Y.; Feng, Z.; Wang, J. *Vibrio vulnificus* hemolysin: Biological activity, regulation of VvhA expression, and role in pathogenesis. *Front. Immunol.* **2020**, *11*, 599439. [CrossRef]
- Leng, F.; Lin, S.; Wu, W.; Zhang, J.; Song, J.; Zhong, M. Epidemiology, pathogenetic mechanism, clinical characteristics, and treatment of *Vibrio vulnificus* infection: A case report and literature review. *Eur. J. Clin. Microbiol. Infect. Dis.* **2019**, *38*, 1999–2004. [CrossRef]
- Song, E.J.; Lee, S.J.; Lim, H.S.; Kim, J.S.; Jang, K.K.; Choi, S.H.; Han, H.J. *Vibrio vulnificus* VvhA induces autophagy-related cell death through the lipid raft-dependent c-Src/NOX signaling pathway. *Sci. Rep.* **2016**, *6*, 27080. [CrossRef]
- Shinoda, S.; Miyoshi, S.I.; Yamanaka, H.; Miyoshi-Nakahara, N. Some properties of *Vibrio Vulnificus* hemolysin. *Microbiol. Immunol.* **1985**, *29*, 583–590. [CrossRef]
- Lee, S.J.; Jung, Y.H.; Oh, S.Y.; Song, E.J.; Choi, S.H.; Han, H.J. *Vibrio vulnificus* VvhA induces NF-kappaB-dependent mitochondrial cell death via lipid raft-mediated ROS production in intestinal epithelial cells. *Cell Death Dis.* **2015**, *6*, 1655. [CrossRef]
- Hu, C.M.; Fang, R.H.; Copp, J.; Luk, B.T.; Zhang, L. A biomimetic nanosponge that absorbs pore-forming toxins. *Nat. Nanotechnol.* **2013**, *8*, 336–340. [CrossRef] [PubMed]
- Hu, C.M.; Zhang, L.; Aryal, S.; Cheung, C.; Fang, R.H.; Zhang, L. Erythrocyte membrane-camouflaged polymeric nanoparticles as a biomimetic delivery platform. *Proc. Natl. Acad. Sci. USA* **2011**, *108*, 10980–10985. [CrossRef] [PubMed]
- Fang, R.H.; Hu, C.M.; Zhang, L. Nanoparticles disguised as red blood cells to evade the immune system. *Expert Opin. Biol. Ther.* **2012**, *12*, 385–389. [CrossRef] [PubMed]
- Distler, U.; Tenzer, S. Tools for pathogen proteomics: Fishing with biomimetic nanosponges. *ACS Nano* **2017**, *11*, 11768–11772. [CrossRef]
- Chen, Y.; Chen, M.; Zhang, Y.; Lee, J.H.; Escajadillo, T.; Gong, H.; Fang, R.H.; Gao, W.; Nizet, V.; Zhang, L. Broad-spectrum neutralization of pore-forming toxins with human erythrocyte membrane-coated nanosponges. *Adv. Healthc. Mater.* **2018**, *7*, e1701366. [CrossRef]
- Makadia, H.K.; Siegel, S.J. Poly lactic-co-glycolic acid (PLGA) as biodegradable controlled drug delivery carrier. *Polymers* **2011**, *3*, 1377–1397. [CrossRef]

27. Yu, F.; Ao, M.; Zheng, X.; Li, N.; Xia, J.; Li, Y.; Li, D.; Hou, Z.; Qi, Z.; Chen, X.D. PEG-lipid-PLGA hybrid nanoparticles loaded with berberine–phospholipid complex to facilitate the oral delivery efficiency. *Drug Deliv.* **2017**, *24*, 825–833. [CrossRef]
28. Lin, H.J.; Wang, J.H.; Wang, C.Y.; Wu, Y.C. The preparation and characteristic of poly(lactide-co-glycolide) microspheres as novel antigen delivery systems. *Int. J. Nanotechnol.* **2013**, *10*, 870–890. [CrossRef]
29. Zohra, M.; Fawzia, A. Hemolytic activity of different herbal extracts used in Algeria. *Int. J. Pharm. Sci. Res.* **2014**, *5*, 495–500.
30. Kannan, K.; Jain, S.K. Oxidative stress and apoptosis. *Pathophysiology* **2000**, *7*, 153–163. [CrossRef]
31. Tsujimoto, Y. Apoptosis and necrosis: Intracellular ATP level as a determinant for cell death modes. *Cell Death Differ.* **1997**, *4*, 429–434. [CrossRef] [PubMed]
32. Lee, S.J.; Lee, H.J.; Jung, Y.H.; Kim, J.S.; Choi, S.H.; Han, H.J. Melatonin inhibits apoptotic cell death induced by *Vibrio vulnificus* VvhA via melatonin receptor 2 coupling with NCF-1. *Cell Death Dis.* **2018**, *9*, 48. [CrossRef] [PubMed]
33. Osunla, C.A.; Okoh, A.I. *Vibrio pathogens*: A public health concern in rural water resources in sub-Saharan Africa. *Int. J. Environ. Res. Public Health* **2017**, *14*, 1188. [CrossRef] [PubMed]
34. Kang, S.J.; Jung, S.I.; Peck, K.R. Historical and clinical perspective of *Vibrio vulnificus* infections in Korea. *Infect. Chemother.* **2020**, *52*, 245–251. [CrossRef]
35. Lu, Z.; Li, M.; Liang, H.; Qiu, Q.; Yang, G.; Zhou, T.; Hong, G. Dynamic expressions of liver tissue apoptosis-related genes of *Vibrio vulnificus* sepsis rats and the effects of antibacterial agents. *J. Huazhong Univ. Sci. Technol. Med. Sci.* **2009**, *29*, 193–197. [CrossRef]
36. Liu, C.C.; Wang, S.M.; Chiou, Y.Y.; Chen, C.T. *Vibrio vulnificus* infection complicated by acute respiratory distress syndrome in a child with nephrotic syndrome. *Pediatr. Pulm.* **2000**, *29*, 400–403.
37. Rho, H.W.; Choi, M.J.; Lee, J.N.; Park, J.W.; Kim, J.S.; Park, B.H.; Sohn, H.S.; Kim, H.R. Cytotoxic mechanism of *Vibrio vulnificus* cytotoxin in CPAE cells. *Life Sci.* **2002**, *70*, 1923–1934. [CrossRef]
38. Víctor, V.M.; Esplugues, J.V.; Hernández-Mijares, A.; Rocha, M. Oxidative stress and mitochondrial dysfunction in sepsis: A potential therapy with mitochondria-targeted antioxidants. *Infect. Disord.-Drug Targets* **2009**, *9*, 376–389. [CrossRef]
39. Lou, Y.L.; Xie, D.L.; Huang, X.H.; Zheng, M.M.; Zhang, T.; Xu, J. *Vibrio vulnificus* hemolysin induces TNF- $\alpha$  independent ROS production by primary murine macrophages. *Res. Sq.* **2021**.
40. Prauchner, C.A. Oxidative stress in sepsis: Pathophysiological implications justifying antioxidant co-therapy. *Burns* **2017**, *43*, 471–485. [CrossRef]
41. Fang, R.H.; Luk, B.T.; Hu, C.M.; Zhang, L. Engineered nanoparticles mimicking cell membranes for toxin neutralization. *Adv. Drug Deliv. Rev.* **2015**, *90*, 69–80. [CrossRef] [PubMed]
42. Wang, F.; Fang, R.H.; Luk, B.T.; Hu, C.J.; Thamphiwatana, S.; Dehaini, D.; Angsantikul, P.; Kroll, A.V.; Pang, Z.; Gao, W.; et al. Nanoparticle-based antivirulence vaccine for the management of methicillin-resistant *Staphylococcus aureus* skin infection. *Adv. Funct. Mater.* **2016**, *26*, 1628–1635. [CrossRef] [PubMed]
43. Bricarello, D.A.; Patel, M.A.; Parikh, A.N. Inhibiting host-pathogen interactions using membrane-based nanostructures. *Trends Biotechnol.* **2012**, *30*, 323–330. [CrossRef] [PubMed]
44. Huang, K.C.; Weng, H.H.; Yang, T.Y.; Chang, T.S.; Huang, T.W.; Lee, M.S. Distribution of fatal *Vibrio vulnificus* necrotizing skin and soft-tissue infections: A systematic review and meta-analysis. *Medicine* **2016**, *95*, e2627. [CrossRef]
45. Xia, Q.; Zhang, Y.; Li, Z.; Hou, X.; Feng, N. Red blood cell membrane-camouflaged nanoparticles: A novel drug delivery system for antitumor application. *Acta. Pharm. Sin. B* **2019**, *9*, 675–689. [CrossRef]
46. Yang, J.; Wang, F.; Lu, Y.; Qi, J.; Deng, L.; Sousa, F.; Sarmiento, B.; Xu, X.; Cui, W. Recent advance of erythrocyte-mimicking nanovehicles: From bench to bedside. *J. Control. Release* **2019**, *314*, 81–91. [CrossRef]
47. Kotb, S.; Piraquive, J.; Lambertson, F.; Lux, F.; Verset, M.; Di Cataldo, V.; Contamin, H.; Tillement, O.; Canet-Soulas, E.; Sancey, L. Safety evaluation and imaging properties of gadolinium-based nanoparticles in nonhuman primates. *Sci. Rep.* **2016**, *6*, 35053. [CrossRef]
48. Passow, G.S.H. Preparation and properties of human erythrocyte ghosts. *Mol. Cell Biochem.* **1973**, *2*, 197–218.
49. Kaur, H.; Fisher, K.; Othman, M. Thromboelastography testing in mice following blood collection from facial vein and cardiac puncture. *Blood Coagul. Fibrinolysis* **2019**, *30*, 366–369. [CrossRef]
50. Govender, T.; Stolnik, S.; Garnett, M.C.; Illum, L.; Davis, S.S. PLGA nanoparticles prepared by nanoprecipitation: Drug loading and release studies of a water-soluble drug. *J. Control. Release* **1999**, *57*, 171–185. [CrossRef]





Article

# Optical and Material Characteristics of MoS<sub>2</sub>/Cu<sub>2</sub>O Sensor for Detection of Lung Cancer Cell Types in Hydroplegia

Arvind Mukundan <sup>1</sup>, Shih-Wei Feng <sup>2</sup>, Yu-Hsin Weng <sup>1</sup>, Yu-Ming Tsao <sup>1</sup>, Sofya B. Artemkina <sup>3,4</sup>, Vladimir E. Fedorov <sup>3,4</sup>, Yen-Sheng Lin <sup>5</sup>, Yu-Cheng Huang <sup>6,\*</sup> and Hsiang-Chen Wang <sup>1,\*</sup>

- <sup>1</sup> Department of Mechanical Engineering, Advanced Institute of Manufacturing with High Tech Innovations (AIM-HI), Center for Innovative Research on Aging Society (CIRAS), National Chung Cheng University, 168, University Rd., Min Hsiung, Chia Yi 62102, Taiwan; d09420003@ccu.edu.tw (A.M.); soul\_loving0629@yahoo.com.tw (Y.-H.W.); d09420002@ccu.edu.tw (Y.-M.T.)
- <sup>2</sup> Department of Applied Physics, National University of Kaohsiung, 700 Kaohsiung University Rd., Nanzih District, Kaohsiung 81148, Taiwan; swfeng@nuk.edu.tw
- <sup>3</sup> Nikolaev Institute of Inorganic Chemistry, Siberian Branch of Russian Academy of Sciences, 630090 Novosibirsk, Russia; artem@niic.nsc.ru (S.B.A.); fed@niic.nsc.ru (V.E.F.)
- <sup>4</sup> Department of Natural Sciences, Novosibirsk State University, 1, Pirogova str., 630090 Novosibirsk, Russia
- <sup>5</sup> Department of Electronic Engineering, I-Shou University, No. 1, Sec. 1, Syuecheng Rd., Dashu District, Kaohsiung 84001, Taiwan; yslin@isu.edu.tw
- <sup>6</sup> Department of Dentistry, Kaohsiung Armed Forces General Hospital, 2, Zhongzheng 1st. Rd., Kaohsiung 80284, Taiwan
- \* Correspondence: tim1018@hotmail.com (Y.-C.H.); hcwang@ccu.edu.tw (H.-C.W.)

**Citation:** Mukundan, A.; Feng, S.-W.; Weng, Y.-H.; Tsao, Y.-M.; Artemkina, S.B.; Fedorov, V.E.; Lin, Y.-S.; Huang, Y.-C.; Wang, H.-C. Optical and Material Characteristics of MoS<sub>2</sub>/Cu<sub>2</sub>O Sensor for Detection of Lung Cancer Cell Types in Hydroplegia. *Int. J. Mol. Sci.* **2022**, *23*, 4745. <https://doi.org/10.3390/ijms23094745>

Academic Editor: Raghvendra Singh Yadav

Received: 4 April 2022

Accepted: 22 April 2022

Published: 25 April 2022

**Publisher's Note:** MDPI stays neutral with regard to jurisdictional claims in published maps and institutional affiliations.

**Abstract:** In this study, n-type MoS<sub>2</sub> monolayer flakes are grown through chemical vapor deposition (CVD), and a p-type Cu<sub>2</sub>O thin film is grown via electrochemical deposition. The crystal structure of the grown MoS<sub>2</sub> flakes is analyzed through transmission electron microscopy. The monolayer structure of the MoS<sub>2</sub> flakes is verified with Raman spectroscopy, multiphoton excitation microscopy, atomic force microscopy, and photoluminescence (PL) measurements. After the preliminary processing of the grown MoS<sub>2</sub> flakes, the sample is then transferred onto a Cu<sub>2</sub>O thin film to complete a p-n heterogeneous structure. Data are confirmed via scanning electron microscopy, SHG, and Raman mapping measurements. The luminous energy gap between the two materials is examined through PL measurements. Results reveal that the thickness of the single-layer MoS<sub>2</sub> film is 0.7 nm. PL mapping shows a micro signal generated at the 627 nm wavelength, which belongs to the B2 excitons of MoS<sub>2</sub> and tends to increase gradually when it approaches 670 nm. Finally, the biosensor is used to detect lung cancer cell types in hydroplegia significantly reducing the current busy procedures and longer waiting time for detection. The results suggest that the fabricated sensor is highly sensitive to the change in the photocurrent with the number of each cell, the linear regression of the three cell types is as high as 99%. By measuring the slope of the photocurrent, we can identify the type of cells and the number of cells.

**Keywords:** photoelectrochemical; chemical vapor deposition; molybdenum disulfide (MoS<sub>2</sub>); cuprous oxide (Cu<sub>2</sub>O); positive oxide trap state; DNA; biosensor



**Copyright:** © 2022 by the authors. Licensee MDPI, Basel, Switzerland. This article is an open access article distributed under the terms and conditions of the Creative Commons Attribution (CC BY) license (<https://creativecommons.org/licenses/by/4.0/>).

## 1. Introduction

Molybdenum disulfide (MoS<sub>2</sub>) is one of the two-dimensional (2D) transition metal chalcogenides that have been studied recently [1–6]. Materials related to nanometer-scale electronic and optoelectronic components, such as field-effect transistors, prospective memory components, light-emitting diodes (LED), and sensors, have been manufactured because of the excellent spin-valley coupling and flexural and optoelectronic properties of MoS<sub>2</sub> [7–19]. However, MoS<sub>2</sub> is a layered structure, which has good lubricity, resistance to pressure, and wear resistance, and is mostly used as solid lubricant [20]. It is used in equipment operating under high-speed, heavy-load, high-temperature, and chemical

corrosive conditions. MoS<sub>2</sub> is a black hexagonal crystal structure with silver-gray luster, its Moiré mass is 160.07 g/mol, density is 5.06 g/cm<sup>3</sup>, and melting point is 1185 °C. MoS<sub>2</sub> itself is insoluble in water, generally insoluble in other acids, alkalis, and organic solvents. However, at 400 °C, oxidation occurs slowly, and molybdenum trioxide (MoO<sub>3</sub>) gradually forms. PN heterostructures have been widely used in the semiconductor industry; as a typical P-type semiconductor, Cu<sub>2</sub>O is considered to be the most effective material [21]. With these characteristics, Cu<sub>2</sub>O can be effectively used as an absorption layer in the visible wavelength range [22–25]. In a bulk MoS<sub>2</sub> semiconductor, an indirect energy gap of 1.2 eV between the G- and S-point conduction bands, and a single-layer MoS<sub>2</sub> semiconductor has a direct energy gap of 1.84 eV. Studies on light absorption, light reflection, and light excitation spectroscopy have evolved from bulk materials to single-layer TMDs [26]. In 2014, Yu-Fei Zhao et al. used a simple chemical synthesis method to cover MoS<sub>2</sub> successfully on p-Cu<sub>2</sub>O semiconductors for high-efficiency solar hydrogen production [21]. In 2016, Xinne Zhao et al. assembled Cu<sub>2</sub>O nanoparticles and MoS<sub>2</sub> nanosheets with a 2D planar structure into a 3D MoS<sub>2</sub>/Cu<sub>2</sub>O porous nanocomposite through hydrothermal synthesis [27,28]. In 2017, Linxia Fang et al. successfully decorated Cu<sub>2</sub>O nanoparticles on flower-like MoS<sub>2</sub> and used them for non-enzymatic current detection in glucose. This structure has Cu<sub>2</sub>O nanoparticles dispersed in MoS<sub>2</sub> [29]. Gang Li et al. reported the hydrothermal synthesis of MoS<sub>2</sub>/Cu<sub>2</sub>O nanocomposites with a tunable heterojunction to enhance the photochemical activity and stability of visible light [30]. The lack of energy gap of graphene in two-dimensional materials has shifted the focus on two-dimensional transition metal dichalcogenides (TMDs) with different energy gaps obtained by changing the number of layers. In the review of previous studies on MoS<sub>2</sub>/Cu<sub>2</sub>O, MoS<sub>2</sub>/Cu<sub>2</sub>O has high-performance photocatalysis, excellent electrocatalysis, strong stability, reproducibility, and high selectivity for non-MEI sensors. This structure can be used as a hydrogen oxide biosensor for environmental engineering applications, such as energy storage and water purification. It can also be used as a non-MEI current detection in glucose oxidation. It is better for the signal interference of uric acid, dopamine, and ascorbic acid. Apart from inorganic biosensors, organic materials are also getting attention in the last few years. Some biosensors using poly(methylene blue) (PMB), poly(alizarin yellow R), poly(azure A), poly(azure B), poly(azure C), poly(brilliant cresyl blue), and poly(thionine) has been widely studied and reported [31–37]. Even though these biosensors have good selectivity, their disadvantages include instability, cost, and a need for a mediator in some cases [38]. On the other hand, in recent years due to the excellent electrochemical properties of Cu<sub>2</sub>O, much research has been conducted towards its application as a sensor [39–42]. MoS<sub>2</sub> which has a similar structure to graphene due to its conductivity and good electrical and chemical properties has been widely reported to be employed in numerous biosensors [43–45].

Hence, in this research, a new MoS<sub>2</sub>/Cu<sub>2</sub>O PN heterojunction structure, can reduce the predominant disadvantage of noise interference to the detection signal through different growth methods, material special characteristics, and the structure itself. This MoS<sub>2</sub>/Cu<sub>2</sub>O structure is applied to a sensor for cancer cells with different canceration levels. In this study, CVD is conducted for single-layer MoS<sub>2</sub> to obtain large-area and uniform MoS<sub>2</sub> films. Several measurement techniques, including Raman mapping, are used to check the number of layers. Atomic force microscopy (AFM) is employed for thickness analysis and scanning electron microscopy (SEM) is utilized to observe surface morphology. X-ray diffraction (XRD; Figure S1 for XRD) is conducted to measure whether a signal appears, and transmission electron microscopy (TEM; Figure S4) is performed to determine the direction of the crystal lattice. However, studies on the synthesis of semiconductor materials and nanostructures have also been carried out. During the research, Cu<sub>2</sub>O nanostructures have been successfully fabricated through electrochemical deposition. The major application of this heterostructure is to develop a low-cost and rapid way to detect lung cancer cell types in hydroplegia by fabricating a PEC biosensor that is highly sensitive to lung cancer cells significantly reducing the current busy procedures and longer waiting time for detection.

## 2. Materials and Methods

The glass substrate used in the experiment was indium tin oxide (ITO) for  $\text{Cu}_2\text{O}$  electroplating. The resistance of the ITO surface was  $7 \Omega$ , and the thickness of the coating was 200 nm. All the chemicals used were all American Chemical Society (ACS) and guaranteed reagent (GR) to avoid the failure of results because of insufficient purity or residual impurities in the grown crystals, especially low-chlorine Sigma-Aldrich (Burlington, MA, USA) 98+% for sodium hydroxide because the solution of  $\text{Cu}_2\text{O}$  deposition was susceptible to the influence of chloride ions to produce copper chloride precipitation.

### 2.1. Process and Steps of Electrochemical $\text{Cu}_2\text{O}$ Growth

#### 2.1.1. Substrate and Electrolysis Pretreatment

$\text{Cu}_2\text{O}$  was prepared through electrochemical deposition, and the substrate used was a  $2 \text{ cm} \times 2 \text{ cm}$  transparent conductive film made of ITO for  $\text{Cu}_2\text{O}$  electroplating (Supplementary Section S1.1 for the Material characteristics of  $\text{Cu}_2\text{O}$ ). P-type  $\text{Cu}_2\text{O}$  has a small energy gap of 2.0 eV, which was a suitable conduction band [46,47]. Acetone, methanol, isopropanol, and deionized water were used to reduce the impurities, such as dust, oil stains, or residues, on the electrode surface after ITO plating. The adhesion of impurity contamination also improved the stability of film growth to obtain a higher-quality  $\text{Cu}_2\text{O}$  film (Supplementary Section S3 for the List of substrates, organic solvents, gases, and chemicals used to grow  $\text{Cu}_2\text{O}$  and  $\text{MoS}_2$ ). In the cleaning steps, the electrode surface was first cleaned with acetone in an ultrasonic oscillator for 10 min to dissolve and remove surface oil stains or other organic impurities. After the specimen was shaken and washed with acetone, it was rinsed with methanol in an ultrasonic oscillator for 10 min to dissolve and remove residual copper contamination on the surface. Isopropanol was used for cleaning in an ultrasonic oscillator for 10 min to dissolve and remove surface oil stains or other organic impurities. The glass substrate was soaked in deionized water with a resistivity of  $18.2 \text{ M W}\cdot\text{cm}$  ( $25 \text{ }^\circ\text{C}$ ), and an ultrasonic oscillator was used for 10 min to remove residual organic solvents. The sample was taken out, and a high-pressure nitrogen gun was used to remove the moisture on the surface of the ITO glass substrate. The ITO glass substrate was baked in an oven at  $100 \text{ }^\circ\text{C}$  for 30 min to remove the residual moisture on the substrate and placed in a clean moisture-proof box for later use. The cut graphite rods with a diameter of 1 cm and a length of 18 cm were subjected to electrochemical  $\text{Cu}_2\text{O}$  deposition. The main purpose of cleaning the electrodes of the graphite rods was to reduce impurities, such as dust, oil stains, and residual powder, on the electrode surface during graphite rod production. External impurities contaminated  $\text{Cu}_2\text{O}$  electrolytic deposition and improved film growth stability. For cleaning, the graphite rod was soaked in 1 M sodium hydroxide solution and washed with ultrasonic vibration for 30 min to remove grease and organic pollutants adsorbed on the surface. The surface of the graphite rod was ground with sandpaper and rinsed with deionized water during grinding to remove the powder remaining in the graphite rod manufacturing. The graphite rod was soaked in deionized water and shaken for 30 min with ultrasonic cleaning to reduce the residual impurities on the surface. The graphite rod was baked in an oven at  $100 \text{ }^\circ\text{C}$  for 30 min to remove the surface moisture and placed in a moisture-proof box to complete the pretreatment of the graphite electrode.

#### 2.1.2. Preparation of $\text{Cu}_2\text{O}$ Film

A  $\text{Cu}_2\text{O}$  thin film was prepared for electrochemical deposition to grow a highly uniform thin film on the ITO glass substrate (Supplementary Section S1.2 for  $\text{Cu}_2\text{O}$  Synthesis). The electrolyte was made of 0.4 M copper sulfate powder ( $\text{CuSO}_4$ ), 85% lactic acid, and 5 M sodium hydroxide (NaOH) prepared into a 1000 c.c. aqueous solution. The pH could be adjusted to 10, 11, and 12 through the amount of sodium hydroxide, which was measured in real time by a portable Starter300 pH meter (ST300). A DC power supply (MOTTECH LPS505N) was used to power the two-pole electrochemical deposition system equipment in which the positive electrode was a graphite rod, and the negative electrode was con-

nected to the ITO glass substrate (Supplementary Section S2.1 for the electrochemical deposition system). The temperature of the growing electrolyte was controlled at 60 °C to ensure that the lactic acid works. The deposition time was fixed at 30 min to achieve high quality and uniformity. At the end of the film, the sample was washed with deionized water, and the surface moisture was removed with a high-pressure nitrogen gun for subsequent experiments.

### 2.1.3. Cu<sub>2</sub>O Grinding

A plane grinder was widely used for the single-sided grinding and polishing of various materials, such as LED sapphire substrates, optical glass wafers, quartz wafers, silicon wafers, germanium wafers, molds, light guide plates, and optical skewer joints. The Cu<sub>2</sub>O thin film was processed by grinding to smoothen the Cu<sub>2</sub>O surface and facilitate the subsequent transfer of MoS<sub>2</sub> while maintaining the integrity of the morphological characteristics of MoS<sub>2</sub> and reducing the transfer failure rate. The rotation speed of the grinder was controlled at the minimum, and the time was set at 1 h. Considering Cu<sub>2</sub>O was a thin film at the micrometer scale, we chose the micro grade at the scale of a diamond polishing sheet.

### 2.1.4. Experimental Materials and Drug Specifications of MoS<sub>2</sub>

The substrate used to grow MoS<sub>2</sub> was silicon dioxide (SiO<sub>2</sub>) for chemical vapor deposition (CVD; Supplementary Section S1.2 for obtaining MoS<sub>2</sub> layers). The thickness of the chosen silicon wafer (100) crystal plane was 300 nm. The purity of sulfur powder (S) and molybdenum oxide (MoO<sub>3</sub>) powder was 99.98% and 99.95%, respectively, to avoid impurities that affect the CVD or the remaining impurities of grown single crystals. The quartz tubes and ceramic crucibles in the tubular thermal tubes were cleaned with aqua regia. The concentrations of nitric acid and hydrochloric acid were 37% and 68–69%, respectively, to avoid the adhesion of impurities from the previous growth during cleaning, which affects the experimental parameters and reproducibility of the next growth of monolayer MoS<sub>2</sub>.

## 2.2. Process and Steps of CVD-Grown MoS<sub>2</sub>

The majority of 2D material layer identification studies focus on film synthesis using mechanical stripping [48–50]. Most 2D material layer identification studies have focused on film synthesis through mechanical stripping [51]. In the present experiment, a 300 nm SiO<sub>2</sub> silicon substrate was prepared and cleaned with ultrasonic vibration in acetone for 10 min to remove impurities and oil stains on the surface; deionized water was then used to remove the organic solvent acetone (Supplementary Section S5 for CVD-grown MoS<sub>2</sub>).

After 10 min, the sample was taken out, and the moisture on the surface of the ITO glass substrate was removed with a high-pressure nitrogen gun. The method used to grow MoS<sub>2</sub> was CVD [52–57]. The substrate was placed under specific pressure and temperature conditions and one or more precursors were chemically reacted on the surface of the substrate to produce a high-quality large-area thin film. The application of CVD in the preparation of single-layer TMDs starts with MoS<sub>2</sub> growth. The inert gas used to grow MoS<sub>2</sub> through CVD was argon. Afterward, 500 sccm of argon was used to clean the internal cavity and keep it in a clean environment. The heating rate was set to 20 °C per min, the growth temperature was 650 °C, and the temperature was held for 30 min. Once the temperature was dropped to 400 °C, the lid was opened. The MoS<sub>2</sub> structure was obtained when the temperature decreases to room temperature. The experimental process was shown in Figure 1. With molybdenum trioxide (MoO<sub>3</sub>) and sulfur powder (S) as precursors, a 2 cm × 2 cm silicon dioxide/silicon (SiO<sub>2</sub>/Si) substrate was placed on the crucible and sent into the furnace tube. The vaporization point of MoO<sub>3</sub> was 650 °C [58–60]. The vaporization point of S was above 200 °C. Gas-phase MoO<sub>3</sub> undergoes two chemical reactions in high-temperature environments to produce molybdenum oxide (MoO<sub>3-x</sub>) intermediates. The resulting molybdenum oxide intermediates diffuse to the substrate and vaporize to form a MoS<sub>2</sub> film. The distance between the two crucibles was 46 cm. This long

distance was to ensure that the vapor concentration gradient of sulfur was negligible on the substrate compared with that of the MoO<sub>3</sub> concentration gradient because the distance between MoO<sub>3</sub> and the substrate was small. CVD can effectively prepare single- and multi-layer MoS<sub>2</sub>. It can grow high-quality single-crystal materials and prepare uniformly distributed thin films on a large area, which was conducive to subsequent optoelectronic component manufacturing.

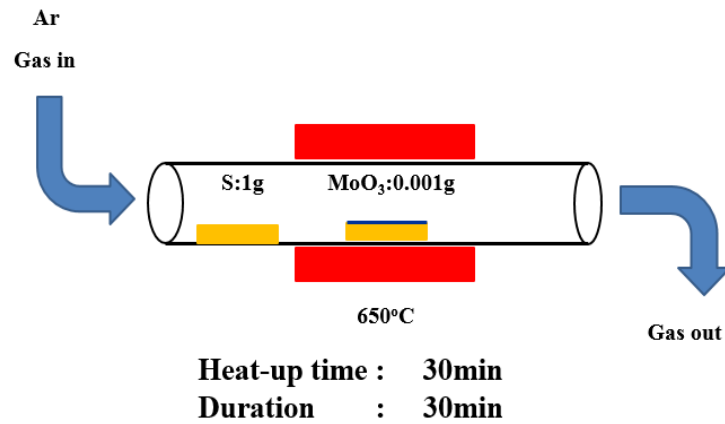


**Figure 1.** Schematic of a growing MoS<sub>2</sub> film.

#### MoS<sub>2</sub> Transfer Process

A spin coater was used to coat uniformly the photoresistant PMMA A5 on the substrate to transfer MoS<sub>2</sub> after CVD growth on the Cu<sub>2</sub>O surface and left for the PMMA to dry. The substrate was covered with photoresistant liquid into 2 M NaOH as an etching solution for separating the substrate and PMMA A5. The removed photoresist was placed in DI water and blown dry with high-pressure nitrogen to prepare for the subsequent transfer. Then, PMMA A5 was placed on the original SiO<sub>2</sub> substrate, which was cut to an appropriate size with a three-axis leveling table and placed on the surface of the Cu<sub>2</sub>O substrate. The temperature was set to 210° for about 30 s to make the PMMA adhere to the substrate. The sample was soaked in acetone for 30 min, and photoresistance was removed, leaving MoS<sub>2</sub> to complete the entire transfer process (Figure 2).

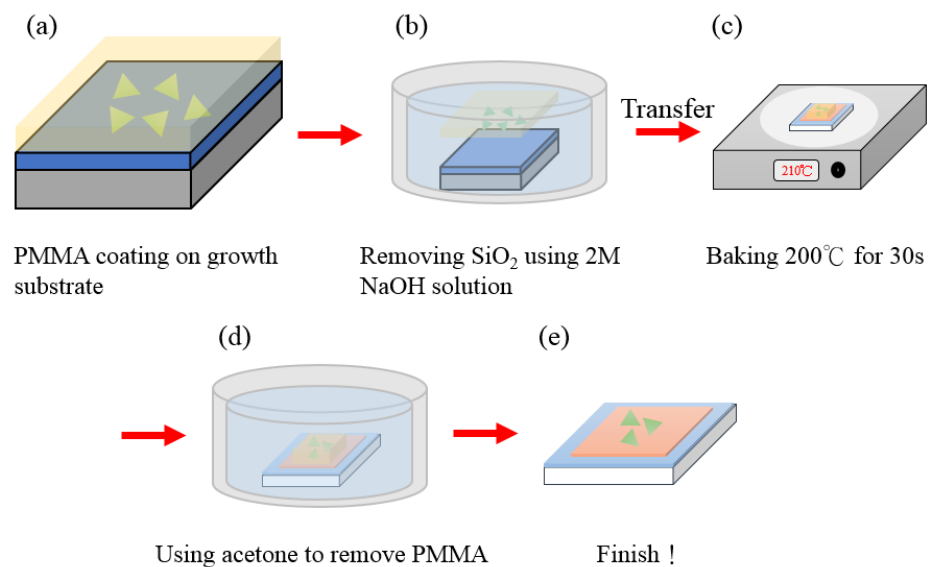


**Figure 2.** MoS<sub>2</sub> transfer flow chart: (a) PMMA coating on growth, (b) Removing SiO<sub>2</sub> using 2 M NaOH solution, (c) Baking 200 °C for 30 s, (d) Remove PMMA by acetone, (e) Complete the entire transfer process.

### 3. Results

#### 3.1. Growth Results of MoS<sub>2</sub>/Cu<sub>2</sub>O

Based on the above growth methods and measurement results, the CVD-grown MoS<sub>2</sub> was transferred electrochemically to grown Cu<sub>2</sub>O (Supplementary Section S4 for the results of Cu<sub>2</sub>O electrochemical growth under different parameters). Material and optical characteristics were analyzed: Raman mapping (Supplementary Section S2.2 for micro-Raman Spectroscopy), SEM (Supplementary Section S2.5 for scanning electron microscope), and SHG measurements (Supplementary Section S2.8 for multiphoton excitation microscope).

##### 3.1.1. Cu<sub>2</sub>O Flattening Comparison

This study has used the Cu<sub>2</sub>O film grown by the electrochemical method as the template for MoS<sub>2</sub> transfer. The SEM image is used to detect the success rate of the transfer, and the result is consistent with the Cu<sub>2</sub>O image without transfer in the SEM image, as shown in Figure 3a,b. The reason for the failure is that the Cu<sub>2</sub>O surface used for the electrochemical method is quite rough, and the rough surface causes the MoS<sub>2</sub> transfer to be broken or unable to be transferred because of the uneven surface. Afterward, the Cu<sub>2</sub>O film was ground to smoothen the Cu<sub>2</sub>O surface and facilitate the subsequent transfer of MoS<sub>2</sub> while maintaining the integrity of the morphological characteristics of MoS<sub>2</sub> and reducing the transfer failure rate. Figure 4a shows the AFM data results of Cu<sub>2</sub>O before grinding. Under the following parameters, i.e., Z range of 740.16 nm, Rms of 97.496, and data scale of 0–800 nm (height), Figure 4b shows the results of Cu<sub>2</sub>O after surface polishing by grinding. Under the following parameters, i.e., Z range of 94.623 nm, Rms of 3.849 nm, and data scale of 0–50 nm (height), the top and flat views of the Cu<sub>2</sub>O film in the SEM image are shown in Figure 3c,d, respectively. The surface after grinding is smooth. According to the above data, grinding may be used to treat the Cu<sub>2</sub>O surface.

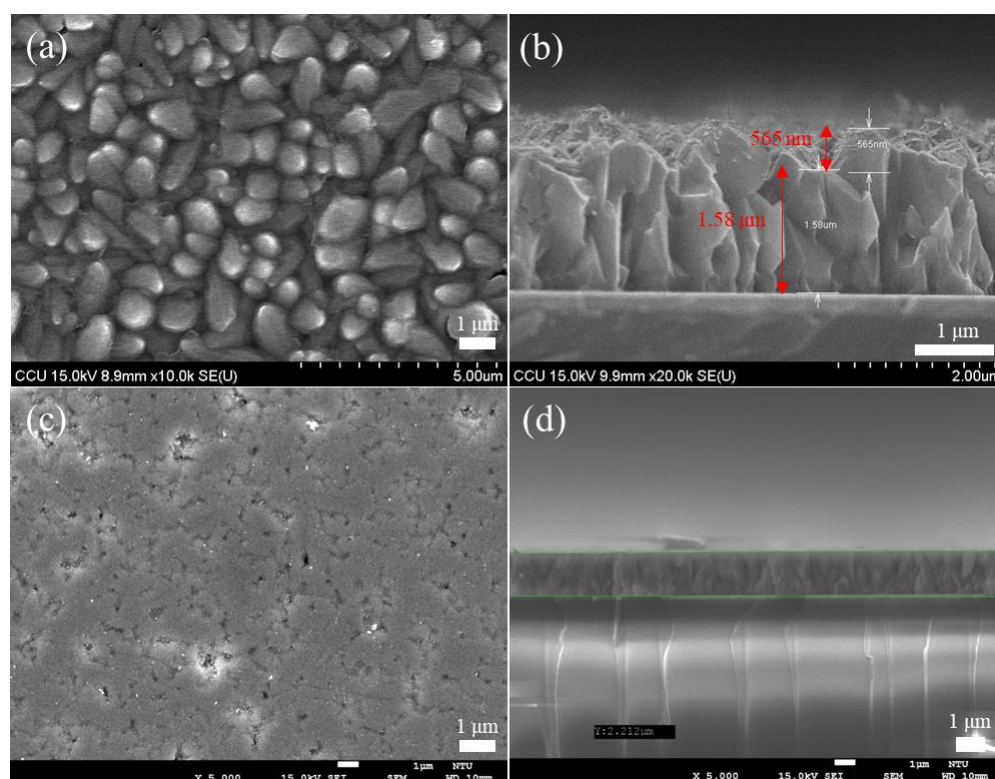


**Figure 3.** (a) Represents the front view of the Cu<sub>2</sub>O film before polishing, (b) represent the side view of the Cu<sub>2</sub>O film before polishing, (c) show the SEM images of the top view after Cu<sub>2</sub>O polishing, (d) show the SEM images of the front view after Cu<sub>2</sub>O polishing.

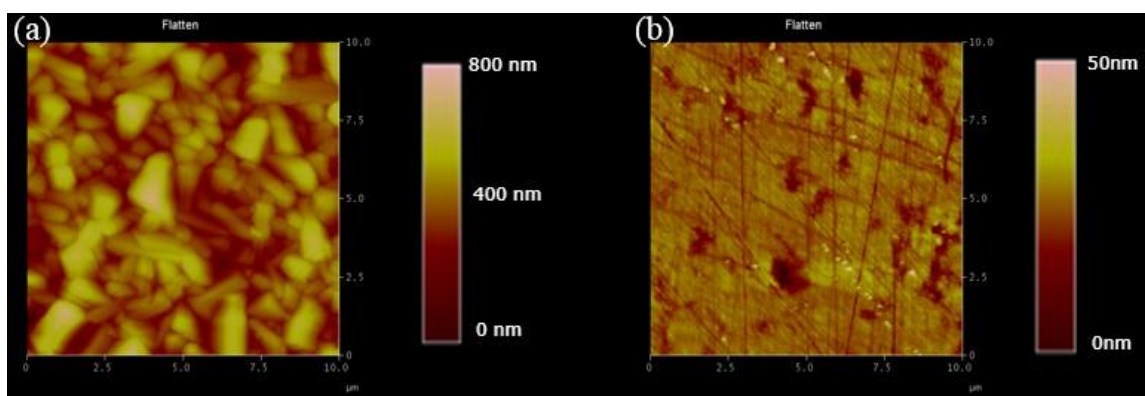


**Figure 4.** (a,b) AFM measurements of the  $\text{Cu}_2\text{O}$  film before and after polishing.

### 3.1.2. $\text{MoS}_2$ Transfer Result on $\text{Cu}_2\text{O}$

After the  $\text{Cu}_2\text{O}$  surface is polished by the abovementioned grinding method, the SEM image result shows that the surface is smoother than the original unpolished surface, and the surface roughness is reduced by 96% in the AFM measurement result (Supplementary Section S2.6 for atomic force microscope). Then CVD-grown  $\text{MoS}_2$  film is transferred to the  $\text{Cu}_2\text{O}$  surface, and SEM is performed (Figure 5). Although few irregularities are observed on the surface of the  $\text{Cu}_2\text{O}$ , SEM analysis shows that  $\text{MoS}_2$  is transferred successfully, and the morphological characteristics of  $\text{MoS}_2$  are completely present on the surface of  $\text{Cu}_2\text{O}$ .

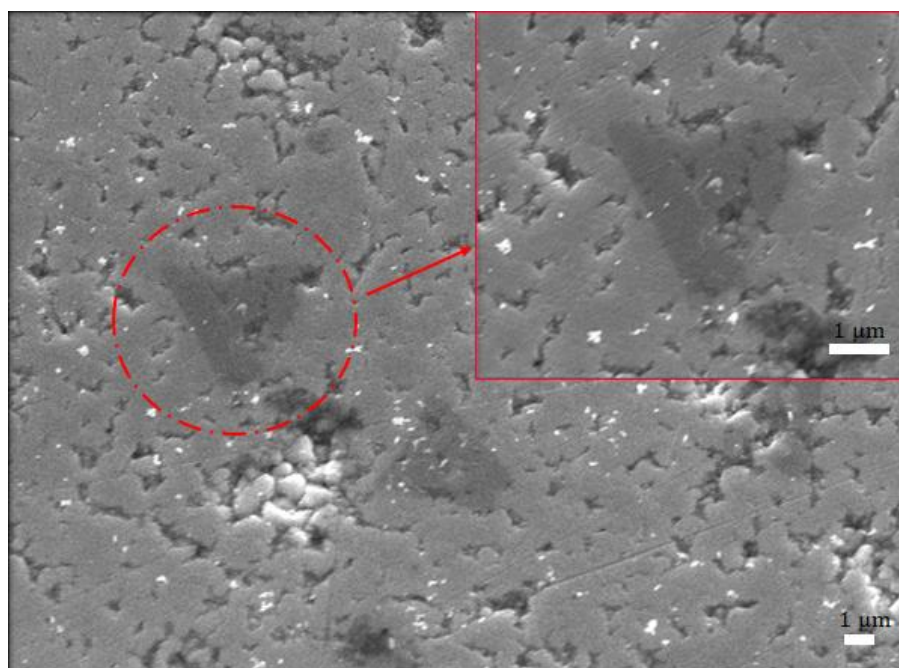


**Figure 5.** SEM image of  $\text{MoS}_2$  transferred to the  $\text{Cu}_2\text{O}$  surface.

### 3.1.3. Analysis of $\text{MoS}_2/\text{Cu}_2\text{O}$ Materials and Optical Properties

After the transfer of the CVD-grown  $\text{MoS}_2$  film onto the electrochemically grown  $\text{Cu}_2\text{O}$  surface. Its material and optical properties are analyzed by employing OM (Supplementary Section S2.4 for optical microscope), SHG images, SEM, and Raman and PL mapping. A multiphoton image is used to identify the signal display during the  $\text{MoS}_2$  transfer (Figure 6). The morphological characteristics of  $\text{MoS}_2$  grown by CVD are obvious. A core point exists in most triangles, and when this core point corresponds to a multiphoton image, the signal becomes stronger than the color of the triangles other than the core point. Figure 6b

shows the multiphoton image of MoS<sub>2</sub>/Cu<sub>2</sub>O/ITO after the transfer. Although many blue irregularities in the image, they are not evenly dispersed to make it clear whether they are MoS<sub>2</sub> triangles.

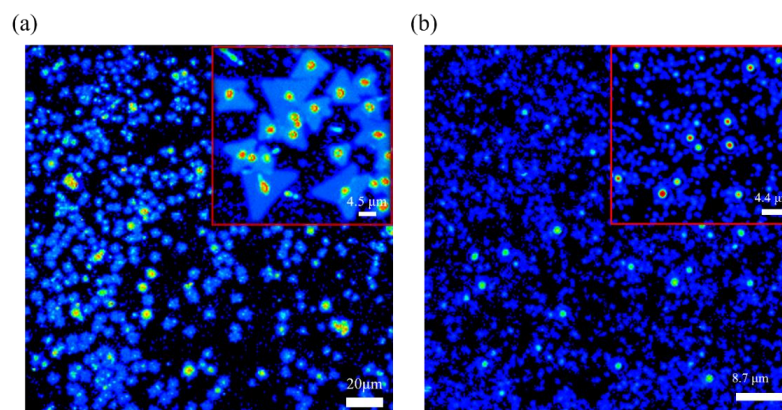
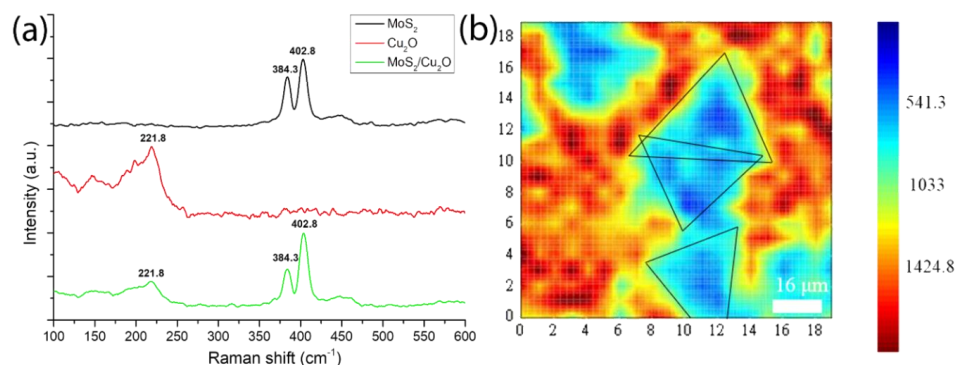


**Figure 6.** Multiphoton images of (a) MoS<sub>2</sub>/SiO<sub>2</sub>/Si and of (b) MoS<sub>2</sub>/Cu<sub>2</sub>O/ITO.

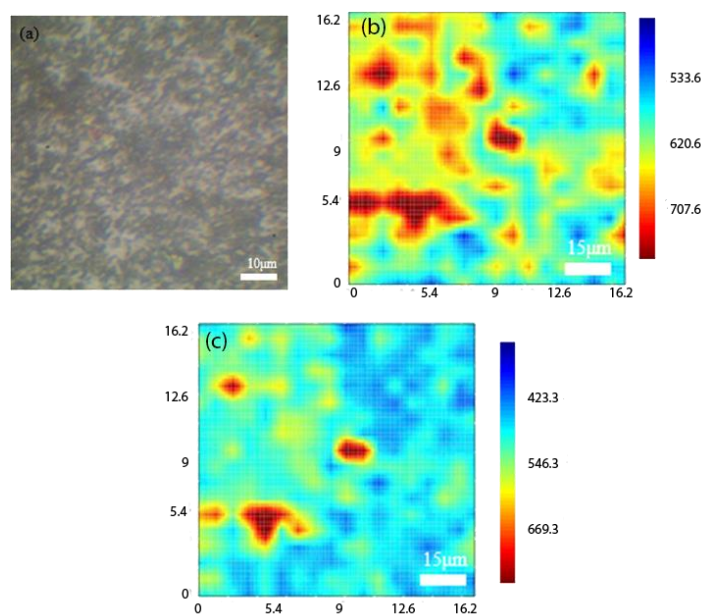
However, the comparison of the obvious bright spots in the image in Figure 6a suggests that a bright spot signal may be the core image after MoS<sub>2</sub> transfer and because Cu<sub>2</sub>O is not completely flat like the SiO<sub>2</sub> surface after being polished. Moreover, this bright spot at the center of MoS<sub>2</sub> is due to the nucleation of MoS<sub>2</sub>. The growth parameters, such as carrier gas, growth temperature, precursors, substrates, and promoters can affect the nucleation and growth modes of MoS<sub>2</sub> [61]. However, Ho Kwon Kim et al. has shown that the pre-exposure of growth substrates to alkali metal halides and the Mo precursor before the growth stage appears can suppress nucleation of MoS<sub>2</sub> [62]. Therefore, the other blue part may be a multi-photon image of a mixture of MoS<sub>2</sub> and Cu<sub>2</sub>O. As shown in Figure 5, the grown MoS<sub>2</sub> has been successfully transferred to the Cu<sub>2</sub>O film. These two data can be combined, proving that MoS<sub>2</sub> has been successfully transferred to the Cu<sub>2</sub>O film by grinding and transfer. Raman mapping, which is the best method to analyze the number of layers, has been used to analyze the image of the transferred MoS<sub>2</sub>/Cu<sub>2</sub>O sample [63–65]. In this study, a 532 nm band is used as a laser excitation light source. From Figure 7b we can observe that the blue-green area is the MoS<sub>2</sub> film, and the red area is part of a Cu<sub>2</sub>O film. The 532 nm band was used as the laser excitation light source in this study. As shown in Figure 7a, the Raman shift of MoS<sub>2</sub> has a peak at 384.3 before transfer while the Raman shift had a peak at 402.8 cm<sup>-1</sup> after the transfer. The Raman shift of Cu<sub>2</sub>O before the transfer has a peak at 221.8 cm<sup>-1</sup>. After transferring MoS<sub>2</sub> onto the Cu<sub>2</sub>O film, the Raman shift did reach peaks at 221.8, 384.3, and 402.8 cm<sup>-1</sup>. It can be clearly inferred that the Raman peak of Cu<sub>2</sub>O appearing at 221.8 cm<sup>-1</sup> indicates that the surface of Cu<sub>2</sub>O was partially oxidized. Similarly, the Raman shifts of MoS<sub>2</sub> at 384.3 and 402.8 cm<sup>-1</sup> are in accordance with E<sub>12g</sub> and A<sub>1g</sub>, respectively, and combined vibrations of two different phonons (A<sub>1g</sub>(M)–LA(M)), respectively, which indicates the existence of MoS<sub>2</sub> structures [66–69]. In the Cu<sub>2</sub>O/MoS<sub>2</sub> composite films, the diffraction peaks of Cu<sub>2</sub>O and MoS<sub>2</sub> are still observed. The result shows that the grown MoS<sub>2</sub> has a uniform film in the image and can replace the morphology. E<sub>12g</sub> and A<sub>1g</sub> vibration modes are the main signals for the judgment of MoS<sub>2</sub>. The two vibration modes are highly dependent on the thickness of MoS<sub>2</sub>. When the  $\Delta k$  value of the subtraction of E<sub>12g</sub> and A<sub>1g</sub> peaks is less than 20 cm<sup>-1</sup>, the analyzed MoS<sub>2</sub> is regarded as a single-layer structure.

Figure 8a shows the OM image of MoS<sub>2</sub>/Cu<sub>2</sub>O, Figure 8b illustrates the 625-band image selected for the PL mapping image. The MoS<sub>2</sub> spectrum consists of two peaks corresponding to the A1 and B1 excitons at 667 nm (1.86 eV) and 627 nm (1.97 eV), respectively. The measured PL for Cu<sub>2</sub>O grown by the electrochemical method was about 720–900 nm. In the measurement of the PN heterostructure material combination of MoS<sub>2</sub>/Cu<sub>2</sub>O, Raman measurement was first performed on the OM image. After the signal of MoS<sub>2</sub> is found, PL

measurement is carried out, and the combined structure is examined through the measurement results to show that the band range covers 625–900 nm. We found that a micro signal is generated at about 627 nm in the orange elliptical dashed circle, and the wavelength of 627 nm belongs to the B2 excitons of MoS<sub>2</sub>. The signal gradually increases when it approaches 670 nm. However, the Cu<sub>2</sub>O signal is not in this part because its light-emitting band starts to generate signals from 720 nm. Therefore, the Cu<sub>2</sub>O film may be too thick, and the single-layer MoS<sub>2</sub> film thickness is only 0.7 nm, so the two heterostructure materials are combined in the wavelength range of 670–700 nm. The entire signal undergoes a red-shifted phenomenon because the Cu<sub>2</sub>O film signal is strong.



**Figure 7.** (a) Raman spectrum after MoS<sub>2</sub> transfer to Cu<sub>2</sub>O surface and (b) Raman mapping of MoS<sub>2</sub>/Cu<sub>2</sub>O.



**Figure 8.** (a) OM image of MoS<sub>2</sub>/Cu<sub>2</sub>O, (b) 625 band for PL mapping image, (c) 675 band for PL mapping image.

### 3.2. Photocurrent Response Analysis

This research uses the preparation of biosensors, and the photocurrent measurement system and impedance analysis system set up in the laboratory (see Supplement 1, Section S6 for Analysis of Structural Characteristics of Photoelectrochemical Biosensors). The photocurrent measurement of the three lung cancer cells A549, H460 and H520 was carried out by the carrier transport mechanism of photogenerated charge, and the zigzag-toothed microelectrode was used to perform aggregation and impedance analysis of the cancer cells. In this study, we utilized two characteristic substances, glutathione (GSH) and glutathione disulfide (GSSG), to verify the detection mechanism of the developed

biosensor. Generally, GSH in cells exists in two forms: 90% of GSH is present in the cytoplasm as reduced GSH, and 10% is present in the mitochondria. For healthy cells, the ratio of GSH to GSSG is greater than 10:1. However, when cells become cancerous, the ratio of GSH to GSSG decreases [70,71]. Because the majority carriers in N-type PEC are electrons and hence GSSG participating in PEC reaction is more significant. When irradiated, electron-hole pairs are generated, GSSG recombines with photo-generated electrons, and photo-generated holes are detected, forming a system of hole currents. As the degree of canceration becomes more severe, the concentration of GSSG contained in cancer cells increases, and the measured photocurrent also increases [72,73]. On the contrary, the majority of carriers in the P-type PEC biosensor are holes and hence GSH participates in the PEC reaction more significantly. After being illuminated, GSH recombines with photo-generated holes, photo-generated electrons are detected, and a system of electron flow is formed. The more severe the carcinogenesis of the structure, the smaller the GSH concentration and also a decrease of the photocurrent [74,75]. As shown in Figure 9 the photocurrent decreased with the increase of suspended cell density, which indicated that more GSH was involved in the PEC process. From Figure 10, it can be known that different cells have different amounts of change, there is a highly linear relationship between the photocurrent change and the number of cells, and the linear regression of the three cell types is as high as 99%. The slopes corresponding to the three cell lines A549, NCI-H460 and NCI-H520 were approximately 0.000452, 0.000749 and 0.000174, respectively. By measuring the magnitude of the photocurrent, we can calculate the regression curve equation, thereby identifying which cell of the three cells is. In the growth mechanism of Cu<sub>2</sub>O, as the thickness increases, the stress or dislocation will increase, resulting in a certain optimal thickness of the material. Previous studies also shows that the best growth thickness of Cu<sub>2</sub>O under the environment and parameters of our growth is 2 μm [76].

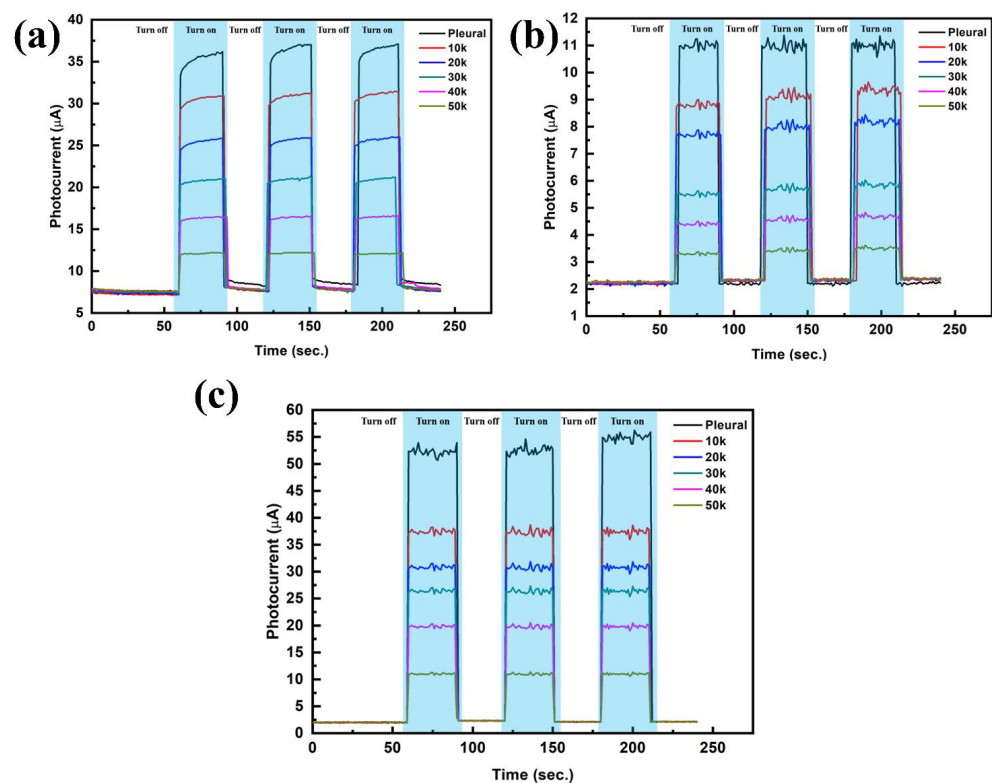


**Figure 9.** P. (a) Photocurrent responses of A549 under different cell numbers, (b) Photocurrent responses of NCI-H460 under different cell numbers and (c) Photocurrent responses of NCI-H520 under different cell numbers.

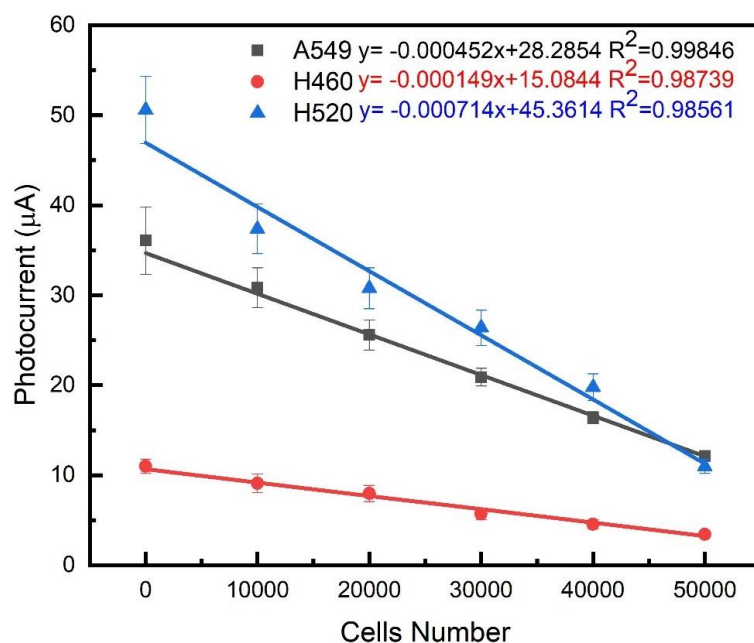


**Figure 10.** Linear relationship between photocurrent changes and cell number in three lung cancer cell lines on biosensing chips.

#### 4. Discussion

When the MoS<sub>2</sub> film has a single-layer structure, the A<sub>1g</sub> signal is stronger than that of a multilayer film. If the MoS<sub>2</sub> film has a multilayer structure, the E<sub>12g</sub> signal is stronger than that of a single-layer film. The PL signal of MoS<sub>2</sub> also decreases as the number of layers increases. Therefore, we can observe the contrast of the image by selecting the PL mapping images of 625 and 675 nm, corresponding to the color bar value. Single- and multi-layer MoS<sub>2</sub> film signals are found in the selected 625-band image compared with much fewer signals in the 675-band image. When we grow the MoS<sub>2</sub> film, single- and multi-layer structures form. In the selection of images for mapping, more multi-layer MoS<sub>2</sub> films are covered. The PL measurement results in this study use a 532 nm laser as the excitation light source to measure the PL of a single-layer MoS<sub>2</sub> film. The measurement results show that a strong signal is generated at the wavelength of 667 nm, and the energy is 1.84 eV after conversion. It is the energy gap of single-layer MoS<sub>2</sub>. However, from Gang Li et al., the energy band alignment of bulk MoS<sub>2</sub> and single layer MoS<sub>2</sub> was observed at 1.4 eV and 1.78 eV, respectively [29]. From our study, the single layer MoS<sub>2</sub> was observed at 1.84 eV, close to the previous observations. The future scope of this project can be split into two aspects. First, after the two materials are combined, by using them as electric double-layer transistors their electrical properties can be tested. After confirming the positive state of the oxide trap. We can also try to bombard the element with high-energy particles to explore its characteristic influence and figure out if it affects the transformation of the mechanism. If the result of the electron beam bombardment affects the element and causes the characteristics to change, it can be checked again whether the electrical property changes from the positive oxide trap state to the negative interface trap state. Second, CVD can be performed to grow MoS<sub>2</sub> in the 2H phase. MoS<sub>2</sub> has three crystal structures: 2H (semiconductor characteristics), 1T (metallic characteristics), and 3R (semiconductor characteristics). The intensity difference can be detected in the PL mapping and electrostatic force microscope (EFM) images of 2H-MoS<sub>2</sub> and 1T-MoS<sub>2</sub>. The future scope of this study is to collect a large amount of data to build a large-scale database by measuring the cell impedance and photocurrent in the patient's pleural effusion. After analyzing the data through Artificial Intelligence (AI), a human-machine display interface will be designed which provides the types of cancer cells defined by the system, assisting physicians to determine the patient's cancer status and provide appropriate treatment methods.

## 5. Conclusions

In this study, an electrochemical method was used to grow a Cu<sub>2</sub>O film with a uniform and superior crystal lattice. The micro-roughened surface structure of Cu<sub>2</sub>O was polished by grinding. Then, CVD-grown single crystal MoS<sub>2</sub> was transferred to the Cu<sub>2</sub>O film. OM, SHG, SEM, Raman, and PL mapping measurements were used to analyze the combination of the two materials. Electrochemical methods were successfully used to achieve relatively good electrical properties. TEM showed that Cu<sub>2</sub>O is a single crystal structure, and SEM revealed that the surface should be processed by subsequent grinding methods. After grinding and polishing were performed, AFM and SEM were used to obtain the experimental results. MoS<sub>2</sub> structure was grown through CVD, and E<sub>12g</sub> and A<sub>1g</sub> peaks were obtained via Raman analysis. The main luminescence peak at 667 nm was determined through PL analysis. The single layer of MoS<sub>2</sub> was transferred to the polished Cu<sub>2</sub>O surface, which was confirmed by SEM and SHG results. Raman and PL mapping image analysis on MoS<sub>2</sub>/Cu<sub>2</sub>O indicated that the grown MoS<sub>2</sub> had a uniform film. The combined structure was measured through PL measurement to verify that the band range covered 625–900 nm. A micro signal was found at the 627 nm wavelength. It belonged to the B2 excitons of MoS<sub>2</sub> and tended to increase gradually as it approached 670 nm. The Cu<sub>2</sub>O film was too thick, whereas the thickness of the single-layer MoS<sub>2</sub> film was only 0.7 nm. As such, the two heterostructure materials combined in the wavelength range of 670–700 nm. The strong signal of the Cu<sub>2</sub>O film itself led to a red shift in the entire signal. This study also successfully fabricated a low-cost PEC biosensor that is highly sensitive to lung cancer cells which is a rapid way to detect lung cancer cell types in hydroplegia. The photocurrent response is measured using the MoS<sub>2</sub>/Cu<sub>2</sub>O biochip material grown by electrochemical deposition. As the number of cancer cells measured increases, the content of oxidized GSSG also increases, and the measured photocurrent decreases accordingly. It is also possible to use dielectrophoresis to gather cancer cells to form a pearl string, measure unlabeled cancer cells, and use the slope of the admittance value to shape lung cancer cells. The linear regression curve is compared with the admittance value and the photocurrent measurement value to distinguish the types of cancer cells in the pleural effusion.

**Supplementary Materials:** The following supporting information can be downloaded at: <https://www.mdpi.com/article/10.3390/ijms23094745/s1>.

**Author Contributions:** Conceptualization, V.E.F., S.-W.F. and S.B.A.; methodology, S.-W.F., Y.-M.T., Y.-C.H. and Y.-S.L.; software, S.-W.F., V.E.F. and Y.-S.L.; validation, S.B.A., S.-W.F. and H.-C.W.; formal analysis, S.-W.F., Y.-M.T. and Y.-S.L.; investigation, Y.-S.L., Y.-H.W. and A.M.; resources, S.-W.F., Y.-M.T., Y.-C.H. and Y.-H.W.; data curation, S.B.A.; writing—original draft preparation, S.B.A., A.M. and Y.-H.W.; writing—review and editing, A.M. and H.-C.W.; supervision, S.-W.F., V.E.F. and H.-C.W.; and project administration, H.-C.W. All authors have read and agreed to the published version of the manuscript.

**Funding:** This research was supported by the Ministry of Science and Technology, The Republic of China under the grants MOST 105-2923-E-194-003 MY3, 108-2823-8-194-002, 109-2622-8-194-001-TE1, and 109-2622-8-194-007. This work was financially/partially supported by the Advanced Institute of Manufacturing with High-tech Innovations (AIM-HI) and the Center for Innovative Research on Aging Society (CIRAS) from The Featured Areas Research Center Program within the framework of the Higher Education Sprout Project by the Ministry of Education (MOE) and Kaohsiung Armed Forces General Hospital research project 108-016 in Taiwan.

**Institutional Review Board Statement:** Not Applicable.

**Informed Consent Statement:** Not Applicable.

**Data Availability Statement:** Not Applicable.

**Conflicts of Interest:** The authors declare no conflict of interest.

## References

1. Geim, A.K.; Novoselov, K.S. The rise of graphene. In *Nanoscience and Technology: A Collection of Reviews from Nature Journals*; World Scientific: Singapore, 2010; pp. 11–19.
2. Sarma, S.D.; Adam, S.; Hwang, E.H.; Rossi, E. Electronic transport in two-dimensional graphene. *Rev. Mod. Phys.* **2011**, *83*, 407. [CrossRef]
3. Lin, X.; Su, L.; Si, Z.; Zhang, Y.; Bournel, A.; Zhang, Y.; Klein, J.-O.; Fert, A.; Zhao, W. Gate-Driven Pure Spin Current in Graphene. *Phys. Rev. Appl.* **2017**, *8*, 034006. [CrossRef]
4. Wu, C.; Zhang, J.; Tong, X.; Yu, P.; Xu, J.; Wu, J.; Wang, Z.M.; Lou, J.; Chueh, Y.-L. A critical review on enhancement of photocatalytic hydrogen production by molybdenum disulfide: From growth to interfacial activities. *Small* **2019**, *15*, 1900578. [CrossRef] [PubMed]
5. Yang, D.; Wang, H.; Luo, S.; Wang, C.; Zhang, S.; Guo, S. Paper-Cut Flexible Multifunctional Electronics Using MoS<sub>2</sub> Nanosheet. *Nanomaterials* **2019**, *9*, 922. [CrossRef] [PubMed]
6. Zhang, Y.; Wan, Q.; Yang, N. Recent Advances of Porous Graphene: Synthesis, Functionalization, and Electrochemical Applications. *Small* **2019**, *15*, e1903780. [CrossRef] [PubMed]
7. Choi, M.S.; Lee, G.-H.; Yu, Y.-J.; Lee, D.-Y.; Lee, S.H.; Kim, P.; Hone, J.; Yoo, W.J. Controlled charge trapping by molybdenum disulphide and graphene in ultrathin heterostructured memory devices. *Nat. Commun.* **2013**, *4*, 1624. [CrossRef] [PubMed]
8. Han, T.; Liu, H.; Wang, S.; Chen, S.; Xie, H.; Yang, K. Probing the Field-Effect Transistor with Monolayer MoS<sub>2</sub> Prepared by APCVD. *Nanomaterials* **2019**, *9*, 1209. [CrossRef] [PubMed]
9. Lee, C.-H.; Lee, G.-H.; van der Zande, A.M.; Chen, W.; Li, Y.; Han, M.; Cui, X.; Arefe, G.; Nuckolls, C.; Heinz, T.F.; et al. Atomically thin p–n junctions with van der Waals heterointerfaces. *Nat. Nanotechnol.* **2014**, *9*, 676–681. [CrossRef]
10. Lu, G.Z.; Wu, M.-J.; Lin, T.-N.; Chang, C.-Y.; Lin, W.-L.; Chen, Y.T.; Hou, C.-F.; Cheng, H.-J.; Lin, T.-Y.; Shen, J.-L.; et al. Electrically Pumped White-Light-Emitting Diodes Based on Histidine-Doped MoS<sub>2</sub> Quantum Dots. *Small* **2019**, *15*, 1901908. [CrossRef]
11. Park, Y.J.; Sharma, B.K.; Shinde, S.M.; Kim, M.-S.; Jang, B.; Kim, J.-H.; Ahn, J.-H. All MoS<sub>2</sub>-Based Large Area, Skin-Attachable Active-Matrix Tactile Sensor. *ACS Nano* **2019**, *13*, 3023–3030. [CrossRef]
12. Radisavljevic, B.; Radenovic, A.; Brivio, J.; Giacometti, V.; Kis, A. Single-layer MoS<sub>2</sub> transistors. *Nat. Nanotechnol.* **2011**, *6*, 147–150. [CrossRef]
13. Roh, J.; Ryu, J.H.; Baek, G.W.; Jung, H.; Seo, S.G.; An, K.; Jeong, B.G.; Lee, D.C.; Hong, B.H.; Bae, W.K.; et al. Threshold Voltage Control of Multilayered MoS<sub>2</sub> Field-Effect Transistors via Octadecyltrichlorosilane and their Applications to Active Matrixed Quantum Dot Displays Driven by Enhancement-Mode Logic Gates. *Small* **2019**, *15*, 1803852. [CrossRef] [PubMed]
14. Zhao, J.; Li, N.; Yu, H.; Wei, Z.; Liao, M.; Chen, P.; Wang, S.; Shi, D.; Sun, Q.; Zhang, G. Highly Sensitive MoS<sub>2</sub> Humidity Sensors Array for Noncontact Sensation. *Adv. Mater.* **2017**, *29*. [CrossRef] [PubMed]
15. Zhang, P.; Yang, S.; Pineda-Gómez, R.; Ibarlucea, B.; Ma, J.; Lohe, M.R.; Akbar, T.F.; Baraban, L.; Cuniberti, G.; Feng, X.; et al. Electrochemically Exfoliated High-Quality 2H-MoS<sub>2</sub> for Multiflake Thin Film Flexible Biosensors. *Small* **2019**, *15*, 1901265. [CrossRef]
16. Yang, K.; Liu, H.; Wang, S.; Li, W.; Han, T. A Horizontal-Gate Monolayer MoS<sub>2</sub> Transistor Based on Image Force Barrier Reduction. *Nanomaterials* **2019**, *9*, 1245. [CrossRef] [PubMed]
17. Yadav, V.; Roy, S.; Singh, P.; Khan, Z.; Jaiswal, A. 2D MoS<sub>2</sub>-based nanomaterials for therapeutic, bioimaging, and biosensing applications. *Small* **2019**, *15*, 1803706. [CrossRef] [PubMed]
18. Shin, M.; Yoon, J.; Yi, C.; Lee, T.; Choi, J.-W. Flexible HIV-1 Biosensor Based on the Au/MoS<sub>2</sub> Nanoparticles/Au Nanolayer on the PET Substrate. *Nanomaterials* **2019**, *9*, 1076. [CrossRef] [PubMed]
19. Sarkar, D.; Liu, W.; Xie, X.; Anselmo, A.C.; Mitrageotri, S.; Banerjee, K. MoS<sub>2</sub> Field-Effect Transistor for Next-Generation Label-Free Biosensors. *ACS Nano* **2014**, *8*, 3992–4003. [CrossRef]
20. Jia, X.; Huang, J.; Li, Y.; Yang, J.; Song, H. Monodisperse Cu nanoparticles @ MoS<sub>2</sub> nanosheets as a lubricant additive for improved tribological properties. *Appl. Surf. Sci.* **2019**, *494*, 430–439. [CrossRef]
21. Zhao, Y.-F.; Yang, Z.-Y.; Zhang, Y.-X.; Jing, L.; Guo, X.; Ke, Z.; Hu, P.; Wang, G.; Yan, Y.-M.; Sun, K.-N. Cu<sub>2</sub>O Decorated with Cocatalyst MoS<sub>2</sub> for Solar Hydrogen Production with Enhanced Efficiency under Visible Light. *J. Phys. Chem. C* **2014**, *118*, 14238–14245. [CrossRef]
22. Paracchino, A.; Laporte, V.; Sivula, K.; Grätzel, M.; Thimsen, E. Highly active oxide photocathode for photoelectrochemical water reduction. *Nat. Mater.* **2011**, *10*, 456–461. [CrossRef]
23. Mahmoud, M.A.; Qian, W.; El-Sayed, M.A. Following Charge Separation on the Nanoscale in Cu<sub>2</sub>O–Au Nanoframe Hollow Nanoparticles. *Nano Lett.* **2011**, *11*, 3285–3289. [CrossRef]
24. Radi, A.; Pradhan, D.; Sohn, Y.; Leung, K.T. Nanoscale shape and size control of cubic, cuboctahedral, and octahedral Cu–Cu<sub>2</sub>O core–shell nanoparticles on Si (100) by one-step, templateless, capping-agent-free electrodeposition. *ACS Nano* **2010**, *4*, 1553–1560. [CrossRef]
25. De Jongh, P.E.; Vanmaekelbergh, D.; Kelly, J.J. Photoelectrochemistry of Electrodeposited Cu<sub>2</sub>O. *J. Electrochem. Soc.* **2000**, *147*, 486–489. [CrossRef]
26. Li, Z.; Ezhilarasu, G.; Chatzakis, I.; Dhall, R.; Chen, C.-C.; Cronin, S.B. Indirect Band Gap Emission by Hot Electron Injection in Metal/MoS<sub>2</sub> and Metal/WSe<sub>2</sub> Heterojunctions. *Nano Lett.* **2015**, *15*, 3977–3982. [CrossRef]

27. Zhao, X.; Li, Y.; Guo, Y.; Chen, Y.; Su, Z.; Zhang, P. Coral-like MoS<sub>2</sub>/Cu<sub>2</sub>O porous nanohybrid with dual-electrocatalyst performances. *Adv. Mater. Interfaces* **2016**, *3*, 1600658. [CrossRef]
28. Mukundan, A.; Tsao, Y.-M.; Artemkina, S.B.; Fedorov, V.E.; Wang, H.-C. Growth Mechanism of Periodic-Structured MoS<sub>2</sub> by Transmission Electron Microscopy. *Nanomaterials* **2021**, *12*, 135. [CrossRef]
29. Fang, L.; Wang, F.; Chen, Z.; Qiu, Y.; Zhai, T.; Hu, M.; Zhang, C.; Huang, K. Flower-like MoS<sub>2</sub> decorated with Cu<sub>2</sub>O nanoparticles for non-enzymatic amperometric sensing of glucose. *Talanta* **2017**, *167*, 593–599. [CrossRef]
30. Li, G.; Zhang, W.; Hou, J.; Li, T.; Li, P.; Wang, Y.; Liu, J.; Wang, K. Enhanced visible light photochemical activity and stability of MoS<sub>2</sub>/Cu<sub>2</sub>O nanocomposites by tunable heterojunction. *Mater. Today Commun.* **2020**, *23*, 100933. [CrossRef]
31. Koyun, O.; Sahin, Y. Voltammetric determination of nitrite with gold nanoparticles/poly (methylene blue)-modified pencil graphite electrode: Application in food and water samples. *Ionics* **2018**, *24*, 3187–3197. [CrossRef]
32. Amini, N.; Gholivand, M.B.; Shamsipur, M.; Movahedi, A.A.M.; Farahi, S.; Habibi-Rezaei, M.; Maleki, A.; Rezaee, M.; Naderi, K. Fabrication of a glycation induced amyloid nanofibril and polyalizerin yellow R nanobiocomposite: Application for electrocatalytic determination of hydrogen peroxide. *Int. J. Biol. Macromol.* **2018**, *123*, 1297–1304. [CrossRef] [PubMed]
33. Agrisuelas, J.; González-Sánchez, M.-I.; Gómez-Monedero, B.; Valero, E. A Comparative Study of Poly(Azure A) Film-Modified Disposable Electrodes for Electrocatalytic Oxidation of H<sub>2</sub>O<sub>2</sub>: Effect of Doping Anion. *Polymers* **2018**, *10*, 48. [CrossRef] [PubMed]
34. Liu, Y.; Song, N.; Ma, Z.; Zhou, K.; Gan, Z.; Gao, Y.; Tang, S.; Chen, C. Synthesis of a poly (N-methylthionine)/reduced graphene oxide nanocomposite for the detection of hydroquinone. *Mater. Chem. Phys.* **2019**, *223*, 548–556. [CrossRef]
35. da Silva, W.; Ghica, M.E.; Brett, C.M. Novel nanocomposite film modified electrode based on poly (brilliant cresyl blue)-deep eutectic solvent/carbon nanotubes and its biosensing applications. *Electrochim. Acta* **2019**, *317*, 766–777. [CrossRef]
36. Shamspur, T.; Biniiaz, Z.; Mostafavi, A.; Torkzadeh-Mahani, M.; Mohamadi, M. An Electrochemical Immunosensor Based on Poly(Thionine)-Modified Carbon Paste Electrode for the Determination of Prostate Specific Antigen. *IEEE Sens. J.* **2018**, *18*, 4861–4868. [CrossRef]
37. Ali, S.; Gupta, A.; Shafiei, M.; Langford, S. Recent Advances in Perylene Diimide-Based Active Materials in Electrical Mode Gas Sensing. *Chemosensors* **2021**, *9*, 30. [CrossRef]
38. Kozitsina, A.N.; Svalova, T.S.; Malysheva, N.N.; Okhokhonin, A.V.; Vidrevich, M.B.; Brainina, K.Z. Sensors Based on Bio and Biomimetic Receptors in Medical Diagnostic, Environment, and Food Analysis. *Biosensors* **2018**, *8*, 35. [CrossRef]
39. Feng, T.; Chen, X.; Qiao, X.; Sun, Z.; Wang, H.; Qi, Y.; Hong, C. Graphene oxide supported rhombic dodecahedral Cu<sub>2</sub>O nanocrystals for the detection of carcinoembryonic antigen. *Anal. Biochem.* **2015**, *494*, 101–107. [CrossRef]
40. Ma, H.; Li, Y.; Wang, Y.; Hu, L.; Zhang, Y.; Fan, D.; Yan, T.; Wei, Q. Cubic Cu<sub>2</sub>O nanoframes with a unique edge-truncated structure and a good electrocatalytic activity for immunosensor application. *Biosens. Bioelectron.* **2016**, *78*, 167–173. [CrossRef]
41. Park, J.C.; Kim, J.; Kwon, H.; Song, H. Gram-Scale Synthesis of Cu<sub>2</sub>O Nanocubes and Subsequent Oxidation to CuO Hollow Nanostructures for Lithium-Ion Battery Anode Materials. *Adv. Mater.* **2009**, *21*, 803–807. [CrossRef]
42. Wang, H.; Zhang, Y.; Wang, Y.; Ma, H.; Du, B.; Wei, Q. Facile synthesis of cuprous oxide nanowires decorated graphene oxide nanosheets nanocomposites and its application in label-free electrochemical immunosensor. *Biosens. Bioelectron.* **2017**, *87*, 745–751. [CrossRef]
43. Su, S.; Sun, H.; Cao, W.; Chao, J.; Peng, H.; Zuo, X.; Yuwen, L.; Fan, C.; Wang, L. Dual-Target Electrochemical Biosensing Based on DNA Structural Switching on Gold Nanoparticle-Decorated MoS<sub>2</sub> Nanosheets. *ACS Appl. Mater. Interfaces* **2016**, *8*, 6826–6833. [CrossRef]
44. Su, S.; Zou, M.; Zhao, H.; Yuan, C.; Xu, Y.; Zhang, C.; Wang, L.; Fan, C.; Wang, L. Shape-controlled gold nanoparticles supported on MoS<sub>2</sub> nanosheets: Synergistic effect of thionine and MoS<sub>2</sub> and their application for electrochemical label-free immunosensing. *Nanoscale* **2015**, *7*, 19129–19135. [CrossRef]
45. Wang, X.; Shen, L.; Deng, W.; Yan, M.; Liu, H.; Ge, S.; Yu, J.; Song, X. A sensitive electrochemiluminescent immunosensor based on 3D-flower-like MoS<sub>2</sub> microspheres and using AuPt nanoparticles for signal amplification. *RSC Adv.* **2016**, *6*, 23411–23419. [CrossRef]
46. Wu, I.-C.; Weng, Y.-H.; Lu, M.-Y.; Jen, C.-P.; Fedorov, V.E.; Chen, W.C.; Wu, M.T.; Kuo, C.-T.; Wang, H.-C. Nano-structure ZnO/Cu<sub>2</sub>O photoelectrochemical and self-powered biosensor for esophageal cancer cell detection. *Opt. Express* **2017**, *25*, 7689–7706. [CrossRef]
47. Chen, Y.-S.; Liao, C.-H.; Chueh, Y.-L.; Lai, C.-C.; Chen, L.-Y.; Chu, A.-K.; Kuo, C.-T.; Wang, H.-C. High performance Cu<sub>2</sub>O/ZnO core-shell nanorod arrays synthesized using a nanoimprint GaN template by the hydrothermal growth technique. *Opt. Mater. Express* **2014**, *4*, 1473–1486. [CrossRef]
48. Zhao, Y.; Luo, X.; Li, H.; Zhang, J. Interlayer breathing and shear modes in few-trilayer MoS<sub>2</sub> and WSe<sub>2</sub>. *Nano Lett.* **2013**, *13*, 1007–1015. [CrossRef]
49. Li, H.; Wu, J.; Yin, Z.; Zhang, H. Preparation and Applications of Mechanically Exfoliated Single-Layer and Multilayer MoS<sub>2</sub> and WSe<sub>2</sub> Nanosheets. *Acc. Chem. Res.* **2014**, *47*, 1067–1075. [CrossRef]
50. Li, H.; Lu, G.; Yin, Z.; He, Q.; Li, H.; Zhang, Q.; Zhang, H. Optical identification of single-and few-layer MoS<sub>2</sub> sheets. *Small* **2012**, *8*, 682–686. [CrossRef]
51. Li, K.-C.; Lu, M.-Y.; Nguyen, H.T.; Feng, S.-W.; Artemkina, S.B.; Fedorov, V.E.; Wang, H.-C. Intelligent Identification of MoS<sub>2</sub> Nanostructures with Hyperspectral Imaging by 3D-CNN. *Nanomaterials* **2020**, *10*, 1161. [CrossRef]

52. Wang, Q.; Lei, Y.; Wang, Y.; Liu, Y.; Song, C.; Zeng, J.; Song, Y.; Duan, X.; Wang, D.; Li, Y. Atomic-scale engineering of chemical-vapor-deposition-grown 2D transition metal dichalcogenides for electrocatalysis. *Energy Environ. Sci.* **2020**, *13*, 1593–1616. [CrossRef]
53. Cai, Z.; Liu, B.; Zou, X.; Cheng, H.-M. Chemical Vapor Deposition Growth and Applications of Two-Dimensional Materials and Their Heterostructures. *Chem. Rev.* **2018**, *118*, 6091–6133. [CrossRef] [PubMed]
54. Jeon, J.; Jang, S.K.; Jeon, S.M.; Yoo, G.; Jang, Y.H.; Park, J.-H.; Lee, S. Layer-controlled CVD growth of large-area two-dimensional MoS<sub>2</sub> films. *Nanoscale* **2014**, *7*, 1688–1695. [CrossRef] [PubMed]
55. Lee, Y.-H.; Zhang, X.-Q.; Zhang, W.; Chang, M.-T.; Lin, C.-T.; Chang, K.-D.; Yu, Y.-C.; Wang, J.T.-W.; Chang, C.-S.; Li, L.-J.; et al. Synthesis of Large-Area MoS<sub>2</sub> Atomic Layers with Chemical Vapor Deposition. *Adv. Mater.* **2012**, *24*, 2320–2325. [CrossRef]
56. van der Zande, A.M.; Huang, P.Y.; Chenet, D.A.; Berkelbach, T.C.; You, Y.; Lee, G.-H.; Heinz, T.F.; Reichman, D.R.; Muller, D.A.; Hone, J.C. Grains and grain boundaries in highly crystalline monolayer molybdenum disulphide. *Nat. Mater.* **2013**, *12*, 554–561. [CrossRef]
57. Najmaei, S.; Liu, Z.; Zhou, W.; Zou, X.; Shi, G.; Lei, S.; Yakobson, B.I.; Idrobo, J.C.; Ajayan, P.M.; Lou, J. Vapour phase growth and grain boundary structure of molybdenum disulphide atomic layers. *Nat. Mater.* **2013**, *12*, 754–759. [CrossRef]
58. Hyun, C.-M.; Choi, J.-H.; Lee, S.W.; Park, J.H.; Lee, K.-T.; Ahn, J.-H. Synthesis mechanism of MoS<sub>2</sub> layered crystals by chemical vapor deposition using MoO<sub>3</sub> and sulfur powders. *J. Alloy. Compd.* **2018**, *765*, 380–384. [CrossRef]
59. Liu, H.; Bin Yang, R.; Yang, W.; Jin, Y.; Lee, C.J. Atomic layer deposition and post-growth thermal annealing of ultrathin MoO<sub>3</sub> layers on silicon substrates: Formation of surface nanostructures. *Appl. Surf. Sci.* **2018**, *439*, 583–588. [CrossRef]
60. Pondick, J.V.; Woods, J.M.; Xing, J.; Zhou, Y.; Cha, J.J. Stepwise sulfurization from MoO<sub>3</sub> to MoS<sub>2</sub> via chemical vapor deposition. *ACS Appl. Nano Mater.* **2018**, *1*, 5655–5661. [CrossRef]
61. Kim, H.; Ovchinnikov, D.; Deiana, D.; Unuchek, D.; Kis, A. Suppressing Nucleation in Metal–Organic Chemical Vapor Deposition of MoS<sub>2</sub> Monolayers by Alkali Metal Halides. *Nano Lett.* **2017**, *17*, 5056–5063. [CrossRef]
62. Zhou, D.; Shu, H.; Hu, C.; Jiang, L.; Liang, P.; Chen, X. Unveiling the Growth Mechanism of MoS<sub>2</sub> with Chemical Vapor Deposition: From Two-Dimensional Planar Nucleation to Self-Seeding Nucleation. *Cryst. Growth Des.* **2018**, *18*, 1012–1019. [CrossRef]
63. KaiáLee, M. Large-area few-layered graphene film determination by multispectral imaging microscopy. *Nanoscale* **2015**, *7*, 9033–9039.
64. Lu, M.-Y.; Wu, S.-C.; Wang, H.-C. Time-evolution of the electrical characteristics of MoS<sub>2</sub> field-effect transistors after electron beam irradiation. *Phys. Chem. Chem. Phys.* **2018**, *20*, 9038–9044. [CrossRef]
65. Hsieh, Y.-P.; Wang, Y.-W.; Ting, C.-C.; Wang, H.-C.; Chen, K.-Y.; Yang, C.-C. Effect of Catalyst Morphology on the Quality of CVD Grown Graphene. *J. Nanomater.* **2013**, *2013*, 6. [CrossRef]
66. Park, B.; Lee, D.; Kim, H.-S.; Cho, Y.; Park, S.; Kim, C.; Lee, T.; Woo, D.H.; Kim, J.H. Synergetic enhancement in optical nonlinearity of Au nanoparticle decorated MoS<sub>2</sub> via interaction between excitonic and surface plasmon resonances. *Appl. Surf. Sci.* **2020**, *532*, 147486. [CrossRef]
67. Zhang, G.; Zhang, Z.; Xia, D.; Qu, Y.; Wang, W. Solar driven self-sustainable photoelectrochemical bacteria inactivation in scale-up reactor utilizing large-scale fabricable Ti/MoS<sub>2</sub>/MoOx photoanode. *J. Hazard. Mater.* **2020**, *392*, 122292. [CrossRef]
68. Yuan, Y.; Wang, W.; Shi, Y.; Song, L.; Ma, C.; Hu, Y. The influence of highly dispersed Cu<sub>2</sub>O-anchored MoS<sub>2</sub> hybrids on reducing smoke toxicity and fire hazards for rigid polyurethane foam. *J. Hazard. Mater.* **2019**, *382*, 121028. [CrossRef]
69. Lu, C.; Xuan, H.; Zhou, Y.; Xu, X.; Zhao, Q.; Bai, J. Saturable and reverse saturable absorption in molybdenum disulfide dispersion and film by defect engineering. *Photonics Res.* **2020**, *8*, 1512. [CrossRef]
70. Hao, X.-Y.; Bergh, J.; Brodin, O.; Heltman, U.; Mannervik, B. Acquired resistance to cisplatin and doxorubicin in a small cell lung cancer cell line is correlated to elevated expression of glutathione-linked detoxification enzymes. *Carcinogenesis* **1994**, *15*, 1167–1173. [CrossRef]
71. Hammond, C.L.; Lee, T.K.; Ballatori, N. Novel roles for glutathione in gene expression, cell death, and membrane transport of organic solutes. *J. Hepatol.* **2001**, *34*, 946–954. [CrossRef]
72. Kang, Z.; Yan, X.; Wang, Y.; Bai, Z.; Liu, Y.; Zhang, Z.; Lin, P.; Zhang, X.; Yuan, H.; Zhang, X.; et al. Electronic Structure Engineering of Cu<sub>2</sub>O Film/ZnO Nanorods Array All-Oxide p-n Heterostructure for Enhanced Photoelectrochemical Property and Self-powered Biosensing Application. *Sci. Rep.* **2015**, *5*, srep07882. [CrossRef] [PubMed]
73. Tang, J.; Kong, B.; Wang, Y.; Xu, M.; Wang, Y.; Wu, H.; Zheng, G. Photoelectrochemical detection of glutathione by IrO<sub>2</sub>–Hemin–TiO<sub>2</sub> nanowire arrays. *Nano Lett.* **2013**, *13*, 5350–5354. [CrossRef]
74. Zang, Y.; Ju, Y.; Jiang, J.; Xu, Q.; Chu, M.; Xue, H. Cu<sup>2+</sup>-Modulated in situ growth of quantum dots for split-type photoelectrochemical immunoassay of prostate-specific antigen. *Anal.* **2019**, *144*, 4661–4666. [CrossRef]
75. Zhu, Y.; Xu, Z.; Yan, K.; Zhao, H.; Zhang, J. One-Step Synthesis of CuO–Cu<sub>2</sub>O Heterojunction by Flame Spray Pyrolysis for Cathodic Photoelectrochemical Sensing of l-Cysteine. *ACS Appl. Mater. Interfaces* **2017**, *9*, 40452–40460. [CrossRef] [PubMed]
76. Tran, M.H.; Cho, J.Y.; Sinha, S.; Gil Gang, M.; Heo, J. Cu<sub>2</sub>O/ZnO heterojunction thin-film solar cells: The effect of electrodeposition condition and thickness of Cu<sub>2</sub>O. *Thin Solid Film.* **2018**, *661*, 132–136. [CrossRef]



MDPI  
St. Alban-Anlage 66  
4052 Basel  
Switzerland  
Tel. +41 61 683 77 34  
Fax +41 61 302 89 18  
[www.mdpi.com](http://www.mdpi.com)

*International Journal of Molecular Sciences* Editorial Office

E-mail: [ijms@mdpi.com](mailto:ijms@mdpi.com)  
[www.mdpi.com/journal/ijms](http://www.mdpi.com/journal/ijms)







Academic Open  
Access Publishing

[www.mdpi.com](http://www.mdpi.com)

ISBN 978-3-0365-8324-2